CRANFIELD INSTITUTE OF TECHNOLOGY

College of Aeronautics

Ph.D. Thesis

R. THORNE

SOME EXPERIMENTAL AND THEORETICAL STUDIES IN AIRCRAFT STABILITY AT HIGH ANGLES OF ATTACK.

Supervisor: P.A.T. Christopher

September 1983

To Jesus Christ who loves us and has
freed us from our sins by His blood,
and has made us to be a kingdom
and priests to serve His God and
Father - to Him be glory and power
for ever and ever! Amen

(Revelation 1 vv. 5^{b},6)

SUMMARY

A review of techniques for stability and response investigations is presented and the averaging technique of Beecham-Titchener-Simpson is applied to the lateral equations of motion for two combat aircraft. The analytic technique predicts oscillation amplitudes and frequencies accurately, for non-linear aerodynamic characteristics with respect to sideslip or roll rate. However, limitations of the method are apparent when non-linearities in roll rate and sideslip are treated simultaneously. Rates of growth to limit cycle oscillations are predicted by the averaging method and two formulations for a local damping factor are compared with simulation results.

Results from extensive wind tunnel tests on a High Incidence Research Model (HIRM) are presented along with estimates of dynamic stability derivatives and polynomial fits to the wind tunnel data. The lateral stability and response of the HIRM at high angles of attack, is investigated using the analytic techniques described earlier, as well as simulations.

Six degree of freedom eigenvalue results for the HIRM are shown. An investigation into the effects of cross-coupling derivatives and different forms of roll rate data, using non-linear and linearised simulations, concludes the thesis.

ACKNOWLEDGEMENTS

I would like to express my sincere thanks to Drs. Peter Christopher and Jean Ross for their guidance, unfailing encouragement and patient help throughout the course of this research.

My thanks also to all the people in the Aerodynamics Department at The Royal Aircraft Establishment, Bedford and Farnborough, who helped me in many ways and made working at the R.A.E. so enjoyable. I am particularly indebted to Dr.George Reid for his help with computing at Farnborough and to Messrs.Charles O'Leary and Ron Fail for cheerfully letting me work with them during various wind tunnel tests at Bedford.

Many thanks to my colleagues in the College of Aeronautics for their friendly advice and assistance, particularly Mr.Mike Cook, for his help and for allowing me to lecture on various short courses.

I am extremely grateful to Mrs.Tricia Forrest-Holden for her excellent typing of the thesis.

Financial support for the research was provided by the Science and Engineering Research Council, The Royal Aircraft Establishment, Farnborough and the College of Aeronautics, Cranfield.

Finally, special thanks are due to my family and friends for their constant encouragement and support over the last few years. My Chinese friends have also contributed to this thesis in their own special ways:

饮水思源

CONTENTS

CONTENTS (continued)

CONTENTS (continued)

CONTENTS (continued)

CONTENTS (concluded)

LIST OF TABLES

LIST OF FIGURES

LIST OF FIGURES (continued)

LIST OF FIGURES (continued)

LIST OF FIGURES (continued)

LIST OF FIGURES (concluded)

NOTATION

a	amplitude of motion (eqns.(2.36),(2.40)-(2.43))
a_1, b_1, c_1, d_1	coefficients in stability quartic (defined in Appendix B)
b_{3v}, c_{3v}, d_{3v}, a_{3p}, b_{3p}, c_{3p}, d_{3p}, c_{3vp}, d_{3vp}	coefficients used in Beecham-Titchener-Simpson averaging (defined in Appendix B)
A, A_v, A_p	amplitudes of motion in §2.3.4
$\underline{A}$	constant, system matrix in §2.4.2.2
A_1 to K_1	coefficients in equation (2.77)(defined in Appendix C.1)
A_{1v} to A_{4v}, A_{1p} to A_{4p}	coefficients in equations (2.98) and (2.104) (defined in Appendix C.3)
A_2, B_2, C_2	coefficients in equation (2.88) (defined in Appendix C.2).
b	span (m)
B_{1v} to B_{4v}, B_{1p} to B_{5p}	coefficients in equations (2.101) and (2.107) (defined in Appendix C.3)
c	chord (m)
$\bar{c}$	aerodynamic mean chord (m)
c_0	chord at centre line (m)
c_r	root chord (m)
c_t	tip chord (m)
C_D	coefficient of drag
C_L	coefficient of lift
C_X, C_Y, C_Z	force coefficients along x,y,z axes
C_ℓ, C_m, C_n	moment coefficients
$C_{\ell_\alpha}, C_{\ell_\beta}, C_{X_q}$	slopes of force and moment coefficients (Appendix F),U.S.non-dimensional derivatives.
$C_{n_{\beta dyn}}$	dynamic N_v derivative in U.S.notation (defined in equation (2.20)).
C_K	general force coefficient (see Appendix F)
C_j	general moment coefficient (see Appendix F)
e, f, g	terms in quadratic solution, §2.4.2.4
$f(x,\dot{x})$	general function, §2.4.2
$\underline{F}$	n^{th} order vector, §2.4.2.2

NOTATION (continued)

g	acceleration due to gravity (m/s^2)
g_1	$g \cos\Theta$
g_2	$g \sin\Theta$
g_3	$g \cos\Phi \cos\Theta$
g_4	$g \sin\Theta \cos\Phi$
g_5	$g \cos\Theta \sin\Phi$
g_6	$g \sin\Theta \sin\Phi$
h	altitude
i	$\sqrt{-1}$
I_x, I_y, I_z	moments of inertia of aircraft ($kg.m^2$)
I_{xz}	product of inertia of aircraft ($kg.m^2$)
J	general moment (Chapter 6 and Appendix F)
k	damping index
K	general force (Chapter 6 and Appendix F)
K	factor in $\breve{N}_p$ estimate (equation (4.1))
$K_{\xi p}, K_{\zeta r}, K_{\zeta \beta}$	gearings in control system
$\ell'_v, \ell'_p, \ell'_r$, etc	concise rolling moment derivatives (defined in Appendices A and E)
L_v, L_p, L_r, etc	dimensional rolling moment derivatives
$\breve{L}_v, \breve{L}_p, \breve{L}_r$, etc	aeronormalised rolling moment derivatives (defined in Appendix A and Ref.45)
L	rolling moment
m	aircraft mass
M	pitching moment
M	Mach number
m'_u, m'_w, m'_q, etc	concise pitching moment derivatives (defined in Appendix E).
M_u, M_w, M_q, etc	dimensional pitching moment derivatives
$\breve{M}_u, \breve{M}_w, \breve{M}_q$, etc	aeronormalised pitching moment derivatives (defined in Appendix A and Ref.45)
N	yawing moment
n'_v, n'_p, n'_r, etc	concise yawing moment derivatives (defined in Appendices A and E)
N_v, N_p, N_r, etc	dimensional yawing moment derivatives
$\breve{N}_v, \breve{N}_p, \breve{N}_r$, etc	aeronormalised yawing moment derivatives (defined in Appendix A and Ref.45)
$\breve{N}_{v_{dyn}}$	dynamic N_v derivative (defined in eqn.(2.20))

NOTATION (continued)

p q r	roll pitch yaw	} rates (total components, e.g. equations (2.1) to (2.9), except where stated e.g. Appendix E and small perturbation equations)
$p_\gamma, q_\gamma, r_\gamma$	non-dimensional angular rates (defined in Appendix F)	
R	Routh's discriminant	
R*	non-linear Routh's discriminant (eqn.(2.76))	
s	semi-span (m)	
$\underline{s}$	vector locating non-linear function of $\underline{x}$ in §2.4.2.2	
S_T	tailplane reference area (m^2)	
S_W	wing reference area (m^2)	
t	time (secs.)	
T	time period (secs.)	
T_c	time constant for exponential modes (secs.)	
$T_{\frac{1}{2}}$	time to half-amplitude for oscillatory modes (secs.)	
u	velocity component along x axis (small perturbation quantity in Appendix E and linearised equations)	
u,v,w	coefficients in quadratic equation in Fig.2.5	
v	velocity component along y axis, sideslip velocity (small perturbation quantity in Appendix E and linearised equations)	
$\bar{v}$	v/V	
V	aircraft velocity (m/s)	
w	velocity component along z axis (small perturbation quantity in Appendix E and linearised equations)	
x	aircraft body fixed axis, forward	
$\underline{x}$	state vector, order n	
X	force component along x axis	
x'_u, x'_w, x'_q, etc	concise X force derivatives (defined in Appendices A and E)	
X_u, X_w, X_q, etc	dimensional X force derivatives	
$\breve{X}_u, \breve{X}_w, \breve{X}_q$, etc	aeronormalised X force derivatives (defined in Appendix A and Ref.45)	

NOTATION (continued)

y	aircraft body fixed axis, to starboard
Y	sideforce, along y axis
y'_v, y'_p, y'_r, etc.	concise sideforce derivatives (defined in Appendices A and E)
Y_v, Y_p, Y_r, etc.	dimensional sideforce derivatives
$\breve{Y}_v, \breve{Y}_p, \breve{Y}_r$, etc.	aeronormalised sideforce derivatives (defined in Appendix A and Ref.45)
z	aircraft body fixed axis, normal to aircraft, downwards
Z	force component along z axis
z'_u, z'_w, z'_q, etc.	concise Z force derivatives (defined in Appendices A and E)
Z_u, Z_w, Z_q, etc.	dimensional Z force derivatives
$\breve{Z}_u, \breve{Z}_w, \breve{Z}_q$, etc.	aeronormalised Z force derivatives (defined in Appendix A and Ref.45)

Greek symbols

α	angle of attack
α	dynamic stability axis angle in §2.3.5
β	angle of sideslip (see Appendix F for definition)
β	dynamic stability axis angle in §2.3.5
γ	flight path angle in Chapter 5
ε	phase angle in Beecham-Titchener-Simpson averaging technique
ζ	rudder angle
$\underline{\eta}$	vector with components η_i in equation (2.40)
η_C	symmetric canard deflection angle $= \frac{1}{2}(\eta_{starboard} + \eta_{port})$
η_T	symmetric tailplane deflection angle $= \frac{1}{2}(\eta_{starboard} + \eta_{port})$
θ	perturbation pitch angle
Θ	Euler (pitch attitude) angle
Θ	limit cycle amplitude in Beecham-Titchener-Simpson averaging technique

NOTATION (continued)

λ	taper ratio (see table 4.1)
λ	amplitude damping factor, $\dot{a}/a$, in Beecham-Titchener-Simpson averaging technique
Λ	sweep angle
μ	dynamic stability axis angle in §2.3.5
μ	eigenvalue in §2.3.4 and in linear stability analysis; $\mu = -k \pm i\nu$
μ	non-linear eigenvalue/operator in Beecham-Titchener-Simpson averaging technique (§2.4.2); $\mu = \lambda + i\omega$
ν	frequency in linear eigenvalue
ξ	aileron angle
$\underline{\xi}$	vector with components ξ_i in equation (2.40)
ξ_C	differential canard deflection angle $= \frac{1}{2}(\xi_{starboard} - \xi_{port})$
ξ_T	differential tailplane deflection angle $= \frac{1}{2}(\xi_{starboard} - \xi_{port})$
ρ	atmospheric density
σ	amplitude of non-linear response
τ	time (defined in equation (6.7))
ϕ	perturbation bank angle
ϕ	phase angle of non-linear response in Beecham-Titchener-Simpson averaging technique (§2.4.2.2)
Φ	Euler (roll) angle
ψ	perturbation yaw angle
Ψ	Euler (yaw) angle
$\dot{\Psi}$	resultant angular velocity in a turn (eqn.(6.11))
ω	general body axis velocity component in Appendix F
ω	frequency of non-linear response in Beecham-Titchener-Simpson averaging technique

Dressings, etc. (shown on an arbitrary character A)

A_b	critical amplitude in local linearisation technique (equation (2.113))
A^B	body axes
$(A)_B$	body contribution (to derivative)

NOTATION (continued)

A_c	critical amplitude at divergence (eqn.(2.116))
A_C	canard
$(A)_C$	canard contribution (to derivative)
A_{dr}	dutch roll
A_{DYN}	dynamic stability axes (defined in Ref.47)
A_e	equilibrium value
A_{eff}	effective value of derivative
A_F	fin
$(A)_F$	fin contribution (to derivative)
A_L	limit cycle value
A_{LE}	leading edge
A_o	oscillatory rig
$(A)_p$	planform contribution (to derivative)
A_p	roll rate
A_{ph}	phugoid
A_r	yaw rate
A_{rm}	roll mode
A_R	rotary rig
A_{sm}	spiral mode
A_{sp}	short period
A_{trim}	trim value
A_T	tailplane
$(A)_T$	tailplane contribution (to derivative)
A_{TE}	trailing edge
$A_v, A_{-\bar{v}}$	sideslip
A^W	wind axes
A_W	wing
$(A)_W$	wing contribution (to derivative)
A_α, A_β	slopes with respect to α, β
A_γ	non-dimensional angular rates (see §F.4.1)
A_ϕ	bank angle
A_0	initial value, or datum value
$A_{0,1,2,3}$	coefficients in polynomial fit (used on derivatives)
A'	perturbation from trim value in linear analysis (§2.4.3.2, §6.2 and Appendix E)

NOTATION (concluded)

$\dot{A}$	differentiation with respect to time, d()/dt
A'	concise derivative, natural sign (defined in Appendices A.3 and E)
A''	modified concise derivative, natural sign (defined in Appendices A.3 and F)
$\hat{A}$	shortened form of variable in §2.4.2.4, Fig.2.5 and §6.2.3
A*	non-linear Routhian and stability quartic coefficients (equations (2.65),(2.75) and (2.76) and Appendix C)
A*	combined derivative from oscillatory rig tests (defined in §4.7 and Figs.4.10 to 4.12)
$\bar{A}$	quantity divided by flight speed, V
$\breve{A}$	aeronormalised (non-dimensional) derivative
$\tilde{A}$	dressing used to denote phase angle in equation (2.40)
Re(A)	real part
Im(A)	imaginary part

Abbreviations

A.A.D.P.	Aileron Alone Departure Parameter
B.T.	Beecham-Titchener
B.T.S.	Beecham-Titchener-Simpson
c.g.	centre of gravity
d.o.f.	degree of freedom
F.F.T	Fast Fourier Transform
HIRM	High Incidence Research Model
L.C.D.P.	Lateral Control Departure Parameter
LSWT	Low Speed Wind Tunnel
NAG	Numerical Algorithms Group
r or rad.	radian
R.A.E.	Royal Aircraft Establishment
W.T.	Wind Tunnel

CHAPTER 1

INTRODUCTION

1.1 High Angle of Attack Aerodynamic Characteristics

Modern combat aircraft are required to manoeuvre at high angles of attack (α) and these requirements have important implications for the stability and controllability of the aircraft. References 1 to 5 indicate how much importance is now attached to the high angle of attack behaviour of current combat aircraft.

Figure 1.1 illustrates some of the flow characteristics typical at high angles of attack and which must be taken into consideration when providing for adequate stability and controllability:

- large regions of separated/stalled flow
- aerodynamic interference between various components of airframe, low energy wakes from stalled surfaces
- vortex flows from long fuselage forebodies, swept wings, canards (Ref.6) and strakes (Refs.7 to 9). Vortex bursting.

The development of combat aircraft over the past 20 years has been somewhat hampered by the emergence of lateral phenomena limiting the maximum usable C_L on aircraft at high angles of attack. Earlier aircraft with a conventional wing stall generally showed a decrease in C_L above a certain α and this stall dictated the maximum C_L usable. Fig.1.2 shows a typical C_L - α curve for an aircraft with these characteristics. Later designs (see Fig.1.3) do not show conventional wing stalls and show C_L's which go on increasing to high α's. The current generation fighters such as the F-14, F-16 and F-17/18 (Refs.10 to 12) display such characteristics by virtue of strakes and blended wing-body designs for lift (Ref.13). In these cases the handling and manoeuvrability at high α's are now limited by lateral effects e.g. loss of directional or dihedral stability. These effects can occur suddenly or with some warning depending on the aircraft configuration. Another point to mention is that the relatively long fuselage forebodies and swept wing designs common today lead to poor lateral and directional stability characteristics at high α. For example:

a) Large side-forces produced by asymmetric vortices shed off the nose may mean the aircraft "yaws off" ("nose slice", Ref.14).

b) Wing drop can occur without warning if flow separates suddenly. For some aircraft, directional stability at high α and sideslip (β) can be restored as the fin comes out of the vortex/stalled flow from the nose and body, as for example on the F-5 (Ref.15).

Departure is the general term given to uncommanded events resulting in complete loss of control and the aircraft may then go into a spin or uncontrolled non-periodic motions above the conventional stall angle of attack ("post stall gyrations"). Controls may not be effective at high angles of attack or, if adverse, may aggravate departure conditions.

Before departure,many combat aircraft suffer from degraded handling qualities due to the occurrence of periodic limit cycle oscillations known as wing rock. The mathematical modelling of wing rock has provided the basis for much of the work described in this thesis and so it may be useful to look at this phenomena in a little more detail before concluding this introductory chapter with a look at the overall aims of the thesis.

1.2 Wing Rock

In general,wing rock may be described as uncommanded lightly damped lateral oscillations about the longitudinal axis, viewed by the pilot as roll oscillations. The phenomenon occurs on many combat aircraft as high g manoeuvres are pulled and Refs.16 and 17 show flight records of wing rock for F-4 and Gnat aircraft. Wing rock can be difficult to control as its causes are not always clear and are highly configuration dependent. Airframe modifications e.g. wing tanks[17], wing-body strakes and wing leading-edge flaps can have significant effects on the wing rock characteristics.

Some of the potential aerodynamic causes of wing rock so far identified include:-

a) Buffet. Wing rock can be associated with buffet in that it may be a forced oscillation caused by flow separation on the wings (asymmetries on the wings affecting one wing more than the other). At transonic speeds it can be caused by the movement of shocks responsible for the separating and reattaching of flows (Ref.18). Hwang and Pi[19] in work on an F-5 model concluded that the wing rock on this aircraft was due to fluctuating pressure changes on the wing top surface, especially near the tip region.

b) Aerodynamic Hysteresis. Schiff et al[20] describe a non-linear aerodynamic model in which wing rock is modelled on the basis of aerodynamic hysteresis in C_ℓ against roll angle. The cause of such hysteresis may be the breakdown of vortices over wings at high α. Cord[21] and Schmidt[22] look at aerodynamic hysteresis of C_ℓ against β.

c) Static Aerodynamic Non-linearity. References 23 and 24 describe work on the modelling of limit angle oscillations on the HP115 using cubic non-linearities in yawing or rolling moment with respect to sideslip angle. This form of non-linearity has also been looked at in this thesis and results are presented in Chapters 3 and 5.

d) Loss in Roll Damping. F-14 wing rock is shown in Ref.25 to be caused by the combined effects of loss in aerodynamic roll damping after wing panels stall and the low level of directional stability. Again for the Gnat[17] it seems to be the rolling motion which dominates, at a frequency similar to the dutch roll, suggesting no new aerodynamics is involved and that the wing rock may be thought of as a dutch roll undamped by non-linear aerodynamics.

e) Dynamic Aerodynamic Non-linearities. Ross[26] has shown that non-linear rolling and yawing moments with respect to roll rate also give rise to limit cycle behaviour. Work on these formulations for this thesis is described later both for the aircraft of Ref.26 and a new combat aircraft configuration.

It seems that linear aerodynamics can provide explanations for some wing rock characteristics, for example, based on an unstable dutch roll[17]. The dutch roll frequency going to zero seemed to correlate on some aircraft with the appearance of wing rock but the disappearance of dutch roll damping seemed a better indicator for the Gnat discussed in Ref.17.

The importance of the study of wing rock and other high angle of attack phenomena can be emphasised by two points. Wing rock on some aircraft may act as a natural aerodynamic warning to the pilot that something more serious is likely to happen e.g. a nose slice. In this respect it can be useful. On the other hand, for aircraft where wing rock occurs significantly below C_L's where departure is likely, the manoeuvrability and tracking ability of the aircraft are impaired. In these cases, steps to prevent wing rock can improve the maximum usable C_L.

1.3 Mathematical Modelling

From the above, it is obvious that high angle of attack phenomena are strongly non-linear with respect to static and dynamic motion variables[27]. This makes the analytic prediction of dynamic stability parameters very difficult, depending as they do, on complex aircraft configurations and flowfields[28]. However the prediction of high angle of attack effects is very important in the design of modern combat aircraft and their control systems and good mathematical modelling of high-α behaviour is very necessary for the design of such control systems.

It is in the areas of the development and use of various mathematical models for high-α behaviour and the evaluation of some analytic techniques for predicting non-linear phenomena, that work for this thesis has been carried out. The R.A.E. began a programme[29,30] in 1980 to develop mathematical models of combat aircraft aerodynamics at high-α using a High Incidence Research Model (HIRM). Collaboration with the R.A.E. has enabled most of the work for this thesis to be carried out on the HIRM.

1.4 Aims

Initial work aimed to develop analogue and digital simulation techniques and followed work done by Ross et al[17,26] on the Gnat and other combat aircraft. Tied in with this work was the use of the analytic averaging technique of Beecham and Titchener[31] which has been developed along the lines suggested by Simpson[32]. The technique has provided good results for such configurations as the HP115 and other aircraft of the "sixties" generation. An aim of the current work was to apply the technique to the HIRM at angles of attack between 20^{o} and 40^{o}. Certain developments of the technique have been evaluated, in particular the treatment of aerodynamic non-linearities with respect to two response variables. This highlighted some limitations of the technique although for application to the HIRM equations with single variable non-linearity, the technique was more successful. Comparisons with local linearisation methods are described.

An important aim of the work was the use of the above techniques to build up mathematical models of the HIRM, to predict its high α behaviour in advance of free flight drop model tests. Simple 3 degree of freedom (d.o.f.) lateral motion models, incorporating aerodynamic non-linearities, were first of all used, followed by six degree of freedom models.

Following the work of a number of US researchers[33,34] to apply linearisation techniques to non-zero equilibrium states, a six degree of freedom linearised analysis was performed. The final model looked at is a 6 degree of freedom simulation model which has been used to:

a) compare with the 3 d.o.f.results

b) compare with the 6 d.o.f. linearised results

c) examine the use of different types of experimental data in the formulation and build up of mathematical models to see which is best for prediction of high α behaviour up to departure

d) look at effects of cross-coupling aerodynamics.

A valuable part of the work has been the opportunity to compare very simple linearised models and very complex models

all on a common data base, to see directly how far linearised techniques hold good.

1.5 Layout

With the above as an overall view of the work for this thesis, the next chapter contains a brief description of the various approaches to mathematical modelling of aircraft dynamics and a look at the techniques used for stability and response analysis in this thesis, both computational and analytic. Results for two combat aircraft are presented in Chapter 3.

The work on the HIRM then follows, starting with a description of HIRM and going on to the measurement of its static and dynamic aerodynamic characteristics, using a number of experimental techniques as well as prediction techniques.

Initial stability and three degree of freedom modelling results are presented in Chapter 5 along with an assessment of the averaging technique. Chapter 6 covers the 6 degree of freedom modelling, starting with the linearised treatment and going on to the development of the full force and moment simulation. Finally, conclusions from the work and recommendations for future work are presented in Chapter 7.

CHAPTER 2

TECHNIQUES FOR STABILITY AND RESPONSE INVESTIGATION

2.1 Introduction

As has been described in the first chapter, aircraft stability and response phenomena at high α are highly configuration dependent since complex aircraft shapes, external stores etc lead to highly non-linear aerodynamic behaviour. This presents difficulties when theoretically analysing the stability and response characteristics. Broadly speaking, two main approaches are used in the theoretical assessment of stability and response: (i) use of analytic techniques and (ii) use of computational/numerical methods to produce time histories etc. Stability is also predicted using measured aerodynamic data on its own or in the form of so-called "departure parameters". These parameters can give valuable insights into aircraft behaviour and really come into the category of very simple analytic techniques.

This chapter continues with a description of general mathematical modelling concepts showing how numerical/computer based solutions of the aircraft equations of motion and analytic techniques fit into the overall stability and response assessment. Descriptions of commonly used departure parameters are given in §2.3 and are followed by descriptions of the analytic techniques used in the thesis.

Finally, some of the computer programs (digital and analogue) which provided most of the results for the thesis are described. The descriptions of six degree of freedom mathematical models of the HIRM are given in Chapter 6.

2.2 Mathematical Modelling

2.2.1 General

Central to the understanding of flight dynamic phenomena at high angles of attack is the formulation of an adequate mathematical model of the aircraft. Reference 30 gives an overall picture of how the RAE's HIRM programme is tackling the objective of selecting and verifying a mathematical model for a typical combat aircraft configuration at high angles of attack. This thesis has provided an examination of a number of HIRM mathematical models and compared results from simulations with analytic techniques. Further comparisons with free flight model results are an aspect of the programme not covered in this thesis but are an important part of the overall mathematical modelling field. Fig.2.1 summarises the

main ideas behind the development of mathematical models for high α behaviour, which will be described below.

Two main processes in the mathematical modelling are the choice of the form of the model and then determination of the numerical coefficients for it. Prediction of flight motion histories can then be made and comparisons made with analytic techniques and flight results. Alterations to the model can be made and extensions incorporated to bring in control systems.

The choice of the mathematical model determines the wind tunnel data required, e.g. aerodynamic forces and moments and how they should be incorporated to predict flight responses. Schiff et al[20] describe how the form of model adopted defines characteristic motions which, in turn, define the way in which the aerodynamic stability parameters are determined, i.e. what kind of wind tunnel tests are required. Some of the techniques for determination of parameters shown in Fig.2.1 have been used for the HIRM and are covered in depth in Chapter 4. Briefly these are: tests on a static wind tunnel model at α and sideslip, β; tests on a model performing small amplitude yaw, sideslip and roll oscillations about body axes at non-zero α and β and rotary rig tests on a model rolling about the wind axis. Measurements of cross-coupling aerodynamics were also made and, during the early stages of response modelling, estimates of dynamic lateral derivatives were used. Flow field computations provide a possible source of stability parameter information but are as yet not developed enough to provide much data. For the aircraft models described in Chapter 3, data came from earlier work done at the RAE, including both wind tunnel tests and flight tests.

As a result of needs shown up by studies for this thesis, a programme of work to provide yawing derivative data for the HIRM will soon be under way using the whirling arm facility at Cranfield College of Aeronautics.

2.2.2 Form of Mathematical Model

The classical form of model starting from the familiar equations of motion and, based on small perturbation analysis (stability and control derivatives), is still very important in providing stability and response information. However, situations involving non-linear dependence of aerodynamic or inertial forces and moments on motion, require the solution of non-linear equations of motion.

Tobak and Schiff have presented papers in recent years[35,36] which propose a mathematical model based on non-linear functional analysis and characteristic motions. In effect, what is done is to assume a general model for the aircraft and then use wind tunnel and free-flight data to provide numerical coefficients with time dependence effects included. The model must be simplified for analysis and Ref.35 includes an application of the technique to aircraft wing rock.

The alternative approach to mathematical modelling is to start from a simple model and build up the complexity to account for the observed flight phenomena e.g. by incorporating non-linear aerodynamics. This has been the approach adopted for certain aircraft by the R.A.E. and this thesis has been concerned with these kind of models including different forms of data to check on the adequacy of modelling. Thomas[37] emphasised the importance of representing non-linear characteristics of forces and moments rather than time dependence of quantities and for quasi-steady motions, with no significant time history effects, it is to be expected that the extended classical models and the U.S. non-linear functional analysis model will give the same results. For extreme manoeuvres near departure, or spinning, where flow separation and stalling of surfaces are important, time history effects may be required. Differences between responses from quasi-steady models with time-independent coefficients and drop test results could indicate time dependent effects have to be included. However the idea of keeping the model as simple as possible is attractive, so the current work has concentrated on how far it is possible to go, in analysis without time history effects.

For this thesis, the models used have had their origins in the classical small perturbation equations of motion starting with the 3 degree of freedom linearised lateral equations. Complexity has been systematically increased, to give predictions of flight characteristics at high angles of attack.

(i) The linear 3 degree of freedom lateral mathematical model has been used to give preliminary estimates of the stability of the classical modes of lateral motion up to $\alpha = 40^{o}$. For a linear model the nominal flight path can be a dynamic equilibrium, not necessarily an unaccelerated flight condition. Stengel and Berry[38] have suggested a linear model adequately describes the dynamics of aircraft with departure prevention systems,which keep angular excursions small.

(ii) The non-linear 3 degree of freedom lateral mathematical model is a development of (i) obtained by extending the idea of stability derivatives to polynomial representations of forces and moments against rates and position. This models the non-linear dependence of aerodynamic forces and moments on aircraft static variables. First of all non-linear static aerodynamic characteristics in the form of cubic variation of moments with respect to sideslip can be incorporated. Alternatively, or in addition, cubic variation of moments with roll rate have also been examined for the HIRM in this thesis. By using these relatively simple equations, analytical work can be done on response calculations using non-linear averaging techniques as well as local linearisation ("bifurcation") methods.

Based on work such as that described for current aircraft in Chapter 3, as well as that at the R.A.E. (e.g.Ref.23), the non-linear 3 d.o.f. lateral model has been shown to give adequate predictions of many responses in flight up to departure. It was thought that this model would be accurate up to α = 25-30^{o} for the HIRM,when looking at departure from controlled flight,at given constant angles of attack and work was carried out to assess this.

The non-linear 3 d.o.f. model is very amenable to analogue and digital computer solution, the analogue providing a convenient means for sensitivity studies on the aerodynamic non-linearities. Analogue results are shown in Chapter 3.

The model ignores inertia coupling,which should be a reasonable assumption for the flight conditions considered; only when the aircraft has departed or entered a spin will inertia cross-coupling become important. Ross[39] describes the levels of sophistication needed for modelling inertia cross-coupling problems. Second order derivatives with respect to angle of attack can be included in the model and Mehra[40] included a linear dependence of some lateral derivatives on angle of attack, which illustrates other ways in which the basic linearised equations can be expanded.

(iii) The non-linear, 6 degree of freedom table look up model is often used as the basis of a flight simulator study and as such is not readily amenable to theoretical analysis,due to the non-analytic nature of the forces and moments used. It has been used in this work partly to provide results for comparison with simpler models and partly to examine the effects of various forms of aerodynamic data. For the HIRM, this simulation model includes measured static, forced oscillation and rotary aerodynamic characteristics as tabulated functions of control angles and response variables, e.g. α and β. In the USA,curved flow wind-tunnel tests also provide data for 6 degree of freedom models and, following on from the HIRM work described in this thesis, it is planned to measure some pure yawing motion data for the HIRM using the whirling arm facility at Cranfield College of Aeronautics. (This data will also be useful for incorporating non-linear rolling data into models of the form (ii), where the current work showed up the limitations of not having pure yawing data available.)

These various forms of data are necessary when modelling aircraft manoeuvres such as spins and departures,where the responses show large amplitudes and non-linear effects dominate. However, for adequate response predictions in less extreme manoeuvres, but where non-linear effects may still be expected, how are the various forms of data to be used? Is the real aircraft behaviour best modelled by using large amplitude data alone,above a certain angle of attack (e.g. for spins where rotary effects dominate the real aircraft flowfield) or is oscillatory data needed as well? Anglin[41] describes some work on these ideas in

respect of spins. The 6 d.o.f. HIRM program has been used to look at which combinations of aerodynamic data are needed to adequately define the behaviour in some high angle of attack situations.

Oscillatory rig tests provided measurements of cross-coupling derivatives for the HIRM so the 6 d.o.f. model has also been used for sensitivity studies to help determine the importance of these derivatives.

Fig.2.2 summarises the important points concerning the various forms of non-linear mathematical model described above.

2.2.3 Models Used in this Thesis

2.2.3.1 General

The general equations of motion of an aircraft in geometric body axes, with the origin at the centre of gravity (c.g.) are:

$$\dot{u} = rv - qw + \frac{X}{m} - g_2 \qquad (2.1)$$

$$\dot{v} = pw - ru + \frac{Y}{m} + g_5 \qquad (2.2)$$

$$\dot{w} = qu - pv + \frac{Z}{m} + g_3 \qquad (2.3)$$

$$\dot{p} = \frac{I_{xz}}{I_x}(\dot{r} + pq) + \frac{(I_y - I_z)qr}{I_x} + \frac{L}{I_x} \qquad (2.4)$$

$$\dot{q} = \frac{I_{xz}}{I_y}(r^2-p^2) + \frac{(I_z - I_x)pr}{I_y} + \frac{M}{I_y} \qquad (2.5)$$

$$\dot{r} = \frac{I_{xz}}{I_z}(\dot{p} - qr) + \frac{(I_x - I_y)pq}{I_z} + \frac{N}{I_z} \qquad (2.6)$$

$$\dot{\Phi} = p + q\sin\Phi\tan\Theta + r\cos\Phi\tan\Theta \qquad (2.7)$$

$$\dot{\Theta} = q\cos\Phi - r\sin\Phi \qquad (2.8)$$

$$\dot{\Psi} = q\sin\Phi\ \sec\Theta + r\cos\Phi\sec\Theta \qquad (2.9)$$

where $g_2 = g\sin\Theta$

$g_3 = g\cos\Theta\cos\Phi$

and $g_5 = g\cos\Theta\sin\Phi$

Starting with equations (2.1)-(2.9), the usual linearised equations are derived by considering small perturbations in the state variables, about an equilibrium position (see, for example, Refs.42 and 43) or by differentiating the full equations (Ref.44). The linearised equations of motion for the lateral behaviour are then written, using the familiar aerodynamic derivatives in concise notation[45] with natural signs, as:

$$\dot{v} = y'_v v + V_e \sin\alpha_e p - V_e r \cos\alpha_e + g\cos\Phi_e \cos\Theta_e . \phi + g\sin\Theta_e . \psi \qquad (2.10)$$

$$\dot{p} = \ell'_{v_1} v + \ell'_{p_{eff}} p + \ell'_{r_{eff}} r + \ell'_\xi \xi + \ell'_\zeta \zeta \qquad (2.11)$$

$$\dot{r} = n'_{v_1} v + n'_{p_{eff}} p + n'_{r_{eff}} r + n'_\xi \xi + n'_\zeta \zeta \qquad (2.12)$$

$$\dot{\phi} = p \qquad (2.13)$$

$$\dot{\psi} = r \qquad (2.14)$$

Details of the nomenclature used in these equations, and for the aerodynamic coefficients and derivatives throughout this thesis, are given in Appendix A. The dash notation, $'$, indicates that the terms include contributions arising from the elimination of $\dot{p}$ from the $\dot{r}$ equation and $\dot{r}$ from the $\dot{p}$ equation. For some of the analysis in later chapters a roll damper, with gearing $K_{\xi p}$, and a yaw damper, with gearing $K_{\zeta r}$, were used and contributions from these are included in the derivatives $\ell'_{p_{eff}}$, $n'_{p_{eff}}$, $\ell'_{r_{eff}}$ and $n'_{r_{eff}}$ e.g.

$$\ell'_{p_{eff}} = \frac{I_z L_p + I_{xz} N_p}{I_x I_z - I_{xz}^2} + K_{\xi p} \frac{I_z L_\xi + I_{xz} N_\xi}{I_x I_z - I_{xz}^2}$$

(See Appendix A.3 for full details). The full gravity term shown in equation (2.2) has been replaced by its approximate form

$$g_3 \phi + g_2 \psi$$

in which perturbations in the g component are expressed in terms of deviation angles ϕ and ψ, and Φ_e, Θ_e are Euler angles, the 'e' denoting equilibrium conditions. Derivatives y'_p and y'_r are negligible in comparison with the other p and r terms in (2.10).

The linear equations, such as (2.10) - (2.14), continue to form the basis of much work on stability and control and give good results due to the often relatively small perturbations in state variables needed to describe fairly violent manoeuvres. Also, over appreciable ranges of these variables the aerodynamics are adequately described by

linear functions and it was hoped that equations (2.10) - (2.14) would be adequate for angles of attack up to at least 25°,but this was to be investigated.

Starting with the simple lateral equations, a non-linear mathematical model can now be built up using wind-tunnel aerodynamic data.

2.2.3.2 Non-linear Lateral Aerodynamics Model

Ross[23,24] has previously shown how non-linear sideforce and moments due to sideslip could be modelled by extending the idea of derivatives to include higher order terms. For instance, static wind tunnel data of sideforce against sideslip velocity, v, was fitted using a cubic polynomial in sideslip.

Similarly, C_ℓ and C_n against v can be fitted in the same way and for the aircraft models described in Chapter 3, as well as the HIRM, variations with roll rate, p, were also included. Hysteresis in C_ℓ against sideslip has also been investigated by the R.A.E. as such phenomena may be expected in separating/reattaching flows[46].

Including cubic aerodynamic non-linearities in the lateral equations of motion gives the final form of the equations used for much of the work in this thesis:

$$\dot{v} = y'_v v + V_e \sin\alpha_e p - V_e r \cos\alpha_e + g_3\phi + g_2\psi \qquad (2.15)$$

$$\dot{p} = \ell'_{v_1} v + \ell'_{v_3} \underline{v}^3 + \ell'_{p_{eff}} p + \ell'_{p_3} p^3 + \ell'_{r_{eff}} r + \ell'_\xi \xi + \ell'_\zeta \zeta \qquad (2.16)$$

$$\dot{r} = n'_{v_1} v + n'_{v_3} \underline{v}^3 + n'_{p_{eff}} p + n'_{p_3} p^3 + n'_{r_{eff}} r + n'_\xi \xi + n'_\zeta \zeta \qquad (2.17)$$

$$\dot{\phi} = p \qquad (2.18)$$

$$\dot{\psi} = r \qquad (2.19)$$

where non-linear sideslip contributions, $(\ell'_{v_1} + \ell'_{v_3} v^2)v$ and $(n'_{v_1} + n'_{v_3} v^2)v$, and non-linear roll rate contributions, $(\ell'_{p_{eff}} + \ell'_{p_3} p^2)p$ and $(n'_{p_{eff}} + n'_{p_3} p^2)p$, have been included. This form of model has been used for response calculations and analysis using averaging techniques. Comparisons were made with stability roots of the linear equations.

2.2.3.3 Other Models

As a next step, the non-linear kinematic terms shown in (2.4) and (2.6) could be incorporated in equations (2.16) and (2.17) so that α and pitch rate time histories could be utilised in the lateral responses and analysis. With V approximately

constant, so that the $\dot{u}$ equation could be ignored, a 5 degree of freedom model would then show the effects of longitudinal motion and cross-coupling on the characteristics.

Six degree of freedom models are described in Chapter 6 and applied to the HIRM. Locally linearised equations about equilibrium trim points at high angles of attack are examined as well as a simulation model using equations (2.1) to (2.9) and the various forms of experimental data mentioned in §2.2.1.

2.3 Departure Parameters for Linear Equations

The main parameters which have been used for predicting departure and spin tendancies in the stall angle of attack region are $C_{n_{\beta dyn}}$, the dynamic directional stability, and various forms of lateral control departure parameter (L.C.D.P.), which indicate aileron control problems (adverse aileron yaw). These parameters are merely indicators based on static data, as they are partly intended to be used during the initial stages of an aircraft's development when only static data is available. As such, they do not give any information as to the form of departure, only that instability may be expected as they go negative. Negative values of $C_{n_{\beta dyn}}$ and L.C.D.P. predict directional divergence and roll reversal respectively, indicating problem areas at the relevant angles of attack.

The classical stability analysis for the linear equations of motion (longitudinal and lateral) examines the roots of the characteristic polynomial. This technique is outlined briefly in §2.3.4.

The examination of moments in dynamic stability axes, used by Kalviste[47], provides a useful assessment of stability with cross-coupling included. Section 2.3.5 describes this technique.

2.3.1 $C_{n_{\beta dyn}}$ ($\breve{N}_{v_{dyn}}$)

Dynamic $\breve{N}_v$ ($\breve{N}_{v_{dyn}}$, or $C_{n_{\beta dyn}}$ in U.S. notation) is a misleading term as it only includes static derivatives. It provides no information on the form of instability and does not give necessary and sufficient conditions for departure.

$C_{n_{\beta dyn}}$ is defined, in U.K. notation, as:

$$\breve{N}_{v_{dyn}} = \breve{N}_v - \frac{I_z}{I_x}\breve{L}_v \sin\alpha \qquad (2.20)$$

It may be regarded either as directional stability in wind axes, an approximation to the dutch roll frequency or as an approximation to the term 'b' in the lateral stability quartic (see Appendix B). Greer[48] shows how $\breve{N}_{v_{dyn}}$ can be treated in the last mentioned way, where negative values

often correlate with the occurrence of directional divergence. The quartic term b, using concise notation, can be written as

$$b_1 = n'_r\ell'_{p_{eff}} - n'_{p_{eff}}\ell'_r + y'_v(\ell'_{p_{eff}} + n'_r) - \ell'_{v_1}V\sin\alpha + n'_{v_1}V\cos\alpha \qquad (2.21)$$

The derivatives are usually less than 1 in magnitude and products of derivatives are assumed small, in comparison with other terms, so a reduced b coefficient, b_{1_R}, may be written as:

$$b_{1_R} = n'_{v_1}V\cos\alpha - \ell'_{v_1}V\sin\alpha \qquad (2.22)$$

Then:

$$\frac{b_{1_R}}{\frac{1}{2}\rho V^2 Sb} = \frac{1}{I_Z}\left(\frac{N_{r_1}}{\frac{1}{2}\rho VSb}\cos\alpha - \frac{I_Z}{I_X}\frac{L_{r_1}}{\frac{1}{2}\rho VSb}\sin\alpha\right)$$

i.e. $$\frac{b_{1_R} I_Z}{\frac{1}{2}\rho V^2 Sb} \simeq \breve{N}_{v_{dyn}} \qquad (2.23)$$

where $\breve{N}_{v_{dyn}}$ is as defined in expression (2.20).

Results for the HIRM, given in Chapter 5, show $\breve{N}_{v_{dyn}}$ is a good representation of the full b_1 term factored by $I_Z/\frac{1}{2}\rho V^2 Sb$. Kalviste[47] has extended the ideas of $\breve{N}_{v_{dyn}}$ to form $\breve{N}_{\alpha_{dyn}}$ as well as $\breve{M}_{\alpha_{dyn}}$ and $\breve{M}_{v_{dyn}}$ (or its equivalent $\breve{M}_{\beta_{dyn}}$). Use will be made of Kalviste's formulation of moments in his dynamic stability axes for the HIRM.

Calico[49] shows the derivation of $\breve{N}_{v_{dyn}}$ from a lateral stability analysis of the perturbation equations about a symmetric equilibrium condition using only static derivatives.

For some aircraft, $\breve{N}_{v_{dyn}}$ trends show good correlation with flight behaviour e.g. the F-5 in Ref.15 and the F-4 in Ref.50. In the case of the F-16, which is controllable up to 40° α (due to the presence of strakes and leading edge flap deflection), improved sideslip characteristics, at high α, mean $\breve{N}_v$ is more positive, $\breve{L}_v$ more negative and so $\breve{N}_{v_{dyn}}$ remains positive up to greater than $\alpha = 40^\circ$. Johnston and Hogge[51] also mention failings of $\breve{N}_{v_{dyn}}$ to predict departure.

The addition and use of canard surfaces, as on the HIRM, can significantly affect $\breve{N}_{v_{dyn}}$.

2.3.2 Lateral Control Departure Parameter (L.C.D.P.)

The aileron-alone departure parameter or A.A.D.P., a form of L.C.D.P., is defined as:

$$A.A.D.P. = \breve{N}_v - \breve{L}_v \frac{\breve{N}_{\xi_T}}{\breve{L}_{\xi_T}} \qquad (2.24)$$

and negative values indicate the likelihood of control induced departure due to adverse aileron yaw ($\breve{N}_{\xi T}$ positive). With all the derivatives in the A.A.D.P. of their normal sign ($\breve{N}_v$ positive and the others negative), A.A.D.P. is positive but at high angles of attack with $\breve{N}_v$ going negative, $\breve{L}_v$ positive (unstable), adverse aileron yaw leads to negative values of A.A.D.P. By gearing the rudder to the ailerons to counteract the adverse aileron yaw, positive values of the control departure parameter can be retained to higher α. For a simple gearing where K is chosen to give zero yawing moment with differential tail application,

$$K = -\frac{\breve{N}_{\xi_T}}{\breve{N}_\zeta} \qquad (2.25)$$

then the lateral control departure parameter, as it is now called, is defined as:-

$$L.C.D.P. = \breve{N}_v - \breve{L}_v\left(\frac{\breve{N}_{\xi_T}+K\breve{N}_\zeta}{\breve{L}_{\xi_T}+K\breve{L}_\zeta}\right) \qquad (2.26)$$

2.3.3 Weissman Criteria

Weissman[52,53] has advocated the simultaneous assessment of N_{vdyn} and L.C.D.P. in predicting stability and departure boundaries. Fig.2.3 shows how $C_{n\beta_{dyn}}$ and L.C.D.P. are used together for indications of departure characteristics. The boundaries were established (Ref.54) originally by examining the response to small sideslip disturbances, using a 6 degree of freedom simulation of an aircraft in high g manoeuvres.

2.3.4 Roots of Stability Polynomial

Apart from the parameters described in §2.3.1 to 2.3.3, using static derivative data, the conventional assessment of stability of a linear system is made using the so called characteristic determinant.

Assumed solutions of the form

$$v = A_v e^{\mu t}$$

$$p = A_p e^{\mu t}$$

are substituted into the small perturbation linear equations.

The determinant of the equations is then equated to zero to give the condition for the equations to be compatible. For the lateral equations of motion, the characteristic determinant equated to zero gives a quartic equation in μ, the coefficients of which are given in Appendix B:

$$\mu^4 + a_1\mu^3 + b_1\mu^2 + c_1\mu + d_1 = 0 \qquad (2.27)$$

The solutions to this equation, the so-called stability roots, are used to describe the constituents of the system motion, each constituent being given by an expression of the form $Ae^{\mu t}$ as indicated above.

For μ real, if it is positive, the constituent increases rapidly, and for stability, μ must be negative, the zero value indicating neutral stability.

For complex μ, indicating an oscillatory response, the real part must be negative for the motion to be stable. Again zero indicates neutral stability and a positive real part indicates divergence.

For the case of the quartic stability equation (2.27), important for aircraft work, the condition for stability is given by the coefficients a_1, c_1 and d_1 being positive and the Routh's discriminant, R, being positive. Routh's discriminant is given by

$$R = c_1(a_1b_1 - c_1) - a_1^2 d_1 \qquad (2.28)$$

2.3.5 Dynamic Stability Axis Moments

Kalviste[47] has described an analysis technique for investigating high angle of attack stability characteristics using the six degree of freedom equations retaining all cross-coupling terms. He defines a new set of axes ("dynamic stability axes") which involve the aircraft rolling about the velocity vector, through μ, yawing (about the z axis), through β, and finally pitching (about the y axis), through α, to achieve a perturbed state (c.f. yaw, pitch and roll for definition of conventional Euler angles). Stability parameters are defined about the new axis system and include an extension of N_{vdyn} (§2.3.1)

The equations of motion in the dynamic stability axes are:

$$\ddot{\mu} = \left(\frac{L}{I_x}\cos\alpha + \frac{N}{I_z}\sin\alpha\right)\sec\beta = L_{DYN} \qquad (2.29)$$

$$\ddot{\alpha} = \frac{M}{I_y} - \left(\frac{L}{I_x}\cos\alpha + \frac{N}{I_z}\sin\alpha\right)\tan\beta = M_{DYN} \qquad (2.30)$$

$$\ddot{\beta} = -(\frac{N}{I_z}\cos\alpha - \frac{L}{I_x}\sin\alpha) = -N_{DYN} \qquad (2.31)$$

L_{DYN} is the rolling acceleration about the velocity vector, M_{DYN} is the pitching acceleration which causes a change in incidence and $-N_{DYN}$ is the yawing acceleration which causes a change in sideslip.

Non-dimensional aerodynamic moment coefficients in dynamic stability axes are defined by Kalviste as:-

$$C_{\ell_{DYN}} = (C_\ell\cos\alpha + \frac{I_x}{I_z}C_n\sin\alpha)\sec\beta \qquad (2.32)$$

$$C_{m_{DYN}} = C_m - \frac{b}{c}(\frac{I_y}{I_z}C_n\sin\alpha + \frac{I_y}{I_x}C_\ell\cos\alpha)\tan\beta \qquad (2.33)$$

$$C_{n_{DYN}} = C_n\cos\alpha - \frac{I_z}{I_x}C_\ell\sin\alpha \qquad (2.34)$$

The aircraft aerodynamics are assumed to be functions of α and β only so only the $\ddot{\alpha}$ and $\ddot{\beta}$ equations need be considered for stability analysis. Uncoupled stability criteria are given by $\partial C_{mDYN}/\partial\alpha < 0$ and $\partial C_{nDYN}/\partial\beta > 0$ and Kalviste describes how, for the coupled equations, $\partial C_{mDYN}/\partial\beta (= C_{m\beta DYN})$ and $C_{n\alpha DYN}$ are also used.

Some of these ideas are used in Chapter 5 in connection with the HIRM. In particular the dynamic stability axis moments are presented as functions of angle of attack and sideslip.

2.4 Analytic Techniques for Non-linear Equations

2.4.1 General

Two main approaches exist to the solution of the aircraft equations of motion. Either they can be solved using computational techniques (digital or analogue) or they can be solved using analytic techniques, which inevitably involve some degree of approximation.

Numerical and analogue methods are ideal for parametric studies but can prove expensive and the analysis of the results is often lengthy. Also, for non-linear systems the characteristics depend on the amplitude and phase of the input response variables.

Analytic techniques are attractive in that they provide more general information than numerical solutions,which tend to be highly specific to certain flight conditions and control inputs. In particular, analytic techniques provide an overall picture of the dynamic response to all kinds of control inputs and can be used to show the limits of validity of linearised theories.

Mathematical techniques for the solution of practical non-linear systems always involve approximations either in the original equations or in the techniques themselves. For instance the idealisation of constant roll rate is adopted to obtain an algebraic solution to the inertia coupling problem[55-58].

Two analytic techniques for obtaining general stability characteristics which have been developed recently are used for the work in this thesis. One[40,59] is based on a local linearisation of the equations of motion about a non-zero equilibrium state while the other, which receives most attention in the current work, is an extension of the one degree of freedom averaging technqiue of Kryloff-Bogoliuboff[60], developed at the R.A.E. by Beecham and Titchener[31].

Averaging techniques start from the basis that fine detail in the system motion is going to be smoothed out by integration over an appropriate cycle. The overall characteristics of the system,in terms of the amplitude of the envelope of the motion and its instantaneous frequency,are retained but the instantaneous displacement and velocity within the envelope are not described. Beecham and Titchener describe a wide range of single degree of freedom applications for their version of the technique. Simpson[32] published details of a generalisation of the Beecham-Titchener method to n degree of freedom systems. It was an aim of the thesis work to apply this generalisation, referred to hereafter as the Beecham-Titchener-Simpson (B.T.S.) method, to the uncoupled lateral aircraft equations of motion with non-linear aerodynamic moments present. In certain cases the method provides good results. However, limitations of the technique, concerning the number of non-linearities which can usefully be accommodated in this application, are highlighted. In view of these limitations more emphasis was placed, towards the end of the work, on numerical techniques.

2.4.2 Beecham-Titchener-Simpson Method

2.4.2.1 General

Beecham and Titchener considered systems typified by:

$$\ddot{x} + f(x,\dot{x}) = 0 \qquad (2.35)$$

and sought solutions of the form

$$x = a(t)\cos\phi(t) \qquad (2.36)$$

The introduced a local damping factor, $\lambda = \dot{a}/a$, and a local frequency, $\omega = \dot{\phi}$, as the important parameters describing the characteristics of the system when the averaging technique

(integrating over one cycle) was applied.

Ross and Beecham[23,24] applied the Beecham-Titchener (B.T.) method to the lateral equations of motion of an aircraft by extending the technique to cope with higher order equations. In Refs.23 and 24 the method is applied to the lateral equations reduced to a 4th order equation in sideslip. Starting with equations (2.15) - (2.18) with $\ell'_{p_3} = n'_{p_3} = 0$ and no control terms,(2.15) can be differentiated and p substituted for $\dot{\phi}$ from (2.18). Elimination of p and r in turn from (2.16) and (2.17) and subsequent substitution for the p and r terms in (2.15), gives an equation in v of the form:

$$\frac{d^4 v}{dt^4} + \frac{d^3 a_1 v}{dt^3} + \frac{d^2}{dt^2}(b_1 v + b_{3_v} v^3) + \frac{d}{dt}(c_1 v + c_{3_v} v^3) + d_1 v + d_3 v^3 = 0 \qquad (2.37)$$

where a_1, b_1, c_1 and d_1 are the usual combinations of derivatives from linear stability analysis (§2.3.4) and b_3, c_3 and d_3 are equivalent non-linear terms, defined in Appendix B. This equation is then 'averaged' by integrating over one cycle of the motion, using the principles to be outlined in the next section.

Simpson[32] noted the advantages offered by applying the averaging to first order systems directly as opposed to a second or higher order formulation. When the lateral equations are considered,as shown in (2.15) to (2.19) with non-linear sideslip and roll rate terms, it is not possible to reduce the equations to an equation in one variable and the algebra to reduce the equations to a form equivalent to that of (2.37) is very lengthy. The final equation, in such a form, includes both sideslip and roll rate terms. In an attempt to deal with the equations with non-linearities in both side-slip and roll rate, this thesis uses the B.T.S.technique to average the equations in first order form, without reducing them to a single high-order equation. The B.T.S. technique yields a similar stability polynomial to that from the B.T. technique and, as it uses determinants in its derivation, it is simpler to apply. However, there are some important differences between the stability polynomials given by the two techniques and these will be highlighted in the next section.

2.4.2.2 Application to Aircraft Lateral Equations of Motion

A full description of the techniuqe, its mathematical basis plus some applications are given in Ref.61.

After some initial work on two degree of freedom systems using just the v and p equations, the B.T.S.technique was applied to simplified versions of equations (2.15) to (2.18) as follows. The equations in matrix form for zero control

input are:

$$\begin{bmatrix}\dot{v}\\ \dot{p}\\ \dot{r}\\ \dot{\phi}\end{bmatrix} = \begin{bmatrix} y'_v & V_e\sin\alpha_e & -V_e\cos\alpha_e & g_3 \\ \ell'_{v_1} & \ell'_{p_1} & \ell'_{r_{eff}} & 0 \\ n'_{v_1} & n'_{p_1} & n'_{r_{eff}} & 0 \\ 0 & 1 & 0 & 0 \end{bmatrix}\begin{bmatrix} v\\ p\\ r\\ \phi\end{bmatrix} + \begin{bmatrix} 0\\ \ell'_{v_3}\\ n'_{v_3}\\ 0\end{bmatrix} v^3 + \begin{bmatrix} 0\\ \ell'_{p_3}\\ n'_{p_3}\\ 0\end{bmatrix} p^3$$

(2.38)

In general, such a system may be written as

$$\dot{x} = \underline{F}(x) \qquad (2.39a)$$

or $$\underline{\dot{x}} = \underline{A}\,\underline{x} + \underline{s}\,f(\underline{x}) \qquad (2.39b)$$

where $\underline{s}$ is a vector locating the non-linear function of vector $\underline{x}$, $f(\underline{x})$.

Ignoring the gravitational term, to simplify the analysis a little, a solution is assumed of the form:-

$$\underline{x} = -a\left[\sin\tilde{\phi}\underline{\xi} + \cos\tilde{\phi}\underline{\eta}\right] \qquad (2.40)$$

where $\sim$ has been used to indicate ϕ is a phase angle and not a perturbation bank angle. The vector $\underline{x}$ can be written as:-

$$v = -a_1\left[\sin\phi.\xi_1 + \eta_1.\cos\phi\right] \qquad (2.41)$$

$$p = -a_2\left[\sin\phi.\xi_2 + \eta_2.\cos\phi\right] \qquad (2.42)$$

$$r = -a_3\left[\sin\phi.\xi_3 + \eta_3.\cos\phi\right] \qquad (2.43)$$

(omitting the $\sim$ from the ϕ as confusion is unlikely to occur in this section). These can be simplified by noting that they can be regarded as expansions of $\cos(\phi+\varepsilon)$ where ε is a phase angle. By taking the phase angle of the v solution as reference (zero) then (2.41) to (2.43) can be re-written as

$$v = \sigma_v\cos\phi \qquad (2.44)$$

$$p = \sigma_p\cos(\phi + \varepsilon_p) \qquad (2.45)$$

$$r = \sigma_r \cos(\phi + \varepsilon_r) \tag{2.46}$$

where $\eta_1 = -1$, $\eta_2 = -\cos\varepsilon_p$, $\eta_3 = -\cos\varepsilon_r$

$\xi_1 = 0$, $\xi_2 = \sin\varepsilon_p$, $\xi_3 = \sin\varepsilon_r$

and $a_1 = -\sigma_v$

$a_2 = -\sigma_p$

$a_3 = -\sigma_r$

With $\omega = \frac{d\phi}{dt}$ (2.47)

and assuming

$$\lambda = \frac{\dot{\sigma}_v}{\sigma_v} = \frac{\dot{\sigma}_p}{\sigma_p} = \frac{\dot{\sigma}_r}{\sigma_r} \tag{2.48}$$

then $\dot{v} = \sigma_v(\lambda\cos\phi - \omega\sin\phi)$ (2.49)

$$\dot{p} = \sigma_p(\lambda\cos(\phi+\varepsilon_p) - \omega\sin(\phi+\varepsilon_p)) \tag{2.50}$$

$$\dot{r} = \sigma_r(\lambda\cos(\phi+\varepsilon_r) - \omega\sin(\phi+\varepsilon_r)) \tag{2.51}$$

After substituting the expressions (2.44) - (2.46) and (2.49) - (2.51) into (2.38), the resulting system of equations is solved by taking the average values over one cycle of ϕ from 0 to 2π, to yield approximate analytic solutions for the oscillatory modes. The averaging technique[32] uses the fact that the average value of the equations is zero over one cycle (ϕ = 0 to 2π):

$$\frac{1}{\pi}\int_0^{2\pi} (\underline{\dot{x}} - \underline{F}(\underline{x}))\sin\phi \, d\phi = 0 \tag{2.52}$$

and $$\frac{1}{\pi}\int_0^{2\pi} (\underline{\dot{x}} - F(x))\cos\phi . d\phi = 0 . \tag{2.53}$$

Applying (2.52) to equations (2.38) gives:

$$-\omega\sigma_v = -V_e\sin\alpha_e\sigma_p\sin\varepsilon_p - V_e\cos\alpha_e\sigma_r\sin\varepsilon_r \tag{2.54}$$

$$\sigma_p(-\lambda\sin\varepsilon_p-\omega\cos\varepsilon_p) = -\ell'_{p_1}\sigma_p\sin\varepsilon_p-\ell'_r\sigma_r\sin\varepsilon_r-\tfrac{3}{4}\ell'_{v_3}\sigma_v{}^3\sin\varepsilon_v - \tfrac{3}{4}\ell'_{p_3}\sigma_p{}^3\sin\varepsilon_p \quad (2.55)$$

$$\sigma_r(-\lambda\sin\varepsilon_r-\omega\cos\varepsilon_r) = -n'_{p_1}\sigma_p\sin\varepsilon_p-n'_r\sigma_r\sin\varepsilon_r-\tfrac{3}{4}n'_{v_3}\sigma_v{}^3\sin\varepsilon_v - \tfrac{3}{4}n'_{p_3}\sigma_p{}^3\sin\varepsilon_p \quad (2.56)$$

Applying (2.53) to (2.38) gives:

$$\sigma_v\lambda = y'_v\sigma_v+V_e\sin\alpha_e\sigma_p\cos\varepsilon_p-V_e\cos\alpha_e\sigma_r\cos\varepsilon_r \quad (2.57)$$

$$\sigma_p(\lambda\cos\varepsilon_p-\omega\sin\varepsilon_p) = \ell'_{v_1}\sigma_v+\ell'_{p_1}\sigma_p\cos\varepsilon_p+\ell'_r\sigma_r\cos\varepsilon_r + \tfrac{3}{4}\ell'_{v_3}\sigma_v\cos\varepsilon_v+\tfrac{3}{4}\ell'_{p_3}\sigma_p{}^3\cos\varepsilon_p \quad (2.58)$$

$$\sigma_r(\lambda\cos\varepsilon_r-\omega\sin\varepsilon_r) = n'_{v_1}\sigma_v+n'_{p_1}\sigma_p\cos\varepsilon_p+n'_r\sigma_r\cos\varepsilon_r + \tfrac{3}{4}n'_{v_3}\sigma_v{}^3\cos\varepsilon_v+\tfrac{3}{4}n'_{p_3}\sigma_p{}^3\cos\varepsilon_p \quad (2.59)$$

These equations may be simplified by considering:

$$\frac{1}{\pi}\int_0^{2\pi}\underline{G}(\cos\phi - i\sin\phi)d\phi = 0 \quad (2.60)$$

where $\underline{G} = \dot{\underline{x}} - \underline{F}(\underline{x})$

Putting $\mu = i\omega$ gives:

$$\sigma_v\,\mu = y'_v\sigma_v + V_e\sin\alpha_e\sigma_p e^{i\varepsilon_p} - V_e\cos\alpha_e\sigma_r e^{i\varepsilon_r} \quad (2.61)$$

$$\sigma_p e^{i\varepsilon_p}\mu = \ell'_{v_1}\sigma_v + \ell'_p\sigma_p e^{i\varepsilon_p} + \ell'_r\sigma_r e^{i\varepsilon_r} + \tfrac{3}{4}\ell'_{v_3}\sigma_v{}^3 e^{i\varepsilon_v} + \tfrac{3}{4}\ell'_{p_3}\sigma_p{}^3 e^{i\varepsilon_p} \quad (2.62)$$

$$\sigma_r e^{i\varepsilon_r}\mu = n'_{v_1}\sigma_v + n'_p\sigma_p e^{i\varepsilon_p} + n'_r\sigma_r e^{i\varepsilon_r} + \tfrac{3}{4}n'_{v_3}\sigma_v{}^3 e^{i\varepsilon_v} + \tfrac{3}{4}n'_{p_3}\sigma_p{}^3 e^{i\varepsilon_p} \quad (2.63)$$

Rewriting equations (2.61) to (2.63) in matrix form and also replacing the 'g' term gives:

$$\begin{bmatrix} \mu - y'_v & -V_e\sin\alpha_e & V_e\cos\alpha_e & -g_3 \\ -\ell'_{v_1} - \tfrac{3}{4}\ell'_{v_3}\sigma_v^2 & \mu-\ell'_{p_1} - \tfrac{3}{4}\ell'_{p_3}\sigma_p^2 & -\ell'_r & 0 \\ -n'_{v_1} - \tfrac{3}{4}n'_{v_3}\sigma_v^2 & -n'_{p_1} - \tfrac{3}{4}n'_{p_3}\sigma_p^2 & \mu-n'_r & 0 \\ 0 & -1 & 0 & \mu \end{bmatrix} \begin{bmatrix} \sigma_v & \\ \sigma_p & e^{i\varepsilon_p} \\ \sigma_r & e^{i\varepsilon_r} \\ \sigma_\phi & e^{i\varepsilon_\phi} \end{bmatrix} = \underline{0}$$

(2.64)

Setting the determinant of the system matrix in (2.64) to zero for solutions, gives the equivalent lateral stability polynomial now including non-linearities in v and p. The terms ℓ'_{v_1}, n'_{v_1}, ℓ'_{p_1} and n'_{p_1} in the linear stability equation have been replaced by their non-linear equivalents, e.g. $\ell'_{v_1} + \tfrac{3}{4}\ell'_{v_3}\sigma_v^2$. The resulting quartic which must be analysed to study the aircraft lateral dynamic stability is:

$$\mu^4 + \mu^3(a_1+\tfrac{3}{4}a_{3_p}\sigma_p^2) + \mu^2(b_1+\tfrac{3}{4}b_{3_p}\sigma_p^2 + \tfrac{3}{4}b_{3_v}\sigma_v^2)$$

$$+ \mu\,(c_1+\tfrac{3}{4}c_{3_p}\sigma_p^2 + \tfrac{3}{4}c_{3_v}\sigma_v^2 + \tfrac{9}{16}c_{3_{vp}}\sigma_v^2\sigma_p^2)$$

$$+ \quad d_1+\tfrac{3}{4}d_{3_p}\sigma_p^2 + \tfrac{3}{4}d_{3_v}\sigma_v^2 + \tfrac{9}{16}d_{3_{vp}}\sigma_v^2\sigma_p^2 \quad = \quad 0$$

(2.65)

The terms a_1, b_1, c_1 and d_1 are as in the normal aircraft lateral stability quartic (see §2.3.4) and terms a_{3_p}, b_{3_p} etc. contain non-linear elements (given in full in Appendix B). Equation (2.65) is the equation which would be obtained by applying local linearisation techniques to (2.38) in the manner described in §2.3.4.

2.4.2.3 Comments on Application to Lateral Equations

Having applied the B.T.S.method to the full non-linear lateral equations (2.38), it will be useful to examine some of the practical implications of using the resulting equation (2.65). Equation (2.65) warrants some comments if only because of its complexity.

First of all, by setting the non-linear p terms, n'_{p_3} and ℓ'_{p_3}, to zero, the resulting quartic may be compared with that obtained by reducing the original equations of motion to a 4th order equation in v (equation (2.37)) and applying the averaging method[23,39]. The resulting stability equation is:

$$(\lambda+i\omega)^4 + a_1(\lambda+i\omega)^3 + b_1(\lambda+i\omega)^2 + \tfrac{3}{4}b_{3v}\sigma_v^2(3\lambda+i\omega)^2 + c_1(\lambda+i\omega) + \tfrac{3}{4}c_{3v}\sigma_v^2(3\lambda+i\omega) + d_1 + \tfrac{3}{4}d_{3v}\sigma_v^2 = 0 \quad (2.66)$$

This is not the same solution as that obtained by averaging the equations in first order form (c.f. (2.65)):

$$(\lambda+i\omega)^4 + a_1(\lambda+i\omega)^3 + (b_1+\tfrac{3}{4}b_{3v}\sigma_v^2)(\lambda+i\omega)^2 + (c_1+\tfrac{3}{4}c_{3v}\sigma_v^2)(\lambda+i\omega) + d_1+\tfrac{3}{4}d_{3v}\sigma_v^2 = 0 \quad (2.67)$$

If the original averaging technique[23] is applied to the lateral equations with non-linear v and p terms, (2.38), a 4th order formulation of the equations would be sought first of all. Reduction of the equations to an equation in one variable is not now possible, as mentioned in §2.4.2.1, but after some lengthy algebra to eliminate r, a 4th order equation in v and p results:

$$\frac{d^4v}{dt^4} + \frac{d^3}{dt^3}(a_1v + a_{3p}p^3) + \frac{d^2}{dt^2}(b_1v + b_{3v}v^3 + b_{3p}p^3) + \frac{d}{dt}(c_1v + c_{3v}v^3 + c_{3p}p^3 + c_{3vp}v^3p^3) + d_1v + d_{3v}v^3 + d_{3p}p^3 + d_{3vp}v^3p^3 = 0 \quad (2.68)$$

It is the differentiation of the non-linear terms in v^3 and p^3 in (2.37) and (2.68) that means the resulting stability polynomial (e.g. (2.66) from (2.37)) contains terms like $\frac{3}{4}c_{3v}\sigma_v^2(3\lambda+i\omega)$. For instance, consider the term

$$\frac{d}{dt}(c_1v + c_3v^3) = \frac{d}{dt}C(v) \quad \text{in (2.37).}$$

Expanding, gives

$$\frac{d}{dt}C(v) = c_1\frac{dv}{dt} + c_3.3v^2.\frac{dv}{dt}$$

Upon averaging, the term $c_1\ dv/dt$ gives rise to the $c_1(\lambda+i\omega)$ in (2.66) and the $3c_3v^2\ dv/dt$ term produces the $\frac{3}{4}c_3\sigma_v^2(3\lambda+i\omega)$ in (2.66).

It is the neglect of the extra terms from the differentiation of $B(v)(= b_1+b_3v^3)$, $C(v)$ etc, in (2.37) and (2.68), that means the expansion of the stability determinant from (2.64)

results in a polynomial in $(\lambda+i\omega)$ only, (2.65) or (2.67).

In conventional stability and control analysis, it is convenient to use Laplace Transforms, i.e. a differential operator in the equations of motion (see e.g. Ref.44) and some progress with the expansion of the "non-linear determinant" in (2.64) can be made by regarding μ as a differential operator, as suggested by Ross[39]. In this case,

$$\mu = \mu\{\ \} = \frac{1}{\pi\sigma}\int_0^{2\pi}\frac{d}{dt}\{\ \}(\cos\phi - i\sin\phi)d\phi \qquad (2.69)$$

So, considering $v = \sigma_v\cos\phi$ (from 2.44), for example gives

$$\mu\{v\} = \frac{1}{\pi\sigma_v}\int_0^{2\pi}(\sigma_v(\lambda\cos\phi-\omega\sin\phi))(\cos\phi-i\sin\phi)d\phi$$

$$= \lambda + i\omega = \mu \qquad (2.70)$$

Similarly,

$$\mu\{v^3\} = \tfrac{3}{4}\sigma_v^2(3\lambda+i\omega) \qquad (2.71)$$

For μ^2, a similar operator is defined as:

$$\mu^2 = \mu^2\{\ \} = \frac{1}{\pi\sigma}\int_0^{2\pi}\frac{d^2}{dt^2}\{\ \}(\cos\phi-i\sin\phi)d\phi$$

So, for $v = \sigma_v\cos\phi$, first of all

$$\frac{d^2(v)}{dt^2} = \sigma_v(\lambda^2\cos\phi-\omega\sin\phi\lambda-\omega^2\cos\phi-\omega\sin\phi\lambda),$$

then

$$\mu^2\{v\} = \frac{1}{\pi\sigma_v}\int_0^{2\pi}\frac{d^2}{dt^2}(v)(\cos\phi-i\sin\phi)d\phi$$

$$\lambda^2 + 2i\omega\lambda - \omega^2 = \mu^2 \qquad (2.72)$$

Similarly,

$$\mu^2\{v^3\} = \tfrac{3}{4}\sigma_v^2(9\lambda^2 + 6i\lambda\omega - \omega^2)$$

$$= \tfrac{3}{4}\sigma_v^2(3\lambda + i\omega)^2 \qquad (2.73)$$

Some difficulties remain with the interpretation of μ as an operator but work has been carried out to show it is a useful concept.

Another point to notice about the B.T.S.method applied to the lateral equations with non-linear v and p characteristics, is the assumption made in (2.48), that each response variable has the same damping factor. Results presented in Chapter 3 show this is not so in practice, but for non-linearities in v characteristics alone, then (2.48) does hold.

2.4.2.4 Stability Boundaries

The corresponding equation to (2.65), which includes the $(3\lambda+i\omega)$ terms discussed in the last section, is:

$$
\begin{aligned}
&(\lambda+i\omega)^4 + a_1(\lambda+i\omega)^3 + \tfrac{3}{4}a_{3p}\sigma_p^2(3\lambda+i\omega)^3 \\
&\quad + b_1(\lambda+i\omega)^2 + \tfrac{3}{4}b_{3p}\sigma_p^2(3\lambda+i\omega)^2 + \tfrac{3}{4}b_{3v}\sigma_v^2(3\lambda+i\omega)^2 \\
&\quad + c_1(\lambda+i\omega) + \tfrac{3}{4}c_{3p}\sigma_p^2(3\lambda+i\omega) + \tfrac{3}{4}c_{3v}\sigma_v^2(3\lambda+i\omega) \\
&\quad\quad + \tfrac{9}{16}c_{3vp}\sigma_v^2\sigma_p^2(3\lambda+i\omega) \\
&\quad + d_1 + \tfrac{3}{4}d_{3p}\sigma_p^2 + \tfrac{3}{4}d_{3v}\sigma_v^2 \\
&\quad\quad + \tfrac{9}{16}d_{3vp}\sigma_v^2\sigma_p^2 = 0 \qquad (2.74)
\end{aligned}
$$

Conditions for stability boundaries (exponential divergences or limit cycles (complex roots with zero damping)) are given by putting the non-linear damping factor, λ, to zero. In these cases, equations (2.65) and (2.74) are identical. Similarly for the lateral equations with non-linearities in v only, equations (2.66) and (2.67) are the same when $\lambda = 0$. For much of the work, using the averaging technique applied to limit cycle behaviour, the results are thus independent of the anomalies noted regarding λ and 3λ terms.

Introducing a simplified notation, equation (2.65) may be written as

$$\mu^4 + \mu^3 a^* + \mu^2 b^* + \mu c^* + d^* = 0 \qquad (2.75)$$

Routh's discriminant for the equivalent linear system may be formed by using a*, b*, etc in place of a_1, b_1 etc from the linear system (see equation (2.28)). The amplitude of the sustained (non-linear) oscillations is given by the condition that the equivalent linear system is neutrally stable. Thus the limit cycle amplitude for the non-linear system is given by

$$R^* = a^*b^*c^* - (a^*)^2d^* - (c^*)^2 = 0 \qquad (2.76)$$

Using the full expressions for a*, b*, c* and d* (see (2.65)), equation (2.76) is cubic in $\frac{3}{4}\sigma_p^2$ and quadratic in $\frac{3}{4}\sigma_v^2$ and so cannot be solved analytically. The equation may be written as

$$\begin{aligned}\hat{\sigma}_p^3 A_1 &+ \hat{\sigma}_p^3\hat{\sigma}_v B_1 + \hat{\sigma}_p^2\hat{\sigma}_v^2 C_1 + \hat{\sigma}_p^2\hat{\sigma}_v D_1 + \hat{\sigma}_p^2 E_1 + \hat{\sigma}_p\hat{\sigma}_v^2 F_1 \\ &+ \hat{\sigma}_p\hat{\sigma}_v G_1 + \hat{\sigma}_p H_1 + \hat{\sigma}_v^2 J_1 + \hat{\sigma}_v K_1 \\ &+ a_1 b_1 c_1 - a_1^2 d_1 - c_1^2 = 0 \qquad (2.77)\end{aligned}$$

where $\hat{\sigma}_p = \frac{3}{4}\sigma_p^2$, $\hat{\sigma}_v = \frac{3}{4}\sigma_v^2$ and coefficients A_1 to K_1 are given in Appendix C.1.

It thus seems reasonable to extend the idea of Routh's discriminant to a non-linear, effective Routh's discriminant for the system under consideration. To demonstrate some of the results obtainable from (2.77) it is easier to consider the system with non-linearities in one variable, say v. In this case,

$$a_{3p} = b_{3p} = c_{3p} = d_{3p} = c_{3vp} = d_{3vp} = 0 \qquad (2.78)$$

and (2.77) becomes a quadratic in $(\frac{3}{4}\sigma_v^2)$:-

$$\begin{aligned}(\tfrac{3}{4}\sigma_v^2)^2[a_1 b_{3v} c_{3v} - c_{3v}^2] + (\tfrac{3}{4}\sigma_v^2)[a_1 b_1 c_{3v} + a_1 b_{3v} c_1 - a_1^2 d_{3v} - c_1 c_{3v} - c_1 c_{3v}] \\ + a_1 b_1 c_1 - a_1^2 d_1 - c_1^2 = 0 \qquad (2.79)\end{aligned}$$

This gives σ_v^2 as either positive, negative or complex, of which only the first possibility is physically meaningful, i.e.

$$\sigma^2_{v_{1,2}} = -\frac{f \pm \sqrt{f^2 - 2eg}}{2e} \qquad (2.80)$$

where $e = \frac{9}{16}(a_1 b_{3v} c_{3v} - c_{3v}^2)$

$$f = \tfrac{3}{4}(a_1 b_1 c_{3v} + a_1 b_{3v} c_1 - a_1^2 d_{3v} - 2c_1 c_{3v})$$

and $g = a_1 b_1 c_1 - a_1^2 d_1 - c_1^2$

Associated with each positive σ_v^2 is a frequency which can be obtained by putting $\lambda = 0$ in the stability quartic. In its general form, for non-linear v and p, the quartic becomes

$$(i\omega)^4+a^*(i\omega)^3+b^*(i\omega)^2+c^*(i\omega)+d^* = 0 \qquad (2.81)$$

or $$\omega^4 - b^*\omega^2 + d^* = 0 \qquad (2.82)$$

and $$-a^*\omega^3 + c^*\omega = 0 \qquad (2.83)$$

Thus, the frequency, ω, is given by, from (2.82):-

$$\omega_{12}^2 = \frac{b^* \pm \sqrt{(b^*)^2 - 4d^*}}{2} \qquad (2.84)$$

$$\simeq b^* \quad \text{for small } d^* \qquad (2.85)$$

or, from (2.83):-

$$\omega_{12}^2 = \frac{c^*}{a^*} \qquad (2.86)$$

provided $\omega \neq 0$. Expressions (2.84) and (2.86) simplify when considering non-linear v or p characteristics alone, e.g. when $a_{3p} = 0$; then $a^* = a_1$.

For non-linear v characteristics, the σ_v obtained using the '+' sign in (2.80) is associated with the frequency, ω, obtained using the '+' sign in (2.84) and similarly for the '-' sign expressions. The frequencies can also be obtained from (2.86). It may be noted that the substitution of (2.86) back into (2.82) yields the condition $R^* = 0$ again (2.76). An alternative expression for frequency may be obtained by solving (2.86) for σ_v^2 and substituting this in (2.79), resulting in a biquadratic in ω.

From (2.84) or (2.86) it may be seen that ω^2 can be positive or negative depending on the magnitude of the square root term in (2.84) and the signs of c*, a* in (2.86). The combination of positive σ_v^2 and positive ω^2 indicates a limit cycle and this has been considered in the past[26] to represent wing rock. The combination of positive σ_v^2 and negative ω^2 is indicative of a real root divergence, with σ_v now being the critical amplitude at which divergence occurs. This is physically reasonable in that in a solution of the form $Ae^{i\omega t}$, a negative ω^2 means $\pm i\omega$ used in the response gives one root as an exponential divergence. The divergence case may also be derived by considering $d^* = 0$ in equation (2.75). This is by analogy with the linear system (e.g. Ref.62,p.118) where $d_1 = 0$ is indicative of zero damping of a real root. In the case of (2.75) with $\mu = 0$ there is no oscillatory solution, so $d^* = 0$ is the condition for a real root with zero damping.

For non-linearities in p alone, (2.77) is a bicubic in σ_p which can be used to give limit cycle amplitudes and frequencies,or critical amplitudes at divergence. The full expression for (2.77) in this case is given in the next section.

2.4.2.5 Solutions for Limit Cycles

It was noted in §2.4.2.4. that for non-linearities in v only, equation (2.75) reduced to (2.79) which enabled limit cycle amplitudes and frequencies to be calculated. Similarly for non-linear p characteristics, i.e. $b_{3v}=c_{3v}=d_{3v}=c_{3vp}=d_{3vp}=0$, (2.77) gives the bicubic in σ_p referred to above, from which limit cycle amplitudes in p can be derived:

$$(a_1+\tfrac{3}{4}a_{3p}\sigma_p^2)(b_1+\tfrac{3}{4}b_{3p}\sigma_p^2)(c_1+\tfrac{3}{4}c_{3p}\sigma_p^2)-(a_1+\tfrac{3}{4}a_{3p}\sigma_p^2)^2(d_1+\tfrac{3}{4}d_{3p}\sigma_p^2)$$

$$-(c_1+\tfrac{3}{4}c_{3p}\sigma_p^2) \quad = \quad 0 \qquad (2.87)$$

or

$$(\sigma_p^2)^3A_2+(\sigma_p^2)^2B_2+(\sigma_p^2)C_2+a_1b_1c_1-a_1^2d_1-c_1^2 \quad = \quad 0 \qquad (2.88)$$

The coefficients A_2, B_2 and C_2 are given in full in Appendix C.2. Once σ_p has been found, corresponding frequencies can be obtained from the general equations (2.84) or (2.86). Comments regarding limit cycles and divergences will apply as for the non-linear v case discussed in §2.4.2.4.

The B.T.S.technique thus gives expressions for amplitudes and frequencies of limit cycles for cases of non-linear v or p characteristics and results in Chapters 3 and 5 show the method works well in these cases.

However, the equations of motion with non-linear v and p characteristics present simultaneously would be expected to give a better representation of the aircraft characteristics and it was one of the aims of the current work to apply the B.T.S. technique to the equations of motion in such cases. The resulting equation for the amplitudes of the p and v oscillations is as given in (2.77). This could be solved for σ_p given σ_v and vice versa, with frequencies again calculated using (2.84) or (2.86).

Explicit equations for σ_p and σ_v can be derived after some lengthy algebra which is best illustrated by considering simplified versions of (2.64) and (2.76), where the gravitational term is ignored (as must be done for responses about some non-zero equilibrium states). In this case, $d^* = 0$, and (2.76) becomes:

$$\tfrac{9}{16}\sigma_p{}^4(a_{3p}b_{3p})+\tfrac{9}{16}\sigma_p{}^2\sigma_v{}^2(a_{3p}b_{3v}-c_{3vp})+\tfrac{3}{4}\sigma_v{}^2(a_1b_{3v}-c_{3v})$$

$$+\tfrac{3}{4}\sigma_p{}^2(a_1b_{3p}+a_{3p}b_1-c_{3p})+a_1b_1-c_1 \quad = \quad 0 \qquad (2.89)$$

Another relationship between σ_p and σ_v can be obtained from (2.64):

$$\begin{bmatrix} \mu-y'_v & -V_e\sin\alpha_e & V_e\cos\alpha_e \\ -\ell'_{v1}-\tfrac{3}{4}\ell'_{v3}\sigma_v{}^2 & \mu-\ell'_{p1}-\tfrac{3}{4}\ell'_{p3}\sigma_p{}^2 & \ell'_r \\ -n'_{v1}-\tfrac{3}{4}n'_{v3}\sigma_v{}^2 & -n'_{p1}-\tfrac{3}{4}n'_{p3}\sigma_p{}^2 & \mu-n'_r \end{bmatrix} \begin{bmatrix} \sigma_v \\ \sigma_p e^{i\varepsilon_p} \\ \sigma_r e^{i\varepsilon_r} \end{bmatrix} = \underline{0} \qquad (2.90)$$

The first two equations of (2.90) are:

$$(\mu-y'_v)\sigma_v - V_e\sin\alpha_e\,\sigma_p e^{i\varepsilon_p} + V_e\cos\alpha_e\sigma_r e^{i\varepsilon_r} = 0 \qquad (2.91)$$

$$(-\ell'_{v1}-\tfrac{3}{4}\ell'_{v3}\sigma_v{}^2)\sigma_v + (\mu-\ell'_{p1}-\tfrac{3}{4}\ell'_{p1}\sigma_p{}^2)\sigma_p e^{i\varepsilon_p} - \ell'_r\sigma_r e^{i\varepsilon_r} = 0 \qquad (2.92)$$

With $\mu = i\omega_L$ (suffix 'L' denoting limit cycle value), elimination of $\sigma_r e^{i\varepsilon_r}$ between (2.91) and (2.92) and separation of real and imaginary parts gives:

$$\sigma_p{}^2[\{\ell'_v V_e\sin\alpha_e+V_e\cos\alpha_e(\ell'_{p1}+\tfrac{3}{4}\ell'_{p3}\sigma_p{}^2)\}^2+V_e{}^2\cos^2\alpha_e\omega_L{}^2]$$

$$= \sigma_v{}^2[\{y'_v\ell'_r+V_e\cos\alpha_e(\ell'_{v1}+\tfrac{3}{4}\ell'_{v3}\sigma_v{}^2)\}^2+\ell'_r{}^2\omega_L{}^2] \qquad (2.93)$$

With $d^* = 0$, (2.84) gives

$$\omega_L{}^2 = b^*$$

$$= b_1 + \tfrac{3}{4}(b_{3p}\sigma_p{}^2 + b_{3v}\sigma_v{}^2)$$

Thus, (2.93) becomes:

$$\sigma_p{}^2[\{\ell'_v V_e\sin\alpha_e+V_e\cos\alpha_e(\ell'_{p1}+\tfrac{3}{4}\ell'_{p3}\sigma_p{}^2)\}^2+V_e^2\cos^2\alpha_e(b_1+\tfrac{3}{4}(b_{3p}\sigma_p{}^2+b_{3v}\sigma_v{}^2))]$$

$$= \sigma_v{}^2[\{y'_v\ell'_r+V_e\cos\alpha_e(\ell'_{v1}+\tfrac{3}{4}\ell'_{v3}\sigma_v{}^2)\}^2+\ell'_r{}^2(b_1+\tfrac{3}{4}(b_{3p}\sigma_p{}^2+b_{3v}\sigma_v{}^2))] \qquad (2.94)$$

which is sextic in σ_v and σ_p.

In principle, (2.89) and (2.94) can be solved for σ_p and σ_v. From (2.89) an expression for σ_v^2 can be derived which is $O(\sigma_p^4)$ and on substitution in (2.94), would give a bisextic equation, $O(\sigma_p^{12})$.

Rather than solve explicitly for σ_p and σ_v in this way, initially equation (2.89) was used to predict σ_p given σ_v and vice versa, using amplitudes from computer simulations, to see if correct limit cycle amplitudes were predicted when using the full expression. If good results were obtained it would then be worth obtaining explicit formulations for σ_v and σ_p but if results were not good it would indicate a limitation of the method. With the complexity of the explicit expressions for σ_p and σ_v, the physical basis for the expressions becomes obscure. The expression for σ_v indicated above from (2.89) would give an $O(\sigma_p^{12})$ equation as explained; if σ_v was also included the equation would be higher order.

Results using the above ideas are presented in Chapters 3 and 5.

2.4.2.6 Rate of Growth to Limit Cycles

Separating a non-linear stability quartic, such as (2.67), into real and imaginary parts and eliminating ω, gives an equation in λ and σ. The local damping factor, $\lambda(\sigma)$, can then be evaluated as a function of σ up to the limit cycle amplitude, Θ. Quadrature can be used to give an amplitude envelope as a function of time to compare with numerical solutions of the equations.

For non-linearities in v and p, equations (2.65) and (2.74) are the two possible expressions for the stability quartic depending on whether or not μ is regarded as an operator in the expansion of the equations of motion determinant. Simplifying these quartics by neglecting the non-linearities in p gives equations (2.67) and (2.66) for the "$(\lambda+i\omega)$" and "$(3\lambda+i\omega)$" formulations respectively. Similarly, neglecting the v non-linearities in (2.74) gives

$$
\begin{aligned}
(\lambda+i\omega) &+a_1(\lambda+i\omega)^3+\tfrac{3}{4}a_{3p}\sigma_p^2(3\lambda+i\omega)^3 \\
&+b_1(\lambda+i\omega)^2+\tfrac{3}{4}b_{3p}\sigma_p^2(3\lambda+i\omega)^2 \\
&+c_1(\lambda+i\omega) +\tfrac{3}{4}c_{3p}\sigma_p^2(3\lambda+i\omega)+d_1+\tfrac{3}{4}d_{3p}\sigma_p^2 \;=\; 0 \qquad (2.95)
\end{aligned}
$$

for the $(3\lambda+i\omega)$ formulation. The $(\lambda+i\omega)$ formulation from (2.65) is as (2.95) but with $(3\lambda+i\omega)$ replaced by $(\lambda+i\omega)$.

Expressions for local damping, $\lambda(\sigma)$ can be derived as shown in the following sections.

2.4.2.6.1 Non-linear Sideslip Characteristics

Separating (2.67) into real and imaginary parts gives:

$$\omega^4-\omega^2\{b_1+\tfrac{3}{4}b_{3v}\sigma_v^2+3\lambda a_1+6\lambda^2\}+\{d_1+\tfrac{3}{4}d_{3v}\sigma_v^2+\lambda(c_1+\tfrac{3}{4}c_{3v}\sigma_v^2)$$

$$+\lambda^2(b_1+\tfrac{3}{4}b_{3v}\sigma_v^2)+\lambda^3a_1+\lambda^4\} \quad = \quad 0 \qquad (2.96)$$

and

$$\omega^3\{a_1+4\lambda\} \;=\; \omega\{c_1+\tfrac{3}{4}c_{3v}\sigma_v^2+2\lambda(b_1+\tfrac{3}{4}b_{3v}\sigma_v^2)+3\lambda^2a_1+4\lambda^3\} \qquad (2.97)$$

Provided $\omega \neq 0$, then (2.97) gives an expression for ω^2 which may be substituted in (2.96) to give a sextic equation in λ which is biquadratic in σ_v:

$$64\lambda^6+96a_1\lambda^5+A_{4v}\lambda^4+A_{3v}\lambda^3+A_{2v}\lambda^2+A_{1v}\lambda$$

$$-(c_1+\tfrac{3}{4}c_{3v}\sigma_v^2)^2+a_1(b_1+\tfrac{3}{4}b_{3v}\sigma_v^2)(c_1+\tfrac{3}{4}c_{3v}\sigma_v^2)-a_1^2(d_1+\tfrac{3}{4}d_{3v}\sigma_v^2) = 0 \qquad (2.98)$$

The coefficients A_{1v} to A_{4v} are given in Appendix C.3.1 and are functions of σ_v.

Similarly for (2.66), using $(3\lambda+i\omega)$ terms, separating into real and imaginary parts gives:

$$\omega^4-\omega^2\{b_1+\tfrac{3}{4}b_{3v}\sigma_v^2+3\lambda a_1+6\lambda^2\}+\{d_1+\tfrac{3}{4}d_{3v}\sigma_v^2+\lambda(c_1+\tfrac{9}{4}c_{3v}\sigma_v^2)$$

$$+\lambda^2(b_1+\tfrac{27}{4}b_{3v}\sigma_v^2)+\lambda^3a_1+\lambda^4\} \quad = \quad 0 \qquad (2.99)$$

and

$$\omega^3\{a_1+4\lambda\} \;=\; \omega\{c_1+\tfrac{3}{4}c_{3v}\sigma_v^2+2\lambda(b_1+\tfrac{9}{4}b_{3v}\sigma_v^2)+3\lambda^2a_1+4\lambda^3\} \qquad (2.100)$$

Elimination of ω^2, provided $\omega \neq 0$, gives a similar equation to (2.98):

$$64\lambda^6+96a_1\lambda^5+B_{4v}\lambda^4+B_{3v}\lambda^3+B_{2v}\lambda^2+B_{1v}\lambda-(c_1+\tfrac{3}{4}c_{3v}\sigma_v^2)^2$$

$$+a_1(b_1+\tfrac{3}{4}b_{3v}\sigma_v^2)(c_1+\tfrac{3}{4}c_{3v}\sigma_v^2)-a_1^2(d_1+\tfrac{3}{4}d_{3v}\sigma_v^2) \;=\; 0 \qquad (2.101)$$

Coefficients B_{1v} to B_{4v} are again given in Appendix C.3.1.

2.4.2.6.2 Non-linear Roll Rate Characteristics

Starting with the quartic given in (2.95), but using $(\lambda+i\omega)$ in place of the $(3\lambda+i\omega)$ terms, separation into real and imaginary parts gives:

$$\omega^4-\omega^2\{b_1+\tfrac{3}{4}b_{3p}\sigma_p{}^2+3\lambda(a_1+\tfrac{3}{4}a_{3p}\sigma_p{}^2)+6\lambda^2\}+\{d_1+\tfrac{3}{4}d_{3p}\sigma_p{}^2+\lambda(c_1+\tfrac{3}{4}c_{3p}\sigma_p{}^2)$$
$$+\lambda^2(b_1+\tfrac{3}{4}b_{3p}\sigma_p{}^2)+\lambda^3(a_1+\tfrac{3}{4}a_{3p}\sigma_p{}^2)+\lambda^4\} = 0 \qquad (2.102)$$

and

$$\omega^3\{a_1+4\lambda+\tfrac{3}{4}a_{3p}\sigma_p{}^2\} = \omega\{c_1+\tfrac{3}{4}c_{3p}\sigma_p{}^2+2\lambda(b_1+\tfrac{3}{4}b_{3p}\sigma_p{}^2)$$
$$+3\lambda^2(a_1+\tfrac{3}{4}a_{3p}\sigma_p{}^2)+4\lambda^3\} \qquad (2.103)$$

As before, providing $\omega \neq 0$, an expression for ω^2 can be obtained from (2.103) and substituted in (2.102) to give a sextic in λ:

$$64\lambda^6+96(a_1+\tfrac{3}{4}a_{3p}\sigma_p{}^2)\lambda^5+A_{4p}\lambda^4+A_{3p}\lambda^3+A_{2p}\lambda^2+A_{1p}\lambda-(c_1+\tfrac{3}{4}c_{3p}\sigma_p{}^2)^2$$
$$+(a_1+\tfrac{3}{4}a_{3p}\sigma_p{}^2)(b_1+\tfrac{3}{4}b_{3p}\sigma_p{}^2)(c_1+\tfrac{3}{4}c_{3p}\sigma_p{}^2)$$
$$-(a_1+\tfrac{3}{4}a_{3p}\sigma_p{}^2)^2(d_1+\tfrac{3}{4}d_{3p}\sigma_p{}^2) = 0 \qquad (2.104)$$

This is bicubic in σ_p and so cannot be solved analytically. Coefficients A_{1p} to A_{4p} are given in full in Appendix C.3.2.

Using the quartic as given in (2.95) with $(3\lambda+i\omega)$ terms, separation into real and imaginary parts gives:

$$\omega^4-\omega^2\{b_1+\tfrac{3}{4}b_{3p}\sigma_p{}^2+3\lambda(a_1+\tfrac{9}{4}a_{3p}\sigma_p{}^2)+6\lambda^2\}+\{d_1+\tfrac{3}{4}d_{3p}\sigma_p{}^2+\lambda(c_1+c_{3p}\tfrac{9}{4}\sigma_p{}^2)$$
$$+\lambda^2(b_1+\tfrac{27}{4}b_{3p}\sigma_p{}^2)+\lambda^3(a_1+\tfrac{3}{4}.27a_{3p}\sigma_p{}^2)+\lambda^4\} = 0 \qquad (2.105)$$

and

$$\omega^3\{a_1+4\lambda+\tfrac{3}{4}a_{3p}\sigma_p{}^2\} = \omega\{c_1+\tfrac{3}{4}c_{3p}\sigma_p{}^2+2\lambda(b_1+\tfrac{9}{4}b_{3p}\sigma_p{}^2)$$
$$+3\lambda^2(a_1+\tfrac{27}{4}a_{3p}\sigma_p{}^2)+4\lambda^3\} \qquad (2.106)$$

With the usual restriction, $\omega \neq 0$, (2.105) and (2.106) may be combined to give a sextic in λ:-

$$64\lambda^6 + B_{5p}\lambda^5 + B_{4p}\lambda^4 + B_{3p}\lambda^3 + B_{2p}\lambda^2 + B_{1p}\lambda - (c_1 + \tfrac{3}{4}c_{3p}\sigma_p^2)^2$$

$$+(a_1 + \tfrac{3}{4}a_{3p}\sigma_p^2)(b_1 + \tfrac{3}{4}b_{3p}\sigma_p^2)(c_1 + \tfrac{3}{4}c_{3p}\sigma_p^2)$$

$$-(a_1 + \tfrac{3}{4}a_{3p}\sigma_p^2)^2(d_1 + \tfrac{3}{4}d_{3p}\sigma_p^2) = 0 \qquad (2.107)$$

Coefficients B_{1p} to B_{5p} are again given in Appendix C.3.2.

2.4.2.6.3. Solutions for Local Damping

Equations (2.98) and (2.101) are two equations expressing local damping as a function of amplitude for the lateral equations with non-linear v characteristics, while (2.104) and (2.107) are the corresponding equations when non-linearities in p are present. These equations can be solved as functions of amplitude, σ, up to the limit cycle amplitude, Θ, and comparisons can then be made to decide which of the expressions (using $(\lambda+i\omega)$ or $(3\lambda+i\omega)$ terms) give the better results for the rate of growth to limit cycle amplitudes. (In the next chapter and Chapter 5, when comparing the damping factors from the two kinds of expression, the formulations for λ will be referred to as "$(\lambda+i\omega)$" and "$(3\lambda+i\omega)$", to indicate the expressions ((2.98), (2.104) and (2.101), (2.107) respectively) from which they were derived).

Apart from comparisons of λ as a function of amplitude it is also possible to use the damping factors to build up a time history of the amplitude envelope for comparison with the 'exact' computer solution of the equations of motion.

2.4.3 Global Stability (Local Linearisation)

2.4.3.1 General

A number of researchers have applied local linearisation techniques to the study of high angle of attack phenomena, e.g. Hreha and Lutze[33,63] performed a linearised analysis of spin dynamics using coupled longitudinal and lateral equations. The equations of motion are linearised about a non-zero equilibrium state and stability roots are examined in the usual way. These techniques are also used for the HIRM in Chapters 5 and 6.

Johnston et al[64] and Kalviste[47] have shown that static aero-dynamic cross-coupling due to sideslip can have a significant effect on aircraft stability and control characteristics. Coefficients C_m, C_ℓ and C_n are given as functions of α as well as β, since at high angles of attack, sideslip is often non-zero. Linearising the equations with constant non-zero sideslip and angular rates, p_e, r_e and q_e, provides coupling between lateral and longitudinal motion. Thus for equilibrium conditions with high angles of attack and sideslip, a static

stability investigation (eigenvalue extraction) should strictly include both longitudinal and lateral equations. Initial work on the HIRM was performed using the lateral equations alone and, later, a combined longitudinal/lateral system was used to examine the effects of cross-coupling.

Mehra and co-workers[40,59] have presented linearisation techniques in terms of bifurcation analysis and a comparison of this formulation with the non-linear techniques described in the previous section has been made by Ross and Johnson[65]. An outline of the relationship between the techniques is given in the next section and some results comparing the techniques are given in Chapters 3 and 5.

2.4.3.2 Comparison of Local Linearisation and Non-linear Averaging

Consider the lateral equations of motion as given in (2.15) to (2.18) but omitting the g term and the non-linearities in p for simplicity. To examine linear stability, the following expressions

$$v = v_e + v' \tag{2.108}$$

$$p = p_e + p' \tag{2.109}$$

$$r = r_e + r' \tag{2.110}$$

(where ' indicates a perturbation quantity) are substituted in the small perturbation equations and the equilibrium equations subtracted. Assuming solutions of the form

$$v' = A_v e^{\mu t} \tag{2.111}$$

gives the stability polynomial,from expansion of the determinant of the equations:

$$\mu^3 + a_1\mu^2 + [b_1+3b_{3v}\bar{v}_e^2]\mu + c_1 + 3c_{3v}\bar{v}_e^2 = 0 \tag{2.112}$$

with $\mu = -k\pm i\nu$, where κ is the damping index and ν, frequency. The condition $k = 0$ indicates zero damping of the perturbation about the equilibrium state with critical amplitude, v_b, given by

$$c_1 + 3c_{3v}v_b^2 = 0 \tag{2.113}$$

for real roots with zero damping,

$$\text{or} \qquad a_1[b_1 + 3b_{3v}v_b^2] - [c_1 + 3c_{3v}v_b^2]^2 = 0 \qquad (2.114)$$

for complex roots with zero damping.

For the non-linear B.T.S. technique applied to non-zero equilibrium states, a solution of the form

$$v = \sigma_v \cos\phi + v_e \qquad (2.115)$$

is assumed (c.f. (2.44) for zero equilibrium states). Then for real roots with zero damping the critical amplitude at divergence is given by

$$c_1 + 3c_{3v}v_e^2 + \tfrac{3}{4}c_{3v}\sigma_c^2 = 0 \qquad (2.116)$$

and for limit cycles, the amplitude of the limit cycle is given by

$$a_1[b_1+3b_{3v}v_e^2+\tfrac{3}{4}b_{3v}\sigma_L^2]-[c_1+3c_{3v}v_e^2+\tfrac{3}{4}c_{3v}\sigma_L^2]= 0 \qquad (2.117)$$

Comparing (2.114) and (2.117) shows that there is a series of limit cycles about the current equilibrium state given by

$$3b_{3v}v_b^2 = 3b_{3v}v_e^2 + \tfrac{3}{4}b_{3v}\sigma_L^2$$

$$\text{or} \qquad v_b^2 = v_e^2 + \frac{\sigma_L^2}{4} \qquad (2.118)$$

So for each v_e below the critical v_b, the linear stability boundary, there is a limit cycle of amplitude, σ_L, where

$$\sigma_L = 2(v_b^2 - v_e^2)^{\frac{1}{2}} \qquad (2.119)$$

For zero controls input i.e. $v_e = 0$, then

$$v_b^2 = \frac{\sigma_{L_o}^2}{4} \qquad (2.120)$$

$$\sigma_{L_o} = 2v_b \qquad (2.121)$$

Thus there exists a relationship between the non-linear stability characteristics about non-zero equilibrium states and the linear stability boundaries. Chapters 3 and 5 show some results confirming relationship (2.118).

2.5 Computer Applications

Most of the work for this thesis has been aimed at computer based mathematical modelling of aircraft dynamics and the assessment of the models.

Initial work was performed using analogue techniques to solve the aircraft lateral equations of motion and predict responses, but by far the largest part of the work has been carried out using digital techniques, on VAX 11/780 and VAX 11/782 computers.

This section outlines the various programs developed for the thesis work. They are mainly based on the theoretical techniques described earlier in this chapter.

Chapter 6 includes details of 6 degree of freedom computer models which were developed towards the end of the work.

2.5.1 Analogue Simulation

Computing was carried out at the start of the project on a VIDAC 1224 analogue computer[66] at Cranfield College of Aeronautics, to follow up work described by Ross in Ref.26. The lateral equations of motion for the two combat aircraft described in Chapter 3 were programmed in the form:-

$$\dot{v} = wp - rV + \frac{Y_v}{m}v + g\phi \qquad (2.122)$$

$$\dot{p} = \frac{I_z}{I_xI_z-I_{xz}^2}[L_{v1}v+L_{v3}v^3+(L_{p1}+K_\xi p L_\xi)p+L_{p3}p^3+L_r r+L_\xi \xi+L_\zeta \zeta]$$

$$+ \frac{I_{xz}}{I_xI_z-I_{xz}^2}[N_{v1}v+N_{v3}v^3+(N_{p1}+K_\xi p N_\xi)p+N_r r+N_\xi \xi+N_\zeta \zeta] \qquad (2.123)$$

$$\dot{r} = \frac{I_x}{I_xI_z-I_{xz}^2}[N_{v1}v+N_{v3}v^3+(N_{p1}+K_\xi p N_\xi)p+N_r r+N_\xi \xi+N_\zeta \zeta]$$

$$+ \frac{I_{xz}}{I_xI_z-I_{xz}^2}[L_{v1}v+L_{v3}v^3+(L_{p1}+K_\xi p L_\xi)p+L_{p3}p^3+L_r r+L_\xi \xi+L_\zeta \zeta] \qquad (2.124)$$

$$\dot{\phi} = p \qquad (2.125)$$

2.5.2 Digital Simulation SIMUL

2.5.2.1 Introduction

This program started as a digital implementation of the analogue simulation equations (2.122) to (2.125) but was quickly developed to include more features.

The equations as used in the ultimate version of the program were:

$$\dot{v} = V_e \sin\alpha_e p - rV_e \cos\alpha_e + y'_v v + g_3 \sin\phi + g_2 \sin\psi \qquad (2.126)$$

$$\dot{p} = \ell'_{v_1} v + \ell'_{v_3} v^3 + \ell'_{p_1} p + \ell'_{p_3} p^3 + \ell'_r r + \ell'_\xi \xi + \ell'_\zeta \zeta \qquad (2.127)$$

$$\dot{r} = n'_{v_1} v + n'_{v_3} v^3 + n'_{p_1} p + n'_{p_3} p^3 + n'_r r + n'_\xi \xi + n'_\zeta \zeta \qquad (2.128)$$

$$\dot{\phi} = p \qquad (2.129)$$

$$\dot{\psi} = r \qquad (2.130)$$

The overall layout of the program is shown in Fig.2.4. The program was written in VAX-11 FORTRAN[67,68] which is based on FORTRAN 77. Versions of the program have successfully been run on VAX 11/780 and 11/782 computers and an HP 1000 machine. On the VAX the program can be run interactively or in the batch stream

2.5.2.2 Applications Software

The Numerical Algorithms Group (NAG) mathematical subroutine library provides two of the integration routines used in the program (a Runge-Kutta-Merson method and an Adams-Bashforth predictor-corrector method) and are described in Refs.69 and 70. GINOGRAF[71] is a library of subroutines used in conjunction with GINO-F[72,73] to produce the graphs for the program on the VAX machines. On the HP 1000, a local graph plotting routine was used for graphical output.

2.5.2.3 Program Description

(i) Initialisation

During the input stage, constants related to the atmosphere and aircraft are read in as well as data for the integration and graphical output routines (axis limits). These constants are:

g	acceleration due to gravity	(m/s^2)
ρ	atmospheric density	(kg/m^3)
m	aircraft mass	(kg)
I_x, I_z, I_{zx}	aircraft inertias	$(kg.m^2)$
S_W	wing area	(m^2)
s	semispan	(m)
$K_{\xi p}, K_{\zeta r}$	feedback gearings	
DELT	integration step length	

TOL	exponent for tolerance controlling error in integration (tolerance = 10^{-TOL})	
TIMEND	end time for simulation	(secs)

Initial conditions about which the response is calculated along with derivatives and control inputs, form the rest of the input data:

Motion variables:

V_o	speed	(m/s)
α_o	angle of attack	(degrees)
$\bar{v}_o$	sideslip velocity / V_o	-
p_o	roll rate	(radians/sec)
r_o	yaw rate	(radians/sec)
Θ_o	pitch attitude	(degrees)
ϕ_o	bank angle	(degrees)

Control inputs:

ξ_T, ζ	initial control angles	(radians)

$\left.\begin{matrix}\xi_{T_1}, t_{\xi_1}, t_{\xi_2} \\ \zeta_1, t_{\zeta_1}, t_{\zeta_2}\end{matrix}\right\}$ new control angle between times t_1 and t_2

Derivatives (read in, in notation of Ref.45):

L_{v_1}	L_{v_3}	N_{v_1}	N_{v_3}	Y_v
$\breve{L}_{p_1}$	$\breve{L}_{p_3}$	$\breve{N}_{p_1}$	$\breve{N}_{p_3}$	
$\breve{L}_{p_{1R}}$	$\breve{L}_{p_{3R}}$	$\breve{N}_{p_{1R}}$	$\breve{N}_{p_{3R}}$	
$\breve{L}_r$		$\breve{N}_r$		
$\breve{L}_\xi$		$\breve{N}_\xi$		
$\breve{L}_\zeta$		$\breve{N}_\zeta$		$\breve{Y}_\zeta$

(ii) Integration

After initialisation, the equations of motion are integrated. Subroutine FCN contains the equations (2.126) to (2.130) which are used at each stage in the integration. A table look up function was incorporated to enable the program to use experimental data and look up functions will be mentioned again in Chapter 6 with reference to the six degree of freedom simulation.

(iii) OUTput

Subroutine OUT controls the printing of the results of the simulation and allows the user to vary the output time interval. At each step in the integration the current values of

the response variables are stored by OUT ready for plotting by subroutine DRFGS.

(iv) EVLAM

This subroutine evaluates local damping factor, λ, and frequency, ω, as a function of response variable amplitudes $\bar{v}(= v/V)$ and p, for comparison with averaging results. Data used is that stored in the arrays for plotting via subroutine DRFGS. Damping factor, λ, is evaluated numerically using:

(a) a formula given by Beecham and Titchener[31] using the peak values of 3 successive half cycles

(b) an approximation, using a linear formula, fitting the envelope of oscillation locally by

$$\sigma = Ae^{\lambda t}$$

(v) Fast Fourier Transform (F.F.T.)

Subroutine FFT was used in the program when operated at Farnborough on an HP 1000 computer and computes a Fast Fourier Transform of the simulation response.

2.5.3 Digital Program ROUTH

2.5.3.1 Introduction

Program 'ROUTH' was originally developed to evaluate the terms a*, b*, c* and d* in the non-linear Routhian discriminant, R*, and solve a simple form of the equation, R* = 0 (equation 2.76). In its definitive form, the program evaluated the above plus various linear stability parameters (linear Routh's discriminant and roots of the lateral stability quartic), solved R* = 0 in a number of forms for different non-linearities and evaluated rates of growth to limit cycles. The program was one of the main tools used in investigating the various applications of the Beecham-Titchener-Simpson averaging technique described in §2.4.2. It was written in VAX-11 FORTRAN[67,68] and was run on VAX 11/780 and 11/782 machines.

2.5.3.2 Applications Software

The Numerical Algorithms Group mathematical subroutine library provided routines for: (a) finding the roots of real polynomial equations which were formulated in ROUTH[74] and (b) numerical evaluation of definite integrals[75].

2.5.3.3 Program Description

The overall layout of the program is shown in Fig.2.5 and the rest of section 2.5.3 will describe in more detail the elements of the program shown in this figure.

(i) Initialisation

The initialisation segment uses much the same input data as described for SIMUL in §2.5.2.3 except for those items specific to the integration routines in SIMUL. In particular, aircraft data, flight conditions and lateral derivatives (in the notation of Ref.45) are read in. For use in solving the full R* = O equation, (2.89), with non-linear v and p characteristics, limit cycle amplitudes in $\bar{v}$ and p are read in as VLIM and PLIM.

Concise derivatives are then formed as defined in Appendix A.3.

(ii) Equilibrium States

If non-zero rudder, ζ, and asymmetric tail, ξ_T, angles are read in, this segment of the program calculates the resultant equilibrium state in terms of $\bar{v}_e$, p_e and r_e. Equations (2.15) to (2.19) are used in calculating the required states, defined by $\dot{v} = \dot{p} = \dot{r} = O$. For solution of the equations algebraically, the g terms in (2.15) were neglected as were the non-linear p terms. With the term $y'_\zeta\zeta$ added to the sideforce $y'_v v$ in (2.15) and using ξ_o and ζ_o for the control settings, the following cubic equation in equilibrium sideslip is derived:-

$$
\begin{aligned}
&v_e^3(V_e\sin\alpha_e(n'_{v_3}\ell'_r-\ell'_{v_3}n'_r)+V_e\cos\alpha_e(n'_{v_3}\ell'_p-\ell'_{v_3}n'_p))\\
&+ v_e(y'_v(\ell'_p n'_r-n'_p\ell'_r)+V_e\sin\alpha_e(n'_v\ell'_r-\ell'_v n'_r)-V_e\cos\alpha_e(\ell'_v n'_p-n'_v\ell'_p))\\
&+ V_e\sin\alpha_e((n'_\xi\ell'_r-\ell'_\xi n'_r)\xi_o-(\ell'_\zeta n'_r-n'_\zeta\ell'_r)\zeta_o-V_e\cos\alpha_e((\ell'_\xi n'_p-n'_\xi\ell'_p)\xi_o\\
&- (n_\zeta\ell_p-\ell_\zeta n_p)\zeta_o)+y_\zeta\zeta_o \quad = \quad O \qquad (2.131)
\end{aligned}
$$

From the solution of this equation, using a NAG routine (Ref.74), the equilibrium roll and yaw rates are also derived:

$$
p_e = \frac{-[\ell'_{v_3}v_e^3+(\ell'_v+\frac{\ell'_r y'_v\sec\alpha_e}{V})v_e+\ell'_r y'_\zeta\zeta_o\sec\alpha_e+\ell'_\xi\xi_o+\ell'_\zeta\zeta_o]}{\ell'_p+\ell'_r\tan\alpha_e} \qquad (2.132)
$$

$$
r_e = y'_v\frac{v_e}{V}\sec\alpha_e + p_e\tan\alpha_e + y'_\zeta\frac{\zeta_o}{V}\sec\alpha_e \qquad (2.133)
$$

(iii) Routh's Discriminant and Lateral Stability Quartic

The terms a_1, a_3p, b_1, b_3p etc. in the lateral stability quartic shown in equation (2.65) are next evaluated. Appendix B gives the definitions of these terms and from them the

linear Routh's discriminant is evaluated, equation (2.28). Roots of the linear stability quartic are calculated, again using the NAG routine described in Ref.74.

(iv) Limit Cycle Amplitudes and Frequencies

Sections labelled 1, 2, 3 and 4 in Fig.2.5 indicate segments in ROUTH which evaluate limit cycle amplitudes and frequencies (if they exist) for various non-linear aerodynamic characteristics.

First of all, for cubic non-linearities sideslip alone, the equation for limit cycle sideslip amplitude, equation (2.79), is solved and for each amplitude the corresponding frequency is evaluated using equations (2.84) and (2.86).

For non-linearities in roll rate characteristics alone, subroutine PLIMIT is called to solve equations (2.88), a bicubic in roll-rate amplitude, using the usual NAG root solving routine[74]. Again frequencies are calculated using the relevant forms of (2.84) and (2.86).

Finally, for combined non-linear sideslip and roll rate characteristics, subroutine COMB is called to evaluate the appropriate amplitudes. Using a measured limit cycle amplitude in roll rate (if it exists), PLIM, equation (2.89) is solved to give the associated sideslip amplitude. Then the measured limit cycle amplitude in sideslip, VLIM, is used in a similar way to predict the roll rate amplitude. Frequencies are calculated in subroutine FREQ using the full forms of expressions (2.84) and (2.86).

(v) Rate of Growth to Limit Cycles

If measured limit cycle amplitudes for non-linear sideslip or roll rate characteristics have been input to ROUTH, subroutine RATE is now called to solve equation (2.65) as a function of either σ_v or σ_p up to the measured limit cycle amplitude. Using $\mu = \lambda + i\omega$, this gives damping factor, λ, as a function of σ_v or σ_p. The NAG root solving routine is again used in RATE and in the remaining subroutines called from RATE.

The "$(3\lambda+i\omega)$" forms for λ as a function of σ are evaluated in subroutines RATE3V, for non-linear sideslip, and RATE3P, for non-linear roll rate. These routines solve sextics in λ, both "$(\lambda+i\omega)$" forms (equations (2.98) and (2.104)) and "$(3\lambda+i\omega)$" forms (equations (2.101) and (2.107)).

In order to compare the two forms of λ for each non-linearity, with simulation results, without estimating λ from the simulation, time histories of the amplitude envelopes up to limit cycle are calculated in RATE3V and RATE3P. The damping factor is defined as

$$\lambda = \frac{\dot{\sigma}}{\sigma}$$

i.e. $\lambda = \frac{1}{\sigma}\frac{d\sigma}{dt}$

Thus $\int_{t_1}^{t_2} dt = \int_{\sigma_o}^{\Theta} \frac{d\sigma}{\lambda\sigma}$ (2.134)

$= T_L$ where T_L is the time for the amplitude of the oscillation to grow from σ_o to the final value, Θ.

Subroutines RATE3V and RATE3P store $\lambda\sigma$ as a function of σ for the two forms of λ and then use a NAG quadrature routine[75] to evaluate the definite integral in (2.134), between an initial non-zero amplitude and amplitudes up to Θ. Time histories can then be plotted for direct comparison with simulation predictions.

2.5.4 Digital Program ROOTS

This program evaluates the stability roots, eigenvectors and various measures of frequency and damping for the lateral modes of an aircraft. A full description of the program can be found in Ref.76.

The major part of ROOTS is a subroutine EIGNP[77] which is used, with its subsidiaries, to calculate all the eigenvalues and eigenvectors of a real general matrix. Alternative routines are available in the NAG Library.

ROOTS was used on VAX 11/780 and 782 computers as well as an HP 1000 at the Royal Aircraft Establishment.

2.5.5 Fast Fourier Transform Subroutine

This subroutine[78,79] was used at the Royal Aircraft Establishment in conjunction with SIMUL to analyse lateral responses. It was used on an HP 1000 computer and gave output of normalised response variable amplitude against frequency. Typical output is shown in Chapter 3.

CHAPTER 3

APPLICATIONS TO TYPICAL COMBAT AIRCRAFT

3.1 Introduction

In this chapter some of the techniques described in Chapter 2 will be applied to two typical combat aircraft which have already been used as the basis for previous stability and control work at the R.A.E.

Aircraft A is the Gnat trainer aircraft and is known to exhibit wing rock oscillations under certain high angle of attack conditions. A linear analysis of dutch roll and wing rock flight test records for the Gnat is contained in Ref.17. The onset of wing rock in this aircraft is shown to be due to the lack of dutch roll damping, which arises from the loss in damping-in-roll at high angles of attack. A useful feature of the Gnat flight tests was the ability to fly with and without wing mounted fuel tanks. This meant that effects of configuration on wing rock and dutch roll characteristics could be investigated. A non-linear analogue simulation of the Gnat was set up using equations (2.122) to (2.125) with $K_{\xi p} = 0 = \check{L}_{p3}$ and some results simulating wing rock were achieved.

Aircraft B is a current generation fighter aircraft and again exhibits wing rock at high angles of attack. This aircraft has been used as the basis for a number of investigations in recent years[26,65] and initial work for this thesis, looking at various techniques for stability and response analysis, concentrated on this aircraft.

For both aircraft, non-linearities in $C_\ell(\beta)$ and $C_n(\beta)$ were modelled, as aircraft with such non-linearities are known to exhibit wing rock. In the case of aircraft B, non-linearities in roll rate were also modelled, to simulate the effects of flow separation at high angles of attack.

3.2 Gnat Aircraft Simulation

Values for the derivatives used for the analogue computer simulation are given in Table 3.1.

A number of variations on the derivatives were tried, following work done at the RAE, to get a 'feel' for the non-linear responses and results are shown in Figs.3.1 to 3.6. Case 1 shows the basic aircraft with $\check{L}_{v3} = -8.8$ giving a $\bar{v}$ ($\simeq\beta$) limit cycle of amplitude 0.043 and a slightly distorted p limit cycle. Halving the directional stability derivative, $\check{N}_v$, to 0.0515 gives a $\bar{v}$ amplitude of

0.055 and the p response is now showing some distortion. Increasing the non-linear $\check{L}_{v3}$ term to -44 gives a much reduced $\theta_{\bar{v}}$, of 0.02rads. The effect of increasing yaw damping is shown in case 4 and leads to a damped oscillation, showing the close relationship of the motion to the dutch roll, in which $\check{N}_r$ plays a major part.

Increasing the linear part of the rolling moment due to sideslip characteristics, $\check{L}_{v1}$, means in case 5 (compared to case 1), the limit cycle amplitude is much greater ($\theta_{\bar{v}} = 0.07$), due to the decrease in lateral stability. The small value of $\check{L}_{v3}$ is not able to 'hold' the limit cycle until a bigger amplitude is reached than in case 1.

Finally in Fig.3.6 the effect of increase in both $\check{L}_{v1}$ and $\check{L}_{v3}$ is seen giving, not only an increase in $\theta_{\bar{v}}$ over case 1, but also a distinct second frequency appearing in the p trace. The low frequency is 0.476 Hz while the high frequency oscillation is 1.25 Hz, giving an almost 3:1 ratio, consistent with the cubic form of non-linearity in the rolling moment due to sideslip characteristics.

3.3 Combat Aircraft B Simulation

3.3.1 Analogue Simulation

As for the Gnat, initial work on aircraft B was performed on the College of Aeronautics analogue computer, dimensionless derivatives, as shown in equations (2.122) to (2.125), being used to provide suitable scalings for the computer. The derivatives, in Hopkin [45] notation, are shown in Table 3.2. Results showing the effect of a roll damper gearing on the response of aircraft B were given by Ross in Ref.26. Typical behaviour is shown in Figs.3.7 to 3.10, which show responses obtained at Cranfield. The basic non-linear sideslip case considered, has softening spring characteristics for the rolling moment and stiffening spring characteristics for the yawing moment.

Fig.3.7 shows the basic limit cycle response with the non-linear sideslip characteristics and Fig.3.8 illustrates the critical amplitude of $\bar{v}$ for divergent response. Limit cycles were obtainable for a limited range of values of $K_{\xi p}$, but for $K_{\xi p}$ above 0.0072 a damped response (for $\bar{v}_{ic} < \bar{v}_{crit}$) or oscillatory divergence ($\bar{v}_{ic} > \bar{v}_{crit}$) was obtained (Figs.3.9 and 3.10).

An important part of the analogue computer work was the effect of controls on responses. The relationship between the theoretical techniques of Mehra (bifurcation analysis) and Beecham-Titchener (non-linear averaging) has been explained in Chapter 2 and the current analogue simulations offered the means to verify the relationship on a real aircraft application.

For non-zero aileron and rudder angles, equilibrium conditions exist given by $\dot{\bar{v}} = \dot{p} = \dot{r} = 0$. The limit cycle

responses for 3 aileron inputs are shown in Figs.3.11 to 3.13 and show the new equilibrium conditions for the particular inputs used. Of most importance is the new amplitude of oscillation in $\bar{v}$ obtained with aileron application, as this provides a direct verification of the relationship between the theoretical techniques mentioned above. For the case of $K_{\xi_p} = 0$ (Fig.3.11) it will be noted that the non-zero equilibrium conditions were not held for very long and so difficulties were encountered in measuring steady-state amplitudes. As a general comment, the analogue computations provide a quick assessment of stability and response but they are less accurate than digital results when quantitative results are required. For this reason, the limit cycle responses to aileron input will not be analysed in detail here. Instead they will be mentioned again when the equivalent digital responses are examined (see section 3.3.5).

This section has shown the kind of responses and results obtainable using the analogue computer. Quantitative results can be extracted from them but it was felt that more progress would be made, in the quantitative assessments of the various ideas developed in Chapter 2, by turning to digital simulation. The analogue computer provided a very convenient method of assessing the response behaviour of the aircraft in parametric studies, but it is the digital computer programs that are considered next and from which most of the results for this thesis were obtained, both for combat aircraft B and for the HIRM. The next sections deal with the assessment of the non-linear averaging process and Mehra's bifurcation analysis as applied to combat aircraft B.

3.3.2 Non-linear Sideslip Characteristics

Using the basic aircraft case shown in Table 3.2 a digital simulation was set up. Results were checked against previous analogue solutions and RAE results. The build up to limit cycles for $K_{\xi_p} = 0$ is shown in Fig.3.14 (c.f. Fig.3.7 from analogue computer) along with FFT output, showing the frequency of oscillation, ω_L, to be 0.64 Hz, with a small peak coming at $3\,\omega_L$ for p and r, as might be expected.

For various values of K_{ξ_p}, program ROUTH was used to evaluate critical amplitudes and frequencies by solving the quadratic in σ_v resulting from R* = 0 (equation (2.79)). Both (2.84) and (2.86) were used to calculate corresponding frequencies for each amplitude and gave the same answers. The resulting stability boundary (as given originally by Ross in Ref.26) is shown in Fig.3.15 and shows the good agreement between the averaging technique and the simulation results, both for limit cycles and divergences.

3.3.2.1 Rate of Growth to Limit Cycles

The digital simulation program SIMUL calculates the local damping factor, λ, and frequency, ω, as a function of time using an approximate formula and the formula due to Beecham-Titchener given in Ref.31. These calculations of λ can be compared with local damping, calculated as functions of amplitude in the program ROUTH, using the original stability polynomial, with both $(\lambda+i\omega)$ and $(3\lambda+i\omega)$ terms, eqns. (2.98) and (2.101).

Results for the basic non-linear sideslip characteristics case are shown in Fig.3.16. The B.T. λ from the simulation is somewhat smaller than the theoretical values at small amplitude, where $(\lambda+i\omega)$ and $(3\lambda+i\omega)$ formulations for λ do not differ very much. As amplitude increases the difference between $(\lambda+i\omega)$ and $(3\lambda+i\omega)$ becomes more marked and it is noticeable that the simulation values show closer agreement with the $(\lambda+i\omega)$ formulation above an amplitude of 0.016.

In Fig.3.17 the results are presented in the form of a time history of the envelope of the oscillatory response in sideslip. The $(\lambda+i\omega)$ and $(3\lambda+i\omega)$ formulation envelopes were calculated using the quadrature routine in ROUTH, described in §2.5.3. Again it can be seen that the $(\lambda+i\omega)$ formulation gives the better agreement with the simulation results.

3.3.3 Non-linear Roll Rate Characteristics

Cubic non-linearities in rolling moment against roll rate characteristics of the form

$$C_\ell = \breve{L}_{p1}\left(\frac{pb}{V}\right) + \breve{L}_{p3}\left(\frac{pb}{2V}\right)^3$$

have been shown to give[26] limit cycle responses, with amplitude given by

$$\breve{L}_{p1} + \frac{3}{4}\breve{L}_{p3}\left(\frac{pb}{2V}\right)^2 = \text{const.}$$

for this aircraft. A number of different combinations of $\breve{L}_{p1}$ and $\breve{L}_{p3}$ were covered in the simulations, and 3 cases examined in the next section are detailed in Table 3.3

3.3.3.1 Rate of Growth to Limit Cycles

As for the non-linear sideslip characteristics, the main interest in examining the non-linear roll rate characteristics, was to compare the $(\lambda+i\omega)$ and $(3\lambda+i\omega)$ formulations for obtaining λ as functions of amplitude up to the limit cycle.

Fig.3.18 shows the build up to limit cycle for case 2 of Table 3.3. Superimposed on the $\bar{v}$ envelope is the envelope

of the p oscillation peaks, factored by the ratio of $\theta_{\bar{v}}$ to θ_p. This confirms an assumption, made in the theoretical analysis, that $\lambda_{\bar{v}} = \lambda_p$. It will be shown later that this is only true in the case of the equations with a non-linearity in one response variable. When two or more non-linearities are present, $\lambda_{\bar{v}} \neq \lambda_p$.

$\breve{L}_{p1}$ controls the rate of growth to the limit cycle and case 1 has a slower rate, while case 3 shows a fast rise to the limit cycle amplitude. These two cases are now examined in more detail.

Fig.3.19 shows λ_p against amplitude, for case 1, from digital simulation and from the ROUTH program. The solutions of the sextics in λ (equations (2.104) and (2.107) for $(\lambda+i\omega)$ and $(3\lambda+i\omega)$ respectively) show reasonably good agreement with the simulation values of λ. The difference between the $(\lambda+i\omega)$ and $(3\lambda+i\omega)$ formulations is now much smaller than for the non-linear sideslip cases due to the difference in the original stability equations, e.g. (2.95) and (2.66) for $(3\lambda+i\omega)$ formulations. The non-linear roll rate equations now contain an $a_{3p}\sigma_p^2$ term, which in turn means larger coefficients of λ^5 in the sextic equations (2.104) and (2.107).

Fig.3.20 shows λ_p against amplitude for case 3, again from simulation and non-linear theory. With the faster build up to the limit cycle amplitude, fewer peaks are available in the simulation to calculate λ_p and this may lead to inaccuracies.

As in section 3.3.2.1, to overcome any difficulties with calculations of λ from the simulations, the envelope of peaks from the simulations can be compared with envelopes calculated by quadrature from λ given by ROUTH.

Results are given in Fig.3.21 for cases 1 and 3. It is again apparent that there is now little difference in either case between the $(\lambda+i\omega)$ and $(3\lambda+i\omega)$ formulations for λ and the non-linear theory predicts the rate of growth up to the limit cycle reasonably well.

3.3.4 Non-linearities with Respect to Two Response Variables, $\bar{v}$ and p

As discussed in section 2.4.2.5. one aim of the current work has been to assess the application of the averaging technique to the lateral equations of motion with two response variable non-linearities present. After some initial work to sort out some problems with the gravity term, limit cycles were eventually obtained and an analysis completed using the equations set out in §2.4.2.5.

3.3.4.1 Initial Work

Starting with the non-linear sideslip characteristics given in Table 3.2, non-linear roll rate characteristics were added to the model using values of $\breve{L}_{p_1}$ and $\breve{L}_{p_3}$ shown in Table 3.3. Other combinations of $\breve{L}_{p_1}$ and $\breve{L}_{p_3}$ were also examined. Details of the major cases examined are included in Table 3.4, which will be referred to later.

Equations used originally were those given in (2.122) to (2.125) with $g\phi$ as the gravity term in the sideslip equation. This term significantly influenced the form of the responses in the cases where $\breve{L}_{p_1}$ was large and positive with significant $\breve{L}_{p_3}$, or where $\breve{L}_{p_1}$ was positive with zero $\breve{L}_{p_3}$.

For cases where $\breve{L}_{p_1}$ was stabilising (negative) and $\breve{L}_{p_3}$ small or zero limit cycles such as shown in Fig.3.22 (case 1b) were obtained. Even with a destabilising $\breve{L}_{p_1}$ and a value of $\breve{L}_{p_3}$ around -2000, stable limit cycles were obtained as shown in Fig.3.23. This response (case 2b) is for $\breve{L}_{p_1}$=0.01, $\breve{L}_{p3}$=-1760 and the F.F.T. shows ω_L=0.64

Figures 3.22 and 3.23 both show the p envelope response, scaled by $\theta_{\bar{v}}/\theta_p$, superimposed on the $\bar{v}$ response to show that now $\lambda_{\bar{v}} \neq \lambda_p$ (c.f. Fig.3.18 for single non-linearity). This illustrates one source of error in the B.T.S. averaging where a single λ was used when multiple non-linearities were included in the analysis, eqn.(2.48). In Fig.3.23, relaxation type oscillations are present in the yaw rate trace, and were characteristic of the basic non-linear sideslip system (Fig.3.14).

Keeping $\breve{L}_{p_3}$ = -1760 and increasing $\breve{L}_{p_1}$ (to 0.03 in Fig.3.24 case 2c) shows how the $g\phi$ term affects the motion. With a more destabilising value of $\breve{L}_{p_1}$ (e.g. 0.03), as ϕ builds up, the p and r responses show irregularities and higher frequency oscillations coming in at about $2\omega_L$ and $3\omega_L$. Increasing $\breve{L}_{p_1}$ with a given $\breve{L}_{p_3}$, increases the irregularity of the response.

The effect of the non-linearities in sideslip characteristics alone, with a destabilising $\breve{L}_{p_1}$ (= 0.01) is shown in Fig.3.25 where an oscillatory divergence is shown.

Returning to the combined non-linearities, Fig.3.26 shows the response, with $g\phi$ in the equations of motion, for a large value of $\breve{L}_{p_3}$ (-3810) and $\breve{L}_{p_1}$ = 0.075 (case 3b). It will be noticed that the large peaks in the ϕ trace correspond to a definite critical value of sideslip at around $\bar{v}$ = -0.03. Similar peaks are seen in the p and r traces.

Both Runge-Kutta and Adams-Bashforth integration routines gave the same responses for these cases with large $\breve{L}_{p_3}$ and $\breve{L}_{p_1}$ and further investigation was performed to find the cause of the highly irregular oscillations now occurring.

If the occurrence of other frequencies in the response was definitely due to the extra non-linearities then it would indicate the need to formulate the averaging technique with two frequencies (as well as at least two λ's for strict accuracy, as noted above).

A summary of the characteristics of the oscillations for various $\check{L}_{p1}$ and $\check{L}_{p3}$ is shown in Fig.3.27. The FFT program was used to examine frequencies and amplitudes of the responses to check if the oscillations bore any resemblance to those obtained with just non-linear $\bar{v}$ or p terms alone. Different initial conditions were also tried as it is a characteristic of non-linear systems that the response can show significant dependence on the input parameters.

Cases such as 3b were examined up to around 50 or 60 secs record. This particular case shows a lot of energy at the dutch roll or basic limit cycle frequency of 0.62 Hz (Fig.3.26b).

Concentrating on this case, Fig.3.28 shows the response when the g term is omitted from the equations of motion and immediately the response is seen to be periodic. Putting the g term in as gsinϕ,gives the response shown in Fig. 3.29. In this case now when ϕ gets up to -π and sinϕ = 0 the response is identical to that without the g term in the equations of motion. Table 3.4 summarises the major features of the various responses compared with the previous non-linear $\bar{v}$ and p systems.

For the cases of large $\check{L}_{p3}$ (cases 2b,3b) it seems that the ω_L (around 0.6) and $\theta_{\bar{v}}$, θ_p are closer to the basic non-linear $\bar{v}$ aircraft than the equivalent non-linear p cases, which have higher frequencies (0.83 Hz) and larger p amplitudes. This indicates the non-linear $\bar{v}$ characteristics tend to dominate the response.

In view of the effect of form of the g term,it was decided that further simulations would incorporate this as gsinϕ (later gcosΘcosΦ.sinϕ for the HIRM) rather than gϕ which just gives a steadily increasing term in the equations of motion,as ϕ builds up. The incorporation of gsinϕ did not significantly affect the basic cases with non-linear side-slip or roll rate characteristics alone.

Much more work could have been done on the combat aircraft B model with simultaneous $\bar{v}$ and p characteristics and having obtained some limit cycle responses with this system it was decided to use these to assess the development averaging technique outlined in §2.4.2.5.

3.3.4.2 Assessment of the Averaging Technique Applied to Aircraft B

The averaging technique as developed in §2.4.2.5. required the solution of a non-linear Routhian discriminant = 0, which is biquadratic in σ_p and quadratic in σ_v (eqn.2.89).

As an assessment of how valid this equation was, results from cases 2b and 3b were used to predict $\bar{v}$ limit cycle amplitudes and frequencies given p data and vice versa.

The results are summarised in table 3.5. It can be seen that for a given Θ_p, the solution of the resulting quadratic gives good estimates of both $\Theta_{\bar{v}}$ and ω_v and the most accurate value for ω_v is from $\omega^2 = b^*$ (equation (2.84)).

Using the simulation $\Theta_{\bar{v}}$ to predict Θ_p and ω shows how sensitive to $\Theta_{\bar{v}}$ the formula is. For case 2b, the biquadratic gave no real solution for Θ_p, while for case 3b, the roll rate amplitude was nearly 4 times the measured value.

3.3.4.3 Discussion

These results indicate some serious limitations of the averaging technique. It may be said that a number of approximations have been made to enable it to be applied e.g. a common λ for all response variables and neglecting g in the equations of motion, but with even these simplifications the derivation of explicit formulae for Θ_p and $\Theta_{\bar{v}}$ is a difficult task. The algebraic complexity now makes the technique less attractive and also tends to obscure physical insights into the system behaviour. In view of these observations, and the fact that the results, using a "short cut" to solve R* = 0, are disappointing, it was decided to concentrate more on the computational aspects of mathematical modelling for the remainder of the work, although the averaging technique was applied to the HIRM results.

It should be emphasised that the limitations shown up so far are applicable only to rolling and yawing moment characteristics of a cubic form with respect to sideslip and roll rate. Because of the highly individual nature of combat aircraft configurations, lateral aerodynamic characteristics can be formulated in other ways. Johnson et al[80] describe the non-linearities in $C_\ell \sim \beta$ for highly swept wings at high angles of attack and Murdin and Riddle[81] describe the $C_\ell \sim \beta$ non-linearities for a model with less swept wings.

3.3.5 Comparison of Non-linear Averaging and Local Linearisation

Following on from the analogue simulations described in section 3.3.1, the response to controls, in the presence of non-linear sideslip characteristics, was again examined but now using the digital simulation, SIMUL. This enabled the relationship between the non-linear averaging technique and local linearisation, equation (2.118), to be confirmed.

Using the digital simulation program, SIMUL, enabled some accurate measurements of limit cycle amplitudes to be made (in particular for $K_{\xi p} = 0$ (c.f. Fig.3.11)). The equilibrium sideslip angles for different control angle settings were calculated using ROUTH.

A typical output for $K_{\xi p} = 0$ is shown in Fig.3.30 and shows the reduction in $\bar{\theta}_{\bar{v}}$ for $\bar{v}_e$ set by a non-zero control angle, ξ_T. The results for $K_{\xi p} = 0$ and $K_{\xi p} = 0.005$ are shown in Figs.3.31a and 3.31b, where $\bar{\theta}_{\bar{v}}$ from the digital simulations are plotted against $\bar{v}_e$ and compared with the theoretical curve given by equation (2.118). The agreement between the theory and the simulation is very good confirming that a linearised treatment of the equations can yield useful information about the response of the non-linear system about non-zero equilibrium conditions.

CHAPTER 4

STABILITY AND CONTROL DATA FOR THE HIRM

4.1 Introduction

The RAE initiated the HIRM project with the aim of developing mathematical models for high α behaviour (Refs.29,30) and the project has provided a wide range of experimental and theoretical data on a novel aircraft configuration.

An important aspect of the work has been the freezing of the design at an early stage so that the data base built up will be compatible with future flight experience, obtained with drop models. In the past, experience has often been based on real aircraft configurations which are changed as development proceeds and so make it difficult to analyse behaviour on a common data base. (In fact the HIRM's design has been changed in minor details but these should not affect the general conclusions of the thesis work.)

This chapter sets out the background to the HIRM data used in the mathematical models in Chapters 5 and 6. Section 4.2 outlines the philosophy behind the HIRM configuration. The rest of the chapter describes the results from various wind tunnel tests along with estimates of dynamic derivatives made at an early stage in the work.

4.2 HIRM Configuration

A full description of the design philosophy behind the HIRM configuration can be found in Ref.30 but a review of the layout will be in order here. The design is meant to represent a typical combat aircraft of the future and is shown in 3-view in Fig.4.1. Before measurements of free-flight model inertias and mass became available, estimates were made of these quantities for use in this thesis and the definitive set of estimates used (Ref.82) are given in Table 4.1 along with other leading particulars for the model.

The design point for the wing is M = 0.8, C_L = 0.8 and its optimum operation at other conditions will be obtained by various leading and trailing edge devices. In particular, for the low speed conditions relevant to the current studies, leading edge droop has been incorporated on the model wings (see Fig.4.1) in order to retain flow attachment to as high an angle of attack as possible. The wings are of supercritical section.

The difficulty of incorporating control surface actuators in the thin wings and the corresponding complications of adding representative excresances to wind tunnel models, was one of the reasons for adopting a separate roll control in the form of all moving tailplanes as well as canards. Due consideration was also given to other work on canard configurations and already a number of modern combat aircraft have such surfaces, e.g. the Mirage 4000, giving lower trim drag. NASA have also tested some three-surface configuration models by adding canards to F-15, F-18 models.[83] One aim of fitting the canards has been to enhance the lifting capability at high angles of attack using vortex lift. Vortices generated to flow over the main wing provide additional lift and inhibit flow separation so that the wing can generate significant lift up to high angles of attack. J.W.Agnew and others[84,85] have described the vortex systems occurring on F-15 based three surface configurations and the performance benefits obtainable with canard configurations. The use of both canards and tailplanes provides scope in the HIRM project for later investigation of direct lift and sideforce control.

The fuselage has flat sides to accommodate as large as possible a movement of the control surfaces before gaps occur. The aft end of the fuselage,in particular,has a large base area so that wind tunnel models can be fitted to various sting supports without the need to alter the fuselage geometry from that of the free flight models. This has been a problem in the past,where revised rear fuselage contours can be the cause of differences between wind tunnel and flight data. By using exactly the same model details for wind-tunnel and drop tests it is hoped that doubts about Reynolds number effects, correct geometric representation of parts etc. will be dispelled.

4.3 HIRM Data Base

With an objective of the HIRM program to look at the mathematical modelling of aircraft aerodynamic forces and moments at low speed, high angles of attack, a number of experimental techniques have been used to provide data for the mathematical models. Before experimentally determined dynamic lateral derivatives were available for mathematical modelling, estimates were made using semi-empirical methods. Flight trials of the drop models will provide both a verification of existing data as well going on to provide more parameters using identification techniques.

4.3.1 Wind Tunnel Testing

A number of wind tunnel testing techniques have been used to provide data for the HIRM mathematical models. Initial conventional static tests were performed on a provisional model, HIRM 1, in the RAE No.2 11½ft x 8ft, 13ft x 9ft and

8ft x 6ft wind tunnels and later tests were made with the definitive geometry, HIRM 2 (as shown in Fig.4.1).

Measurements of derivatives made while the model undergoes forced oscillations were made on HIRM 2 in the RAE 13ft x 9ft wind tunnel (W.T.). This oscillatory rig apparatus was also used to provide cross-coupling derivatives between longitudinal and lateral motions at angles of attack up to 24^{o}. Dynamic derivatives due to roll rate have been measured on the BAe rolling rig at Warton using HIRM 2.

At the time of writing full scale static tests have just been carried out on a drop test model in the RAE 5m W.T. A summary of the W.T.tests and models used is given in Ref.30.

4.3.2 Estimation of Derivatives

To enable mathematical modelling to proceed before measured lateral dynamic derivatives were available, estimates of these parameters were made using semi-empirical techniques. This also proved useful as an exercise in assessing the limitations of current estimation techniques as comparisons with measured data showed up significant discrepancies in some area.

4.3.3 Free-Flight Trials

Although it is beyond the scope of this thesis to go in to detail, mention should be made of the free-flight trials aspects of the HIRM program,as this is such an important part of the overall programme. The flight trials are pre-programmed sequences flown by dynamically scaled models in a fast time scale. They provide more data as input for the mathematical modelling and help validate the mathematical model. A major aspect of the work is in assessing the stability and controllability of the aircraft in extreme manoeuvres and in developing advanced control systems.

Full details of the philosophy behind drop model flight trials is given in the literature (see e.g. Fail[86], Moss et al[87]). As a major concern in the development of current combat aircraft is departure and spin-prevention, this will form a large part of the work for the HIRM trials using various levels of complexity of control system. Initial trials will be to look at the small amplitude longitudinal and lateral response about various mean angles of attack,using stable configurations first, then going to a 5% negative static margin. Due to range limitations at UK ranges, spins and departure will also be investigated at an early stage. The main programme of work will then involve assessment of control systems. Direct lift and sideforce (the latter via interference pressures on fuselage sides from differential canard application (see Ross and Thomas[89] , Henderson and

Leavitt[89]) will also be investigated. Further details of the proposed flight test programme for HIRM are given in Ref.30.

The rest of this chapter describes the various wind-tunnel tests as well as estimation procedures used to measure static and dynamic stability parameters for the HIRM.

4.4 Longitudinal Aerodynamics

A full review of the static aerodynamic data for the HIRM project is given in Ref.90, which covers both longitudinal and lateral data obtained from all static wind tunnel testing. The initial mathematical models in this thesis concentrated on the lateral behaviour of HIRM (Chapter 5) but full 6 d.o.f. force and moment models of the configuration were set up later and so some comments on the longitudinal characteristics are given in this section.

4.4.1 Trim Configurations

The canard-wing-tailplane arrangement means that the HIRM has an extra degree of freedom in trimming compared to conventional layouts. At each trimmed angle of attack, a number of combinations of canard and tailplane will provide the necessary trim forces and moments. Because of the size of the canard, it is limited for use in pitch trimming.

Only a limited number of combinations of tailplane/canard settings (configurations) have been wind tunnel tested and each configuration is referred to by a letter. For instance, C refers to $\eta_C = -10^o$ and $\eta_T = -20^o$. Some of the important configurations are shown in Fig.4.2.

Trim schedules, which aim to maximise L/D throughout the α-range up to departure and use simple movements of the canard/tailplane to trim with α, have been investigated by the R.A.E. Two typical schedules are shown in Fig.4.2 and although trim law A showed a slightly better L/D at $\alpha = 10^o$ than B,it would be difficult to programme during a flight due to the complicated combined movements of the canard and tailplane.

In this thesis, work has been confined to configuration C data as this particular configuration has a high trimmed angle of attack. It also lies on trim schedule B which involves simple movements of the canard/tailplane and consequently will probably be used on early flight trials.

4.4.2 Configuration C Data

Static wind tunnel tests provided force and moment data as functions of angle of attack, sideslip and control angle

settings. The static data used in this thesis was from tests on HIRM 1 as this provided the most complete set of data available for configuration C. Tests covered an α range of 0^o to 90^o for a number of configurations.

Fig.4.3 shows C_L, C_D and C_m curves against α for configuration C and for the same configuration, canard off. The main points of interest are the extended linear range of C_L and increased $C_{L_{max}}$ with the canard on, due to the canard interaction keeping flow attached over the wing at high α's. Without the canard the 'break' in the C_L~α curve due to the onset of wing flow separation occurs at a lower α (around 20^o) than with the canard on (α around 24^o).

Positive static stability (negative slope of the C_m~α curve) is maintained throughout the α range shown. The stable pitching moment break (increase in magnitude of slope of C_m~α curve) at $\alpha=24^o$ for canard on, is again associated with the onset of flow separation over the canard and wing and has been observed by other researchers e.g. Agnew and Hess (Ref.84). Agnew and Hess note that the stable break is not usually present on canard-wing arrangements, so this is an advantage of having a tailplane as well. Without the canard, an increase in static stability is seen as expected and C_m~α shows a stable break slightly earlier than with canard on.

The actual behaviour of the airflow including vortex and separation effects over the aircraft is difficult to describe precisely without some flow visualisation tests. A few such tests have been performed in the 13ft. x 9ft wind tunnel at R.A.E. Bedford on HIRM 2 and more recently a plastic model has been used in a water tunnel. Agnew et al[85] describe the results of flow visualisation tests on an F-15 three-surface configuration and postulate a suitable arrangement for the vortex flows at high α. It is to be expected that the HIRM would exhibit similar flow characteristics, involving vortices from the canards going over the wing to provide an increase in lift. The limited flow visualisation tests on the HIRM have shown vortex formation at high α.

Longitudinal control characteristics for HIRM configuration C have also been measured from the static wind tunnel data for HIRM 1. Variation of forces and moments with η_T and η_C enabled the longitudinal control derivatives to be extracted. Derivatives with respect to symmetric tailplane movement, η_T, for configuration C were of most interest in the later work on the HIRM and were measured using the changes in C_L and C_m from configuration C to configuration F (configuration F has $\Delta\eta_T = +10^o$ from configuration C). The resulting derivatives, $C_{Z\eta_T}$ and $C_{m\eta_T}$, are shown in Fig.4.4.

4.5 Static Tests and Lateral Static Derivatives

4.5.1 Wind Tunnel Results

Rolling and yawing moment plus sideforce variations with β, were measured for $\beta = -6(1)6^{o}$ up to $\alpha = 40^{o}$ for HIRM 1, configuration C,in the R.A.E.No.2 11½ft x 8ft wind tunnel. A sample of the results is shown in Fig.4.5. Only a relatively small range of β was used for the static tests but more recent tests on a drop test model at full scale Reynolds numbers have provided data up to $\pm 18^{o}$ sideslip. The lateral coefficients measured for HIRM 1 remain reasonably linear with sideslip up to α around 20^{o}. Above this α, C_Y and C_ℓ start showing non-linearities and non-zero values at $\beta_e = 0^{o}$. The yawing moment coefficient, C_n, remains linear to a much higher α, 36^{o} angle of attack being when the first indication of non-linearity appears. As expected, there is a reduction in directional stability, $C_{n\beta}$, as α increases and Cn_β goes negative at around $\alpha = 18^{o}$, indicating a loss in fin effectiveness.

The linear behaviour of $Cn\sim\beta$ up to $\alpha = 36^{o}$ suggests that the onset of non-linearities in the lateral characteristics is associated with flow separation from the lifting surfaces only. It is unlikely that asymmetric shedding of vortices off the nose affects the lifting surfaces,as the nose probe on the HIRM was installed partly to disrupt such phenomena. Murdin and Riddle[81] describe tests on a model fighter configuration.having a wing with a drooped leading edge (as on the HIRM configurations tested so far) and strakes. Flow separation from the wings combined with the effects of the strake vortices were responsible for the non-linearities observed in the $C_\ell\sim\beta$ characteristics measured. Loss of lift on the windward wing at non-zero sideslip, combined with the leeward strake vortex acting on a large area of the leeward wing,meant C_{ℓ_β} was positive at small non-zero sideslips. A similar phenomenon may be responsible for the zero slope of the $C_\ell\sim\beta$ curve observed on the HIRM results at $\alpha = 40^{o}$(Fig.4.5b).

4.5.2 Lateral Static Derivatives

Static derivatives $\breve{L}_v$, $\breve{N}_v$ and $\breve{Y}_v$ were extracted from the wind tunnel measurements on HIRM 1 described in §4.5.1. Results are shown in Fig.4.6 for configuration C along with results from oscillatory rig tests on HIRM 2 which will be described in §4.7.

The variation of $\breve{N}_v$ with α is shown in Fig.4.6a and the static test results show $\breve{N}_v$ going negative at $\alpha = 18^{o}$,as indicated already by the $C_n\sim\beta$ characteristics.

Fig.4.6b shows the derivative $\breve{L}_v$ increasing in magnitude (while remaining negative for stability) up to an α of around 18^{o}. The initial positive slope is due to the drooped leading edge of the wing, used to help keep attached

flow at high angles of attack. Effects of flow separation lead to a reduction in the magnitude of $\check{L}_v$ (decrease in stability) above $\alpha = 18^o$. Johnson et al[80] have shown how the effects of vortex bursting and vortex motion off the wings over a highly swept wing lead to trends in $\check{L}_v$ with α similar to those shown here for the HIRM. However the wings on the HIRM are not very highly swept so the wing vortices will not be as strong as those dealt with by Johnson and will probably remain over the wings at the sideslips tested. It seems likely that the effects of flow separation on the wing tips will have more influence on the rolling moment behaviour with sideslip for the HIRM.

The peak in $\check{L}_v$ at $\alpha = 26^o$ corresponded to a peak in the dutch roll instability (to be described in Chapter 5) and was one reason for selecting $\alpha = 26^o$ as an initial case for studying the effect of non-linear sideslip and roll rate characteristics on response.

The sideforce due to sideslip derivative, $\check{Y}_v$, is shown in Fig.4.6c against α and again shows a peak at around $\alpha = 26^o$. HIRM 1 differed slightly from HIRM 2 in having a more tapered rear fuselage and this may account for some of the discrepancies between the different measurements of the static derivatives. Static tests on HIRM 2 have also been carried out in a number of wind tunnels and it is thought that some of the differences in $\check{Y}_v$ and $\check{N}_v$ from the various sources are attributable to sidewash effects from the quadrants used in the R.A.E. 13ft x 9ft wind tunnel (shown in the photograph, Fig.4.9, of the oscillatory rig apparatus). Most of the work presented in this thesis, in particular the simulations, has used the static data from the 11½ft x 8ft wind tunnel HIRM 1 tests so a consistent set of derivatives has been used but results may differ from those using static data measured on HIRM 2 in other wind tunnels.

4.5.3 Lateral Control Derivatives

Sideforce and rolling and yawing moments due to rudder, differential canard and differential tailplane deflections were extracted from the 11½ft x 8ft wind tunnel data for HIRM 1 and results are shown in Fig.4.7 for configuration C. For the current work only tailplane and rudder movements were used in the simulations and analysis, so derivatives due to rudder, ζ, and differential tailplane, ξ_T, are of most importance here.

Derivatives $\check{Y}_\zeta$ and $\check{Y}_{\xi_T}$ show relatively little change with α up until $35^o\alpha$,when $\check{Y}_\zeta$ decreases. The rolling moment derivative $\check{L}_\zeta$ goes negative at $\alpha = 34.5^o$ while $|\check{L}_{\xi_T}|$ steadily increases with α up to $\alpha = 36^o$. Yawing moment due to rudder, $\check{N}_\zeta$, remains negative up to $\alpha = 40^o$, but is reduced significantly at $\alpha = 40^o$. Differential tailplane is used for roll control on the HIRM and adverse aileron yaw ($\check{N}_{\xi_T}$ positive) only occurs above $\alpha = 37^o$.

Although canard angle was fixed at -10^{o} for the simulations and analysis, the control derivatives for canard movement are worth commenting on. Significant sideforce is developed by differential canard application ($\check{Y}_{\xi C}$) along with a yawing moment of the same sign below $\alpha = 34^{o}$ ($\check{N}_{\xi C}$). Because $\check{Y}_{\zeta}$ is of opposite sign to $\check{Y}_{\xi C}$, while $\check{N}_{\xi C}$ is the same sign as $\check{N}_{\zeta}$ below $\alpha = 34^{o}$, this means that, up to this α, opposite sign rudder can be used to balance differential canard yawing moment and produce a sideforce in the same direction as from the canard. This could be the basis for implementing a direct sideforce capability on the HIRM.

4.6 Estimation of Lateral Dynamic Derivatives

4.6.1 Introduction

To provide data for initial stability calculations and also to evaluate some prediction methods for high angles of attack, the main lateral dynamic derivatives for the HIRM were estimated. Derivatives due to roll rate and yaw rate have been estimated using semi-empirical methods based on experimental test data. Simple corrections were applied to allow for the effects of flow separation with angle of attack. Thomas[91] gives a useful guide to techniques for estimating lateral-directional derivatives at subsonic speeds, while Ross et al[17] provide some useful information on effects of angle of attack on these derivatives.

Widely available sources of data for the estimation of derivatives are those of ESDU[92] and DATCOM[93] and use was made of both sources to estimate $\check{L}_p$, $\check{N}_p$, $\check{L}_r$ and $\check{N}_r$ for the HIRM. Data used in the calculations is presented in Table 4.1 and calculations were carried out for a low-speed, zero Mach number flight case with c.g. at $0.125\bar{c}$. Zero deflection of canard and tail were used at first but for some derivatives, corrections were made to give estimates for specific configurations with non-zero η_C and η_T. The low angle of attack estimates were factored to allow for flow separation effects with increase in angle of attack and results are compared with oscillatory rig measurements of the derivatives, described in §4.7.

Details of the estimations of the various derivatives are presented in Appendix D and the following sections outline the important points in the calculations. Estimates were made in wind axes and in general ESDU results were used except where DATCOM was the only source available. The methods generally agreed with each other where both were available.

4.6.2 Rolling Moment due to Rate of Roll, $\check{L}_p$

$\check{L}_p$ is of importance in rolling performance as well as determining dynamic stability characteristics. The main contribution is from the wing but contributions from the tail, canard and fin were also estimated for the HIRM, as

these were likely to be significant (Ref.92, Item A 06.01.01).

The usual reduction in roll damping derivative at high angles of attack arises from the tendancy of the flow on the outboard part of a swept wing to break down and the reduction follows the decrease in the slope of the C_L~α curve. Thus,one approximate method of allowing for increasing angle of attack,is to scale the value of the derivative at low α by the variation of $\partial C_L/\partial\alpha$ with α, obtained from wind tunnel experments. This method was used for estimating the variation of $\check{L}_p$ with α for the HIRM and details are given in Appendix D. Results are shown in Fig.4.8a and are presented in wind axes, as calculated. Also shown for comparison are measurements from the oscillatory rig tests described in §4.7. The measured trend,with increasing α,towards a reduction in roll damping is quite closely predicted by the estimates.

4.6.3 Yawing Moment due to Rate of Roll, $\check{N}_p$

Contributions from the wing and fin were estimated for $\check{N}_p$. DATCOM was used for the wing contribution as the ESDU Item (No.81014) was not available at the time. Again the estimate of $\check{N}_p$ at low α was factored to allow for effects of flow separation. In this case a factor, K, (Ref.17) gives a measure of the proportions of separated and attached flow, and $\check{N}_p$ is given by

$$\check{N}_p = K\left(\frac{\check{N}_p}{C_L}\right)C_L \qquad (4.1)$$

Results shown in Fig.4.8b for $\check{N}_p$ are plotted together with measurements from oscillatory tests on configuration C. The estimates for $\check{N}_p$ showed the poorest agreement with measured data out of the four derivatives estimated for HIRM. The fin makes a significant contribution to $\check{N}_p$ and is difficult to estimate due to inaccuracies in estimating fin centre of pressure position,so this could be a major factor in the inaccuracy. Fin contribution was estimated using formulae given in Refs.17 and 94 (see Appendix D.3).

4.6.4 Rolling Moment due to Rate of Yaw, $\check{L}_r$

The standard methods,ESDU and DATCOM,both provide methods of estimating this derivative. The wing provides the main contribution and Ref.92, Item 72021 provides a chart for the basic wing and then uses factors for effects of twist, flaps and dihedral. The method is known to be unreliable for low aspect ratio, highly swept wings because of flow separation effects. The tailplane contribution could have been calculated in the same way as for the wings but the accuracy would be questionable due to interference effects from the wing, fin and body. Fin contribution was estimated using Ref.92, Item 70006 which was the only suitable item available at the time, although now Item 82017 would be used.

A semi-empirical method, which tries to account for the effects of flow separation at higher angles of attack[17], uses experimentally determined $\check{L}_v$ values to correct theoretical values of $\check{L}_r$ due to the wing:

$$(\check{L}_r)_w = C_L\{(\frac{\check{L}_r}{C_L}) + (\frac{\check{L}_v}{C_L})\}_{theory} - \check{L}_{v_{expt.}} \qquad (4.2)$$

For the HIRM estimates, oscillatory rig measurements of $\check{L}_v$ were used for the corrections and results are shown in Fig.4.8c. Again results are compared with oscillatory rig results and agreement is not very good between estimated and measured values because of the highly non-linear behaviour of $\check{L}_r$.

4.6.5 Yawing Moment due to Rate of Yaw, $\check{N}_r$

This is the most important derivative due to yaw rate, r, in terms of aircraft dynamics and main contributions come from the fin and body. ESDU Item 71017 was used to estimate a wing contribution but no effects of wing flow separation were allowed for because of the small size of the wing contribution. Fin contribution was calculated using Ref.92, Item A.07.01.00 and since the calculations were performed, another relevant ESDU Item,82017, has become available. The large fuselage, with flat sides, for the HIRM, means the body makes a significant contribution to $\check{N}_r$ but information on $(\check{N}_r)_B$ is scarce. In the calculations, a slender body formula, given by Sacks[95] was adapted to give the body contribution, independent of angle of attack.

Results for configuration C are shown in Fig.4.8d with oscillatory results in wind axes and show relatively good agreement.

For each derivative, estimated contributions from $\check{L}_{\dot{v}}$ and $\check{N}_{\dot{v}}$ were added for comparison with the oscillatory data as the latter is in the form of combined derivatives, e.g. $\check{L}_p+\check{L}_{\dot{v}}\sin\alpha$ (see §4.7). The results overall serve to illustrate the need for better calculation methods for flow fields produced by surfaces rolling, yawing and sideslipping. The interference effects are difficult to estimate and, for the HIRM, the canards have a significant effect on the high α characteristics. At least for the HIRM, the leading edge droop delays the breakdown of low α flow and so extends the α range over which low α estimates are applicable.

4.7 Oscillatory Rig Tests

4.7.1 Introduction

The oscillatory rig provides a method of measuring dynamic derivatives due to yaw, roll and pitch rates. The wind tunnel model is forced to oscillate at pre-determined frequencies on a flexible-sting and response is measured using strain gauges. Some static as well as dynamic derivatives can be measured. The oscillatory rig technique is fully described in the literature (e.g.Refs. 96,97) but a brief outline will be given here.

Fig.4.9 shows the HIRM 2 on the high angle of attack sting support in the 13ft x 9ft low-speed wind tunnel at R.A.E. Bedford. The model is mounted on a flexible sting (known as a spring unit) and is oscillated at predetermined frequencies by a vibration generator mounted in the sting carrier. Two kinds of spring units are used, lateral and longitudinal, and rather than try and eliminate unwanted flexibilities, each has built in flexibilities. For the lateral units (such as shown in Fig.4.9) these flexibilities are in yaw, sideslip and roll, while for the longitudinal units, flexibilities are in pitch and heave. The model is oscillated at each of the frequencies determined by the flexibilities and measurements are made of amplitude, frequency and excitation force for each mode. Model inertias are measured after the rig has been calibrated and using these inertias in the equations of motion enables the required aerodynamic derivatives to be measured as differences between wind-on and wind-off measurements.

Using the high angle of attack sting support system shown in Fig.4.9, α's of up to 90^{o} can be achieved. The sting carrier is mounted on rollers which move in tracks in the two semi-circular supports and can be clamped by spring loaded steel blocks. The sting carrier supports in turn are mounted on rotatable upper and lower turntables. An alternative method of mounting the spring unit,in the 13ft x 9ft wind tunnel,uses an 'A' frame on which changes in angle of attack are made manually (up to $\alpha = 26^{o}$).

The derivatives are measured at fixed frequencies and no provision is made for measuring the derivatives as functions of oscillation frequency. However,the apparatus was designed to use frequencies close to those of typical aircraft dynamic motions, e.g. the dutch roll. Provision is also made for examining unstable motions,as known amounts of damping can be transmitted to the model from the vibration generator.

By using a lateral spring on the 'A' frame and mounting the model on the spring unit after rolling it through 90^{o} (so that the wings were in the vertical plane), it proved possible to measure cross-coupling derivatives L_q, M_p and Z_p. The 'A' frame's conventional incidence adjustment was now equivalent to setting sideslip and

effects of $\beta_e = -6^o$ were examined on the cross-coupling derivatives.

Results are now described from the oscillatory rig tests and three different series of tests are identified in the results which follow:

a) OD1 or OD3. Lateral tests using apparatus shown in Fig.4.9.

b) OD5 Longitudinal tests

c) OD6 Cross-coupling tests with effects of sideslip. 'A' frame string support.

Measurements from the oscillatory rig tests are made in earth axes and when the dynamic derivatives are transformed to geometric body axes, they appear in the form of combined derivatives,with contributions from acceleration derivatives, e.g.

$$\check{L}^{\bullet}_{\phi} = \check{L}_p + \check{L}^{\bullet}_{v}\sin\alpha$$

A list of the lateral derivative definitions is given in Table 2 of Ref.97. Unless otherwise stated,the results presented for the oscillatory rig tests show combined derivatives in geometric body axes as these have been used in later work.

A number of different HIRM configurations were tested on the oscillatory rig apparatus but only configuration C results are presented here. In the case of the longitudinal and cross-coupling tests, deflection of the spring unit, with the wind on, meant the model had to be trimmed to ensure adequate clearance of the tail during oscillations. In these cases the tailplane was used to trim, so results presented for configuration "C" have $\eta_C = -10^o$ but η_T at various settings between around -18^o and -38^o.

4.7.2 Results of Longitudinal Tests

Results of the longitudinal oscillatory rig tests (OD5) are shown in Fig.4.10. In solving the equations of motion for the pitch and heave of the model, static derivatives $\check{M}_w$ and $\check{Z}_w$ are evaluated and these are shown in Figs.4.10a and 4.10b. Both derivatives show local peaks at around $\alpha = 18^o$ associated with flow separation from the wings. Normal force restrictions on the spring unit meant that a fairly low wind tunnel speed, 40 m/s, had to be used for the high angles of attack and results are shown here for 40 m/s wind tunnel speed throughout the α-range.

The dynamic derivatives, $\check{Z}_q$ and $\check{M}_q$ are shown in Figs.4.10c and 4.10d and again show local peaks due to flow separation effects, although now at slighly higher α than for the static derivatives. Also shown in Fig.4.10c are estimated values of the combined derivative, $\check{M}_q{}^*$, up to $\alpha = 40^o$ (Ref.98).

The cross-coupling tests (OD6) also provided estimates of the longitudinal derivatives and these are shown by the crosses in Figs.4.10a to 4.10d for $\alpha = 12^{o}$ to 24^{o}. Effects of sideslip were examined during the cross-coupling tests and the longitudinal derivatives at $\beta_e = -6^{o}$ are shown by the dashed lines in the above figures.

4.7.3 Results of Lateral Tests

These tests were conducted using the equipment as shown in Fig.4.9 and as well as providing measurements of the dynamic derivatives, the tests also yield values of the static derivatives $\breve{N}_v$, $\breve{L}_v$ and $\breve{Y}_v$. All lateral tests were conducted,at $\beta = 0^{o}$,on HIRM 2. The static derivative results (labelled OD3) were shown in Figs.4.6a to 4.6c, in comparison with the $11\frac{1}{2}$ft x 8ft static wind tunnel results from HIRM 1 tests. $\breve{N}_v$ from the two sources shows good agreement and $\breve{Y}_v$ also shows similar trends from oscillatory and static tests. Comparison of the two sets of results for lateral stability derivative, $\breve{L}_v$, in Fig.4.6b shows that the oscillatory measurements tend to indicate a higher level of lateral stability,particularly at the higher angles of attack. The differences probably indicate different flow separation fields in the two forms of test. Another possible influence on the measurements are the support systems used in the different wind tunnels.

Results for dynamic derivatives $\breve{L}_p$, $\breve{N}_p$, $\breve{L}_r$ and $\breve{N}_r$ are shown in Fig.4.11. Also re-plotted from §4.6 are the estimates of these derivatives in body axes. The high value of L_p estimated at $\alpha = 40^{o}$,leads to a positive value of estimated $\breve{N}_r$ (Fig.4.11d) in the transformation of $\breve{N}_r$ to body axes.

The oscillatory roll damping derivative retains an almost constant negative value right up to $\alpha = 40^{o}$.

Estimated and measured $\breve{N}_p$ differ a lot throughout the whole angle of attack range. As mentioned in §4.6,$\breve{N}_p$ is difficult to estimate,but another factor in the discrepancy could be in the oscillatory measurements. With large roll damping, a large roll excitation force has to be fed into the oscillatory rig. The vibration generator feeds in a combined roll/yaw signal so the yawing response is mainly due to the mechanical excitation and that due to aerodynamic excitation is small. Hence $\breve{N}_p$ is eventually calculated as the difference between two large numbers.

4.7.4 Results of Cross-Coupling Tests

Derivatives $\breve{L}_q$, $\breve{M}_p$ and $\breve{Z}_p$ were measured by mounting the HIRM 2 on a lateral spring with its wings in the vertical plane. Calculations also gave estimates for $\breve{M}_w$, $\breve{Z}_w$, $\breve{M}_q$ and $\breve{Z}_q$ as presented in §4.7.2. and also $\breve{L}_p$.

Cross-coupling derivatives and $\breve{L}_p$ are shown in Figs.4.12a to 4.12d for $\beta_e = 0^{o}$ and $\beta_e = -6^{o}$. The α range used for

these tests was limited to 12^{o}-24^{o}. Effects of sideslip are very marked but results for $\beta_e = -6^{o}$ show similar trends to those with $\beta_e = 0^{o}$.

In later work described in §6.2,the cross-coupling derivatives are used in an eigenvalue program, EIGEN,and derivatives were required for angles of attack up to 40^{o}. Because of the rapid changes in the cross-coupling dynamic derivatives,with small angle of attack change, it was decided to assume small, usually constant,values for these derivatives above $\alpha = 26^{o}$. The assumed values used in §6.2 are also shown in Figs.4.12a to 4.12d.

4.8 Rotary Rig Measurement of Dynamic Derivatives

4.8.1 Introduction

The oscillatory rig tests,described in the previous section, included measurements of derivatives due to rate of roll. The continuously driven rotary derivative rig provides another method of measuring such derivatives and uses a more appropriate model motion than the oscillatory rig.

Rotary rigs continuously rotate a model about an axis aligned to the wind and, in the particular rig used for the HIRM tests, the model is mounted on a six-component, internal strain gauge balance, signals being taken out through a slip ring unit. The rig used in the 5.5m LSWT at BAe Warton, is fully described in Ref.99 but a few details will be given here. It is shown schematically in Fig.4.13.

Angle of attack range is -45^{o} to 90^{o}, achieved by mounting the model either through the base or the top and moving the sting round an arc centred at the model reference centre. Sideslip is achieved by rolling the model about its longitudinal axis but all tests on the HIRM so far have been conducted at zero sideslip.

The maximum(pb/2V)achievable is 0.2, with maximum speed for the 5.5m Warton tunnel being 22 m/s. Results from tests on HIRM 2 will now be described.

4.8.2 Results

Results described in this section will be those for HIRM configuration C, $\eta_C = -10^{o}$, $\eta_T = -20^{o}$. Tests were also made on configurations with $\eta_C = 0^{o}$, $\eta_T = 0^{o}$; $\eta_C = 10^{o}$, $\eta_T = -10^{o}$ as well as with various surfaces off, to perform component build up tests.

For configuration C, tests were performed for a range of α from 10^{o} to 45^{o}. At each α, roll rates from (pb/2V)≃-0.17 to(pb/2V)≃+0.18 were used, and for each roll rate a number of parameters are recorded, the ones discussed in this section being $C_Y{}^B$, $C_n{}^B$ and $C_\ell{}^B$ (see Appendix A for

description of notation used for various data sources). It will be noted that force and moment measurements are made in body axes as functions of wind axis roll rate, $(p^W b/2V)$.

Typical results for $\alpha = 12^o$, 20^o, 22^o, 24^o and 38^o are shown in Fig.4.14. Ultimately, body axis derivatives, L_p^B and N_p^B, are required from this data for the current work (Y_p^B could also be extracted but was neglected for the 3 degree of freedom models. C_Y^B ~ (pb/2V) data was used in the 6 degree of freedom simulation). The first step in this process is to extract wind axis derivatives.

i) Wind Axis Derivatives

Given the data in the form of C_ℓ^B, C_n^B as a function of $(p^W b/2V)$ wind axis derivatives, $\breve{L}_p^W$ and $\breve{N}_p^W$ can be formed in two ways:

a) Convert C_ℓ^B to C_ℓ^W using C_n^B and take the slope. Similarly for C_n^W using C_ℓ^B:-

$$C_\ell^W = C_\ell^B \cos\alpha + C_n^B \sin\alpha \qquad (4.3)$$

$$C_n^W = C_n^B \cos\alpha - C_\ell^B \sin\alpha \qquad (4.4)$$

The slopes are then $\dfrac{\partial C_\ell^W}{\partial(\frac{p^W b}{2V})} = 2\breve{L}_p^W$

and $\dfrac{\partial C_n^W}{\partial(\frac{p^W b}{2V})} = 2\breve{N}_p^W$

b) Take the slopes of C_ℓ^B ~ $(p^W b/2V)$ and C_n^B ~ $(p^W b/2V)$ i.e. slopes of the measured data and then convert to wind axes:

$$2\breve{L}_p^W = \frac{\partial C_\ell^B}{\partial(\frac{p^W b}{2V})}\cos\alpha + \frac{\partial C_n^B}{\partial(\frac{p^W b}{2V})}\sin\alpha \qquad (4.5)$$

$$2\breve{N}_p^W = \frac{\partial C_n^B}{\partial(\frac{p^W b}{2V})}\cos\alpha - \frac{\partial C_\ell^B}{\partial(\frac{p^W b}{2V})}\sin\alpha \qquad (4.6)$$

In method (b), the wind axis derivatives are derived directly from the slopes of the raw data against roll rate

and then combined, whereas in (a) slopes are taken after combining C_ℓ and C_n. Method (b) was preferred as it ensured there were no effects of C_n on C_ℓ or C_ℓ on C_n before derivatives were formed. It should be said,of course,that in theory there should be no difference between the two methods.

Wind axis derivatives obtained by taking slopes over a small range of (pb/2V) are shown in Fig.4.15. Also shown are values of derivatives obtained by fitting cubic polynomials to the wind axis moments against (pb/2V). These will be described in §4.9.2.

Evident in Fig.4.15a is the very large change in $\breve{L}_p{}^W$ around $\alpha = 20^o$, leading to a small positive value of $\breve{L}_p{}^W$ at $\alpha = 24^o$. The positive slope of the $C_\ell{}^B{\sim}$(pb/2V) data is evident on Fig.4.14d between (pb/2V) = -0.04 and +0.05. Other tests[100] showed this autorarotation tendency to be much greater with the tailplane and canard off, suggesting canard downwash was affecting the flow over the wings significantly at this α.

ii) Body Axis Derivatives

To convert the wind axis derivatives to body axis derivatives it is necessary to know $\breve{L}_r{}^W$ and $\breve{N}_r{}^W$. This is where some more experimental data would be very useful, such as could be measured in a curved flow wind tunnel[101], or on a whirling arm. Derivatives due to pure yawing (r only) could then be measured and, partly as a result of this need, a programme of work has now been proposed which will involve testing the HIRM on the whirling arm facility at Cranfield College of Aeronautics.

In the meantime,wind axis $\breve{L}_r$ and $\breve{N}_r$ were obtained from oscillatory rig tests. The oscillatory data gives estimates of $\breve{L}_p{}^B$, $\breve{N}_p{}^B$, $\breve{L}_r{}^B$ and $\breve{N}_r{}^B$ (in fact the oscillatory rig data is in the form of combined derivatives: $\breve{L}_p+\breve{L}_{\dot{v}}\sin\alpha$ etc). These can be converted to wind axis form using standard transformations[102], e.g.

$$\breve{L}_r{}^W = \cos^2\alpha.\breve{L}_r{}^B-\sin^2\alpha\breve{N}_p{}^B-\sin\alpha\cos\alpha(\breve{L}_p{}^B-\breve{N}_r{}^B) \qquad (4.7)$$

$$\breve{N}_r{}^W = \cos^2\alpha.\breve{N}_r{}^B+\sin^2\alpha\breve{L}_p{}^B-\sin\alpha\cos\alpha(\breve{L}_r{}^B+\breve{N}_p{}^B) \qquad (4.8)$$

Thus, from a consistent set of body axis data, we have an estimate of $\breve{L}_r{}^W$ and $\breve{N}_r{}^W$. Estimates of $\breve{N}_p$ and $\breve{L}_p$ are required in these transformations but only as correction terms.

Now, using similar transformations for conversion from wind axes to body axes, the required $\breve{L}_{p_R}^B$ and $\breve{N}_{p_R}^B$ can be calculated:

$$\breve{L}_{p_R}^{B} = \breve{L}_{p_R}^{w}\cos^2\alpha+\breve{N}_{r_o}^{w}\sin^2\alpha-\sin\alpha\cos\alpha(\breve{N}_{p_R}^{w}+\breve{L}_{r_o}^{w}) \quad (4.9)$$

$$\breve{N}_{p_R}^{B} = \breve{N}_{p_R}^{w}\cos^2\alpha-\breve{L}_{r_o}^{w}\sin^2\alpha+\sin\alpha\cos\alpha(\breve{L}_{p_R}^{w}-\breve{N}_{r_o}^{w}) \quad (4.10)$$

It may be noted that the rotary rig terms (suffix R) on the right hand side of these equations could have been obtained in another way from the rotary rig data measured,as:

$$\breve{L}_{p_w}\cos\alpha = (\breve{L}_{p_R}^{w}\cos\alpha-\breve{N}_{p_R}^{w}\sin\alpha)\cos\alpha$$

$$\breve{N}_{p_w}\cos\alpha = (\breve{N}_{p_R}\cos\alpha+\breve{L}_{p_R}\sin\alpha)\cos\alpha$$

Results for the rotary rig derivatives in body axes are given in Fig.4.16. Again, also shown are values obtained via cubic polynomial representations of the wind axis data (see §4.9.2). Oscillatory measurements of $\breve{L}_p$ and $\breve{N}_p$, described in §4.7.3,are also shown for comparison.

4.9 Polynomial Descriptions of Lateral Moments

4.9.1 Cubic Fits to Static Data

Following work done on the combat aircraft described in Chapter 3,using cubic polynomials to describe the variation of rolling and yawing moments with sideslip and roll rate, cubic polynomials were fitted to the corresponding data for the HIRM.

A number of different programs were used to fit the polynomials to the data,including one for use on a Commodore PET microcomputer and another, POLFT, written for the VAX 11 computer,using a NAG mathematical library subroutine[103]. An R.A.E.program, CFIT, was used to fit polynomials to the rotary rig data.

POLFT computes a weighted least-squares polynomial approximation to a set of data points, so for instance,for $C_\ell(\beta)$, it fits a polynomial:

$$C_\ell = C_{\ell_0} + \breve{L}_{v_1}\bar{v} + \breve{L}_{v_2}\bar{v}^2 + \breve{L}_{v_3}\bar{v}^3$$

The PET program had the facility to fit modified cubics, as required for the lateral equations of motion, i.e.

$$C_\ell = \breve{L}_{v_1}\bar{v} + \breve{L}_{v_3}\bar{v}^3 \quad (4.11)$$

$$C_n = \breve{N}_{v_1}\bar{v} + \breve{N}_{v_3}\bar{v}^3 \quad (4.12)$$

but the best results were obtained by fitting either 3 or 4 term expressions and omitting the constant and squared term,for use in the simulation. When trying to fit an odd powered cubic polynomial directly to the data it was found that the terms would often be quite different to the values obtained from the full polynomial because of the constraints being imposed on the few terms in the polynomial.

Examples of some results for $\alpha = 26^{o}$ obtained using the PET program are given in Figs.4.17 and 4.18. These figures show the curves fitted using polynomials of the form given in equations (4.11) and (4.12),after coefficients had been obtained by fitting polynomials with more terms. Three of the fits show softening spring characteristics and polynomial 3B for C_{ℓ} (Fig.4.17b) shows stiffening spring characteristics, i.e. there is an effective increase in stiffness as sideslip amplitude increases, with $\check{L}_{v_1}$ having its usual negative sign. $\check{N}_{v_1}$ is of opposite sign to that usual at low α.

The physical basis for softening or stiffening spring characteristics for $C_{\ell}(\beta)$ and $C_n(\beta)$ is difficult to determine without resort to flow visualisation tests. Certainly for $C_n(\beta)$,if there are strong vortices from the canards at high β going over the fin,it would be expected that restoring C_n would be reduced. At even higher β, if the fin had not stalled, as the fin came out of the influence of the vortices, stiffening would be expected.

It was decided to concentrate on using POLFT to fit the polynomials to $C_{\ell}(\beta)$ and $C_n(\beta)$ data and results for the α range 22^{o} to 38^{o} are shown in Table 4.2. Examples of fits obtained are given in Fig.4.19 and the $\alpha = 24^{o}$ results show the effects of some variation in $\check{L}_{v_3}$.

The definitive values of $\check{L}_{v_1}$ and $\check{N}_{v_1}$ and the cubic coefficients $\check{L}_{v_3}$ and $\check{N}_{v_3}$ are shown in Fig.4.20. Also shown are the values of $\check{L}_{v}$ and $\check{N}_{v}$ obtained from linear regression between $\beta = -6^{o}$ and $\beta = +6^{o}$.

As noted before, the non-linearities in rolling moment are larger than those in yawing moment but at $\alpha = 40^{o}$, $\check{N}_{v_3}$ is increasing rapidly. The discrepancies between $\check{L}_{v_1}$ from the cubic fit and the regression reflect both the inaccuracies from constraining a cubic to the data as well as those from the regression analysis.

4.9.2. Cubic Fits to Rotary Data

As with the static data,described in §4.9.1, cubic polynomials were fitted to the rotary rig data. Both full cubic and modified cubic (without the squared term) polynomials were fitted to the measured (body axis) data and wind axis data:

$$C_\ell = C_{\ell_0} + C_{\ell_p}\left(\frac{pb}{2V}\right) + C_{\ell_{p_2}}\left(\frac{pb}{2V}\right)^2 + C_{\ell_{p_3}}\left(\frac{pb}{2V}\right)^3 \quad (4.13)$$

$$C_n = C_{n_0} + C_{n_p}\left(\frac{pb}{2V}\right) + C_{n_{p_2}}\left(\frac{pb}{2V}\right)^2 + C_{n_{p_3}}\left(\frac{pb}{2V}\right)^3 \quad (4.14)$$

The polynomials were fitted using an RAE program, CFIT, and typical results are shown in Fig.4.12 for wind axis moments at $\alpha = 24^o$ and $\alpha = 26^o$.

A slight inconsistency in notation arose when it was decided to put $C_{\ell_{p_3}} = \breve{L}_{p_3}$ and $C_{n_{p_3}} = \breve{N}_{p_3}$ for use in simulations and analysis, but the linear parts were of the correct form, i.e.

$$\frac{C_{\ell_p}}{2} = \breve{L}_p, \qquad \frac{C_{n_p}}{2} = \breve{N}_p$$

Plots of $\breve{L}_{p_1}^w$, $\breve{L}_{p_3}^w$, $\breve{N}_{p_1}^w$ and $\breve{N}_{p_3}^w$ are shown in Figs.4.22 and 4.23. Significant non-linearity is evident in both $C_\ell(pb/2V)$ and $C_n(pb/2V)$ above about 15^o angle of attack, including non-zero moments at zero roll-rate

Incorporation of the rotary rig data in its non-linear cubic form presented some problems due to the absence of large amplitude motion yawing data. These problems are high-lighted in §5.7.4.1.

CHAPTER 5

HIRM LATERAL STABILITY AND RESPONSE

5.1 Introduction

This chapter sets out an analysis of the stability and response (mainly lateral) of the HIRM using techniques described in Chapter 2 and building on the data described in Chapter 4. After an analysis of the static and dynamic stability data, lateral response simulations are described, followed by applications of the Beecham-Titchener averaging technique to the HIRM lateral data. By way of introduction a few remarks will be made on the calculation of trim conditions for the stability calculations.

Configuration C has a trim angle of attack (using HIRM 1 data) of 35^{o}. Because more data was available for this configuration than any other, and because it had a high trim angle of attack, calculations concentrated on this version. For different angles of attack "near-trim" conditions were considered and tail/canard settings were kept constant for evaluating such quantities as C_L, C_D (and hence flight path angle, γ, and V).

Calculations used free-flight model data for mass, wing area, inertias etc and were performed for a mean altitude of 5000 ft above Sea Level. Trim conditions were calculated using the following equations for gliding flight.

For trim, along flight path:

$$\dot{V} = 0 = -D - W\sin\gamma_e \qquad (5.1)$$

and normal to flight path:-

$$L = W\cos\gamma_e \qquad (5.2)$$

$$\text{So} \quad \tan\gamma_e = -\frac{D}{L} = -\frac{C_D}{C_L} \qquad (5.3)$$

$$\text{Also} \quad \tfrac{1}{2}\rho V^2 S C_L = W\cos\gamma_e \qquad (5.4)$$

$$\text{So} \quad V^2 = \frac{2}{\rho S C_L}.W\cos\gamma_e \qquad (5.5)$$

Measured and estimated aerodynamic derivatives were used at the calculated trim conditions to assess the stability and response of the HIRM at varying α.

5.2 Preliminary Assessment of Stability

Referring to data given in Chapter 4 for the HIRM it is noted from Figs.4.3 and 4.6 for the C configuration that (i) pitch stability is restoring up to $\alpha = 40^{o}$; (ii) directional stability, $\check{N}_v$, is restoring up to 18^{o} angle of attack while; (iii) the lateral stability derivative, $\check{L}_v$, shows a significant loss between 18^{o} and 26^{o} angle of attack.

Turning to controls, symmetric tailplane (equivalent to elevator) power, $C_{m_{\eta_T}}$, remains negative up to $\alpha = 40^{o}$ (Fig.4.4) as does the asymmetric tailplane effectiveness, $\check{L}_{\xi_T}$ (Fig.4.7). Yaw due to differential tailplane, $\check{N}_{\xi_T}$, is adverse above $\alpha = 37^{o}$.

These all tend to suggest departure tendancies beginning around $\alpha = 18^{o}$ and although $\check{N}_{\xi_T}$ is proverse up to a high α, controllability may be lost due to the negative $\check{N}_v$ above $\alpha = 18^{o}$.

To take the stability assessment further, the departure parameters, $\check{N}_{v_{dyn}}$ and L.C.D.P. can be examined, as well as the roots of the classical lateral stability quartic. In the next section, departure criteria for the HIRM are evaluated and then lateral stability roots are examined.

During early stages of the work on the HIRM there were no measured dynamic derivatives available, so initial stability calculations were carried out using estimated derivatives (see §4.6). Another source of uncertainty were the inertias of the free flight model. Only now, at the time of writing, have measurements actually been performed on the free-flight models, so again initial calculations for stability were made using estimated inertias.

Initially the yaw to roll inertia ratio was estimated at 9.7 but for the definitive calculations, the inertia ratio was set to 6, likely to be more representative of the HIRM free flight model value. The definitive set of estimated inertias and mass ("Data Set no.3") was given in Table 4.1.

5.3 Departure Parameters

5.3.1 $\check{N}_{v_{dyn}}$ and L.C.D.P.

The departure parameters $\check{N}_{v_{dyn}}$ and L.C.D.P., described in §2.3, were evaluated for the HIRM configuration C using static wind tunnel data in program ROOTS. The results for configuration C are plotted in Figs.5.1 and 5.2.

$\check{N}_{vdyn}$ remains positive up to 40^o angle of attack but approaches zero at 26^o, indicating susceptibility to directional divergence. Examination of $\check{N}_v$ and $\check{L}_v$ (Fig.4.6) shows that at $\alpha = 26^o$, $\check{N}_v$ is negative and $|\check{L}_v|$ is at a maximum (small negative value), which leads to the near zero value of $\check{N}_{vdyn}$. Despite $\check{N}_v$ remaining negative, the large negative values of $\check{L}_v$ at higher angles of attack mean $\check{N}_{vdyn}$ goes well positive at these high angles of attack, showing how a stable dihedral effect and relatively high inertia ratio, (I_z/I_x), can significantly affect $\check{N}_{vdyn}$.

As far as L.C.D.P. is concerned, $\check{L}_v$ remains negative (but almost goes positive at $\alpha = 26^o$) up to $\alpha = 40^o$ and $\check{N}_{\xi_T}$ is also negative up to 37^o angle of attack. Despite this, the large negative values of $\check{N}_v$ means L.C.D.P. goes negative at around $\alpha = 24^o$, a few degrees above the angle of attack at which $\check{N}_v$ does so. Negative values of L.C.D.P. (shown as A.A.D.P. in Fig.5.2) indicate that control induced departure is likely. The lateral control behaviour for configuration C could be improved by adding an aileron-to-rudder gearing, as mentioned in §2.3.2, and some form of control system will be needed for the free flight models. For configuration C, the A.A.D.P. is well negative at the trim angle of attack, around 34^o.

The effect of positive deflection of the canard is shown in Figs.5.1 and 5.2. Deflection of the canard through + 10^o results in an increase in A.A.D.P. below 30^o angle of attack and an increase in the α at which A.A.D.P. = 0. N_{vdyn} is similarly increased in the α range 24 - 29^o but then shows a loss at $\alpha = 32^o$.

Positive deflection of the tailplane leads to an increase in $\check{N}_{vdyn}$ up to $\alpha = 36^o$ when it then goes to zero. L.C.D.P. is slightly worse than for the basic C configuration as it now goes through zero at $\alpha = 22^o$. Ref.90 contains departure parameter results for other HIRM configurations.

Greer[48] has pointed out the method of extraction of $\check{N}_v$ and $\check{L}_v$ from experimental data can affect the ability of $\check{N}_{vdyn}$ to predict directional divergence.

It is important that data is available at very small α intervals to ensure sudden changes in the aerodynamic characteristics are covered, as these could well lead to negative values of the departure parameters.

$\check{L}_v$ and $\check{N}_v$ can be extracted from $C_\ell(\beta)$ and $C_n(\beta)$ in a number of ways, e.g. a straight line fit to data over a large range of sideslip, straight line fit to small sideslip data etc. Examples are shown in Fig.5.3 for HIRM C static data at $\alpha = 40^o$. These can lead to significant differences in the calculation of departure parameters at high α, where $C_\ell(\beta)$ and $C_n(\beta)$ are non-linear. Fig.5.4 shows the values of $\check{L}_v$ and $\check{N}_v$ obtained using 3 methods of extraction from the experimental data for HIRM C. The major differences occur

above $\alpha = 20^{o}$ but, as can be seen, the methods all show $\check{N}_v$ going through zero at the same α and all show $\check{L}_v$ remaining negative up to $\alpha = 40^{o}$.

In Fig.5.5, which shows the effect of these values of $\check{L}_v$ and $\check{N}_v$ on $\check{N}_{vdyn}$, there is little difference in the form of the $\check{N}_{vdyn}$ curve, except above $\alpha = 34^{o}$ where $\check{N}_{vdyn}$ is now positive anyway. A more negative $\check{N}_v$ from the fit to C_n data over $\beta = \pm 2^{o}$, at $\alpha = 26^{o}$, gives $\check{N}_{vdyn} = 0$ at this angle of attack.

In §2.3.1, the interpretation of $\check{N}_{vdyn}$ as a factored approximation to b_1, in the lateral stability quartic, was mentioned. $\check{N}_{vdyn}$ is given approximately by $b_{1R} I_Z / \frac{1}{2}\rho V^2 Sb$ (eqn.(2.23)), which in turn is an approximation to $b_1 I_Z / \frac{1}{2}\rho V^2 Sb$.

The validity of using $\check{N}_{vdyn}$ as a representation of the behaviour of the b_1 term, in the lateral stability quartic, is shown in Fig.5.5. The values of the factored b_1 term agree well with $\check{N}_{vdyn}$, showing the terms neglected from b_1, to get $\check{N}_{vdyn}$, are small. For other configurations this may not be so and b_1 may go negative when $\check{N}_{vdyn}$ is near zero.

As a general remark it must be said that the prediction of departure using static data has come into question in recent years. It is possible that the static data does not accurately represent the flight case considered, e.g. observations on the Gnat aircraft[26] certainly showed $\check{N}_{vdyn}$ well positive when such phenomena as wing rock (divergence in the form of lateral-directional oscillatory instability) occurred, at high angles of attack. L.C.D.P. also has limitations when $\check{N}_v$ and $\check{L}_v$ do not have conventional signs and in these cases, further data is required to predict the kind of departure from a control input.

5.3.2 Weissman Criteria

Following Weissman[52,53] (§2.3.3), Fig.5.6 shows a plot of A.A.D.P. against $\check{N}_{vdyn}$ for HIRM configuration C. Cubic fits to $C_n(\beta)$ and $C_\ell(\beta)$ have been used for this figure. No departure tendencies are indicated, by this plot, up to $\alpha = 24^{o}$, after which yaw divergence may be expected followed by roll reversal (refer to Fig.2.3).

5.3.3 Conclusions

This section has shown that, based on configuration C data, a control system is likely to be required to obtain stable flight of the HIRM above 24^{o} angle of attack. It should be noted that the analysis presented here has been based on one configuration and for actual flights the configuration will change, to obtain different trim angles of attack. Ross and Reid[90] show that for configuration changes following control law B (see §4.4.1) $\check{N}_{vdyn}$ is positive up to greater than 40^{o} angle of attack and L.C.D.P., without an aileron-rudder interconnect, goes negative at 27^{o} angle of attack.

5.4 Lateral Characteristic Equation and Roots

5.4.1 General

Using the various forms of static and dynamic data available for configuration C,an anlaysis of the stability can be made by examining the lateral characteristic equation roots.

As a preliminary to this, the linear Routh Discriminant, given by

$$R = a_1 b_1 c_1 - a_1^2 d_1 - c_1^2 \qquad (5.6)$$

was evaluated using linear components of the cubic fitted static data and oscillatory dynamic derivatives. Results are shown in Fig.5.7 and indicate instability between $\alpha = 24^o$ and 34^o. The similarity of the variation of b_1, with α, to the $\check{N}v_{dyn}$ variation is also apparent.

5.4.2 Lateral Roots

Using the same data as in Fig.5.7 the program ROUTH was used to evaluate the roots of the lateral stability quartic and results are plotted in Fig.5.8, showing variation with α. The roll and spiral modes are stable exponential modes at angles of attack up to 22^o, at which point they combine to form a damped oscillatory mode. At $32^o\alpha$ this mode briefly becomes two exponential modes again.

The dutch roll mode damping decreases as α increases and the mode goes unstable at $24^o\alpha$. Frequency also decreases with α down to a minimum around $26^o\alpha$. Above this α,both frequency and damping increase again, the oscillation becoming convergent at $\alpha = 34^o$.

The damping characteristics are presented in Figs.5.9a,c, in the form of the real part of the roots. The negative real part of the roots, -k, corresponds to, λ, the damping index, used in the averaging technique, for non-linear damping. Again these figures use the linear contribution from the cubic fitted static data and oscillatory dynamic data (dashed lines). Also shown in Fig.5.9, is the data using straight line fits for static derivatives. Differences between the results start to arise above $\alpha = 30^o$, where the non-linearities in $C_n(\bar{v})$ and $C_\ell(\bar{v})$ make the straight line fits less accurate for the static derivatives.

The time constants for the exponential modes and times to half-amplitudes for the oscillatory modes are shown in Figs.5.9b,d, as calculated from the program ROOTS.

The effects of using other combinations of static and dynamic derivatives from the various sources described in Chapter 4 are shown in Figs.5.10 and 5.11. Combinations of static and dynamic data from the 11½ft x 8ft wind tunnel

tests, oscillatory rig and rotary rig tests, as well as estimates of the dynamic derivatives, have been used in the calculations.

The plots show similar trends, with increasing α, for the roll and spiral modes, e.g. decrease in damping of the roll mode; increase in damping of the spiral mode, until a new oscillatory mode forms above $\alpha = 20^{o}$; new oscillatory mode splitting into real modes at higher α, all the while remaining stable.

Some significant differences occur with the use of the different data sources for the dutch roll characteristics. Fig.5.11 shows the effect of using rotary dynamic data and gives similar characteristics to the oscillatory dynamic data shown in Fig.5.9. The peak dutch roll instability at $\alpha = 26^{o}$ reflects the peak in the dihedral effect derivative, $\check{L}_v$, shown in Fig.4.6.

Comparing the use of oscillatory sideslip derivatives in Fig.5.10 with the use of static sideslip derivatives in Fig.5.9 shows how the more stable dihedral effect, measured on the oscillatory rigs, leads to the dutch roll damping remaining positive for all α, except 34^{o}, where it reaches zero.

The dashed lines in Fig.5.10a,b show how the static sideslip data combined with estimated dynamic data indicates an unstable dutch roll above $\alpha = 23^{o}$. The damping index becomes positive again at $33^{o}\alpha$ and increases rapidly due to the increase in body axis roll damping,which was estimated to occur near $\alpha = 40^{o}$ (see Fig.4.8).

Taken together with the results of $\check{N}_{v_{dyn}}$ and L.C.D.P. tests, the roots of the characteristic equation suggest a simple damper system or some sideslip feedback will be needed to give stable responses above $\alpha = 22^{o}$. The first drop test model has a lower roll inertia than that used in the calculations here (measured $I_x = 16\,kg.m^2$) but the control system being designed should cope with this and be able to control the lateral instability up to at least $30^{o}\alpha$.

5.5 Dynamic Stability Axis Moments

In this section, the dynamic stability axis moments (see §2.3.5) for the HIRM are examined. Body axis data is measured as a function of α and β, so aerodynamic and kinematic coupling between dynamic stability and geometric body axes is included in the dynamic moment coefficients.

The non-dimensional coefficients $C_{\ell DYN}$, C_{mDYN} and C_{nDYN} are shown in Figs.5.12 to 5.14 respectively,for HIRM configuration C. Data from the 11½ft x 8ft W.T.tests has been used for $\alpha = 0(2)40^{o}$ and $\beta = -6(1)6^{o}$. Immediately obvious are the asymmetries about $\beta = 0^{o}$, particularly at high α. In the cases of $C_{\ell DYN}$ and C_{nDYN}, there are non-zero

moments at $\beta = 0^o$, for α above approximately 20^o, indicating possibly asymmetric vortex shedding off the nose.

For $C_{\ell DYN}$, with non-zero sideslip, as α increases, the moment first increases and then decreases. Above $\alpha = 25^o$, there is a finite $C_{\ell DYN}$ at $\beta = 0$.

Turning to C_{mDYN}, in Fig.5.13, for zero sideslip, the trim is at 34.5^o, with a stable pitching moment slope, $\partial C_{mDYN}/\partial\alpha$. Up to $\beta = \pm 6^o$, the trim is stable (although at slightly higher α) as β increases in magnitude. C_{mDYN_α} is stable (negative) for all sideslips shown up to $+4^o$ and -5^o at $\alpha = 20^o$, when local instabilities occur.

The small variation of C_{mDYN} with sideslip, except between $\alpha = 10^o$ and 25^o, indicates small aerodynamic and kinematic cross-coupling.

Fig.5.14 illustrates similarities to features noted in §5.3.1 concerning $\check{N}_{vdyn}$. C_{nDYN} is stable with respect to β up to $\alpha = 25^o$. At around this α, asymmetries start occurring, with unstable values of C_{nDYN} coming in at small positive and negative sideslip angles. As for $C_{\ell DYN}$, C_{nDYN} is non-zero for $\beta = 0^o$ at greater than $25^o\alpha$.

Having examined the stability, concentrating mainly on the lateral motion, using static data and linearised dynamic data, the remaining parts of this chapter deal with the assessment of a three degree of freedom mathematical model for dynamic response cahracteristics.

5.6 Dynamic Responses and Assessment of Averaging

5.6.1 General

One aim of the HIRM project is concerned with flight at angles of attack up to loss of normal control (i.e.departure) and the simulation program, SIMUL, was used to look at the nature of the departure, as predicted by a three degree of freedom mathematical model with aerodynamic non-linearities.

In Chapter 3, the usefulness of the B.T.S.theoretical averaging technique was demonstrated, for current generation combat aircraft applications and limitations of the method were also highlighted. The HIRM data gave further opportunities to apply and assess the averaging technique. The technique would now be applied to the equations of motion at much higher angles of attack than in previous applications and this alone could have presented problems. Measured non-linear aerodynamic characteristics enabled further investigations to be made into rates of growth to limit cycles and responses with two cubic aerodynamic non-linearities present. Comparisons of averaging and local linearisation techniques were also made, using responses about non-zero equilibrium states.

This section continues with an assessment of the effect of non-linear sideslip characteristics, followed by non-linear roll rate characteristics. The chapter concludes with results from simulations using (a) combined non-linearities and (b) responses to controls.

5.6.2 Non-linear Sideslip Characteristics for a Range of α.

Assessment of the lateral stability using programs ROOTS and ROUTH, described in §5.4, showed a region of dutch roll instability between $\alpha = 24^{o}$ and $\alpha = 34^{o}$. It was decided to incorporate some non-linear sideslip characteristics into the equations of motion and look at the form of the responses, particularly over this angle of attack range. The non-linear characteristics are those described in §4.9.1., i.e. cubic variations of moments against sideslip. It was thought that some limit cycles may occur as a result of the non-linear aerodynamics but the softening spring characteristics of the sideslip data (Table 4.2), and the smallness, in general, of the non-linearities, meant that only divergences were predicted above 24^{o} angle of attack. However, these still gave an opportunity to assess the averaging technique at high angles of attack.

Up to $\alpha = 22^{o}$, the responses were stable, with a damped dutch roll oscillation. The $C_{\ell}\sim\beta$ characteristic at $\alpha = 24^{o}$ showed a very strongly non-linear behaviour at $\beta = +4$ to 5^{o} (Fig. 4.19a), but was still softening, and this led to divergence. A typical divergent response is shown in Fig.5.15 for $\alpha = 26^{o}$ and such responses were obtained up to $\alpha = 34^{o}$, in agreement with the implications from the results of the ROOTS program. In all the responses oscillatory dynamic derivatives were used.

From the responses, a critical sideslip, $\bar{v}_{crit}$, at divergence could be determined and was taken as the sideslip at which the roll rate response showed a sudden change. The B.T.S. averaging technique predicts divergences when the solution of $R^{*} = 0$ gives an amplitude, σ_{v}, which has an associated frequency which is imaginary, i.e. ω^{2} is negative. Taking such amplitudes as the amplitudes above which divergence occurs (see section 2.4.2.4), the program ROUTH was used to solve $R^{*} = 0$, for the α range in which instability was predicted by the ROOTS program, i.e. $\alpha = 22^{o}$ to 34^{o}. Critical amplitudes at divergence were measured from the simulations for the same α range and the results are shown in Fig.5.16.

Although the averaging technique tends to slightly over-predict the critical amplitudes the agreement between simulation and analytic technique is good. Certainly the right trends are predicted and the smallest critical amplitudes seem to occur where the softening spring non-linearity is greatest (e.g. $\alpha = 24^{o}$).

5.6.3 Non-linear Sideslip Characteristics at $\alpha = 26^{o}$

Initial calculations concerning the HIRM stability suggested that $\alpha = 26^{o}$ would be the most unstable case (see Figs.5.9 to 5.11). Indeed, for calculations using the first inertia and mass estimates, this was the only angle of attack at which instability was noted.

It was for this reason that early work, using the simulation program, concentrated on this angle of attack and looked at effects of variation in the representation of the static wind tunnel sideslip data. This section will review the work completed on these representations and includes more comparisons with averaging.

5.6.3.1 Assessment of Different $C_{\ell}(\beta)$ and $C_{n}(\beta)$ Characteristics

Having obtained a number of different cubic polynomial fits to the $C_{\ell}(\beta)$ and $C_{n}(\beta)$ data, using various computer programs (see §4.9.1), different combinations were tried in SIMUL, for responses at $\alpha = 26^{o}$. In particular the four curves shown in Figs.4.17 and 4.18 were tried and results from SIMUL were compared to predictions from averaging (program ROUTH). Table 5.1 summarises the results and shows again how the averaging copes well with a non-linearity in one response variable.

Limit cycles of amplitude around 0.12 radians in sideslip, were obtained when stiffening $C_{\ell}(\beta)$ characteristics were used, although the case of $C_{\ell}(\beta)$ curve no.2A (see Table 5.1 for details of the curves) and $C_{n}(\beta)$ curve no.3B also showed a limit cycle,but of larger amplitude in sideslip. This is consistent with softening spring characteristics, which mean the restoring moment effect levels off and then gets smaller at large β. Large amplitude limit cycles, or divergence, are obtained for $C_{\ell}(\beta)$ curve no.2A, shown in Table 5.1. The use of $C_{\ell}(\beta)$ curve no.2A alone led to a decaying oscillation, reflecting the increase in magnitude of $\check{L}v_1$ over the basic linear (unstable) case.

Returning now to the definitive cubic polynomial representations of $C_{\ell}(\beta)$ and $C_{n}(\beta)$, as given in Fig.4.19b, another sensitivity study was carried out. Now, the $C_{n}(\beta)$ characteristics were fixed at $\check{N}_{v_1} = -0.17$, $\check{N}_{v_3} = 1.697$ and the $C_{\ell}(\beta)$ characteristics were varied, using $\check{L}_{v_1} = -0.061$, the linear regression value, and different $\check{L}_{v_3}$ values. The effect of the extreme values of $\check{L}_{v_3}$ are shown in Fig.5.17.

Limit cycle oscillations were obtained for all stiffening spring $C_{\ell}(\beta)$ characteristics and also for $\check{L}_{v_3}$ up to +0.5. Changing $\check{N}_{v_3}$ to 2.599, and repeating the variation of $\check{L}_{v_3}$, increases the range of $\check{L}_{v_3}$ for which limit cycles are obtained. Results are summarised in Fig.5.18. Also shown are calculations from averaging, which agree well with the simulation amplitudes.

A note of caution should be sounded after this review of the various $C_\ell(\beta)$ and $C_n(\beta)$ characteristics. In a lot of cases, the polynomials used, which give rise to limit cycle oscillations in the simulation, describe a curve which is quite different to the best fit to the wind tunnel data. Thus, in some cases the limit cycles are now attaining amplitudes in sideslip, due to the formulation of $C_\ell(\beta)$ or $C_n(\beta)$, which are larger than the peak experimental values of β for which wind tunnel data is available. Thus it must be remembered that these results are very much investigations into the formulations of $C_\ell(\beta)$ and $C_n(\beta)$ and should not be taken as predictions of actual flight responses. It seems that the best fits to the static sideslip data predict oscillatory divergence above $\alpha = 24^o$, as discussed in §5.6.2.

5.6.3.2 Growth to Limit Cycles

Using the characteristics described in the last part of the previous section, i.e. $\check{N}_{v_1} = -0.17$, $\check{N}_{v_3} = 2.599$, $\check{L}_{v_1} = -0.061$ and varying $\check{L}_{v_3}$, a comparison was made of the two analytic formulations for λ, as a function of amplitude up to limit cycle. These so called "$(\lambda+i\omega)$"and "$(3\lambda+i\omega)$", forms for λ were given in equations (2.98) and (2.101).

Results showing λ as a function of amplitude are given in Fig.5.19 and are compared with λ measured from simulations. Two values of $\check{L}_{v_3}$, -0.5 and -1.0, are shown. The $(\lambda+i\omega)$ formulation of λ lies closer to the simulation values but as the limit cycle is reached very quickly, only a few points were obtainable from the simulation. As in Chapter 3, because of the few simulation points available, it may be better to compare the actual simulation growth envelope with that predicted by quadrature (using program ROUTH), from the B.T.S.values of λ. These envelopes, for the two cases in Fig.5.19, are shown in Fig.5.20 and confirm that the $(\lambda+i\omega)$ formulation gives a closer match to the simulation results.

5.6.4 Non-linear Roll Rate Characteristics

5.6.4.1 General

In this section the results of including non-linear roll rate characteristics in the HIRM lateral equations for $\alpha = 26^o$, will be described. The aim was to incorporate the rotary rig data, described in §4.8, into the simulation in the same way that cubic roll rate non-linearities were included in the modelling of aircraft B in Chapter 3. For reasons which will be described, a direct incorporation of the rotary data proved not to be possible and this led to difficulties with assessing the success of averaging for these particular cases.

The simulations and calculations shown in some of the following sections were performed before a definitive set

of inertias and a final mass for the HIRM were adopted. The values of constants for these cases are[104] :

I_x = 13.40 kg.m^2

I_z = 129.4 kg.m^2

I_{xz} = -0.2 kg.m^2

m = 166.6 kg

V = 32 m/s

and these cases are labelled "HIRM Data Set no.2" in the ensuing sections. Test cases run with the latest HIRM data showed similar behaviour, confirming conclusions drawn with the old data.

5.6.4.2 Incorporation of Roll Rate Non-linearities into the Lateral Equations

Cubic polynomials were fitted to the rotary rig data as described in §4.9.2. The question now arose as to how to incorporate this rotary rig data into body axis equations, when the rotary data was in the form of polynomials, fitted in wind axes, or in body axes, as a function of wind axis roll rates?

A. Wind Axes

The first method considered was to convert the simulation to work in wind axes. This involves calculating the inertias in the new axis system[105], calculating new values of the derivatives using such formulae as those shown in eqns.(4.7) and (4.8)[102] , and converting body axis rates to wind axis rates.

The equations used in SIMUL were now:

$$\dot{v}^w = -Vr^w + g\sin\phi + \frac{Y_v^w}{m}.v^w \qquad (5.7)$$

$$\dot{p}^w = \frac{I_z^w}{I_x^w I_z^w-(I_{xz}^w)^2}L + \frac{I_{xz}^w}{I_x^w I_z^w-(I_{xz}^w)^2}N \qquad (5.8)$$

$$\dot{r}^w = \frac{I_x^w}{I_x^w I_z^w-(I_{xz}^w)^2}N + \frac{I_{xz}^w}{I_x^w I_z^w-(I_{xz}^w)^2}L \qquad (5.9)$$

$$\dot{\phi}^w = p^w \qquad (5.10)$$

where

$$L = L_v^w v + L_{p_{1_R}}^w p^w + L_{p_{3_R}}^w (p^w)^3 + L_{r_o}^w r^w \qquad (5.11)$$

and $$N = N^{w}_{v}v + N^{w}_{p_{1_R}}p^{w} + N^{w}_{p_{3_R}}(p^{w})^{3} + N^{w}_{r_o}r^{w} \qquad (5.12)$$

Small amplitude data was used for L_r and N_r derivatives. $L^{w}_{p_{1R}}$, $N^{w}_{p_{1R}}$, $L^{w}_{p_{3R}}$ and $N^{w}_{p_{3R}}$ were obtainable directly from the cubic fits to wind axis data, allowing for constants, and examples were given in Fig.4.21. The effect of omitting the squared term in the polynomial fits was very small, so the major approximation, in the use of the above form of moment representation,was in the omission of the constant terms, C_{ℓ_0} and C_{n_0}. These can become significant at high angles of attack but then, at say $\alpha = 36^{o}$ (Fig.4.14e shows body axis moments), the use of a cubic polynomial to describe the data is questionable.

B. Body Axes

The alternative way of incorporating the rotary data, is to do so in body axes, in a similar way to that used in the simulations described in Chapter 3. Unfortunately it proved not to be possible to incorporate the data as simply as had been done in these previous cases because of difficulties in transforming axes. Ross[107] gave some suggestions as to how the rotary data could be incorporated.

The rotary rig results can be obtained in the form of $L^{w}_{R}(p^{w})$ and $N^{w}_{R}(p^{w})$. From the oscillatory rig, L^{w}_{o} and N^{w}_{o} are obtainable as linear functions of p^{w}, r^{w}. The polynomials describing the rotary data are functions of wind axis roll rates so wind axis moments, as functions of large amplitude test measurements, may be written as:

$$L^{w}_{R} = L^{w}_{R}(p^{w}) + L^{w}_{r_R}r^{w} + L^{w}_{v}v + \ldots \qquad (5.13)$$

$$N^{w}_{R} = N^{w}_{R}(p^{w}) + N^{w}_{r_R}r^{w} + N^{w}_{v}v + \ldots \qquad (5.14)$$

Unfortunately large amplitude yawing data was not available, $L^{w}_{r_R}$ and $N^{w}_{r_R}$ could not be measured, and so, small amplitude data, $L^{w}_{r_o}$ and $N^{w}_{r_o}$, was used as an approximation, as in the last section.

Now the formulations are transferred to body axes and this is where the complexities arise, regarding the cubic polynomials. Body axis moments are given by

$$L^{B} = L^{w}\cos\alpha - N^{w}\sin\alpha \qquad (5.15)$$

$$N^{B} = N^{w}\cos\alpha + L^{w}\sin\alpha \qquad (5.16)$$

So $$L^B = (L^w_R(p^w)\cos\alpha - N^w_R(p^w)\sin\alpha) + (L^w_{r_o}\cos\alpha - N^w_{r_o}\sin\alpha).r^w + L^B_v.v \ldots \quad (5.17)$$

$$N^B = (N^w_R(p^w)\cos\alpha + L^w_R(p^w)\sin\alpha) + (N^w_{r_o}\cos\alpha + L^w_{r_o}\sin\alpha)r^w + N^B_v.v \ldots \quad (5.18)$$

Now $N^w_{r_o}$ and $L^w_{r_o}$ can be transformed to body axis forms and after simplification, (5.17) and (5.18) become

$$L^B = L^B_R(p^w) + (L^B_{r_o}\cos\alpha - L^B_{p_o}\sin\alpha)r^w + L^B_v.v + \ldots \quad (5.19)$$

$$N^B = N^B_R(p^w) + (N_{r_o}\cos\alpha - N_{p_o}\sin\alpha)r^w + N^B_v.v + \ldots \quad (5.20)$$

Representing $L^B_R(p^w)$ and $N^B_R(p^w)$ by their polynomial forms then gives:

$$L^B = L_{p_{wR}}p^w + L_{p_{w_3}}(p^w)^3 + (L^B_{r_o}\cos\alpha - L^B_{p_o}\sin\alpha)r^w + L^B_v v + \ldots \quad (5.21)$$

$$N^B = N_{p_{wR}}p^w + N_{p_{w_3}}(p^w)^3 + (N^B_{r_o}\cos\alpha - N^B_{p_o}\sin\alpha)r^w + N^B_v v + \ldots \quad (5.22)$$

In the simulation program, p^w and r^w are formed as follows:

$$p^w = p^B\cos\alpha + r^B\sin\alpha \quad (5.23)$$

$$r^w = r^B\cos\alpha - p^B\cos\alpha \quad (5.24)$$

and hence can be used in equations (5.21) and (5.22). The lateral equations as used in SIMUL are thus:-

$$\dot{v} = Vp\sin\alpha - Vr\cos\alpha + \frac{Y_v v}{m} + g_3\sin\phi + g_2\sin\psi \quad (5.25)$$

$$\dot{p} = \frac{1}{I_x I_z - I_{zx}^2}(I_z L^B + I_{xz}N^B) \quad (5.26)$$

$$\dot{r} = \frac{1}{I_x I_z - I_{zx}^2}(I_x N^B + I_{xz}L^B) \quad (5.27)$$

$$\dot{\phi} = p \tag{5.28}$$

$$\dot{\psi} = r \tag{5.29}$$

5.6.4.3 Results

Results are presented in this section for simulations using both equations (5.7) to (5.10) for wind axes and (5.25) to (5.29) for body axes. Because of the nature of the approximations for the rotary data, only limited predictions could be made with the averaging technique. The averaging technique has been developed for equations with cubic non-linearities in body axis moments,so the method cannot be used, without more approximation, for equations such as (5.25) to (5.29). Some numbers were tried, on the basis that they may not represent the actual HIRM very well, but would provide some more results from the technique. In the event, trying to use wind axis data in the body axis technique did not provide any useful results as the angle of attack was too high for the approximations to be valid. Derivatives used for the simulations of sections 5.6.4 to 5.6.6 are shown in Table 5.2.

A. Wind Axis Simulation

Using equations (5.7) to (5.10), simulations were run with both full cubic and modified cubic terms for the rolling moment due to roll rate. HIRM Data Set no.2 was used as detailed in §5.6.4.1 and results are shown in Fig.5.21. Wind axis roll rate is almost exactly the same as body axis roll rate, while the wind axis and body axis yaw rates are 180^{o} out of phase.

On transforming the derivatives to wind axes, the dihedral stability is increased along with yaw rate damping derivative, $\check{N}_r$, and program ROUTH, used on the wind axis data, shows the dutch roll to be marginally stable. The linear roll damping term, $\check{L}^{W}_{pR}$, is smaller than the corresponding body axis oscillatory derivative, $\check{L}^{B}_{p_O}$, and so the averaging technique predicts a limit cycle amplitude of 11.9 r/s, much larger than the observed 3.25 r/s.

B. Body Axis Simulation

Using a modified cubic fit to body axis rolling moment against wind axis roll rate,and incorporating this into equations (5.21) and (5.22) for simulation, yields the results shown in Fig.5.22. HIRM Data Set no.2 was again used for this run,and those shown in Fig.5.23.

To test the sensitivity of the simulated motion to the use of body axis rates instead of wind axis roll and yaw rates in equations (5.21) and (5.22), p^B was first of all used

instead of p^W. Fig.5.23a shows the limit cycle characteristics to be unaffected by this approximation. By contrast, when r^B is used instead of r^W, as well as using p^B, a divergent response is obtained (Fig.5.23b), because r^B is different in phase to the r^W replaced. Thus although it may be acceptable to replace p^W by p^B, it would not be acceptable to replace r^W by its body axis equivalent.For the limit cycles obtained with this body axis simulation, the averaging technique only shows imaginary amplitudes as solutions for σ_p.

5.6.5 Non-linear Sideslip and Roll Rate Characteristics

HIRM data for $\alpha = 26^o$ was used to test the solution of the non-linear Routhian discriminant = 0, given in eqn.(2.89), and previously assessed, in §3.3.4.2, for combat aircraft B. Details of the derivatives used are given in Table 5.2.

Fig.5.24 shows the limit cycle response obtained with these non-linear sideslip and roll rate characteristics in equations (5.25) to (5.29).

Given the measured $\sigma_{\bar{v}}$ of 0.4 radians and σ_p of 3 radians/sec, the resulting bicubic in σ_p, and biquadratic in $\sigma_{\bar{v}}$, gave no real solutions for either σ_p or $\sigma_{\bar{v}}$. As noted in §3.3.4.2, b* (eqn.(2.84)) again gave a good prediction of $\omega_L{}^2$, using the measured amplitudes σ_p and $\sigma_{\bar{v}}$. A predicted frequency of 0.43 cycles/sec compared well with a measured frequency of 0.42 cycles/sec from the simulation.

Simulations using data for $\alpha = 28^o$ and 30^o responses, including modified cubic polynomials for $C_\ell^B(p^W\, b/2V)$ and $C_n{}^B(p^W\, b/2V)$, did not produce any limit cycles, only divergent oscillations.

Taken together with the results from §3.3.4.2, this HIRM simulation suggested the development of the averaging technique, along the lines outlined in §2.4.2.5, would not be very successful. Complications outlined in §5.6.4.2, regarding the HIRM rotary data in body axes, meant that the HIRM simulations, using equations (5.25) to (5.29), had both oscillatory and rotary roll rate data included (see eqns. (5.21) and (5.22)). This was another complication not incorporated in the averaging technique. The question of how to use the oscillatory and rotary roll damping data in simulations is considered again in the next chapter, with reference to the six degree of freedom simulations.

5.6.6 Comparison of Non-linear Averaging and Local Linearisation

Following the success of the comparisons between simulation limit cycle amplitudes and amplitudes predicted by theory, equation (2.118), for aircraft B in Chapter 3, similar tests were made using HIRM data.

To obtain limit cycles using the $\alpha = 26^{o}$ data, the sideslip characteristics used in Figs.5.19(a) and 5.20(a) were chosen for the simulations. The details are summarised in Table 5.2.

A typical response is shown in Fig.5.25 for ξ_T = 0.02 radians. No roll damper was used in the HIRM simulations. The major difference to the responses shown in Chapter 3,is in the appearance of some distortion as ξ_T increased. This was thought to be due to the appearance of a lateral phugoid mode and program ROUTH indicated that the characteristic roots showed a lateral phugoid above $\sigma_{\bar{v}}$ = 0.09. Taking an average value of the amplitude of the limit cycle in sideslip and plotting against $\bar{v}_e$, for the different ξ_T, gave the results shown in Fig.5.26. The point for ξ_T = 0.05rads. lies a little way off the theoretical curve but at this control setting the $\bar{v}$ trace was showing more marked irregularity, making $\theta_{\bar{v}}$ difficult to estimate.

On the whole the results confirm the findings shown in Chapter 3,with good agreement between theory and simulation.

CHAPTER 6

SIX DEGREE OF FREEDOM MODELLING OF THE HIRM

6.1 Introduction

The large amount of data available for the HIRM meant a six degree of freedom analysis could be performed to cover some interesting topics. The analysis provides a useful piece of work on its own, as well as providing data for comparison with the 3 degree of freedom computations. It is to be expected that for high α motions (certainly spins) a 3 d.o.f. analysis will be inadequate, where large amplitude, highly coupled motions occur. For the HIRM project, aimed mainly at flight up to departure, a six degree of freedom analysis proved to be useful in examining the effects of the different forms of aerodynamic data available.

The decision to examine a six degree of freedom HIRM mathematical model was also taken because it had not proved possible to develop the 3 degree of freedom averaging technique as much as had been hoped. The complications involved in applying the technique to the 3 degree of freedom equations, with simultaneous non-linearities in two response variables, have already been outlined and the algebra was beginning to inhibit the usefulness of the technique. The results were not as good as had been hoped for anyway.

The work described in this chapter involved two main parts, a six degree of freedom local linearisation and a six degree of freedom simulation. In both cases the importance of cross-coupling terms in the equations of motion have been examined in the light of work done by others in this field in recent years[107-109]. In the case of the local linearisation, the effect of non-zero sideslip was examined. Stengel[110], Calico and Fuller[111], and Cochran et al [34], have noted the important effects of steady sideslip in analyses of the Space Shuttle, a forward swept wing aircraft and a large jet transport (KC-135A) respectively. The measured aerodynamic data for the HIRM, up to $\beta = \pm 6^{o}$, meant that a limited but useful analysis of the effect of sideslip could be made. Conditions of high angle of attack with non-zero sideslip were of most interest and the analysis involved linearising the equations of motion about various equilibrium points and performing an eigenvalue-eigenvector analysis at each point. Hreha and Lutze[33] have shown how linearised analysis can yield useful results for post stall gyrations.

The six degree of freedom simulation was developed via an extensive revision of the 3 degree of freedom simulation program, SIMUL. Anglin[41], Hreha and Lutze[33] and others

have looked at the use of different forms of experimental data to build up mathematical models for spin and post stall regime predictions. The availability of three different types of experimental data for the HIRM provided the opportunity to examine the use of these, in different combinations, for modelling in the pre-departure α region.

Orlik-Rückemann[112] has examined the effects of cross-coupling derivatives on responses of simple fighter aircraft configurations. The availability of such derivatives for the HIRM, meant that a sensitivity study into their effects could be completed, as another useful part of the simulation exercise.

6.2 Linearisation and Eigenvalue Analysis

The use of non-zero steady sideslips as equilibrium conditions at high angles of attack, means complete coupling between lateral and longitudinal motions must be retained in the equations.

In this section,the linearised six degree of freedom aircraft equations of motion are presented first, followed by a description of the determination of derivatives for use in the equations at non-zero equilibrium conditions. Results of the eigenvalue analysis and an assessment of the importance of cross-coupling aerodynamic terms complete the section.

6.2.1 Linearised Equations of Motion

The classical equations of motion, shown in equations (2.1) - (2.9), were linearised about an arbitrary equilibrium in the usual way, by restricting motion to infinitesimal disturbances from the reference state, see e.g. Ref.44, p.234. It is more convenient to retain perturbations in Euler angles (rotations from a horizontal reference condition) for orientations, rather than use small deviation angles in the linearisation. Rotations in azimuth of the reference body axes about the gravity vector have no effect on the system,so only Θ and Φ are needed in the linearised equations. The small perturbation variables resulting from the linearisation procedure are:

$$[u,w,q,\Theta',v,p,r,\Phi'] \qquad (6.1)$$

The longitudinal forces and moments are expanded in terms of

$$[u,w,q,v,p,r] \qquad (6.2)$$

although for the expansion of Z force and pitching moment, derivatives with respect to $\dot{w}$ cannot be ignored. For the lateral forces and moments terms in $\dot{v}$ are retained in the expansions, these forces and moments being assumed to be

functions of

$$[u,w,q,v,p,r,\dot{v}] \tag{6.3}$$

The resulting linearised system is a set of first order ordinary differential equations, shown in Fig.6.1. An explanation of the notation and a brief description of the linearisation is presented in Appendix E. The equations contain cross-coupling derivatives shown in full in Tables E.3 and E.4. The eigenvalues of the system were evaluated using a computer program, EIGEN (to be described in §6.2.3), but before that the derivatives for the equilibria had to be determined.

6.2.2 Derivatives for Non-Zero Equilibrium Conditions

6.2.2.1 General

The requirement to evaluate all the terms shown in the system of equations in Fig.6.1, meant that only a limited number of non-zero equilibrium conditions could be analysed, as experimental data was not available for all sideslips in the range $\beta = -6(1)6^{o}$. Even so, for the main case examined, $\beta_e = -6^{o}$, some derivatives were equated to zero due to lack of aerodynamic data. The terms actually evaluated for the steady sideslip are shown in the third columns of Tables E.1 to E.4. Later calculations included the effects of p_e, equilibrium roll rate.

Static derivatives, $\check{Y}_v$, $\check{L}_v$ and $\check{N}_v$, were already available for $\beta_e = 0^{o}$ as presented in Chapter 4, extracted, via linear regression, from the R.A.E. 11½ft x 8ft W.T.data. Oscillatory rig data for $\check{Y}_v$, $\check{L}_v$, $\check{N}_v$ and $\check{L}_p$, $\check{L}_r$, $\check{N}_p$ and $\check{N}_r$ (the dynamic derivatives being in the form of combined derivatives) as well as rotary rig $\check{L}_p$ and $\check{N}_p$ were also available for $\beta = 0^{o}$. Longitudinal derivatives, $\check{Z}_w$, $\check{M}_w$, $\check{Z}_q$ and $\check{M}_q$ were available from oscillatory tests, at $\beta = 0^{o}$.

Turning to steady sideslip data, oscillatory measurements of $\check{Z}_w$, $\check{M}_w$, $\check{Z}_q$, $\check{M}_q$, $\check{L}_q$, $\check{Z}_p$, $\check{M}_p$ and $\check{L}_p$ were available for $\beta_e = -6^{o}$ at between $\alpha = 12^{o}$ and 24^{o}. Thus the dynamic data for steady sideslips was limited.

By contrast a full set of longitudinal, lateral and cross-coupling static derivatives was obtained for $\beta_e = -6(1)6^{o}$, $\alpha = 0(2)40^{o}$ using various aerodynamic coefficient slopes measured from the original R.A.E. 11½ft x 8ft wind tunnel data. The formulation of these derivatives using the computer program SDERIV6 is now described. Table 6.1. summarises the sources and α,β ranges of the various derivatives used in the eigenvalue analysis.

Program SDERIV6 was written to evaluate the derivatives of C_x, C_z, C_m, C_ℓ, C_n and C_Y with respect to the static

variables u, v, w for $\alpha = 0(2)40^{o}$ and $\beta = -6(1)6^{o}$. The program reads in C_D, C_L, C_m, C_Y, C_ℓ and C_n wind tunnel data, the sideslip angle at which the derivatives are to be evaluated and constants such as span and $\bar{\bar{c}}$. In its final form, for calculating derivatives at steady roll, yaw and pitch rates, the required equilibrium rates plus all available dynamic derivatives are input as well. Dynamic stability axis moments[47] are calculated in the program and were described in the previous chapter.

The program evaluates the slopes of the aerodynamic coefficients (general coefficients will be represented in this section by C_K (force) and C_j (moment)) with respect to α, at the sideslip being considered, for $\alpha = 0(2)40^{o}$ and then evaluates C_{K_β}, C_{j_β} at each α. Two slope routines were available: a) LSLPE, which evaluated the gradient at a given point using 5 adjacent data points and stored the slope in an array. b) Function SLPE, which evaluated local slope using a straight line fit between two points. The gradient was not stored in an array but used as calculated.

The slopes C_{K_α}, C_{j_α} and C_{K_β}, C_{j_β} are then used, together with sines and cosines of α, β, dynamic derivatives and equilibrium rates (where necessary), to calculate the required derivatives with respect to u, v and w. First of all derivatives of C_X, C_Z and C_m are calculated and then derivatives of C_Y, C_ℓ and C_n.

The derivation of the expressions used for the derivatives of forces and moments, in terms of aerodynamic coefficients, is presented in Appendix F. The calculations follow those given in Ref.45, Part 4, but use conventional definitions of α and β, α_t and β_s (see Figure F.1 (Hopkin [45] gives results in terms of angle of downslip, α_s, and flank angle of attack, β_t)). It is probably true to say the difference between the results, using the different definitions, is very small. Expressions used for the derivatives are as follows (shown for a general force, C_K, but also the same for moment derivatives, C_{j_u}, C_{j_v} and C_{j_w}):

$$\breve{K}_u = (2C_K)_e \cos\alpha_e \cos\beta_e - (C_{K_\alpha} \sin\alpha \sec\beta + C_{K_\beta} \cos\alpha \sin\beta)_e - (K_p p_\gamma + K_q q_\gamma + K_r r_\gamma)_e \cos\alpha_e \cos\beta_e \qquad (6.4)$$

$$\breve{K}_w = (2C_K)_e \sin\alpha_e \cos\beta_e + (C_{K_\alpha} \cos\alpha \sec\beta - C_{K_\beta} \sin\alpha \sin\beta)_e - (K_p p_\gamma + K_q q_\gamma + K_r r_\gamma)_e \sin\alpha_e \cos\beta_e \qquad (6.5)$$

$$\check{K}_v = (2C_K)_e \sin\beta + (C_{K_\beta} \cos\beta)_e - (K_p p_\gamma + K_q q_\gamma + K_r r_\gamma)_e \sin\beta_e \quad (6.6)$$

The next section presents some results from the SDERIV6 program, illustrating the effects of sideslip on the static derivatives.

6.2.2.2 Longitudinal and Lateral Derivatives

The derivatives $\check{X}_u$, $\check{X}_w$, $\check{Z}_u$, $\check{Z}_w$, $\check{M}_n$ and $\check{M}_w$, as evaluated by SDERIV6 for $\beta_e = 0^o$, are shown in Figs.6.2 to 6.4. The two slope routines give reasonable agreement (shown by 'SLPE' and 'LSLPE' on the figures), and, in general, compare well with results evaluated at the RAE[113]. For $\check{Z}_w$, shown in Fig.6.3, the oscillatory measurements from longitudinal tests, described in Chapter 4, are also presented for comparison,and agreement with the static measurements is reasonable. Agreement between oscillatory and static data is not so good for the pitch stiffness derivative, $\check{M}_w$ (equivalent to C_{m_α}), shown in Fig.6.4b.

The RAE results for $\check{M}_u$ show a value of approximately zero up to $\alpha = 20^o$ (Fig.6.4a) due to the C_m at low α being trimmed out in their calculations. From equation (6.4) for $\check{K}_u$ (and also $\check{J}_u$), $\check{M}_u$ is mainly $2C_m$ at small α and β and so for configuration C would not be expected to be zero at this α and β. It is, of course, necessary to have $C_m = 0$ for trim conditions and in simple rectilinear flight, with zero body angular rates, this would imply $\check{M}_u$ equal to zero. However for non-zero equilibrium conditions, $\check{M}_u$ need not necessarily be zero, as inertia terms now make a contribution to $\dot{q} = 0$ in the pitching moment equation (see eqn.(2.5)).

The lateral derivative $\check{L}_v$, for $\beta = 0^o$, is shown in Fig.6.5. There is a large loss in dihedral stability at $\alpha = 36^o$ to 38^o, shown in Fig.6.5a, for $\check{L}_v$ calculated using SDERIV6. The corresponding RAE calculations, which were based on straight line fits to $\beta = \pm 6^o$ data, do not show this peak and the reason for the peak is shown in Figs.6.5b,c. Above $\alpha = 34^o$,the sideforce and lateral moments are markedly non-linear with sideslip (as indicated in Fig.4.5) and at $\alpha = 36^o$, C_ℓ shows an upward turn at $\beta = -1^o$ and a local peak near $\beta = 0^o$ (Fig.6.5b). Using a straight line fit between $\beta = \pm 6^o$ smooths out this local peak, but SLPE and LSLPE show C_{ℓ_β} as increasing locally at $\beta = 0^o$ (Fig.6.5c).

Values of $\check{N}_v$ and $\check{Y}_v$ showed similar, but less marked, differences to the R.A.E.measurements (Fig.4.6), above $\alpha = 34^o$, depending on how the relevant slopes were measured.

Effect of sideslip on some of the longitudinal and lateral derivatives, using the function SLPE in SDERIV6, is illustrated in Figs.6.6 to 6.8. $\check{L}_v$ shows very large variations with sideslip above $\alpha = 22^o$ and shows a peak at $\alpha = 24^o$ for both positive and negative sideslip. The peak noted for $\beta = 0$

at α = 36-38^{o} in Fig.6.5a moves back to α = 36^{o} at positive sideslip and extends to a complete loss (increasing positive $\check{L}_v$) of dihedral stability at sideslips of -5^{o} and -6^{o}.

$\check{N}_v$ shows less dramatic changes with sideslip until α = 34^{o} is reached and then it shows a very sharp loss for β = -5^{o} and -6^{o} (Fig.6.8).

6.2.2.3 Cross-Coupling Derivatives

Some of the important cross-coupling derivatives, with effects of sideslip, are shown in Figs.6.9 to 6.11. $\check{M}_v$ attains large values at high angles of attack and β = -5^{o}, -6^{o} and has been found in the past to be a term providing major aerodynamic coupling,for some configurations[114]. $\check{L}_w$ and $\check{N}_w$ are also known to be significant in some cases and Figs.6.10 and 6.11 show that for the HIRM at negative sideslip, these derivatives exhibit large peaks at α = 22^{o}. In addition, $\check{L}_w$ attains high values at α = 28^{o} and 40^{o}.

6.2.2.4 Effect of Equilibrium Angular Rates

The equations for the static derivatives $\check{K}_u$, $\check{K}_v$ and $\check{K}_w$,shown in (6.4) to (6.6),include terms to allow for the effect of non-zero, steady roll, pitch and yaw rates and derivatives were calculated for a number of equilibrium angular rates. Dynamic derivatives, needed in equations (6.4) to (6.6), were used from oscillatory rig tests, where available. Although the oscillatory rig results (see Chapter 4) were in the form of combined derivatives, with acceleration derivatives included, they were considered adequate for use in the static derivative equations.

Effects of rates up to 60^{o}/s proved to be very small, typically much less than 10% change in magnitude of the derivative. Results from the eigenvalue analysis for non-zero angular rate cases,with the 'correct' static derivatives,were hardly any different to those obtained by setting p_γ, q_γ and r_γ to zero in equations (6.4) to (6.6).

Having determined the linearised form of the equations of motion and developed means of evaluating the terms in the system matrix, for non-zero equilibrium conditions, the next step was to perform the eigenanalysis. For this, program EIGEN was written.

6.2.3 Program EIGEN

EIGEN evaluates the eigenvalues and eigenvectors of the system matrix shown in Fig.6.1. Equilibrium conditions and derivatives are read in, as well as flags, to set calls to eigenvalue solving routines and to set either the uncoupled (longitudinal and lateral equations separate) or the fully coupled system matrix for solution.

The eigenvalue routines used were: a) EIGNP[77], as used in the ROOTS program, described in Chapter 4, and b) a routine from the Numerical Algorithms Group library[115]. Eigenvalues for a particular case are the same whichever routine is used, but eigenvectors differ slightly. EIGNP normalises complex eigenvectors so that the component with the largest value in the modulus has its real part equal to 1 and the imaginary part equal to zero, and normalises a real vector so that the sum of the squares of its components is equal to 1. The NAG routine normalises both real and complex eigenvectors so that the sums of the squares of their components are equal to 1. Eigenvectors calculated in the ROOTS program differ again from those given by the uncoupled lateral equations in EIGEN, as ROOTS uses non-dimensional variables $\hat{v} = v/V$, $\hat{p} = P\tau$ and $\hat{r} = r\tau$ where τ is the unit of aerodynamic time, given by

$$\tau = \frac{m}{\frac{1}{2}\rho SV} \qquad (6.7)$$

EIGEN uses dimensional variables.

6.2.4 Results for Steady Sideslips

Complete data was available for $\beta = 0^{\circ}$ and, as described, static derivatives were available for $\beta = -6(1)6^{\circ}$. The only measured dynamic derivatives at non-zero sideslip were for $\beta = -6^{\circ}$, so this sideslip was selected for the main analysis.

6.2.4.1 Zero Sideslip

Fig.6.12 shows the migration of roots with angles of attack for $\beta = 0^{\circ}$ and the effects of coupling the equations. The roots in Fig.6.12a show the uncoupled dutch roll going unstable at $23^{\circ}\alpha$ and remaining so up to $40^{\circ}\alpha$, apart from a small region of stability near $\alpha = 30^{\circ}$. The short period motion undergoes large changes in damping, becoming generally less stable at higher angles of attack. These high frequency oscillatory modes remain two distinct modes throughout the angle of attack range shown. The phugoid mode shows instability at around 12° to 18° angle of attack.

Turning to the coupled roots shown in Fig.6.12b, it will be observed that the effect of coupling is quite small, and the remarks made for the uncoupled modes also apply in general, for the coupled modes. It will be convenient, where possible, to refer to coupled modes by names used for the equivalent uncoupled modes, although at high angles of attack this may be a little misleading, where the modes now contain significant contributions from both longitudinal and lateral response variables.

The effects of setting various cross-coupling terms to zero in the full equations were examined and found to be small, as

indicated by the results for neglecting all the cross-coupling terms.

Hreha and Lutze[33] made comparisons between different types of aerodynamic model for looking at eigenvalues in post stall, equilibrium spin conditions and concluded that the incorporation of separate rotary and acceleration derivatives yielded the best results. For the HIRM analysis, combined derivatives have been used, with $\dot{v}$ terms being incorporated exactly in the concise derivatives (shown in Appendix E) by expanding the lateral forces and moments in terms of u, w, q, v, p, r and $\dot{v}$. The availability of pure rotary data for $\beta = 0^{o}$ conditions meant it could be used in the eigenvalue analysis to compare with the oscillatory data results. It should be remembered, though, that the rotary data in body axes contains correction terms from oscillatory tests (as outlined in §4.8). Eigenvalues obtained when using rotary rig dynamic derivatives are shown in Fig.6.13. Small changes from Fig.6.12b are apparent but overall trends are the same. The dutch roll at $\alpha = 32^{o}$ is now stabilised and it is interesting to note that the rotary rig $\check{L}_{p}^{B}$ (Fig.4.16) shows a stable peak at this α, compared with the oscillatory data.

It would be interesting to obtain pure yawing derivatives and use such data in an eigenvalue analysis. The ultimate test of the various aerodynamic models will lie in comparisons with free-flight drop tests, during which,it is hoped,a number of non-zero equilibrium states may be flown.

6.2.4.2 Non-Zero Sideslip

The effect of -6^{o} sideslip on the roots is shown in Fig.6.14 and immediately obvious is the significance of coupling in the equations when there is some sideslip. Angle of attack range is now $\alpha = 12^{o}$ to 24^{o} because of lack of dynamic derivative data. The short period and dutch roll modes are the most affected by the coupling, the dutch roll roots being stabilised by the coupling. At $\beta = -6^{o}$, $\check{L}_{v}$ shows a marked decrease in magnitude at $\alpha = 24^{o}$ (Fig.6.6) and this is reflected in the uncoupled eigenvalues by the unstable dutch roll at $\alpha = 24^{o}$. In the coupled system, it seems that the "short period" roots become two real positive roots at $\alpha = 20^{o}$. This is significant as it indicates instability, a divergence.

Unstable real roots appear again at around $22^{o}\alpha$ in the $\beta = +6^{o}$ coupled system (Fig.6.15). For this sideslip, although a complete set of static derivatives was available, estimates had to be made for the dynamic derivatives, so the eigenvalues should be regarded with more caution than those shown for $\beta = -6^{o}$. $\check{L}_{p}$, $\check{N}_{p}$, $\check{L}_{r}$ and $\check{N}_{r}$ were used from $\beta = 0^{o}$ oscillatory results. For the derivatives $\check{Z}_{q}$, $\check{M}_{q}$ and $\check{L}_{q}$, values at negative sideslip showed the same trends as for $\beta = 0^{o}$ and hence it was estimated, in the absence of

other data, that $\beta = +6^{o}$ derivatives would show these trends as well. $\check{Z}_p$ and $\check{M}_p$ differed so much between $\beta = 0^{o}$ and -6^{o}, that for $\beta = +6^{o}$ they were set to zero (Figs.4.12c,d). The remaining dynamic derivatives were also assumed to be zero for $\beta = +6^{o}$. These approximations meant little further analysis could be done on the $\beta = +6^{o}$ case, but the $\beta = -6^{o}$ results were examined in more detail. Having cross-coupling dynamic derivatives available for $\beta = -6^{o}$ meant the effects of each one, in turn, could be examined on the coupled roots. It was difficult to follow modes through the angle of attack range by looking at the eigenvectors,because of the rapid changes in phase relationships and magnitudes of the response variables. Typical eigenvectors are shown in Fig.6.16. Figure 6.16a shows the uncoupled system dutch roll eigenvectors from $\alpha = 12^{o}$ to 24^{o}, along with the equivalent coupled system eigenvectors. Up to $\alpha = 22^{o}$ the coupled eigenvectors are similar to the uncoupled results apart from the appearance of the w component (equivalent to angle of attack). The components of the eigenvectors are normalised with respect to the largest component and only those with amplitude above 5% of the main component are shown. Figure 6.16b shows coupled low frequency oscillation eigenvectors (equivalent to uncoupled phugoid mode).

By selecting some high angle of attack cases for examination it was hoped that the most important derivatives responsible for the effects, typified by the results in Fig.6.14, could be identified. In particular, the appearance of real roots at $\alpha = 20^{o}$ was to be looked at.

It was found that of the cross-coupling derivatives available for $\beta = -6^{o}$, $\check{X}_v$, $\check{Z}_v$, $\check{Z}_p$, $\check{Y}_u$, $\check{Y}_w$, $\check{N}_u$ and $\check{L}_q$ could be deleted from the coupled equations without making a significant difference to the eigenvalues of the system. To illustrate this, Fig.6.17 shows the eigenvalues for $\alpha = 18\text{-}24^{o}$, $\beta = -6^{o}$ with just $\check{M}_v$, $\check{M}_p$, $\check{L}_u$, $\check{L}_w$ and $\check{N}_w$ in the equations. The eigenvalues are almost the same as those shown in Fig.6.14 for the fully coupled system. The effects of each of these cross-coupling derivatives on the eigenvalues was examined and the most important results are shown in Figs.6.18 to 6.20.

Removing $\check{M}_p$ did not affect the appearance of the real positive roots at $\alpha = 20^{o}$ but removing $\check{M}_v$ resulted in these roots not appearing until $\alpha = 24^{o}$(Fig.6.18). The effect of also removing $\check{L}_u$ brought the positive roots together and taking out $\check{L}_w$ as well, led to the roots becoming complex, although still unstable.

Fig.6.19 shows again the effect of $\check{L}_u$ on the roots, removal from the basic system resulting in the appearance of real positive roots at $\alpha = 24^{o}$. These real roots become complex when $\check{L}_w$ is removed as well.

Removing $\check{L}_w$ alone, also resulted in the delay of real positive roots appearing until $\alpha = 24^{o}$(Fig.6.20), and removal of $\check{M}_v$ as well, brought the roots together slightly. As seen in

Fig.6.19,it took the removal of $\check{L}_u$ to make these roots complex.

The effect of removing $\check{N}_w$ was not as dramatic as the effects of $\check{L}_u$, $\check{L}_w$ or $\check{M}_v$ but resulted in a delay of the appearance of the positive real roots until $\alpha = 22^o$.

It thus appears that $\check{L}_u$, $\check{L}_w$ and, to a lesser extent, $\check{M}_v$ are the main parameters responsible for the appearance of the real positive roots at $\beta = -6^o$ sideslip. Johnston and Hogge[51] noted the importance of $\check{N}_w$ and $\check{L}_w$ at sideslip on the A.7 aircraft. For the HIRM, Figs.6.6 and 6.10 show $\check{L}_v$ and $\check{L}_w$ for $\alpha = 18$ to 24^o, are of opposite sign at $\beta = 0^o$ but are the same sign (negative) at $\beta = -6^o$. Thus, negative sideslip would result in the rolling moments augmenting one another as α increased. $\check{N}_w$ (Fig.6.11) is positive for $\beta = -6^o$, for $\alpha = 18 - 24^o$, and so is restoring for positive α compared to negative $\check{N}_v$.

6.2.4.3 Effects of Steady Roll Rate

Some effects of roll rates of $\pm 30^o$/s with and without sideslip as equilibrium conditions were examined. In the uncoupled equations, equilibrium angular rates only come explicitly into the equations in the form of q_e, so fully coupled system results are presented in this section to illustrate the effect of p_e.

Fig.6.21a shows the relatively small effect,on the $\beta = 0^o$ roots,of $p_e = 30^o$/s (c.f. Fig.6.12b). The dutch roll goes unstable at just over $20^o\alpha$ and the short period remains oscillatory from $\alpha = 10^o$ to 24^o.

With -6^o of sideslip, the dutch roll is stabilised by $p_e = 30^o$/s (Fig.6.21b, c.f. Fig.6.14), although the real positive roots characteristic of this β are still present. The results, shown in this figure, using static derivatives correctly evaluated for $\beta = -6^o$, $p_e = 30^o$/s,were almost exactly the same as results obtained using $\beta = -6^o$ derivatives. Stengel[110] notes that it is to be expected that roots would be different, depending on whether an aircraft is sideslipped into, or out of, the rolling motion and Fig.6.21b also shows the effect of $p_e = -30^o$/s. The dutch roll is destabilised by this roll rate but real positive roots have not appeared as $\alpha = 20^o$ is reached.

6.3 Simulation

In view of the availability of oscillatory measurements of cross-coupling dynamic derivatives for the HIRM and the importance attached to them in high angle of attack flight, it was decided that an interesting study for the simulation would be an assessment of their effect on the response of the HIRM. In a similar way, the availability of rotary rig data for the HIRM meant that a preliminary assessment could be made of its effect in a simulation model. This section

continues with a description of the mathematical model used in the simulation program, goes on to outline the program itself and ends with results from the simulation model, covering the effects of cross-coupling derivatives and rotary rig data.

6.3.1 Mathematical Model

The general equations of motion in body axes are those shown in equations (2.1) to (2.9) and the six degree of freedom model solves these equations using the available wind-tunnel data in the form of 'look-up' tables. The simplest formulation of the data was employed. For instance, input variables were omitted,where small, or negligible, dependence of the force or moment on those variables was apparent.

A question to be answered using the simulation, was how the different forms of aerodynamic data could be combined within the model over different parts of the flight regime? Static wind tunnel data correctly represents non-rotating steady conditions and rotary data includes the large amplitude rolling motion effects. Oscillatory data provides dynamic derivatives but does not include the effects of the rotation of the flow about the aircraft, such as occurs in spinning or rolling. At high angles of attack, with separated flow conditions, how accurate is it to superpose the reactions from the above characteristic motions, as it would not be expected that the flow fields could be superposed to produce the complex flowfields about the free-flight model[116].

Anglin[41] mentions that the "conventional technique of combining static and forced oscillation data has been found to provide a generally valid aerodynamic representation through the stall/departure region where the motions do not contain significant steady rotation rates". The current work has taken a preliminary look at the use of rotary data and its effects on simulations in the pre-stall/ departure region and has shown up some interesting results. Previous workers have tended to concentrate on spins, using rotary data, and the oscillatory spin entry phases, where conventional models have been used.

The formulation of the body axis forces and moments for the HIRM simulation is shown in Fig.6.22 and includes static, oscillatory and rotary rig data. As far as possible, data for $\alpha = 0^{o}$ to 40^{o}, configuration C, has been used, but in the case of some oscillatory data, only $\alpha = 12^{o} - 24^{o}$ results were available (see Table 6.1).For the α range of $12^{o}- 24^{o}$,although measured oscillatory derivatives were available for $\beta = -6^{o}$, as well as $\beta = 0^{o}$, the likely asymmetries in the sideslip behaviour meant that no extra-polations were made to $\beta = +6^{o}$. All oscillatory data was thus input as a function of α only.

Static data from HIRM 1 tests includes effects of sideslip up to $\beta = \pm 6^{o}$. Configuration C data has been used and effects of change in η_T are ignored as Ref.90, Fig.13, shows the variation of static derivatives with η_T to be fairly small. Although HIRM 1 is not the definitive configuration, it is still useful to look at simulations using HIRM 1 data for comparisons with later flight trials and results from HIRM 2.

The HIRM 1 tests indicated that the tailplane was a powerful trimming control and so tailplane was used for trimming in all the simulations, η_C being fixed at -10^{o}. Compared to other canard setting angles, for $\eta_C = -10$, the variation of trim α with η_T was almost linear over the range $\alpha = 10 - 35^{o}$. Z_{η_T} and M_{η_T} were used as functions of angle of attack only (see Fig.4.4), there being little effect of canard deflection on them. Lateral control derivatives due to ζ and differential tailplane deflection, ξ_T, were also used in the simulation as functions of α only, effects of change in η_T being ignored.

Rotary rig data, when used in the simulations, was incorporated in place of the oscillatory roll data and was incorporated as a function of α and $(p^{W}b/2V)$, where

$$p^{W} = p^{B}\cos\alpha + r^{B}\sin\alpha \qquad (6.8)$$

The α range used was 10^{o} to 40^{o}, while $(pb/2V)$ was in the range ± 0.17. Typical data used is shown in Fig.4.14. In contrast to its use in the 3 degree of freedom simulations, the rotary data could now be incorporated exactly, in the 6 degree of freedom simulation, via 'look-up' routines, using $(p^{W}b/2V)$ and α. (For the 3 d.o.f. simulation, rotary data had to be converted to body axis derivatives using small amplitude yawing data as described in §5.6.4.2.)

No data for α greater than 40^{o} was included in the simulation model, as it was not intended to look at post stall flight or spins.

After developing the non-linear force and moment version of the HIRM simulation, the program was modified to enable a linear six degree of freedom simulation to be run. This not only meant a direct comparison of results could be made, with those from the non-linear model, but also it meant that the effect of some static cross-coupling derivatives could be examined.

6.3.2 Program SIMUL6

This FORTRAN program is an extensive revision of program SIMUL (see §2.5.2) and was implemented for use on a VAX 11/782. The overall layout of the program is shown in Fig.6.23. Integration routines and graphical software used the same subroutine libraries as SIMUL (§2.5.2.2).

6.3.2.1 Program Description

Constants such as feedback gearings, aircraft details (inertias, mass etc specifically for the drop test models), integration controls and graphical output controls are input in the initialisation segment of the program along with initial conditions for the variables V(m/s), Θ(degrees), α(degrees), p(degrees/sec), q(degrees/sec), r(degrees/sec), Φ(degrees) and β(radians). Also set,are control angle changes for the run and flags to control:

a) the choice of integration routine, NINTGRT;
b) the choice of equations, NCOUPLE. Lateral and longitudinal uncoupled or fully coupled. The equations used are those shown in equations (2.1) -(2.9)). NCOUPLE also controls the call for coupled linearised equations;
c) the choice of experimental data, NRO. (Oscillatory rig data or rotary data);
d) a call to subroutine EVLAM to calculate local damping factor, λ, and frequency, ω, as a function of response variable amplitude for $\bar{v}$ and p.

Subroutine TRIM sets the symmetric tailplane angle, η_T, to trim, given the α input as an initial condition and INERT is called to set up inertia constants used in the equations of motion (see Tomlinson, Ref.117).

The equations of motion are then integrated,in first order form in body axes, the equations for $\dot{u}$, $\dot{v}$, $\dot{w}$, $\dot{q}$, $\dot{\Phi}$, $\dot{\Theta}$ and $\dot{\Psi}$ being as shown in Chapter 2 (equations (2.1) - (2.3), (2.5) and (2.7 - (2.9)), while the equations for $\dot{p}$ and $\dot{r}$ have the product of inertia $\dot{p}$ and $\dot{r}$ terms eliminated (e.g. as shown by Tomlinson, Ref.117).

Subroutine AERODYN is called at each stage in the integration to evaluate the aerodynamic forces and moments in body axes, as functions of α, β and, in the case of rotary data, ($p^Wb/2V$). Look-up routines were those used by the author in previous simulation work[118], based on linear interpolation of the data. Depending on the value of the flag, NCOUPLE, cross-coupling derivatives are either evaluated from the measured oscillatory data, set to values input to the program or omitted, in the case of the uncoupled equations being used. Oscillatory rig measurements of $\check{L}_q$, $\check{M}_p$ and $\check{Z}_p$ were incorporated in the program for use in the α = 12° to 24° range. $\check{N}_q$ was not available from the oscillatory tests but could be input separately,at fixed values,for sensitivity studies. Rotary data could either be omitted or incorporated in place of $\check{L}_{p_o}$ and $\check{N}_{p_o}$.

Equations of motion are formulated either as coupled six degree of freedom equations or as uncoupled lateral and longitudinal equations (Fig.6.23).

As well as the above non-linear formulation of the forces and moments (although fixed derivatives can be read in, as

mentioned, for the dynamic cross-coupling derivatives),SIMUL6 also incorporates a linearised set of forces and moments for a six degree of freedom simulation. When the flag,NCOUPLE, is set to 6, AERODYN is not used to formulate the forces and moments for the equations of motion. Instead, subroutine TRIM is used to set the trim pitching moment, lift and drag, and the perturbation forces and moments are formulated directly in FCN using aerodynamic derivatives for the particular trim condition. Derivatives remain constant throughout the response simulation. The use of a linearised six degree of freedom simulation enabled useful comparisons to be made with the full force and moment model and also meant that the effects of some static cross-coupling derivatives could be investigated.

Digital and graphical time histories from SIMUL6 are output via subroutines OUT and DRFGS as for SIMUL (§2.5.2.3).

6.3.3 Results

6.3.3.1 Preliminary Tests on Full Force and Moment Model

First assessments of the simulation program were made using trimmed, straight glides at various angles of attack, up to the onset of lateral instability, at $\alpha = 22^{o}$. Measurements of short period and lateral dynamic characteristics were made using responses to differential and symmetric tailplane deflection, ξ_T and η_T. Some of these results are compared with results from linearised (eigenvalue) analysis in Table 6.2 and show reasonable agreement.

The C configuration of the HIRM will trim out at between 29^{o} and $35^{o}\alpha$ in free flight (predictions differ according to the static wind tunnel data used) and for the drop model tests, trimming at such an α will require the use of a control system to stabilise the motion. Some work has been done at the R.A.E. on the required control system and one proposed system involves a sideslip to rudder feedback,via a gain K_{ζ_β}. This can be thought of as either a change in the rudder angle from ζ to $(\zeta+K_{\zeta_\beta}v)$,or as a change in the $\check{L}_v$ and $\check{N}_v$ derivatives such that they become $(\check{L}_v+K_{\zeta_\beta}V\check{L}_\zeta)$ and $(\check{N}_v+K_{\zeta_\beta}V\check{N}_\zeta)$ respectively.

With K_{ζ_β} negative, $\check{L}_\zeta$ positive (up to $\alpha = 35^{o}$ on the HIRM) and $\check{N}_\zeta$ negative, this leads to an increase in dutch roll frequency and a re-distribution of damping, such that the dutch roll is stabilised at the expense of the spiral mode.

Fig.6.24 shows the basic HIRM trim at $\alpha = 28^{o}$ with divergent dutch roll of period just under 5 secs. The short period motion is just discernible, before simulation limits are exceeded, and has a period of 2 secs. The eigenvalues for $\alpha = 28^{o}$ show an unstable dutch roll,0.449±1.191i, of period 5.28 secs and a stable short period oscillation,-0.395±1.927i, of period 3.2 secs.

The effect of sideslip to rudder gearing with $K_{\zeta\beta} = -0.7$ on this case is shown in Fig.6.25, where an initial $\bar{v}$ of 0.03rads. has been used to excite the dutch roll. Eigenvalues for this system are all stable except for the spiral mode. The dutch roll eigenvalues, -0.539±10.717i, show the expected increase in frequency, the period of oscillation now being 0.59 seconds, with time to half-amplitude being 1.29 seconds. These agree very well with the characteristics shown in Fig.6.25. The low frequency oscillation apparent in the simulation has a period of 11 seconds and the only other oscillatory mode predicted by the eigenvalue analysis is the phugoid of period 15.62 seconds.

Having examined some of the basic characteristics of the HIRM with the simulation, the main intention was to examine the sensitivity of calculated motions to rotary and oscillatory data and to look at the effects of cross-coupling aerodynamics on the predicted motions.

It is widely accepted that modelling of spin entries and developed spins requires the use of rotary data, with angles of attack of 45^{o} to 90^{o} being typical for these cases. It was not intended to use the simulation program for spin modelling but rather to concentrate on lower angle of attack regimes and see how significant rotary data was, in these cases. In the past, rotary data has not commonly been available below around $50^{o}\alpha$.

With these considerations in mind, some suitable flight cases were sought for examination. Although steady sideslip at $\beta = -6^{o}$ had been examined using eigenvalue analysis, the limited amount of sideslip data available meant a useful simulation exercise could not be completed for steady sideslips. Banked turns were eventually chosen as a useful steady state on which to carry out various tests and they would also provide useful indications as to possible modes of departure at high angles of attack. Because of the relatively small roll rates in the turns (body axis roll rates were often below 10^{o}/s), it was thought that other manoeuvres would have to be looked at, to show up the effects of the rotary data. However this proved not to be the case and some interesting results were obtained, e.g. due to the asymmetries in the rotary rig data. Orlik-Rückemann[112] has described some of the effects of cross-coupling aerodynamics on flight in banked turns and banked turns for the HIRM also provided a useful datum condition for examination of cross-coupling effects.

The next sections describe, first, the results of the banked turn simulations and then the findings of the tests on cross-coupling effects.

6.3.3.2 Banked Turns and the Effects of Rotary Rig Data

The basic equations used for calculating the steady state diving turn conditions were approximated by those for a

level flight path turn. In this case:

$$L\cos\phi = mg \tag{6.9}$$

$$n = \frac{1}{\cos\phi} \tag{6.10}$$

$$\dot{\Psi} = \frac{g}{V}\tan\phi \tag{6.11}$$

$$p_o = -\dot{\Psi}\sin\Theta \tag{6.12}$$

$$q_o = \dot{\Psi}\cos\Theta\sin\Phi \tag{6.13}$$

$$r_o = \dot{\Psi}\cos\Theta\cos\Phi \tag{6.14}$$

In terms of body axis vertical force, Z, given by

$$-Z \simeq L\cos\alpha \tag{6.15}$$

(6.9) becomes

$$\frac{-Z}{\cos\alpha n} = mg$$

So $$V^2 = \frac{nmg\cos\alpha}{-S\frac{1}{2}\rho C_Z} \tag{6.16}$$

It was found that these equations enabled a reasonable turn to be set up at a given α. Having calculated the equilibrium body rates for the turn, the control angles required would be calculated using the simple 3 degree of freedom lateral equations. For these calculations oscillatory derivatives were used as these provided a consistent set of data, i.e. all derivatives were available in body axes as opposed to using rotary data, from which consistent body axis derivatives could not be calculated. In general, this meant that the calculations were adequate for setting up simulations using oscillatory data but, as will be seen, for the higher α turns, using rotary data, the simulation turn conditions would often be quite different to the calculated ones.

Using the simulation with oscillatory dynamic data, banked turns were modelled at an intermediate angle of attack, 13^o (case 1), and two higher values, 18^o (cases 2,3) and 20^o (case 4). The highest steady α achievable with the simulation was 20^o, without the response being prone to divergence, which started at around $\alpha = 22^o$. A few attempts at turns at $\alpha = 22^o$ and 30^o showed rapid divergences, to be expected, with

the basic aircraft, because of the lateral instability at these angles of attack. Some details of the responses are shown in Table 6.3.

The effect of incorporating rotary rig data has the smallest effect on case 1, a nominally 60^{o} banked turn, at $\alpha = 13^{o}$. The run with oscillatory data only, shows a bank angle of slightly more than 60^{o}. The roll rate given by $(p^{W}b/2V)$ is small and for this value, $C_{\ell}{}^{R}$, from the rotary rig tests, is negative, with $\check{L}_{pR}{}^{B}$ (as shown in Fig.4.16) slightly more than $\check{L}_{p_{O}}{}^{B}$. Thus, when rotary data is used in place of $L_{p_{O}}$ and $N_{p_{O}}$, a different bank angle is set up, the negative $C_{\ell}{}^{R}{}_{p_{O}}$ leading to a smaller bank angle. Reduced $\dot{\Psi}$ means smaller body axis angular rates, although for the small roll rate, the negative $C_{\ell}{}^{R}$ means negative sideslip is set-up, to provide a balancing C_{ℓ} from the static data.

Cases 2 and 3 (Table 6.3) show even greater changes depending on whether rotary data is incorporated in the simulation or not. In the case of $\alpha = 13^{o}$, enough damping was provided by the rotary data on its own, as a function of $\dot{\alpha}$ and $(p^{W}b/2V)$, to produce a stable banked turn, albeit at a smaller bank angle than with oscillatory data on its own. Now, in cases 2 and 3, initially set up at $\alpha = 18^{o}$, with bank angles of -55^{o} and -44^{o}, respectively, using oscillatory data, rotary data on its own is not sufficient to produce a stable banked turn. In case 2, a limit cycle oscillation is set up as shown in Fig.6.26, the amplitude in p^{B} being 0.68 radians/s. In wind axis, non-dimensional form this is $(p^{W}b/2V) = 0.02$, which indicates that the kink in the $C_{\ell_{R}}{}^{B}$ against $(p^{W}b/2V)$ curve at around $\alpha = 20^{o}$, $(p^{W}b/2V) = 0.02$ (see Fig.4.14b), is responsible for the limit cycle behaviour. Case 3, again with an α of 18^{o}, but now at a higher Θ, and so smaller body axis roll rate, becomes divergent when only rotary damping data is included.

Case 4, with oscillatory data only, was a steady turn at $\alpha = 20^{o}$ and $\Phi = -59^{o}$ which rapidly diverged, when only rotary damping was used in the simulation. Static lateral instability meant no steady banked turn was achievable above 22^{o} as indicated in Table 6.3.

6.3.3.3 Effects of Dynamic Cross-Coupling Derivatives

6.3.3.3.1 General

At high angles of attack, some of the dynamic cross-coupling derivatives for fighter aircraft configurations, can be of similar importance to the traditional dynamic derivatives[119]. This part of the thesis describes some preliminary investigations into the sensitivity of response to cross-coupling dynamic derivatives, for the HIRM.

Simulations were performed for level trimmed flight at $\alpha = 18^{o}$ and for turning flight at $\alpha = 18^{o}$, $n = 2$ (case 2, Table 6.3). Only oscillatory dynamic data was used for the level flight

cases but the effects of rotary data were looked at in the cases of turning flight.

After initial runs to check the trim conditions, simulations were run with full aerodynamic forces and moments including the measured cross-coupling dynamic derivatives,presented in §4.7.4. These were the nominal cases and subsequent runs assessed the effects of varying the values of the cross-coupling derivatives. Perturbations to the flight conditions were introduced by differential tail pulses ($\Delta\xi_T$), or by initialising β with a non-zero value (say 5^o), for tests on lateral into longitudinal derivatives (e.g. $\check{M}_p$). Symmetric tail pulses ($\Delta\eta_T$) were used for examining the effects of longitudinal into lateral derivatives (e.g. $\check{L}_q$).

6.3.3.3.2. Wings Level Flight and the Effects of $\check{L}_q$,$\check{N}_q$

Sensitivity of the motion to variation in $\check{L}_q$ and $\check{N}_q$ is shown in Fig.6.27 for $\alpha = 18^o$, wings level, trimmed flight. The perturbation to the steady flight was via a symmetric tail plane pulse of -4.2^o for 0.5 second at t = 5 secs. At $\alpha = 18^o$, the nominal value of $\check{L}_q$ was +0.13 (Fig.4.12). $\check{N}_q$ was set to zero for the nominal case as there were no oscillatory measurements available for it.

All the responses are stable and the nominal case shows the smallest excursions in response variables. Even using L_q=1.0 (compared to the largest value of $\check{L}_q$,measured in the oscillatory tests at $\beta = -6^o$, of +0.64) gave a well damped response. Reversing the sign of $\check{L}_q$ and $\check{N}_q$ gave an almost mirror image response to that obtained with $\check{L}_q = \check{N}_q = 0.5$

6.3.3.3.3. Turning Flight

Taking the turning flight case 2, in Table 6.3, as datum, the effects of cross-coupling aerodynamics were examined using various combinations of dynamic data and control inputs.

With just oscillatory data, sensitivity of response to a ½ second control pulse, $\Delta\xi_T = 2.8^o$ was examined with $\alpha = 18^o$ and $\Phi = -55^o$ (case 2, Table 6.3). It was thought that with the steady roll rate in the turn, the effect of $\check{M}_p$ could have led to a divergence but,even with $\check{M}_p$ at a value of 0.2 (c.f. maximum value of 0.185 from oscillatory tests),hardly any pitching response was obtained to the ξ_T input.

Next, taking the datum flight case with oscillatory data included, the response to symmetric tailplane pulses was examined. The nominal angle of attack for these cases was 18^o, with bank angle, Φ, of around -55^o. Responses were examined with and without the dynamic cross-coupling derivatives $\check{Z}_p$, $\check{M}_p$ and $\check{L}_q$. The values of these derivatives were those measured in the oscillatory tests, shown in Fig. 4.12. Various size η_T pulses were used to examine responses, with a view to looking at how the simulation predicted divergences, in turning flight.

Response to $\Delta\eta_T = -5^o$ at t = 8 secs for 0.5 sec is shown in Fig.6.28 and shows the main effect of omitting the cross-coupling terms is to reduce the damping of the system, although the effect is quite small. For this particular turn, it will be recalled that with purely rotary damping present, a limit cycle motion was set up (Fig.6.26) and the effect of $\Delta\eta_T = -2^o$, for 0.5 sec. at t = 8 secs, on this motion is shown in Fig.6.29. The effect of the cross-coupling derivatives is small on the divergent motion, predicted for this particular control input. Omission of the cross-coupling terms from the basic response, without a control input, was also found to lead to divergence (Fig.6.30)

The limits of the sideslip data are actually exceeded at t = 13.2 seconds in Fig.6.30 but the time history continues a little longer using extrapolated data. With pitch rate positive, in the basic motion (see Fig.6.26), $\check{L}_q$ (with a value of 0.13) is providing a roll damping contribution so its removal results in the divergence, shown in Fig.6.30, as roll damping is reduced.

For the system with oscillatory damping terms present, the responses to $\Delta\eta_T$ inputs showed the typical characteristics of non-linear system behaviour, in that the response details depended on the size of the control input. For all $\Delta\eta_T$ inputs up to 9.2^o the response remained stable, with and without the dynamic cross-coupling terms.

6.3.4 Results from Linearised Six Degree of Freedom Simulation

6.3.4.1 General

The linearised six degree of freedom simulation used derivatives evaluated for the program EIGEN and which were described in §6.2.2. Responses for $\alpha = 18^o$ were concentrated on to provide comparisons with results from the full simulation. Symmetric, trimmed flight was used as the basis for looking at dynamic cross-coupling derivative effects and also provided the opportunity to examine static cross-coupling derivative effects.

The response to a symmetric tailplane pulse in a banked turn with and without dynamic cross-coupling terms provided a comparison with results shown in Fig.6.28 from the full simulation.

Responses in a steady sideslip manoeuvre at $\alpha = 18^o$ were examined to compare with results from EIGEN.

6.3.4.2 Symmetric and Turning Trimmed Flight at $\alpha = 18^o$

Fig.6.31 shows the lateral response of the linear model for symmetric trimmed flight, to a half-second, symmetric tail-plane pulse at t = 2 seconds, and compares it with the response

of the non-linear basic model shown in Fig.6.27. Apart from the sideslip response, the linear model shows smaller amplitudes in response than the non-linear model but in both models the response is not very significant. Omitting the dynamic cross-coupling derivatives from the linear model had no discernable effect on the response and putting $\check{L}_q=\check{N}_q=1$ still gave a stable response (Fig.6.31). These results demonstrated the relatively small effects of the dynamic cross-coupling terms measured for the HIRM, for this particular flight case.

Tests on the static cross-coupling derivatives showed some more significant results. In particular, for the symmetric trimmed case again, the lateral response to longitudinal control input was seen to be mainly due to the $\check{N}_w$ and $\check{L}_w$ terms. Fig.6.32 shows the response to a half-second symmetric tailplane pulse of 5.7^o at t = 3 seconds, with and without $\check{L}_w$ ($\check{N}_w$ was zero for zero equilibrium sideslip). Immediately obvious is the almost zero response when $\check{L}_w$ is omitted.

Similar tests were performed,to examine the longitudinal response to lateral control inputs (aileron pulses),to check the effects of the static derivative, $\check{M}_v$. No discernable differences could be seen between responses with $\check{M}_v=0$, $\check{M}_v$ at the measured value with opposite sign and $\check{M}_v$ = double the measured value. Curry and Orlik-Rückemann, for another high angle of attack configuration[119], have also noted that $\check{M}_v$ had a very small effect ($\check{N}_w$ effects were only moderate in these tests).

The linearised simulation of banked turns showed similar effects of cross-coupling derivatives to those noted for the symmetric flight, in particular the small effect of the dynamic derivatives.

6.3.4.3 Steady Sideslips at $\alpha = 18^o$

The opportunity was taken with the linearised simulation, to run some steady sideslip cases as it will be recalled that, at sideslip, the effect of derivatives $\check{L}_w$, $\check{N}_w$ and $\check{L}_u$ was thought to be responsible for the appearance of real, divergent roots in the eigenvalue analysis (§6.2.4). Selecting an equilibrium sideslip between 0 and -6^o enabled comparisons also to be made with the full non-linear model and Fig.6.33 shows the responses of both models to a symmetric tailplane pulse of -2.5^o for half a second,at t = 8 seconds, at an equilibrium sideslip of -3^o. Agreement between the two representations is fair but the linear model tends to be more oscillatory. In particular the peak in $\check{M}_q$ at $\alpha = 20^o$, shown in Fig.4.10c, means that the non-linear pitch rate response is smaller than for the linearised model.

Effects of omitting the dynamic cross-coupling terms were again very small in the linearised simulation and $\check{M}_v$ still had hardly any effect when longitudinal motion, in response to initial offsets in sideslip, was examined.

The static derivatives, $\check{N}_w$ and $\check{L}_w$, proved to have significant effects on the lateral motion due to symmetric tailplane pulses,and responses due to 2.5° pulses for half a second, at t = 8 seconds,are shown in Figs.6.34 and 6.35. Omitting these derivatives meant the lateral response was almost zero (Fig.6.34), whilst doubling their nominal values separately produced a slightly greater lateral response with $\check{L}_w = -0.345$ and a divergent response with $\check{N}_w = 0.192$ (Fig.6.35).

In contrast to conclusions from the eigenvalue analysis, the derivative $\check{L}_u$ had a very small effect on the responses about a steady sideslip.

6.4 Comparison of Results from Six- and Three-Degree of Freedom Models

Having completed a limited investigation into various six degree of freedom representations of the HIRM, it is useful to compare the main results and also compare them with findings from the simpler, three degree of freedom models. In many aircraft stability and response investigations, a linear model is assumed adequate for preliminary work, while in other cases full force and moment respresentations are used from the start and result in very complicated models. The work for this thesis has covered a range of mathematical models for the HIRM and so provides a unique opportunity to compare the trends shown by models of differing complexity.

As a summary, the following representations of the HIRM have been examined for various flight cases:

(A) Three degree of freedom lateral linear (roots) (§5.4 and §5.5).

(B) Three degree of freedom, non-linear lateral simulation (§5.6)

(C) Six degree of freedom, linear coupled and uncoupled (roots) (§6.2)

(D) Six degree of freedom, linear aerodynamics simulation (§6.3.4)

(E) Six degree of freedom, non-linear simulation (§6.3.3)

Results from (A), the lateral linear equations in the form of lateral departure parameters and roots of the stability polynomial, were presented in §5.4 and §5.5. Directional stability derivative, $\check{N}_v$, went negative at $\alpha = 18^o$ while $\check{N}_{vdyn}$ remained positive up to $\alpha = 40^o$ and showed a local minimum at $\alpha = 26^o$, due to the loss in lateral static stability derivative, $\check{L}_v$. Depending on the combinations of experimental data used, the roots of the lateral equations, all showed the dutch roll damping index going negative at between 21° and 23°α, and the spiral and roll modes combining to form a single mode at $\alpha = 22^o$ to 26^o.

Simulations using the lateral equations with aerodynamic non-linearities (model (B)) gave stable responses up to $\alpha = 22^{o}$, in agreement with the predictions from the stability roots. Non-linear sideslip characteristics produced divergences above $\alpha = 22^{o}$ and critical amplitudes at divergence agreed well with predictions from the B.T.S.averaging technique.

Results in the current chapter have come from work on six-degree of freedom models (C), (D) and (E) and comparisons are now made between these and with results from the purely lateral models.

The various representations showed good agreement for symmetric trimmed flight at α's up to the onset of lateral instability. In particular, for zero sideslip, steady equilibrium conditions, the three degree of freedom linear roots from (A) agreed very well with the fully coupled roots from (C) and the characteristics from the six degree of freedom simulation program, (E) (see Table 6.2). The full simulation showed lateral instability starting at $\alpha = 22^{o}$ for $\beta_e = 0^{o}$, as indicated by the three degree of freedom model results.

The coupled and uncoupled six degree of freedom roots for $\beta_e = 0$ (model (C)) showed relatively small differences (Fig. 6.12), while the effect of sideslip brought out the importance of the cross-coupling terms and showed up the inadequacy of a purely lateral model (see Fig.6.14). For the HIRM, up to $\alpha = 24^{o}$, with $\beta_e = -6^{o}$, the static derivatives $\check{N}_w$, $\check{L}_w$, $\check{L}_u$ and $\check{M}_v$ had the most important effects on the roots. Comparisons were not made between the eigenvalue properties for $\beta_e = -6^{o}$ and steady sideslip simulations, with model (E), due to the limitations of the sideslip data. However, a case with a steady sideslip of approximately -3^{o} at $\alpha = 18^{o}$ was used to examine the significance of various cross-coupling terms, using the linearised model, (D). Effects of dynamic cross-coupling derivatives were relatively small, as were the effects of $\check{M}_v$ and $\check{L}_u$, but $\check{L}_w$ and $\check{N}_w$ were significant.

Effects of roll rate on the coupled eigenvalues from (C) can be compared with results from the simulations of banked turns, where small equilibrium roll rates were set up. Again uncoupled eigenvalues were quite different to the fully coupled ones and the effect of $p_e = 30^{o}/s$ brought the onset of the dutch roll instability down to around $20^{o}\alpha$. The simulations, using model (E) with oscillatory data, showed oscillatory divergences above $\alpha = 21^{o}$, and with rotary data, divergences occurred at $\alpha = 20^{o}$. When an equilibrium side-slip angle of -6^{o} was added to the equilibrium roll rate, the eigenanalysis showed the appearance of exponential divergences.

From the results presented it may be said that the three degree of freedom lateral simulations and roots provide good indications of stability for the zero equilibrium state and conditions for onset of instability agrees well with the fully coupled model results. However for non-zero equilibrium conditions, the uncoupled linearised analysis is not adequate,

as shown, say, by the comparison of uncoupled and coupled eigenvalues in Fig.6.14. Using the fully coupled linearised equations does seem to give some useful indications of the likely behaviour of the full simulation, both with an eigenvalue analysis and a locally linearised simulation. Effects of dynamic cross-coupling derivatives tended to be small for the cases considered for the HIRM, while the static aerodynamic terms, $\check{L}_w$ and $\check{N}_w$, had major effects, the latter causing divergence when large (double the measured value). Sensitivity of motion to the various derivatives will, of course, depend additionally on flight condition, of which only a few cases have been examined here.

CHAPTER 7

DISCUSSION AND CONCLUSIONS

This thesis has presented an analysis of some mathematical modelling techniques for high angle of attack flight dynamics, mainly applied to a new fighter configuration, the R.A.E.'s High Incidence Research Model. Results have generally been discussed as presented, but this final chapter is intended to draw together the important findings of the work and make some recommendations as to further useful avenues of research, which might be explored.

7.1 Averaging Technique of Beecham-Titchener-Simpson

Chapter 2 presented an outline of Simpson's version of the Beecham=Titchener averaging technique, applied to aircraft lateral equations of motion and, in particular, a method of incorporating aerodynamic non-linearities with respect to two response variables was detailed. Simplifications were made,to apply the technique, in a reasonably straightforward manner, to results from a 3 degree of freedom simulation program. Using Simpson's version of the averaging technique resulted in a non-linear stability polynomial in $(\lambda+i\omega)$, whereas previous applications of the technique, to higher order equations in a single variable[24], have included $(3\lambda+i\omega)$ terms. For limit cycle properties, with $\lambda = 0$, both methods give the same results, but both the HIRM data, and that for an earlier combat aircraft, allowed assessments to be made of which representations gave the better prediction for rate of growth to limit cycle.

Applications of the averaging technique to a combat aircraft with cubic non-linearities in sideslip or roll rate characteristics showed how well limit cycles and critical amplitudes at divergence were predicted. Again for the HIRM, with non-linear characteristics in sideslip alone, a divergence boundary, with respect to angle of attack, was well predicted by the method, as well as limit cycle amplitudes.

Limitations of the technique became apparent when simultaneous non-linearities in sideslip and roll rate characteristics were incorporated. The limitations were not primarily due to the high angle of attack characteristics being used; for HIRM, the method was working well with single variable non-linearities up to $\alpha = 36^{o}$. Rather, limitations in the development of the technique meant successful results were not obtainable. For non-linearities in more than one response variable, the formulation of the assumed solution may need revision. It has recently been noted[61] that the phase angle in the assumed solution can have a large effect

on the results. Multiple frequencies may have to be admitted in the assumed solution, rather than one. The digital responses obtained for both the HIRM and combat aircraft B, described in Chapter 3, with multiple non-linearities, indicated that the various response variable damping factors are not equal, during build-up to limit cycles. This points out the inadequacy of the assumption of a single λ, in the current formulation of the technique.

Even apart from these limitations, the algebraic complexity now entailed,meant simplifications were necessary in order to apply the technique in a reasonably convenient form. Unless simplifications, without loss of accuracy, can be made it is questionable whether the technique is worth developing in such complexity, when doing so does not involve making the physical understanding of the system clearer. Even in the form used to accommodate two non-linearities, where the contribution due to gravity had to be neglected in the lateral equations, the explicit technique would still have involved the solution of a bisextic equation in σ_p.

Work examining the rate of growth to limit cycles, using the averaging technique, indicated that the $(\lambda+i\omega)$ formulation gave equations for $\lambda(\sigma)$ which showed better agreement with simulation than $\lambda(\sigma)$ from $(3\lambda+i\omega)$ formulations. This is perhaps a surprising result in view of the probably greater approximations involved in deriving the $(\lambda+i\omega)$ equation (from a determinant of the lateral equations) than in the $(3\lambda+i\omega)$ equation.

Comparisons of averaging and the local-linearisation techniques mentioned in §2.3.3 showed how responses about zero equilibrium states may be used to predict characteristics about non-zero equilibrium states. In particular it was shown how limit cycle amplitudes about steady side-slip conditions could be predicted from the linear stability boundary.

7.2 Comparison of Three- and Six-Degree of Freedom Modelling

The current work has provided a unique opportunity to compare simple linear models with relatively complicated full force and moment models and some important points were made in §6.4.

Linear, 3 degree of freedom models gave good indications of likely instabilities, from trimmed symmetric equilibrium states, as α was increased. For instance, on the HIRM, the basic lateral roots indicated dutch roll instability occurring at $\alpha = 22^{o}$ and this is the angle of attack at which divergence began from symmetric equilibrium states in the 6 degree of freedom simulations. Eigenvalues and response characteristics from both 3 and 6 degree of freedom

models showed good agreement for the HIRM basic trim states, as typified by results shown for $\alpha = 10^{o}$, 20^{o}.

The importance of cross-coupling terms, and the consequent inadequacy of 3 degree of freedom models, was shown for cases of non-zero equilibrium states. Eigenvalue analyses showed the importance of the derivatives $\check{L}_w$ and $\check{N}_w$ when equilibrium sideslip was not zero. Effects were significant even though the range of β (from 0 to -6^{o}) was relatively small. Data has now been obtained for the HIRM up to $\pm 18^{o}$ of sideslip and this will enable further analysis of cross-coupling effects to be carried out.

A linear 6 degree of freedom simulation confirmed that effects of static cross-coupling derivatives are important in non-zero equilibrium flight. These results are likely to be true in general, for high angles of attack, but due to the high dependence on configuration details, results for other aircraft may show different trends. For the HIRM, flight cases up to $\alpha = 20^{o}$ showed that $\check{L}_w$ and $\check{N}_w$ were the most important of the static cross-coupling derivatives, with $\check{M}_v$ having less effect.

All of the 6 degree of freedom modelling, and most of the 3 degree of freedom work as well, was performed using digital computers but mention should perhaps be made of the analogue, 3 degree of freedom simulations, described in Chapter 3. The analogue computer provided a convenient method of measuring stability boundaries as a function of, say, feedback gearing and was very useful for parametric studies. Although lacking the precision of digital programs, the analogue technique proved useful for getting a qualitative 'feel' for the aircraft behaviour and as such should continue to make a valuable contribution to aircraft stability and response research.

7.3 Six Degree of Freedom Simulation

These simulations provided an opportunity to use a large amount of the measured experimental data for the HIRM configuration C, in assessing mainly the effects of cross-coupling aerodynamics and the use of rotary and oscillatory roll damping data.

It should be noted that static data used from the HIRM 1 tests is likely to give slightly different trim angles of attack to those obtained ultimately in flight tests, because data from the definitive HIRM 2 wind-tunnel model indicated different trim states. However, trends with α should be predicted satisfactorily and the computed responses will provide useful comparisons for simulations using HIRM 2 static data.

Limitations on the amount of data available in sideslip meant that steady sideslips, with β_e outside $\pm 4^{o}$, were not attempted with the full simulation, due to very quick

excursions in β producing extrapolations outside the range of the data tables. Steady sideslips were used in the linearised simulation to examine cross-coupling effects.

Work on simulations of banked turns highlighted the large effects of using either rotary or oscillatory damping in the pre-stall/departure angle of attack range. Future work could be aimed at assessing effects in manoeuvres with higher roll rates, e.g. rapid rolls, but, in the meantime, it may be said that rotary rig damping alone was not adequate at angles of attack above 18^{o}. Attempts were made to incorporate both forms of damping simultaneously, following, for example, Anglin[41] in the modelling of high α behaviour in spins, but it proved not to be possible due to the inability to suitably separate rotary and oscillatory angular rates in the model as formulated.

Pure, large amplitude, yawing data would also be useful for a full simulation, particularly for spins, where high yaw rates are attained. This would provide a complete set of large amplitude (yawing and rolling) data to complement the consistent set of oscillatory data in the model. Tischler and Barlow[120] comment on the sideslip dependence of certain derivatives and point out a need for rotary balance data at sideslip.

With reference to the mathematical modelling ideas described in §2.2, it should be noted that the wind-tunnel data available from the HIRM tests has largely dictated the form of the mathematical models used. As described in §2.2.1, the first step in mathematical modelling is deciding on the form of the model, which in turn determined the type of wind tunnel tests needed.

Effects of measured cross-coupling dynamic derivatives were shown to be small in the cases examined with the full force and moment, 6 degree of freedom simulation. The flight cases examined were straight flight at $\alpha = 18^{o}$, and turning, '2g' flight at $\alpha = 18^{o}$. As in the eigenvalue analysis, combined derivatives, including $\dot{v}$ and $\dot{w}$ components, were included in the model and it would be useful to investigate the effects of separating these into pure rotary and acceleration parts. Only dynamic cross-coupling derivatives were used in the full simulations, the static data being incorporated in table look-up form, so that derivatives due to α and β did not appear explicitly.

Static cross-coupling derivatives were used in a locally linearised 6 degree of freedom simulation and provided an opportunity to examine effects of such derivatives as $\check{M}_v$, $\check{L}_w$ and $\check{N}_w$. As already mentioned, $\check{L}_w$ and $\check{N}_w$ had significant effects on the HIRM responses under steady sideslip conditions, but it is not possible to draw firm conclusions with respect to particular derivatives, for all fighter aircraft configurations, at high angles of attack, due to dependence on configuration details and flight conditions.

7.4 Future Work

a) Averaging

On the averaging technique,more work could usefully be performed on the formulations for rate of growth to limit cycles, in particular comparing $(3\lambda+i\omega)$ and $(\lambda+i\omega)$ forms, in the case of cubic aerodynamic non-linearities.

Work on the formulation of solutions,for cases where non-linearities occur in more than one response variable,should also be pursued.

b) Eigenvalue Analysis

Effects of acceleration derivatives due to $\dot{v}$ and $\dot{w}$ were not explicitly included in the eigenvalue analysis (only implicitly in the form of combined derivatives from oscillatory tests) and the effects of pure rolling or yawing derivatives would make an interesting comparison with the results presented here.

c) Simulations

The simulations described in this thesis have covered only a small number of flight conditions and much work remains to be performed on other cases.

The simulation model includes a relatively limited amount of angle of attack and sideslip data and could be expanded to cover a larger range of angle of attack and sideslip. Tests on a free-flight version of the HIRM,in the R.A.E. 5m wind tunnel,have recently provided more data up to $\pm 18^{o}$ side-slip. Limited data is already available for angles of attack up to 90^{o} and, as a result of needs shown up by work for this thesis, large amplitude yawing data is to be obtained from tests involving the HIRM on a whirling arm facility. Incorporation of all this data would enable more extreme manoeuvres, such as spins, to be simulated. It was not felt necessary, for the current work,aimed at flight up to departure, to incorporate data for α above 40^{o}.

On the programming aspects of the simulation model, an investigation into methods of interpolating data look-up tables would be a useful exercise. The current simulation has used linear interpolation but other techniques, such as using curve fits to the data, have been suggested.

d) R.A.E.Programme

Drop tests of the first free-flight model have just started, at the time of writing, and will provide useful data, both to validate mathematical models of the HIRM and to provide

more input data for such models, via parameter identification techniques.

Although the drop tests will initially use a stable configuration, the later tests will be flown in unstable configurations,with the help of a digital control system. The novel 3 surface arrangement on the HIRM will provide opportunities for direct side force and direct lift control to be investigated.

REFERENCES

1. Dynamic Stability Parameters.
AGARD Conference Proceedings,
AGARD-CP-235 (1978)

2. Dynamic Stability Parameters.
AGARD/VKI Lecture Series,
AGARD-LS-114 (1981)

3. Chambers,J.R. Aerodynamic Characteristics at High Angles of Attack.
AGARD-LS-99 (Aerodynamic Inputs for Problems in Aircraft Dynamics) (1977)

4. Manoeuvre Limitations of Combat Aircraft.
AGARD-AR-115A (1979)

5. Kraus,W.
Przibilla,H.
Haux,U. Stability and Control for High Angle of Attack Maneuvering.
AGARD-CP-333 (Criteria for Handling Qualities of Military Aircraft)(1982)

6. John,H.
Kraus,W. High Angle of Attack Characteristics of Different Fighter Configurations.
AGARD-CP-247 (High Angle of Attack Aerodynamics) (1978)

7. Luckring,J.M. Aerodynamics of Strake-Wing Interaction.
J.Aircraft,Vol.16,No.11,November 1979,
pp 756-762

8. Erickson,G.E. Water Tunnel Studies of Leading Edge Vortices.
J.Aircraft,Vol.19,No.6,June 1982,
pp 442-448

9. Lamar,J.E.
Frink,N.T. Aerodynamic Features of Designed Strake-Wing Configurations.
J.Aircraft,Vol.19,No.8,August 1982,
pp.639-646

10. Bihrle,W.
Meyer,R.C. F-14A High Angle of Attack Characteristics.
J.Aircraft,Vol.13,No.8,August 1976,
pp.576-583

11. Buckner,J.R.
Walker,J.E.
Clark,C.K. Design of the F-16 High-Alpha Flight Control Characteristics and Control System Concept.
AIAA 79-0403 (1979)

12. Patierno,J. YF-17 Design Concepts.
AIAA 74-936 (1974)

13. Buckner,J.K.
Hill,P.W.
Benepe,D. The Aerodynamic Design Evolution of the YF-16.
AIAA 74-935 (1974)

REFERENCES (continued)

14. Anderson,C.A. — The Stall/Spin Problem - American Industry's Approach. AGARD-CP-199 (Stall/Spin Problems of Military Aircraft) (1976)

15. Titiriga,A. Ackerman,J.S. Skow,A.M. — Design Technology for Departure Resistance of Fighter Aircraft. AGARD-CP-199 (Stall/Spin Problems of Military Aircraft) (1976)

16. Chambers,J.R. Anglin,E.L. — Analysis of Lateral-Directional Stability Characteristics of a Twin Jet Fighter Aeroplane at High Angles of Attack. NASA TN-D-5361 (1969)

17. Ross,A.J. Foster,G.W. Turvey,T. — An Investigation of Dutch Roll and Wing Rock Oscillations of a Gnat Trainer Aircraft: Flight Tests and Linear Analysis. RAE Technical Report 78032 (1978)

18. Shaw,D.E. — Pre-stall Behaviour of Combat Aircraft. AGARD-LS-74 (Aircraft Stalling and Buffeting) (1975)

19. Hwang,C. Pi,W.S. — Some Observations on the Mechanism of Aircraft Wing Rock. J.Aircraft,Vol.16,No.6,June 1979, pp.366-373

20. Schiff,L.B. Tobak,M. Malcolm,G.N. — Mathematical Modeling of the Aerodynamics of the High-Angle-of-Attack Maneuvers. AIAA 80-1583 (1980)

21. Cord,T.J. — Hysteresis Induced Wing Rock. U.S.Air Force Flight Dynamics Laboratory AFFDL-TM-75-76-FGC (1975)

22. Schmidt,L.V. — Wing Rock Due to Aerodynamic Hysteresis. J.Aircraft,Vol.16,No.3,March 1979, pp.129-133

23. Ross,A.J. Beecham,L.J. — An Approximate Analysis of the Non-Linear Lateral Motion of a Slender Aircraft (HP115) at Low Speeds. A.R.C. R.& M. No.3674 (1971)

24. Ross,A.J. — Investigation of Nonlinear Motion Experienced on a Slender Wing Research Aircraft. J.Aircraft,Vol.9,No.9,September 1972, pp.625-631

REFERENCES (continued)

25. Gera,J.
Wilson,R.J.
Enevoldson,E.K.
Nguyen,L.T.
Flight Test Experience with High-α Control System Techniques on the F-14 Airplane.
AIAA 81-2505 (1981)

26. Ross,A.J.
Lateral Stability at High Angles of Attack, particularly Wing Rock.
AGARD-CP-260 (Stability and Control) (1979)

27. Booker,D.
McKay,K.
Experience of Non-Linear High Incidence Aerodynamic Characteristics.
AGARD-CP-333 (Criteria for Handling Qualities of Military Aircraft) (1982)

28. Ericsson,L.E.
A Summary of AGARD F.D.P.Meeting on Dynamic Stability Parameters.
AGARD-CP-260 (Stability and Control) (1979)

29. Moss,G.F.
A Note on a Proposed US/UK Cooperative High-Incidence Research Project (CHIRP).
RAE Technical Memorandum Aero 1848 (1980)

30. Moss,G.F.
Ross,A.J.
Butler,G.F.
A Programme of Work on the Flight Dynamics of Departure using a High Incidence Research Model (HIRM).
RAE Technical Memorandum Aero 1950 (1982)

31. Beecham,L.J.
Titchener,I.M.
Some Notes on an Approximate Solution for the Free Oscillation Characteristics of Non-Linear Systems Typified by $\ddot{x} + F(x,\dot{x}) = 0$.
A.R.C. R.& M. No.3651 (1969)

32. Simpson,A.
An Algorithm for Autonomous Non-linear Dynamical Equations.
Aeronautical Quarterly,Vol.28, August 1977, pp.211-234

33. Hreha,M.A.
Lutze,F.H.
Linear Analysis of Poststall Gyrations.
J.Aircraft,Vol.17,No.10,October 1980, pp.727-733

34. Cochran,J.E.
Ho,C-S,
Castleberry,G.A.
Stability of Asymmetric Equilibrium Flight States.
AIAA 80-1567 (1980)

35. Schiff,L.B.
Tobak,M.
Some Applications of Aerodynamic Formulations to Problems in Aircraft Dynamics.
AGARD-LS-114 (Dynamic Stability Parameters) (1981)

REFERENCES (continued)

36. Tobak,M.
Schiff,L.B.
On the Formulation of the Aerodynamic Characteristics in Aircraft Dynamics.
NASA TR R-456 (1976)

37. Thomas,H.H.B.M.
On Problems of Flight over an Extended Angle-of-Attack Range.
Aeronautical Journal,Vol.77,No.752, August 1973, pp.412-423

38. Stengel,R.F.
Berry,P.W.
Stability and Control of Maneuvering High Performance Aircraft.
NASA CR-2788 (1977)

39. Ross,A.J.
A Comparison of Analytical Techniques for Predicting Stability Boundaries for Some Types of Aerodynamic or Cross-Coupling Nonlinearities.
R.A.E.Technical Memorandum Aero 1936 (1982)

40. Mehra,R.K.
Kessel,W.C.
Carroll,J.V.
Global Stability and Control Analysis of Aircraft at High Angles-of-Attack.
ONR-CR215-248-1 (1977)

41. Anglin,E.L.
Aerodynamic Characteristics of Fighter Configurations during Spin Entries and Developed Spins.
J.Aircraft,Vol.15,No.11,November 1978, pp.769-776

42. Babister,A.W.
Aircraft Dynamic Stability and Response.
Pergamon Press (1980)

43. Etkin,B.
Dynamics of Flight - Stability and Control.
Second Edition. John Wiley & Sons (1982)

44. McRuer,D.
Ashkenas,I.
Graham,D.
Aircraft Dynamics and Automatic Control.
Princeton University Press (1973)

45. Hopkin,H.R.
A Scheme of Notation and Nomenclature for Aircraft Dynamics and Associated Aerodynamics.
A.R.C. R.& M. No.3562 (1966)

46. Ross,A.J.
Lateral Handling Characteristics of Combat Aircraft.
Stability and Control Short Course Notes, Cranfield Institute of Technology (1975)

REFERENCES (continued)

47. Kalviste,J. — Aircraft Stability Characteristics at High Angles of Attack. AGARD-CP-235 (Dynamic Stability Parameters) (1978)

48. Greer,D. — Summary of Directional Divergence Characteristics of Several High-Performance Aircraft Configurations. NASA TN D-6993 (1972)

49. Calico,R.A. — A New Look at $C_{n_{\beta,dyn}}$. J.Aircraft,Vol.16,No.12,December 1979, pp.895-896

50. Burris,W.R. Lawrence,J.T. — Aerodynamic Design and Flight Test of U.S.Navy Aircraft at High Angles of Attack. AGARD-CP-102 (Fluid Dynamics of Aircraft Stalling) (1972)

51. Johnston,D.E. Hogge,J.R. — Nonsymmetric Flight Influence on High-Angle-of-Attack Handling and Departure. J.Aircraft,Vol.13,No.2,February 1976, pp.112-118

52. Weissman,R. — Status of Design Criteria for Predicting Departure Characteristics and Spin Susceptibility. AIAA 74-791 (1974)

53. Weissman,R. — Preliminary Criteria for Predicting Departure Characteristics/Spin Susceptibility of Fighter-Type Aircraft. J.Aircraft,Vol.10,No.4,April 1973, pp.214-219

54. — The Effects of Buffeting and other Transonic Phenomena on Maneuvering Combat Aircraft. AGARD-AR-82 (1975)

55. Phillips,W.H. — Effect of Steady Rolling on Longitudinal and Directional Stability. NACA TN 1627 (1948)

56. — Introduction to Inertia Cross-Coupling of the Lateral and Longitudinal Motions during a Rapid Rolling Manoeuvre. Engineering Sciences Data Unit. Item 67005 (1966)

REFERENCES (continued)

57. Inertia Cross-Coupling during a Rapid-Rolling Manoeuvre. Theoretical Background and Discussion of Simplified Stability Boundaries. Engineering Sciences Data Unit. Item 67006 (1966)

58. Hacker,T. Oprişiu,C. A Discussion of the Roll-Coupling Problem. Prog.in Aerospace Sciences,Vol.15, 1974, pp.151-180

59. Mehra,R.K. Carroll,J.V. Global Stability and Control Analysis of Aircraft at High Angles-of-Attack. ONR-CR215-248-2 (1978)

60. Kryloff,N. Bogoliuboff,N.N. Introduction to Nonlinear Mechanics. Princeton University Press (1947)

61. Christopher,P.A.T. Thorne,R. Some Examples of the Application of the Beecham-Titchener-Simpson (B.T.S.) Method to Autonomous Systems. Cranfield College of Aeronautics Report No.8317 (1983)

62. Duncan,W.J. The Principles of the Control and Stability of Aircraft. Cambridge University Press (1952)

63. Hreha,M.A. Linear Analysis of Incipient Spin Dynamics. Virginia Polytechnic Institute and State University M.S. Thesis (1979)

64. Johnston,D.E. Mitchell,D.G. Myers,T.T. Investigation of High-Angle-of-Attack Maneuver - Limiting Factors. U.S.Air Force Flight Dynamics Laboratory Technical Report AFWAL-TR-80-3141 (1980)

65. Ross,A.J. Johnson,M. A Comparison between Two Analytical Methods of Studying the Characteristics of Nonlinear Equations of Motion of an Aircraft. RAE Technical Report 82124 (1982)

66. Analogue Hybrid Computer VIDAC 1224. Computing Techniques (International)Ltd.

67. VAX-11 FORTRAN Language Reference Manual. Digital Equipment Corporation (1982)

68. VAX-11 FORTRAN User's Guide. Digital Equipment Corporation (1982)

REFERENCES (continued)

69. Runge-Kutta-Merson Method for System of Ordinary Differential Equations. NAG Algorithm D02BBF. Numerical Algorithms Group,FORTRAN Library Mk.9 (1982)

70. Adams Method for System of Ordinary Differential Equations. NAG Algorithm D02CBF. Numerical Algorithms Group,FORTRAN Library Mk.9 (1982)

71. GINOGRAF. Cranfield Computer Centre Document CCS7 (1978)

72. GINO-F User Manual.Issue 2. Computer Aided Design Centre (1975)

73. GINO-F at Cranfield. Cranfield Computer Centre Document CCS5 (1978)

74. Zeros of a Polynomial. NAG Algorithm C02AEF. Numerical Algorithms Group,FORTRAN Library Mk.9 (1982)

75. Quadrature for One-Dimensional Integrals. NAG Algorithm D01GAF. Numerical Algorithms Group, FORTRAN Library Mk.9 (1982)

76. Ross,A.J. A FORTRAN Program for the Evaluation of Lateral Stability Parameters of Aircraft. RAE Technical Memorandum Aero 1336 (1971)

77. Grad,J. Brebner,M.A. Eigenvalues and Eigenvectors of a Real General Matrix. Collected Algorithms from Communications of the Association for Computing Machinery.Algorithm 343 (1978)

78. Kruseman Aretz,F.E.J. Zonneveld,J.A. F.F.T.Algorithms. Philips Research Reports,Vol.30,1975, pp.288-301

79. Cochran,W.T.,*et al* What is the Fast Fourier Transform? Proceedings of the I.E.E.E.,Vol.55, No.10, October 1967, pp.1664-1674

REFERENCES (continued)

80. Johnson,J.L.
Grafton,S.B.
Yip,L.P.
Exploratory Investigation of the Effects of Vortex Bursting on the High Angle of Attack Lateral-Directional Stability Characteristics of Highly Swept Wings.
AIAA 11th Aerodynamic Testing Conference (1980)

81. Murdin,P.M.
Riddle,G.L.
Preliminary Results of Low-Speed Tests on a Research Model of a Strike-Fighter Configuration.
RAE Unpublished Note

82. Reid,G.E.A.
HIRM Inertias (Revised).
RAE Unpublished Note, 2 June 1982

83. Croom,M.A.
Grafton,S.B.
Nguyen,L.T.
High Angle-of-Attack Characteristics of Three-Surface Fighter Aircraft.
AIAA 82-0245 (1982)

84. Agnew,J.W.
Hess,J.R.
Benefits of Aerodynamic Interaction to the Three Surface Configuration.
AIAA 79-1830 (1979)

85. Agnew,J.W.
Lyerla,G.W.
Grafton,S.B.
The Linear and Non-Linear Aerodynamics of Three-Surface Aircraft Concepts.
AIAA 80-1581 (1980)

86. Fail,R.
The Role of Free-Flight Models in Aircraft Research and Development.
AGARD-CP-119 (Stability and Control) (1972)

87. Moss,G.F.
Ross,A.J.
Edwards,G.F.
Jeffries,E.B.
The Use of Free-Flight Models for the Prediction of Departure Control.
RAE Technical Memorandum Aero 1952 (1982)

88. Ross,A.J.
Thomas,H.H.B.M.
A Survey of Experimental Data on the Aerodynamics of Controls, in the Light of Future Needs.
AGARD-CP-262 (Aerodynamics of Controls) (1979)

89. Henderson,W.P.
Leavitt,L.D.
Stability and Control Characteristics of a Three-Surface Advanced Fighter Configuration at Angles of Attack up to 45^{0}.
NASA TM-83171 (1981)

90. Ross,A.J.
Reid,G.E.A.
The Development of Mathematical Models for the RAE High Incidence Research Model (HIRM).
Part 1. Analysis of Static Aerodynamic Data.
RAE Technical Report to be published

REFERENCES (continued)

91. Thomas,H.H.B.M. — The Estimation of Lateral-Directional Aerodynamic Derivatives at Subsonic Speeds. AGARD-LS-99 (Aerodynamic Inputs for Problems in Aircraft Dynamics)(1977)

92. — Engineering Sciences Data, Aerodynamics Sub-Series Vol.3. Engineering Sciences Data Unit. (1981, 1982)

93. Hoak,D.E. Carlson,J.W. — USAF Stability and Control Handbook (DATCOM). Douglas Aircraft Co.Inc.,for Flight Control Laboratory,Wright-Patterson AFB, Dayton,Ohio (1960)

94. Ross,A.J. — The Calculation of Lateral Stability Derivatives of Slender Wings at Incidence, including Fin Effectiveness, and Correlation with Experiment. A.R.C. R.& M. No.3402 (1965)

95. Sacks,A.H. — Aerodynamic Forces, Moments and Stability Derivatives for Slender Bodies of General Cross-Section. NACA TN 3283 (1954)

96. O'Leary,C.O. — Wind-Tunnel Measurement of Aerodynamic Derivatives using Flexible-Sting Rigs. AGARD-LS-114 (Dynamic Stability Parameters) (1981)

97. O'Leary,C.O. — Wind-Tunnel Measurement of Lateral Aerodynamic Derivatives using a New Oscillatory Rig, with Results and Comparisons for the Gnat Aircraft. A.R.C. R.& M. No.3847 (1977)

98. Reid,G.E.A. — M2130 Pitch Damping. RAE Unpublished Note,13 September 1982

99. Matthews,A.W. — Experimental Determination of Dynamic Derivatives due to Roll at British Aerospace,Warton Division. AGARD-CP-235 (Dynamic Stability Parameters) (1978)

100. Booker,D. — RAE Model 2130 Rolling Rig Tests. BAe Unpublished Note, 1 March 1982

101. Orlik-Rückemann,K.J. — Review of Techniques for Determination of Dynamic Stability Parameters in Wind Tunnels. AGARD-LS-114 (Dynamic Stability Parameters) (1981)

REFERENCES (continued)

102. Conversion of Stability Derivatives for a Change of Body Axes. Engineering Sciences Data Unit. Item Aero A.00.00.06 Amend.C (1977)

103. Least-Squares Curve Fit by Polynomial Approximation to an Arbitrary Set of Data Points. NAG Algorithm E02ADF. Numerical Algorithms Group,FORTRAN Library Mk.9 (1982)

104. Reid,G.E.A. HIRM Inertias. RAE Unpublished Note, 20 November 1981

105. Conversion of Resolutes of Force and Velocity and of Constants of Inertia for General Change of Axes. Engineering Sciences Data Unit. Item Aero A.00.00.05 Amend.C (1981)

106. Ross,A.J. Combination of Rotary and Oscillatory Rig Results. RAE Unpublished Note, 11 May 1982

107. Orlik-Rückemann,K.J. Aerodynamic Coupling between Lateral and Longitudinal Degrees of Freedom. AIAA Journal,Vol.15,No.12, December 1977, pp.1792-1799

108. Velgar,M. Shinar,J. Cross-Coupling between Longitudinal and Lateral Aircraft Dynamics in a Spiral Dive. J.Aircraft,Vol.20,No.1,January 1983, pp.21-26

109. Sandford,J. Lateral-Longitudinal Cross-Coupling Effects. AGARD-LS-99 (Aerodynamic Inputs for Problems in Aircraft Dynamics) (1977)

110. Stengel,R.F. Effect of Combined Roll Rate and Sideslip Angle on Aircraft Flight Stability. J.Aircraft,Vol.12,No.8,August 1975, pp.683-685

111. Calico,R.A. Fuller,S.G. Stability of Steady Sideslip Equilibria for High Alpha. J.Aircraft,Vol.20,No.4,April 1983, pp.327-330

112. Orlik-Rückemann,K.J. Sensitivity of Aircraft Motion to Cross-Coupling and Acceleration Derivatives. AGARD-LS-114 (Dynamic Stability Parameters) (1981)

REFERENCES (concluded)

113. Reid,G.E.A. — HIRM C Longitudinal Derivatives. RAE Unpublished Note,17 November 1982

114. Johnston,D.E. — Identification of Key Maneuver-Limiting Factors in High-Angle-of-Attack Flight. AGARD-CP-235 (Dynamic Stability Parameters) (1978)

115. — Eigenvalues and Eigenvectors of a Real Matrix. NAG Algorithm F02AGF. Numerical Algorithms Group,FORTRAN Library Mk.9 (1982)

116. Beyers,M.E. — A New Concept for Aircraft Dynamic Stability Testing. J.Aircraft,Vol.20,No.1,January 1983, pp.5-14

117. Tomlinson,B.N. — SESAME - A System of Equations for the Simulation of Aircraft in a Modular Environment. RAE Technical Report 79008 (1979)

118. Thorne,R. — A Study of the Harrier Aircraft in Crosswind Ski-Jump Launches. Cranfield College of Aeronautics M.Sc.Thesis (1980)

119. Curry,W.H.
Orlik-Rückemann,K.J. — Sensitivity of Aircraft Motion to Aerodynamic Cross-Coupling at High Angles of Attack. AGARD-CP-235 (Dynamic Stability Parameters) (1978)

120. Tischler,M.B.
Barlow,J.B. — A Dynamic Analysis of the Motion of a Low-Wing General Aviation Aircraft about its Calculated Equilibrium Flat Spin Mode. AIAA 80-1565 (1980)

121. Bryant,L.W.
Gates,S.B. — Nomenclature for Stability Coefficients. A.R.C. R.& M. No.1801 (1937)

122. Thomas,H.H.B.M. — Notes on Stability and Control Derivatives at Subsonic and Transonic Speeds. RAE Unpublished Note

APPENDIX A

NOMENCLATURE FOR AERODYNAMIC COEFFICIENTS AND DERIVATIVES

A.1 Axes Systems and Experimental Data

An explanation of the system of dressings adopted in this thesis is in order here, to bring out the reasoning behind the various suffices used.

The axis system used for an aerodynamic coefficient or variable such as L, M, p, etc is shown by the superfix B (geometric body axes) or w (wind axes), e.g.

$$C_{\ell}^{B}, \quad C_{n}^{w}, \quad p^{w}, \quad r^{B}$$

In the absence of either B or w, it may be assumed that the coefficient or variable is in body axes.

For derivatives (given in this thesis in the notation of Hopkin, Ref.45), the same system is adopted,for cases where moment or force is in the same axis system as the rate or displacement, e.g.

$$\breve{L}_{p}^{w}, \quad \breve{N}_{r}^{w}$$

However, for mixed body/wind axis derivatives, a suffix is put on the quantity concerned when it is in wind axes, and omitted otherwise, e.g.

$$Lp_{w} = \frac{\partial L^{B}}{\partial p^{w}}$$

$$Lw_{p} = \frac{\partial L^{w}}{\partial p^{B}}$$

These 'mixed' derivatives are used particularly in the cases of rotary rig raw data (see §4.8) where measurements of moments and force are made in body axes (using strain gauges) as functions of wind axis roll rate. Oscillatory rig tests give body axis forces and moments against body axis rates.

The letters 'R' and 'o' are used as suffices on derivatives and coefficients,to denote rotary or oscillatory data respectively, e.g.

$\breve{L}_{p_R}$ ≡ rotary rig measurement

$\breve{L}_{r_o}$ ≡ oscillatory rig measurement

A final set of suffices used on the derivatives, are the numbers 0, 1, 2 and 3 to denote terms in cubic polynomials fitted to raw wind tunnel data. The use of 0, to denote a constant term in such a polynomial, should not give rise to confusion with o, for oscillatory data, because of context and also since only static or rotary wind tunnel data were used for polynomial fitting.

Having explained the system of dressings used, a few examples will show how they can be used in combinations:

$$C_{\ell_{p_{w_3}}} \equiv \frac{\partial^3 C_\ell{}^B}{\partial \left(\frac{p^w b}{2V}\right)^3}$$

Cubic term in polynomial fitted to raw rolling rig data

$$L_{p_{w_R}} \equiv \frac{\partial L^B}{\partial p^w}$$

Dimensional derivative measured on rotary rig

$$\breve{L}_{p_O}{}^B \equiv \frac{\partial C_\ell{}^B}{\partial \left(\frac{p^B b}{V}\right)}$$

Measured on oscillatory rig

$$L_{\dot{p}_{1R}}^{w} \equiv \frac{\partial L^w}{\partial p^w}$$

First order term in polynomial fitted to rolling rig data, in wind axes

A.2 Cross-Coupling Derivatives

In the definition of cross-coupling derivatives, which involve characteristic lengths ($\bar{\bar{c}}$ for longitudinal and b for lateral), the individual components have been non-dimensionalised by the relevant length. This is as opposed to dividing the whole derivative by either a longitudinal or lateral length, e.g. consider the derivative M_p.

In British notation (Ref.45), this is:

$$\breve{M}_p = \frac{\partial C_m}{\partial \left(\frac{pb}{V}\right)} = \frac{\partial \left(\frac{M}{\frac{1}{2}\rho V^2 S\bar{\bar{c}}}\right)}{\partial \left(\frac{pb}{V}\right)}$$

where b has been used for the roll rate term and $\bar{\bar{c}}$ has been used in C_m, as is conventional.

A.3 Concise Derivatives

In the lateral equations (2.10) - (2.12) and (2.15) - (2.17), the concise derivatives, representing the expansion of aerodynamic forces and moments in terms of state variables, are given by (N.B. natural signs used):

$$y'_v = \frac{Y_v}{m} \qquad y'_\zeta = \frac{Y_\zeta}{m}$$

$$\ell'_{v_1} = \frac{I_z L_v + I_{xz} N_v}{I_x I_z - I_{xz}^2} \qquad n'_{v_1} = \frac{I_x N_v + I_{xz} L_v}{I_x I_z - I_{xz}^2}$$

$$\ell'_{v_3} = \frac{I_z L_{v_3} + I_{xz} N_{v_3}}{I_x I_z - I_{xz}^2} \qquad n'_{v_3} = \frac{I_x N_{v_3} + I_{xz} L_{v_3}}{I_x I_z - I_{xz}^2}$$

$$\ell'_{p_{eff}} = \frac{I_z L_p + I_{xz} N_p}{I_x I_z - I_{xz}^2} + K_{\xi p} \frac{I_z L_\xi + I_{xz} N_\xi}{I_x I_z - I_{xz}^2} = \ell'_{p_1} + K_{\xi p} \ell'_\xi$$

$$n'_{p_{eff}} = \frac{I_x N_p + I_{xz} L_p}{I_x I_z - I_{xz}^2} + K_{\xi p} \frac{I_x N_\xi + I_{xz} L_\xi}{I_x I_z - I_{xz}^2} = n'_{p_1} + K_{\xi p} n'_\xi$$

$$\ell'_{p_3} = \frac{I_z L_{p_3} + I_{xz} N_{p_3}}{I_x I_z - I_{xz}^2} \qquad n'_{p_3} = \frac{I_x N_{p_3} + I_{xz} L_{p_3}}{I_x I_z - I_{xz}^2}$$

$$\ell'_{r_{eff}} = \frac{I_z L_r + I_{xz} N_r}{I_x I_z - I_{xz}^2} + K_{\zeta r} \frac{I_z L_\zeta + I_{xz} N_\zeta}{I_x I_z - I_{xz}^2} = \ell'_r + K_{\zeta r} \ell'_\zeta$$

$$n'_{r_{eff}} = \frac{I_x N_r + I_{xz} L_r}{I_x I_z - I_{xz}^2} + K_{\zeta r} \frac{I_x N_\zeta + I_{xz} L_\zeta}{I_x I_z - I_{xz}^2} = n'_r + K_{\zeta r} n'_\zeta$$

$$\ell'_\xi = \frac{I_z L_\xi + I_{xz} N_\xi}{I_x I_z - I_{xz}^2} \qquad \text{and similarly, } \ell'_\zeta$$

$$n'_\xi = \frac{I_x N_\xi + I_{xz} L_\xi}{I_x I_z - I_{xz}^2} \qquad \text{and similarly, } n'_\zeta$$

(N.B. ξ_T used as roll control on the HIRM)

Similar notation was adopted for the longitudinal derivatives, where required, e.g.

$$z'_u = \frac{Zu}{m} \qquad x'_u = \frac{Xu}{m}$$

In the linearisation of the six degree of freedom coupled equations (see Appendix E), a more complicated set of derivatives is formed, involving extra terms in equilibrium roll, yaw and pitch rates, as well as acceleration derivatives. These are denoted by a double dash, e.g.

$$z''_u = \frac{Z_u}{m - Z_w}$$

Full details of these derivatives are given in Appendix E.

APPENDIX B

STABILITY QUARTIC

The non-linear "stability quartic" given in equation (2.65), as well as the equation of motion in v, shown as equation (2.37), both involve terms used in conventional linear stability analysis, e.g. a_1 , b_1 , etc, as well as non-linear terms, e.g. $a_3 p$, $b_3 p$, etc. The definitions of these terms, using concise derivatives, is as follows:

$$a_1 = -y'_v - n'_r - \ell'_{p_{eff}}$$

$$a_{3p} = - \ell'_{p_3}$$

$$b_1 = n'_r \ell'_{p_{eff}} - n'_{p_{eff}} \ell'_r + y'_v (\ell'_{p_{eff}} + n'_r) - \ell'_{v_1} V\sin\alpha + n'_{v_1} V\cos\alpha$$

$$b_{3p} = n'_r \ell'_{p_3} - n'_{p_3} \ell'_r + y'_v \ell'_{p_3}$$

$$b_{3v} = - \ell'_{v_3} V\sin\alpha + n'_{v_3} V\cos\alpha$$

$$c_1 = -y'_v (n'_r \ell'_{p_{eff}} - \ell'_r n'_{p_{eff}}) + \ell'_{v_1} (n'_r V\sin\alpha + n'_{p_{eff}} V\cos\alpha - g_3) - n'_{v_1} (\ell'_r V\sin\alpha + \ell'_{p_{eff}} V\cos\alpha + g_2)$$

$$c_{3p} = -y'_v (n'_r \ell'_{p_3} - \ell'_r n'_{p_3}) + \ell'_{v_1} (n'_{p_3} V\cos\alpha) - n'_{v_1} (\ell'_{p_3} V\cos\alpha)$$

$$c_{3v} = \ell'_{v_3} (n'_r V\sin\alpha + n'_{p_{eff}} V\cos\alpha - g_3) - n'_{v_3} (\ell'_r V\sin\alpha + \ell'_{p_{eff}} V\cos\alpha + g_2)$$

$$c_{3vp} = \ell'_{v_3} (n'_{p_3} V\cos\alpha) - n'_{v_3} (\ell'_{p_3} V\cos\alpha)$$

$$d_1 = \ell'_{v_1} (g_3 n'_r - g_2 n'_{p_{eff}}) - n'_{v_1} (g_3 \ell'_r - g_2 \ell'_{p_{eff}})$$

$$d_{3p} = -\ell'_{v_1} g_2 n'_{p_3} + n'_{v_1} g_2 \ell'_{p_3}$$

$$d_{3v} = \ell'_{v_3} (g_3 n'_r - g_2 n'_{p_{eff}}) - n'_{v_3} (g_3 \ell'_r - g_2 \ell'_{p_{eff}})$$

$$d_{3vp} = -\ell'_{v_3} g_2 n'_{p_3} + n'_{v_3} g_2 \ell'_{p_3}$$

where $\ell'_{p_{eff}} = \ell'_{p_1} + K_{\xi p}\ell'_{\xi}$

and $n'_{p_{eff}} = n'_{p_1} + K_{\xi p}n'_{\xi}$

APPENDIX C

LIMIT CYCLE EQUATIONS

C.1 Non-linear Routhian for Limit Cycles in v,p

Equation (2.76) is an equation for limit cycle amplitudes in v and p and is shown in a more expanded form in equation (2.77). The coefficients A_1 to K_1 used in (2.77) are defined as follows:

$$A_1 = a_{3p}b_{3p}c_{3p} - a_{3p}^2 d_{3p}$$

$$B_1 = a_{3p}b_{3p}c_{3vp} - a_{3p}^2 d_{3vp}$$

$$C_1 = a_{3p}b_{3v}c_{3vp} - c_{3vp}^2$$

$$D_1 = a_1 b_{3p}c_{3vp} + a_{3p}b_{3p}c_{3v} + a_{3p}b_{3v}c_{3p} + a_{3p}b_1 c_{3vp} - 2a_{3p}a_1 d_{3vp} - a_{3p}^2 d_{3v} - 2c_{3vp}c_{3p}$$

$$E_1 = a_1 b_{3p}c_{3p} + a_{3p}b_{3p}c_1 + a_{3p}b_1 c_{3p} - 2a_{3p}a_1 d_{3p} - a_{3p}^2 d_1 - c_{3p}^2$$

$$F_1 = a_1 b_{3v}c_{3vp} + a_{3p}b_{3v}c_{3v} - 2c_{3v}c_{3vp}$$

$$G_1 = a_1 b_1 c_{3vp} + a_1 b_{3p}c_{3v} + a_1 b_{3v}c_{3p} + a_{3p}b_{3v}c_1 + a_{3p}b_1 c_{3v} - a_1^2 d_{3vp} - 2a_{3p}a_1 d_{3v} - 2c_1 c_{3vp} - 2c_{3p}c_{3v}$$

$$H_1 = a_1 b_1 c_{3p} + a_1 b_{3p}c_1 + a_{3p}b_1 c_1 - a_1^2 d_{3p} - 2a_{3p}a_1 d_1 - 2c_1 c_{3p}$$

$$J_1 = a_1 b_{3v}c_{3v} - c_{3v}^2$$

$$K_1 = a_1 b_1 c_{3v} + a_1 b_{3v}c_1 - a_1^2 d_{3v} - 2c_1 c_{3v}$$

C.2 Non-linear Routhian for Limit Cycles in p

Equation (2.88) is an equation for limit cycle amplitudes in p. The terms A_2, B_2 and C_2 are defined as:-

$$A_2 = \tfrac{3}{4}a_{3_p}.\tfrac{3}{4}b_{3_p}.\tfrac{3}{4}c_{3_p}$$

$$B_2 = \tfrac{3}{4}a_{3_p}.\tfrac{3}{4}b_{3_p}.c_1+a_1\tfrac{3}{4}b_{3_p}.\tfrac{3}{4}c_{3_p}+\tfrac{3}{4}a_{3_p}.b_1.\tfrac{3}{4}c_{3_p}-\tfrac{3}{4}a_{3_p}.\tfrac{3}{4}d_{3_p}-\tfrac{9}{16}c_{3_p}^2$$

$$C_2 = a_1.\tfrac{3}{4}b_{3_p}.c_1+\tfrac{3}{4}a_{3_p}.b_1.c_1+a_1.b_1.\tfrac{3}{4}c_{3_p}-a_1.\tfrac{3}{4}d_{3_p}-2c_1.\tfrac{3}{4}c_{3_p}$$

C.3 Rate of Growth to Limit Cycles

Sextic equations in local damping factor, λ, as a function of oscillation amplitude, σ_v or σ_p, were given in §2.4.2.6, for non-linear v and non-linear p characteristics. In each case two equations were given, one derived from the "$(\lambda+i\omega)$" form of the stability equation and the other from the "$(3\lambda+i\omega)$" form. The following are definitions of the various 'A' and 'B' terms in the sextic equations in λ.

C.3.1 Non-Linear v

For the "$(\lambda+i\omega)$" form equation, (2.98):

$$A_{4_v} = 48a_1^2 + 32(b_1 + \tfrac{3}{4}b_{3_v}\sigma_v^2)$$

$$A_{3_v} = 8a_1^3 + 32a_1(b_1 + \tfrac{3}{4}b_{3_v}\sigma_v^2)$$

$$A_{2_v} = 4a_1(c_1+\tfrac{3}{4}c_3\sigma_v^2)+4(b_1+\tfrac{3}{4}b_{3_v}\sigma_v^2)^2+8a_1^2(b_1+\tfrac{3}{4}b_{3_v}\sigma_v^2) -16(d_1+\tfrac{3}{4}d_{3_v}\sigma_v^2)$$

$$A_{1_v} = 2a_1^2(c_1+\tfrac{3}{4}c_3\sigma_v^2)+2a_1(b_1+\tfrac{3}{4}b_{3_v}\sigma_v^2)^2-8a_1(d_1+\tfrac{3}{4}d_{3_v}\sigma_v^2)$$

For the "$(3\lambda+i\omega)$" form equation, (2.101):

$$B_{4_v} = 48a_1^2+16(b_1+\tfrac{3}{4}b_{3_v}\sigma_v^2)+32(b_1+\tfrac{9}{4}b_{3_v}\sigma_v^2)-16(b_1+\tfrac{27}{4}b_{3_v}\sigma_v^2)$$

$$B_{3_v} = 8a_1^2+16a_1(b_1+\tfrac{3}{4}b_{3_v}\sigma_v^2)+24a_1(b_1+\tfrac{9}{4}b_{3_v}\sigma_v^2)-8a_1(b_1+\tfrac{27}{4}b_{3_v}\sigma_v^2) +16(c_1+\tfrac{3}{4}c_{3_v}\sigma_v^2)-16(c_1+\tfrac{9}{4}c_{3_v}\sigma_v^2)$$

$$B_{2_v} = 3a_1^2(b_1+\tfrac{3}{4}b_{3_v}\sigma_v^2)+6a_1^2(b_1+\tfrac{9}{4}b_{3_v}\sigma_v^2)-a_1^2(b_1+\tfrac{27}{4}b_{3_v}\sigma_v^2) +12a_1(c_1+\tfrac{3}{4}c_{3_v}\sigma_v^2)-8a_1(c_1+\tfrac{9}{4}c_{3_v}\sigma_v^2)-4(b_1+\tfrac{9}{4}b_{3_v}\sigma_v^2)^2 +8(b_1+\tfrac{3}{4}b_{3_v}\sigma_v^2)(b_1+\tfrac{9}{4}b_{3_v}\sigma_v^2)-16(d_1+\tfrac{3}{4}d_{3_v}\sigma_v^2)$$

$$B_{1v} = 2a_1(b_1+\tfrac{3}{4}b_{3v}\sigma_v^2)(b_1+\tfrac{9}{4}b_{3v}\sigma_v^2)+3a_1^2(c_1+\tfrac{3}{4}c_{3v}\sigma_v^2)$$
$$-a_1^2(c_1+\tfrac{9}{4}c_{3v}\sigma_v^2)+4(b_1+\tfrac{3}{4}b_{3v}\sigma_v^2)(c_1+\tfrac{3}{4}c_{3v}\sigma_v^2)$$
$$-4(b_1+\tfrac{9}{4}b_{3v}\sigma_v^2)(c_1+\tfrac{3}{4}c_{3v}\sigma_v^2)-8a_1(d_1+\tfrac{3}{4}d_{3v}\sigma_v^2)$$

C.3.2 Non-Linear p

The terms in this section can be written more succinctly by introducing the following notation:

$$a^* = a_1 + \tfrac{3}{4}a_{3p}\sigma_p^2$$

$$a^{**} = a_1 + \tfrac{9}{4}a_{3p}\sigma_p^2$$

$$a^{***} = a_1 + \tfrac{27}{4}a_{3p}\sigma_p^2$$

and similarly for b, c and d terms. Then for the "$(\lambda+i\omega)$" form equation, (2.104):

$$A_{4p} = 48a^* + 32b^*$$

$$A_{3p} = 8(a^*)^3 + 32(a^*)(b^*)$$

$$A_{2p} = 8(a^*)^2(b^*) + 4a^*c^* + 4(b^*)^2 - 16d^*$$

$$A_{1p} = 2a^*(b^*)^2 + 2(a^*)^2(c^*) - 8a^*d^*$$

For the "$(3\lambda+i\omega)$" form equation, (2.107):

$$B_{5p} = 32(a^{***}) + 48a^{**} + 16a^*$$

$$B_{4p} = -(a^*)^2-9(a^{***})^2+10a^*a^{***}+12a^*a^{**}+36a^{**}a^{***}+16b^*$$
$$+32b^{**}-16b^{***}$$

$$B_{3p} = -(a^*)^2(a^{***})+9(a^*)(a^{**})(a^{***})+4(a^*)(b^*)+12a^*b^{**}$$
$$+24a^{**}b^{**}-8a^*b^{***}-12a^{***}b^{**}+12a^{***}b^*+16c^*-16c^{**}$$

$$B_{2p} = 6a^*a^{**}b^{**}+3a^*a^{***}b^*-(a^*)^2b^{***}-6a^{***}c^*+12a^{**}c^*+6a^*c^*$$
$$-8a^*c^{**}-4(b^{**})^2+8b^*b^{**}-16d^*$$

$$B_{1p} = 2a^*b^*b^{**}+3a^*a^{**}c^*-(a^*)^2c^{**}+4b^*c^*-4b^{**}c^*-8a^*d^*$$

APPENDIX D

ESTIMATION OF LATERAL DYNAMIC STABILITY DERIVATIVES

D.1 Introduction

This Appendix gives details of the estimates made of $\check{L}_p$, $\check{N}_p$, $\check{L}_r$ and $\check{N}_r$ for the HIRM, using semi-empirical methods, mainly those of ESDU and DATCOM (Refs.92,93).

Most of the preliminary data used in the calculations is given in Table 4.1 but, where required, other data is introduced in this Appendix. Standard symbols are as defined for the main part of the thesis, but some new symbols are introduced in connection with specific ESDU or DATCOM items. These symbols are as defined in the items concerned and the references given should be consulted for exact definitions. All initial calculations were carried out for M = 0, low α flight conditions and corrections were then made to allow for effects of flow separation at high α.

D.2 Rolling Moment due to Rate of Roll, $\check{L}_p$

D.2.1 Wing Contribution

Ref.92, Item A.06.01.01 gave plots of $-\beta\ell_p/\kappa$ as a function of $\beta A/\kappa$, λ and Λ_E where ℓp is rolling moment due to roll rate, in the notation of Ref.121 and :

β = 1,

κ = $\dfrac{\beta(a_{1_0})_M}{2\pi}$

λ = taper ratio, and

Λ_E = equivalent sweepback, $\dfrac{\tan\Lambda_{\frac{1}{4}}}{\beta}$

Also $\Lambda_{\frac{1}{4}}$ = 36.6^o, $(a_{1_0})_M$ = 3.37 rad^{-1} (from ESDU Item 70011)

So κ = 0.536, $\dfrac{\beta A}{\kappa}$ = 6.152

Giving ℓ_p = -0.193

or $(\check{L}_p)_w$ = -0.097

Ref.93, Section 7.3.2.2-4 gave $(\check{L}_p)_w$ = -0.109

D.2.2 Canard Contribution

Using the same method as for the wing, ESDU Item A.06.01.01 gave an estimate of $(\check{L}_p)_C$ as

$$(\check{L}_p)_C = -0.071$$

while DATCOM, Part 7.3.2.2-4 gave

$$(\check{L}_p)_C = -0.095$$

These estimates were based on canard wing area and were factored, for addition to the wing contribution, to take into account the relative sizes of the wing and canard.

D.2.3 Tailplane Contribution

Again, ESDU Item A.06.01.01 was used, and $(\check{L}_p)_T$, based on tailplane area, was estimated at -0.100 compared to -0.110 from DATCOM Part 7.3.2.2-4.

D.2.4 Fin Contribution

Regarding the fin as half a wing, ESDU Item A.06.01.01 was used to calculate $(\check{L}_p)_F$, by halving the estimate for the fin plus its "image". The estimate was -0.051, compared to -0.058 from DATCOM.

D.2.5 Total $\check{L}_p$

The canard, tailplane and fin contributions were factored by[122]

$$K\left(\frac{S_*}{S}\right)\left(\frac{b_*}{b}\right) \qquad (D.1)$$

where K = 0.5, to account for induced velocity effects, and S_*, b_* are the appropriate surface area and span respectively. Using this factor on the fin, tailplane and canard contributions, and summing with the wing contribution, gave:

$$\check{L}_p = -0.104 \quad \text{(ESDU)}$$

and $$\check{L}_p = -0.117 \quad \text{(DATCOM)}.$$

The value of $\check{L}_p$ at higher α was estimated, to a first approximation, by

$$(\check{L}_p)_{C_L} = (\check{L}_p)_{C_L=0} \frac{(C_{L_\alpha})_{C_L}}{(C_{L_\alpha})_{C_L=0}} \qquad (D.2)$$

where C_{L_α} is the lift curve slope from wind tunnel experiments (11½ft x 8ft static W.T.tests on HIRM 1). Results for HIRM configuration C were shown in Fig.4.8a, where estimated

$\check{L}_p$ has been combined with estimated $\check{L}_{\dot{v}}\sin\alpha$ to give $\check{L}_p+\check{L}_{\dot{v}}\sin\alpha$. The estimation of $\check{L}_{\dot{v}}$ is described in §D.6.

D.3 Yawing Moment due to Rate of Roll, $\check{N}_p$

D.3.1 Wing Contribution

No ESDU data was available at the time of the calculations, so DATCOM was used. Using the HIRM data given, DATCOM section 7.3.2.3 gave an estimate for $\check{N}_p/C_L$ of -0.102.

A correction for separation effects at higher C_L was applied, using equation (4.1).

$$\check{N}_p = K\left(\frac{\check{N}_p}{C_L}\right)C_L \qquad (D.3)$$

$$\text{where } K = \frac{\frac{\partial}{\partial\alpha}(C_L\tan\alpha) - \frac{\partial}{\partial\alpha}(C_D - C_{D_o})}{\frac{\partial}{\partial\alpha}(C_L\tan\alpha) - \frac{\partial}{\partial\alpha}(C_L^2/\pi A)} \qquad (D.4)$$

Again,HIRM 1 static wind tunnel data was used to calculate K.

D.3.2 Fin Contribution

This was estimated using the relationship

$$(\check{N}_p)_F = -\frac{x_F}{b}\cdot\frac{z_F}{b}\cdot(\check{Y}_v)_F \qquad (D.5)$$

where x_F is the fin arm and z_F is the height of the fin centre of pressure above the fin root chord (c.f. Ross et al, Ref.17). $(\check{Y}_v)_F$ was estimated as -0.534 using the formula

$$\frac{(\check{Y}_v)_F}{2} = (y_v)_F = -\tfrac{1}{2}\left(\frac{dC_L}{d\alpha}\right)_F\cdot\frac{S_F}{S} \qquad (D.6)$$

given in Ref.94, with $\left(\frac{dC_L}{d\alpha}\right)_F$ = 4.66 rad^{-1} from ESDU Item Controls 01.01.05.

The estimate of $(\check{N}_p)_F$ was +0.017.

D.3.3 Total $\check{N}_p$

Wing and fin contributions were combined to give an estimate of total $\check{N}_p$. Fig.4.8b showed the results in the form of the combined derivative,

$$\check{N}_p + \check{N}_{\dot{v}}\sin\alpha.$$

$\check{N}_{\dot{v}}$ was estimated as mainly coming from the fin, being due to the change of sidewash over the fin with sideslip (§D.6).

D.4 Rolling Moment due to Rate of Yaw, $\check{L}_r$

D.4.1 Wing Contribution

DATCOM section 7.1.3.2 gave a method for calculating $(\check{L}_r)_W$ for the linear range of C_L, including effects of dihedral. For the HIRM, DATCOM gave

$$(\check{L}_r)_W = 0.145C_L - 0.0028$$

the second term on the right hand side arising from the dihedral contribution.

ESDU Item 72021 also provided a means of estimating contributions to $(\check{L}_r)_W$ from planform, dihedral and twist. For $\Lambda_{\frac{1}{4}} = 37^o$, Fig.1b of this item gave the value of a sweep factor, $g(\Lambda_{\frac{1}{4}})$, as 1.65 and Fig.1a gave

$$\frac{1}{g(\Lambda_{\frac{1}{4}})} \cdot \frac{(\check{L}_{r_o})_p}{C_L} = 0.0932$$

So $$\frac{(\check{L}_{r_o})_p}{C_L} = 0.153$$

Fig.3 gave $(\check{L}_r)_\Gamma = -0.0054$, so

$$(\check{L}_r)_W = 0.153C_L - 0.0054$$

Experimentally determined values of $\check{L}_v$ were used to 'correct' $(\check{L}_r)_W$ for effects of flow separation at high angles of attack using the formula

$$(\check{L}_r)_W = C_L\{(\frac{\check{L}_r}{C_L}) + (\frac{\check{L}_v}{C_L})\}_{theory} - \check{L}_{v_{experiment}} \quad (D.7)$$

ESDU Item A.06.01.04 gave an estimate of $(\check{L}_v/C_L)_{theory}$ as -0.263 so the final formula used to estimate $(\check{L}_r)_W$ as a function of α was (using the ESDU low-α estimate):

$$(\check{L}_r)_W = C_L(-0.11) - \check{L}_{v_{expt.}} - 0.0054$$

D.4.2 Fin Contribution

This was estimated using ESDU Item 70006 there being no suitable DATCOM data available.

$$(\check{L}_r)_F = (\frac{\partial C_Y}{\partial \beta})_F . K . (\frac{S_F . x_F^2}{Sb^2}) \quad (D.8)$$

where $K = \frac{h_F}{x_F} = 0.436$

with h_F = fin centre of pressure position above fuselage datum

and $(\frac{\partial C_Y}{\partial \beta})_F = (\frac{\partial C_L}{\partial \alpha})_F = 4.66\ rad^{-1}$ from ESDU Item Controls 01.01.05.

$(\check{L}_r)_F$ was estimated at 0.036

D.4.3 Total $\check{L}_r$

The wing and fin contributions were combined to give an estimate of total $\check{L}_r$. Adding the $\check{L}_{\dot{v}}$ contribution, using $\check{L}_{\dot{v}}$ derived as described in §D.6, gave the combined derivative

$$\check{L}_r^* = \check{L}_r - \check{L}_{\dot{v}}\cos\alpha$$

which was compared directly with oscillatory rig results in Fig.4.8c.

D.5. Yawing Moment due to Yaw Rate, $\check{N}_r$

D.5.1 Wing Contribution

ESDU Item 71017 and DATCOM Section 7.1.3.3 were both used to estimate this, relatively small, contribution to $\check{N}_r$. Both of these sources gave similar formulae, the ESDU version being (for attached flow conditions):

$$(\check{N}_r)_W = (\frac{\check{N}_r}{C_L^2})C_L^2 + (\frac{\check{N}_{r_o}}{C_{D_o}})C_{D_o} \qquad (D.9)$$

The contributions to $(\check{N}_r)_W$ shown in this formula arise from the asymmetric distributions of lift-dependent drag (due to the trailing vortex system) and profile drag. Figures in the ESDU Item gave $(\check{N}_r/C_L^2)$ and $(\check{N}_{r_o}/C_{D_o})$ as functions of λ and for the HIRM, $(\check{N}_r)_W$ was given by

$$(\check{N}_r)_W = -0.169C_{D_o} - 0.012C_L^2.$$

No effects of wing flow separation at high α were allowed for in $(\check{N}_r)_W$, due to the small size of this contribution to $\check{N}_r$, compared to $(\check{N}_r)_F$ and $(\check{N}_r)_B$.

D.5.2 Fin Contribution

ESDU Item A.07.01.00 gave

$$(\check{N}_r)_F = -(\frac{\partial C_Y}{\partial \beta})_F . (\frac{S_F x_F^2}{Sb^2}) \qquad (D.10)$$

which, for the HIRM, resulted in:

$$(\check{N}_r)_F = -0.083$$

D.5.3 Body Contribution

The large, flat-sided fuselage for the HIRM means $(\check{N}_r)_B$ can make a significant contribution to $\check{N}_r$, but information on $(\check{N}_r)_B$ is scarce. Sacks[95] gave formulae for $(\check{N}_r)_B$ based on slender body theory and adapting this for the HIRM gave

$$(\check{N}_r)_B = -0.089$$

D.5.4 Total $\check{N}_r$

Summing the contributions from fin, body and wing gave the required total $\check{N}_r$. For comparison with oscillatory rig results, the term $-\check{N}_{\dot{v}}\cos\alpha$, was added to the pure $\check{N}_r$ estimates and results were shown in Fig.4.8d.

D.6 Rolling and Yawing Moments due to Rate of Change of Sideslip, $\check{L}_{\dot{v}}$, $\check{N}_{\dot{v}}$

Wing contributions to these derivatives were not estimated due to the absence of any theoretical or empirical methods and so only the fin contributions were estimated.

The effective sideslip at the fin is considered to be[17]

$$\beta + \frac{d\sigma}{d\beta}(\beta - \beta\Delta t) \qquad (D.11)$$

where $\sigma(\alpha)$ is the sidewash induced by the wing and Δt is the time lag for it to reach the fin. Thus the fin contributions, to derivatives due to sideslip, are modified by $(1 + d\sigma/d\beta)$, e.g.

$$(\check{Y}_v)_F = (\check{Y}_v)_{F,\alpha=0} + \frac{d\sigma}{d\beta}.(\check{Y}_v)_{F,\alpha=0} \qquad (D.12)$$

Static wind tunnel test results for HIRM 1, with fin on and off, gave estimates of $(\check{Y}_v)_F$ as a function of α, which in turn gave $d\sigma/d\beta$.

A correction for reduction in wing wake total pressure can be applied to the sidewash factor, $d\sigma/d\beta$, but for the HIRM estimates, the values obtained straight from equation (D.12) were used to estimate $\check{L}_{\dot{v}}$ and $\check{N}_{\dot{v}}$.

The required derivatives were obtained, using the estimates of $(\check{L}_r)_F$ amd $(\check{N}_r)_F$ from §D.4.2. and §D.5.2. respectively (see Ref.17):

$$(\check{L}_{\dot{v}})_F = \frac{d\sigma}{d\beta} \cdot (\check{L}_r)_F \qquad (D.13)$$

$$(\check{N}_{\dot{v}})_F = \frac{d\sigma}{d\beta} \cdot (\check{N}_r)_F \qquad (D.14)$$

APPENDIX E

LINEARISED 6 DEGREE OF FREEDOM EQUATIONS

Starting with the classical equations of motion, equations (2.1) to (2.9), linearisation about an arbitrary equilibrium point, by restricting the motion to infinitesimal disturbances, from the reference state, results in the following equations:-

$$m[\dot{u}+w_e q+q_e w-v_e r-r_e v+g_1\Theta'] = dX \qquad (E.1)$$

$$m[\dot{v}+u_e r+r_e u-w_e p-p_e w-g_3\Phi'+g_6\Theta'] = dY \qquad (E.2)$$

$$m[\dot{w}+v_e p+p_e v-u_e q-q_e u+g_5\Phi'+g_4\Theta'] = dZ \qquad (E.3)$$

$$\dot{p}I_x-\dot{r}I_{xz}+(q_e r+r_e q)(I_z-I_y)-(p_e q-q_e p)I_{xz} = dL \qquad (E.4)$$

$$\dot{q}I_y+(p_e r+r_e p)(I_x-I_z)-(2r_e r-2p_e p)I_{xz} = dM \qquad (E.5)$$

$$\dot{r}I_z-\dot{p}I_{xz}+(p_e q+q_e p)(I_y-I_x)+(q_e r+r_e q) = dN \qquad (E.6)$$

I_{xy} and I_{yz} have been assumed to be zero. Unsubscripted response variables on the left hand sides are now small perturbation quantities, as are Φ', Θ' which are Euler perturbation angles (rotations from a horizontal reference condition). The variables resulting from the linearisation are:

$$[u,w,q,\Theta,v,p,r,\Phi]$$

Equations (E.4) and (E.6) may be re-written in the following way, after substitution to tidy up the product of inertia terms:

$$\dot{p} = \frac{dL}{I_x'}+dNI_{xz}'+(p_e q+q_e p)\left(\frac{I_{xz}}{I_x'}-(I_y-I_x)I_{xz}'\right)$$

$$-(q_e r+r_e q)\left(\left(\frac{I_z-I_y}{I_x'}\right)+I_{xz}I_{xz}'\right) \qquad (E.7)$$

$$\dot{r} = \frac{dN}{I_z'}+dLI_{xz}'-(p_e q+q_e p)\left(\left(\frac{I_y-I_x}{I_z'}\right)-I_{xz}I_{xz}'\right)$$

$$-(q_e r+r_e q)\left(\frac{I_{xz}}{I_z'}+(I_z-I_y)I_{xz}'\right) \qquad (E.8)$$

where I_x', I_z' and I_{xz}' are defined as:

$$\frac{1}{I_x'} = \frac{I_z}{I_x I_z - I_{xz}^2}$$

$$\frac{1}{I_z'} = \frac{I_x}{I_x I_z - I_{xz}^2}$$

$$I_{xz}' = \frac{I_{xz}}{I_x I_z - I_{xz}^2}$$

It is convenient to introduce some special notation for the inertia terms in the equations for $\dot{p}$ and $\dot{r}$:-

$$b_z' = \frac{(I_y - I_x)}{I_z'} - I_{xz} I_{xz}'$$

$$e_z' = \frac{I_{xz}}{I_z'} + (I_z - I_y) I_{xz}'$$

$$e_x' = \frac{I_{xz}}{I_x'} - (I_y - I_x) I_{xz}'$$

$$b_x' = \frac{(I_z - I_y)}{I_x'} - I_{xz}' I_{xz}$$

The remaining moment equation, (E.5) and the force equations (E.1) to (E.3) can be put into the same form as equations (E.7) and (E.8), with acceleration terms on the left hand side. First of all, consider equation (E.1):

$$\dot{u} = \frac{dX}{m} - w_e q - q_e w + v_e r + r_e v - g_1 \Theta' \qquad \text{(E.9)}$$

The forces and moments for the longitudinal equations will be expanded in terms of $[u, w, q, v, p, r]$, but for the pitching moment and Z equation, $\dot{w}$ derivatives cannot be ignored. Taking $M_{\dot{w}}\dot{w}$ out of dM, in equation (E.5), gives:

$$\dot{q} = \frac{dM}{I_y} + \frac{M_{\dot{w}}}{I_y}\dot{w} - (p_e r + r_e p)\left(\frac{I_x - I_y}{I_y}\right) + (2 r_e r - 2 p_e p)\left(\frac{I_{xz}}{I_y}\right) \qquad \text{(E.10)}$$

Similarly, taking $Z_{\dot{w}}\dot{w}$ out of the dZ term in equation (E.3), gives:

$$\dot{w} = \frac{dZ}{m - Z_{\dot{w}}} - \frac{m v_e p}{m - Z_{\dot{w}}} - \frac{m p_e v}{m - Z_{\dot{w}}} + \frac{m u_e q}{m - Z_{\dot{w}}} + \frac{m q_e}{m - Z_{\dot{w}}} u - \frac{m g_5}{m - Z_{\dot{w}}} \Phi' - \frac{m g_4}{m - Z_{\dot{w}}} \Theta' \qquad \text{(E.11)}$$

This can be substituted into (E.10) to give an equation for $\dot{q}$ without other acceleration terms.

Equation (E.2) becomes

$$\dot{v} = \frac{dY}{m} - u_e r - r_e u + w_e p + p_e w + g_3 \Phi' - g_6 \Theta' \qquad (E.12)$$

Now the forces and moments may be expanded in terms of derivatives with respect to $[u,w,q,v,p,r]$, for the longitudinal forces and moments ($M_{\dot{w}}$ and $Z_{\dot{w}}$ already having been accounted for and $X_{\dot{w}}$ being ignored), and $[u,w,q,v,p,r,\dot{v}]$, for dY, dL and dN. Thus

$$dX = X_u u + X_w w + X_q q + X_v v + X_p p + X_r r \qquad (E.13)$$

$$dM = M_u u + M_w w + M_q q + M_v v + M_p p + M_r r \qquad (E.14)$$

$$dZ = Z_u u + Z_w w + Z_q q + Z_v v + Z_p p + Z_r r \qquad (E.15)$$

$$dY = Y_u u + Y_w w + Y_q q + Y_v v + Y_p p + Y_r r + Y_{\dot{v}} \dot{v} \qquad (E.16)$$

$$dL = L_u u + L_w w + L_q q + L_v v + L_p p + L_r r + L_{\dot{v}} \dot{v} \qquad (E.17)$$

$$dN = N_u u + N_w w + N_q q + N_v v + N_p p + N_r r + N_{\dot{v}} \dot{v} \qquad (E.18)$$

Taking equation (E.12) as an example, it becomes, after substituting for dY:-

$$\dot{v} = y''_u u + y''_w w + y''_q q - g_6 \left(\frac{m}{m - Y_{\dot{v}}}\right)\Theta' + y''_v v + y''_p p + y''_r r + g_3 \left(\frac{m}{m - Y_{\dot{v}}}\right)\Phi' \qquad (E.19)$$

where " now indicates a form of concise derivative, containing acceleration derivatives and other mass, inertia and equilibrium rate terms, e.g.

$$y''_u = \left(\frac{m}{m - Y_{\dot{v}}}\right)\left(\frac{Y_u}{m} - r_e\right)$$

A single dash, for a derivative, is used to denote a conventional concise derivative, with natural sign, for force derivatives and pitching moment derivatives:-

$$x'_u = \frac{X_u}{m}, \quad x'_p = \frac{X_p}{m},$$

For rolling and yawing moment derivatives, a dash denotes a concise derivative with product of inertia contributions, e.g.

$$\ell'_{\dot{v}} = \frac{I_z L_{\dot{v}} + I_{xz} N_{\dot{v}}}{I_x I_z - I_{xz}^2}$$

(see Appendix A.3).

Apart from the six force and moment equations, two further small perturbation equations are required,for the kinematic relations involving Φ' and Θ'.

For $\dot{\Theta}$, the full equation is (see equation (2.8)):

$$\dot{\Theta} = q\cos\Phi - r\sin\Phi$$

Substituting q_e+q', $\Phi_e+\Phi'$, $r_e + r'$ and $\dot{\Theta}_e + \Theta'$ as perturbed states, the equation becomes:-

$$\dot{\Theta}_e+\dot{\Theta}' = q_e\cos\Phi_e - q_e\Phi'\cos\Phi_e + q'\cos\Phi_e - q'\Phi'\sin\Phi_e$$
$$- r_e\sin\Phi_e - r_e\Phi'\cos\Phi_e - r'\sin\Phi_e - r'\Phi'\cos\Phi_e$$

Neglecting terms containing products of perturbations, and subtracting the equilibrium condition, gives the required perturbation equation;-

$$\dot{\Theta} = \cos\Phi_e q' - \sin\Phi_e r' + \Phi'(-q_e\sin\Phi_e - r_e\cos\Phi_e) \quad \text{(E.20)}$$

Similarly the equation for $\dot{\Phi}$,

$$\dot{\Phi} = p + q\sin\Phi\tan\Theta + r\cos\Phi\tan\Theta,$$

becomes, in small perturbation form:-

$$\dot{\Phi}' = p' + q'\sin\Phi_e\tan\Theta_e + \Theta'\frac{(q_e\sin\Phi_e + r_e\cos\Phi_e)}{\cos^2\Theta_e}$$
$$+ r'\cos\Phi_e\tan\Theta_e + \Phi'\tan\Theta_e(q_e\cos\Phi_e - r_e\sin\Phi_e) \quad \text{(E.21)}$$

The final form of the linearised 6 degree of freedom equations is shown in Fig.6.1 and the full expressions, for the terms in the system matrix, are shown in Tables E.1 to E.4. Tables E.1 and E.2 show the longitudinal and lateral subsystem terms, while Tables E.3 and E.4 show the cross-coupling terms.

When using these expressions for the HIRM analysis, some derivative values were not available, so these derivatives were simply omitted from the equations, resulting in some simplification of the system matrix. The simplified expressions, for the terms in the system matrix, are also shown in the Tables (third columns). In these terms, p_e, r_e q_e, Φ_e and $Y_{\dot{v}}$ have been set to zero, and $M_{\dot{w}}$, $Z_{\dot{w}}$, $L_{\dot{v}}$ and $N_{\dot{v}}$ are only included where measured, in combined derivatives, on the RAE oscillatory rig. Measurements of pure acceleration derivatives were not made. The terms in the third columns of Tables E.1 to E.4 show the derivatives in'R&M 3562' (Ref.45) form, as used for input to the program EIGEN.

APPENDIX F

DERIVATIVES OF FORCES AND MOMENTS IN TERMS OF AERODYNAMIC COEFFICIENTS

F.1 Preliminary Results

Fig.F.1 defines various angles and velocity components,from which the following relations are derived:-

$$\cos\sigma = \frac{u}{V} \qquad (F.1)$$

$$\cos\beta.\cos\alpha = \frac{u}{V} \qquad (F.2)$$

$$\sin\beta = \frac{v}{V} \qquad (F.3)$$

Conventional definitions for α and β will be used in this section as shown in Fig.F.1, i.e. α_t and β_s, rather than angle of downslip, α_s, and flank angle of attack, β_t, as used in Ref.45.

From the relationships:

$$\cos\alpha = \frac{u}{s} \; ; \; \cos\beta = \frac{s}{V} \; ; \; \sin\alpha = \frac{w}{s}$$

it can be seen that

$$\cos\alpha.\cos\beta = \frac{u}{V}$$

and $$\sin\alpha.\cos\beta = \frac{w}{V} \cdot$$

F.2 Derivatives of V

These are required in §F.3.

$$\frac{\partial V}{\partial u} = \frac{\partial(u^2+v^2+w^2)^{\frac{1}{2}}}{\partial u} = \tfrac{1}{2}(u^2+v^2+w^2)^{-\frac{1}{2}}\ 2u$$

$$= \frac{u}{V} = \cos\beta.\cos\alpha \quad \text{using (F.2)}$$

$$\frac{\partial V}{\partial u} = \cos\alpha\cos\beta \qquad \text{(F.4)}$$

$$\frac{\partial V}{\partial v} = \tfrac{1}{2}(u^2+v^2+w^2)^{-\frac{1}{2}}2v = \frac{v}{V}$$

$$\frac{\partial V}{\partial v} = \sin\beta \qquad \text{(F.5)}$$

$$\frac{\partial V}{\partial w} = \tfrac{1}{2}(u^2+v^2+w^2)^{-\frac{1}{2}}2w = \frac{w}{V} = \sin\alpha\cos\beta$$

$$\frac{\partial V}{\partial w} = \sin\alpha\cos\beta \qquad \text{(F.6)}$$

F.3 Derivatives of α,β with Respect to u,v,w

These derivatives arise in the calculation of aerodynamic derivatives. No small angle approximations are used.

F.3.1 Derivatives of α

$$\tan\alpha = \frac{w}{u}$$

$$\alpha = \tan^{-1}\frac{w}{u}$$

$$\frac{d\alpha}{du} = \frac{1}{1+(\frac{w}{u})^2}\cdot\frac{d}{du}(\frac{w}{u})$$

$$= \frac{1}{1+(\frac{w}{u})^2}\cdot(-\frac{w}{u^2})$$

$$\frac{d\alpha}{du} = -\frac{1}{u}\sin\alpha\cos\alpha \qquad \text{(F.7)}$$

$$\frac{d\alpha}{dw} = \frac{\cos^2\alpha}{u} \qquad \text{(F.8)}$$

N.B. $\frac{d\alpha}{dv} = 0$

F.3.2 Derivatives of β

$$\sin\beta = \frac{v}{V}$$

$$\beta = \sin^{-1}\frac{v}{V} = \sin^{-1}\frac{V}{\sqrt{(u^2+v^2+w^2)}}$$

$$\frac{d\beta}{du} = \frac{1}{\sqrt{(1-\sin^2\beta)}} \cdot \frac{-\frac{1}{2}(u^2+v^2+w^2)^{-\frac{1}{2}}2uv}{u^2+v^2+w^2}$$

$$\frac{d\beta}{du} = \frac{1}{\cos\beta} \cdot \frac{-vu}{V^3} = -\frac{u}{V^2}\tan\beta \qquad \text{(F.9)}$$

Similarly,

$$\frac{d\beta}{dw} = -\frac{w}{V^2}\tan\beta \qquad \text{(F.10)}$$

$\beta = f(v)$ so $\frac{d\beta}{dv}$ can be calculated as follows:

$$\frac{d\beta}{dv} = \frac{1}{\cos\beta} \cdot \frac{V-(v^2/V)}{V^2} = \frac{1}{\cos\beta}\frac{1}{V}(1-\frac{v^2}{V^2})$$

$$\frac{d\beta}{dv} = \frac{\cos\beta}{V} \qquad \text{(F.11)}$$

F.4 Evaluation of Derivatives with respect to u,v,w for X,Z,M,Y,L,N

F.4.1 General

Following the notation of Ref.45, γ is used to indicate non-dimensional p,q and r:

$$p_\gamma = \frac{pb}{V} \; ; \quad q_\gamma = \frac{q\bar{\bar{c}}}{V} \; ; \quad r_\gamma = \frac{rb}{V}$$

with b used as the representative length for lateral quantities and $\bar{\bar{c}}$ for longitudinal quantities.

To allow for the effect of p,q and r in the derivatives, as well as α and β, a general force, K, will be assumed to be given by:-

$$K = K(\alpha,\beta,p_\gamma,q_\gamma,r_\gamma)$$

where K = X,Y,Z. A general moment, J, where J = L,M or N, will similarly be assumed to be given by:

$$J = J(\alpha,\beta,p_\gamma,q_\gamma,r_\gamma)$$

Thus, datum conditions for derivatives can have $p_\gamma \neq q_\gamma \neq r_\gamma \neq 0$, although $\dot{\alpha} = \dot{\beta} = 0$. Using ω to represent u,v,or w, then for a force, K:

$$K = \tfrac{1}{2}\rho V^2 S C_K$$

and for a moment, J:

$$J = \tfrac{1}{2}\rho V^2 S \ell_o C_j$$

Then $$K_\omega = \left(\frac{\partial K}{\partial \omega}\right)_e = \left(\tfrac{1}{2}\rho_e S C_K . 2V . \frac{\partial V}{\partial \omega}\right)_e + \tfrac{1}{2}\rho_e V_e^2 S . \sum_\gamma \left(\frac{\partial C_K}{\partial \gamma} . \frac{\partial \gamma}{\partial \omega}\right)_e$$

$$\breve{K}_\omega = \frac{K_\omega}{\tfrac{1}{2}\rho V S} = \left(2C_K . \frac{\partial V}{\partial \omega}\right)_e + V_e \sum_\gamma \left(\frac{\partial C_K}{\partial \gamma} . \frac{\partial \gamma}{\partial \omega}\right)_e \qquad \text{(F.12)}$$

For a moment derivative:

$$J_\omega = \left(\frac{\partial J}{\partial \omega}\right)_e = \left(\tfrac{1}{2}\rho S \ell_o C_j 2V . \frac{\partial V}{\partial \omega}\right)_e + \tfrac{1}{2}\rho_e V_e^2 S \ell_o \sum_\gamma \left(\frac{\partial C_j}{\partial \gamma} . \frac{\partial \gamma}{\partial \omega}\right)_e$$

$$\breve{J}_\omega = \frac{J_\omega}{\tfrac{1}{2}\rho V S \ell_o} = \left(2C_j \frac{\partial V}{\partial \omega}\right)_e + V_e \sum_\gamma \left(\frac{\partial C_j}{\partial \gamma} . \frac{\partial \gamma}{\partial \omega}\right)_e \qquad \text{(F.13)}$$

F.4.2 Evaluation of $\frac{\partial p_\gamma}{\partial \omega}$, $\frac{\partial q_\gamma}{\partial \omega}$, $\frac{\partial r_\gamma}{\partial \omega}$

F.4.2.1 Derivatives with respect to u

$$\frac{\partial p_\gamma}{\partial u} = \frac{\partial\left(\frac{pb}{\sqrt{(u^2+v^2+w^2)}}\right)}{\partial u} = \frac{-pb\ \tfrac{1}{2}(u^2+v^2+w^2)^{-\frac{1}{2}} . 2u}{u^2+v^2+w^2}$$

$$= \frac{-pb}{V} . \frac{u}{V^2} = -p_\gamma \frac{u}{V^2} = -p_\gamma \frac{\cos\alpha\cos\beta}{V}$$

Similarly for $\frac{\partial q_\gamma}{\partial u}$, $\frac{\partial r_\gamma}{\partial u}$:

$$\frac{\partial q_\gamma}{\partial u} = -\frac{q\bar{\bar{c}}}{V} . \frac{u}{V^2} = -q_\gamma . \frac{u}{V^2} = -q_\gamma \frac{\cos\alpha\cos\beta}{V}$$

$$\frac{\partial r_\gamma}{\partial u} = -\frac{rb}{V} . \frac{u}{V^2} = -r_\gamma . \frac{u}{V^2} = -r_\gamma \frac{\cos\alpha\cos\beta}{V}$$

F.4.2.2. Derivatives with respect to v

$$\frac{\partial p_\gamma}{\partial v} = \frac{\partial\left(\frac{pb}{\sqrt{(u^2+v^2+w^2)}}\right)}{\partial v} = \frac{-pb\ \tfrac{1}{2}(u^2+v^2+w^2)^{-\frac{1}{2}} . 2v}{u^2+v^2+w^2}$$

$$= -\frac{pb}{V} . \frac{v}{V^2} = -p_\gamma \frac{\sin\beta}{V^2}$$

Similarly:

$$\frac{\partial q_\gamma}{\partial v} = -q_\gamma \frac{\sin\beta}{V}$$

$$\frac{\partial r_\gamma}{\partial v} = -r_\gamma \frac{\sin\beta}{V}$$

F.4.2.3 Derivatives with respect to w

$$\frac{\partial p_\gamma}{\partial w} = \frac{\partial\left(\frac{pb}{\sqrt{(u^2+v^2+w^2)}}\right)}{\partial w} = \frac{-pb\ \frac{1}{2}(u^2+v^2+w^2)^{-\frac{1}{2}}.2w}{u^2+v^2+w^2}$$

$$= -\frac{pb}{V}\cdot\frac{w}{V^2} = -p_\gamma \frac{\sin\alpha\cos\beta}{V}$$

Similarly:

$$\frac{\partial q_\gamma}{\partial w} = -q_\gamma \frac{\sin\alpha\cos\beta}{V}$$

$$\frac{\partial r_\gamma}{\partial w} = -r_\gamma \frac{\sin\alpha\cos\beta}{V}$$

F.4.3 Force Derivatives with respect to u

Consider $\breve{X}_u$ as an example:-

$$\breve{X}_u = \left(2C_X.\frac{\partial V}{\partial u}\right)_e + V_e\left(\frac{\partial C_X}{\partial \alpha}.\frac{\partial \alpha}{\partial u} + \frac{\partial C_X}{\partial \beta}.\frac{\partial \beta}{\partial u} + \frac{\partial C_X}{\partial p_\gamma}.\frac{\partial p_\gamma}{\partial u} + \frac{\partial C_X}{\partial q_\gamma}.\frac{\partial q_\gamma}{\partial u} + \frac{\partial C_X}{\partial r_\gamma}.\frac{\partial r_\gamma}{\partial u}\right)_e$$

$$= \left(2C_X\cos\alpha\cos\beta\right)_e + V_e\left(C_{X_\alpha}.\frac{-1}{u}\sin\alpha\cos\alpha + C_{X_\beta}.\frac{-u}{V^2}\tan\beta\right.$$

$$\left. + C_{Xp}\left(-p_\gamma\frac{\cos\alpha\cos\beta}{V}\right) + C_{Xq}\left(-q_\gamma\frac{\cos\alpha\cos\beta}{V}\right) + C_{Xr}\left(-r_\gamma\frac{\cos\alpha\cos\beta}{V}\right)\right)_e$$

where now C_{Xp}, C_{Xq} and C_{Xr} are as defined by Hopkin, Ref.45, Pt.4,p.12 and are the same as 'R&M 3562' derivatives with a dip $\breve{}$:

i.e. $\frac{1}{2}C_{X_p} = \breve{X}_p = C_{Xp}$

$\frac{1}{2}C_{X_q} = \breve{X}_q = C_{Xq}$

$\frac{1}{2}C_{X_r} = \breve{X}_r = C_{Xr}$

So

$$\breve{X}_u = (2C_X\cos\alpha\cos\beta)_e - (C_{X_\alpha}\frac{V}{u}\sin\alpha\cos\alpha + C_{X_\beta}\frac{u}{V}\tan\beta)_e$$

$$-(\breve{X}_p.\frac{pb}{V} + \breve{X}_q.\frac{q\bar{\bar{c}}}{V} + \breve{X}_r.\frac{rb}{V})_e\cos\alpha_e\cos\beta_e$$

$$\breve{X}_u = (2C_X\cos\alpha\cos\beta)_e - (C_{X_\alpha}.\frac{\sin\alpha\cos\alpha}{\cos\alpha\cos\beta} + C_{X_\beta}\cos\alpha\cos\alpha.\frac{\sin\beta}{\cos\beta})_e$$

$$-(\breve{X}_p.\frac{pb}{V} + \breve{X}_q.\frac{q\bar{\bar{c}}}{V} + \breve{X}_r.\frac{rb}{V})_e\cos\alpha_e\cos\beta_e$$

$$\breve{X}_u = (2C_X)_e\cos\alpha_e\cos\beta_e - (C_{X_\alpha}\sin\alpha\sec\beta + C_{X_\beta}\cos\alpha\sin\beta)_e$$

$$-(\breve{X}_p.\frac{pb}{V} + \breve{X}_q.\frac{q\bar{\bar{c}}}{V} + \breve{X}_r.\frac{rb}{V})_e\cos\alpha_e\cos\beta_e \qquad \text{(F.14)}$$

Similarly for $\breve{Z}_u, \breve{Y}_u$.

F.4.4 Moment Derivatives with respect to u

Consider $\breve{M}_u$ as an example:-

$$\breve{M}_u = (2C_m.\frac{\partial V}{\partial u})_e + V_e(\frac{\partial C_m}{\partial\alpha}.\frac{\partial\alpha}{\partial u} + \frac{\partial C_m}{\partial\beta}.\frac{\partial\beta}{\partial u} + \frac{\partial C_m}{\partial p_\gamma}.\frac{\partial p_\gamma}{\partial u} + \frac{\partial C_m}{\partial q_\gamma}.\frac{\partial q_\gamma}{\partial u} + \frac{\partial C_m}{\partial r_\gamma}.\frac{\partial r_\gamma}{\partial u})_e$$

$$= (2C_m\cos\alpha\cos\beta)_e + V_e(C_{m_\alpha}.\frac{(-\sin\alpha\cos\alpha)}{u} + C_{m_\beta}.\frac{(-u\tan\beta)}{V^2})_e$$

$$+V_e(C_{mp}(\frac{-p_\gamma}{V}) + C_{mq}(\frac{-q_\gamma}{V}) + C_{mr}(\frac{-r_\gamma}{V}))_e\cos\alpha_e\cos\beta_e$$

$$\breve{M}_u = (2C_m)_e\cos\alpha_e\cos\beta_e - (C_{m_\alpha}\sin\alpha\sec\beta + C_{m_\beta}\cos\alpha\sin\beta)_e$$

$$-(\breve{M}_p.p_\gamma + \breve{M}_q.q_\gamma + \breve{M}_r.r_\gamma)_e\cos\alpha_e\cos\beta_e \qquad \text{(F.15)}$$

Similarly for $\breve{L}_u$, $\breve{N}_u$.

F.4.5 Force Derivatives with respect to w

Consider X_w as an example:-

$$\breve{X}_w = (2C_X.\frac{\partial V}{\partial w})_e + V_e(\frac{\partial C_X}{\partial\alpha}.\frac{\partial\alpha}{\partial w} + \frac{\partial C_X}{\partial\beta}.\frac{\partial\beta}{\partial w} + \frac{\partial C_X}{\partial p_\gamma}.\frac{\partial p_\gamma}{\partial w} + \frac{\partial C_X}{\partial q_\gamma}.\frac{\partial q_\gamma}{\partial w} + \frac{\partial C_X}{\partial r_\gamma}.\frac{\partial r_\gamma}{\partial w})_e$$

$$\breve{X}_w = (2C_X \sin\alpha\cos\beta)_e + V_e\left(C_{X_\alpha}.\frac{\cos^2\alpha}{u} + C_{X_\beta}.\frac{-w}{V^2}\tan\beta\right)_e$$

$$+V_e\left(C_{Xp}(-p_\gamma)+C_{Xq}(-q_\gamma)+C_{Xr}(-r_\gamma)\right)_e\frac{(\sin\alpha\cos\beta)_e}{V_e}$$

$$= (2C_X\sin\alpha\cos\beta)_e + \left(C_{X_\alpha}\frac{\cos^2\alpha}{\cos\alpha\cos\beta} - C_{X_\beta}\sin\alpha\cos\beta.\frac{\sin\beta}{\cos\beta}\right)_e$$

$$-(\breve{X}_p.p_\gamma + \breve{X}_q.q_\gamma + \breve{X}_r.r_\gamma)_e\sin\alpha_e\cos\beta_e$$

$$\breve{X}_w = (2C_X)_e\sin\alpha_e\cos\beta_e + (C_{X_\alpha}\cos\alpha\sec\beta - C_{X_\beta}\sin\alpha\sin\beta)_e$$

$$-(\breve{X}_p.p_\gamma + \breve{X}_q.q_\gamma + \breve{X}_r.r_\gamma)_e\sin\alpha_e\cos\beta_e \qquad \text{(F.16)}$$

Similarly for $\breve{Y}_w$, $\breve{Z}_w$.

F.4.6 Moment Derivatives with respect to w

Consider $\breve{M}_w$ as an example:-

$$\breve{M}_w = \left(2C_m.\frac{\partial V}{\partial w}\right)_e + V_e\left(\frac{\partial C_m}{\partial\alpha}.\frac{\partial\alpha}{\partial w} + \frac{\partial C_m}{\partial\beta}.\frac{\partial\beta}{\partial w} + \frac{\partial C_m}{\partial p_\gamma}.\frac{\partial p_\gamma}{\partial w} + \frac{\partial C_m}{\partial q_\gamma}.\frac{\partial q_\gamma}{\partial w} + \frac{\partial C_m}{\partial r_\gamma}.\frac{\partial r_\gamma}{\partial w}\right)_e$$

$$\breve{M}_w = (2C_m)_e\sin\alpha_e\cos\beta_e + (C_{m_\alpha}\cos\alpha\sec\beta - C_{m_\beta}\sin\alpha\sin\beta)_e$$

$$-(\breve{M}_p.p_\gamma + \breve{M}_q.q_\gamma + \breve{M}_r.r_\gamma)_e\sin\alpha_e\cos\beta_e \qquad \text{(F.17)}$$

Similarly for $\breve{L}_w$, $\breve{N}_w$.

F.4.7 Force Derivatives with respect to v

Consider $\breve{Z}_v$ as an example:-

$$\breve{Z}_v = \left(2C_Z.\frac{\partial V}{\partial v}\right)_e + V_e\left(\frac{\partial C_Z}{\partial\alpha}.\frac{\partial\alpha}{\partial v} + \frac{\partial C_Z}{\partial\beta}.\frac{\partial\beta}{\partial v} + \frac{\partial C_Z}{\partial p_\gamma}.\frac{\partial p_\gamma}{\partial v} + \frac{\partial C_Z}{\partial q_\gamma}.\frac{\partial q_\gamma}{\partial v} + \frac{\partial C_Z}{\partial r_\gamma}.\frac{\partial r_\gamma}{\partial v}\right)_e$$

$$= (2C_Z\sin\beta)_e + V_e\left(C_{Z_\alpha}.0 + C_{Z_\beta}.\frac{\cos\beta}{V}\right)_e$$

$$+V_e\left(C_{Zp}(-p_\gamma)\frac{\sin\beta}{V} + C_{Zq}(-q_\gamma)\frac{\sin\beta}{V} + C_{Zr}(-r_\gamma)\frac{\sin\beta}{V}\right)_e$$

$$\breve{Z}_v = (2C_Z)_e\sin\beta_e + (C_{Z_\beta}\cos\beta)_e - (\breve{Z}_p.p_\gamma + \breve{Z}_q.q_\gamma + \breve{Z}_r.r_\gamma)_e\sin\beta_e$$

(F.18)

Similarly for $\breve{X}_v, \breve{Y}_v$. Hopkin, Ref.45, Pt.4, p.15, has an extra term, "$-(CZ_\alpha \tan\alpha \sin\beta)_e$", combined with the $(CZ_\beta \cos\beta)_e$ term shown in (F.18). This is because α in Ref.45 is α_s and so is a function of v.

F.4.8 Moment Derivatives with respect to v

Consider $\breve{M}_v$ as an example:-

$$\breve{M}_v = \left(2C_m \frac{\partial V}{\partial v}\right)_e + V_e\left(\frac{\partial C_m}{\partial \alpha}.\frac{\partial \alpha}{\partial v} + \frac{\partial C_m}{\partial \beta}.\frac{\partial \beta}{\partial v} + \frac{\partial C_m}{\partial p_\gamma}.\frac{\partial p_\gamma}{\partial v} + \frac{\partial C_m}{\partial q_\gamma}.\frac{\partial q_\gamma}{\partial v} + \frac{\partial C_m}{\partial r_\gamma}.\frac{\partial r_\gamma}{\partial v}\right)_e$$

$$\breve{M}_v = (2C_m \sin\beta)_e + (C_{m_\beta} \cos\beta)_e - (\breve{M}_p.p_\gamma + \breve{M}_q.q_\gamma + \breve{M}_r.r_\gamma)_e \sin\beta_e \qquad \text{(F.19)}$$

Similarly for $\breve{L}_v$, $\breve{N}_v$.

Table 3.1

Gnat simulation data for analogue computer

(a) Basic aircraft

$\check{Y}_v$	-0.72	M	0.85	I_x	4900 kg.m^2
$\check{N}_v$	0.103	C_L	0.65	I_z	19700 kg.m^2
$\check{N}_p$	0.067	α_e	10^o	m	4082 kg
$\check{N}_r$	-0.086	h	30000ft	ρ	0.458 kg/m^2
$\check{L}_{v_1}$	-0.039	$\bar{w}$	0.175	S_W	16.26 m^2
$\check{L}_p$	-0.150	$\frac{g}{V}$	0.038	V	258 m/s
$\check{L}_r$	-0.053			s	3.66 m

Configuration : tanks on

(b) Non-linear sideslip characteristics

Case No.	$\check{L}_{v_1}$	$\check{L}_{v_3}$	$\check{N}_{v_1}$	$\check{N}_r$	Θ_v
1	0.039	-8.8	0.103	-0.086	0.043
2	0.039	-8.8	0.0515	-0.086	0.055
3	0.039	-44	0.103	-0.086	0.020
4	0.039	-8.8	0.103	-0.171	decaying
5	0.059	-8.8	0.103	-0.086	0.07
6	0.117	-44	0.103	-0.086	0.05

Table 3.2

Combat aircraft B simulation data: non-linear sideslip characteristics

$\check{Y}_v$	-0.338	α	10.2°	I_x	5369 kg.m^2
$\check{N}_{v1}$	0.05	$\bar{w}$	0.171	I_z	41728 kg.m^2
$\check{N}_{v3}$	43.9	$\frac{g}{V}$	0.0355	I_{xz}	2084 kg.m^2
$\check{N}_p$	-0.0517			m	7078 kg
$\check{N}_r$	-0.4425			ρ	0.7787 kg/m^3
$\check{L}_{v1}$	-0.15			S_W	18.67 m^2
$\check{L}_{v3}$	137.2			V	276 m/s
$\check{L}_{p1}$	-0.007			b	7.702 m
$\check{L}_r$	0.079				
Control derivatives:					
$\check{L}_\xi$	-0.1016				
$\check{N}_\xi$	0.0418				
$\check{Y}_\zeta$	0.140				
$\check{L}_\zeta$	0.022				
$\check{N}_\zeta$	-0.085				

Table 3.3

Combat aircraft B simulation data: non-linear roll rate characteristics

Case No.	$\check{L}_{p1}$	$\check{L}_{p3}$	$\check{L}_{v1}$	$\check{N}_{v1}$
1	-0.02	-961.1	-0.2	0.07
2	0.01	-1760.0	-0.2	0.07
3	0.075	-3810.0	-0.2	0.07

Note for Table 3.3:

Other derivatives as in Table 3.2

Table 3.4

Characteristics of aircraft B responses with non-linearities in sideslip and roll rate.

Case No.	$\check{L}_{p_1}$	$\check{L}_{p_3}$	Limit cycle characteristics			
			Frequency		Amplitude	
			$\omega_{\bar{v}}$(Hz)	ω_p(Hz)	$\Theta_{\bar{v}}$(r)	Θ_p(r/s)
Basic non-linear sideslip case						
-	-0.007	0.0	0.64	0.64	0.027	0.45
Non-linear roll rate cases:						
1b	-0.04	-271	0.88	0.88	0.011	0.32
2b	0.01	-1760	0.83	0.83	0.023	0.68
3b	0.075	-3810	0.83	0.83	0.024	0.66
Non-linear $\bar{v}$ and p; gϕ gravity term in equations of motion:						
1b	-0.04	-271	0.72	0.72	0.013	0.34
2b	0.01	-1760	0.64	0.64	0.026	0.46
3b	0.075	-3810	0.62	0.62	No limit cycle	
Non-linear $\bar{v}$ and p; gsinϕ gravity term in equations of motion:						
2b	0.01	-1760	0.64	0.64	0.025	0.45
3b	0.075	-3810	0.60	0.60	0.028	0.44
Non-linear $\bar{v}$ and p; no gravity term in equations of motion:						
3b	0.075	-3810	0.58	0.58	0.029	0.45

Table 3.5

Application of B.T.S.technique to aircraft B with non-linearities in sideslip and roll rate

Case	SIMULation results			Solution of R*=0, equation (2.89)			
	ω(r/s(Hz))	$\Theta_{\bar{v}}$(r)	Θ_p(r/s)	Given Θ	Θ Solution	ω Eqn.(2.84)	ω Eqn.(2.86)
2b	4.04(0.64)	0.0254		$\Theta_{\bar{v}}$=0.0254	No real solution for Θ_p		
			0.4518	Θ_p=0.4518	$\Theta_{\bar{v}}$=0.0258	4.04	5.46
3b	3.80(0.60)	0.0278		$\Theta_{\bar{v}}$=0.0278	Θ_p=1.375	5.39	3.49
			0.440	Θ_p=0.440	$\Theta_{\bar{v}}$=0.030	3.65	7.55

Table 4.1

Free-flight, drop test HIRM data

General		
Length		3.324 m
Span	b	2.603 m
Mass (1)	m	209 kg
Inertias (1)	I_x	27 kg.m^2
	I_y	151 kg.m^2
	I_z	162 kg.m^2
	I_{xz}	-0.187 kg.m^2
Inertia ratio	I_z/I_x	6
Datum altitude for calculations		5000ft above Sea Level
Wing		
Gross wing area	S_W	2.062 m^2
Leading edge sweep	Λ_{LE}	42^o
Chord at centre line	c_0	1.2168 m
Aero mean chord	$\bar{\bar{c}}$	0.8679 m
Tip chord	c_t	0.365 m
Aspect ratio	AR	3.3
Dihedral		-4^o
Taper ratio	λ	0.3
Canard		
Gross area	S_C	0.488 m^2
Span		1.084 m
Leading edge sweep	Λ_{LE}	50^o
Root chord	c_r	0.516 m
Tip chord	c_t	0.311 m
Aspect ratio	AR	2.41
Tailplane		
Gross area	S_T	0.573 m^2
Span	b_T	1.472 m
Leading edge sweep	Λ_{LE}	42^o
Root chord	c_r	0.487 m
Tip chord	c_t	0.147 m
Aspect ratio	AR	3.77
Fin		
Nett area	S_F	0.235 m^2
Exposed height	s_F	0.625 m
Leading edge sweep	Λ_{LE}	42^o
Root chord	c_r	0.578 m
Tip chord	c_t	0.177 m
Aspect ratio	AR	3.71

Note for Table 4.1:
(1) These are values from Ref.82. They are the definitive set of estimates used for most of the work in this thesis and are referred to elsewhere in this thesis as "HIRM Data Set No.3."

Table 4.2

HIRM cubic polynomial coefficients for static data fits

α(degrees)	$\breve{L}_{V1}$	$\breve{L}_{V3}$	$\breve{N}_{V1}$	$\breve{N}_{V3}$
22	-0.135	2.21	-0.116	2.21
24	-0.140	5.95	-0.160	2.12
26	-0.072	0.874	-0.170	1.70
28	-0.084	0.86	-0.169	1.53
30	-0.109	1.75	-0.169	1.41
32	-0.103	0.96	-0.171	0.031
34	-0.161	7.41	-0.169	-2.40
36	-0.274	16.94	-0.139	-5.86
38	-0.235	8.52	-0.126	-6.53
40	-0.192	8.153	-0.088	-12.71

Notes for Table 4.2:

Experimental data source: R.A.E.11½ft x 8ft static W.T.tests
Cubic fitting program used: POLFT

Table 5.1

HIRM lateral responses at $\alpha=26^{o}$ with different sideslip characteristics

Polynomial details						SIMULation		B.T.S.averaging	
	$C_{\ell}(\beta)$			$C_{n}(\beta)$		$\sigma_{\bar{v}}$	ω (rad/s)	$\sigma_{\bar{v}}$	ω (rad/s)
Curve no.	$\breve{L}_{v_1}$	$\breve{L}_{v_3}$	Curve no.	$\breve{N}_{v_1}$	$\breve{N}_{v_3}$				
3B (1)	-0.058	-0.945	-	-0.158	0.0	0.135	1.42	0.139	1.46
2A	-0.071	0.789	2A	-0.168	1.529	Divergent oscillation		0.382	Imag.
2A	-0.071	0.789	3B	-0.176	2.599	0.210	1.20	0.224	1.14
3B (1)	-0.058	-0.945	2A	-0.168	1.529	0.121	1.42	0.124	1.44
3B (1)	-0.058	-0.945	3B	-0.176	2.599	0.118	1.40	0.120	1.43

Note for Table 5.1:

(1) This curve has a stiffening spring characteristic (see Fig.4.17b). All other curves have softening spring characteristics (see Figs.4.17 and 4.18).

Table 5.2

HIRM derivatives used for $\alpha=26^{o}$ lateral response simulations

Derivative	Non-linear roll rate characteristics(1)		Non-linear roll rate & sideslip characteristics(2)	Non-linear sideslip characteristics (3)
	Wind axis simulation (4)	Body axis Simulation (5)	Body axis simulation (5)	Body axis simulation
$\check{Y}_v$	-0.202	-0.202	-0.202	-0.202
$\check{L}_{v_1}$	-0.124	-0.061	-0.058	-0.061
$\check{L}_{v_3}$	0	0	-0.945	-0.500
$\check{N}_{v_1}$	-0.115	-0.158	-0.158	-0.170
$\check{N}_{v_3}$	0	0	0	2.599
$\check{L}_{p_o}$	-0.085	-0.150	-0.150	-0.150
$\check{N}_{p_o}$	-0.100	-0.060	-0.060	-0.065
$\check{L}_{p_R}$	-0.022	0.025	0.025	-
$\check{L}_{p_3R}$	-2.542	-2.684	-2.684	-
$\check{N}_{p_R}$	-0.102	-0.102	-0.102	-
$\check{N}_{p_3R}$	0.931	-0.218	-0.218	-
$\check{L}_{r_o}$	0.192	0.232	0.232	0.232
$\check{N}_{r_o}$	-0.232	-0.167	-0.167	-0.165

Notes for Table 5.2:
(1) HIRM Data Set No.2 used (see §5.6.4)
(2) HIRM Data Set No.3 used (see §5.6.5)
(3) HIRM Data Set No.3 used (see §5.6.6)
(4) Full cubic fitted to wind axis rotary rig data (see Fig.4.21b)
(5) Modified cubic fitted to body axis rotary rig data.

Table 6.1

Angle of attack ranges for derivative data used in HIRM configuration C analysis

Source \ Derivatives	$\check{X}_u$ $\check{X}_w$ $\check{X}_v$ $\check{Z}_u$ $\check{Z}_v$ $\check{M}_u$ $\check{M}_v$ $\check{Y}_u$ $\check{Y}_w$ $\check{L}_u$ $\check{L}_w$ $\check{N}_u$ $\check{N}_w$	$\check{Z}_w$	$\check{M}_w$	$\check{Y}_v$	$\check{L}_v$ $\check{N}_v$	$\check{Z}_q+\check{Z}_{\dot{w}}\cos\alpha$ $\check{M}_q+\check{M}_{\dot{w}}\cos\alpha$	$\check{L}_q+\check{L}_{\dot{w}}\cos\alpha$	$\check{Z}_p+\check{Z}_{\dot{v}}\sin\alpha$	$\check{M}_p+\check{M}_{\dot{v}}\sin\alpha$	$\check{L}_p$	$\check{N}_p$	$\check{L}_r-\check{L}_{\dot{v}}\cos\alpha$ $\check{N}_r-\check{N}_{\dot{v}}\cos\alpha$
11½ft x 8ft W.T. R.A.E.results	$\check{X}_u, \check{X}_w, \check{Z}_u, \check{M}_u$ 0 - 40	0-40	0-40	10-40	10-40	-	-	-	-	-	-	-
11½ft x 8ft W.T. SDERIV6 results (1)	0 - 40	0-40	0-40	0-40	0-40	-	-	-	-	-	-	-
Oscillatory rig tests Lateral, series OD3	-	-	-	10-40	10-40	-	-	-	-	10-40 (2)	10-40 (3)	10-40
Oscillatory rig tests Longitudinal, series OD5	-	0-40	0-40	-	-	0-40	-	-	-	-	-	-
Oscillatory rig tests Cross-Coupling, series OD6 (4)	-	12-24	12-24	-	-	12-24	12-24	12-24	12-24	12-24 (2)	-	-
Rotary rig tests	-	-	-	-	-	-	-	-	-	10-45	10-45	-

Notes for Table 6.1:

Angle of attack ranges in degrees, for $\beta_e = 0^\circ$

(1) Also for $\beta_e = -6(1)6^\circ$

(2) $\check{L}_p+\check{L}_{\dot{v}}\sin\alpha$ measured on oscillatory rig

(3) $\check{N}_p+\check{N}_{\dot{v}}\sin\alpha$ measured on oscillatory rig

(4) Also for $\beta_e = -6^\circ$

TABLE 6.2

HIRM dynamic characteristics for linear analysis and simulation

Mode	$\alpha = 10^{o}$ Program EIGEN Decoupled	Coupled	SIMUL6	$\alpha = 20^{o}$ Program EIGEN Decoupled	Coupled	SIMUL6
(a) Time constants or periods of oscillation (secs)						
Roll mode, T_{rm}	0.422	0.421	0.38	0.747	0.683	-
Dutch roll, T_{dr}	1.592	1.598	1.62	2.55	2.65	2.86
Spiral mode, T_{sm}	9.40	9.36	-	3.72	4.36	-
Short period, T_{sp}	3.308	3.251	2.29	7.50	5.63	6.67
Phugoid, T_{ph}	18.82	18.87	-	10.61	11.79	-
(b) Eigenvalues						
Roll mode	-2.371	-2.375	-	-1.339	-1.463	-
Dutch roll	-0.334±3.947i	-0.324±3.931i	-	-0.298±2.466i	-0.243±2.374i	-
Spiral mode	-0.106	-0.107	-	-0.269	-0.229	-
Short period	-0.692±1.900i	-0.710±1.933i	-	-0.809±0.838i	-0.811±1.115i	-
Phugoid	-0.437±0.334i	-0.427±0.333i	-	-0.083±0.592i	-0.094±0.533i	-

Table 6.3

Summary of effects of oscillatory and rotary damping on banked turn simulations

Case no.	Oscillatory rig data for L_p^B, N_p^B						Rotary rig data for $C_\ell(p_b/2V)$ & $C_n(p_b/2V)$					
	α_e (degs)	β_e (degs)	Φ_e (degs)	$(\frac{pw_b}{2V})$	$L_{p_o}^B$	$\dot{\psi}$ (rad/s)	α_e (degs)	β_e (degs)	Φ_e (degs)	$(\frac{pw_b}{2V})$	$L_{p_R}^B$	$\dot{\psi}$ (rad/s)
1	13	0.47	-66	-0.0026	-0.140	-0.260	14	-0.47	-46	-0.0010	-0.148	-0.182
2	18	-0.13	-55	-0.0021	-0.140	-0.237	Oscillatory: 18 to 19	±4	-27	±0.02	-0.195	-0.116
3	18	-0.04	-44	-0.0014	-0.140	-0.196	20	Divergent				
4	20	0.34	-59	-0.0042	-0.153	-0.274	20	Divergent				
5	22	Unstable					22	Unstable				
6	30	Unstable					30	Unstable				

Table E.1

Longitudinal terms in the linearised equations

Abbreviated form (Chapter 6)	Full expression	Terms used in EIGEN(1)
x'_u	$\frac{X_u}{m}$	$\frac{[\breve{X}_u]\,\frac{1}{2}\rho VS}{m}$
z''_u	$\frac{Z_u + q_e m}{m - Z_{\dot{w}}}$	$\frac{[\breve{Z}_u]\,\frac{1}{2}\rho VS}{m}$
m''_u	$\frac{M_u}{I_y} + \frac{M_{\dot{w}}}{I_y}\left(\frac{Z_u+q_e m}{m-Z_{\dot{w}}}\right)$	$\frac{[\breve{M}_u]\,\frac{1}{2}\rho VS\bar{\bar{c}}}{I_y}$
x''_w	$\frac{X_w}{m} - q_e$	$\frac{[\breve{X}_w]\,\frac{1}{2}\rho VS}{m}$
z''_w	$\frac{Z_w}{m - Z_{\dot{w}}}$	$\frac{[\breve{Z}_w]\,\frac{1}{2}\rho VS}{m}$
m''_w	$\frac{M_w}{I_y} - \frac{M_{\dot{w}}}{I_y}\left(\frac{Z_w}{m-Z_{\dot{w}}}\right)$	$\frac{[\breve{M}_w]\,\frac{1}{2}\rho VS\bar{\bar{c}}}{I_y}$
x''_q	$\frac{X_q}{m} - w_e$	$\frac{[\breve{X}_q]\,\frac{1}{2}\rho VS\bar{\bar{c}}}{m} - V\sin\alpha$
z''_q	$\frac{Z_q + u_e m}{m - Z_{\dot{w}}}$	$\frac{[\breve{Z}_q+\breve{Z}_{\dot{w}}\cos\alpha]\,\frac{1}{2}\rho VS\bar{\bar{c}}}{m} + V\cos\alpha$
m''_q	$\frac{M_q}{I_y} + \frac{M_{\dot{w}}}{I_y}\left(\frac{Z_q+u_e m}{m-Z_{\dot{w}}}\right)$	$\frac{[\breve{M}_q+\breve{M}_{\dot{w}}\cos\alpha]\,\frac{1}{2}\rho VS\bar{\bar{c}}^2}{I_y}$
$-g_1$	$-g\cos\Theta_e$	$-g\cos\Theta_e$
$-g_4\left(\frac{m}{m-Z_{\dot{w}}}\right)$	$-g_4\left(\frac{m}{m-Z_{\dot{w}}}\right)$	$-g\sin\Theta_e$
$-\frac{M_{\dot{w}} g_4 m}{I_y(m-Z_{\dot{w}})}$	$-\frac{M_{\dot{w}} g_4 m}{I_y(m-Z_{\dot{w}})}$	0

Note for Tables E.1 to E.4:

(1) 'R & M 3562' (Ref.45) derivatives shown in brackets:[ ]
These were the quantities actually input to EIGEN.

Table E.2

Lateral terms in the linearised equations

Abbreviated Form (Chapter 6)	Full expression	Terms used in EIGEN (1)
y''_v	$(\frac{m}{m-Y'_{\dot{v}}})\frac{Y_v}{m}$	$\frac{[\breve{Y}_v]\frac{1}{2}\rho VS}{m}$
ℓ''_v	$\ell'_v + \ell'_{\dot{v}} y''_v$	$\frac{I_z[\breve{L}_v]\frac{1}{2}\rho VSb + I_{xz}[\breve{N}_v]\frac{1}{2}\rho VSb}{I_x I_z - I_{xz}^2}$
n''_v	$n'_v + n'_{\dot{v}} y''_v$	$\frac{I_x[\breve{N}_v]\frac{1}{2}\rho VSb + I_{xz}[\breve{L}_v]\frac{1}{2}\rho VSb}{I_x I_z - I_{xz}^2}$
y''_p	$(\frac{m}{m-Y'_{\dot{v}}})(\frac{Y_p}{m} + w_e)$	$V \sin\alpha$
ℓ''_p	$\ell'_p + \ell'_{\dot{v}} y''_p + e'_x q_e$	$\frac{\{I_z[\breve{L}_p+\breve{L}_{\dot{v}}\sin\alpha]\frac{1}{2}\rho VSb^2 + I_{xz}[\breve{N}_p+\breve{N}_{\dot{v}}\sin\alpha]\frac{1}{2}\rho VSb^2\}}{I_x I_z - I_{xz}^2}$
n''_p	$n'_p + n'_{\dot{v}} y''_p - b'_z q_e$	$\frac{\{I_x[\breve{N}_p+\breve{N}_{\dot{v}}\sin\alpha]\frac{1}{2}\rho VSb^2 + I_{xz}[\breve{L}_p+\breve{L}_{\dot{v}}\sin\alpha]\frac{1}{2}\rho VSb^2\}}{I_x I_z - I_{xz}^2}$
y''_r	$(\frac{m}{m-Y'_{\dot{v}}})(\frac{Y_r}{m} - u_e)$	$-V \cos\alpha$
ℓ''_r	$\ell'_r + \ell'_{\dot{v}} y''_r - b'_x q_e$	$\frac{\{I_z[\breve{L}_r-\breve{L}_{\dot{v}}\cos\alpha]\frac{1}{2}\rho VSb^2 + I_{xz}[\breve{N}_r-\breve{N}_{\dot{v}}\cos\alpha]\frac{1}{2}\rho VSb^2\}}{I_x I_z - I_{xz}^2}$
n''_r	$n'_r + n'_{\dot{v}} y''_r - e'_z q_r$	$\frac{\{I_x[\breve{N}_r-\breve{N}_{\dot{v}}\cos\alpha]\frac{1}{2}\rho VSb^2 + I_{xz}[\breve{L}_r-\breve{L}_{\dot{v}}\cos\alpha]\frac{1}{2}\rho VSb^2\}}{I_x I_z - I_{xz}^2}$
$g_3(\frac{m}{m-Y'_{\dot{v}}})$	$g_3(\frac{m}{m-Y'_{\dot{v}}})$	$g \cos\theta_e$
$g_3\ell'_{\dot{v}}(\frac{m}{m-Y'_{\dot{v}}})$	$g_3\ell'_{\dot{v}}(\frac{m}{m-Y'_{\dot{v}}})$	0
$g_3 n'_{\dot{v}}(\frac{m}{m-Y'_{\dot{v}}})$	$g_3 n'_{\dot{v}}(\frac{m}{m-Y'_{\dot{v}}})$	0

(1) See note for Table E.1.

Table E.3

Lateral into longitudinal terms in the linearised equations

Abbreviated Form (Chapter 6)	Full expression	Terms used in EIGEN (1)
x''_v	$\frac{X_v}{m} + r_e$	$\frac{[\check{X}_v]\frac{1}{2}\rho VS}{m}$
z''_v	$\frac{Z_v - p_e m}{m - Z_{\dot{w}}}$	$\frac{[\check{Z}_v]\frac{1}{2}\rho VS}{m}$
m''_v	$\frac{M_v}{I_y} + \frac{M_{\dot{w}}}{I_y}\left(\frac{Z_v - p_e m}{m - Z_{\dot{w}}}\right)$	$\frac{[\check{M}_v]\frac{1}{2}\rho VS\bar{c}}{I_y}$
x'_p	$\frac{X_p}{m}$	0
z''_p	$\frac{Z_p - v_e m}{m - Z_{\dot{w}}}$	$\frac{[\check{Z}_p + \check{Z}_{\dot{v}}\sin\alpha]\frac{1}{2}\rho VSb}{m} - V\sin\beta$
m''_p	$\frac{M_p}{I_y} + \frac{M_{\dot{w}}}{I_y}\left(\frac{Z_p - v_e m}{m - Z_{\dot{w}}}\right) - r_e\frac{(I_x - I_z)}{I_y} - 2p_e\frac{I_{xz}}{I_y}$	$\frac{[\check{M}_p + \check{M}_{\dot{v}}\sin\alpha]\frac{1}{2}\rho VS\bar{c}b}{I_y}$
x''_r	$\frac{X_r}{m} + v_e$	$V\sin\beta$
z''_r	$\frac{Z_r}{m - Z_{\dot{w}}}$	0
m''_r	$\frac{M_r}{I_y} + \frac{M_{\dot{w}}}{I_y}\left(\frac{Z_r}{m - Z_{\dot{w}}}\right) - p_e\frac{(I_x - I_z)}{I_y} + 2r_e\frac{I_{xz}}{I_y}$	0
$-g_s\left(\frac{m}{m - Z_{\dot{w}}}\right)$	$-g_s\left(\frac{m}{m - Z_{\dot{w}}}\right)$	0
$-\frac{M_{\dot{w}} g_s m}{I_y(m - Z_{\dot{w}})}$	$-\frac{M_{\dot{w}} g_s m}{I_y(m - Z_{\dot{w}})}$	0

(1) See note for Table E.1.

Table E.4

Longitudinal into lateral terms in the linearised equations

Abbreviated Form (Chapter 6)	Full expression	Terms used in EIGEN (1)
y''_u	$(\frac{m}{m-Y'_v})(\frac{Y_u}{m} - r_e)$	$\frac{[\check{Y}_u]\frac{1}{2}\rho VS}{m}$
ℓ''_u	$\ell'_u + \ell'_v y''_u$	$\frac{I_z[\check{L}_u]\frac{1}{2}\rho VSb + \check{I}_{xz}[N_u]\frac{1}{2}\rho VSb}{I_x I_z - I_{xz}^2}$
n''_u	$n'_u + n'_v y''_u$	$\frac{I_x[\check{N}_u]\frac{1}{2}\rho VSb + I_{xz}[\check{L}_u]\frac{1}{2}\rho VSb}{I_x I_z - I_{xz}^2}$
y''_w	$(\frac{m}{m-Y'_v})(\frac{Y_w}{m} + p_e)$	$\frac{[\check{Y}_w]\frac{1}{2}\rho VS}{m}$
ℓ''_w	$\ell'_w + \ell'_v y''_w$	$\frac{I_z[\check{L}_w]\frac{1}{2}\rho VSb + I_{xz}[\check{N}_w]\frac{1}{2}\rho VSb}{I_x I_z - I_{xz}^2}$
n''_w	$n'_w + n'_v y''_w$	$\frac{I_x[\check{N}_w]\frac{1}{2}\rho VSb + I_{xz}[\check{L}_w]\frac{1}{2}\rho VSb}{I_x I_z - I_{xz}^2}$
y''_q	$(\frac{m}{m-Y'_v})(\frac{Y_q}{m})$	0
ℓ''_q	$\ell'_q + \ell'_v y''_q - (r_e b'_x - p_e e'_x)$	$\frac{\{I_z[\check{L}_q + \check{L}_w\cos\alpha]\frac{1}{2}\rho VSb\bar{c} + I_{xz}[\check{N}_q]\frac{1}{2}\rho VSb\bar{c}\}}{I_x I_z - I_{xz}^2}$
n''_q	$n'_q + n'_v y''_q - (p_e b'_z + r_e e'_z)$	$\frac{\{I_x[\check{N}_q]\frac{1}{2}\rho VSb\bar{c} + I_{xz}[\check{L}_q + \check{L}_w\cos\alpha]\frac{1}{2}\rho VSb\bar{c}\}}{I_x I_z - I_{xz}^2}$
$-g_\theta(\frac{m}{m-Y'_v})$	$-g_\theta(\frac{m}{m-Y'_v})$	0
$-\ell'_v g_\theta(\frac{m}{m-Y'_v})$	$-\ell'_v g_\theta(\frac{m}{m-Y'_v})$	0
$-n'_v g_\theta(\frac{m}{m-Y'_v})$	$-n'_v g_\theta(\frac{m}{m-Y'_v})$	0

(1) See note for Table E.1.

- Vortex flows from long fuselage forebodies, swept wings, canards, strakes

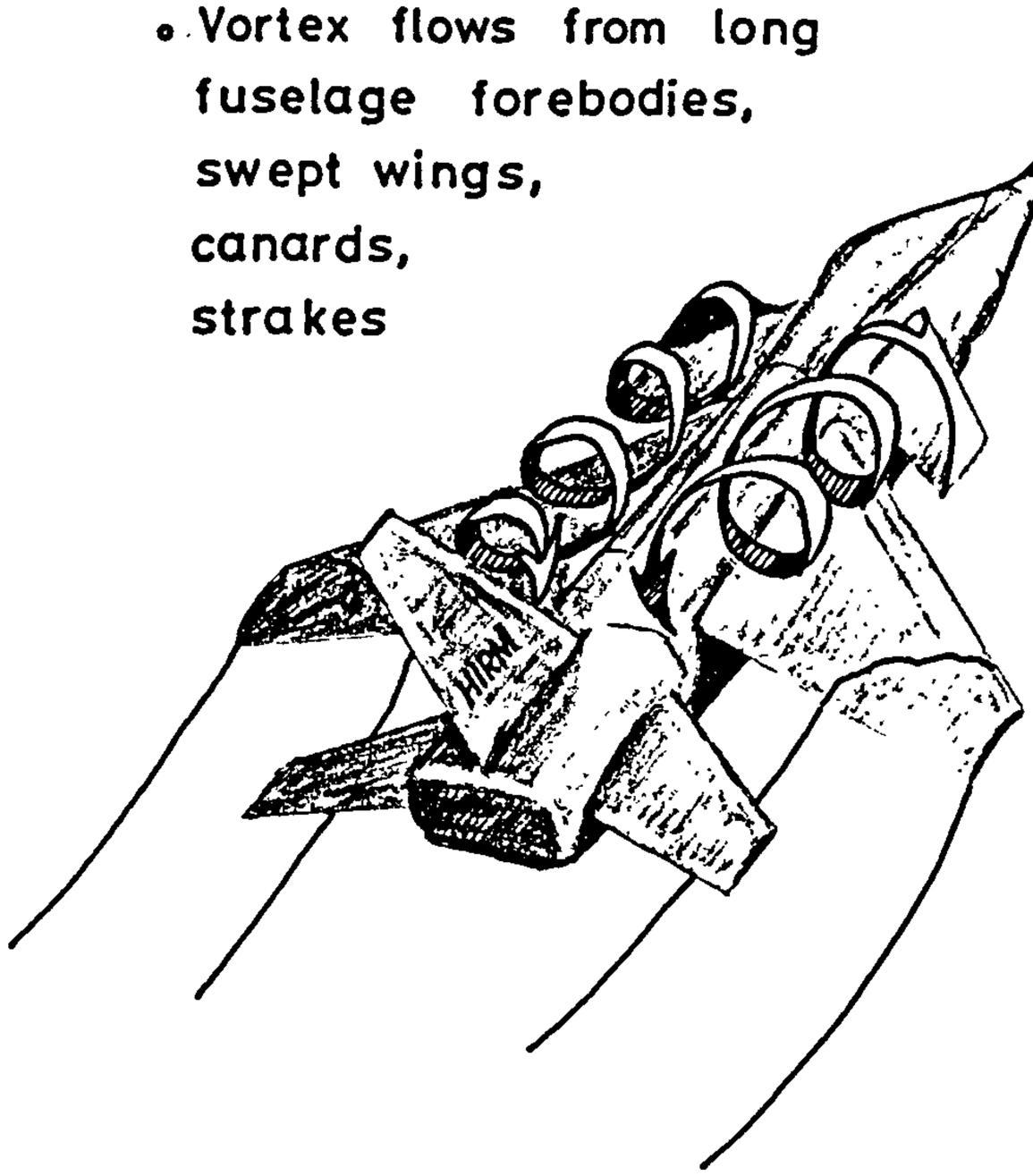

- Large regions of separated/stalled flow
- Aerodynamic interference

⇒ Non-linear effects

Fig 1.1 High angle of attack aerodynamic characteristics

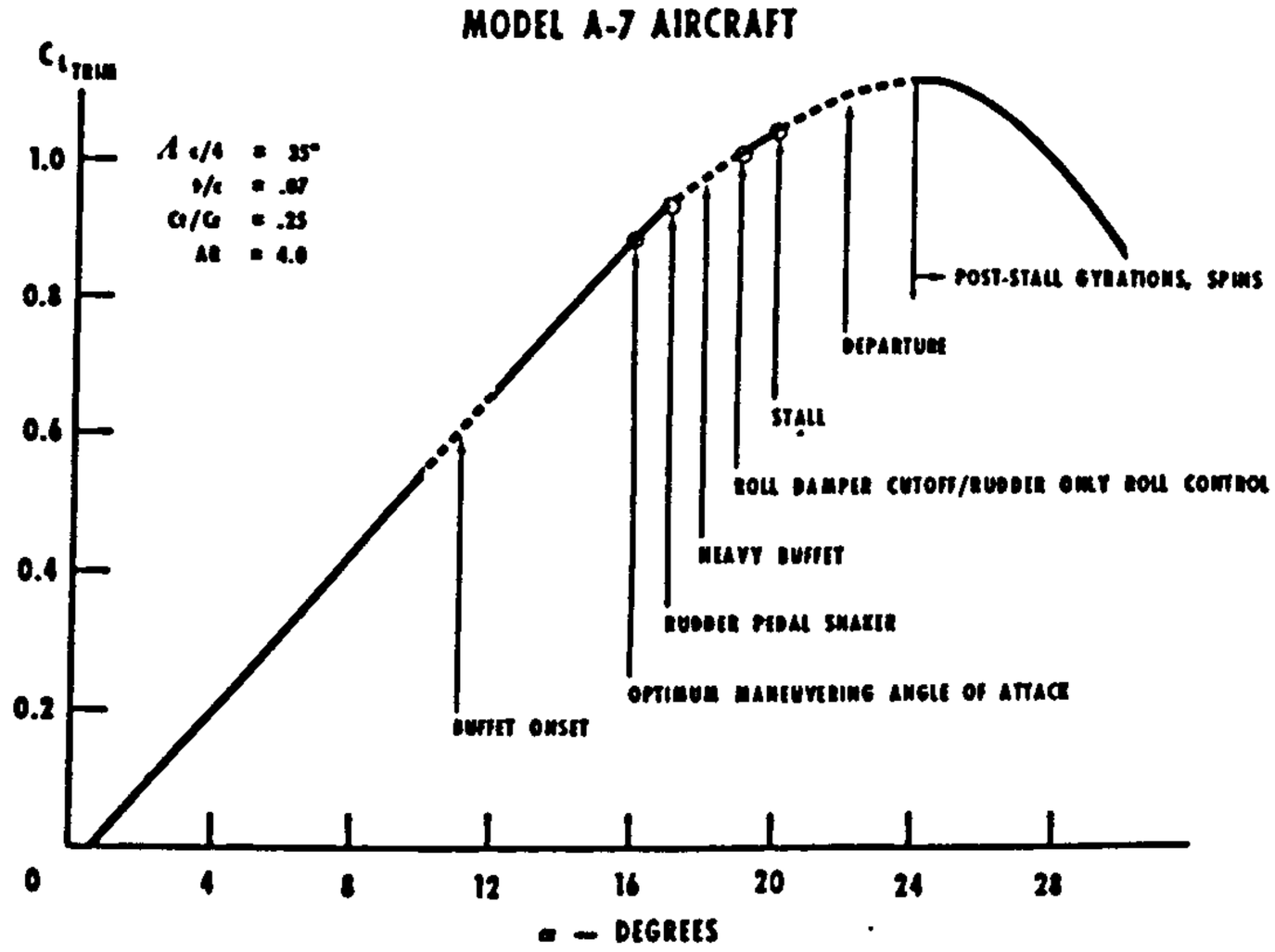

Fig 1.2 A-7 trimmed lift curve

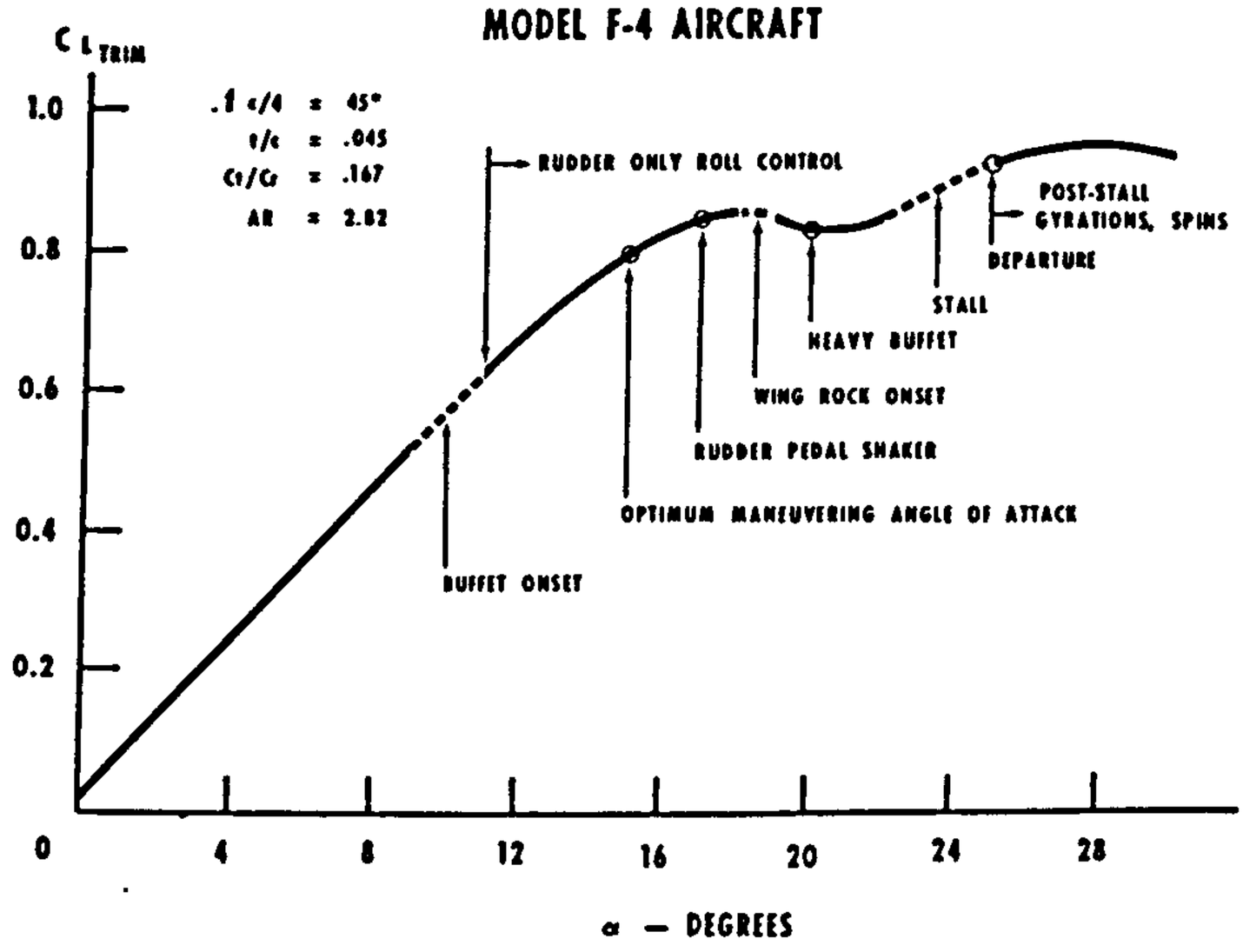

Fig 1.3 Basic F-4 trimmed lift curve

(Reproduced from Burris and Lawrence; Ref. 50)

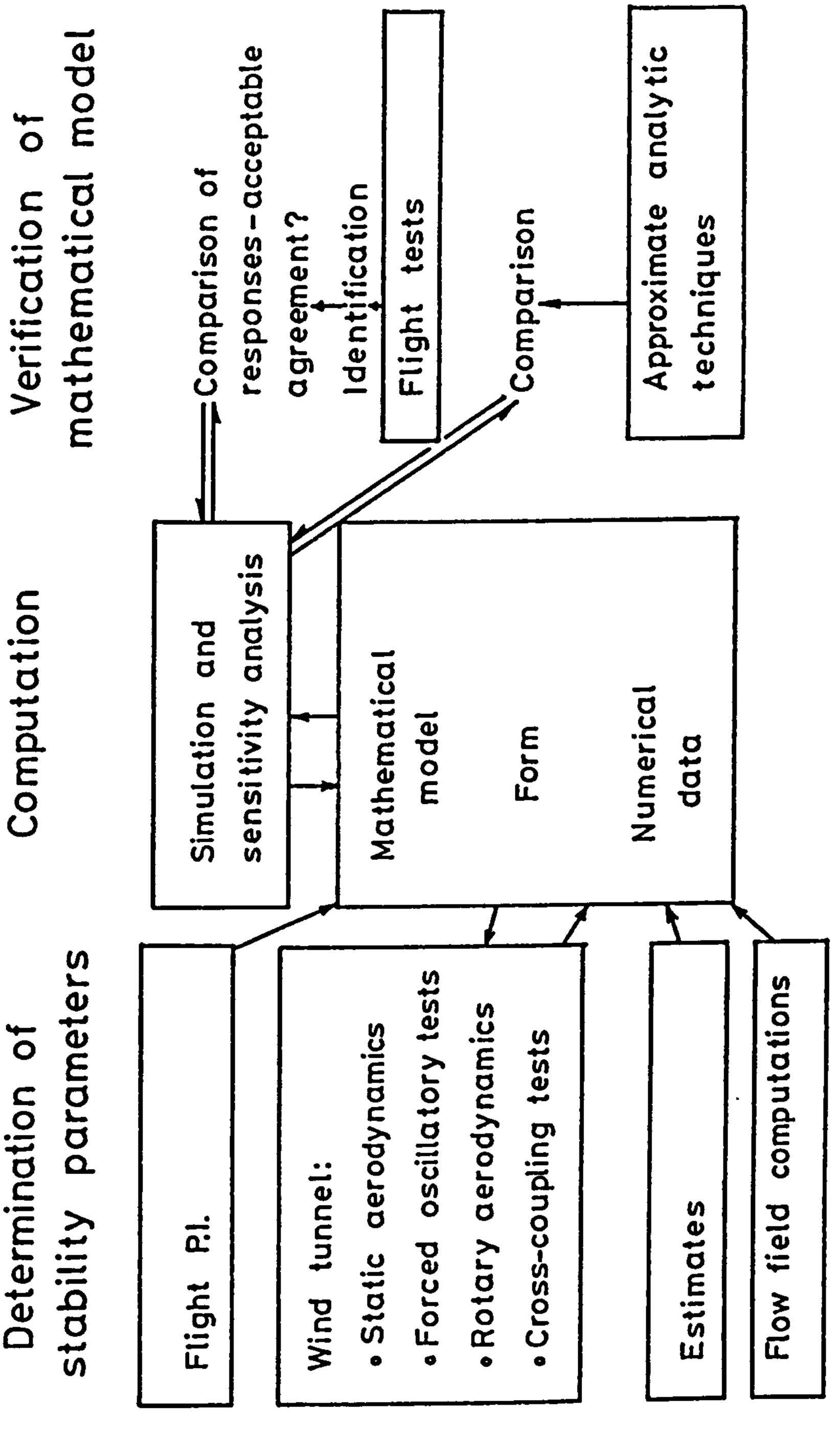

Fig 2.1 Mathematical modelling concepts for flight dynamics

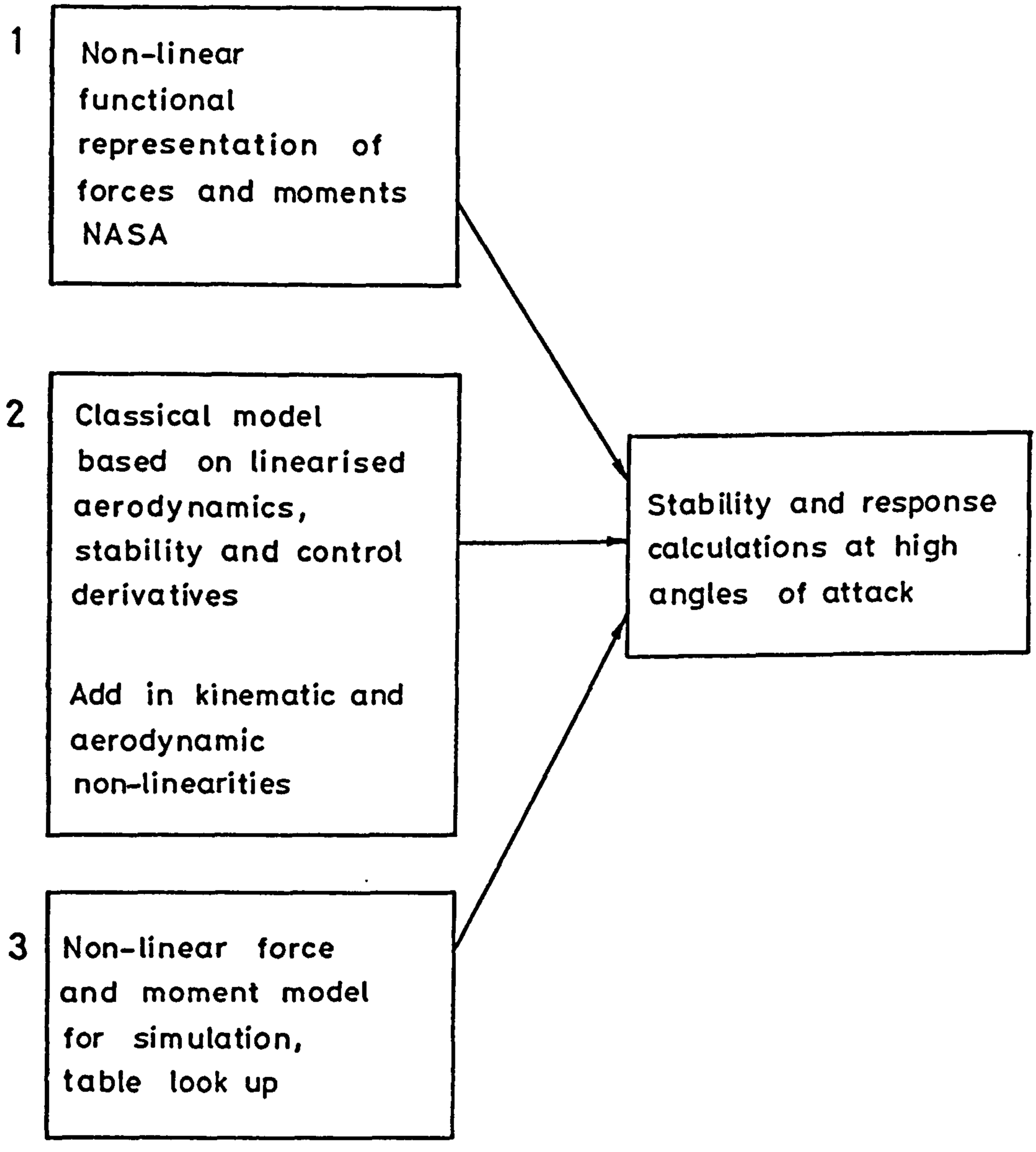

Fig 2.2 Forms of mathematical model for flight dynamics

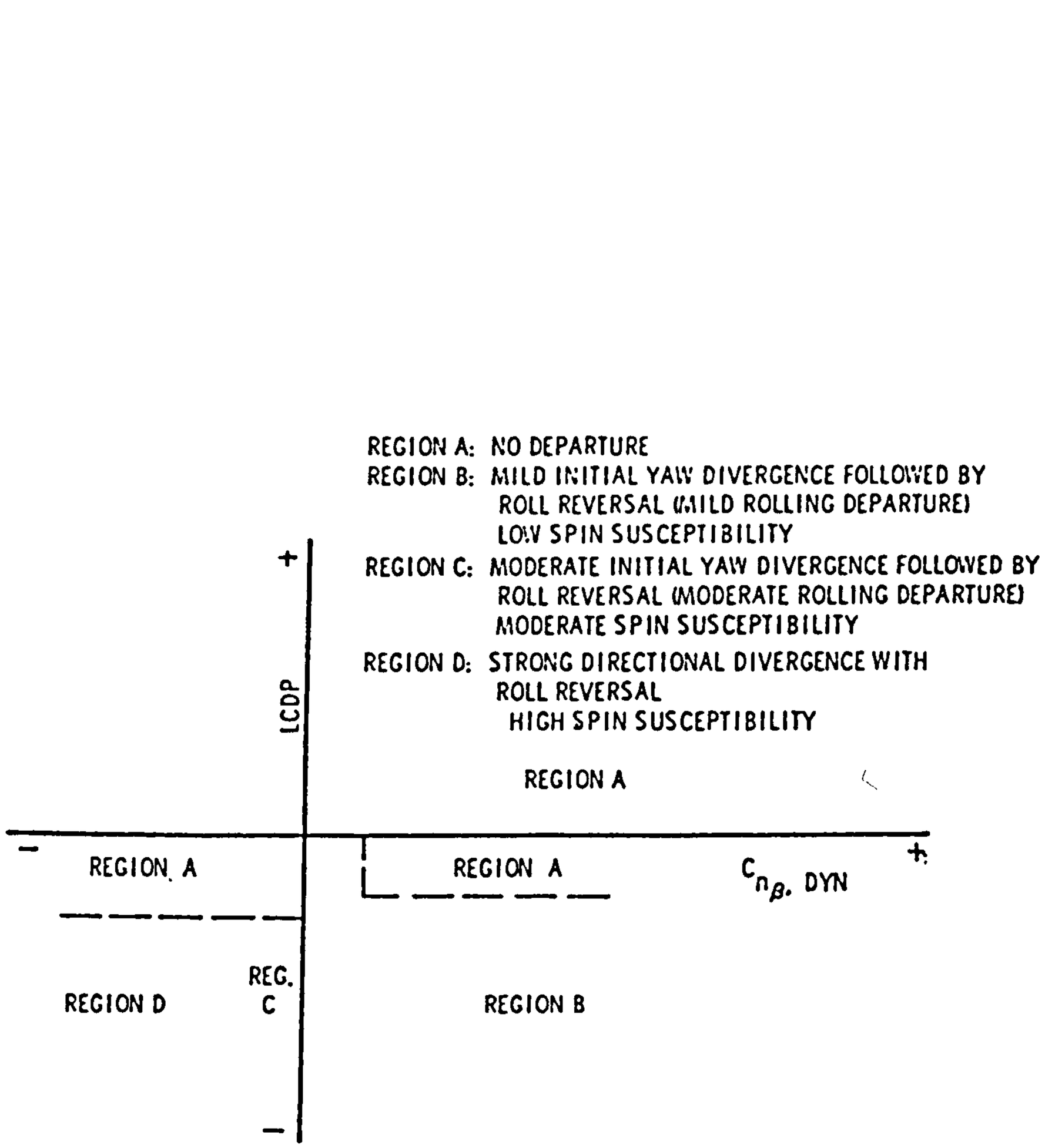

Fig 2.3 Departure and spin susceptibility criteria
(Reproduced from Weissman; Ref. 52)

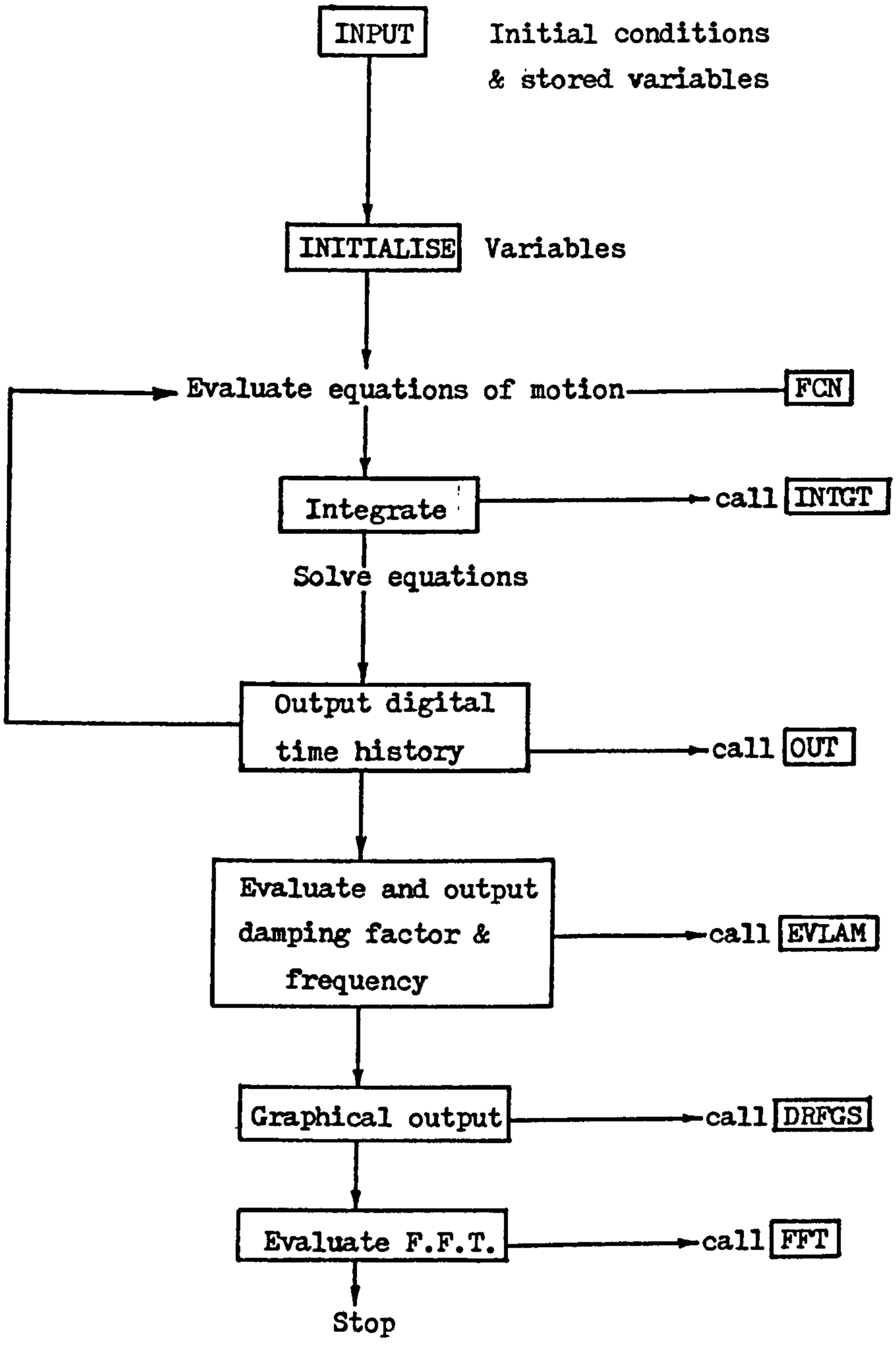

Fig 2.4 Outline flowchart of simulation program SIMUL

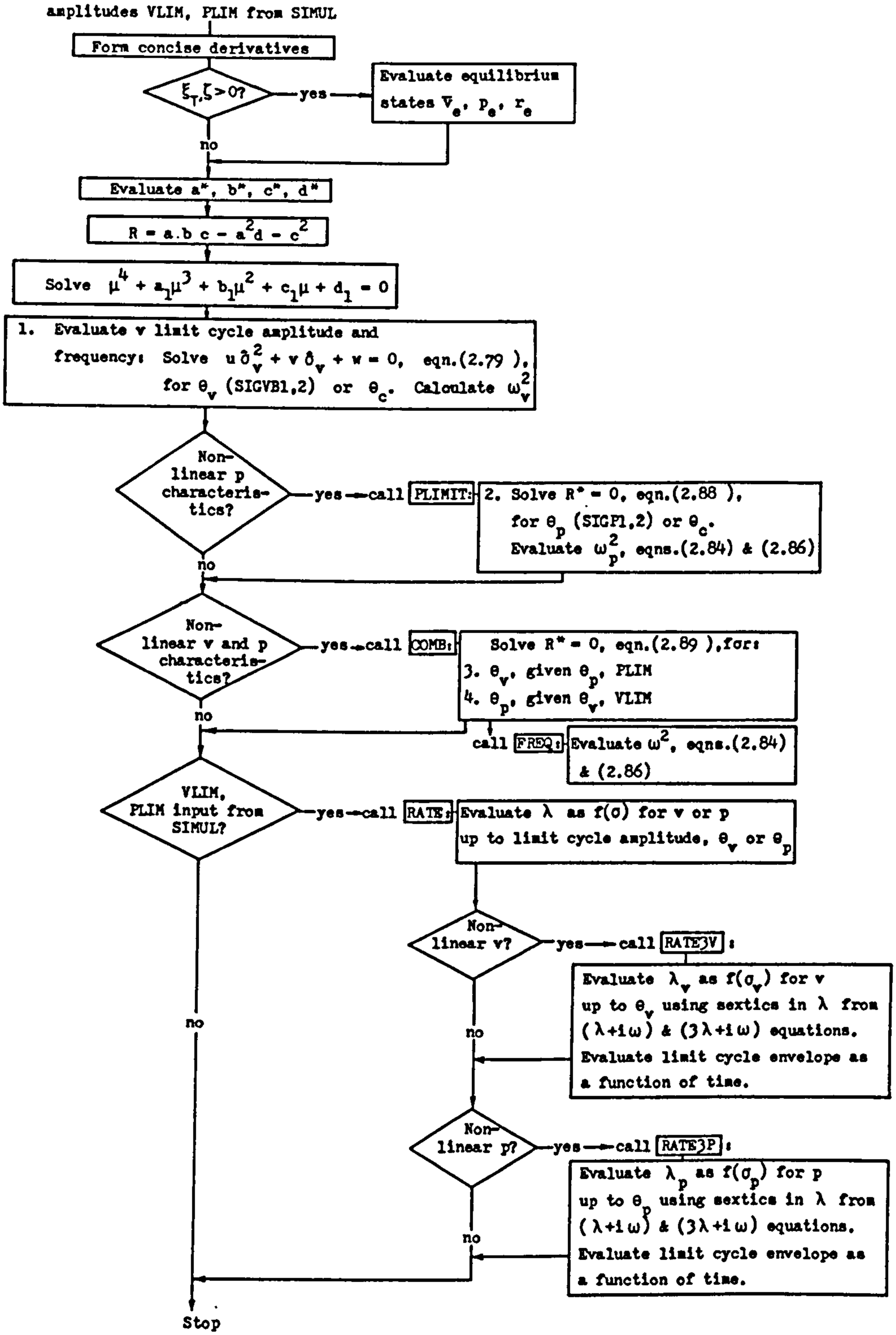

Fig 2.5 Outline flowchart of program ROUTH

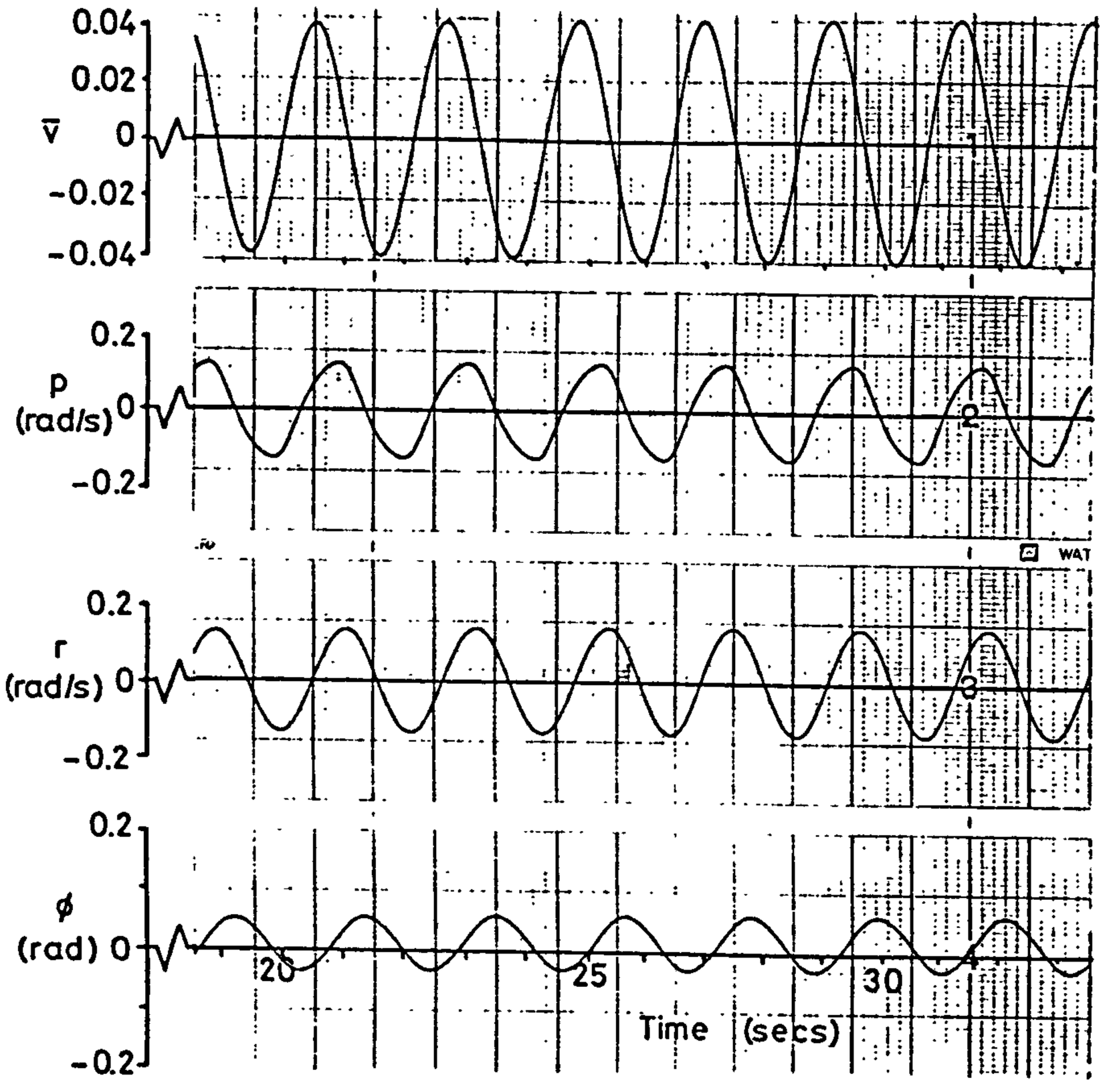

Fig 3.1 Basic Gnat response, Case 1

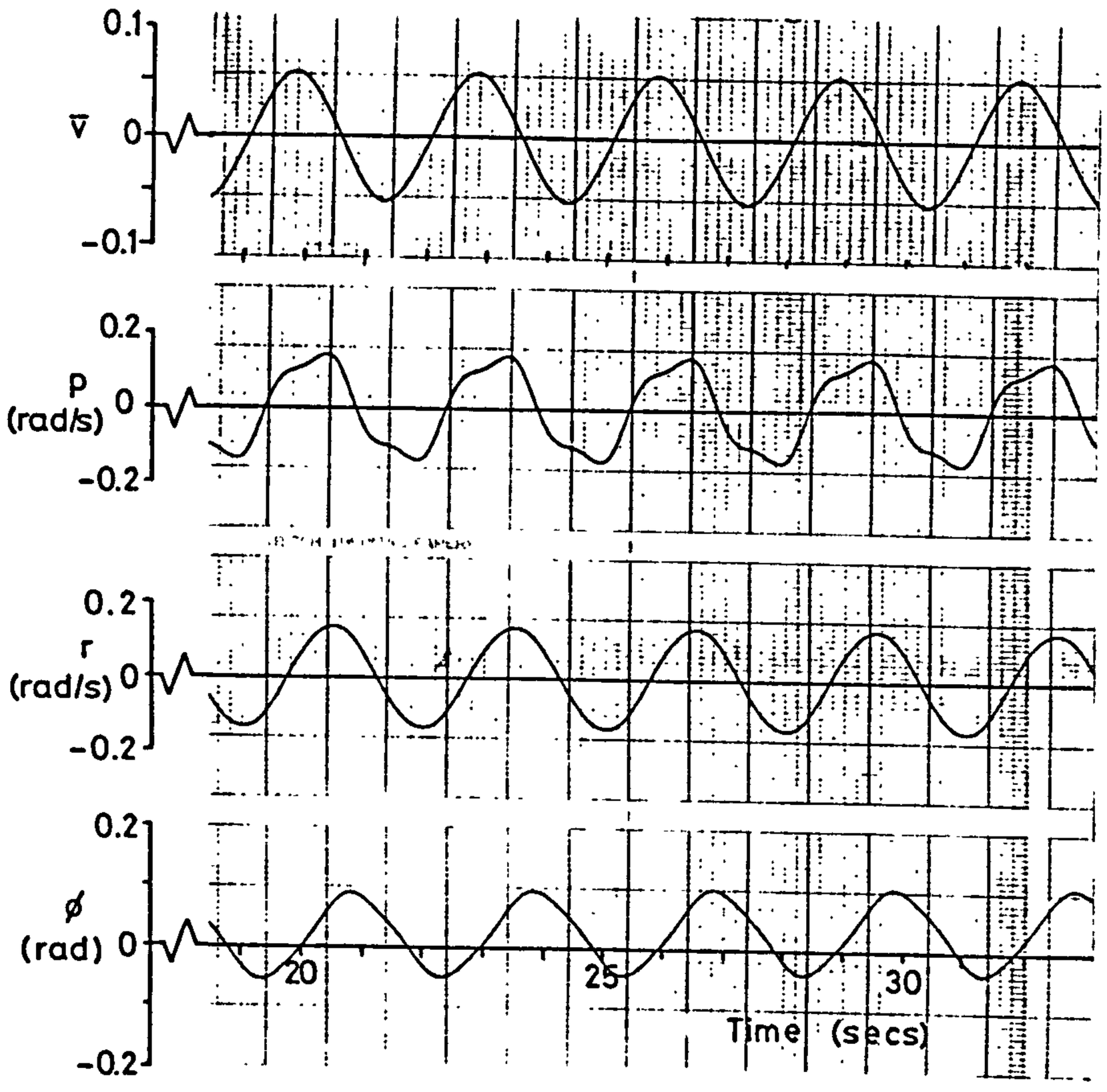

Fig 3.2 Gnat response, Case 2
$\check{N}_v$ halved

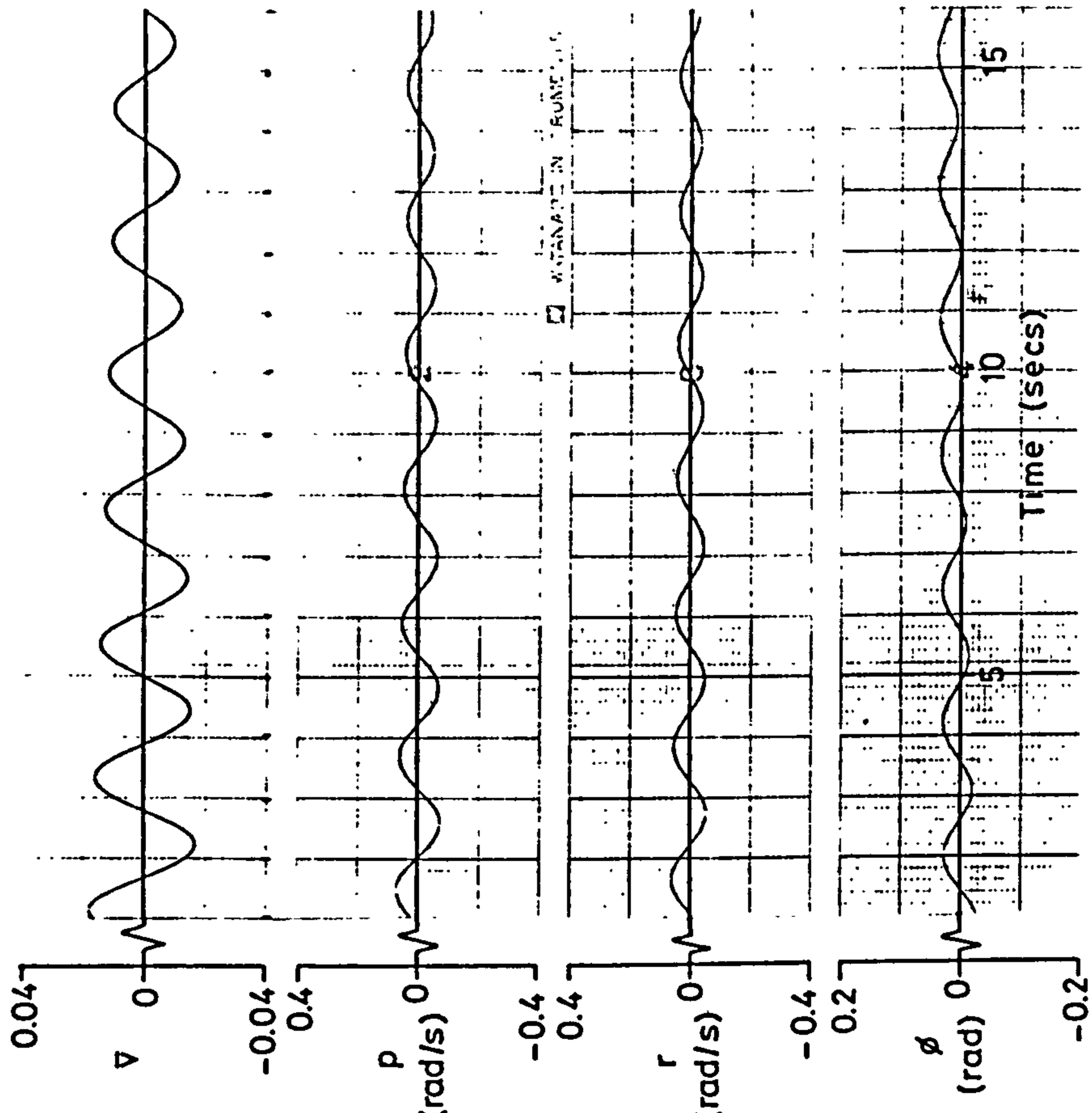

Fig 3.4 Gnat response, Case 4
$\check{N}_r$ doubled

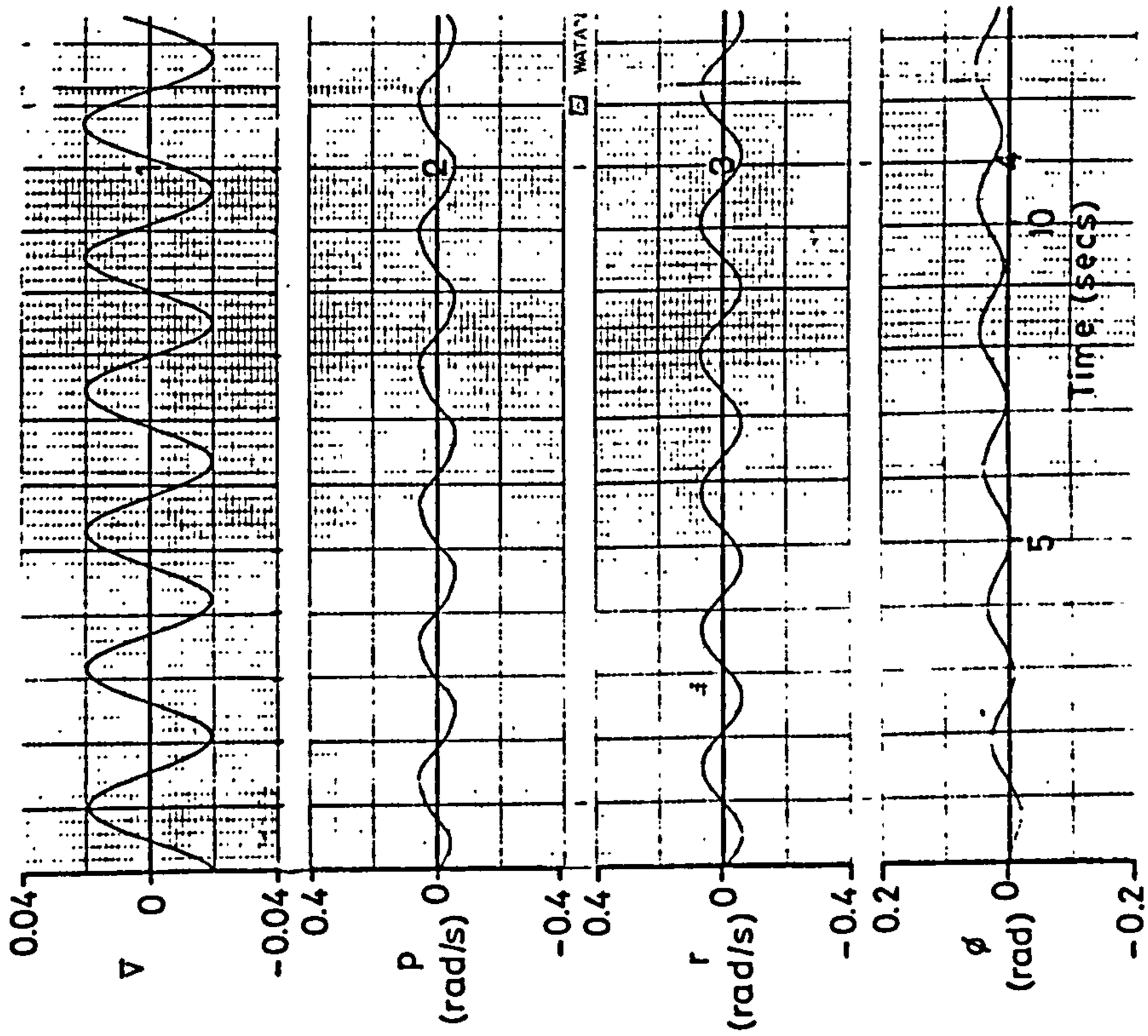

Fig 3.3 Gnat response, Case 3
$|\check{L}_{v3}|$ increased

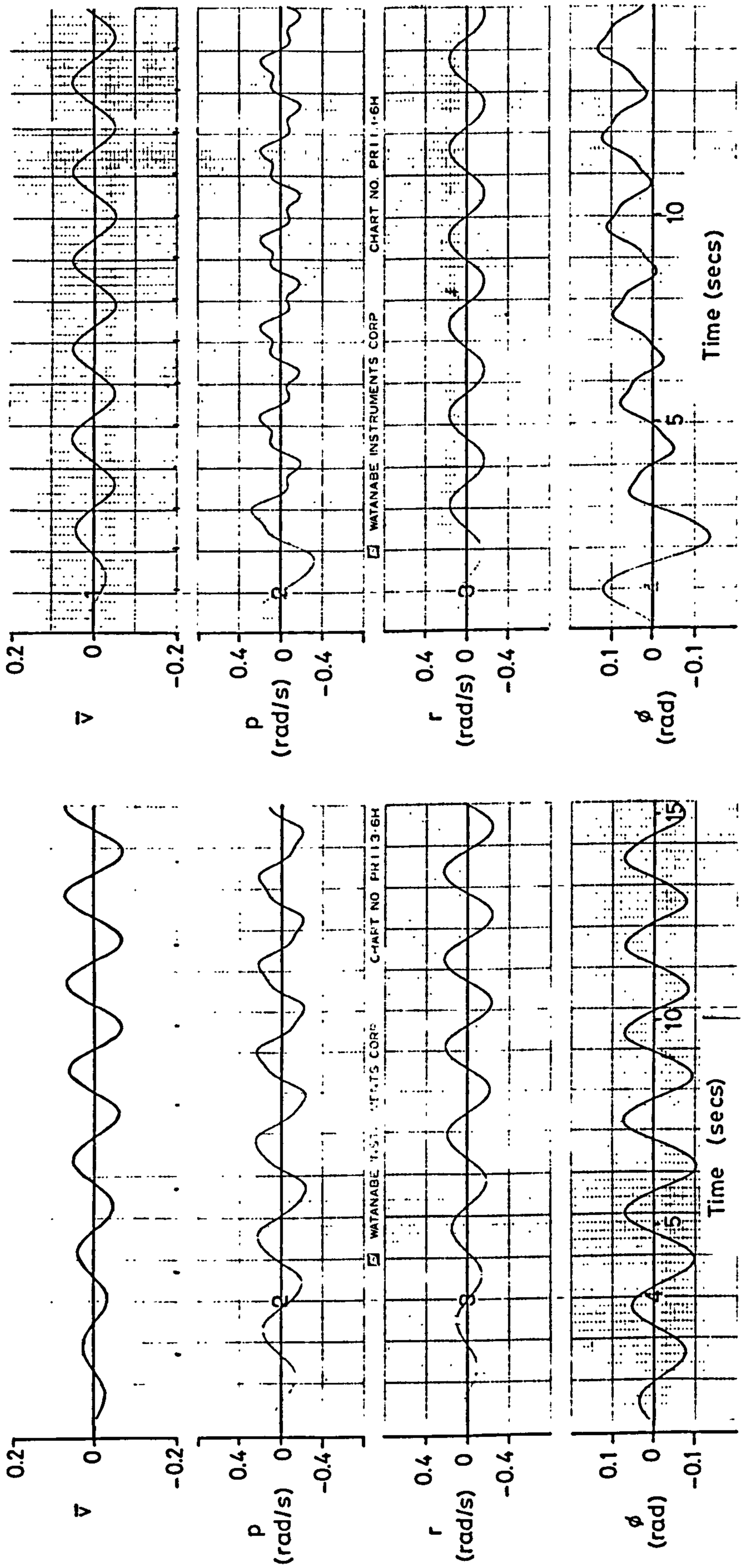

Fig 3.5 Gnat response, Case 5
$\tilde{L}_{v_1}$ increased

Fig 3.6 Gnat response, Case 6
$\tilde{L}_{v_1}$, $|\tilde{L}_{v_3}|$ increased

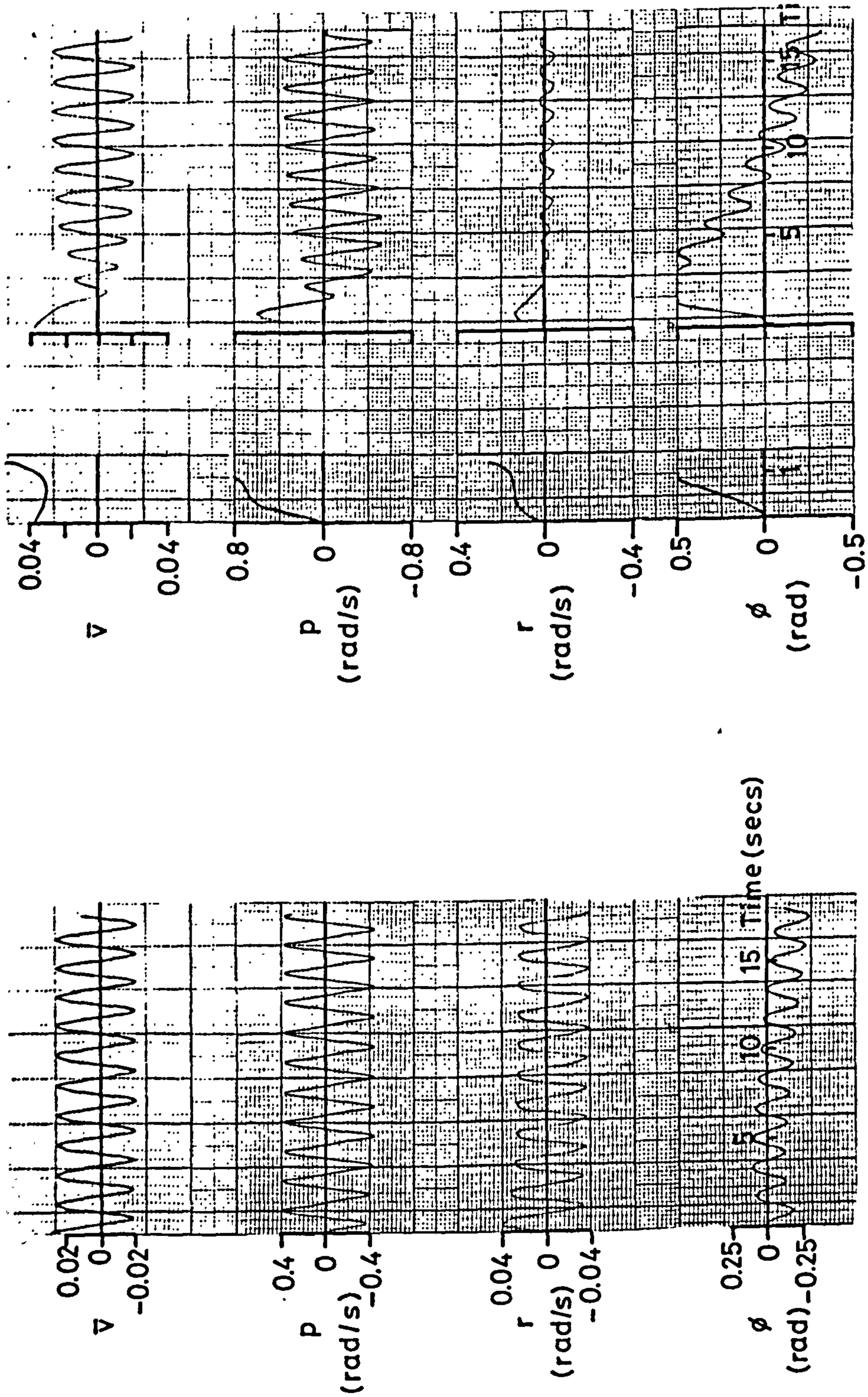

Fig 3.8 Aircraft B critical response with cubic sideslip non-linearity

Fig 3.7 Basic aircraft B response with cubic sideslip non-linearity

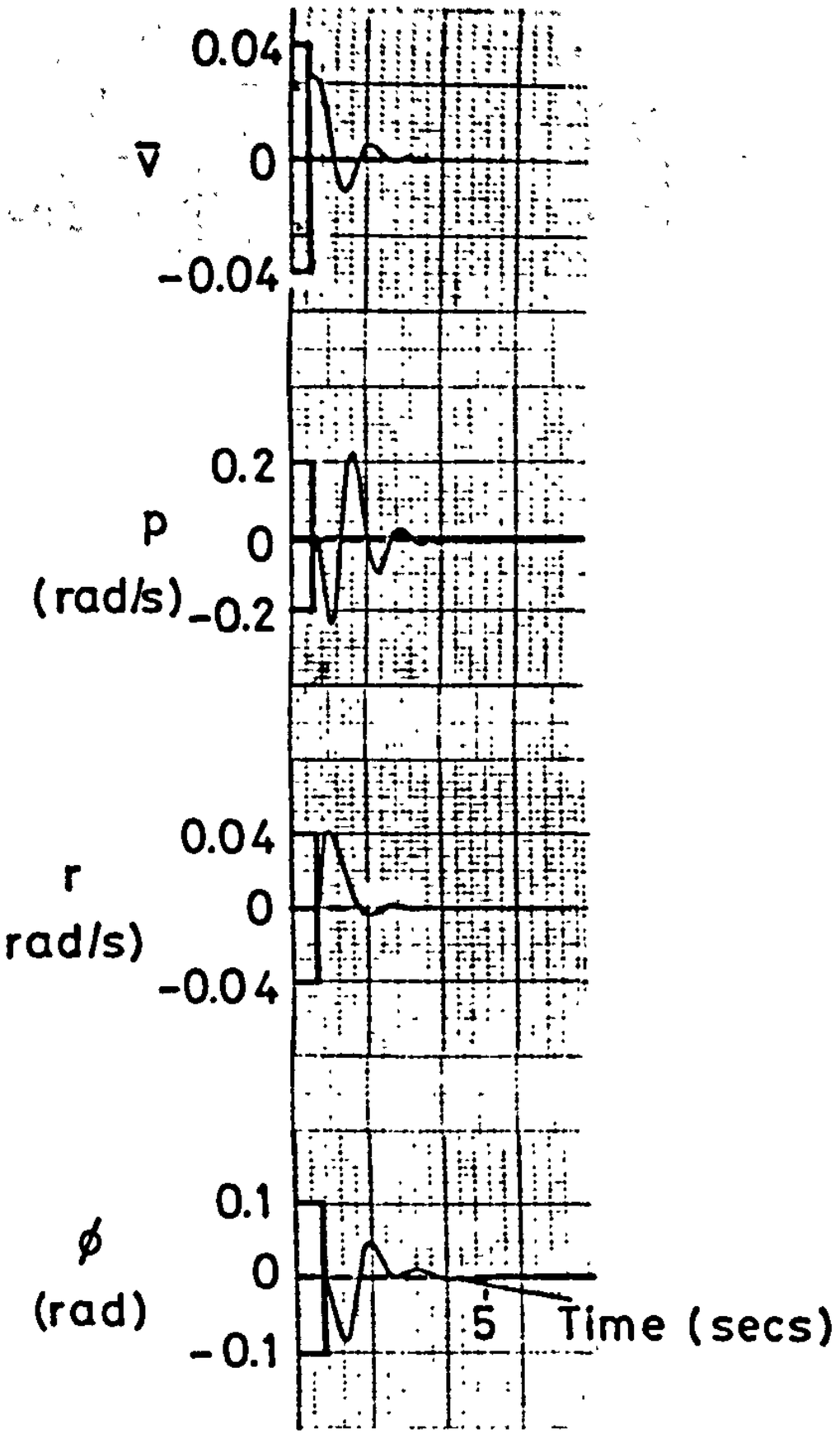

Fig 3.9 Aircraft B damped response with roll damper, $K_{\xi p}$=0.04

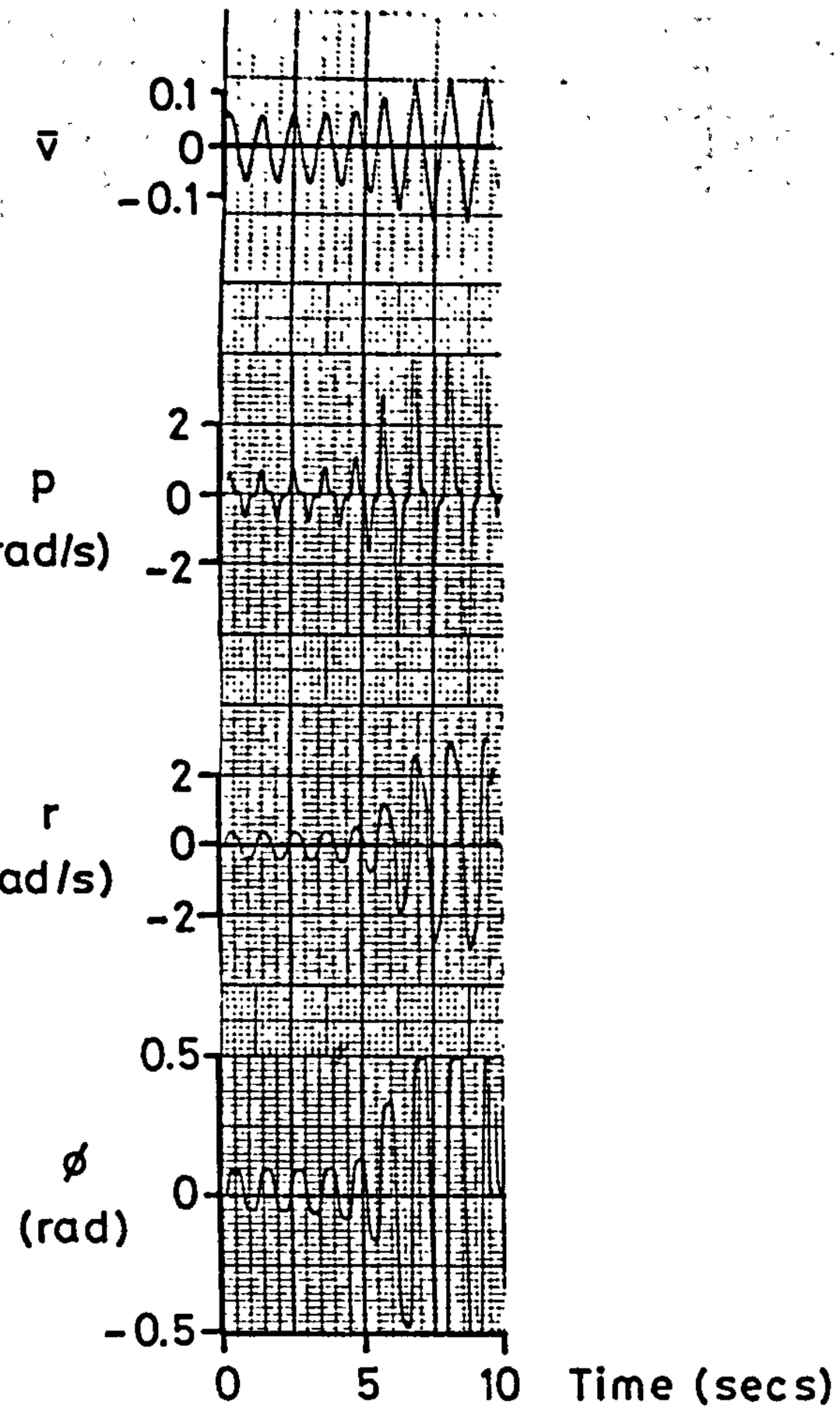

Fig 3.10 Aircraft B oscillatory divergence with roll damper, $K_{\xi p}$= 0.5

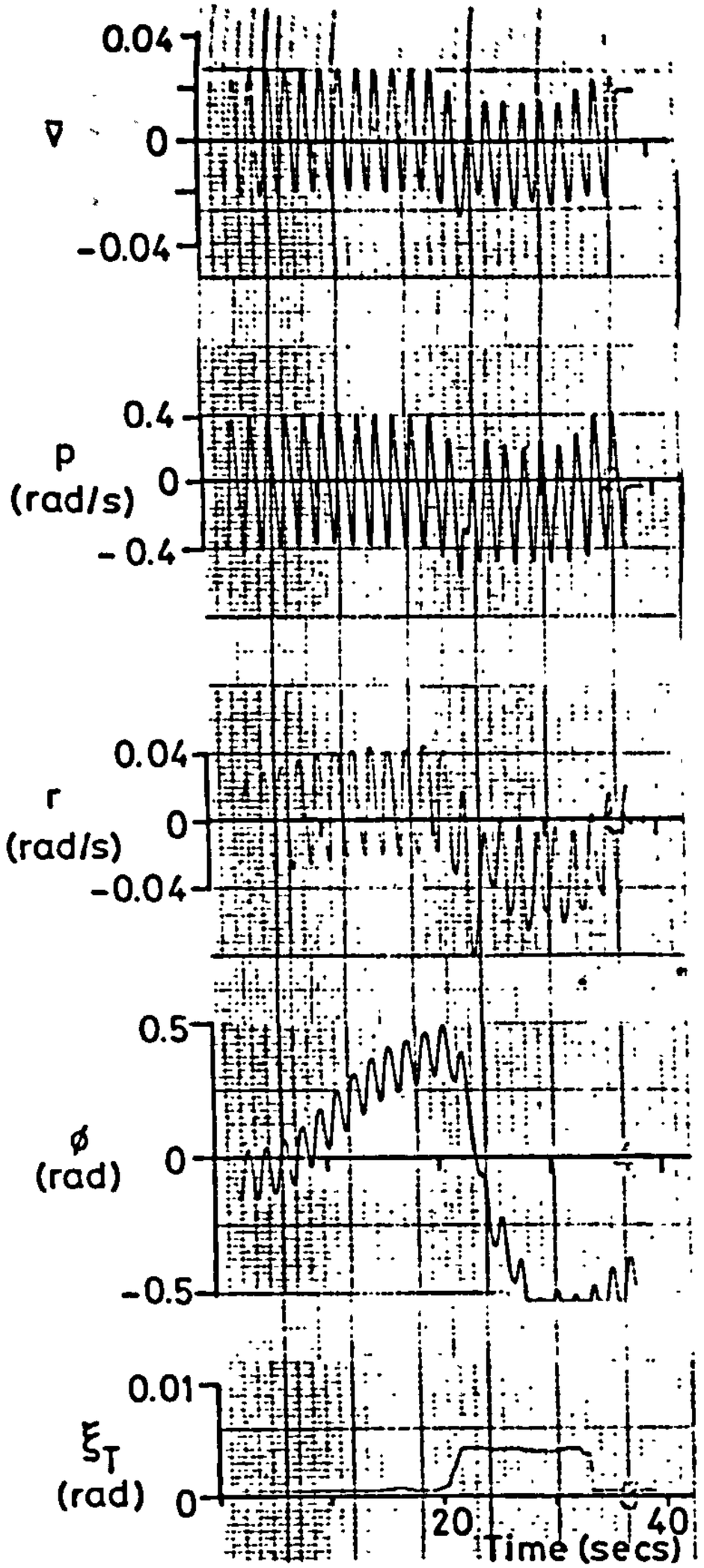

Fig 3.11 Response about non-zero equilibrium state with $K_{\xi p}=0$

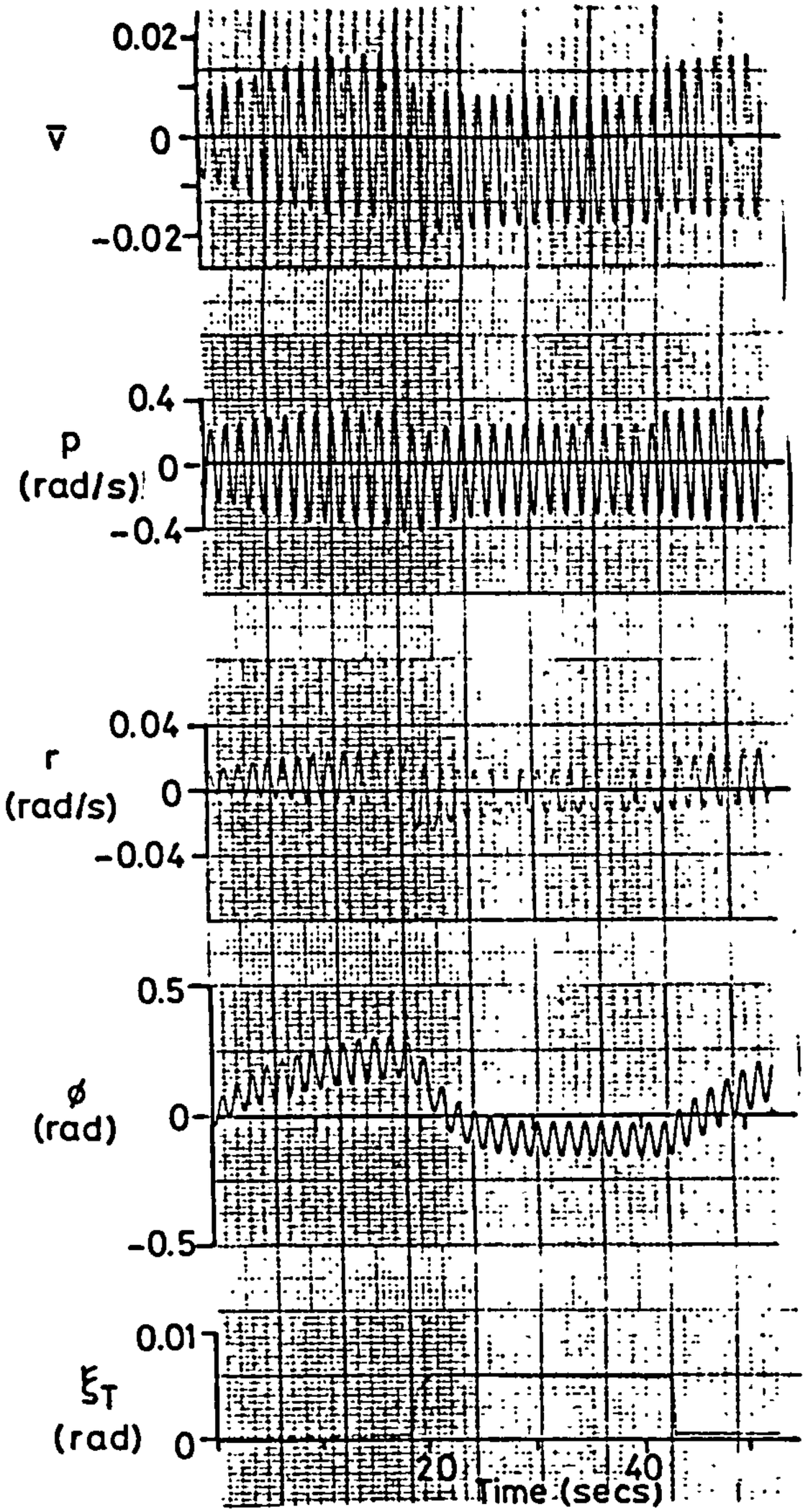

Fig 3.12 Response 1 about non-zero equilibrium state with $K_{\xi p}=0.005$

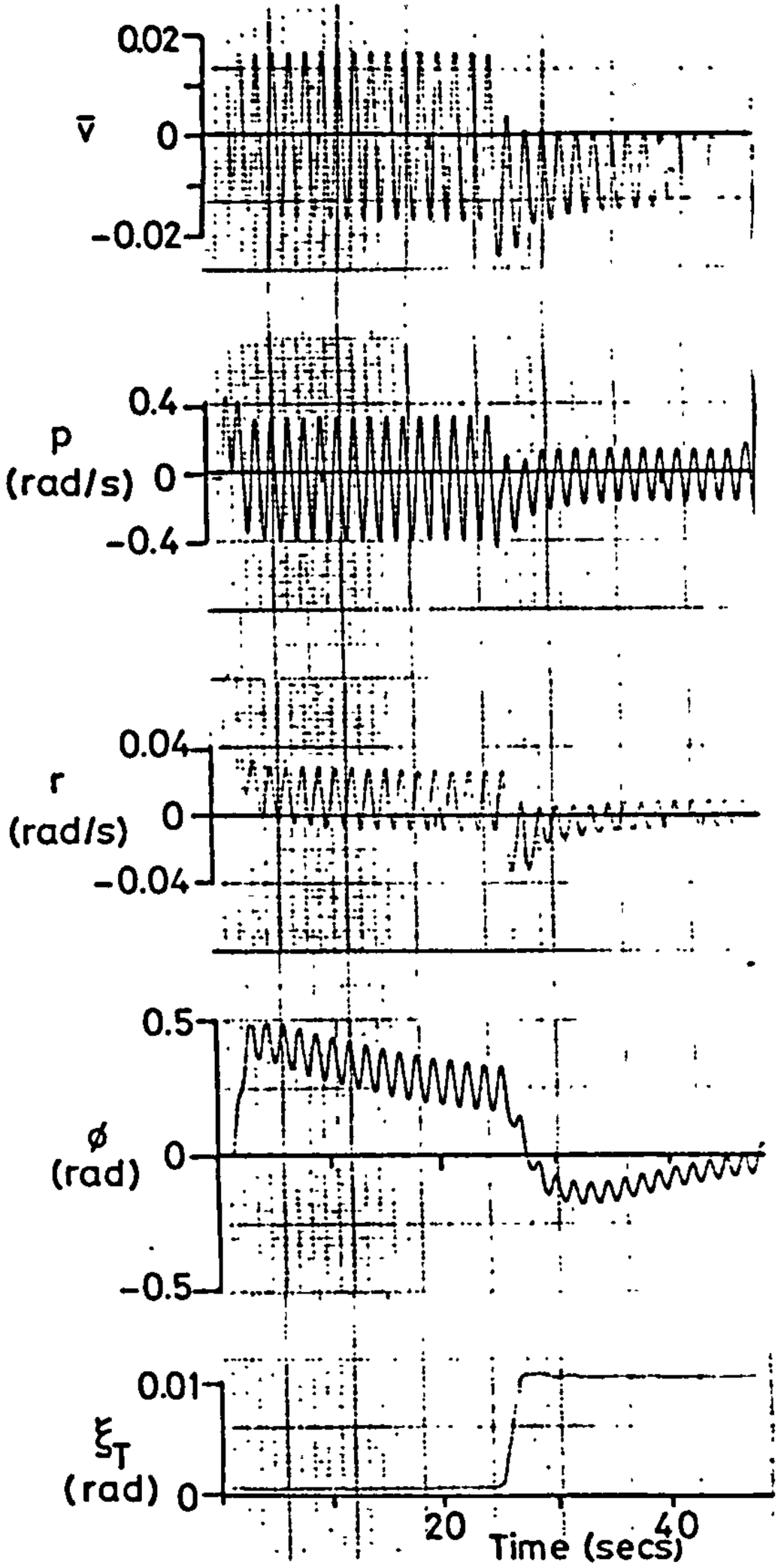

Fig 3.13 Response 2 about non-zero equilibrium state with $K_{\xi p}=0.005$

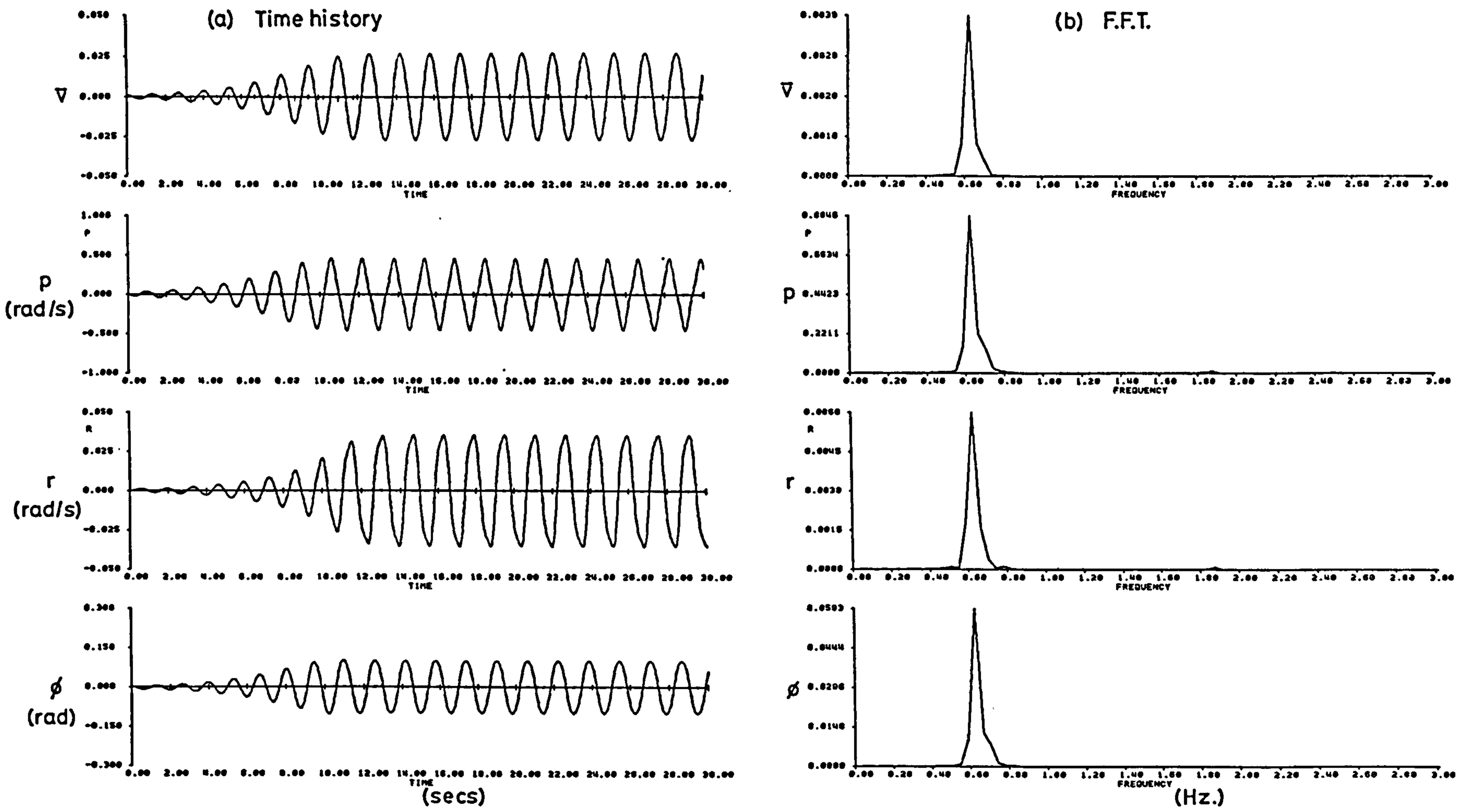

Fig 3.14 Basic aircraft B digital response with cubic sideslip non-linearity

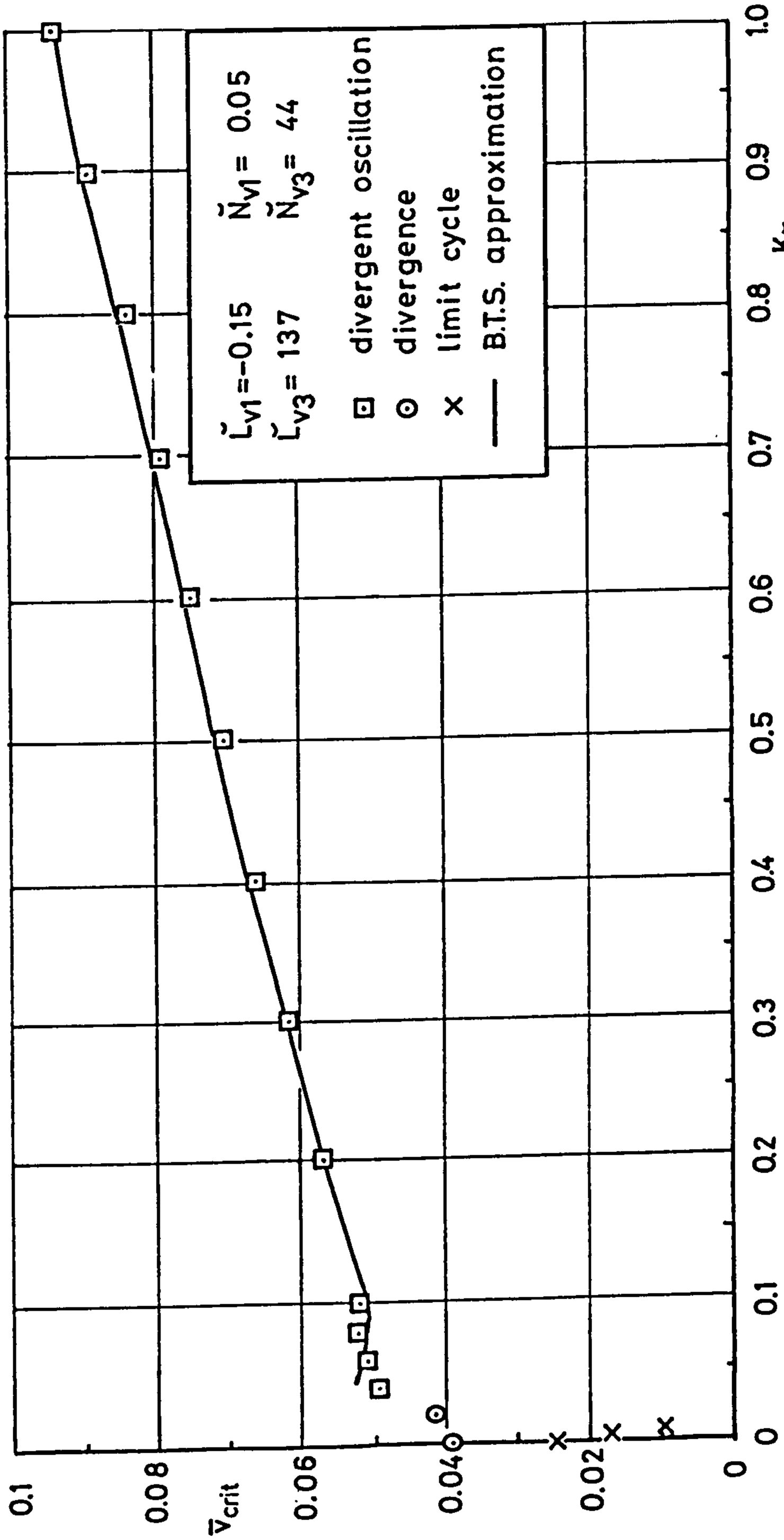

Fig 3.15 Aircraft B. Boundaries for divergent response
(After Ross; Ref.26)

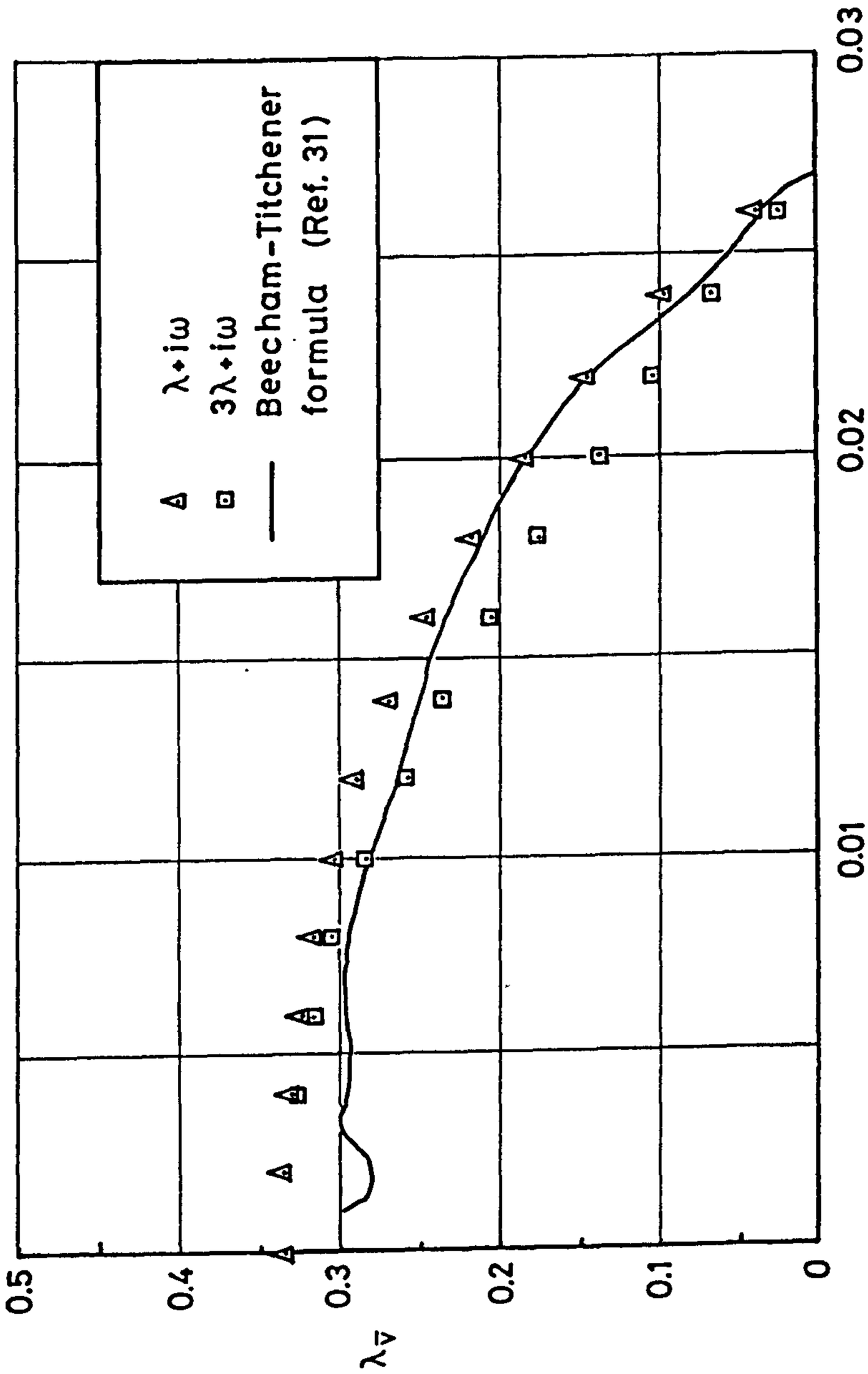

Fig 3.16 Damping factor for response with sideslip non-linearity

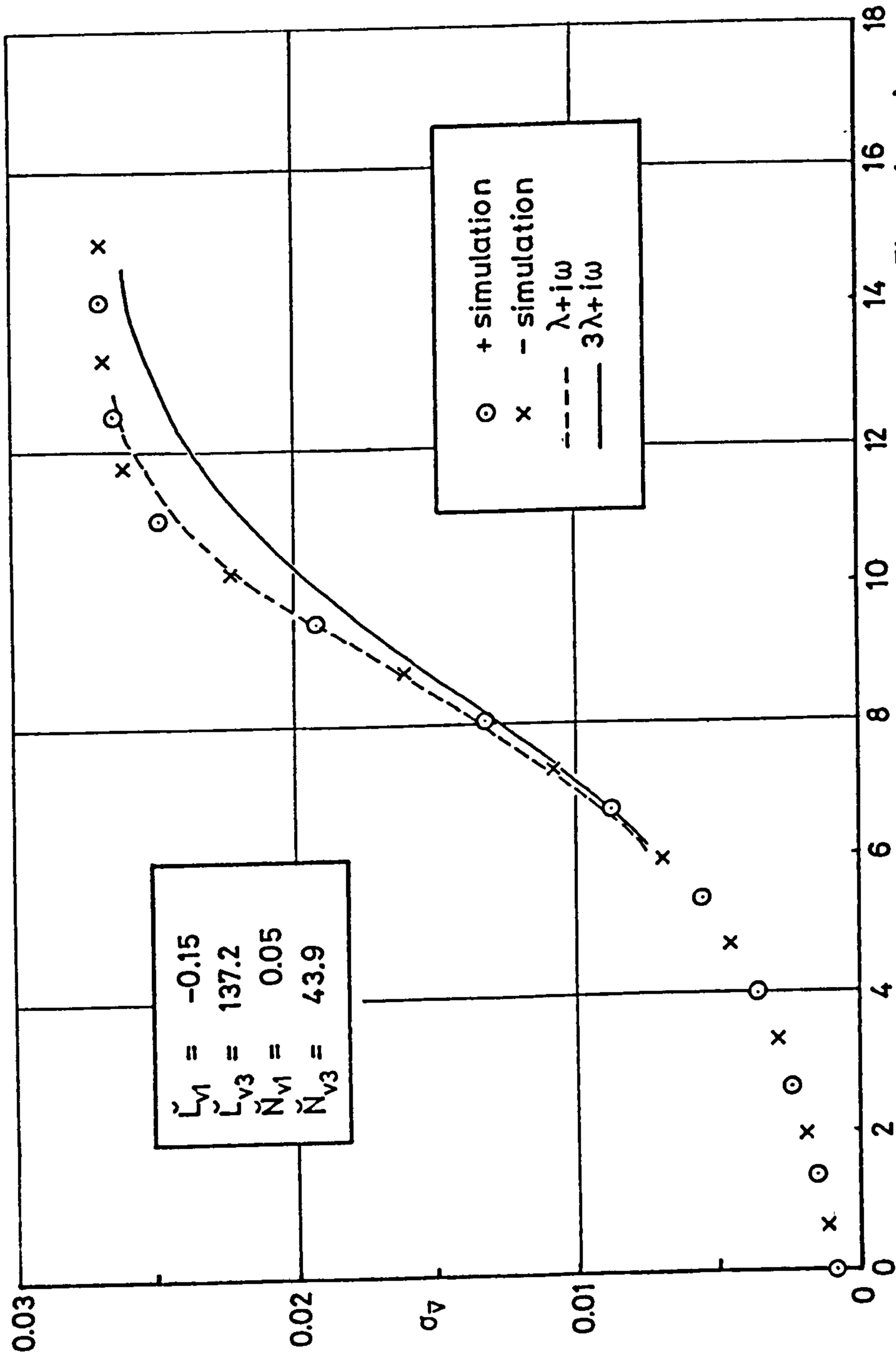

Fig 3.17 Rate of growth to limit cycle with sideslip non-linearity

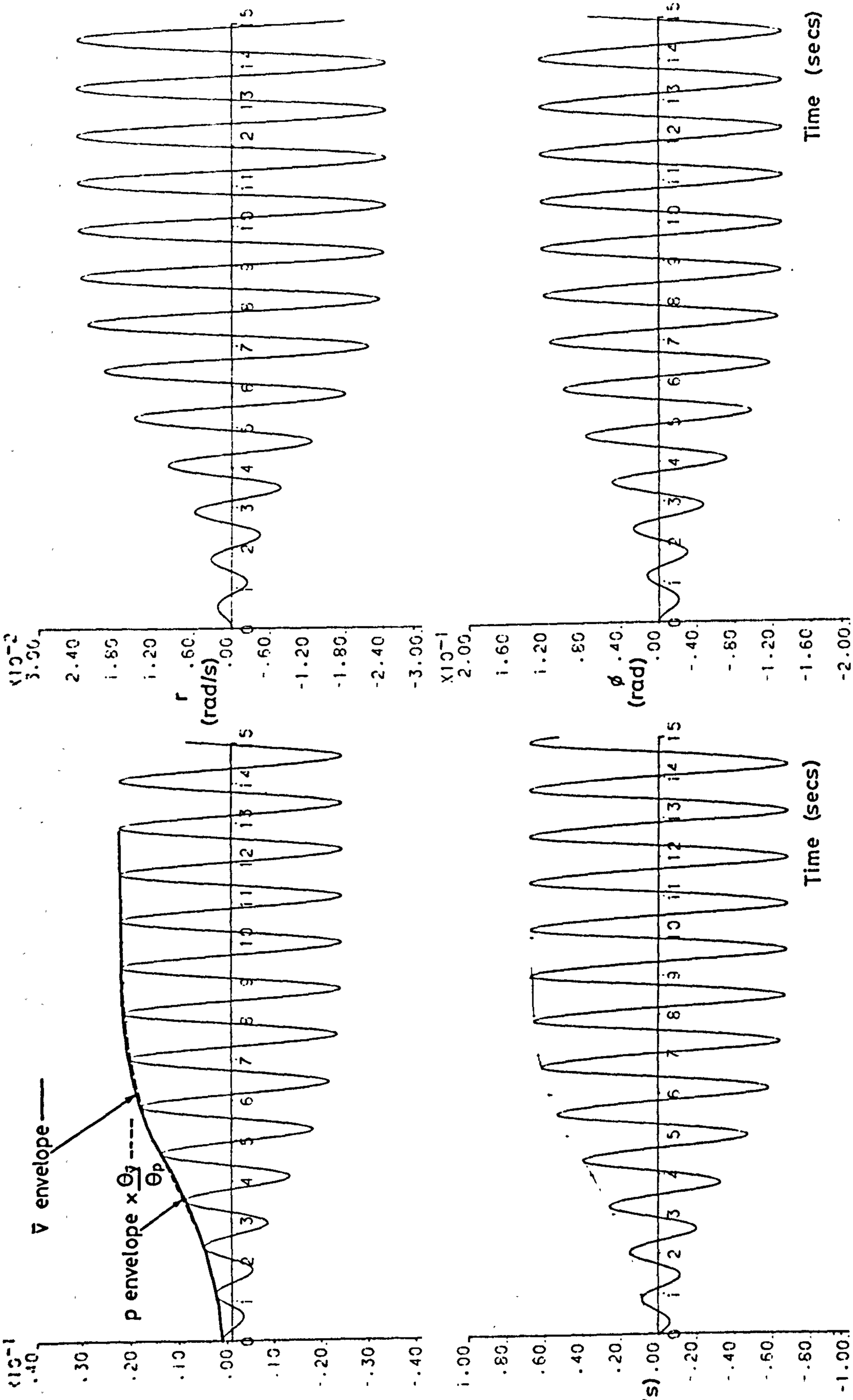

Fig 3.18 Response with non-linearity in roll rate, aircraft B. Case 2

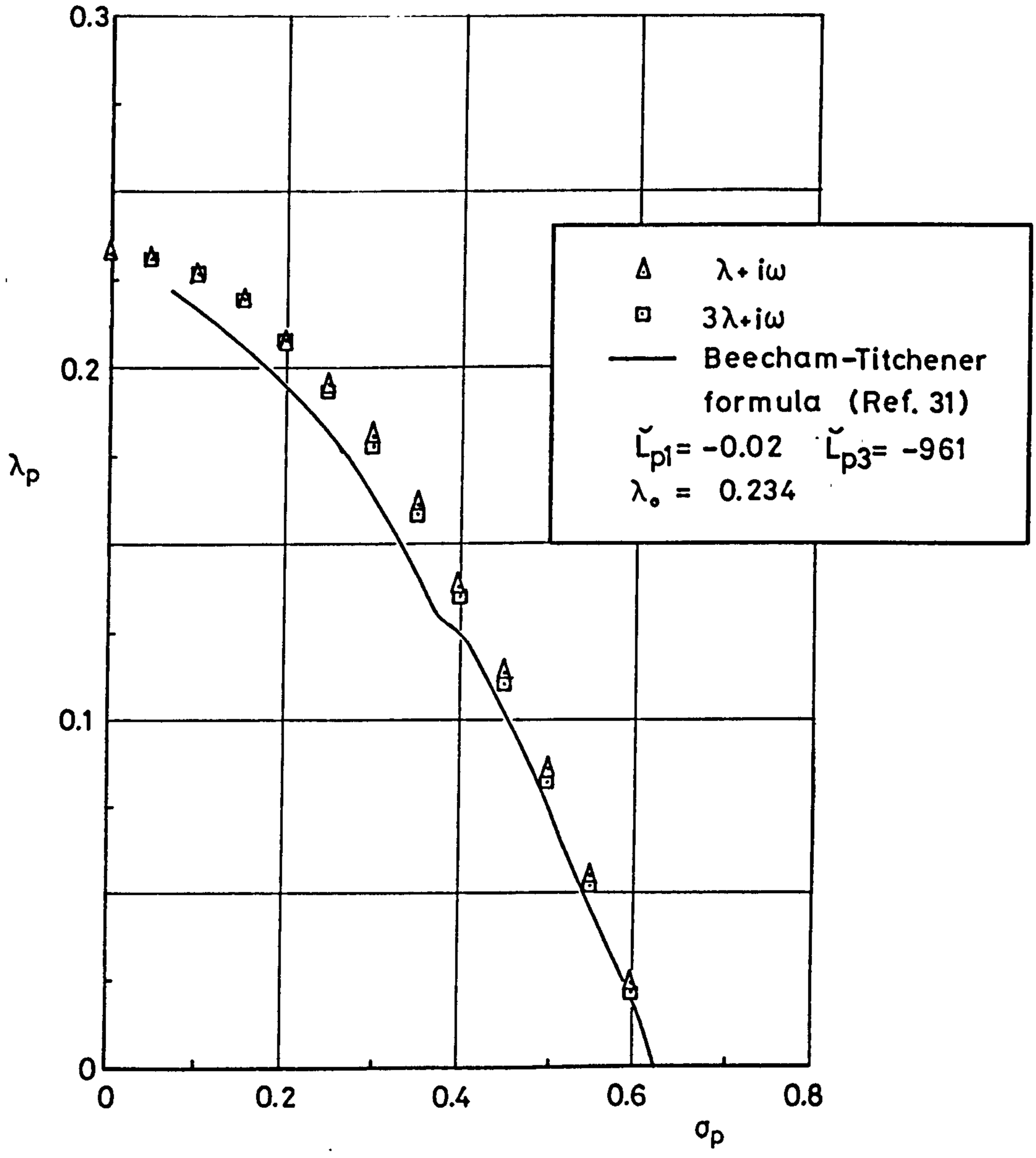

Fig 3.19 Damping factor for response with roll rate non-linearity. Case 1

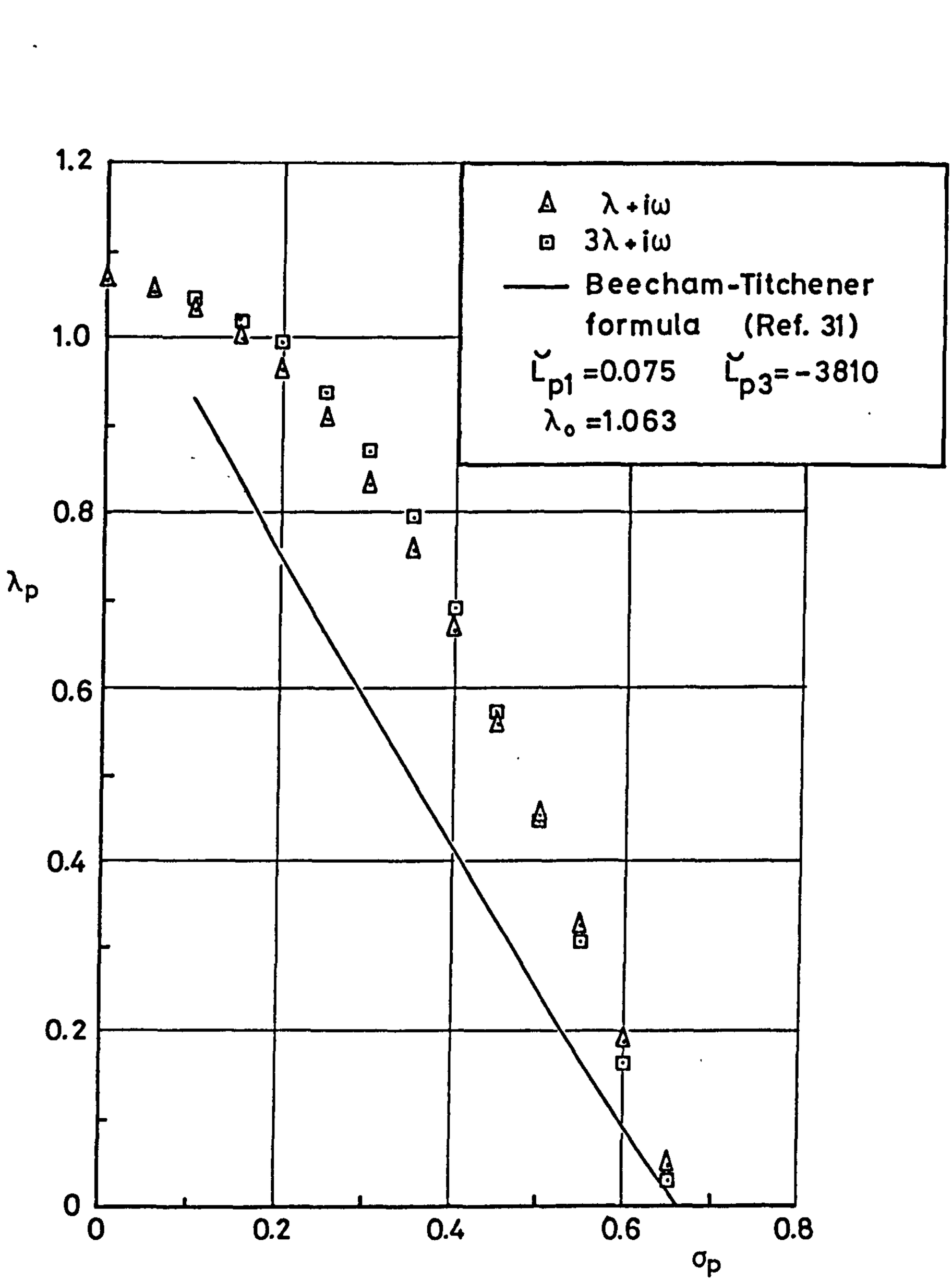

Fig 3.20 Damping factor for response with roll rate non-linearity. Case 3

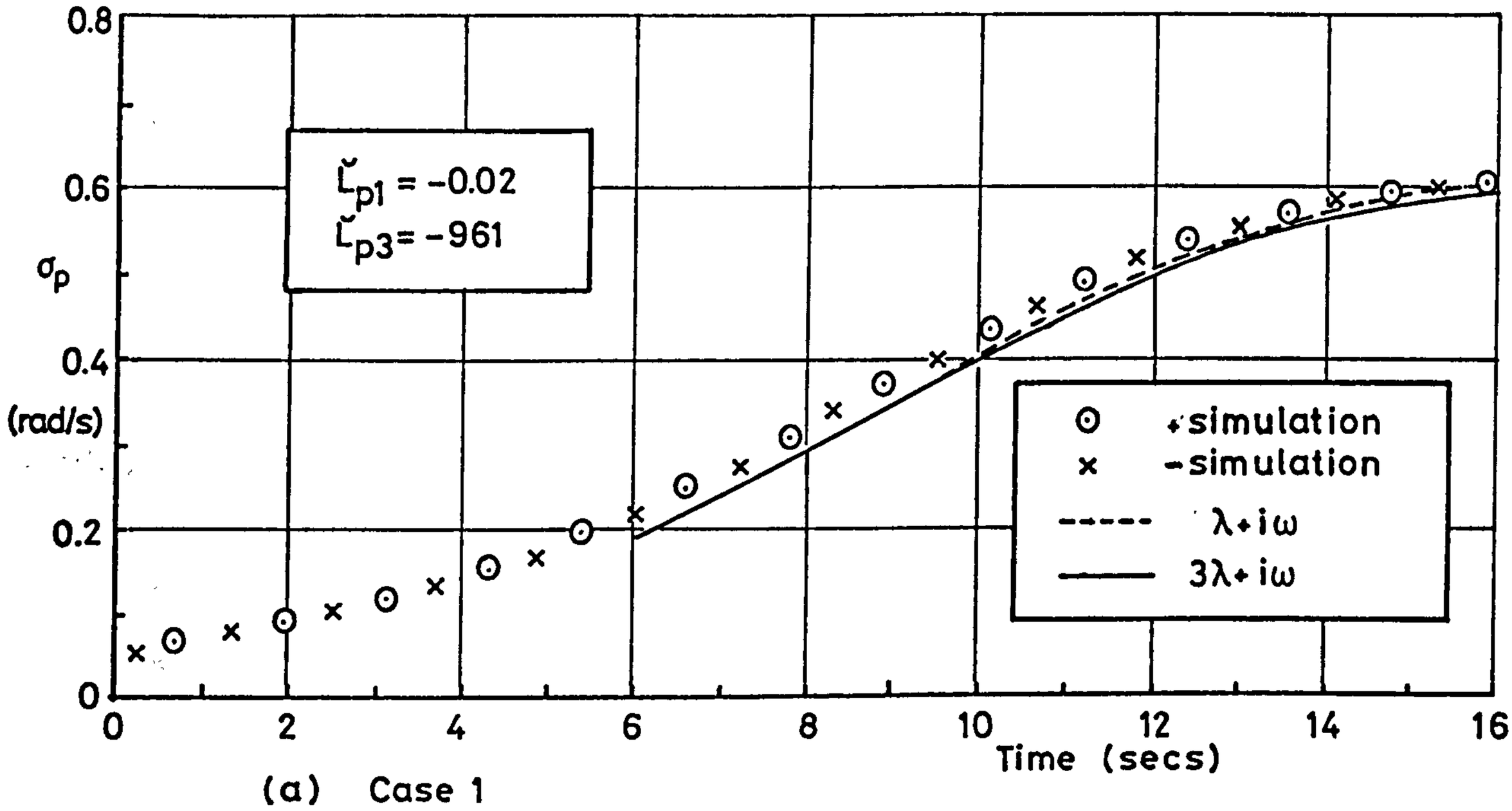

(a) Case 1

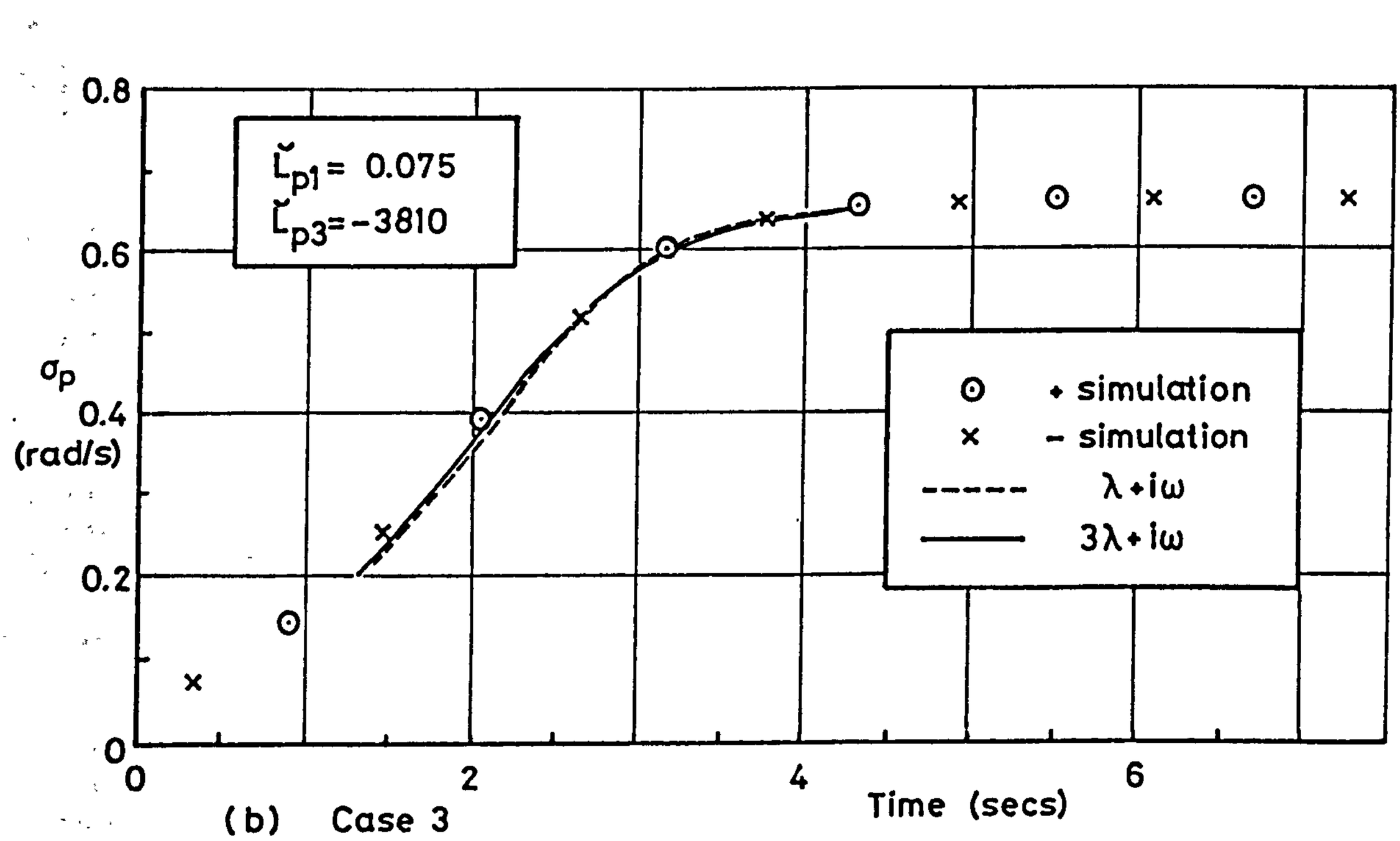

(b) Case 3

Fig 3.21 Rate of growth to limit cycle with roll rate non-linearity

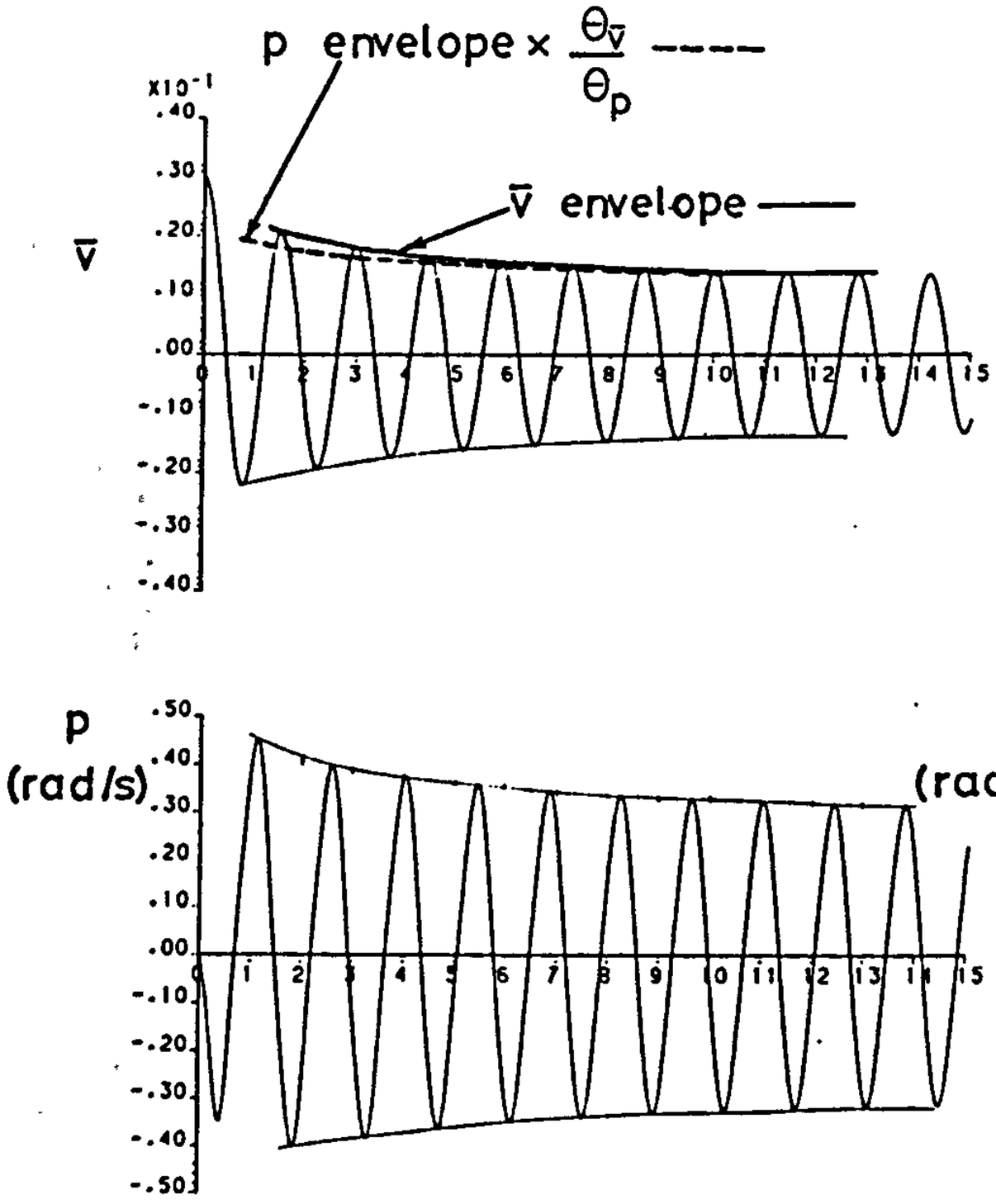

Fig 3.22 Response with sideslip and roll rate non-linearities. Case 1b

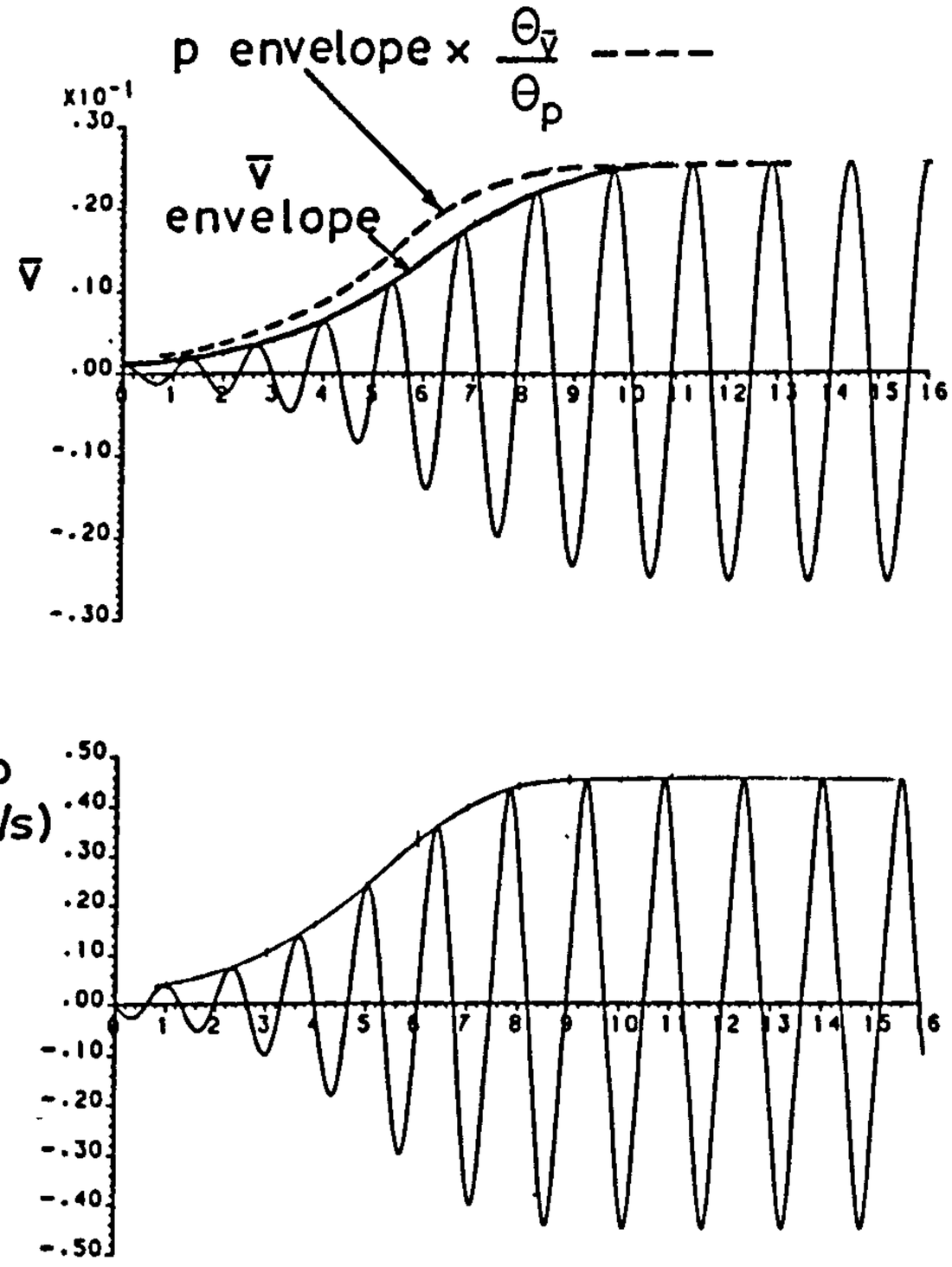

Fig 3.23 Response with sideslip and roll rate non-linearities. Case 2b

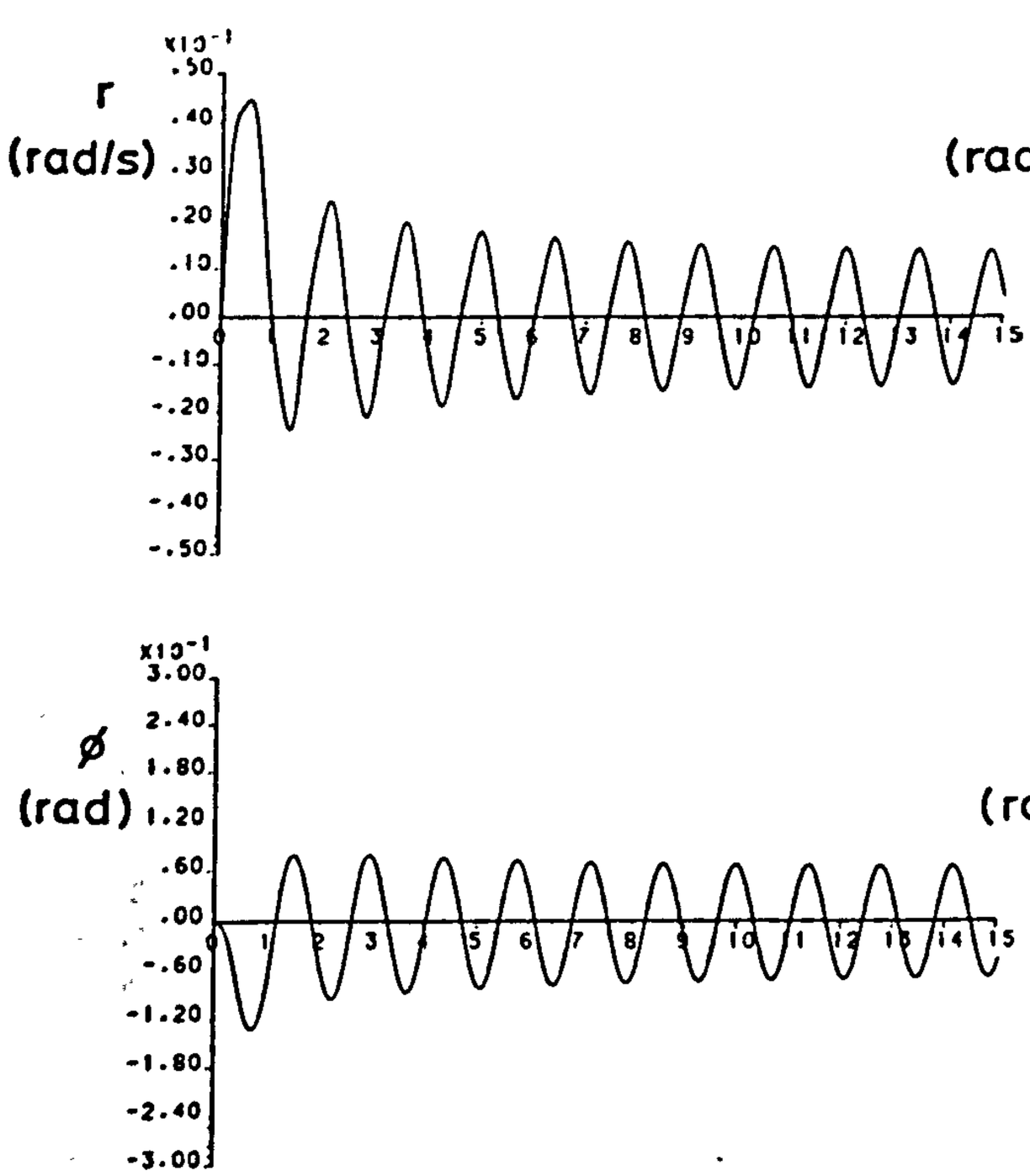

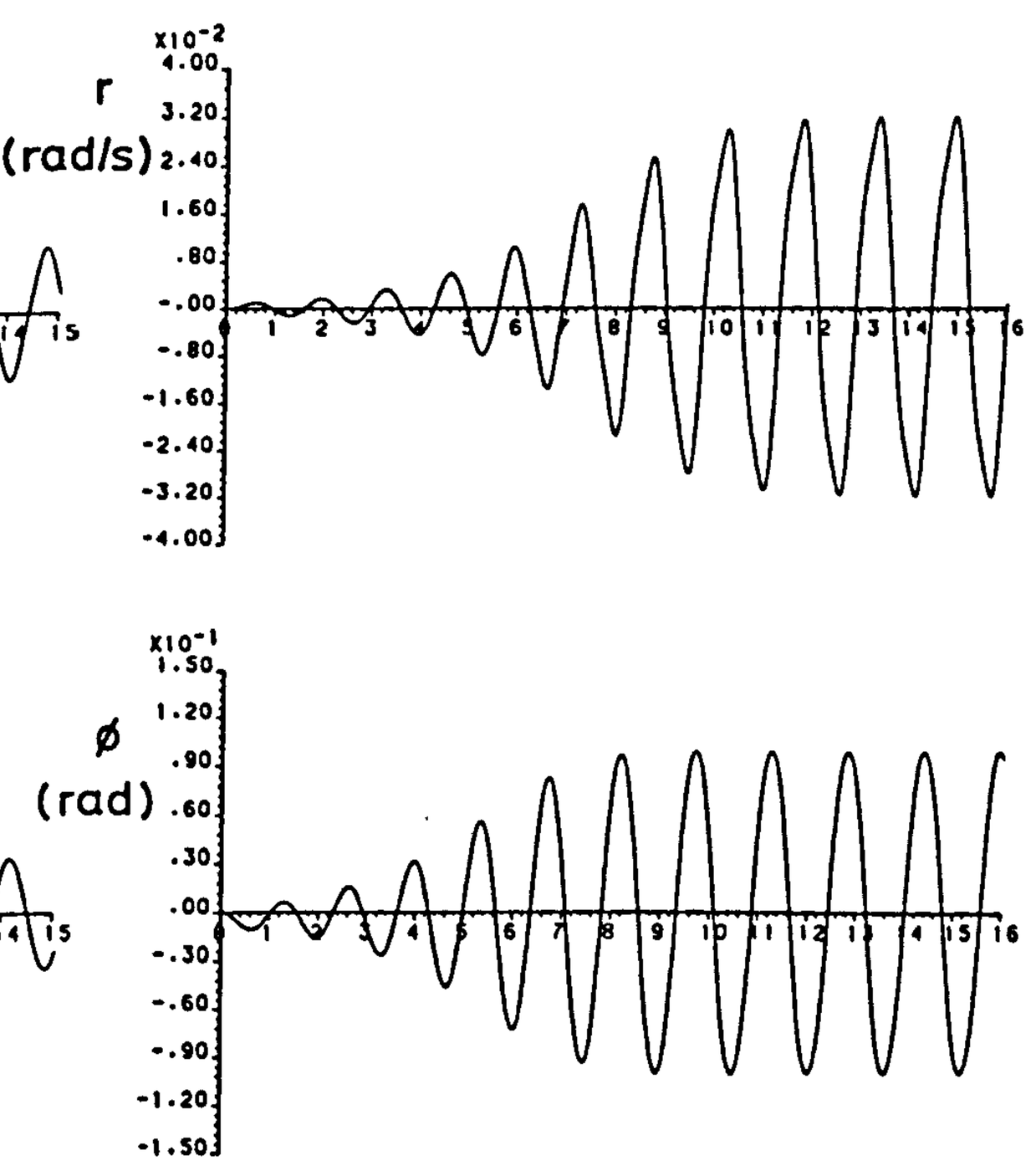

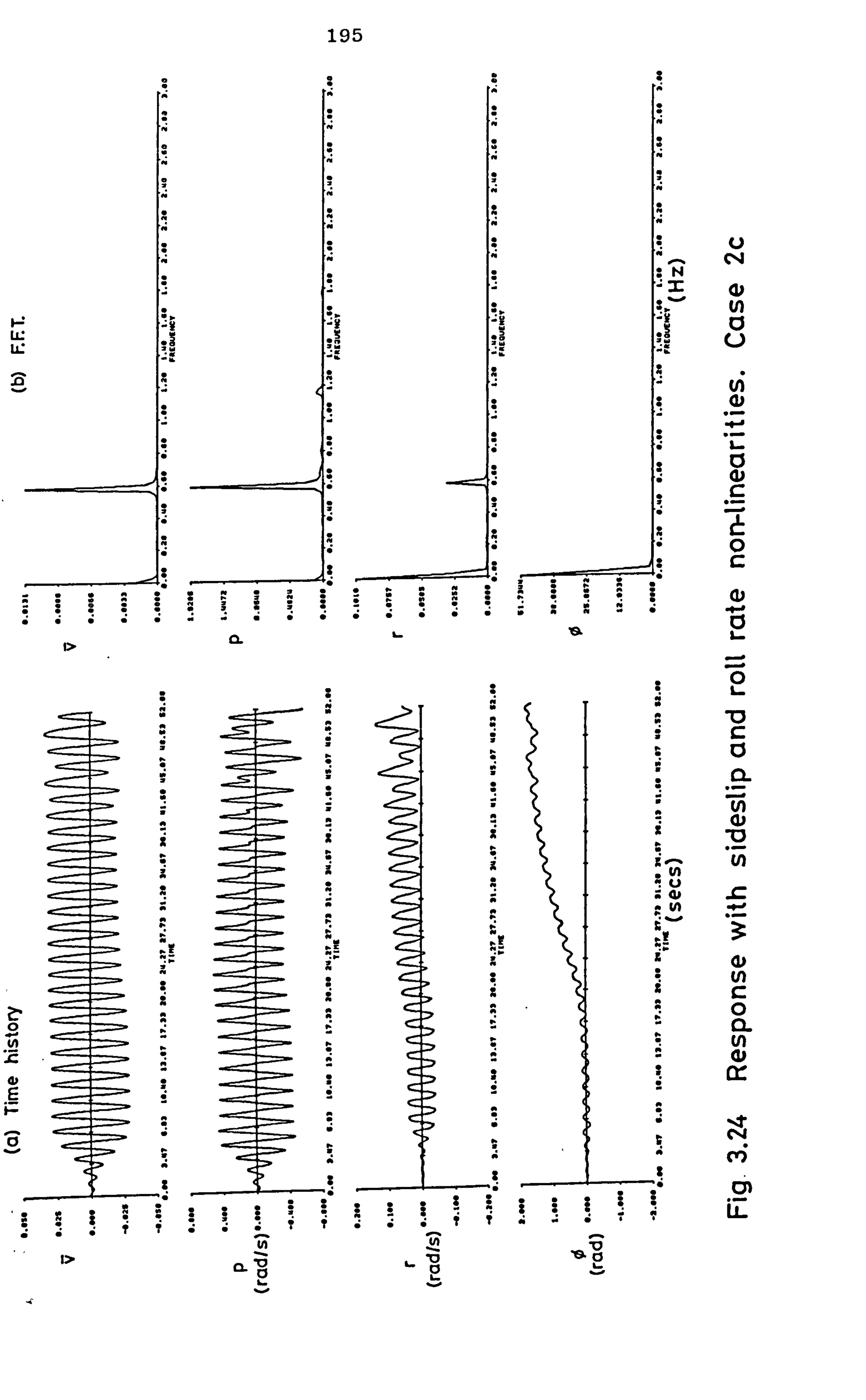

Fig. 3.24 Response with sideslip and roll rate non-linearities. Case 2c

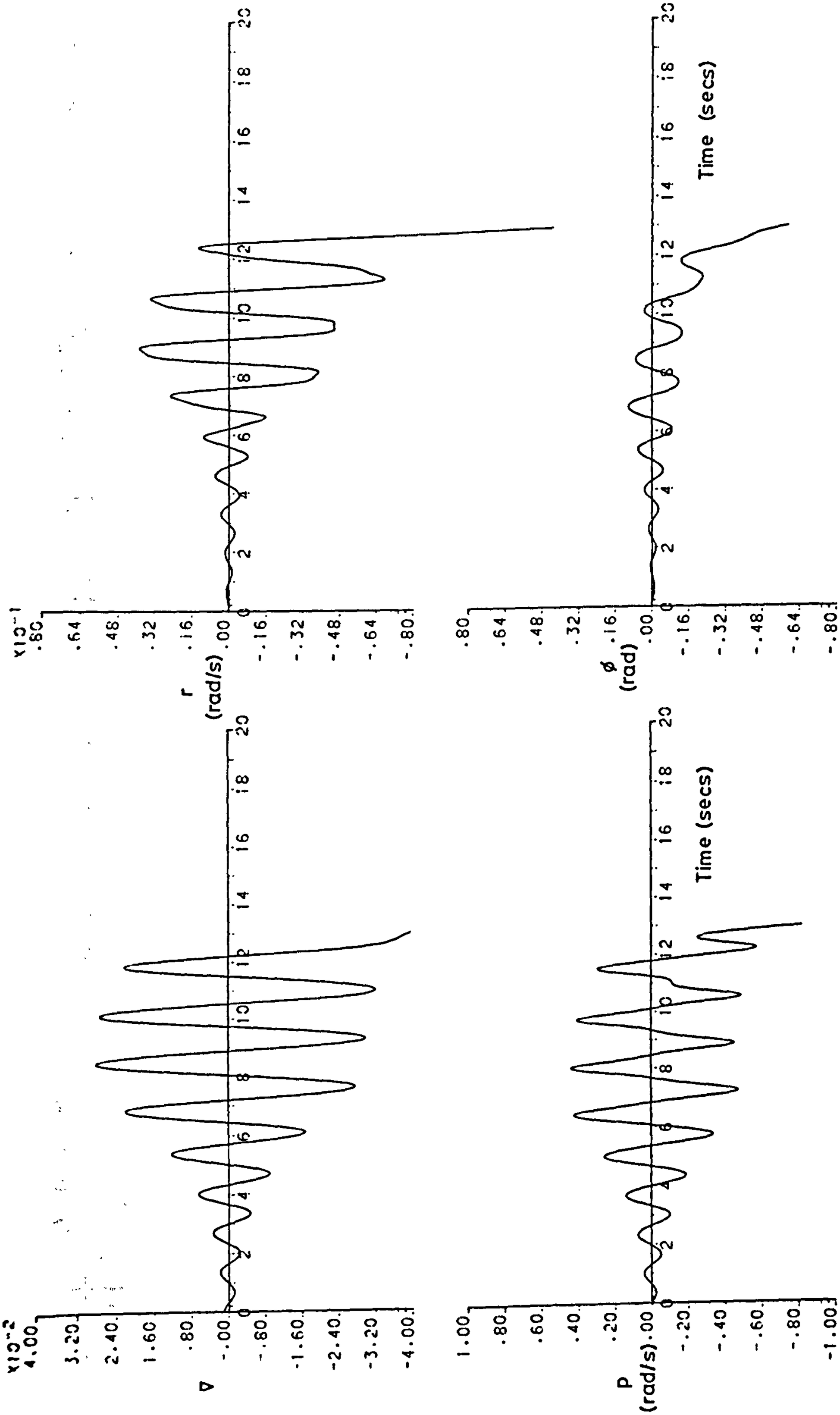

Fig 3.25 Response with sideslip non-linearity and destabilising $\check{L}_{p1}$ alone.
Case 2a

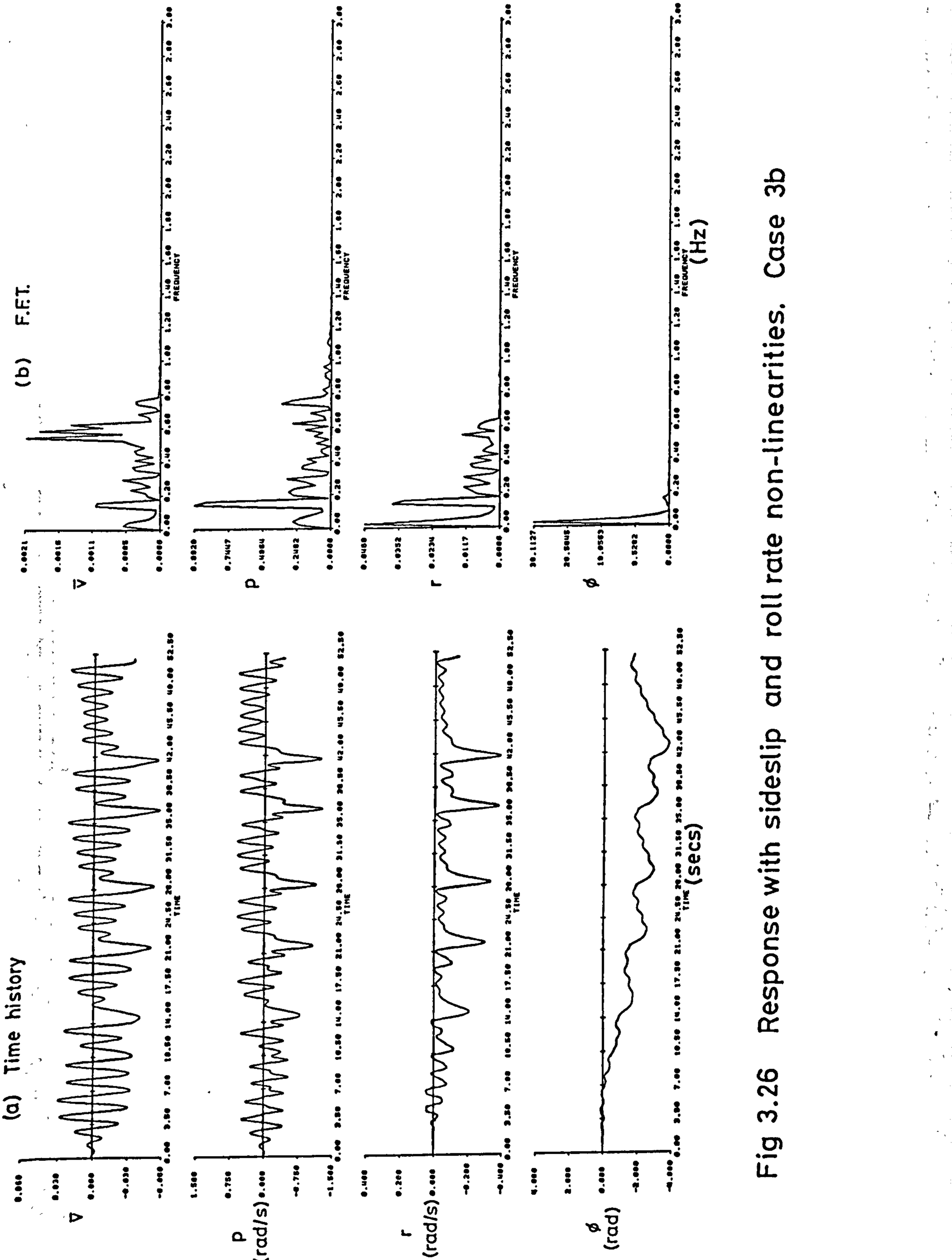

Fig 3.26 Response with sideslip and roll rate non-linearities, Case 3b

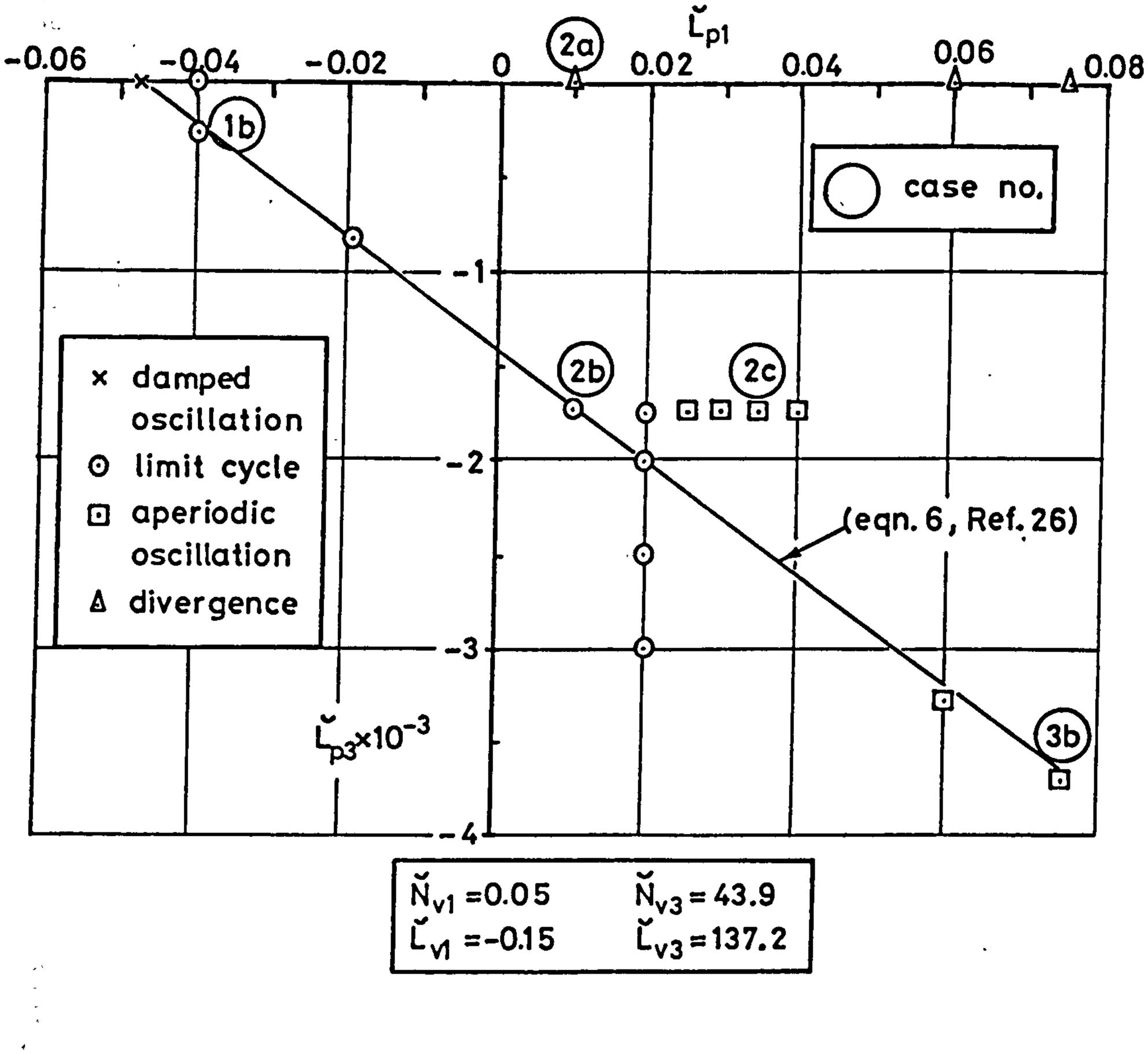

Fig 3.27 Characteristics of responses with sideslip and roll rate non-linearities

Effect of omitting gravity term on response. Case 3b

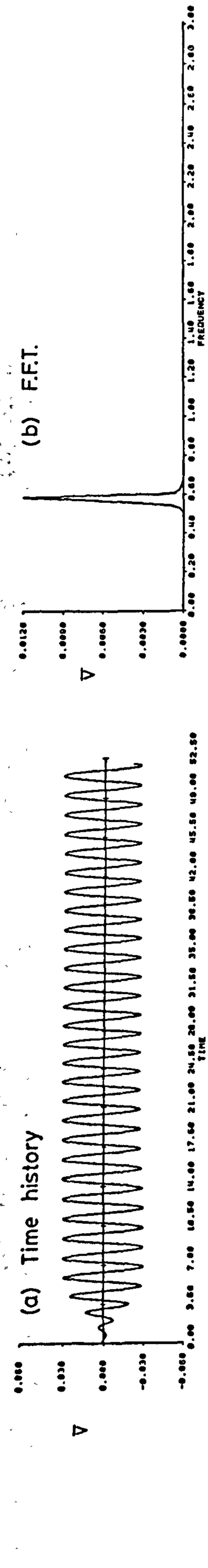

Fig 3.28

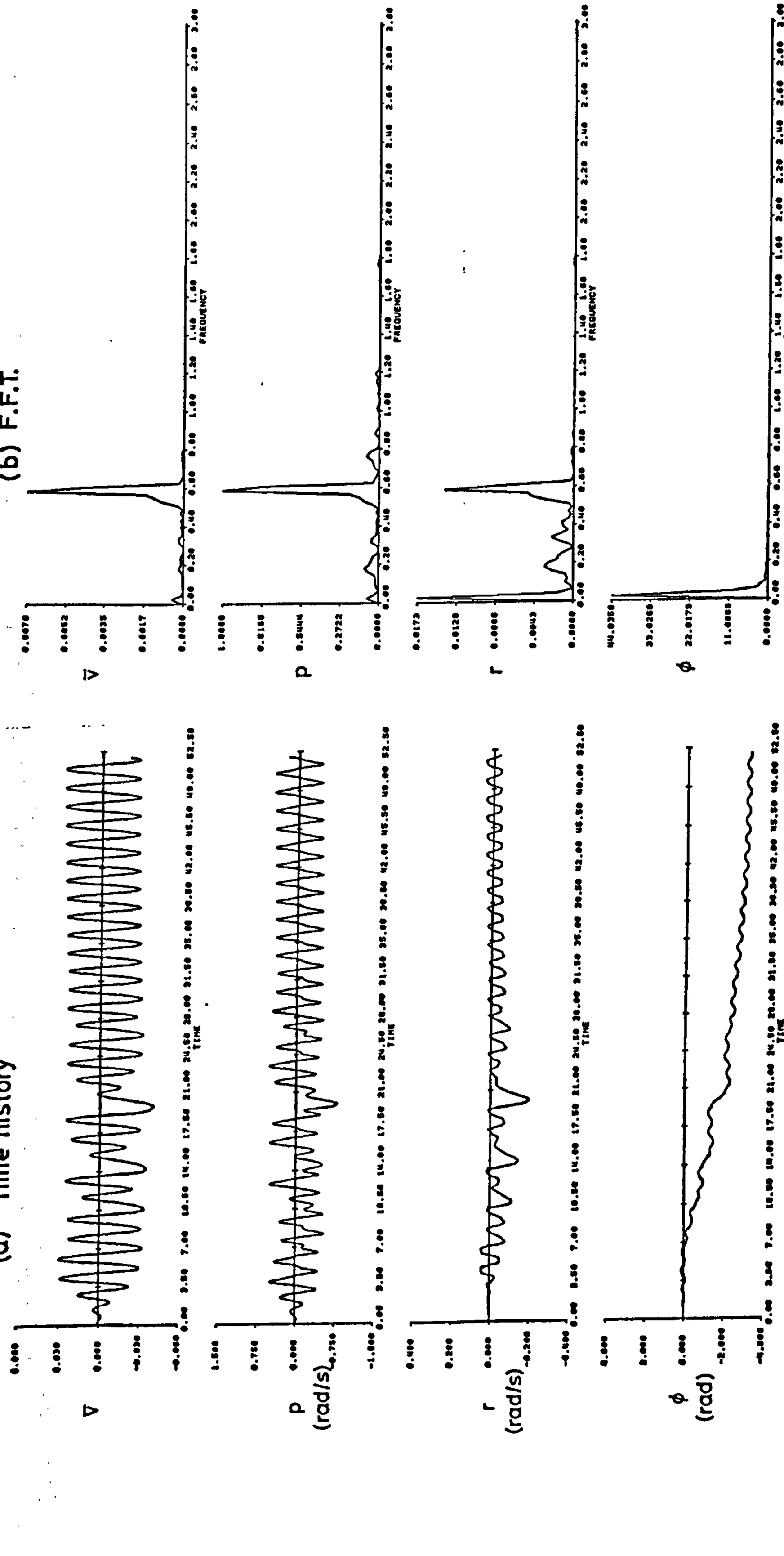

Case 3b

Fig 3.29 Effect of gsinφ gravity term on response. Case 3b

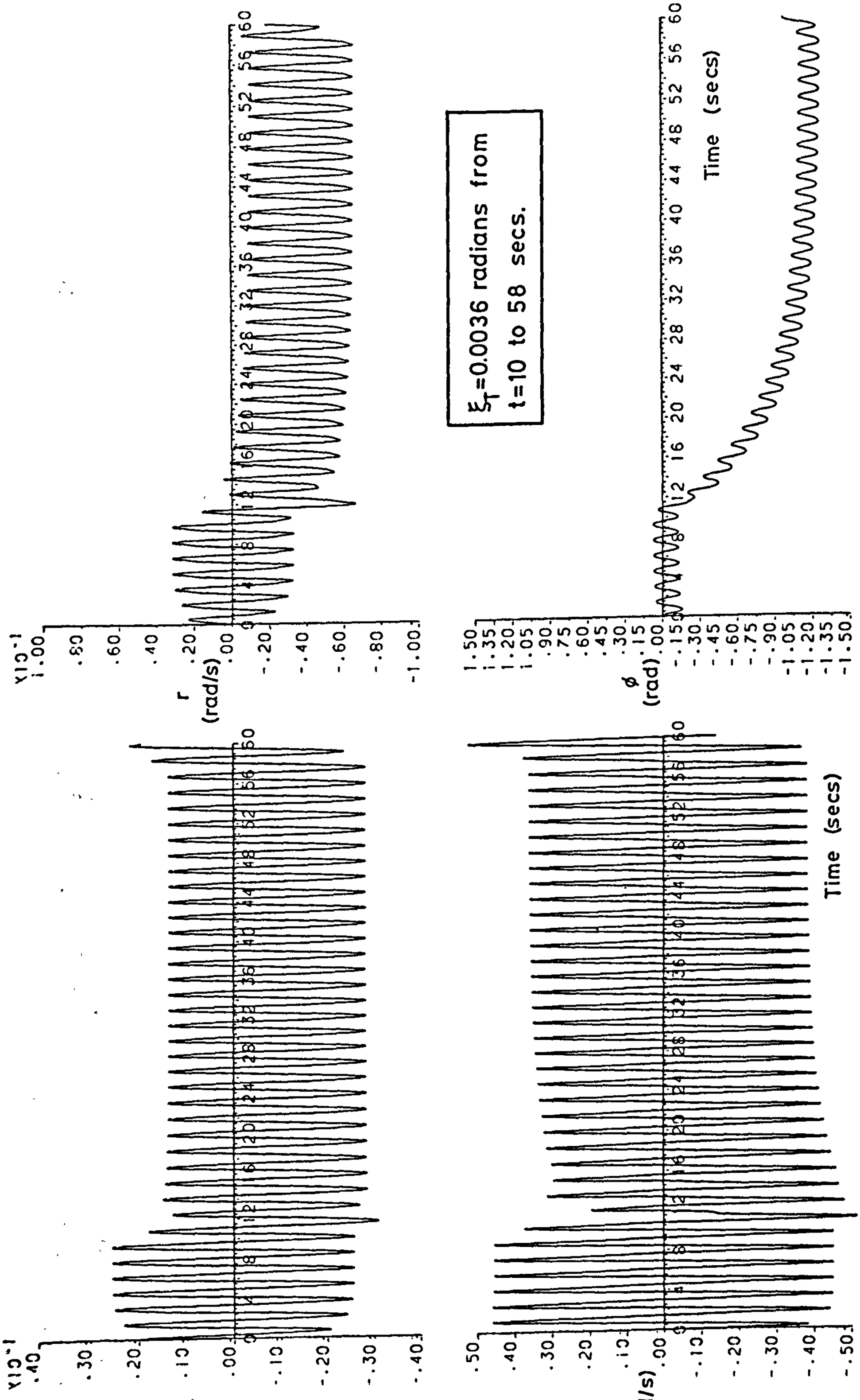

Fig 3.30 Digital response about non-zero equilibrium state with

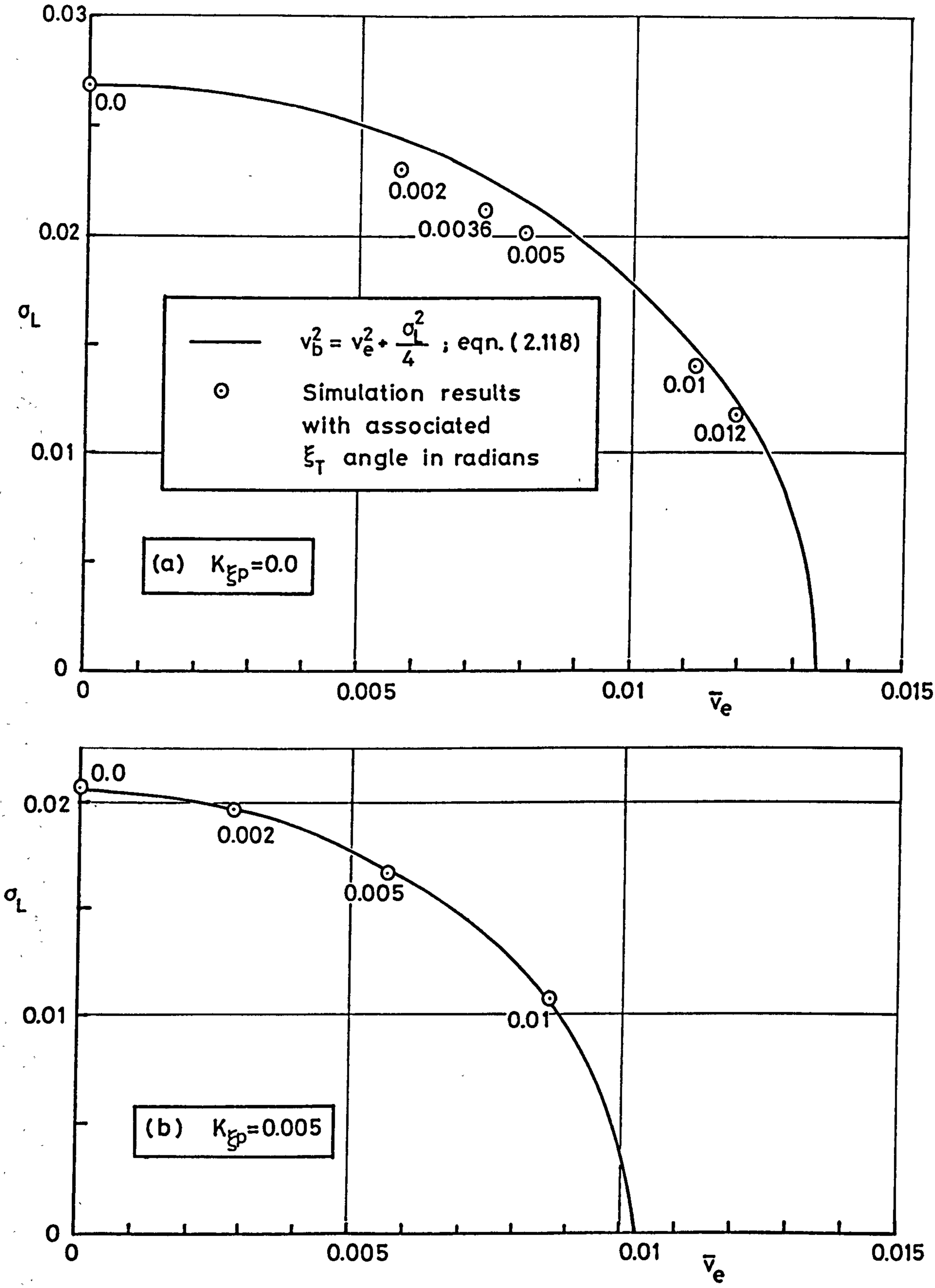

Fig 3.31 Limit cycle responses about non-zero equilibrium states

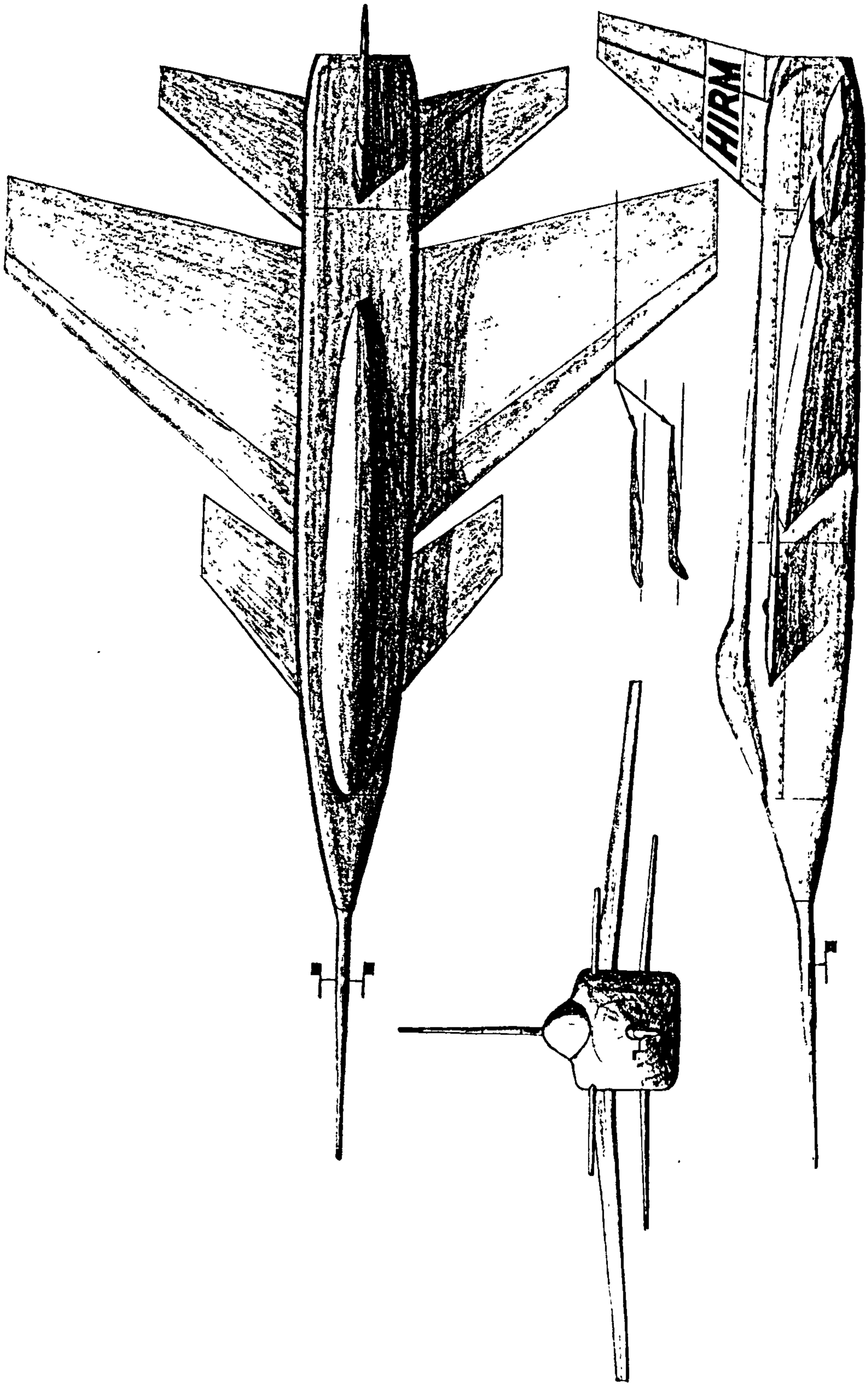

Fig 4.1 The High Incidence Research Model (HIRM)

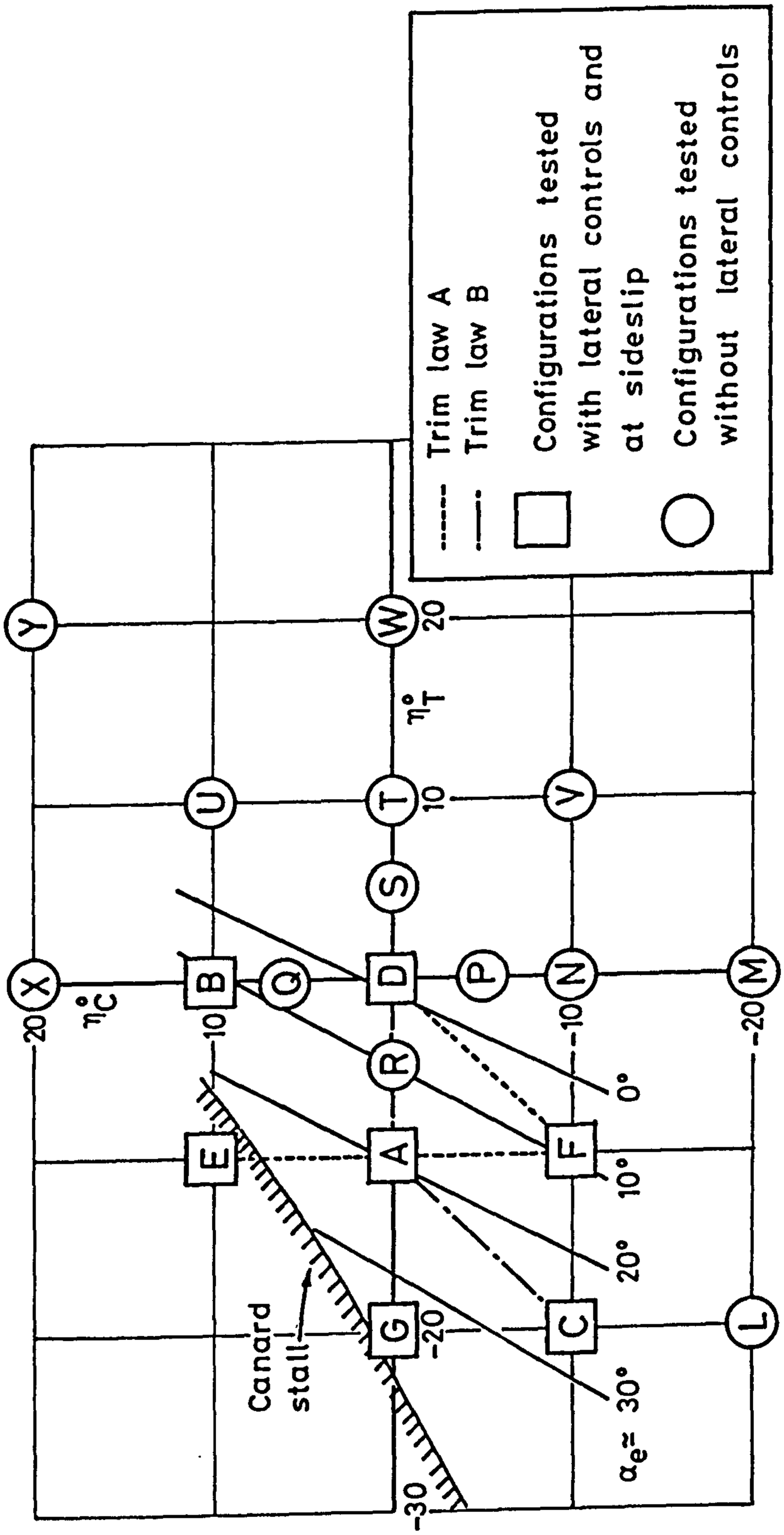

Fig 4.2 HIRM configuration nomenclature
(After Ross and Reid; Ref.90)

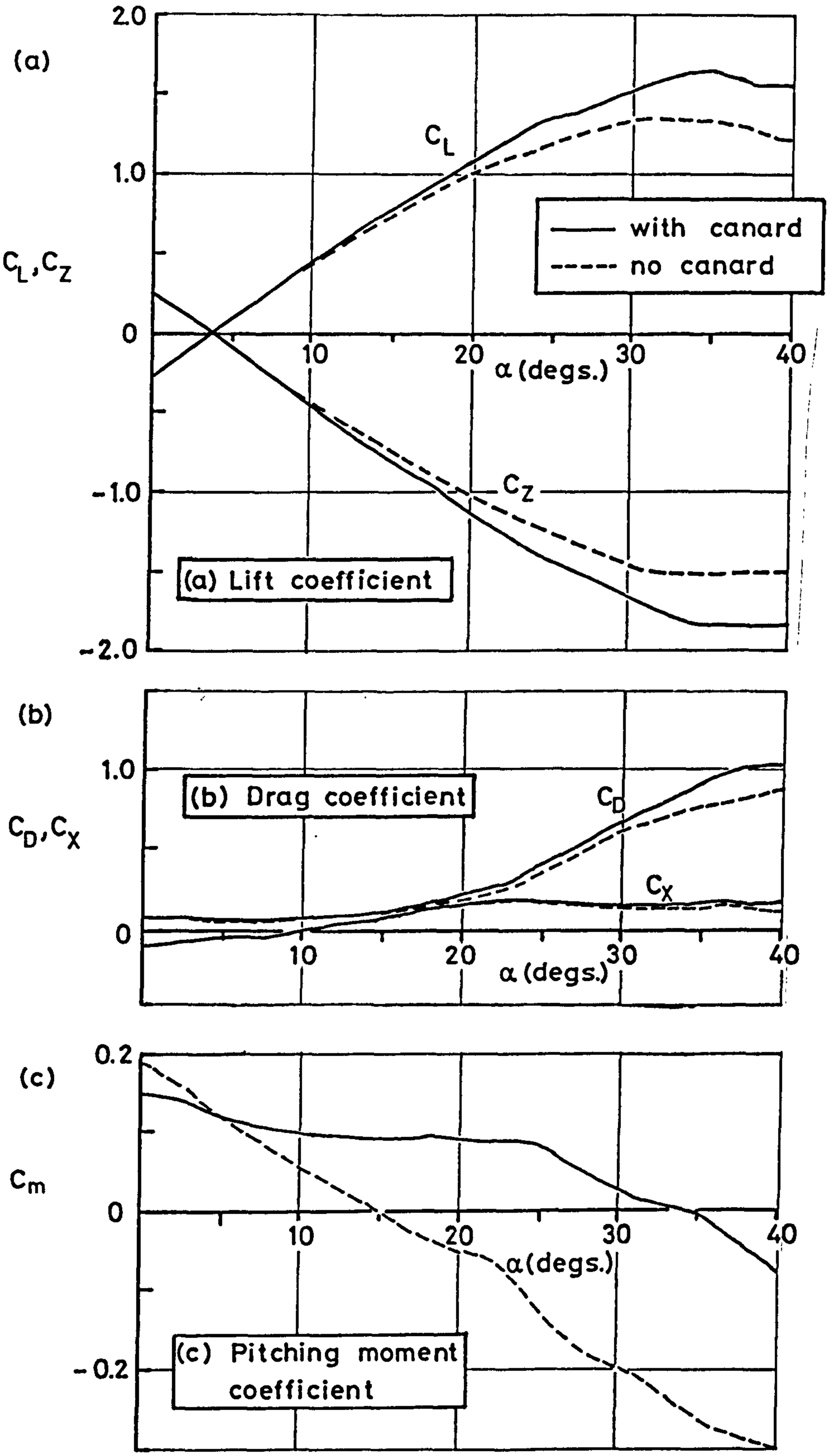

Fig 4.3 HIRM C longitudinal aerodynamic characteristics

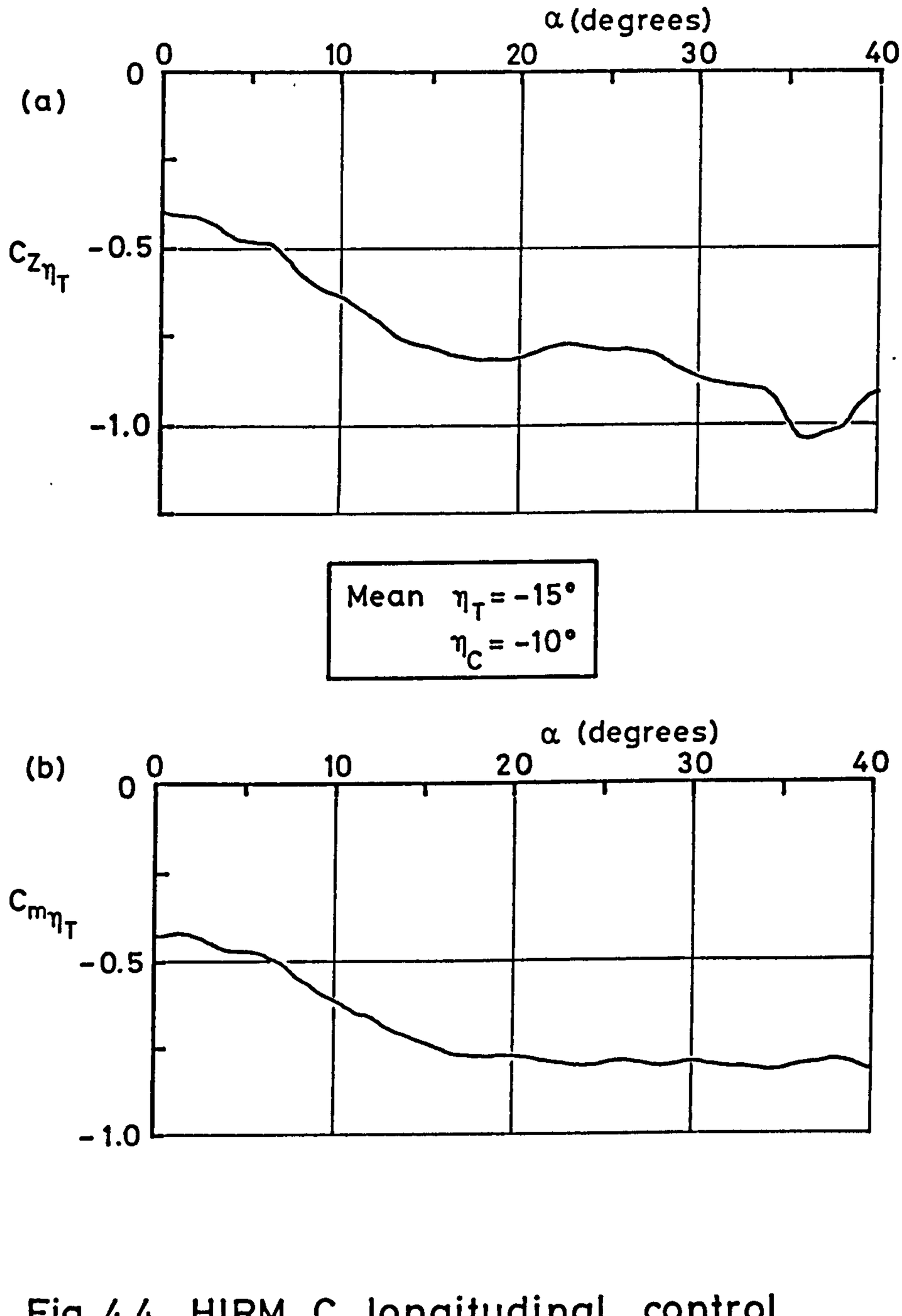

Fig 4.4 HIRM C longitudinal control derivatives

(a)

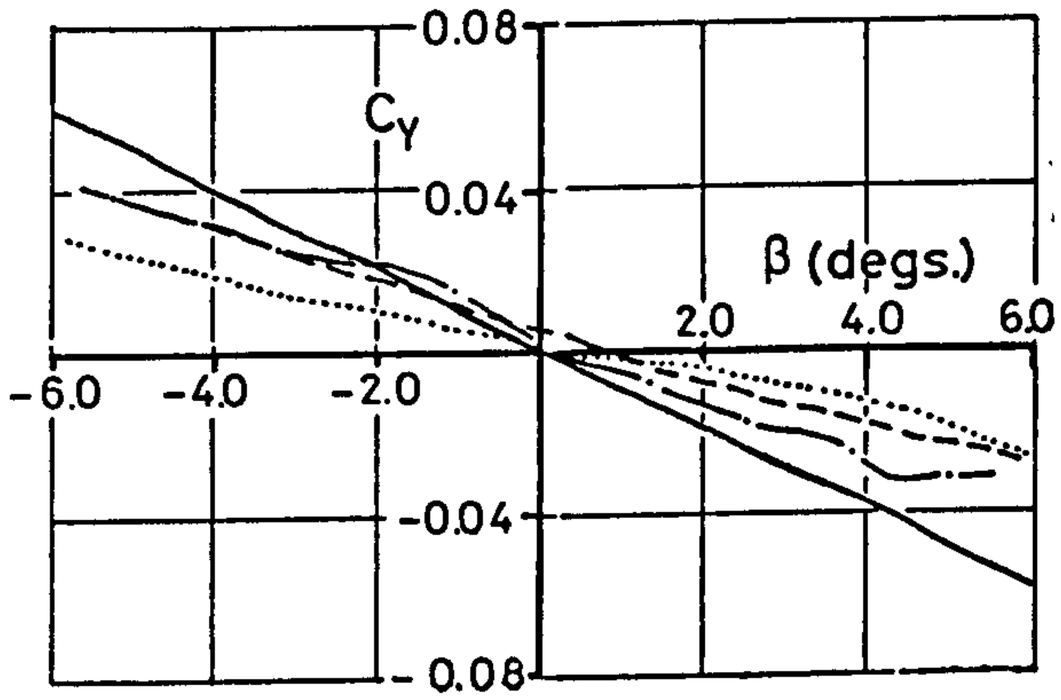

(b)

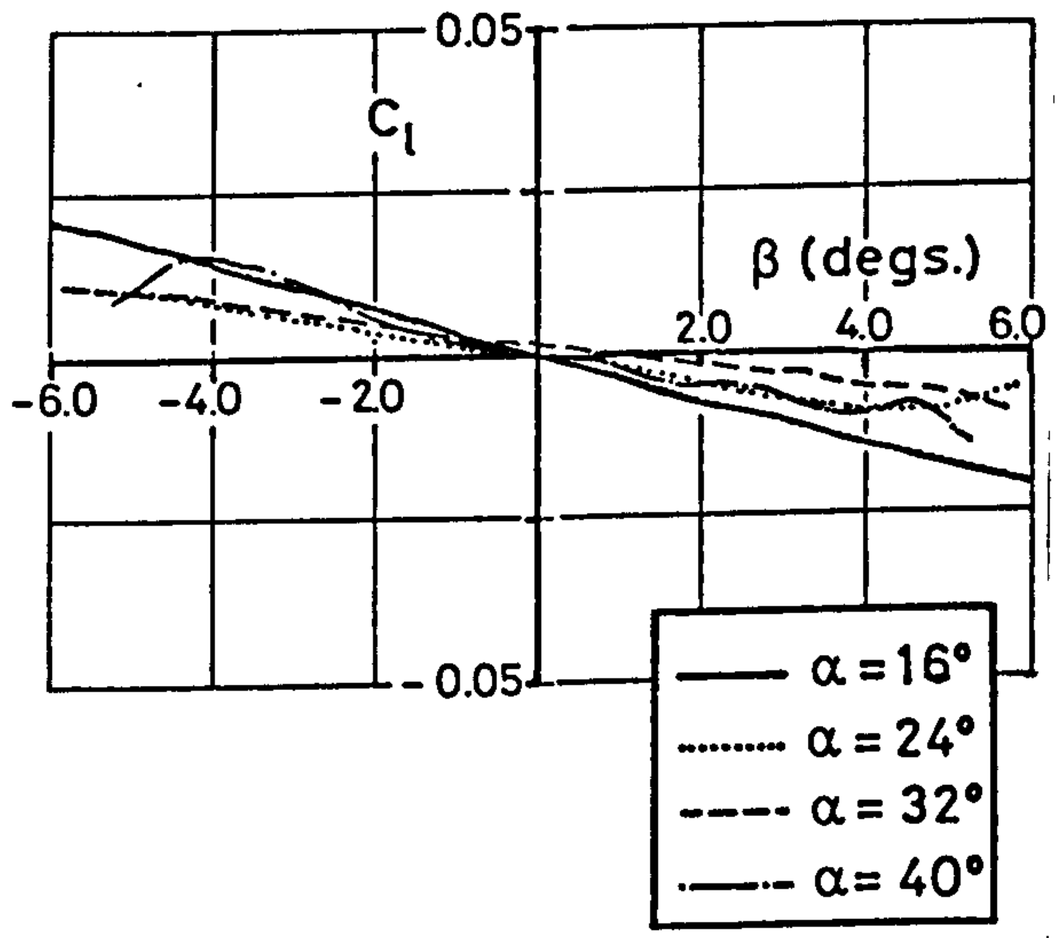

(c)

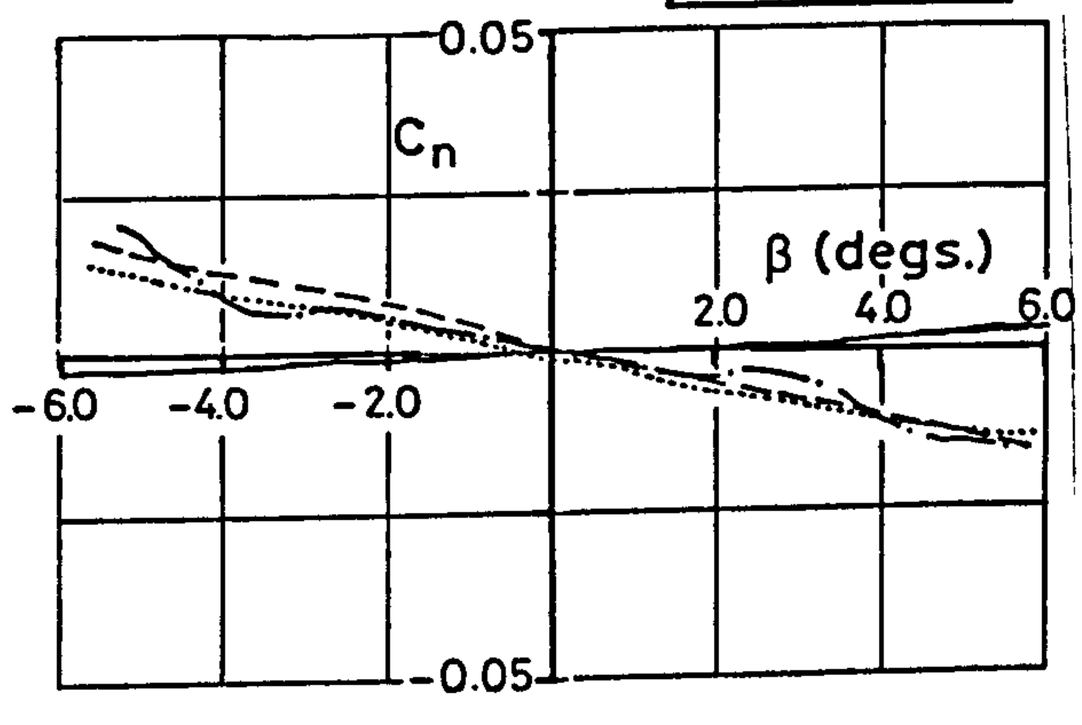

Fig 4.5 HIRM C lateral aerodynamic characteristics

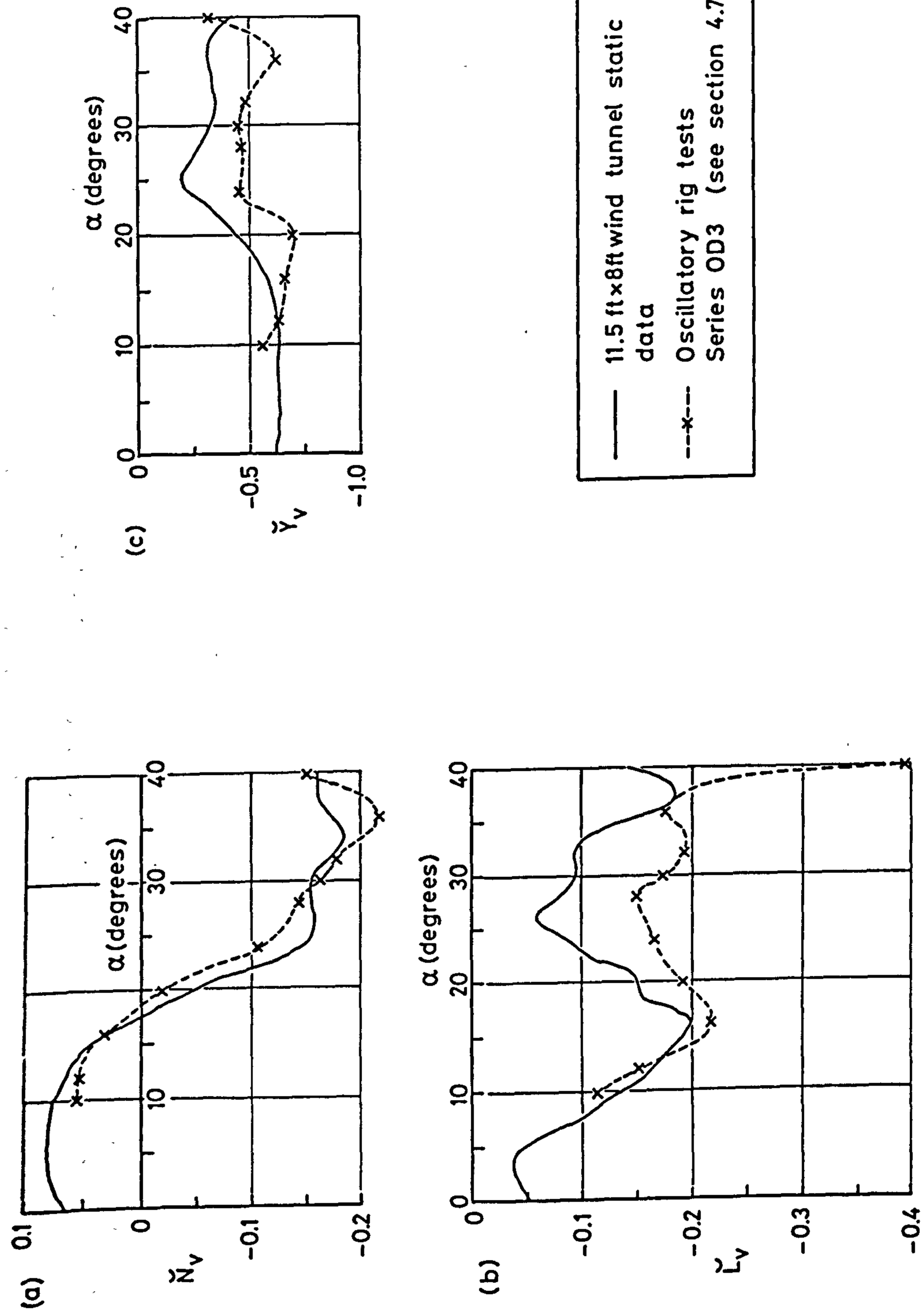

Fig 4.6 HIRM C lateral static derivatives

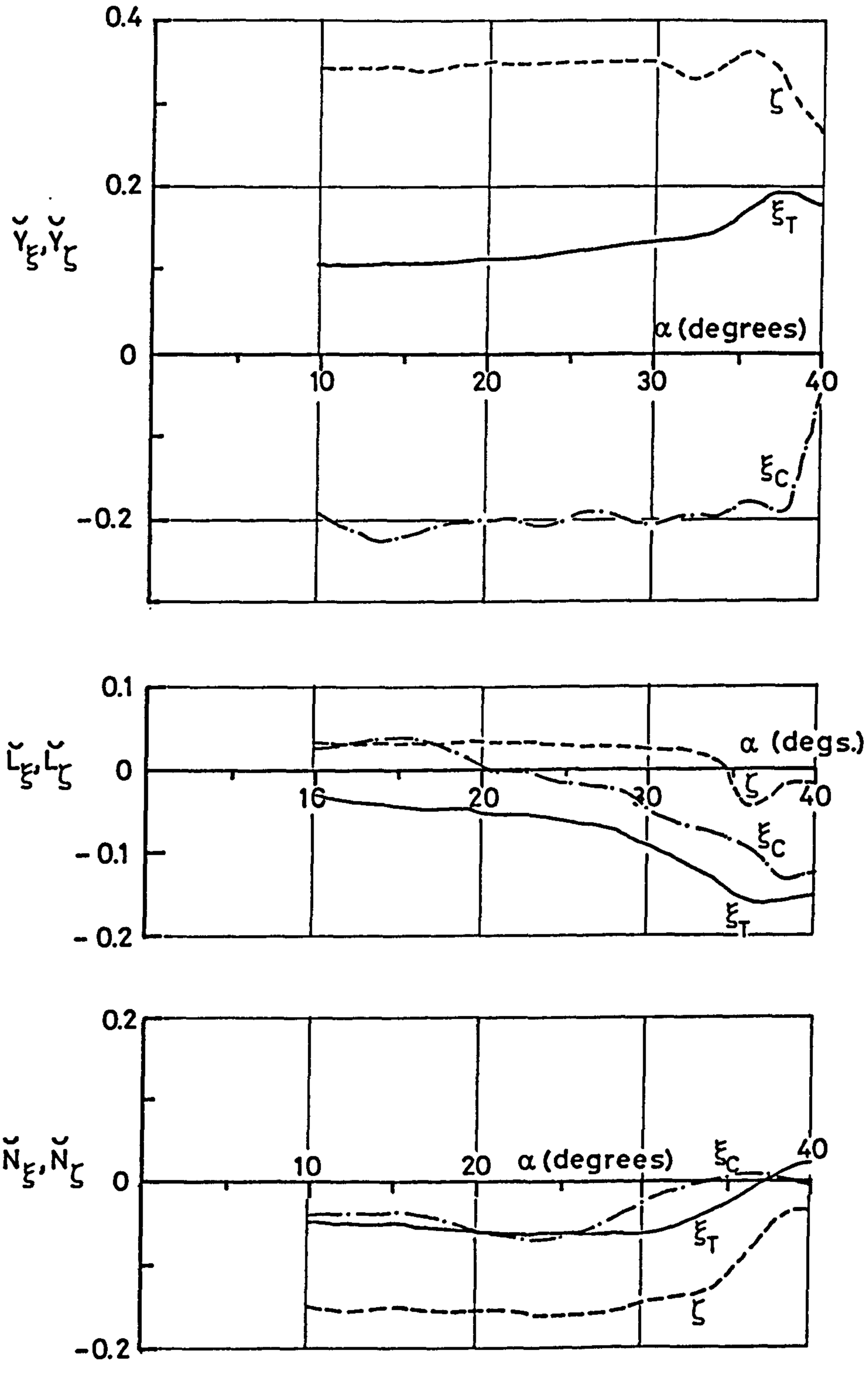

Fig 4.7 HIRM C lateral control derivatives

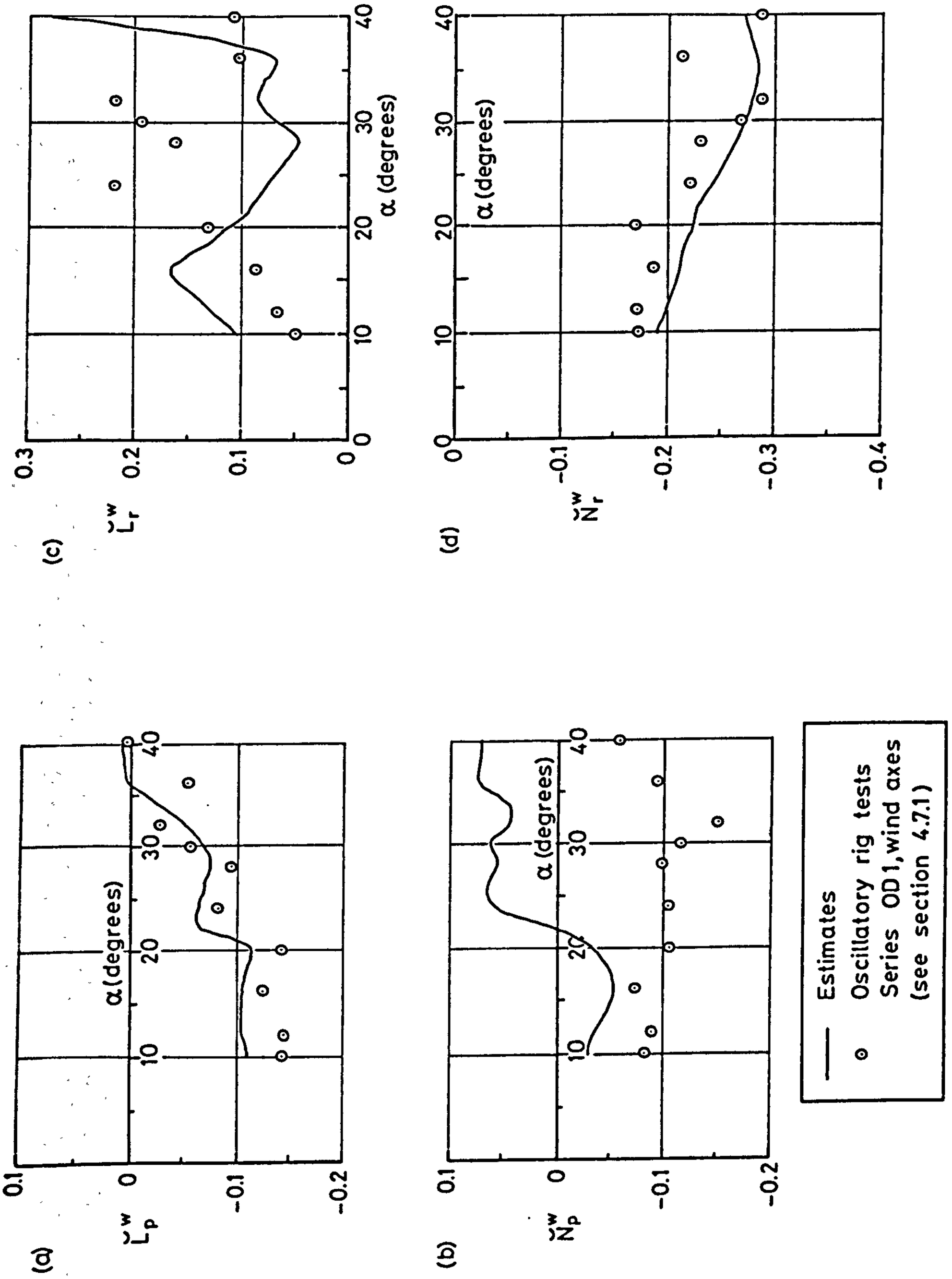

Fig 4.8 HIRM C estimated dynamic derivatives

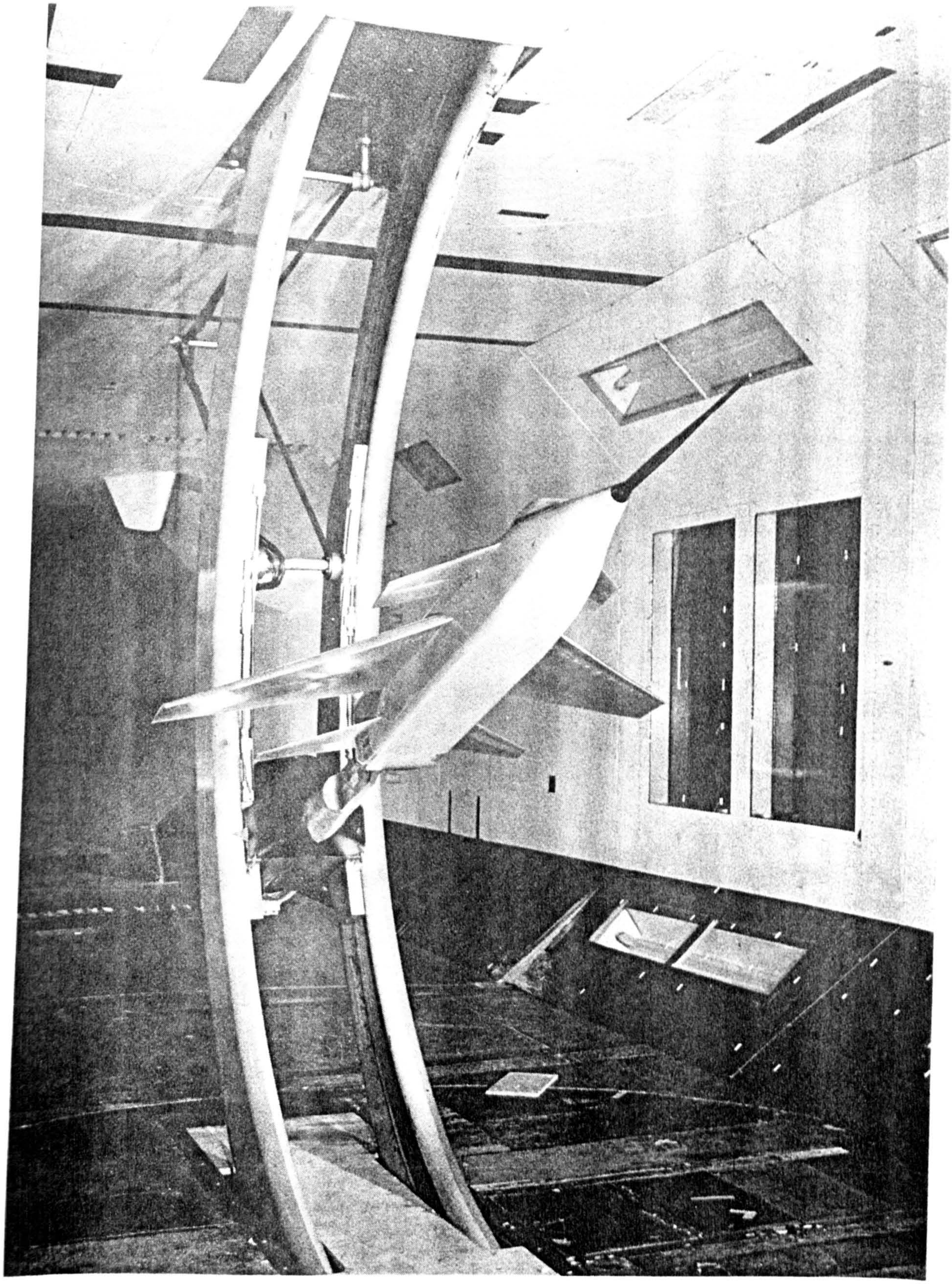

Fig 4.9 HIRM 2 on the oscillatory rig in the R.A.E. Bedford 13 ft × 9 ft wind tunnel

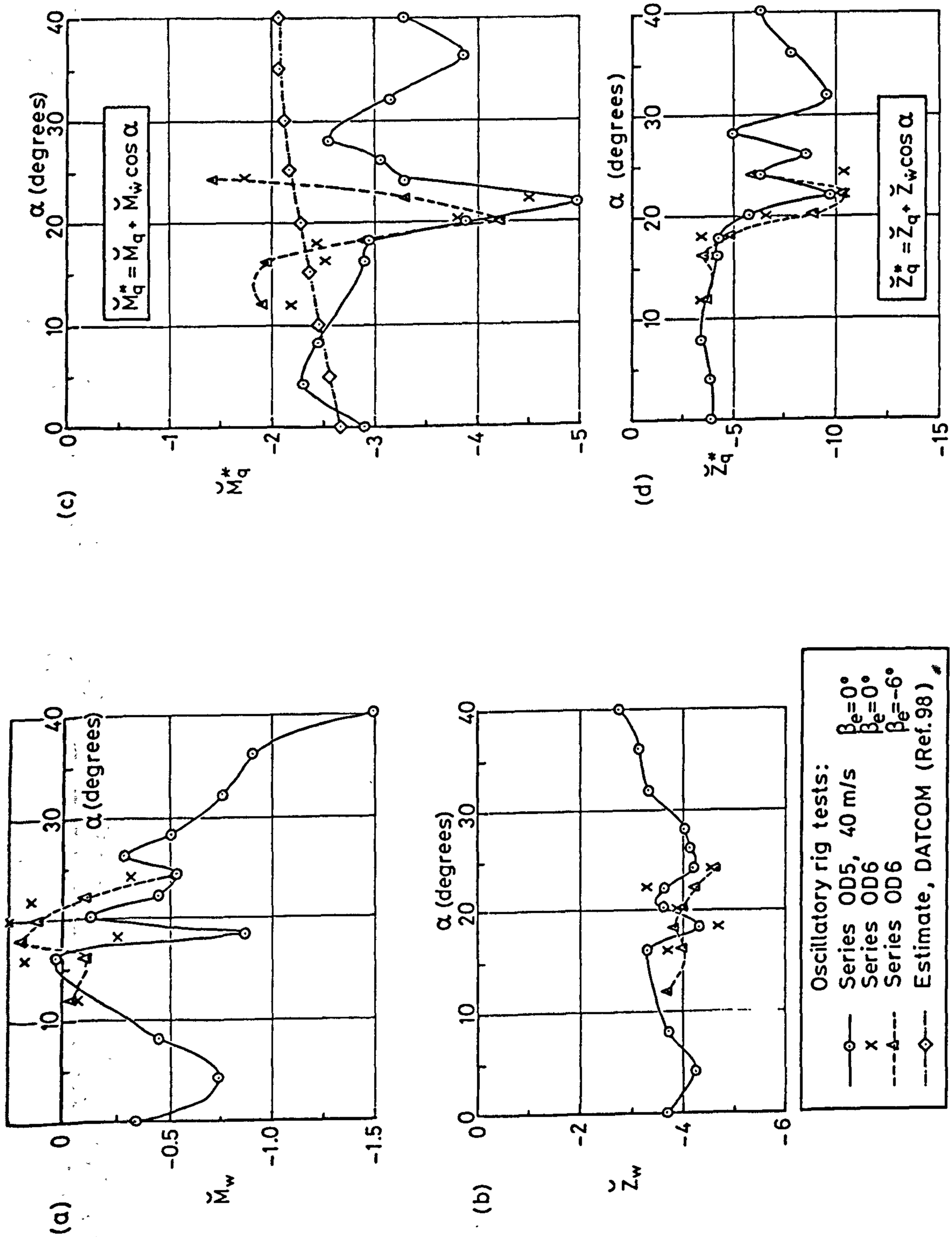

Fig 4.10 HIRM C oscillatory rig results - longitudinal derivatives

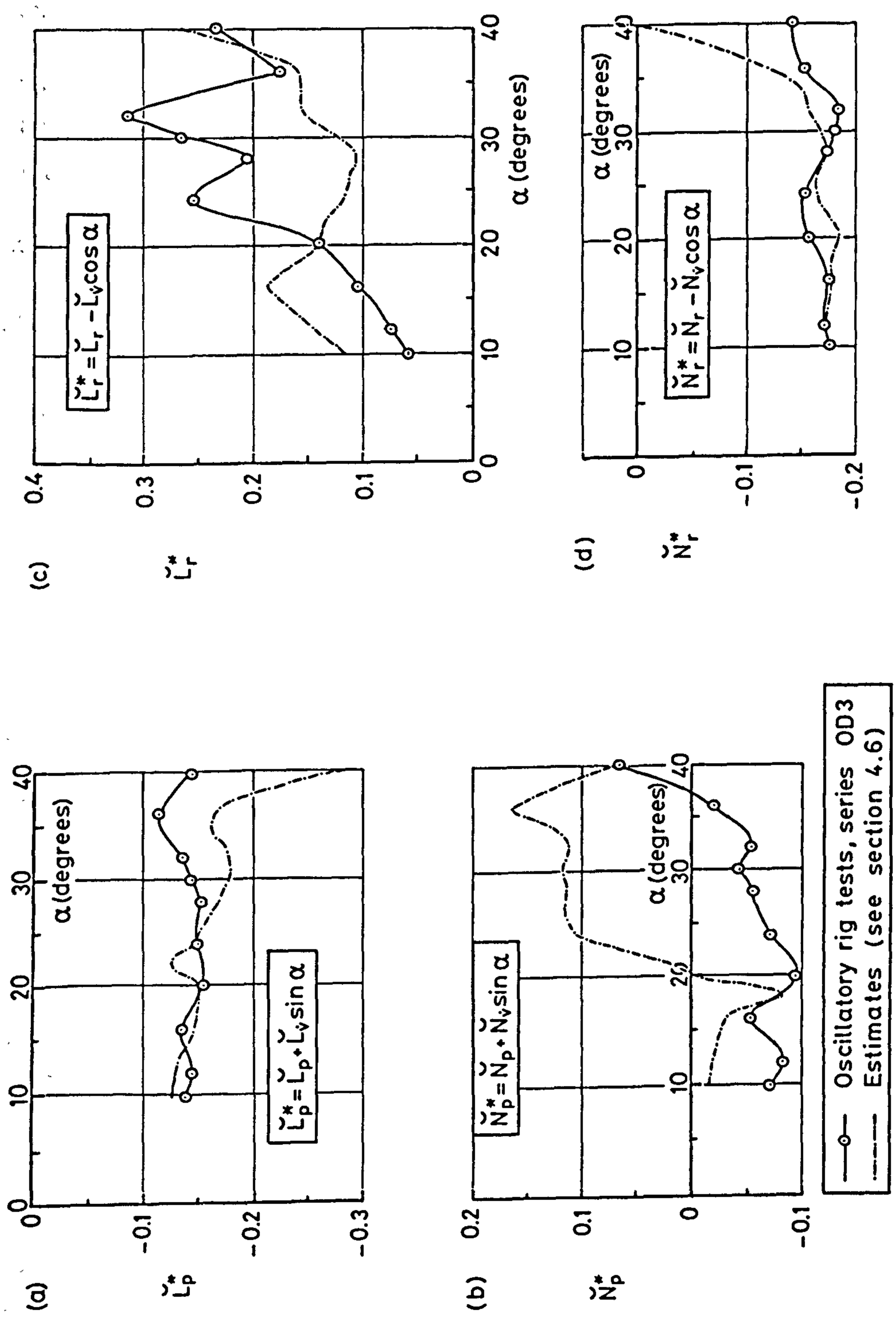

Fig 4.11 HIRM C oscillatory rig results - lateral derivatives

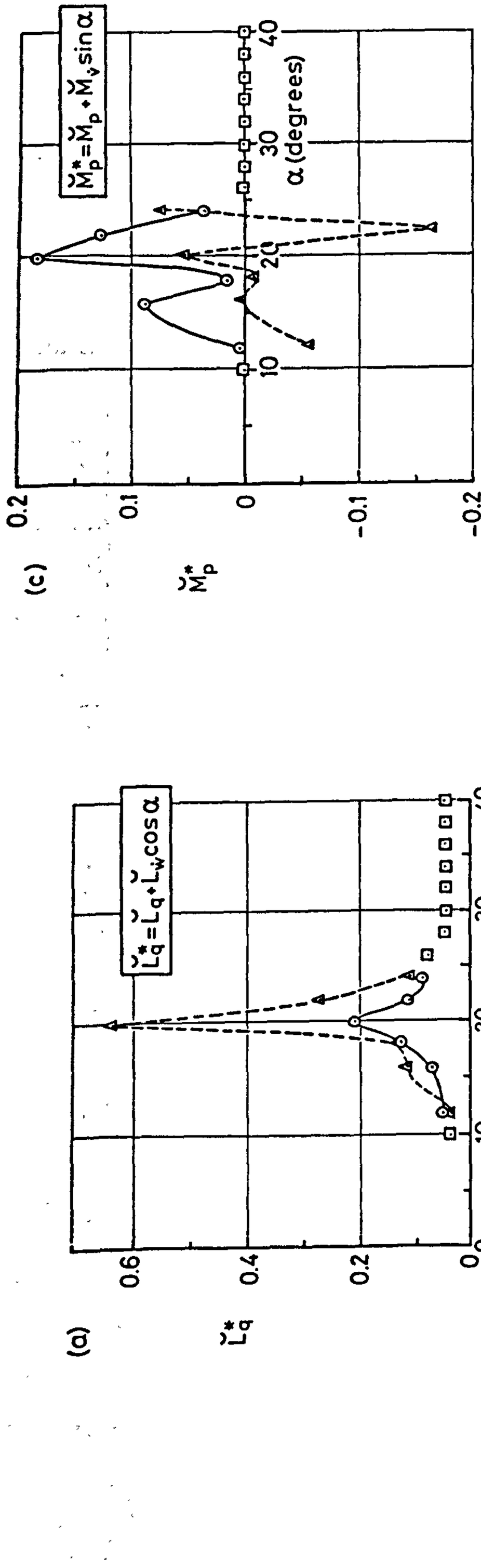

Fig 4.12 HIRM oscillatory rig results, test series OD6

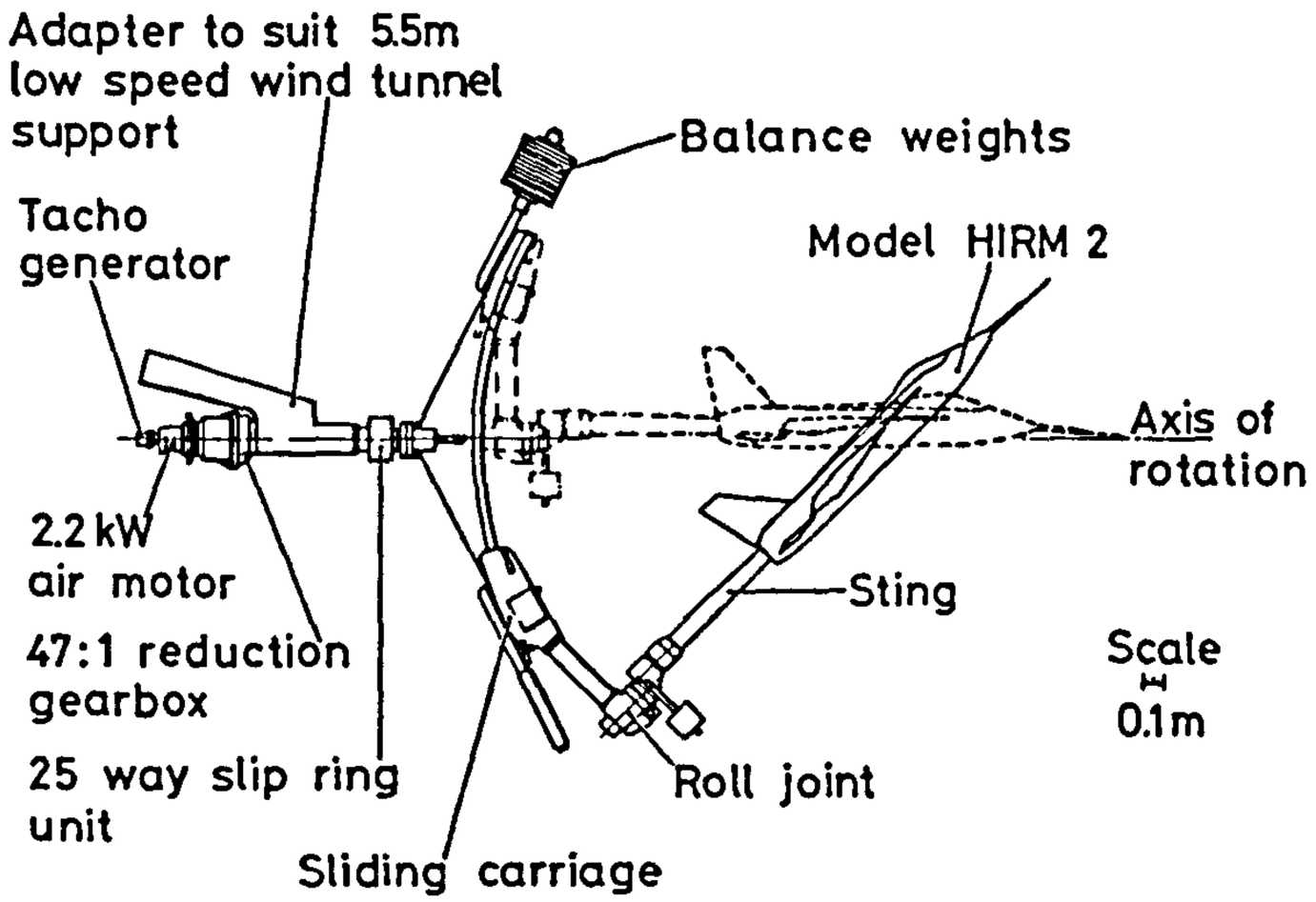

Fig 4.13 British Aerospace low speed wind tunnel rotary derivative rig
(After Matthews; Ref.99)

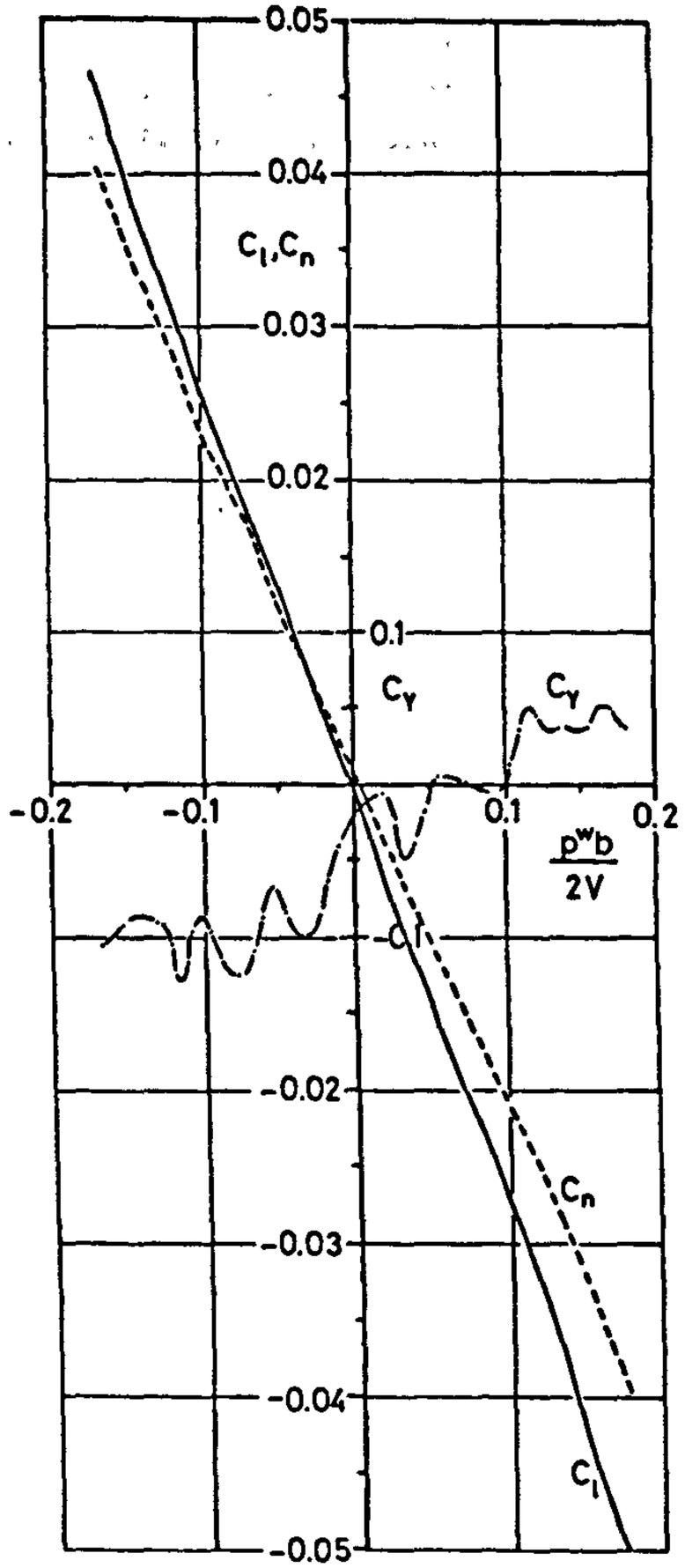

(a) $\alpha = 12°$

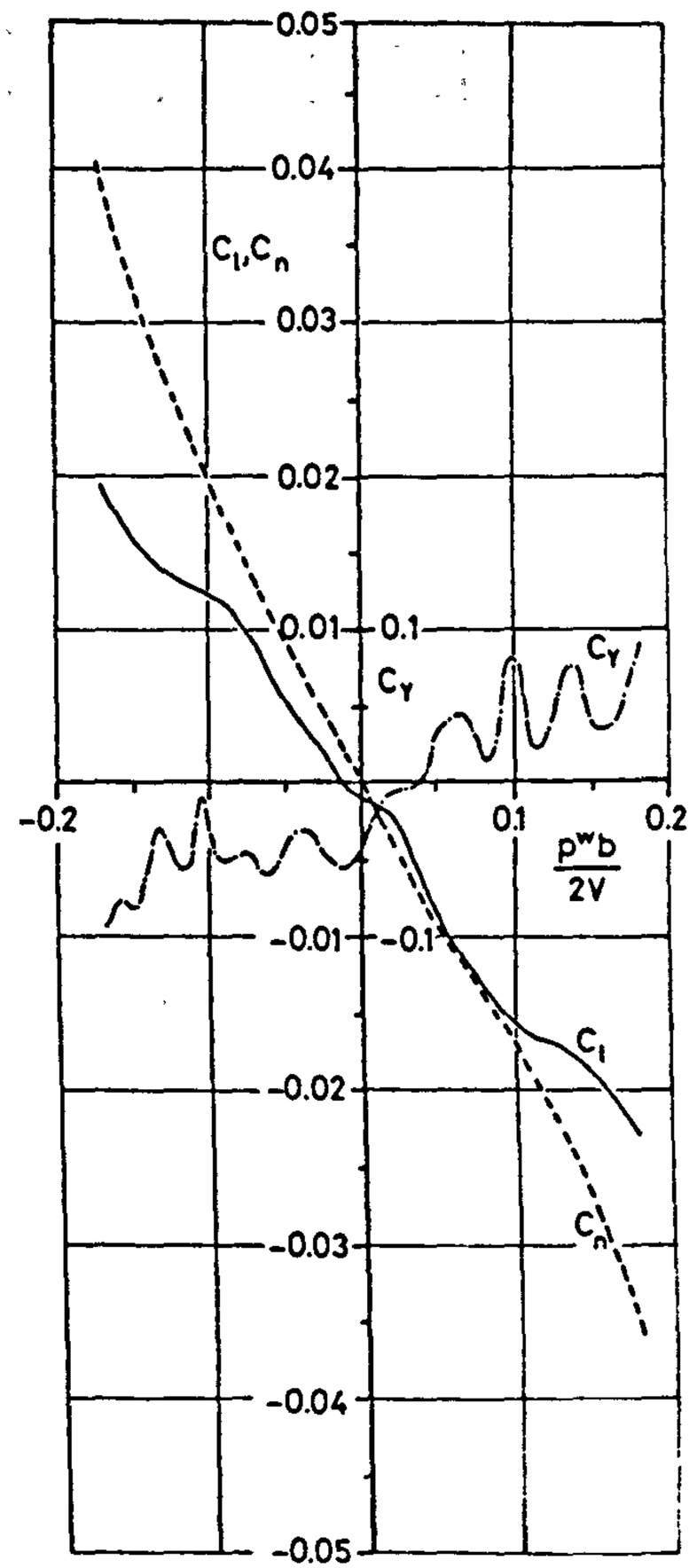

(b) $\alpha = 20°$

Fig 4.14 HIRM C rotary rig results

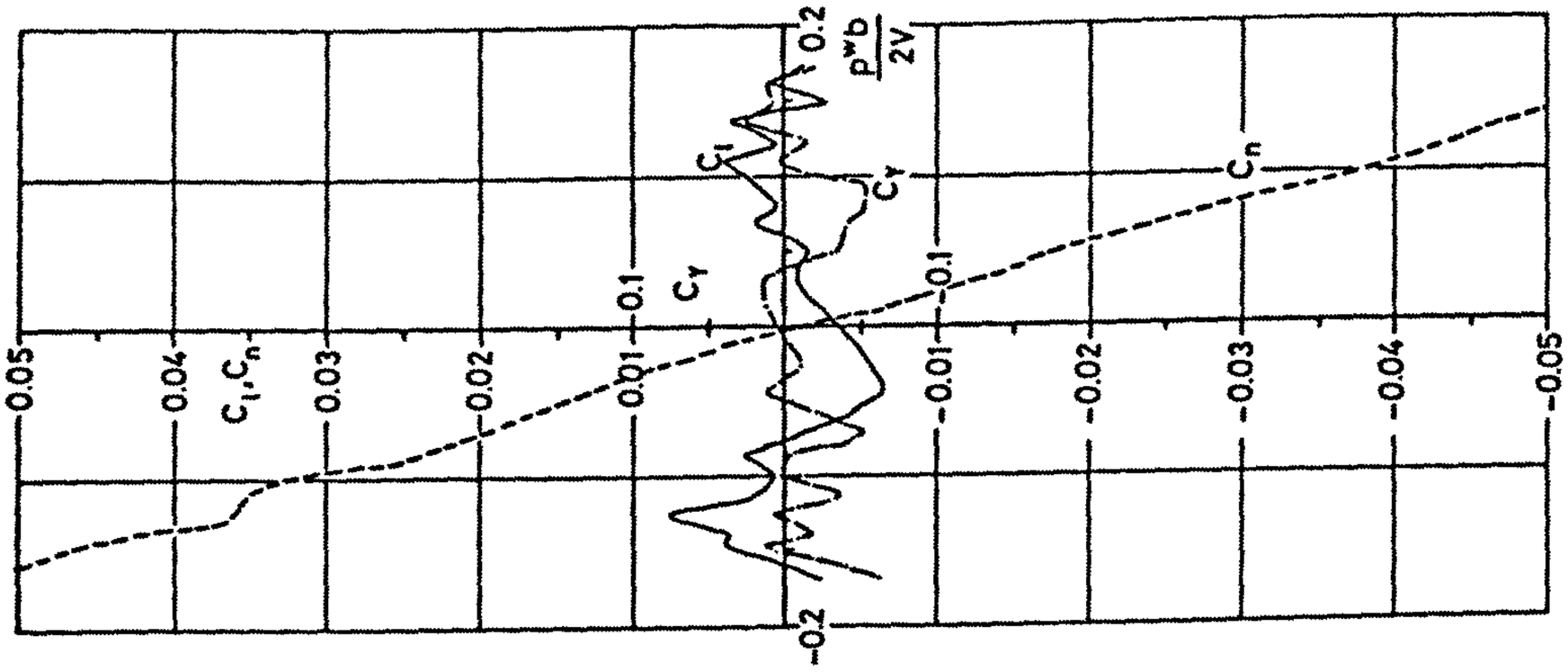

HIRM C rotary rig results

Fig 4.14 (concluded)

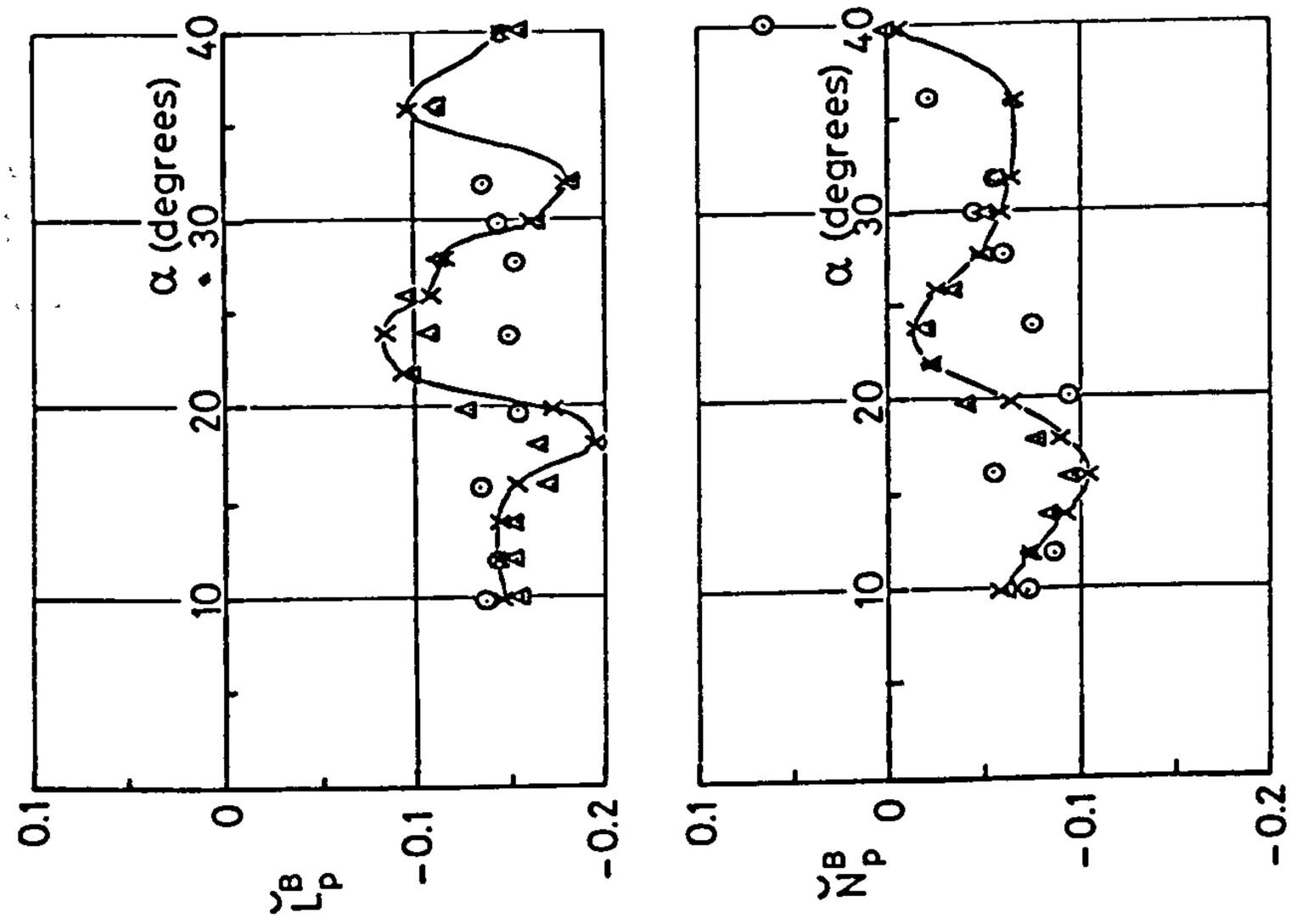

Fig 4.16 HIRM C rotary derivatives ν_{L_p} and ν_{N_p} in body axes

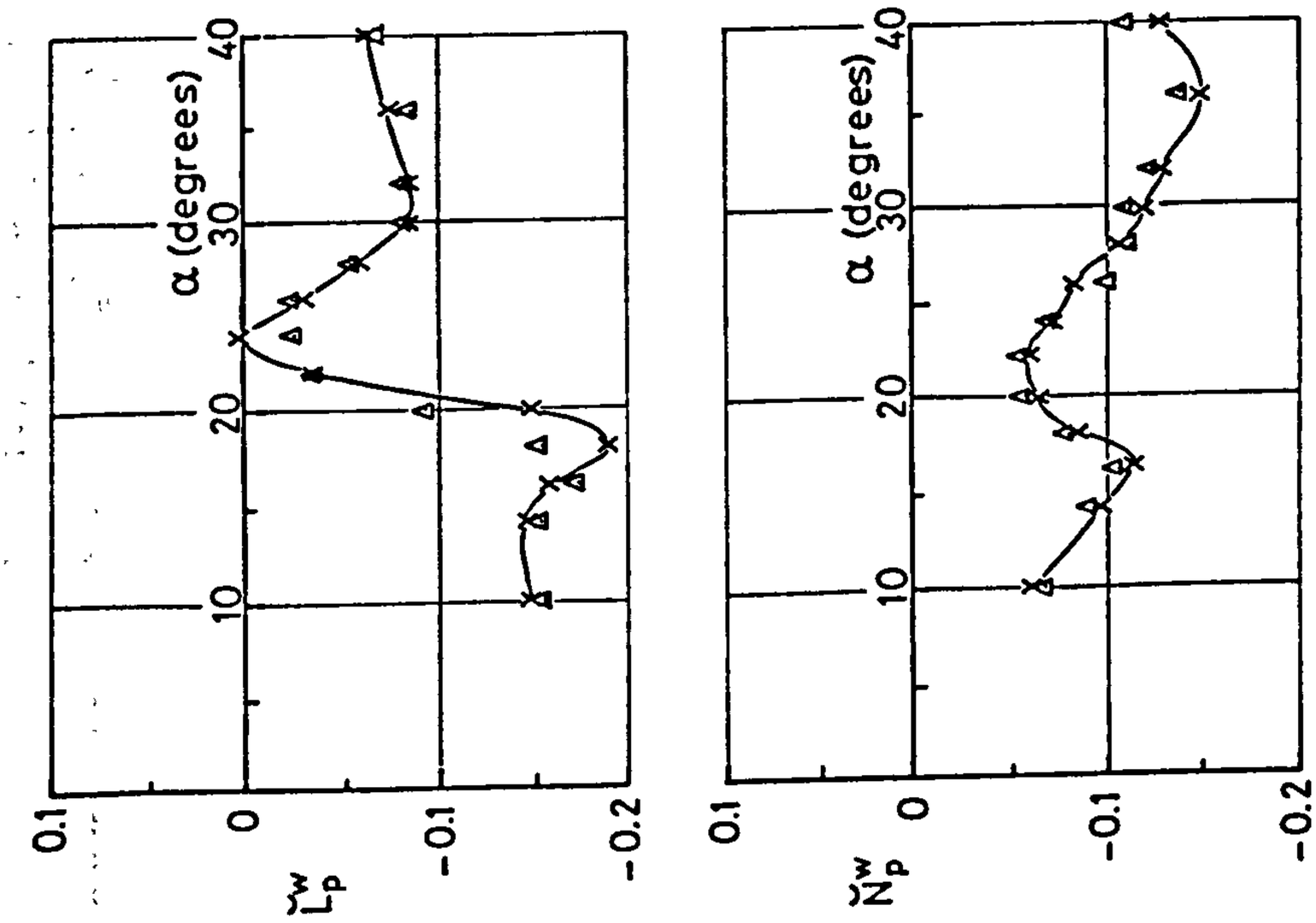

Fig 4.15 HIRM C rotary derivatives ν_{L_p} and ν_{N_p} in wind axes

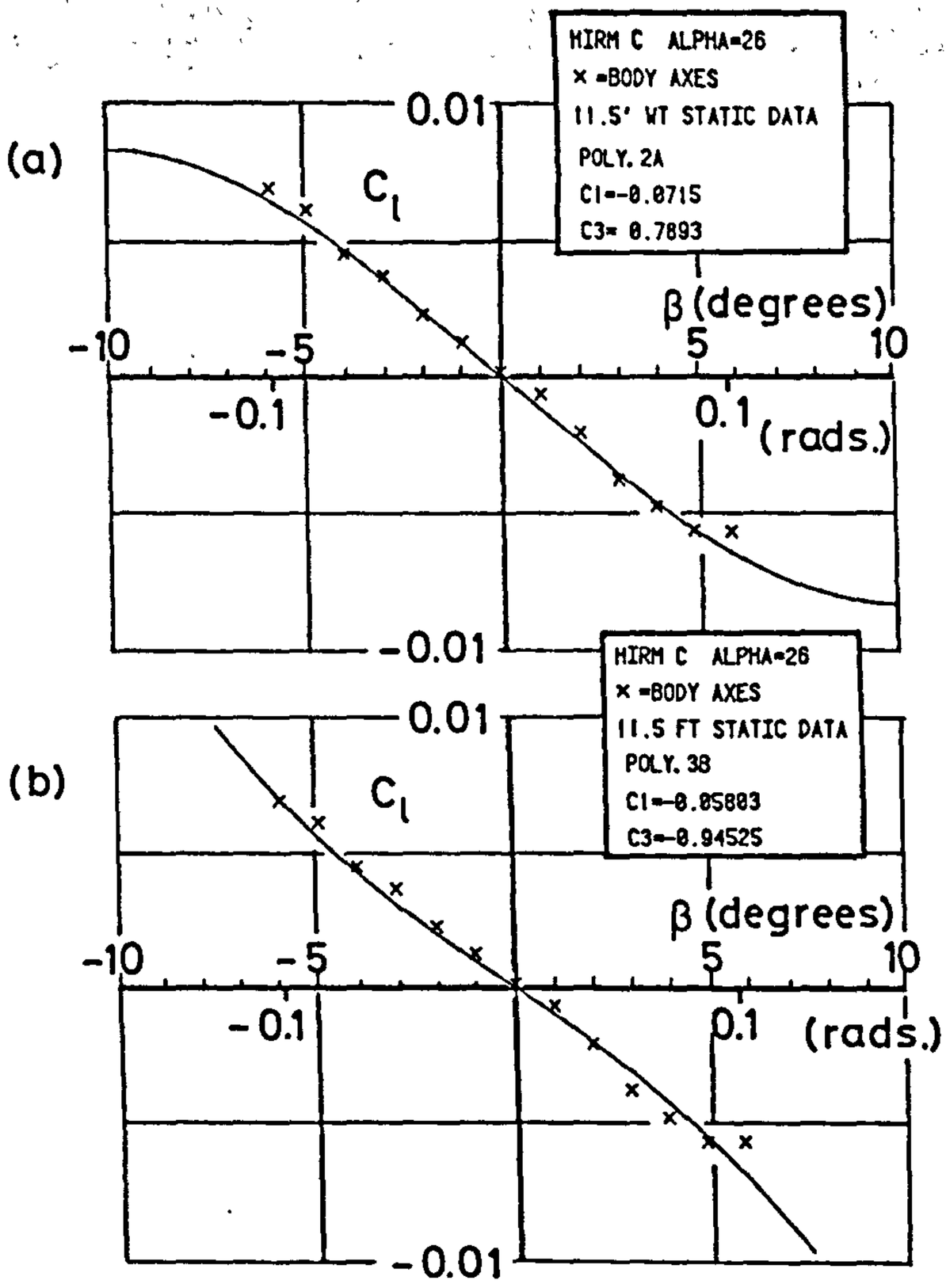

Fig 4.17 Cubic fits to $C_l(\beta)$ data at $\alpha = 26°$

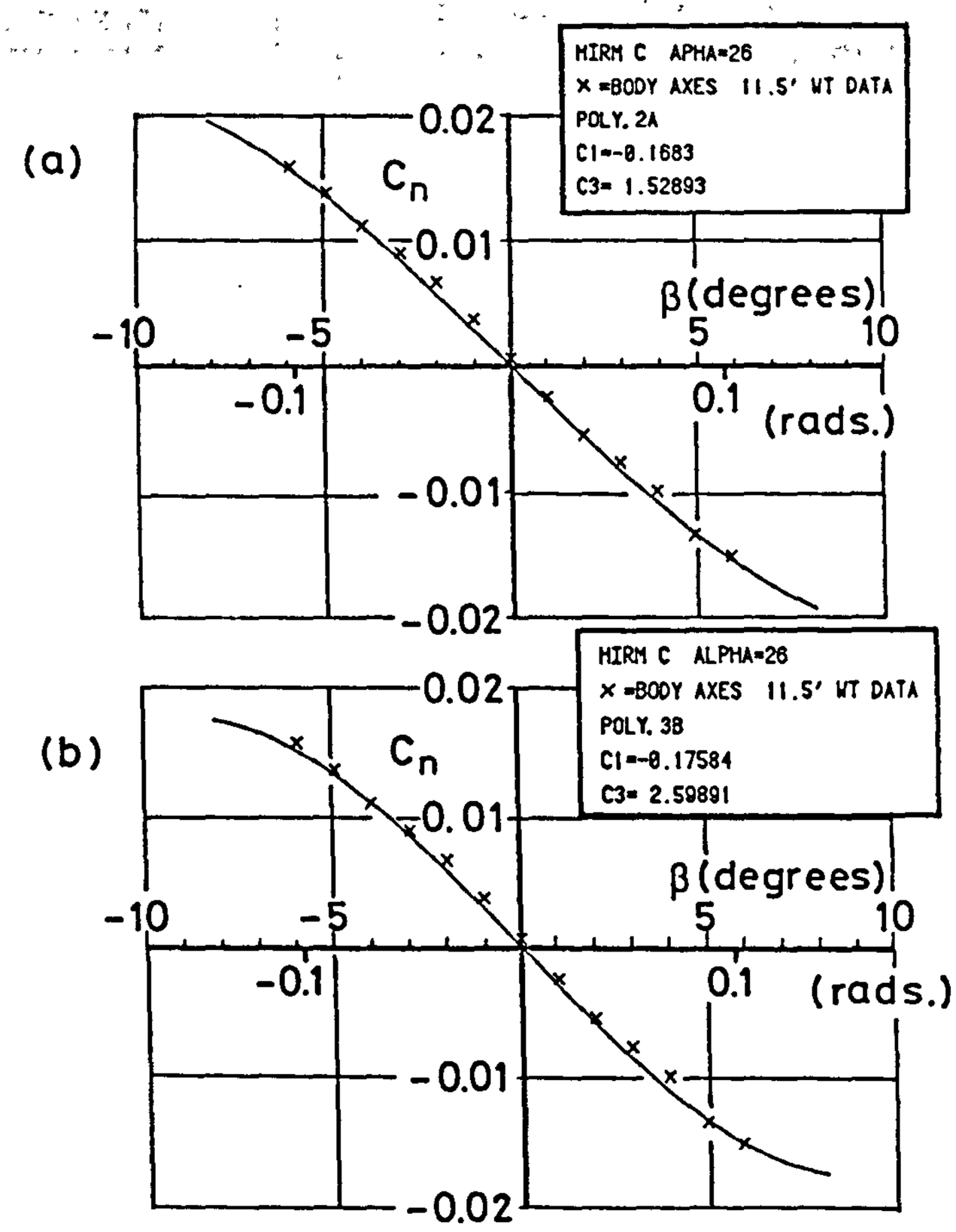

Fig 4.18 Cubic fits to $C_n(\beta)$ data at $\alpha = 26°$

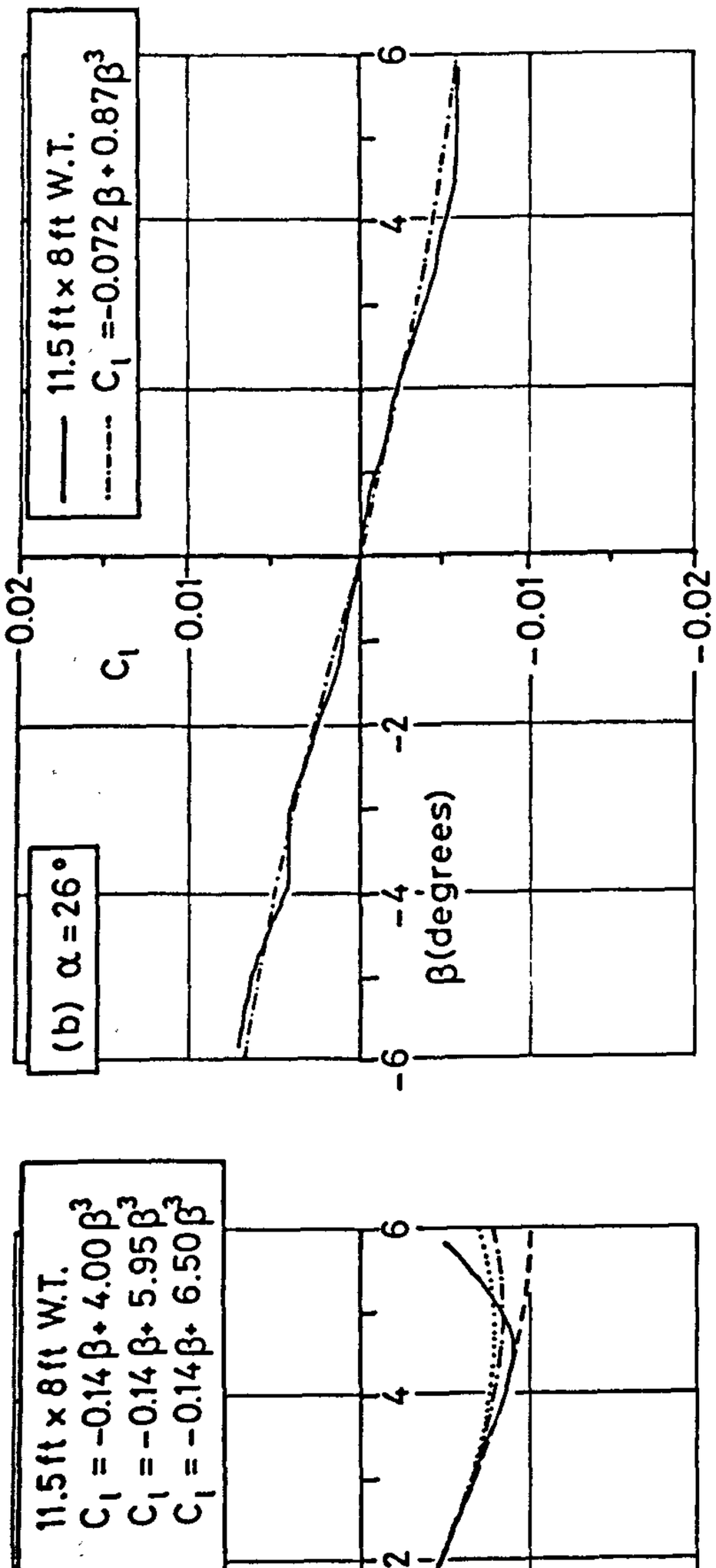

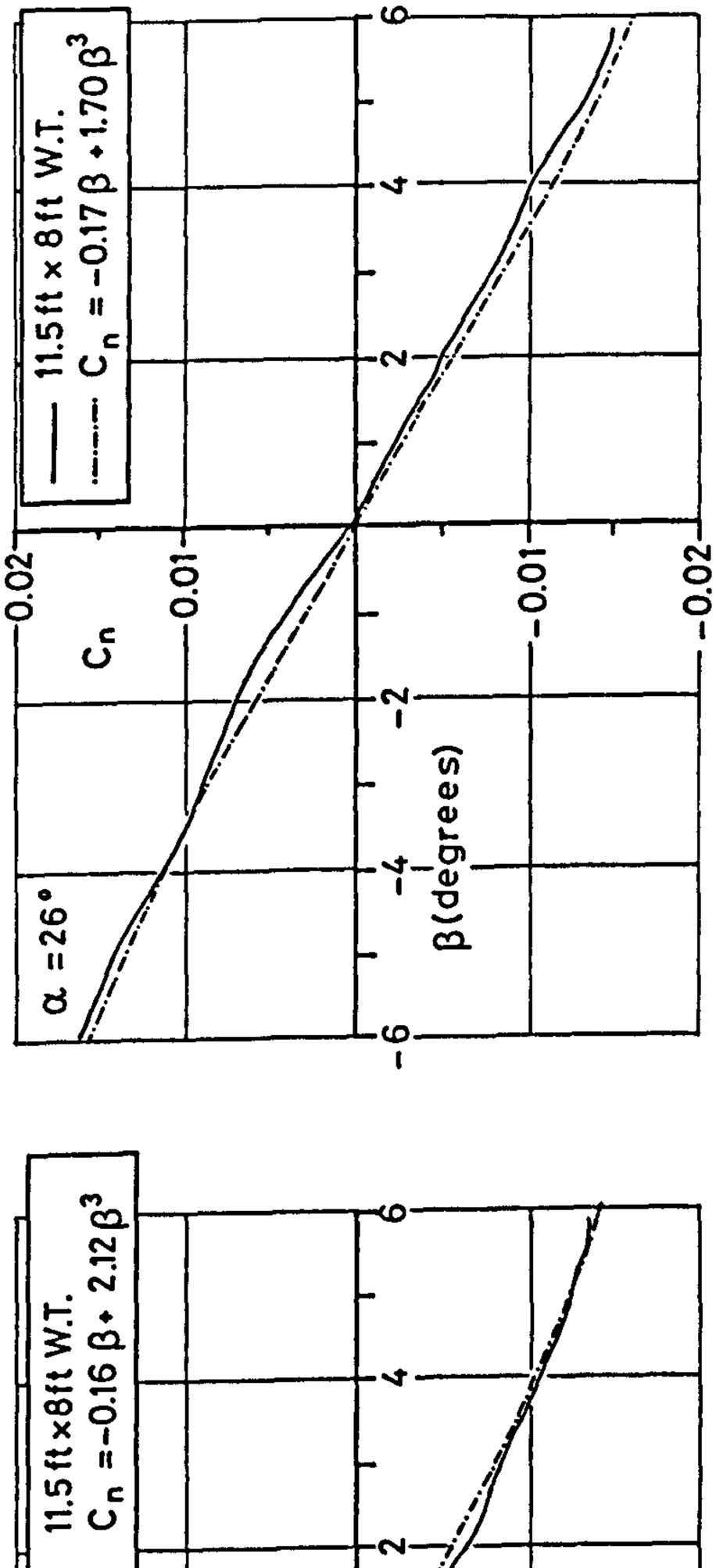

Fig 4.19 Cubic fits to $C_l(\beta)$ and $C_n(\beta)$ data

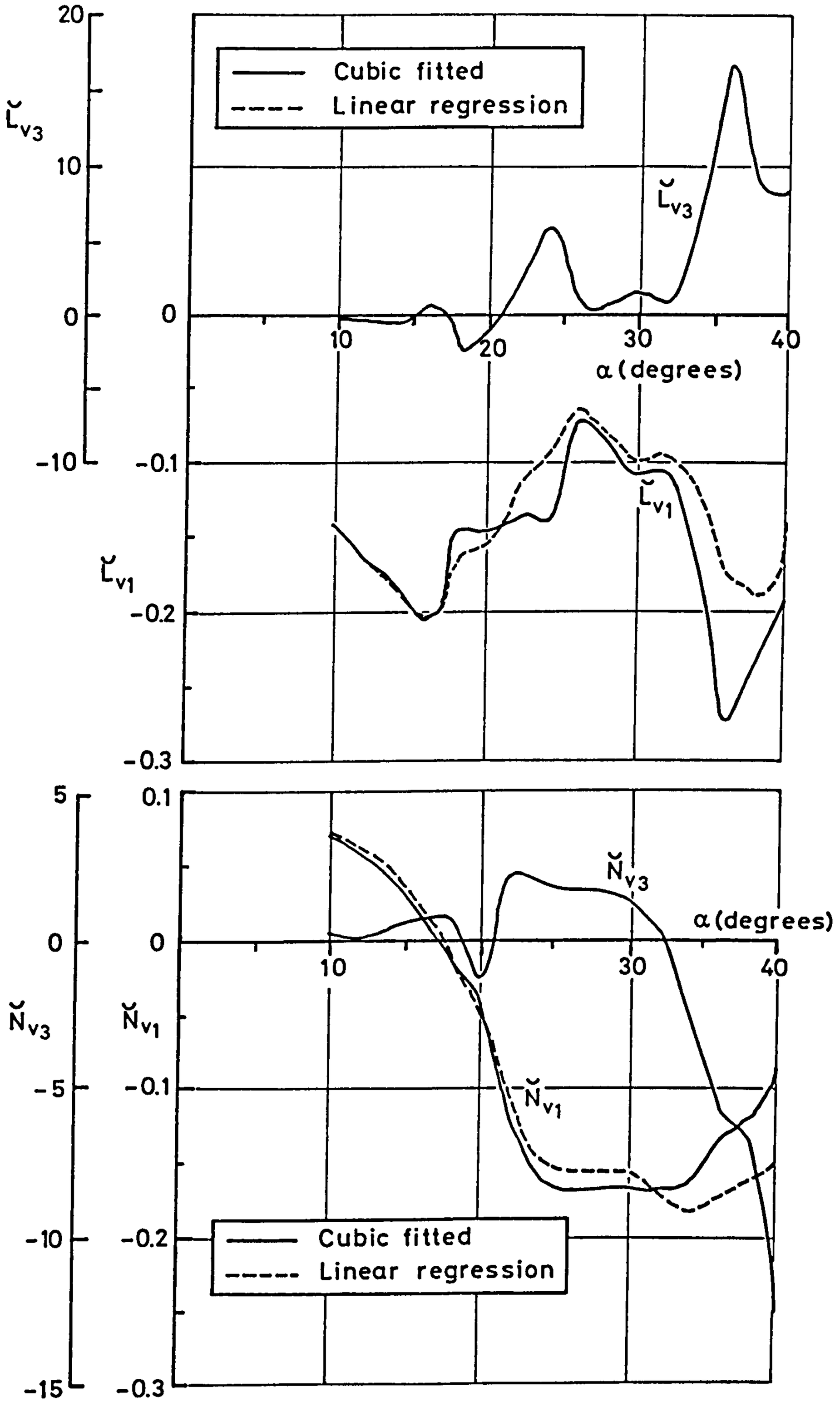

Fig 4.20 Cubic polynomial coefficients for static data

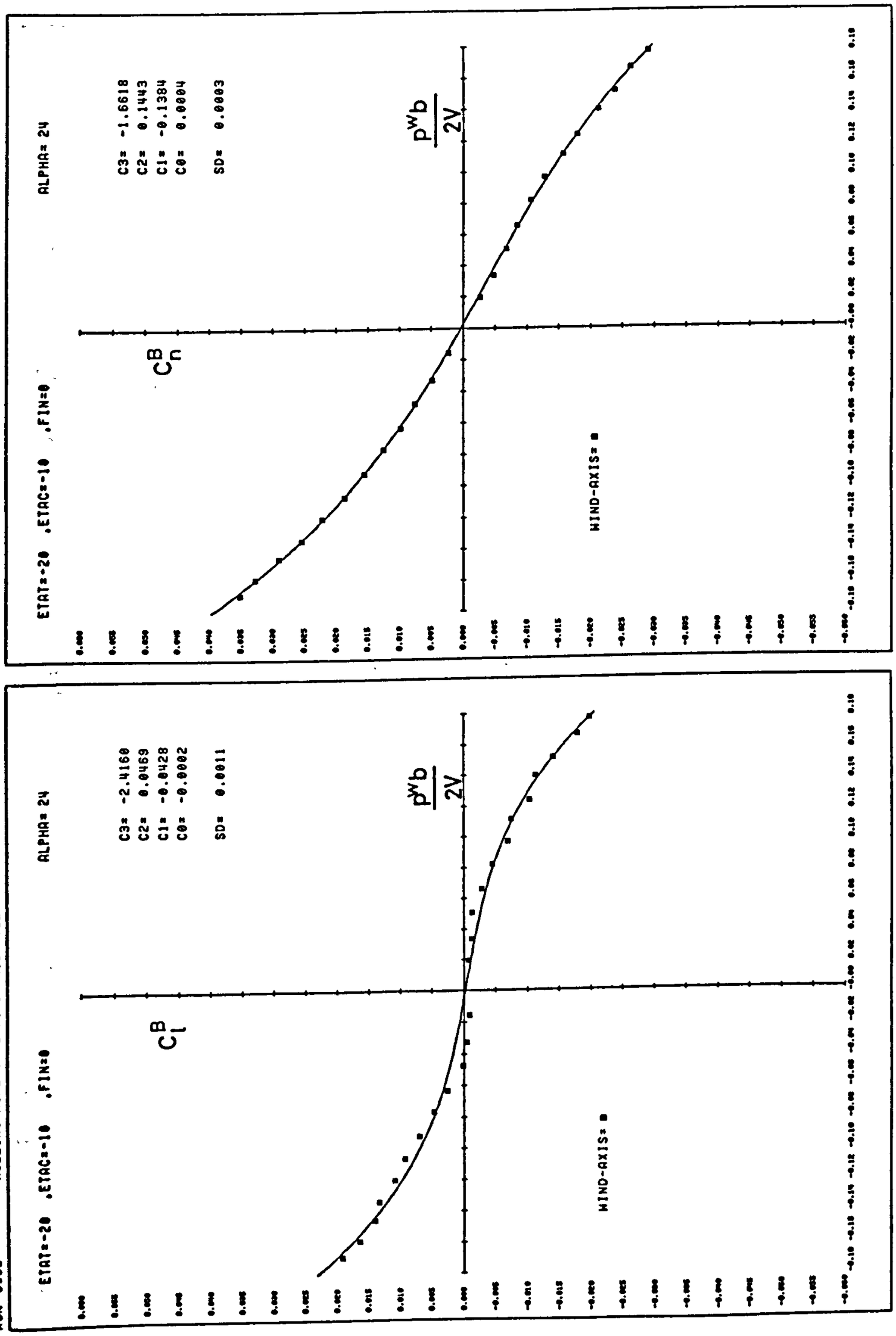

Fig 4.21 Cubic fits to C_l (pb/2V) and C_n(pb/2V). (a) $\alpha = 24°$

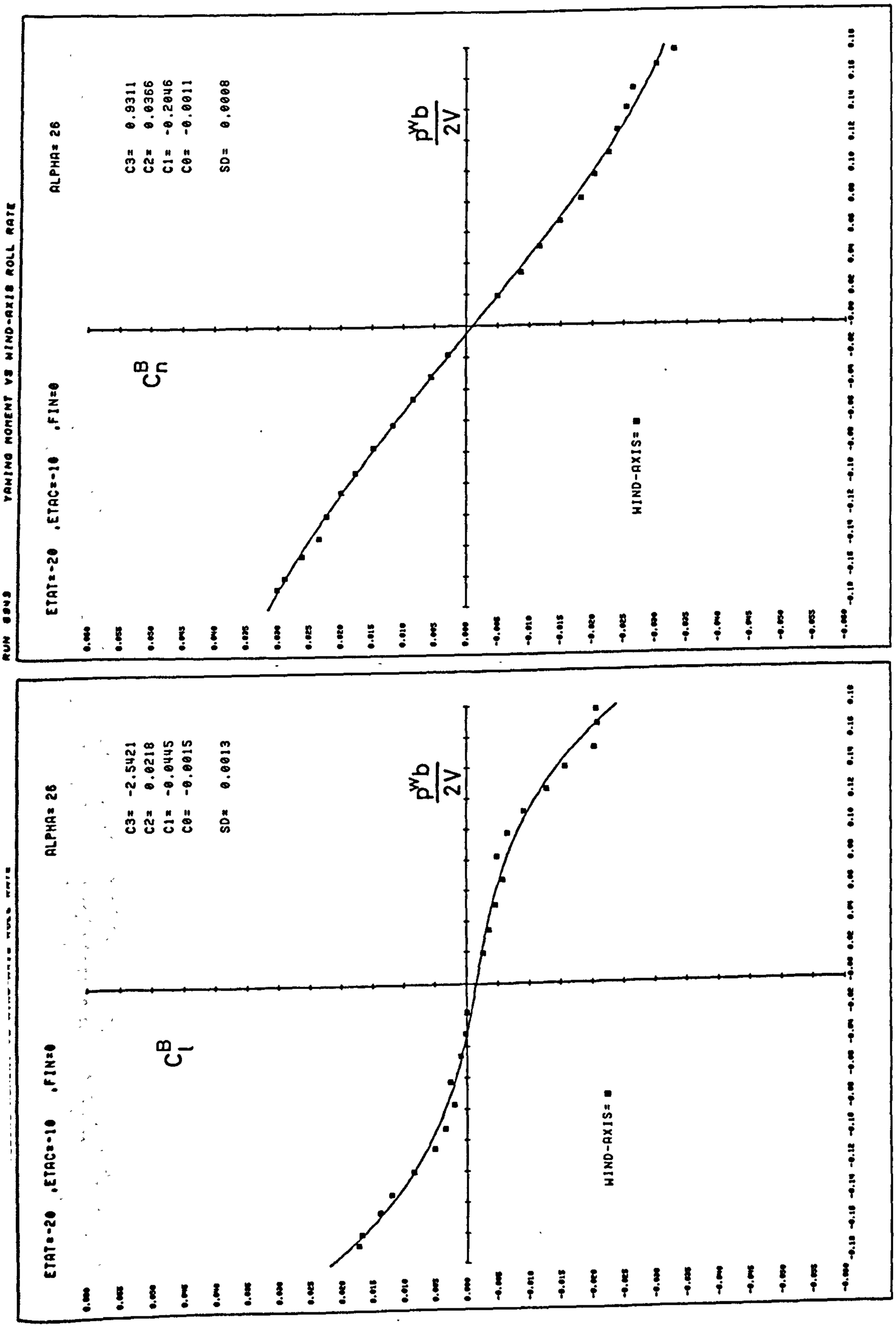

Fig 4.21 (concluded). Cubic fits to C_l (pb/2V) and C_n(pb/2V). (b) $\alpha = 26°$

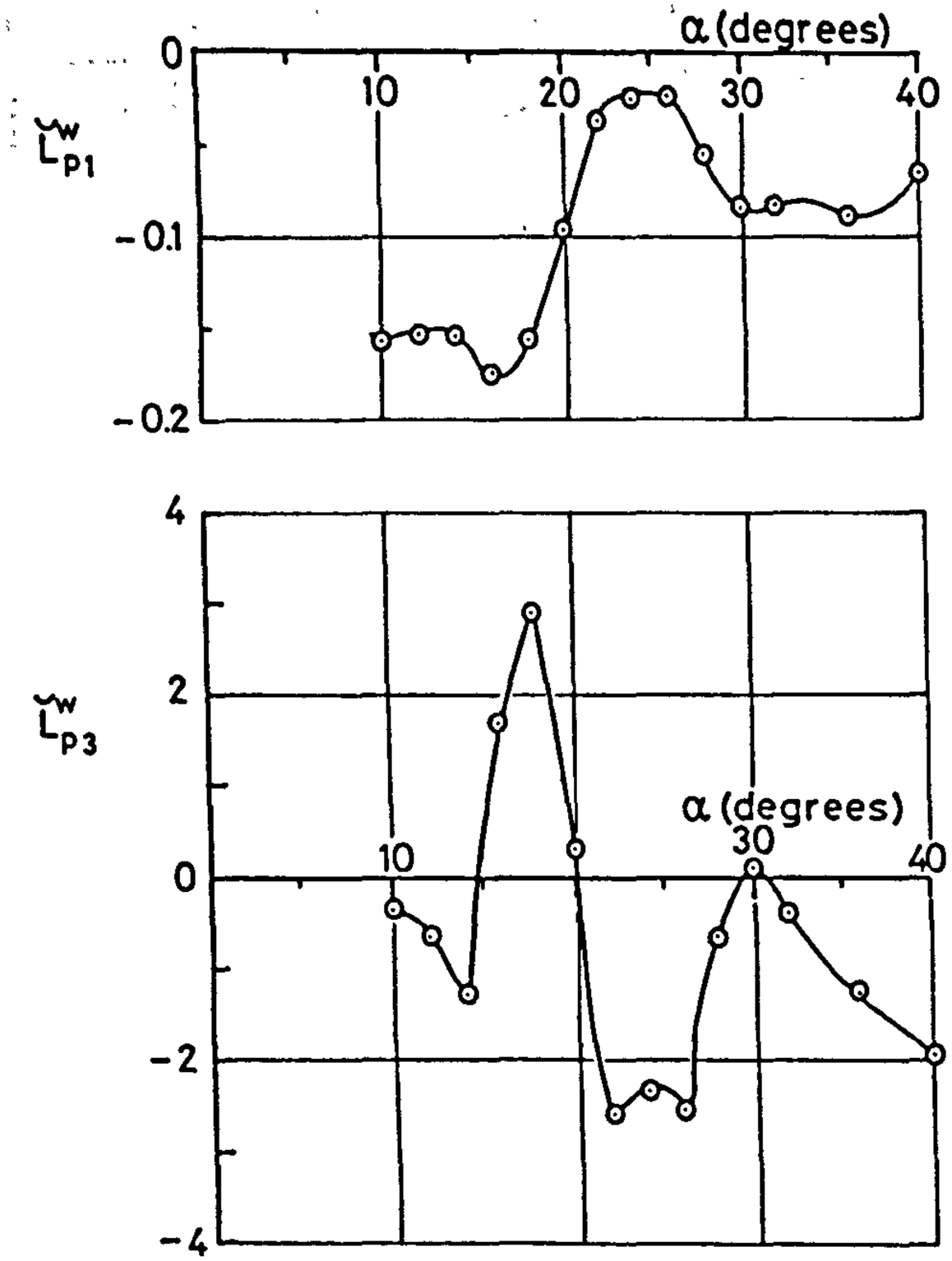

Fig 4.22 Modified cubic polynomial coefficients for C_l(pb/2V)

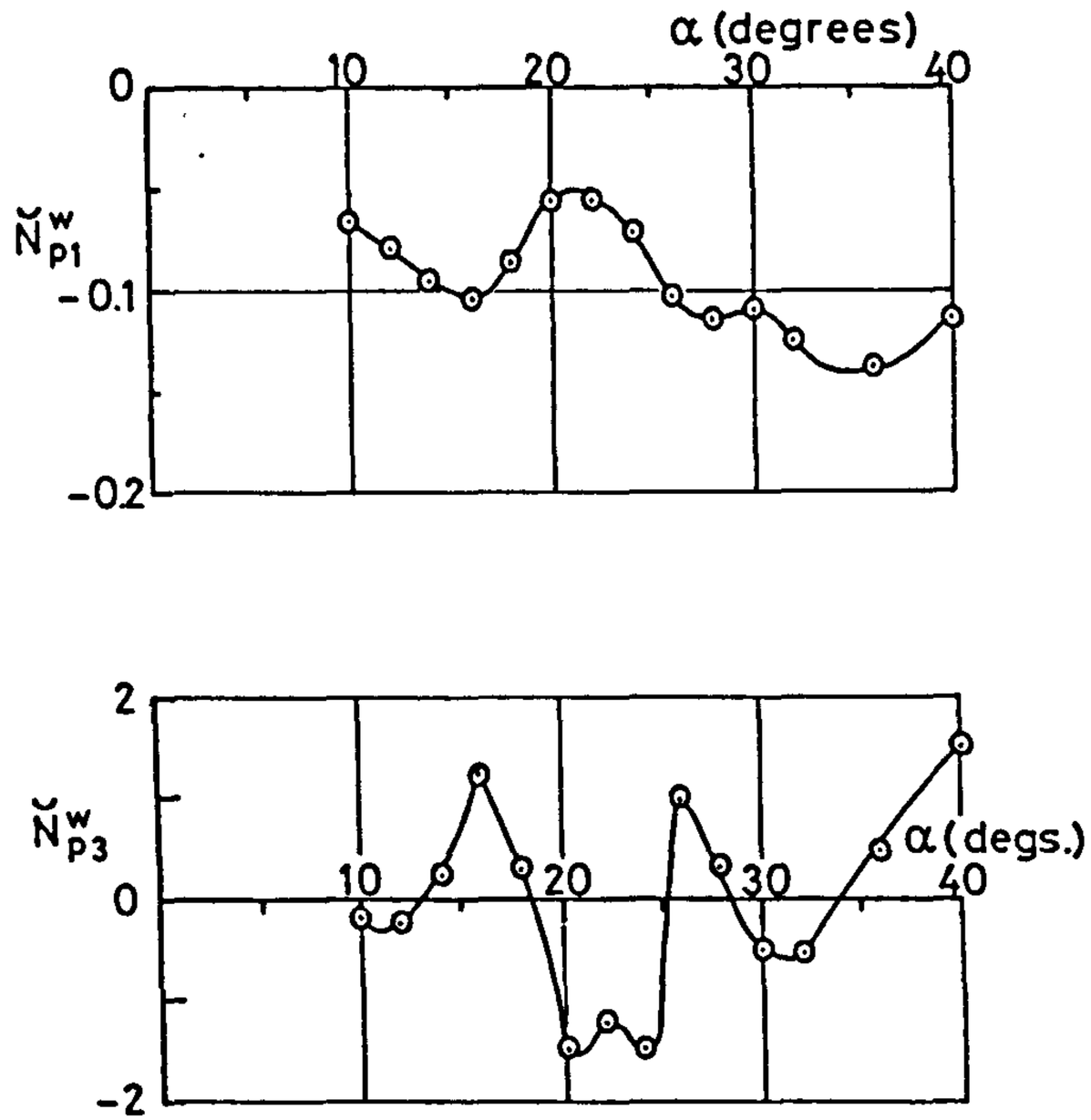

Fig 4.23 Modified cubic polynomial coefficients for C_n(pb/2V)

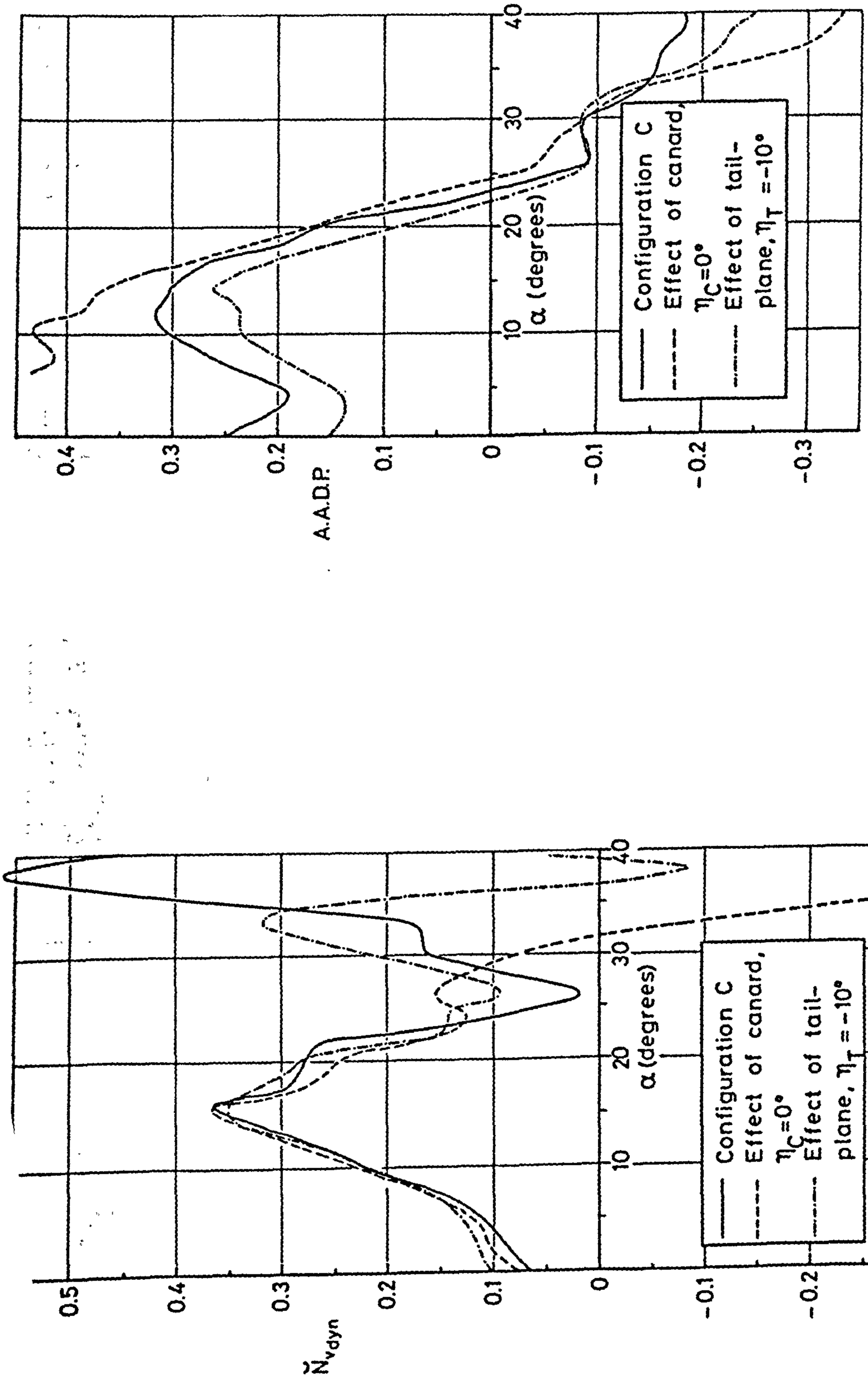

Fig 5.2 Effect of control surface deflections on A.A.D.P.

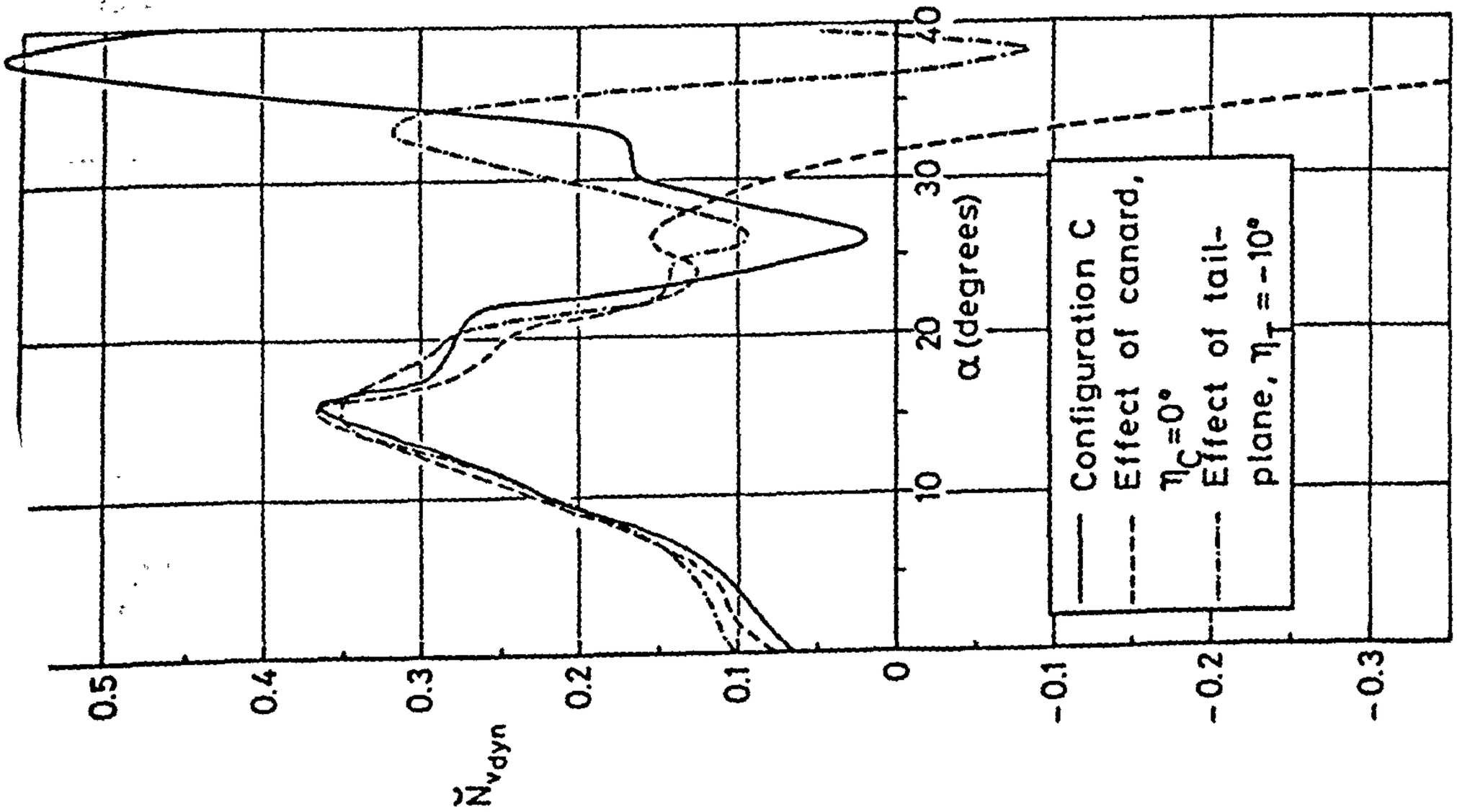

Fig 5.1 Effect of control surface deflections on $\tilde{N}_{vdyn}$

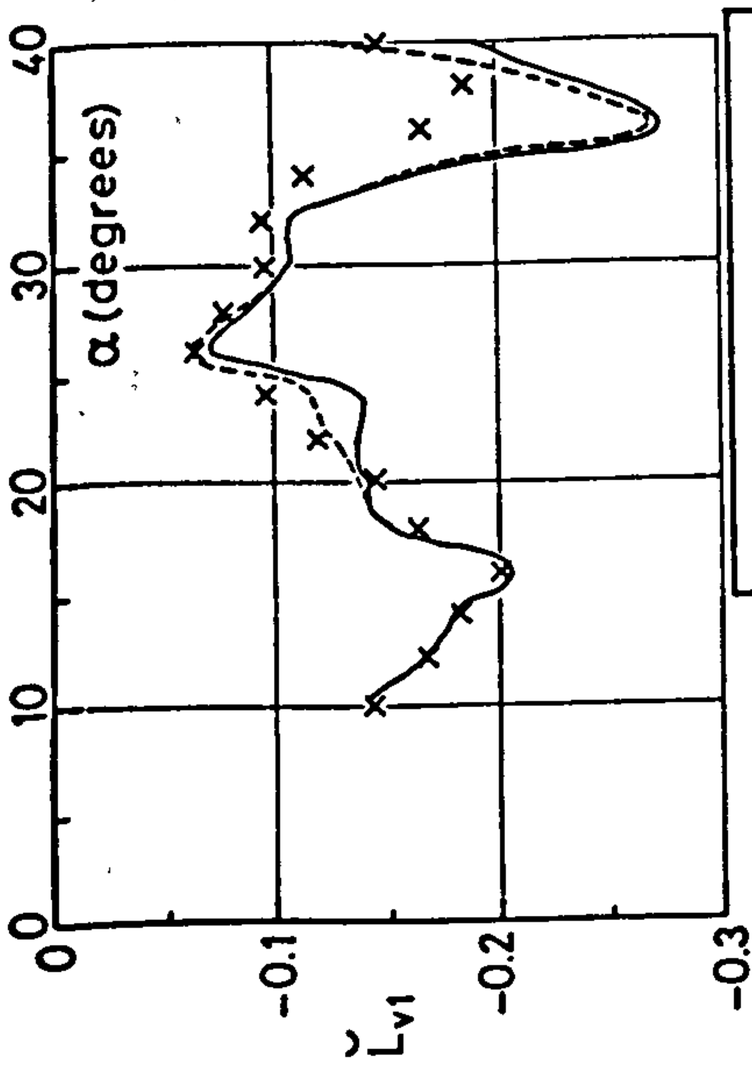

Fig 5.4 Effect of static data curve fitting on L_v and N_v

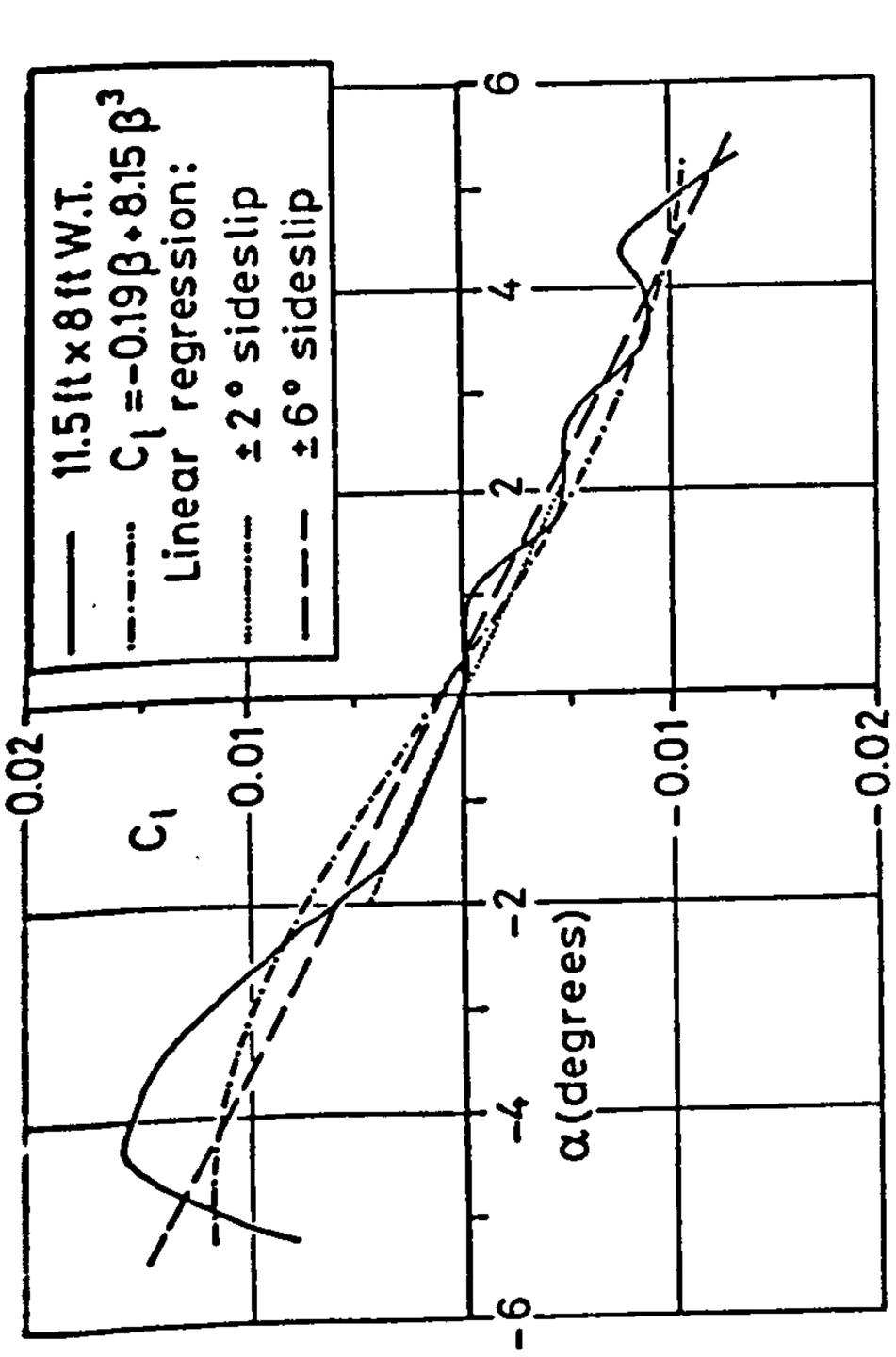

Fig 5.3 Curve fits to $C_l(\beta)$ and $C_n(\beta)$ data at $\alpha = 40°$

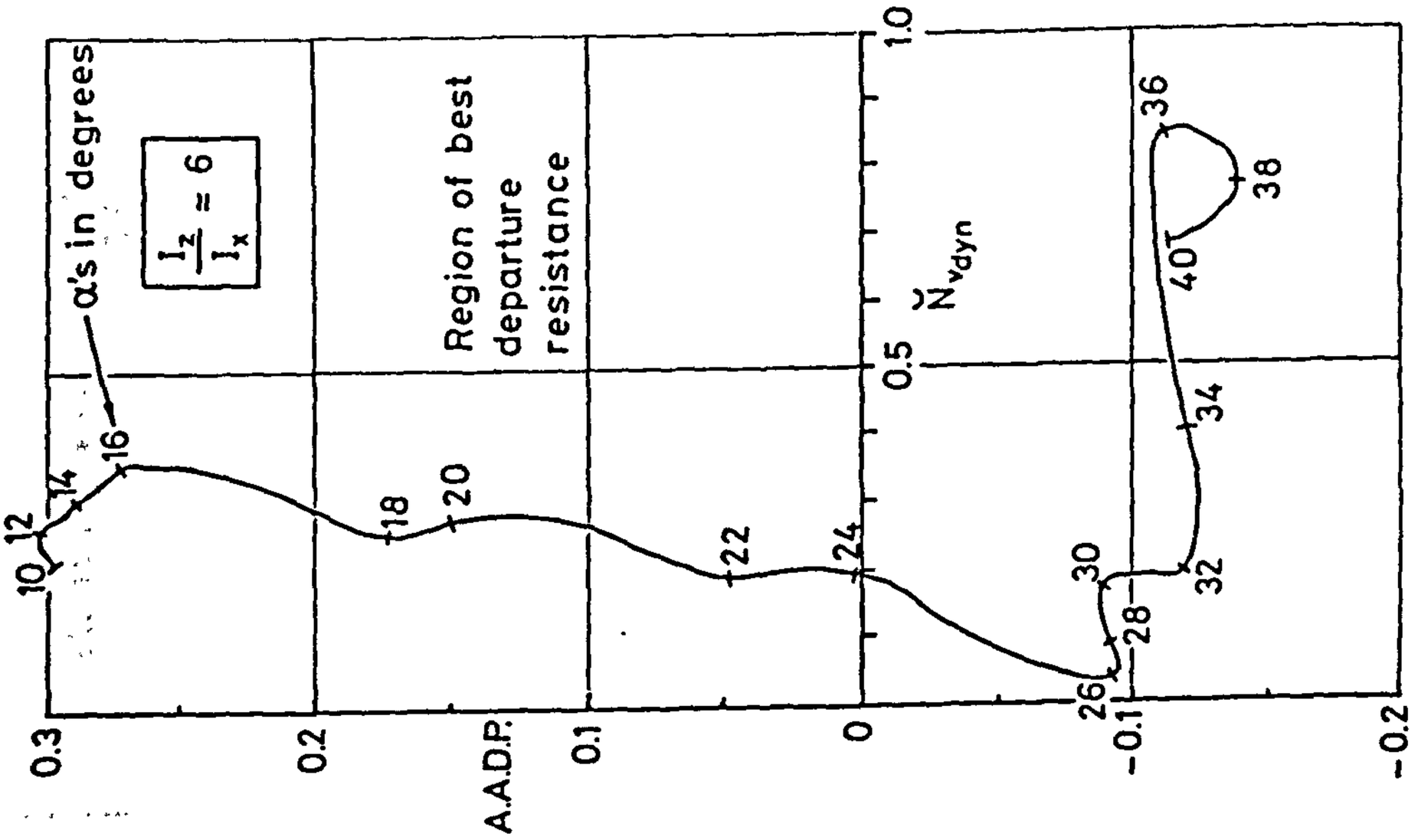

Fig 5.6 A.A.D.P against $\check{N}_{vdyn}$ for configuration C

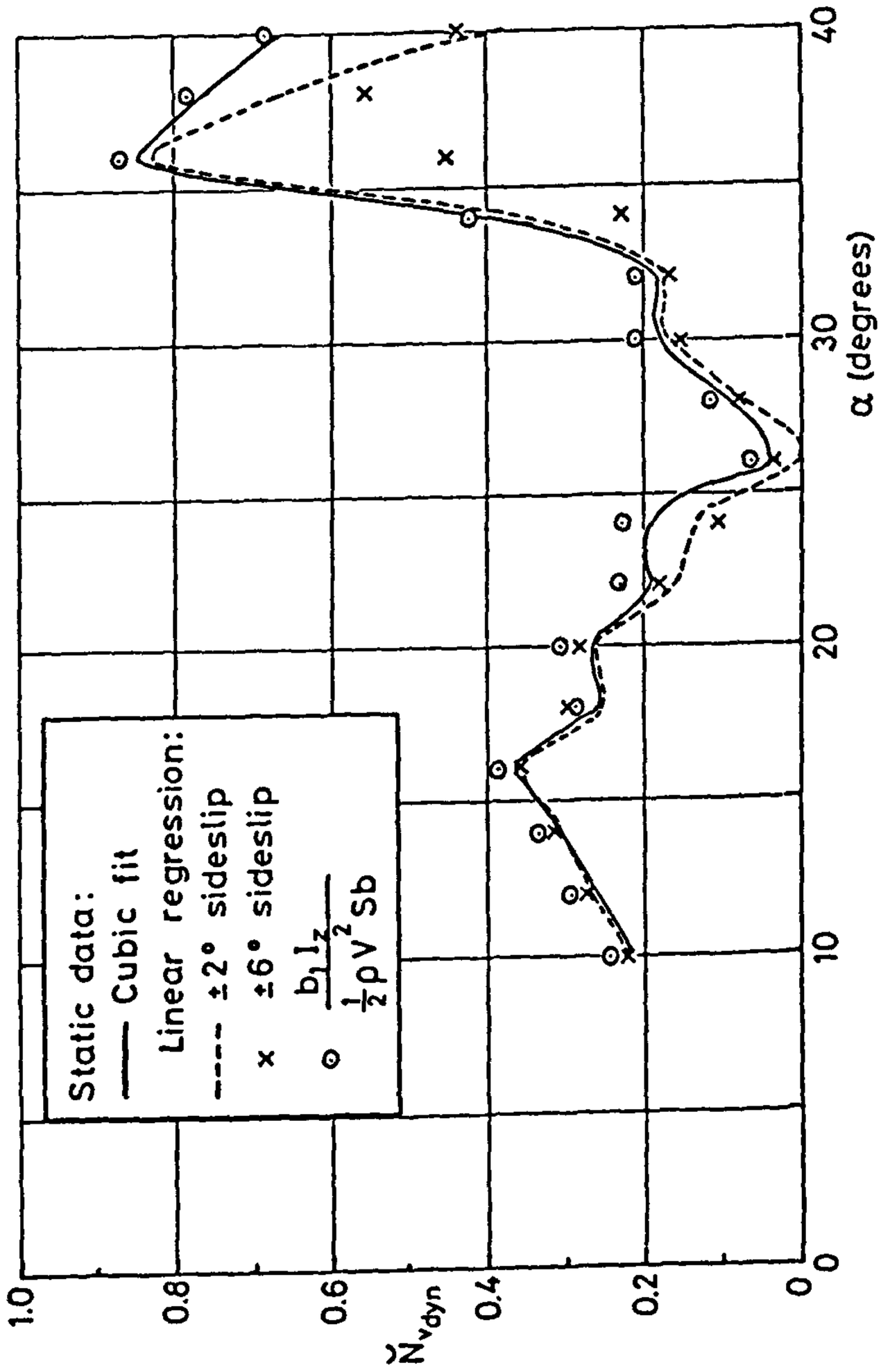

Fig 5.5 Effect of curve fitting on $\check{N}_{vdyn}$

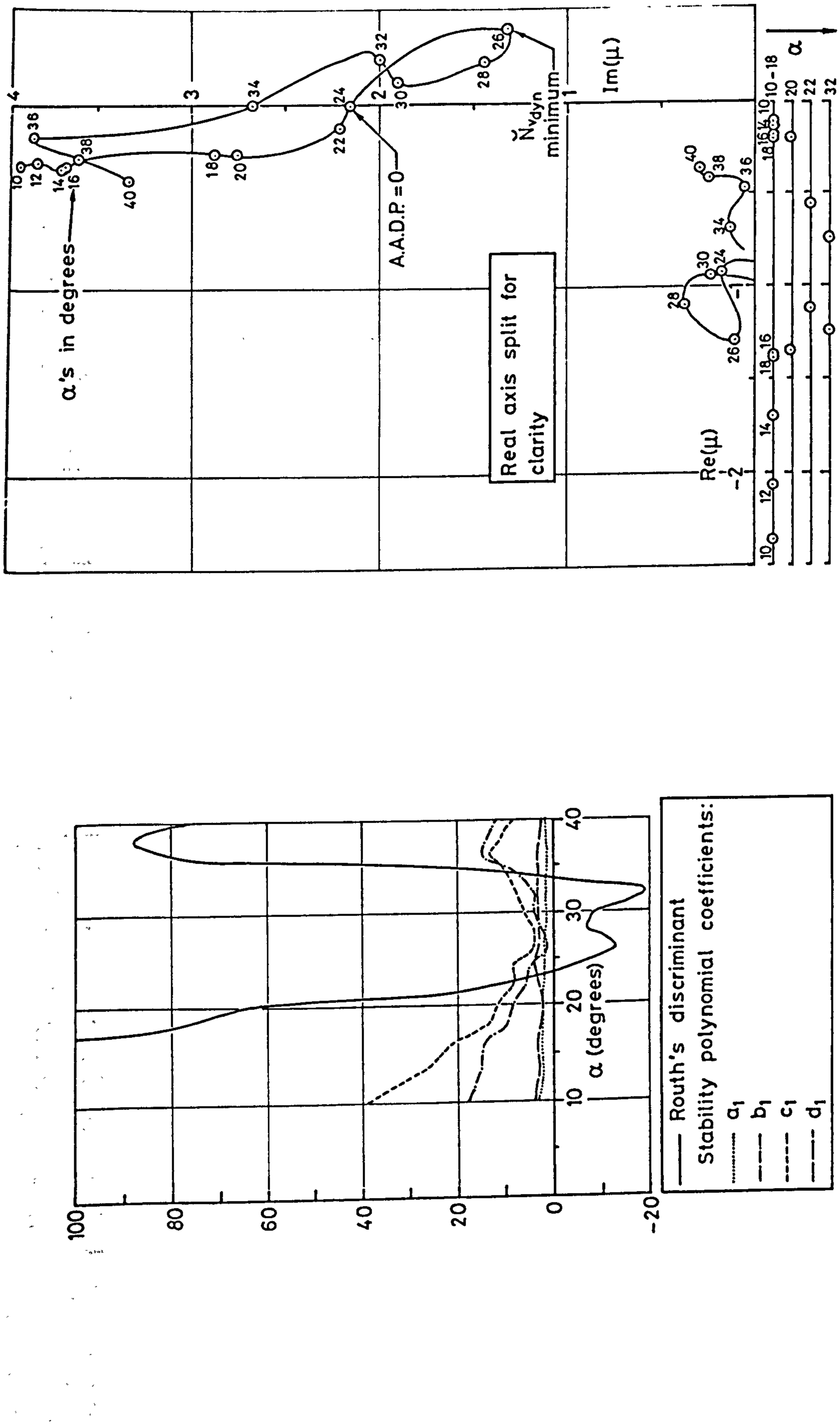

Fig 5.8 Lateral roots migration with angle of attack

Fig 5.7 Coefficients of linear terms of stability polynomial and Routh's discriminant

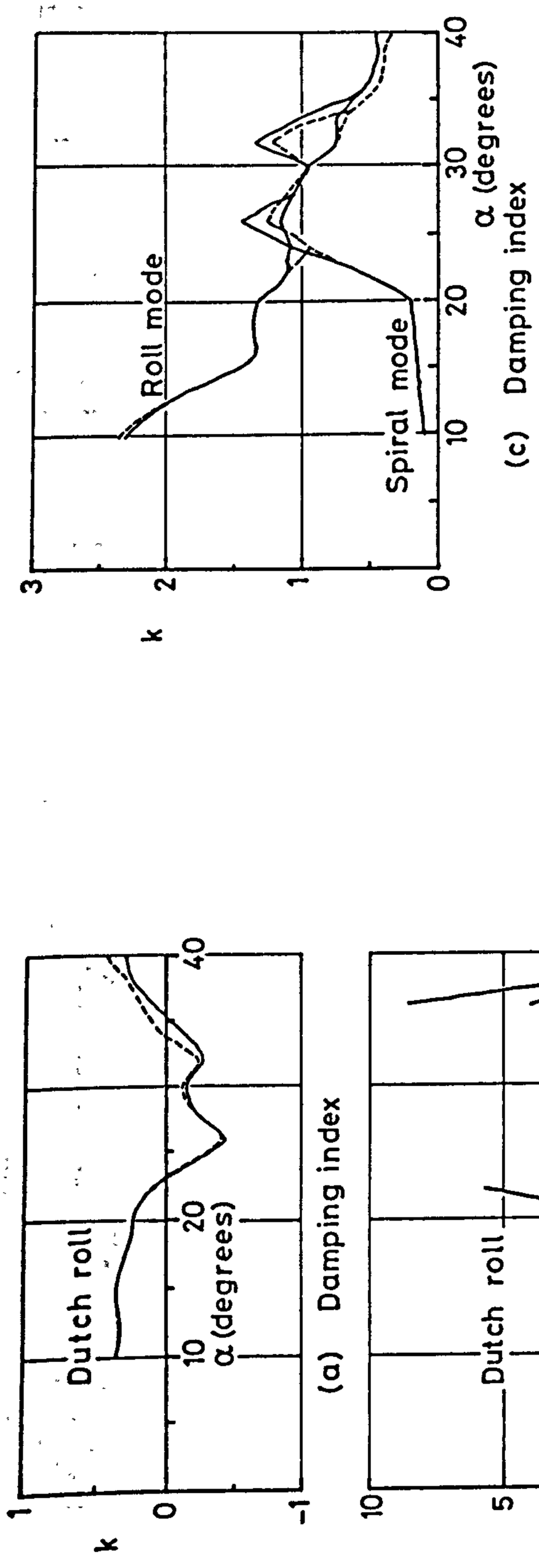

(c) Damping index

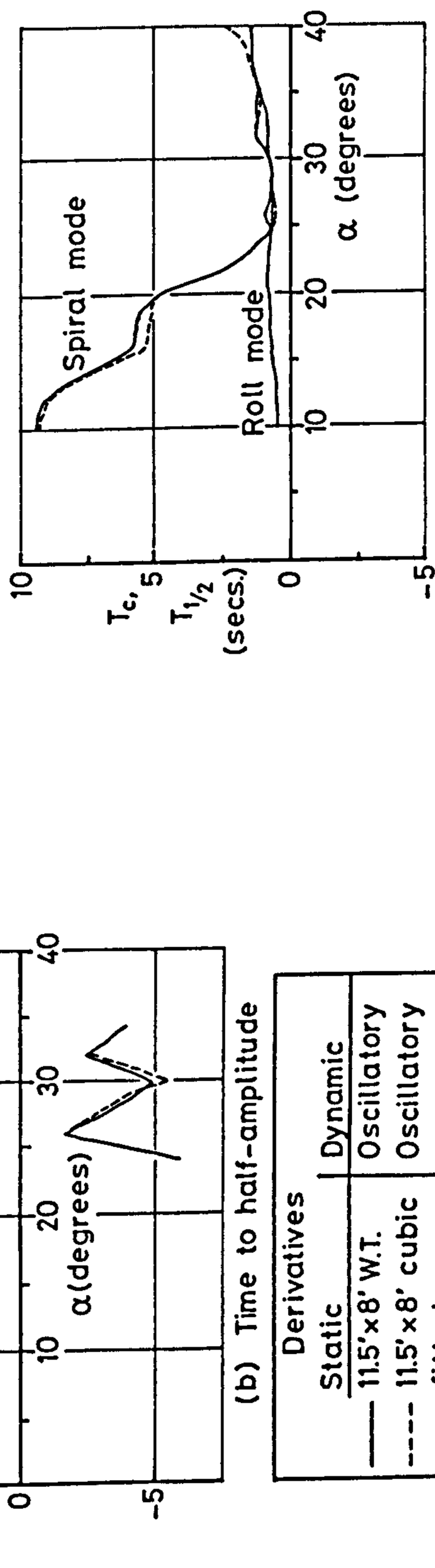

(d) Time constants and time to half-amplitude

(a) Damping index

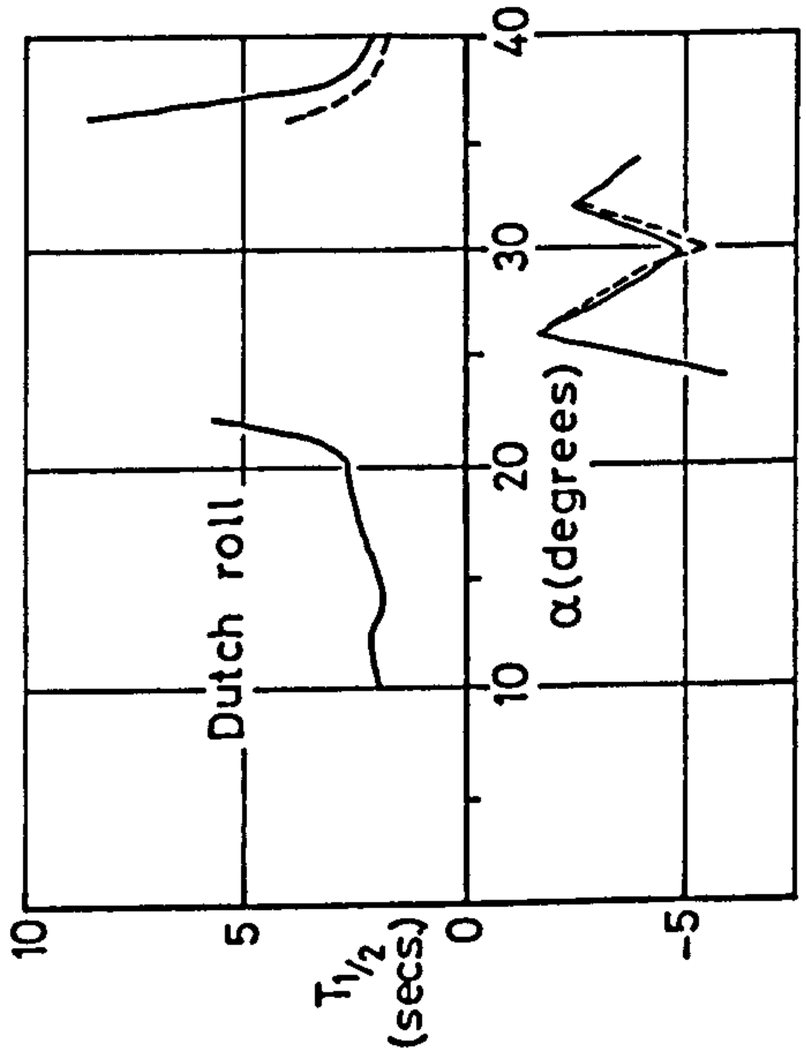

(b) Time to half-amplitude

Derivatives	Dynamic
Static	Oscillatory
—— 11.5'×8' W.T.	Oscillatory
---- 11.5'×8' cubic fitted	

Fig 5.9 Effect of static/oscillatory data on lateral roots

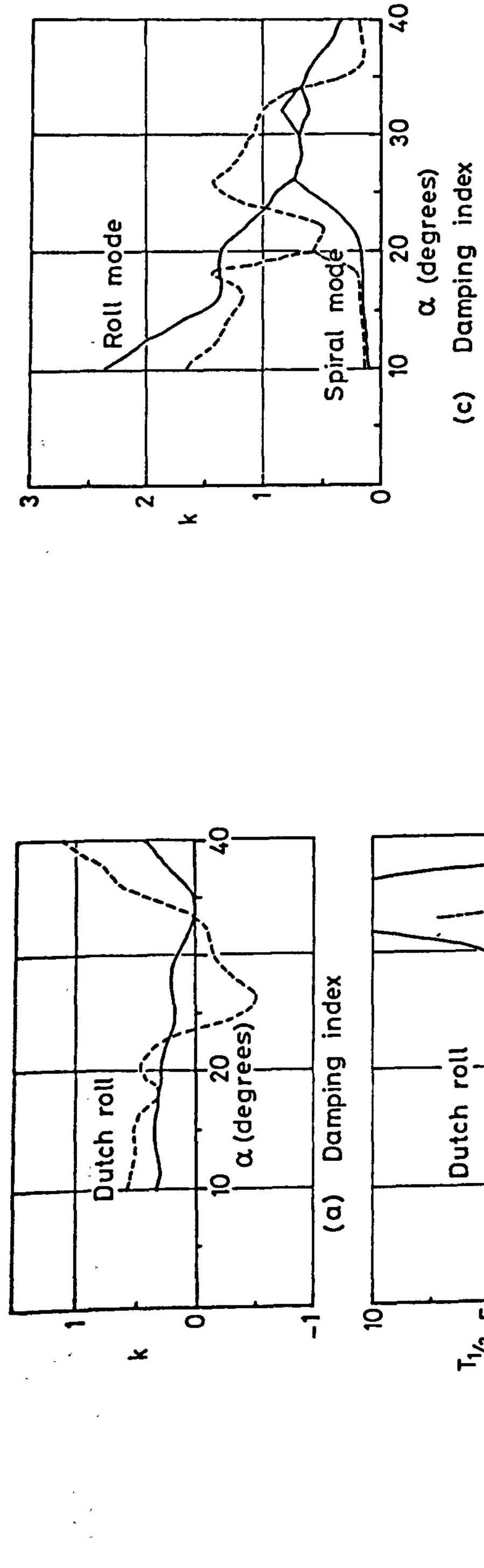

(c) Damping index

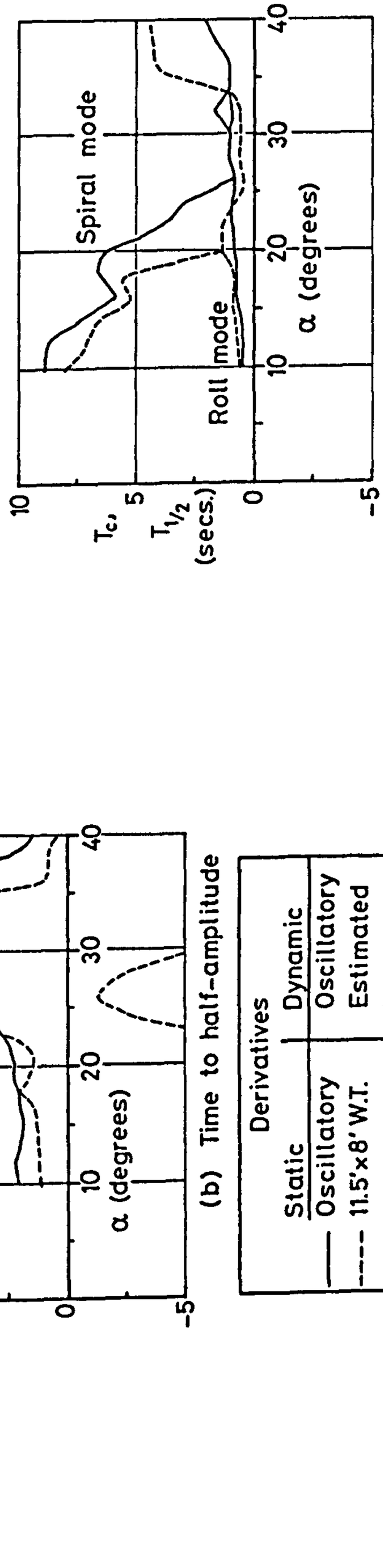

(d) Time constants and time to half-amplitude

(a) Damping index

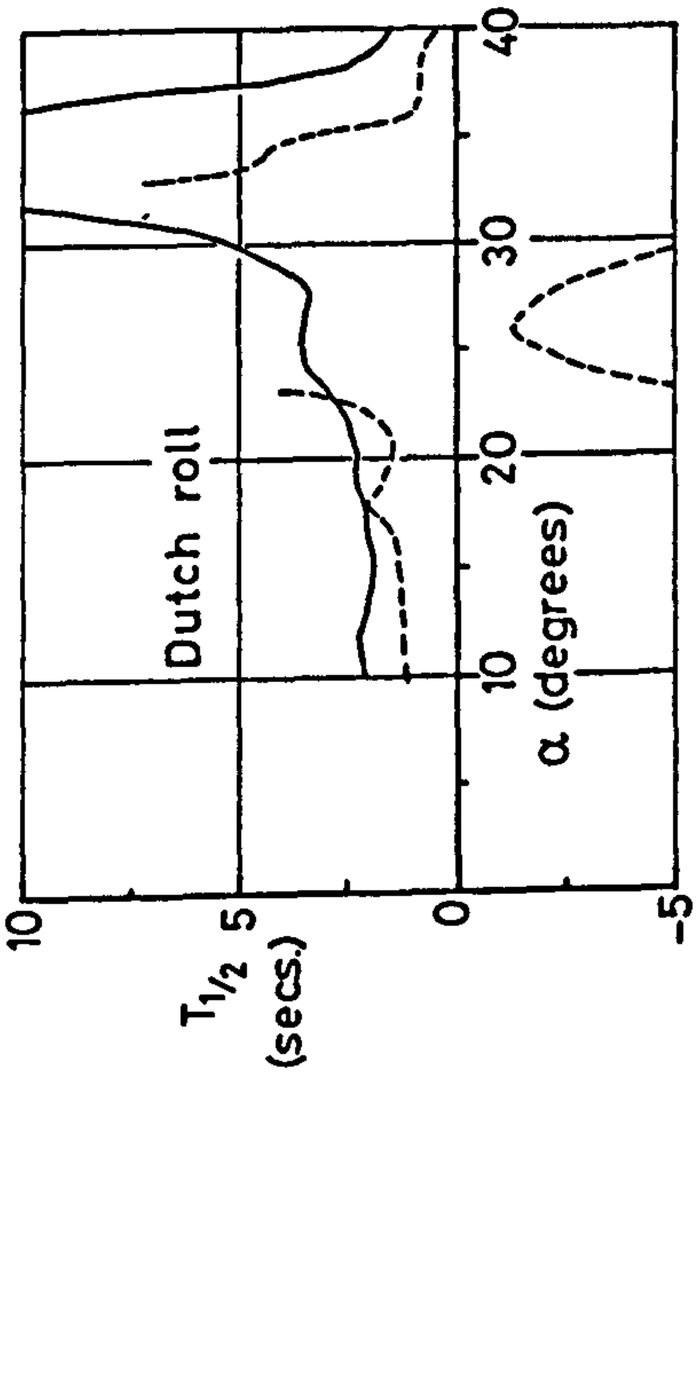

(b) Time to half-amplitude

Fig 5.10 Effect of static/oscillatory/estimated data on lateral roots

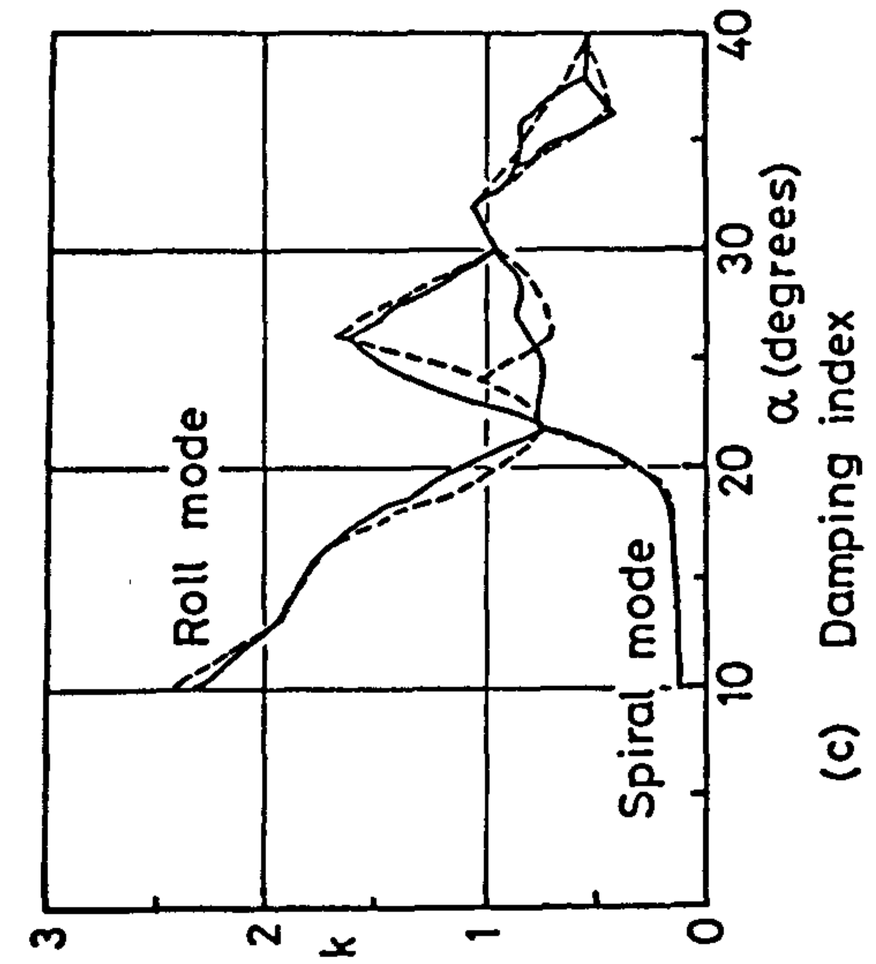

(c) Damping index

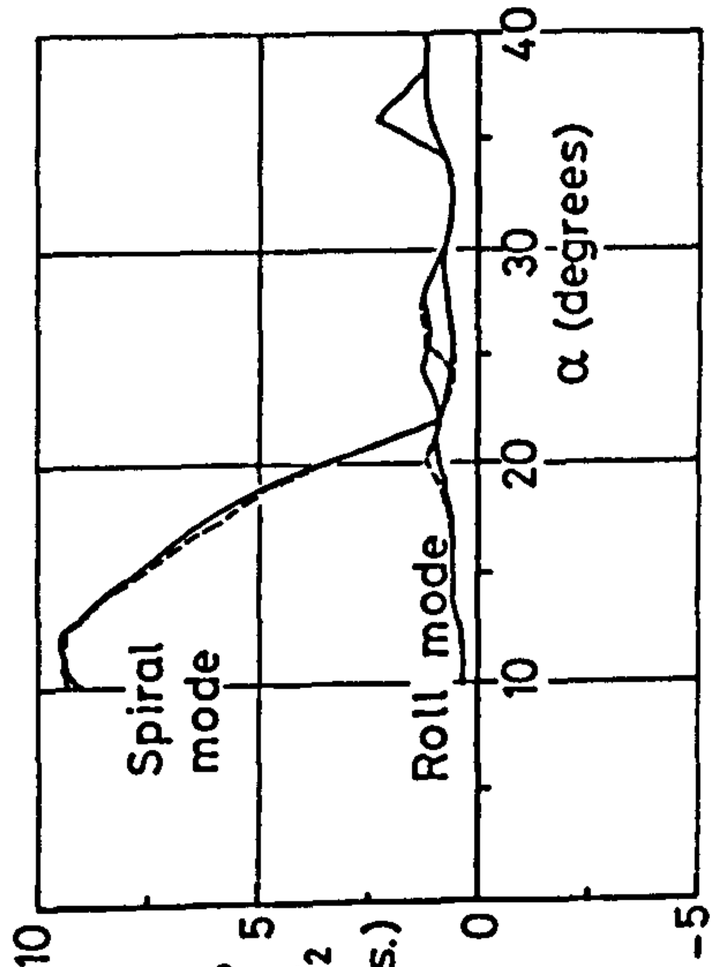

(d) Time constants and time to half-amplitude

on lateral roots

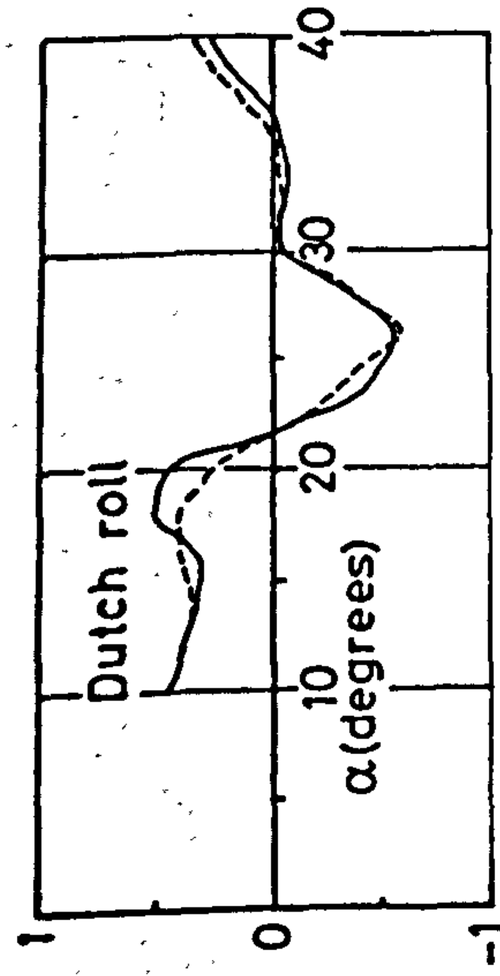

(a) Damping index

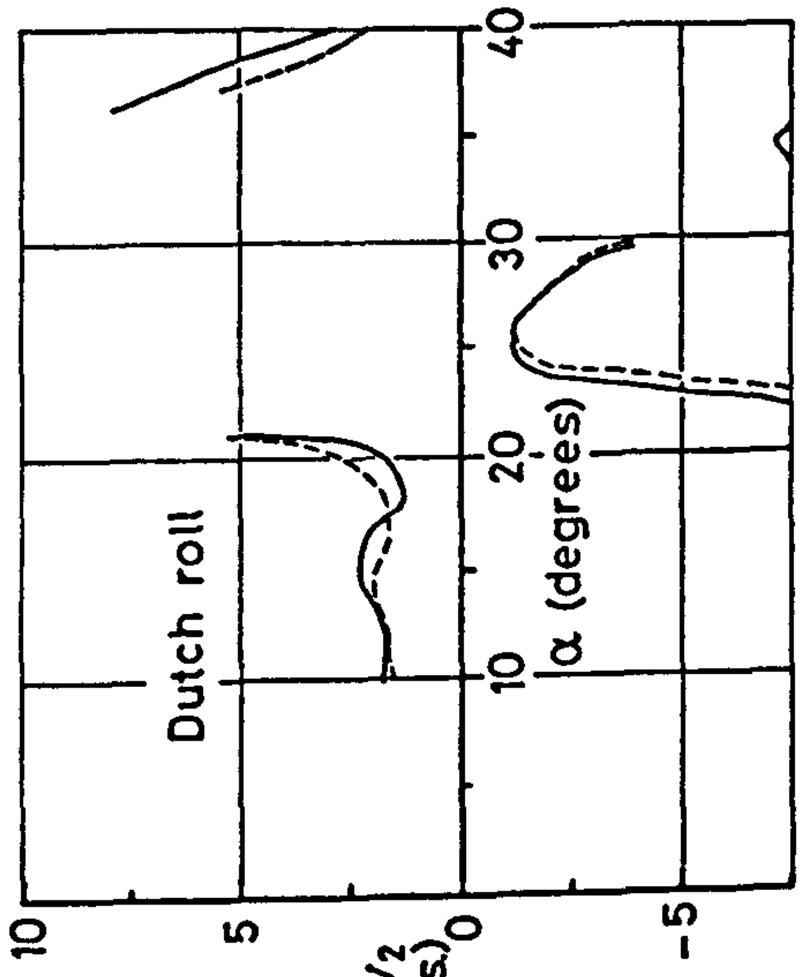

(b) Time to half-amplitude

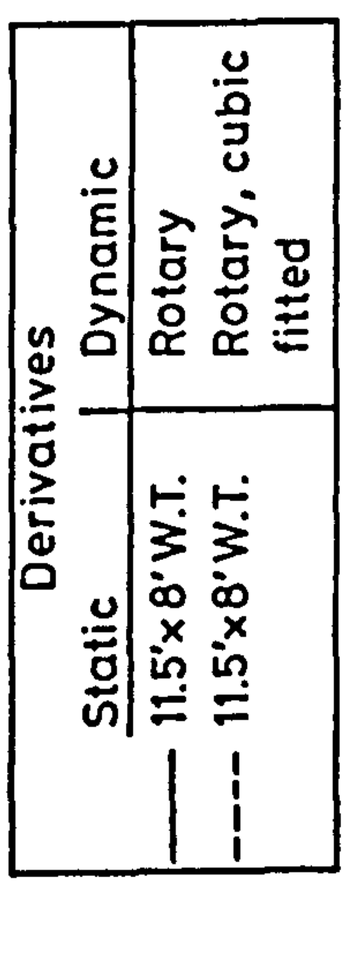

t of static/rotary data

Fig 5.11 Effect

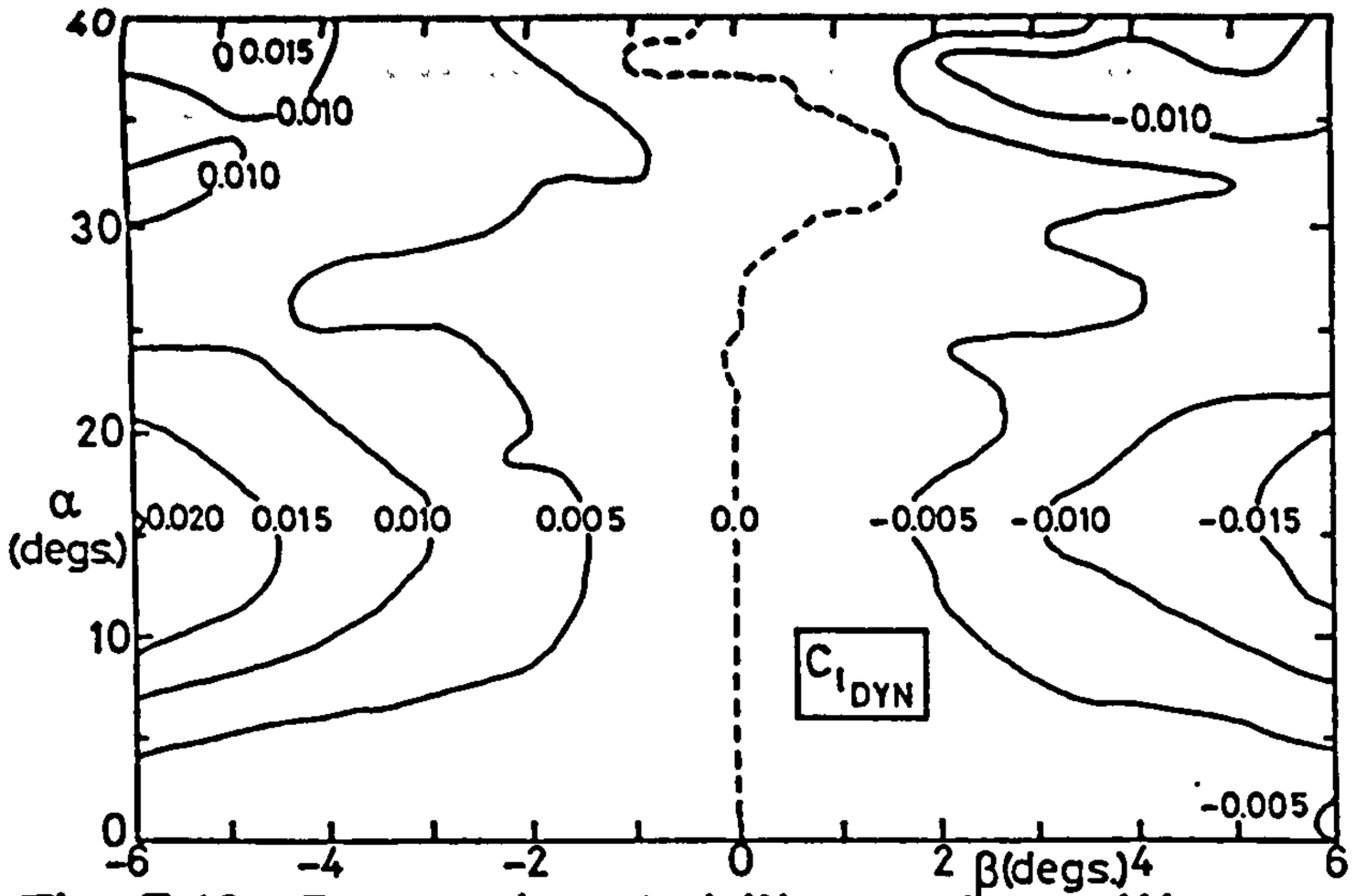

Fig 5.12 Dynamic stability axis rolling moment coefficient for HIRM C

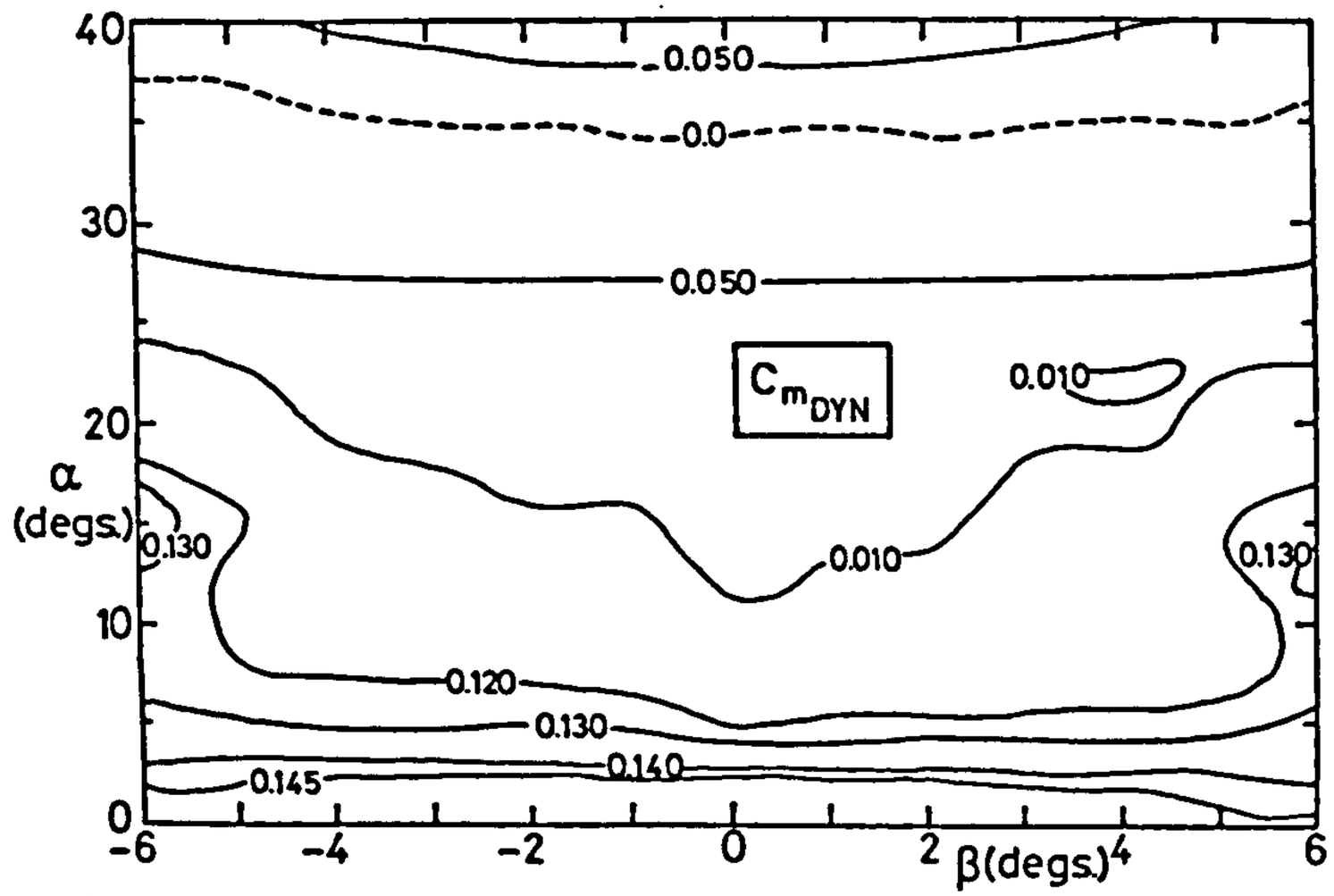

Fig 5.13 Dynamic stability axis pitching moment coefficient for HIRM C

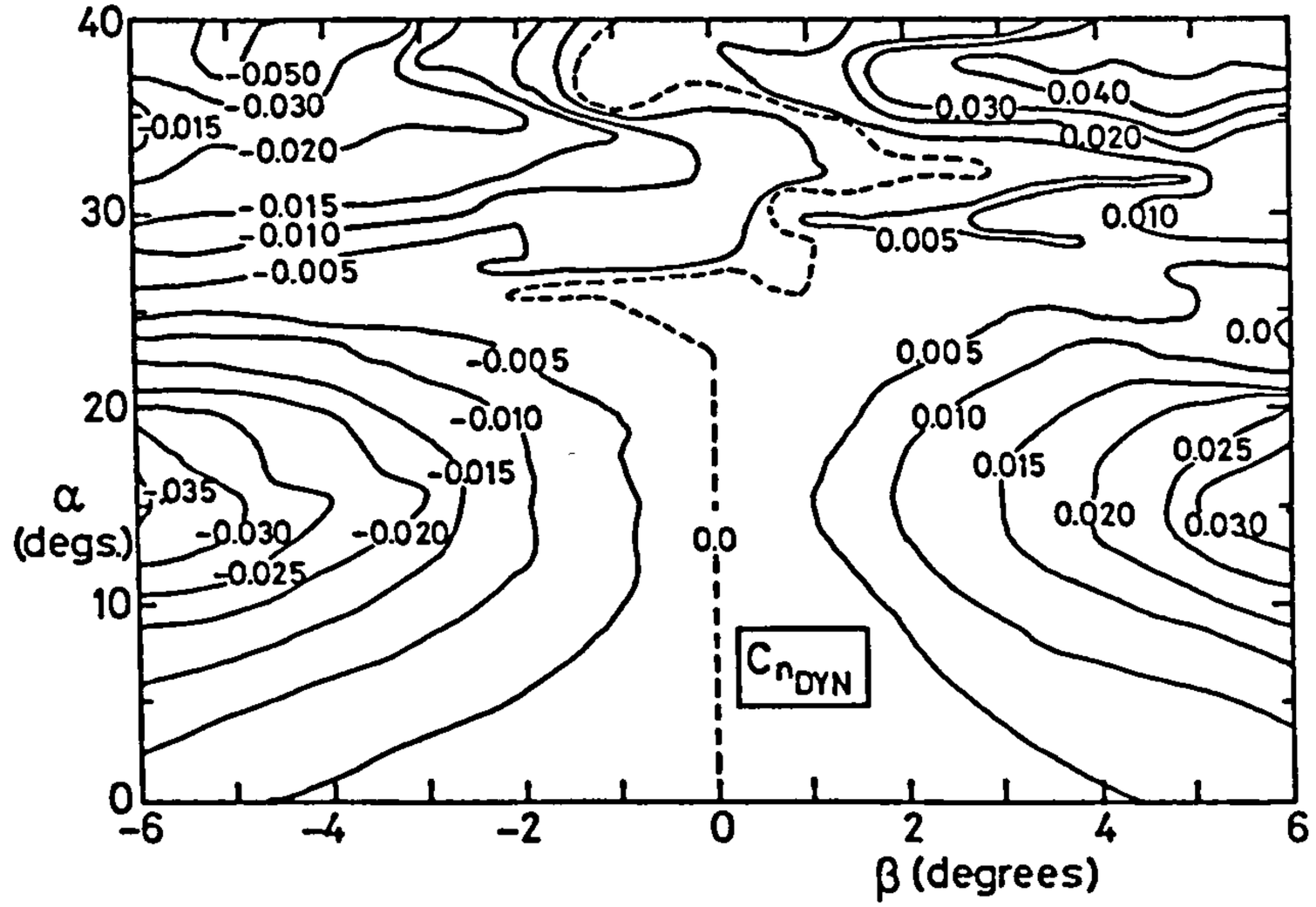

Fig 5.14 Dynamic stability axis yawing moment coefficient for HIRM C

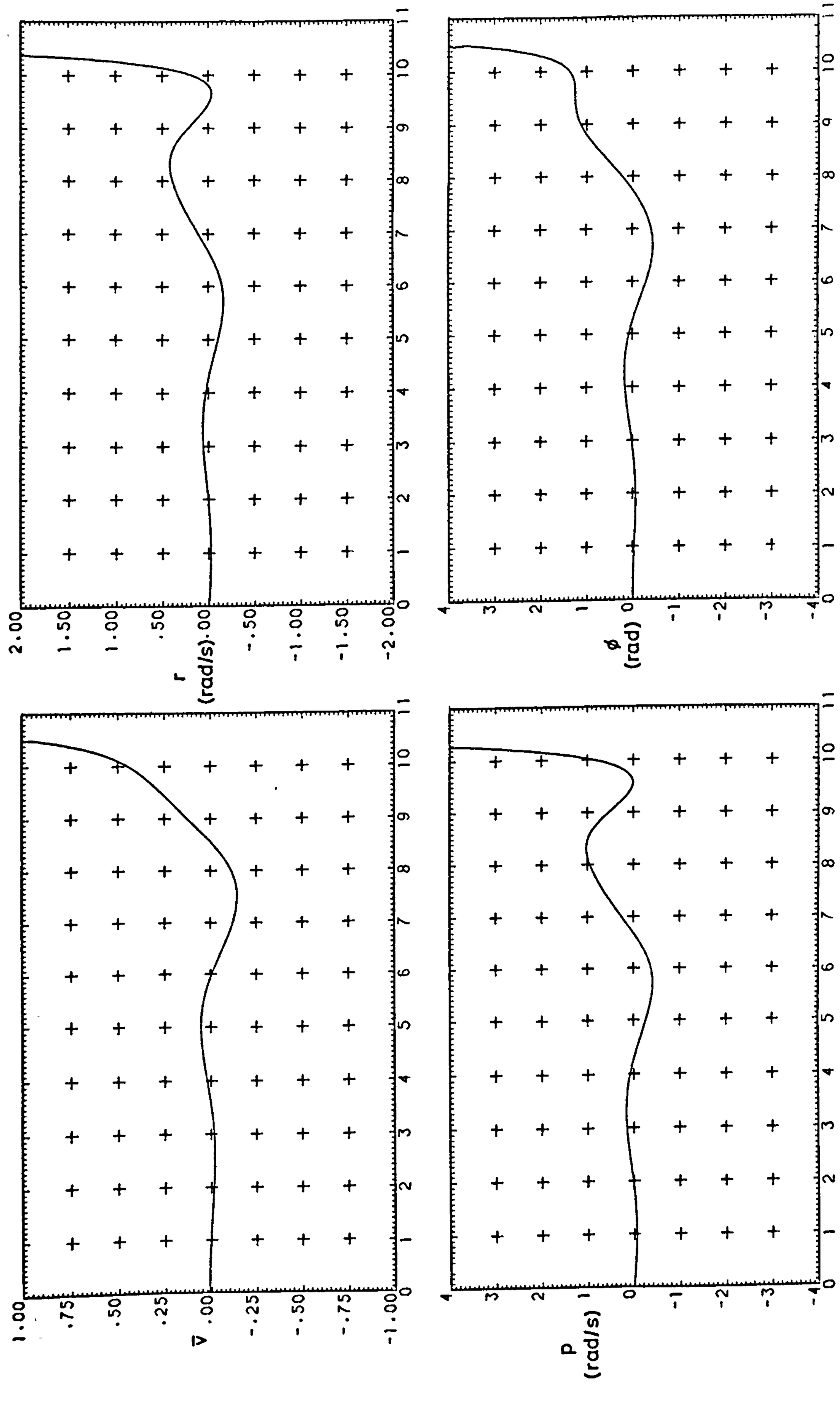

Fig 5.15 HIRM C divergent response at 26° angle of attack with sideslip non-linearities

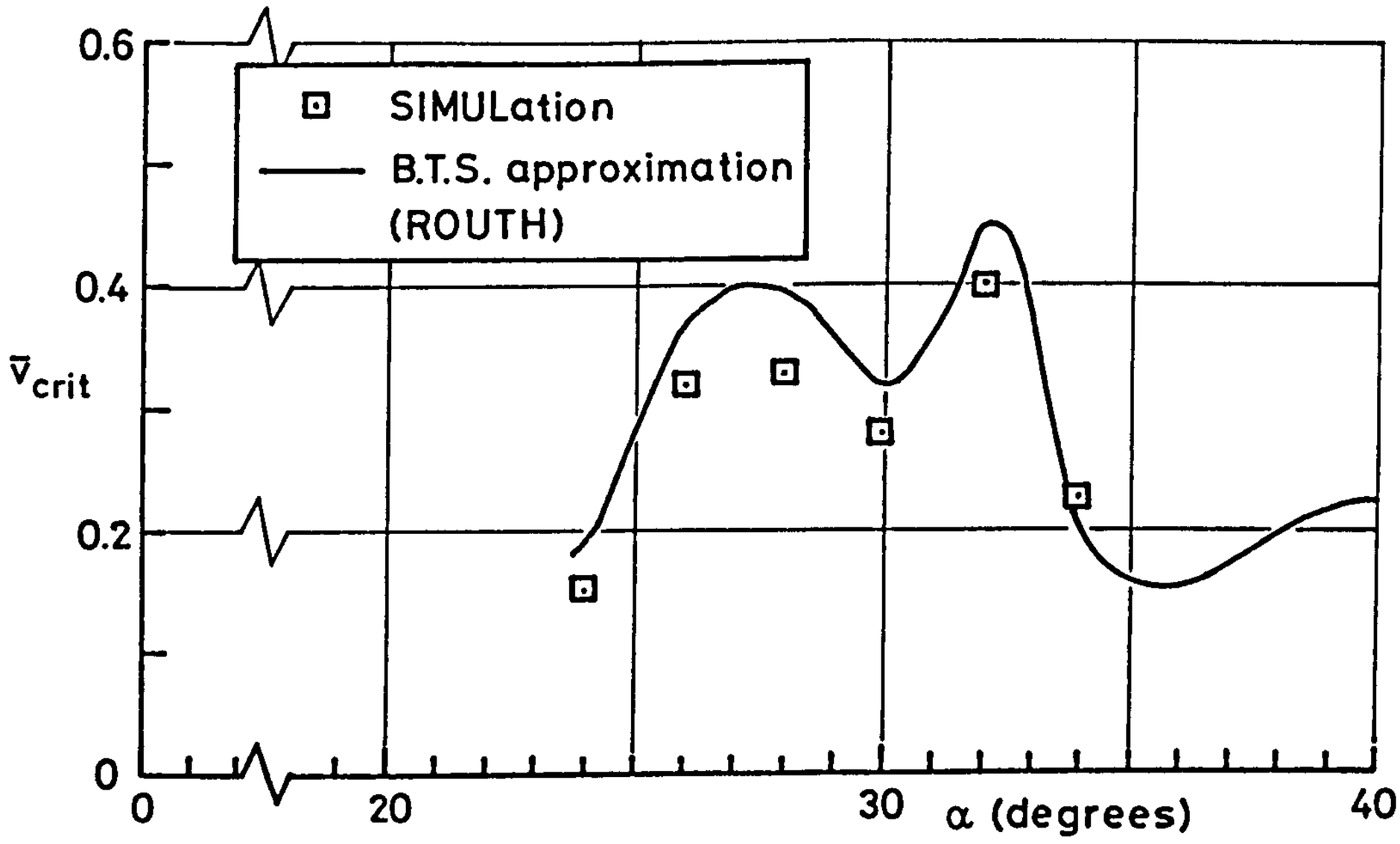

Fig 5.16 Configuration C divergence boundary with cubic non-linearities in sideslip

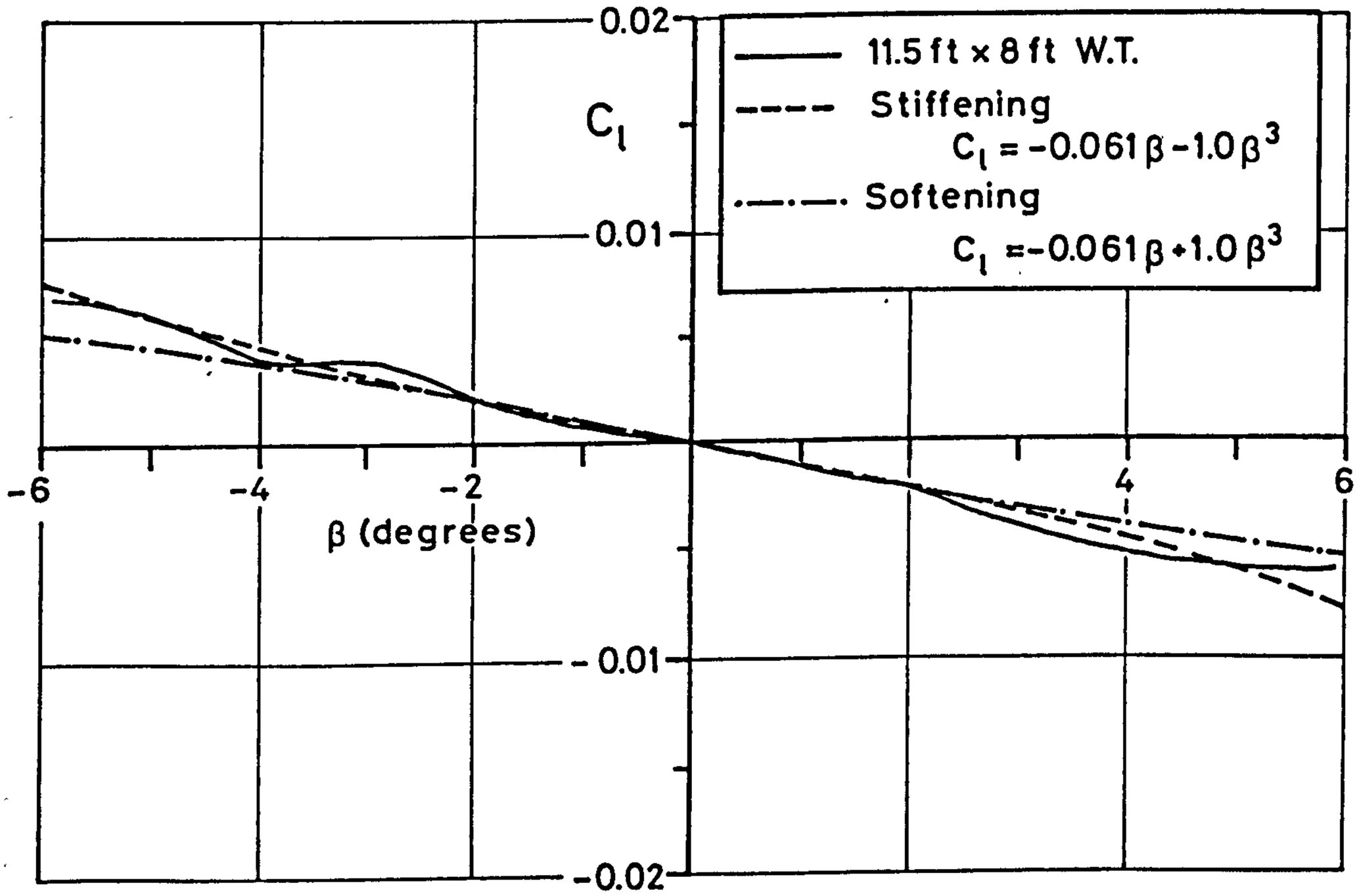

Fig 5.17 Variation in cubic polynomial fits to $C_l(\beta)$ data at $\alpha = 26°$

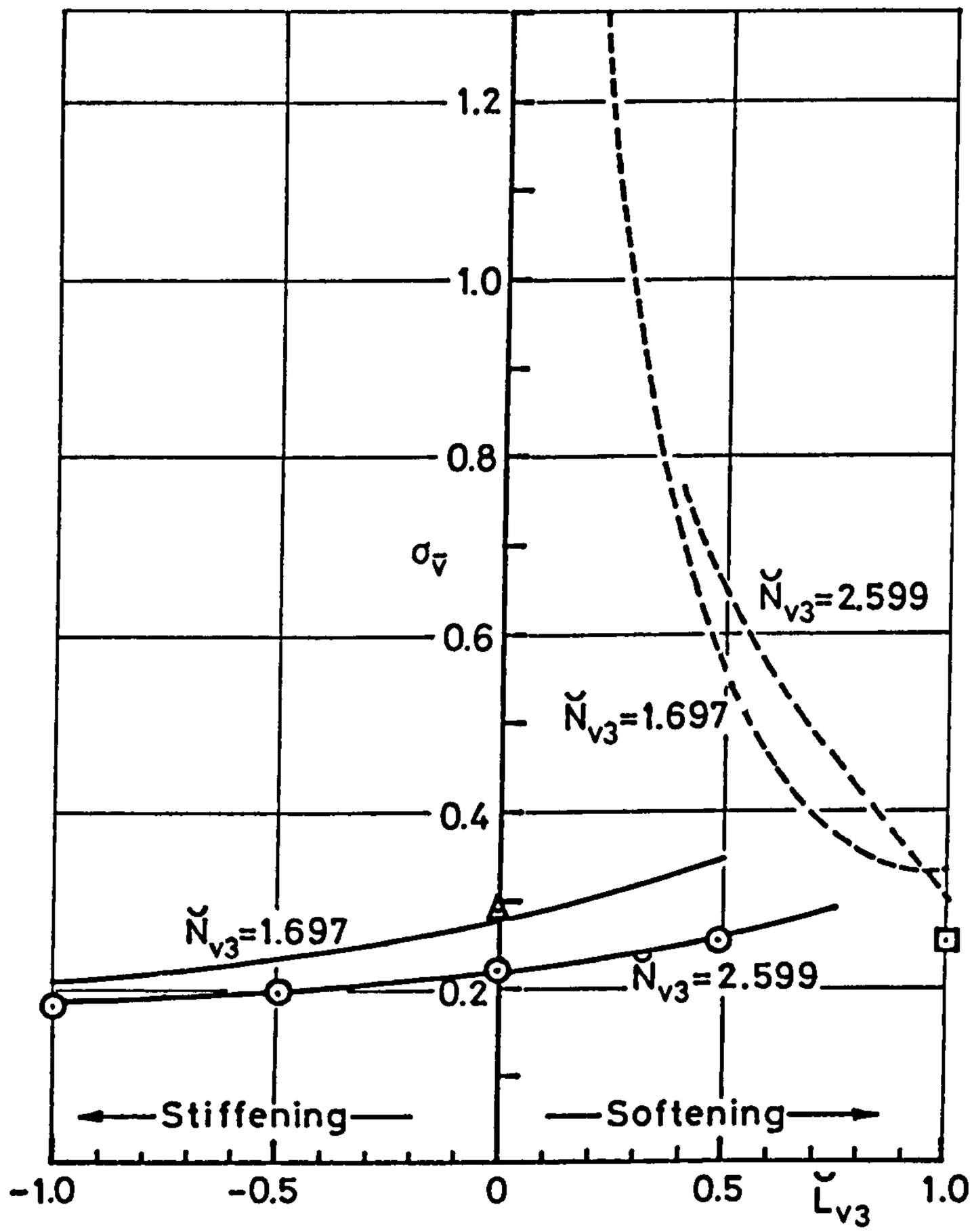

Amplitude of oscillation and at divergence

	Oscillation	Divergence
SIMULation $\breve{N}_{v3}$=1.697	△	
$\breve{N}_{v3}$=2.599	⊙	⊡
B.T.S. approximation	———	- - - - -

Fig 5.18 Configuration C response characteristics with sideslip non-linearities at $\alpha = 26°$

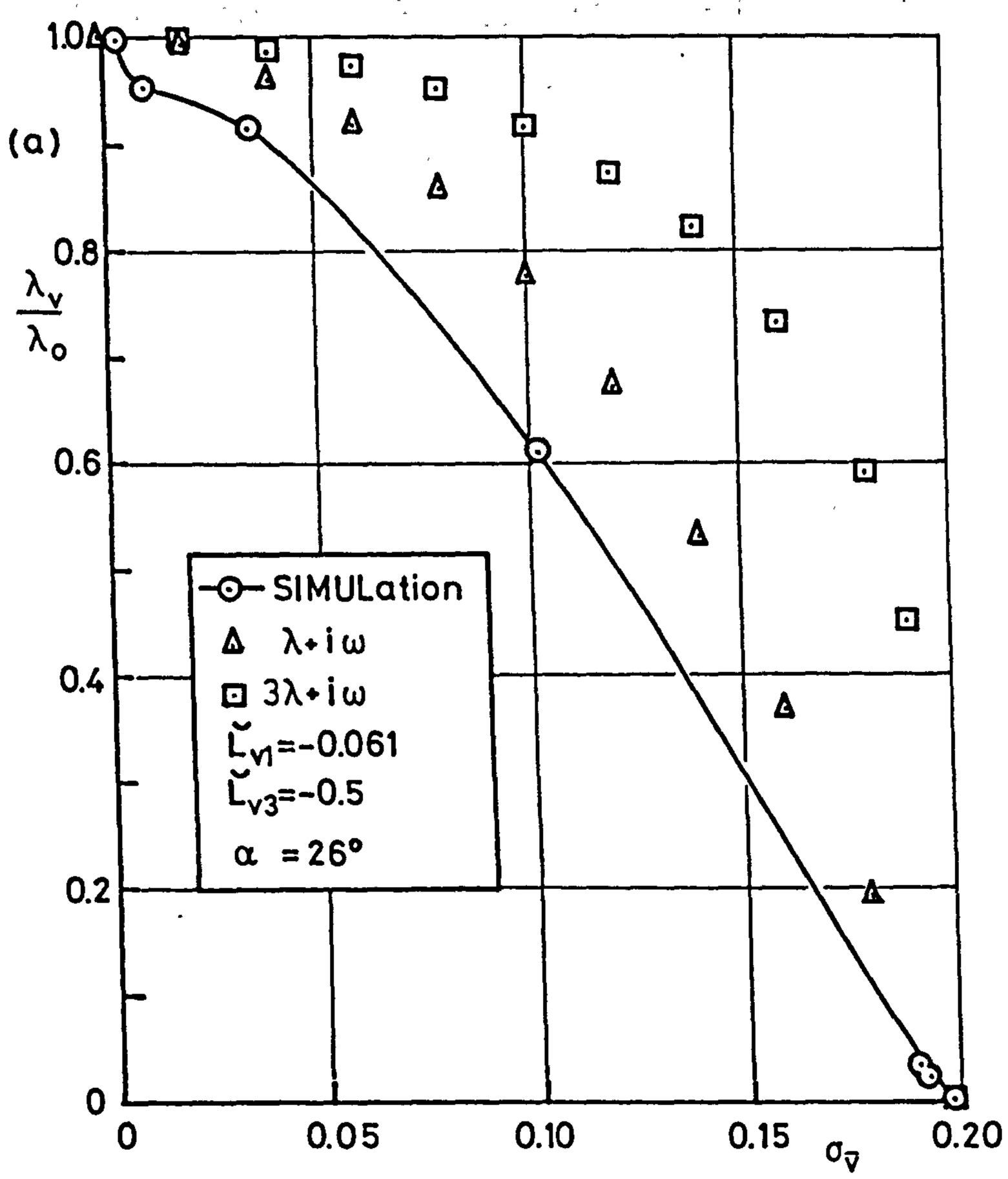

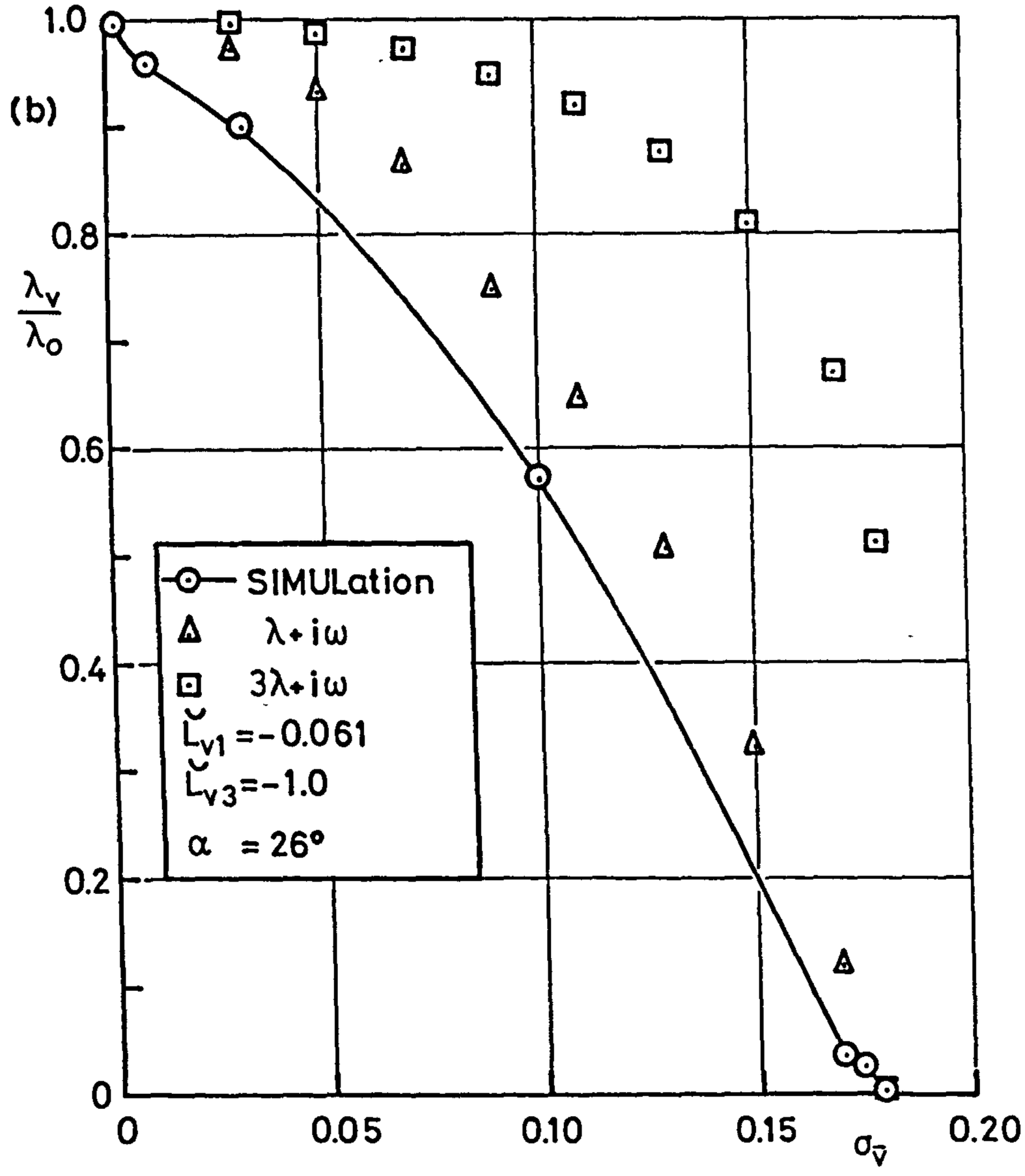

Fig 5.19 Damping factor for HIRM C response with non-linearity in sideslip

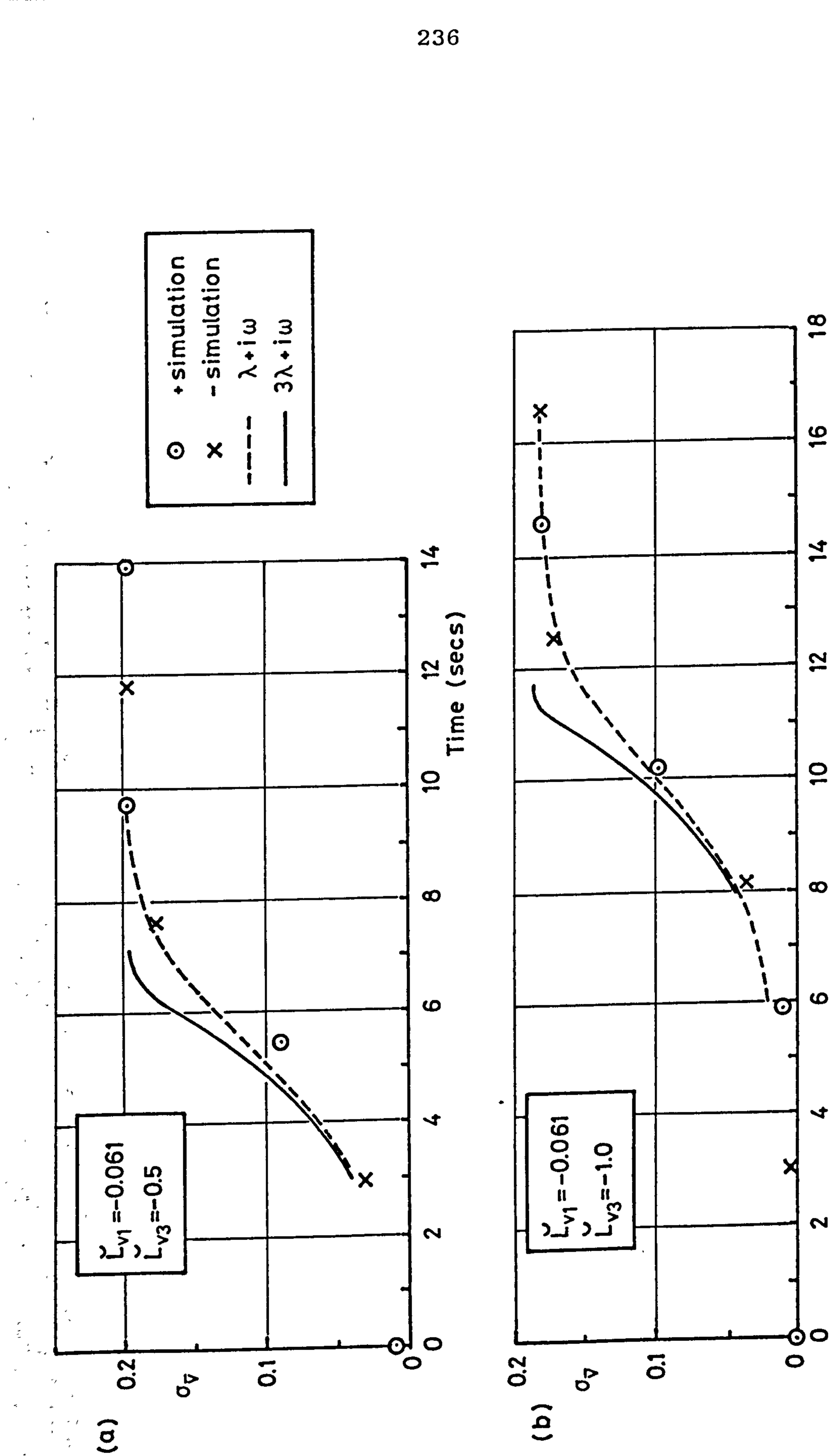

Fig 5.20 Rate of growth to limit cycle for HIRM C with cubic sideslip non-linearity

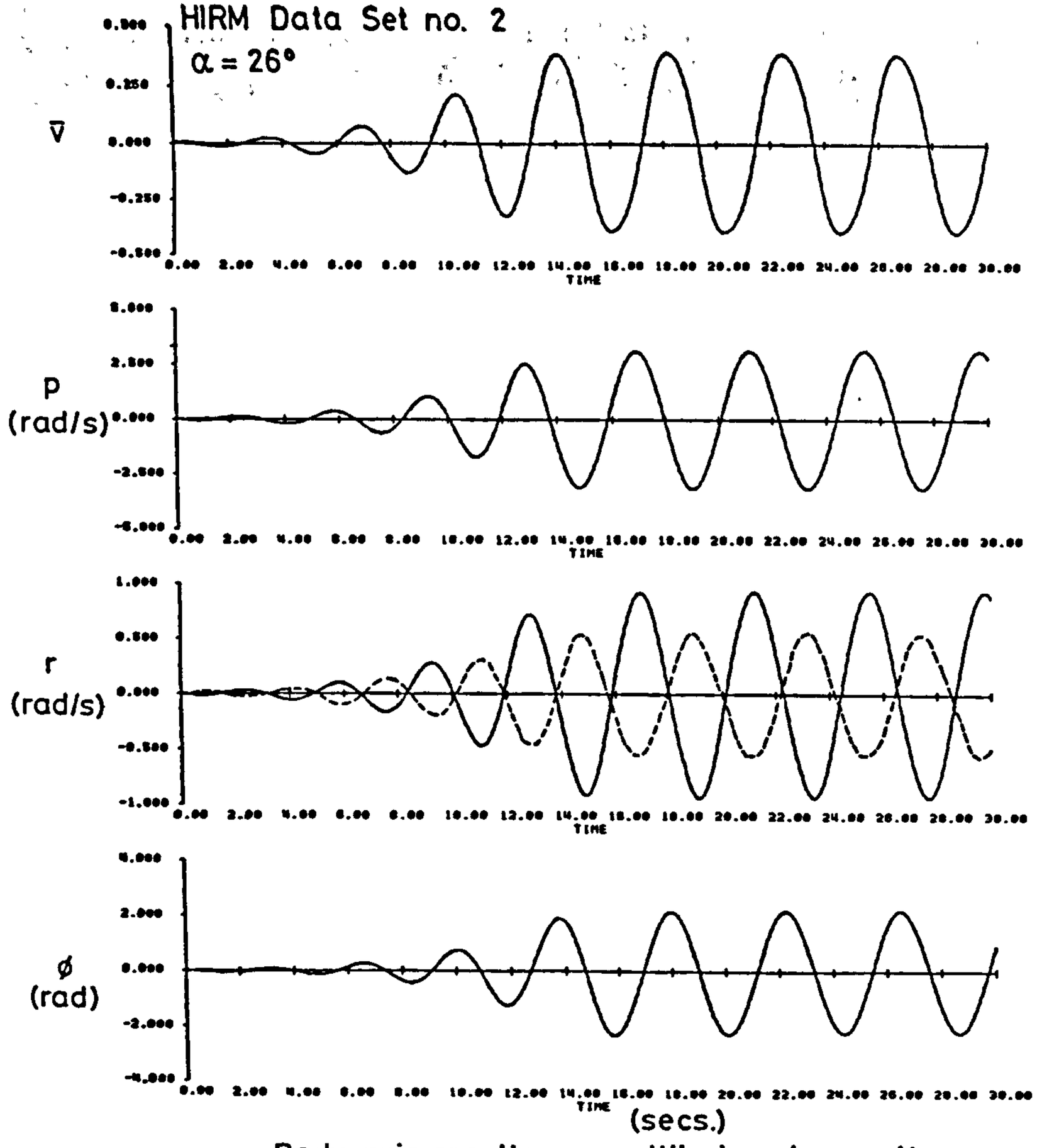

—— Body axis results ----- Wind axis results
Full cubic fits to $C_l^B(p^Wb/2V)$ and $C_n^B(p^Wb/2V)$

Fig 5.21 Wind axis simulation with non-linearities in roll rate

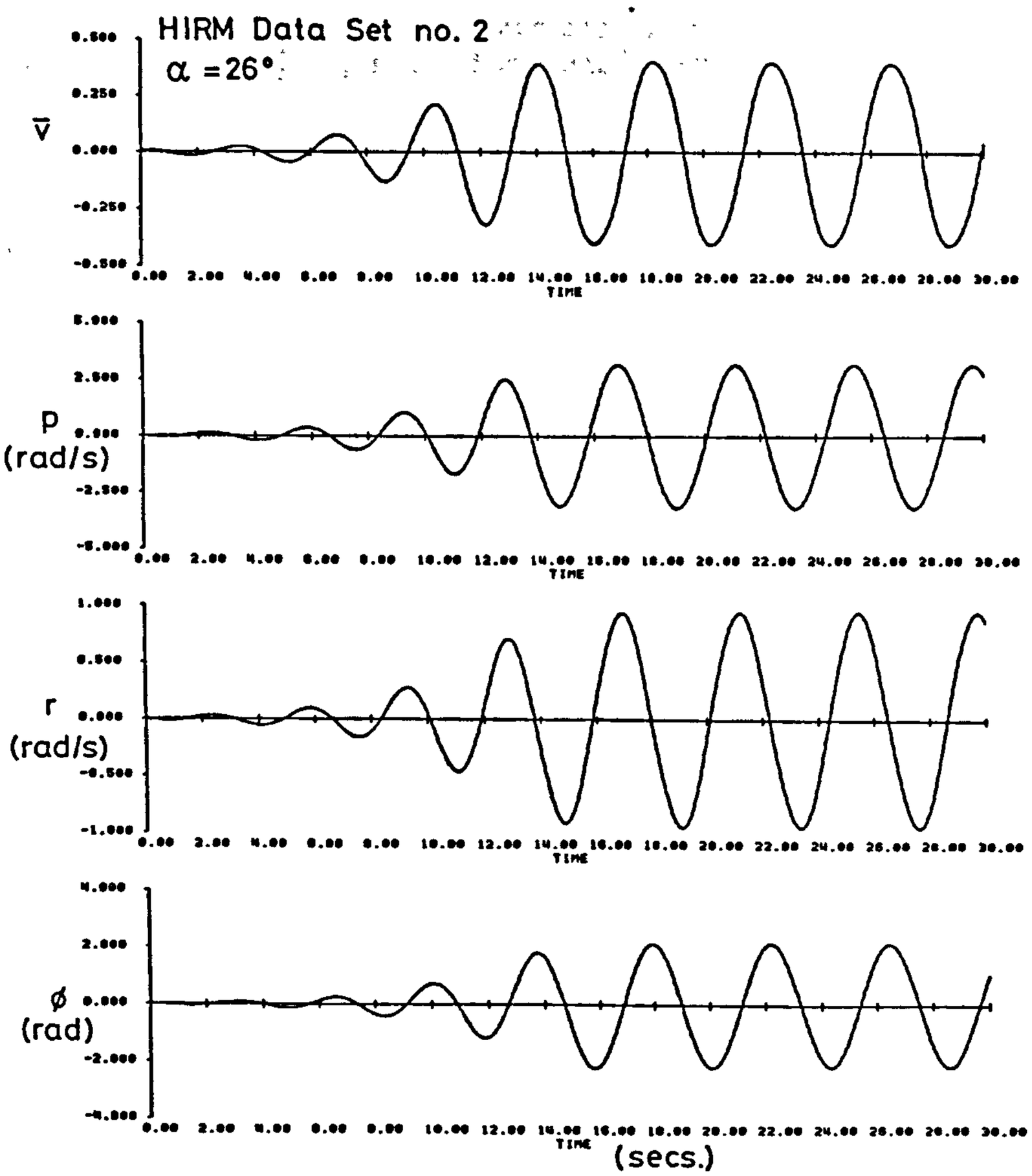

Body axis results
Modified cubic fits to $C_l^B(p^Wb/2V)$ and $C_n^B(p^Wb/2V)$

Fig 5.22 Body axis simulation with non-linearities in roll rate

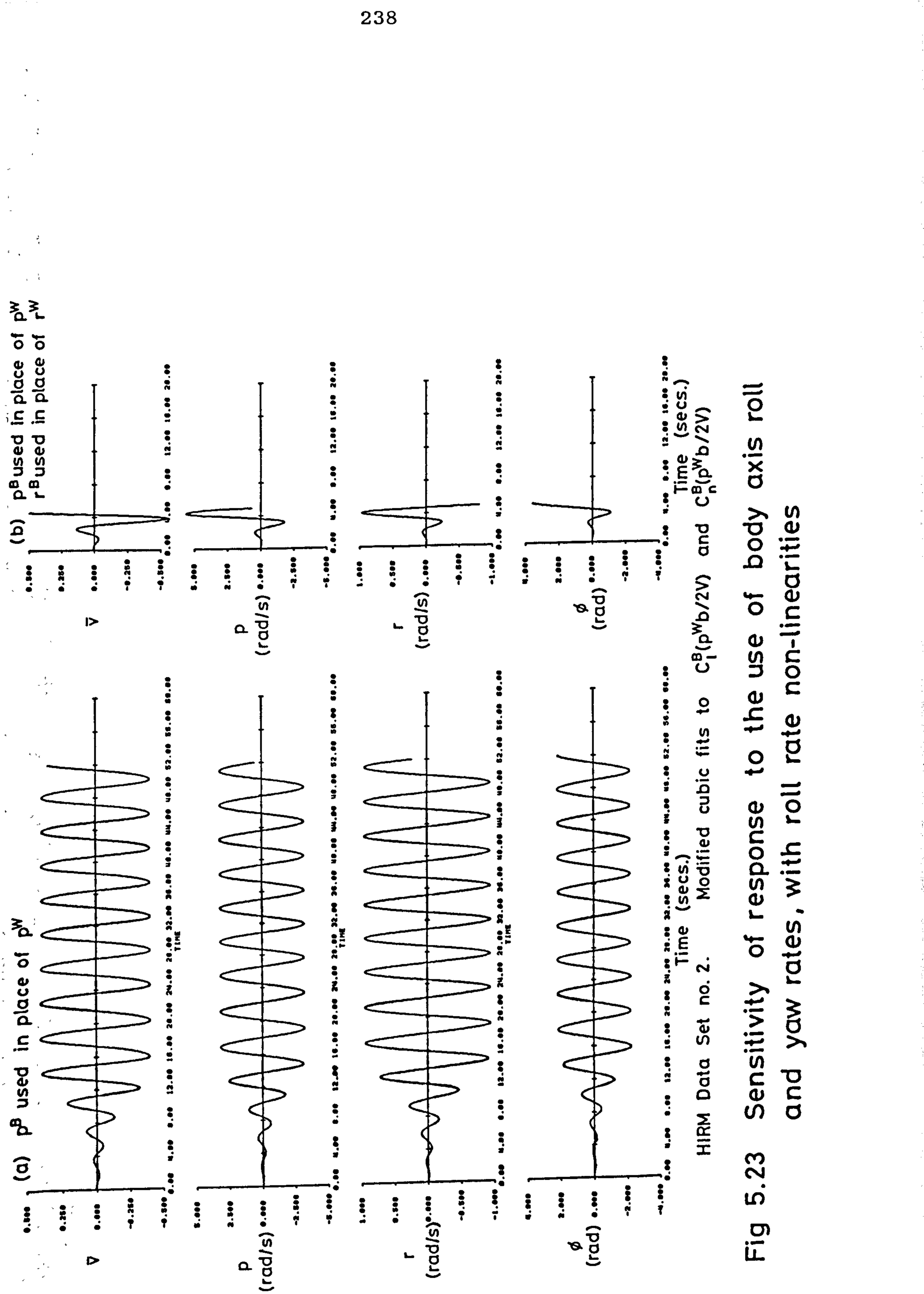

Fig 5.23 Sensitivity of response to the use of body axis roll and yaw rates, with roll rate non-linearities

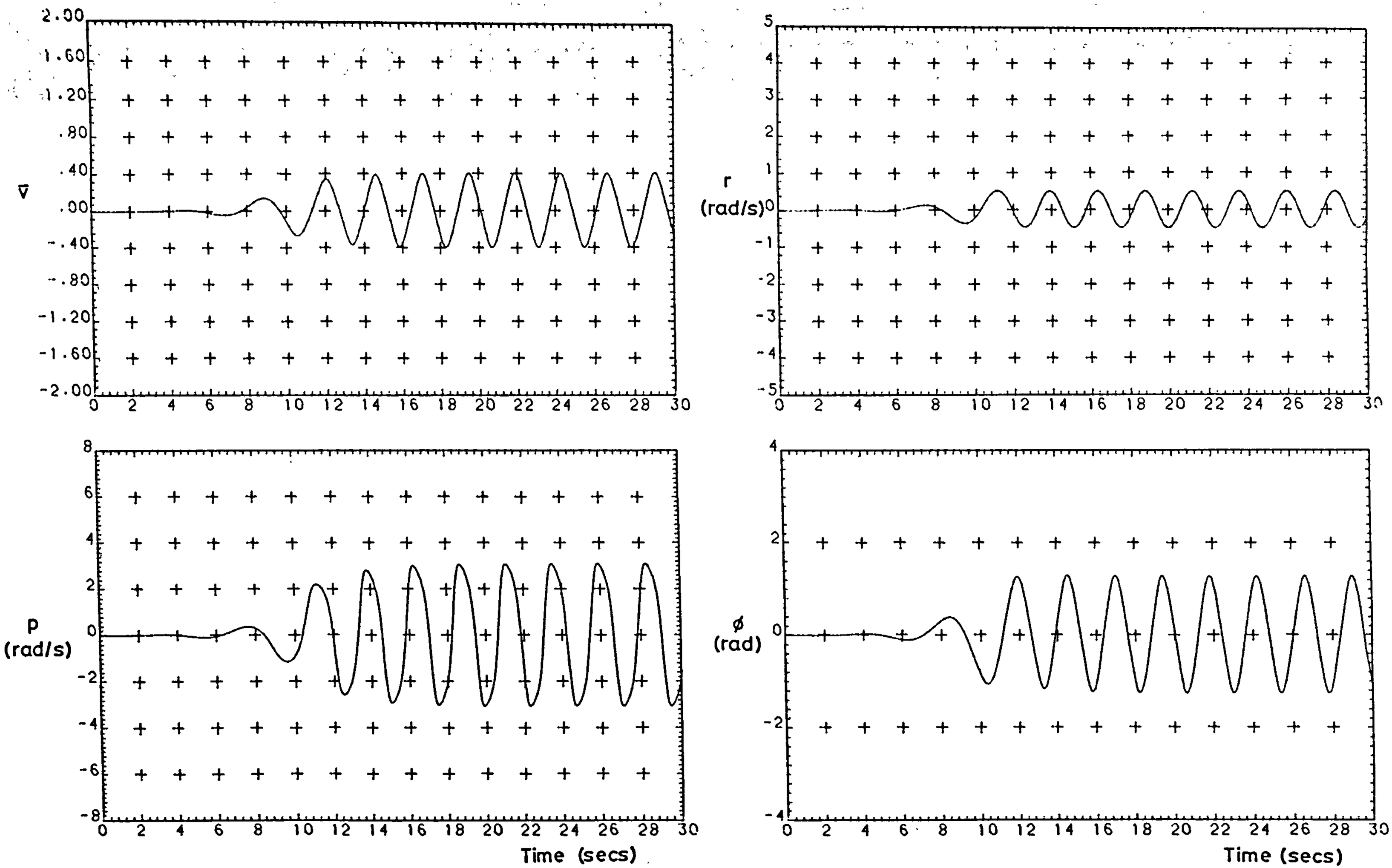

Case details in Table 5.2 α=26°

Fig 5.24 HIRM C response with non-linearities in sideslip and roll rate

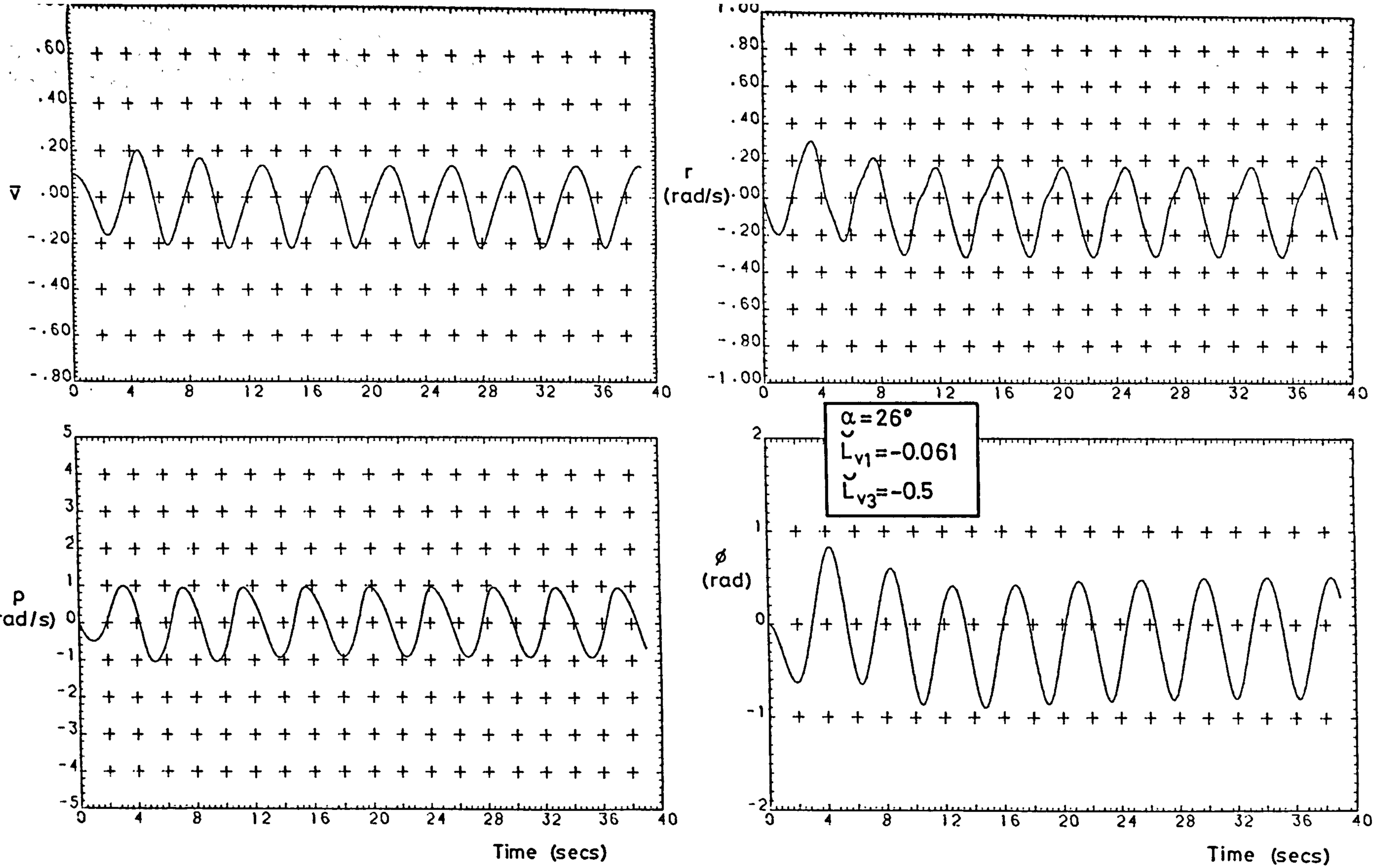

Fig 5.25 HIRM C response about non-zero equilibrium state with ξ_T=0.02 radians

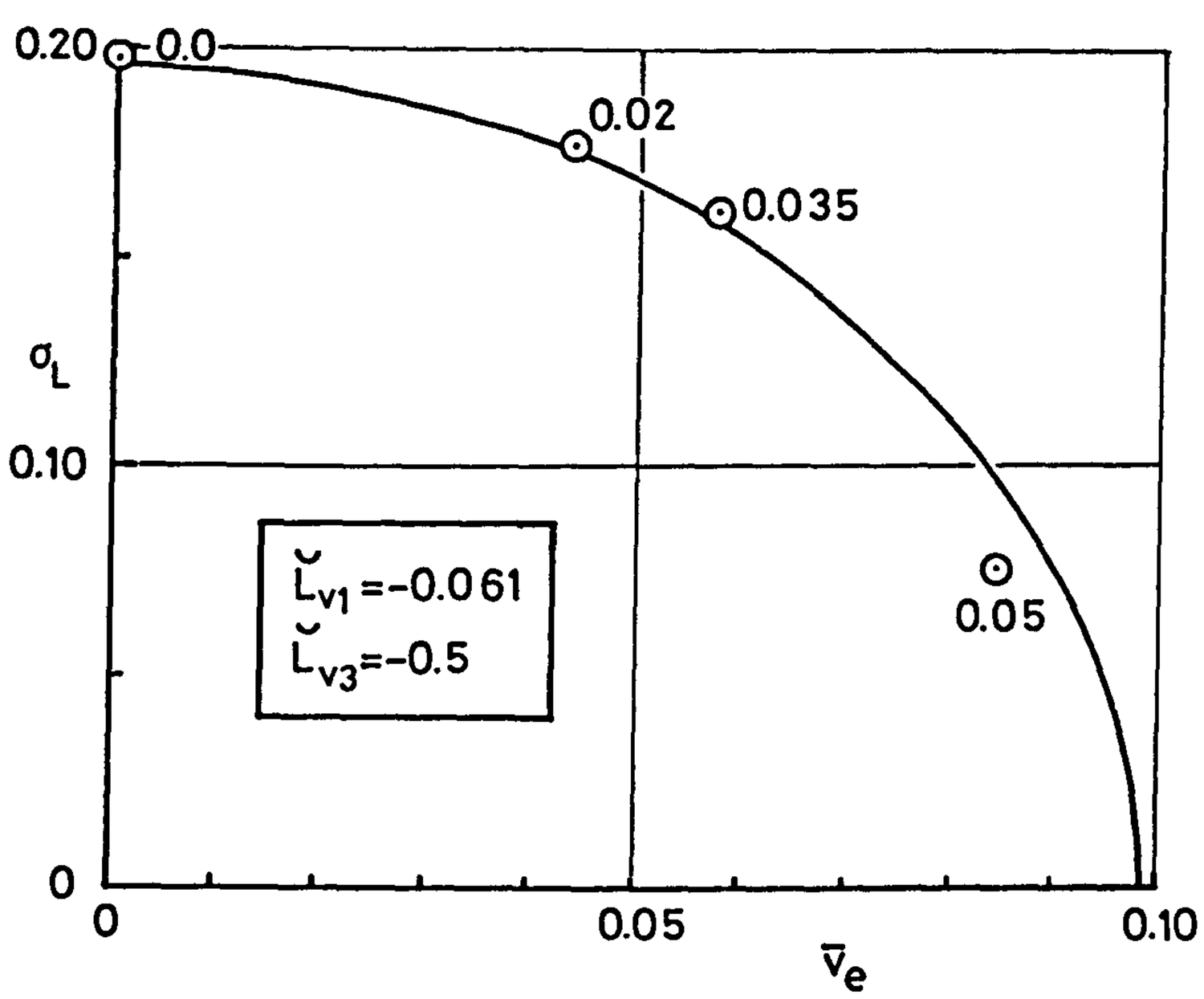

———	$v_b^2 = v_e^2 + \frac{\sigma_L^2}{4}$; eqn. (2.118)
⊙	Simulation results with associated ξ_T angle in radians

Fig 5.26 HIRM C limit cycle responses about non-zero equilibrium states

$$
\begin{bmatrix} \dot{u} \\ \dot{w} \\ \dot{q} \\ \dot{\Theta}' \\ \dot{v} \\ \dot{p} \\ \dot{r} \\ \dot{\Phi}' \end{bmatrix} =
\begin{bmatrix}
x'_u & x''_w & x''_q & -g_1 & x''_v & x'_p & x''_r & 0 \\
z''_u & z''_w & z''_q & -\dfrac{g_4 m}{m - Z_{\dot{w}}} & z''_v & z''_p & z''_r & -g_5 \dfrac{m}{m - Z_{\dot{w}}} \\
m''_u & m''_w & m''_q & -\dfrac{M_{\dot{w}} g_4 m}{I_y (m - Z_{\dot{w}})} & m''_v & m''_p & m''_r & -\dfrac{M_{\dot{w}} g_5 m}{I_y (m - Z_{\dot{w}})} \\
0 & 0 & \cos\Phi_e & 0 & 0 & 0 & -\sin\Phi_e & -q_e \sin\Phi_e - r_e \cos\Phi_e \\
y''_u & y''_w & y''_q & -g_6 \dfrac{m}{m - Y_{\dot{v}}} & y''_v & y''_p & y''_r & g_3 \dfrac{m}{m - Y_{\dot{v}}} \\
l''_u & l''_w & l''_q & -l'_{\dot{v}} g_6 \dfrac{m}{m - Y_{\dot{v}}} & l''_v & l''_p & l''_r & g_3 l'_{\dot{v}} \dfrac{m}{m - Y_{\dot{v}}} \\
n''_u & n''_w & n''_q & -n'_{\dot{v}} g_6 \dfrac{m}{m - Y_{\dot{v}}} & n''_v & n''_p & n''_r & g_3 n'_{\dot{v}} \dfrac{m}{m - Y_{\dot{v}}} \\
0 & 0 & \sin\Phi_e \tan\theta_e & \dfrac{q_e \sin\Phi + r_e \cos\Phi}{\cos^2\theta_e} & 0 & 1 & \cos\Phi_e \tan\theta_e & \tan\theta_e (q_e \cos\Phi_e - r_e \sin\Phi_e)
\end{bmatrix}
\begin{bmatrix} u \\ w \\ q \\ \Theta' \\ v \\ p \\ r \\ \Phi' \end{bmatrix}
$$

Fig 6.1 Linearised 6 degree of freedom equations of motion

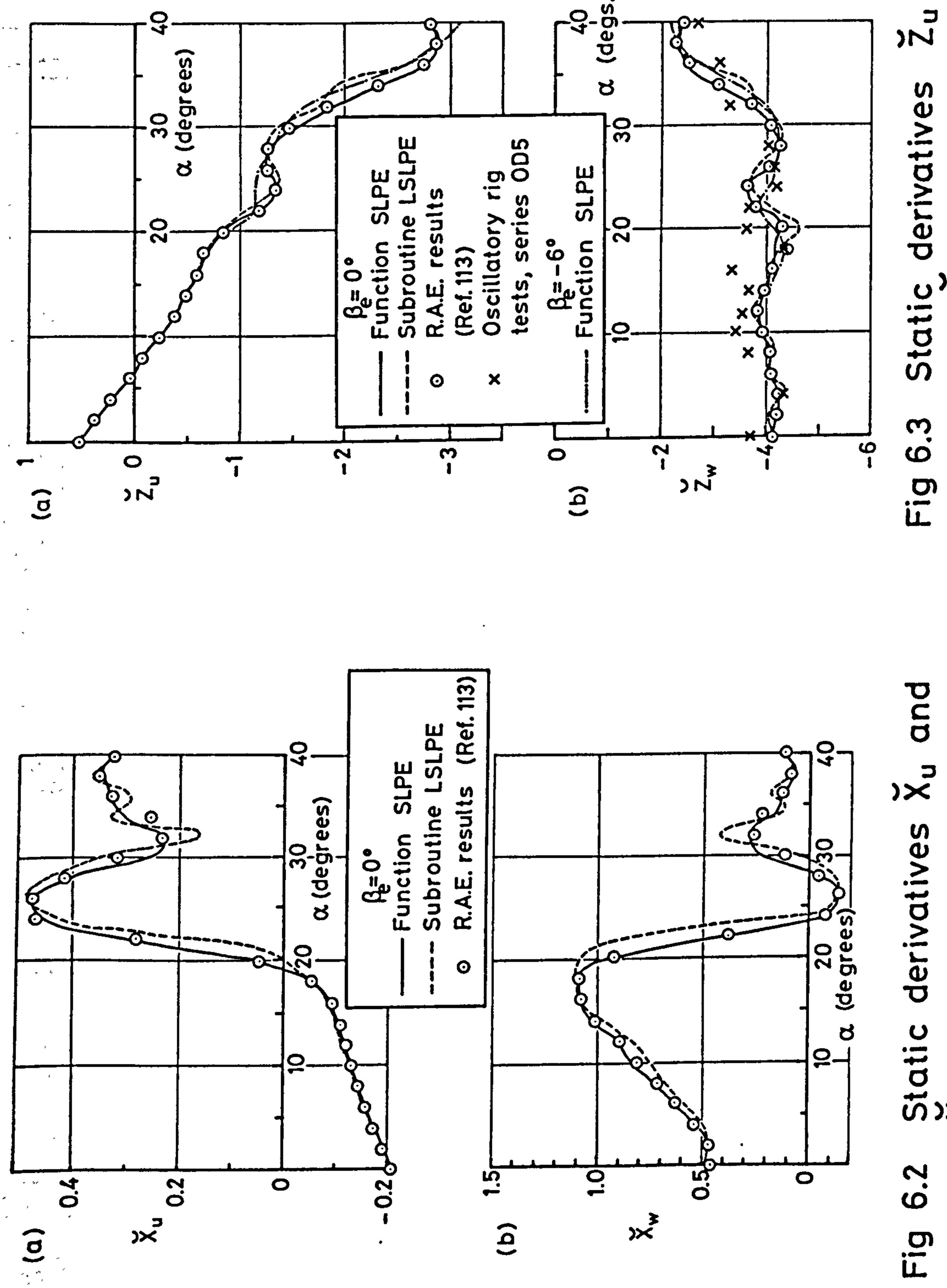

Fig 6.3 Static derivatives $\breve{Z}_u$ and $\breve{Z}_w$

Fig 6.2 Static derivatives $\breve{X}_u$ and $\breve{X}_w$

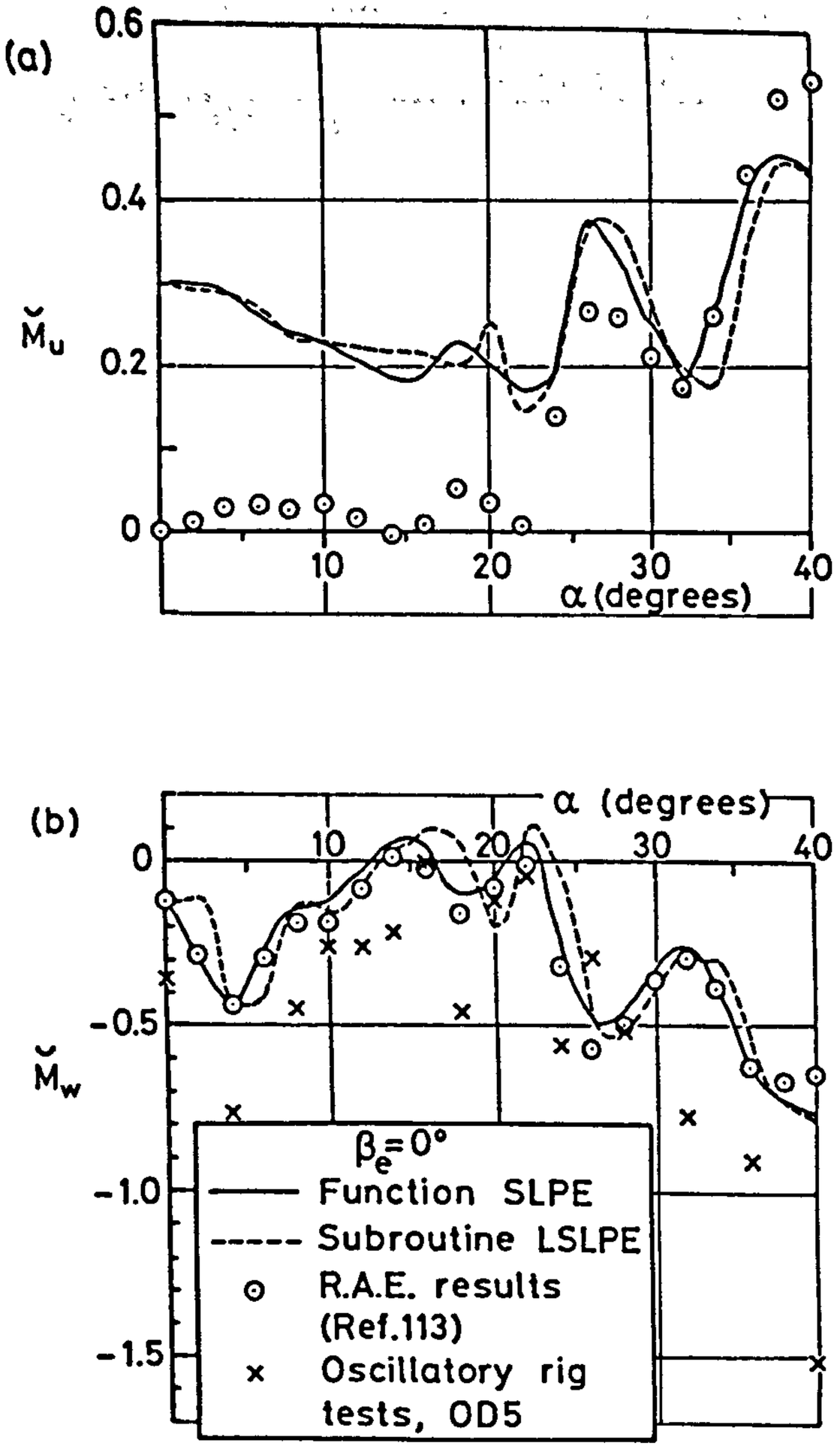

Fig 6.4 Static derivatives $\check{M}_u$ and $\check{M}_w$

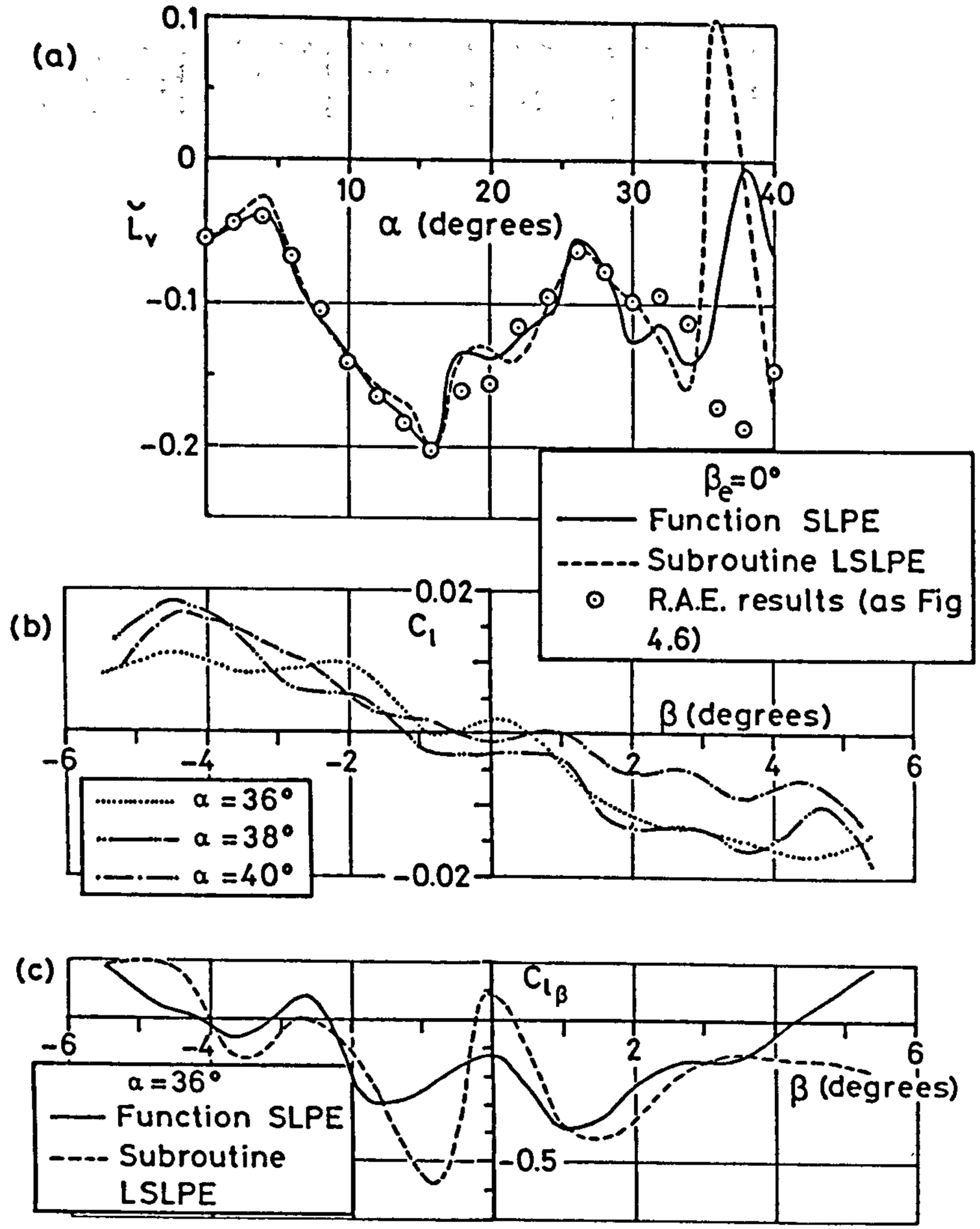

Fig 6.5 Static derivative $\check{L}_v$ and $C_l(\beta)$ characteristics

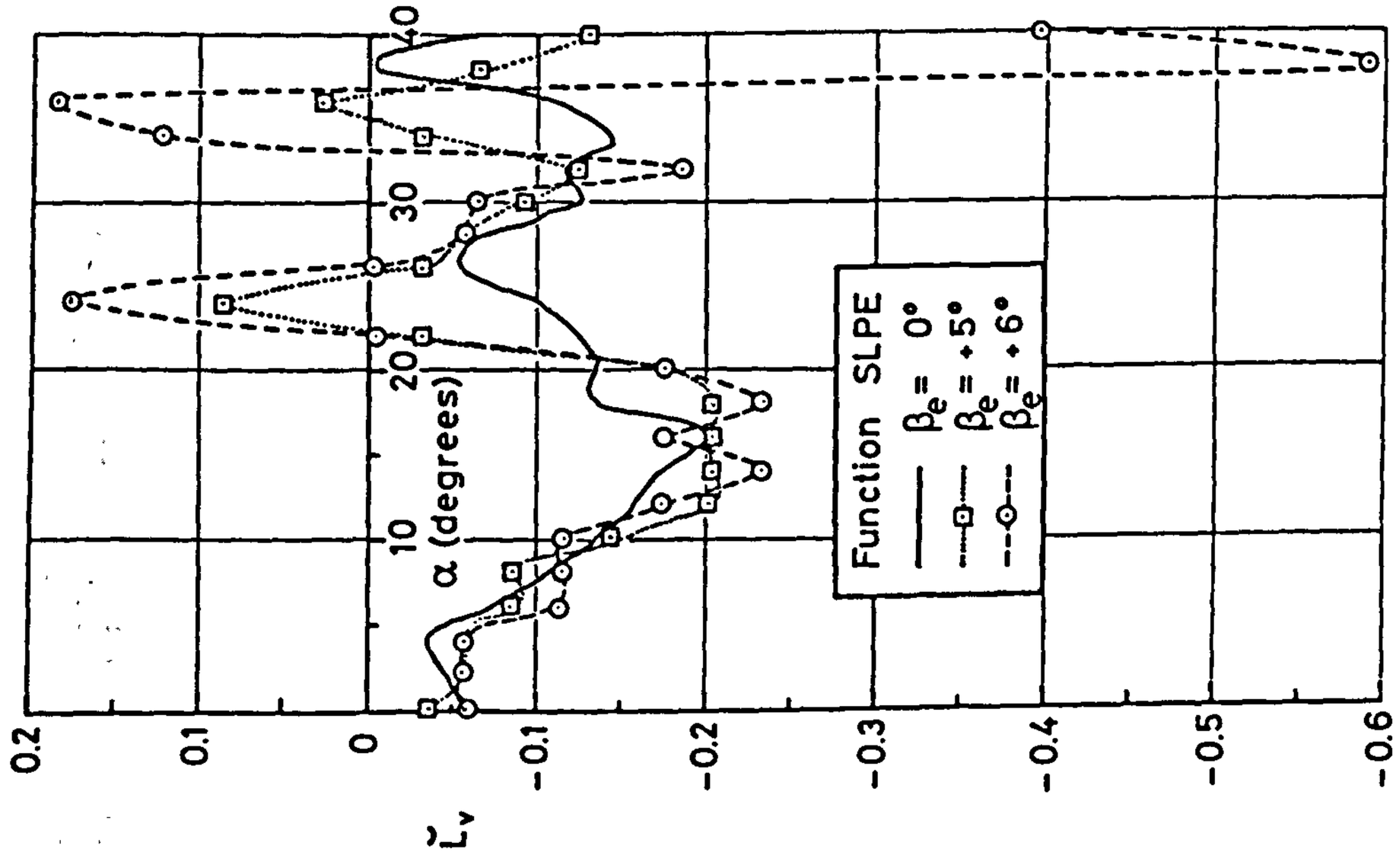

Fig 6.7 Effect of positive sideslip on C_{L_v}

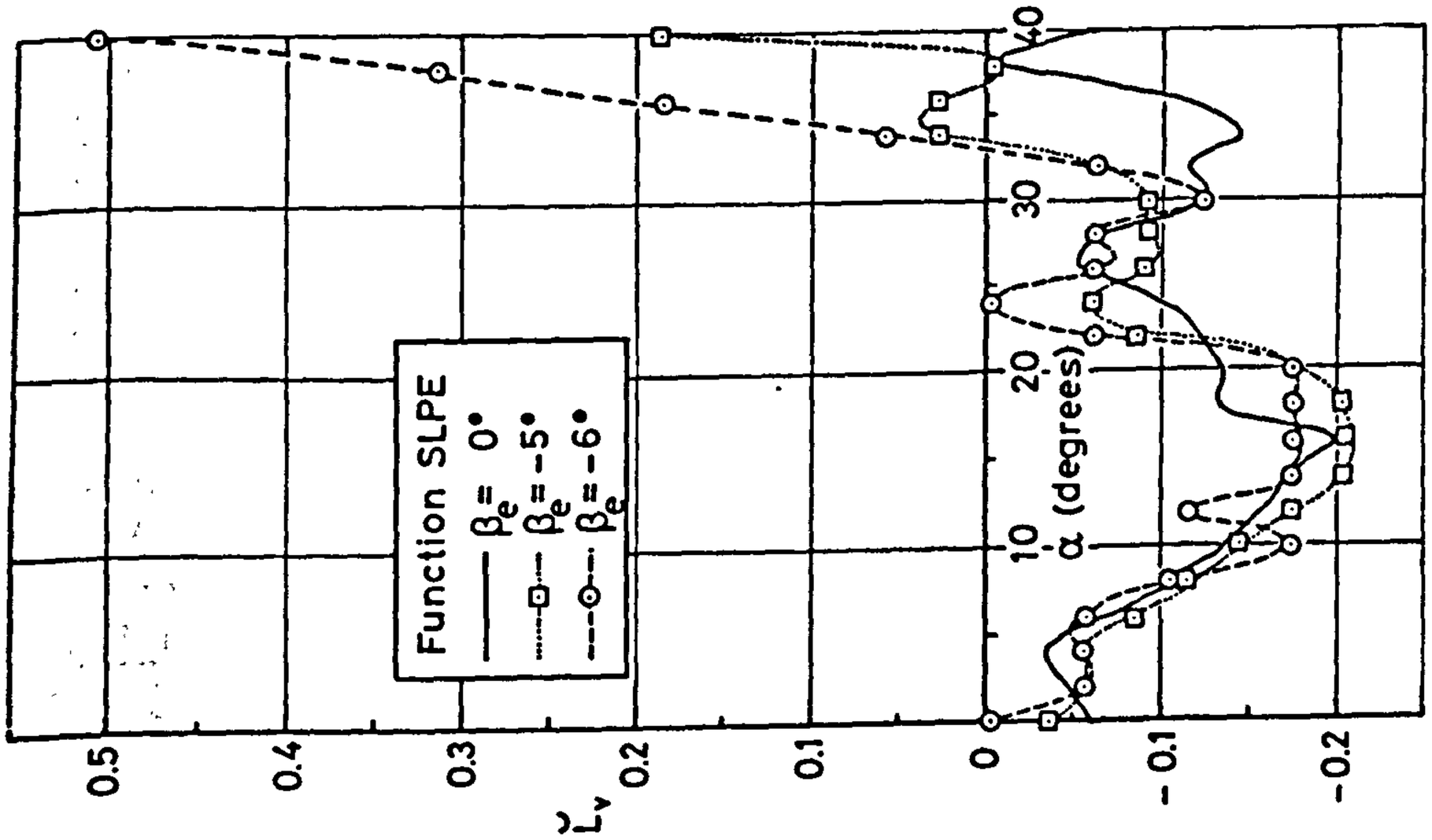

Fig 6.6 Effect of negative sideslip on C_{L_v}

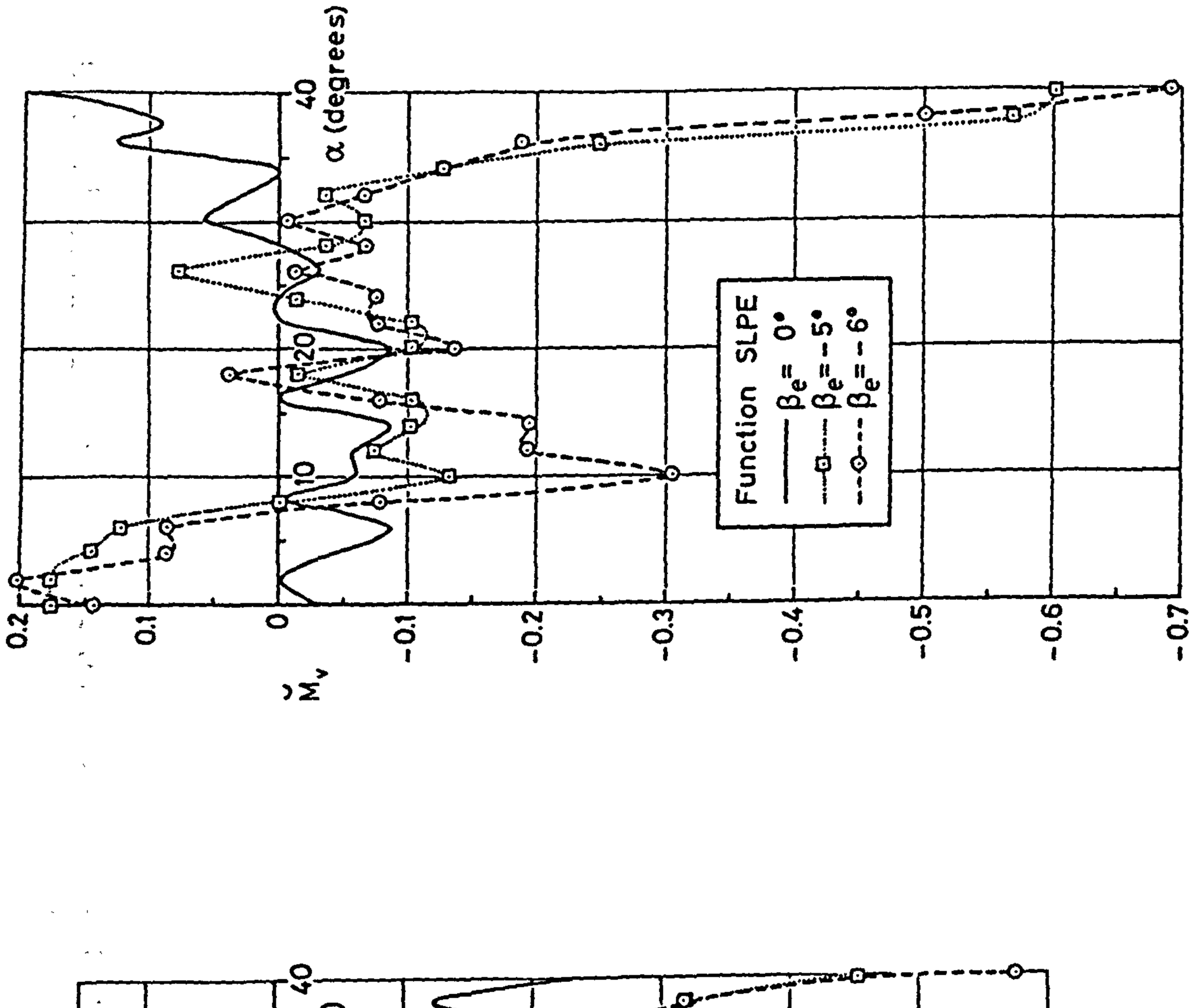

Fig 6.9 Effect of negative sideslip on $\tilde{N}_v$

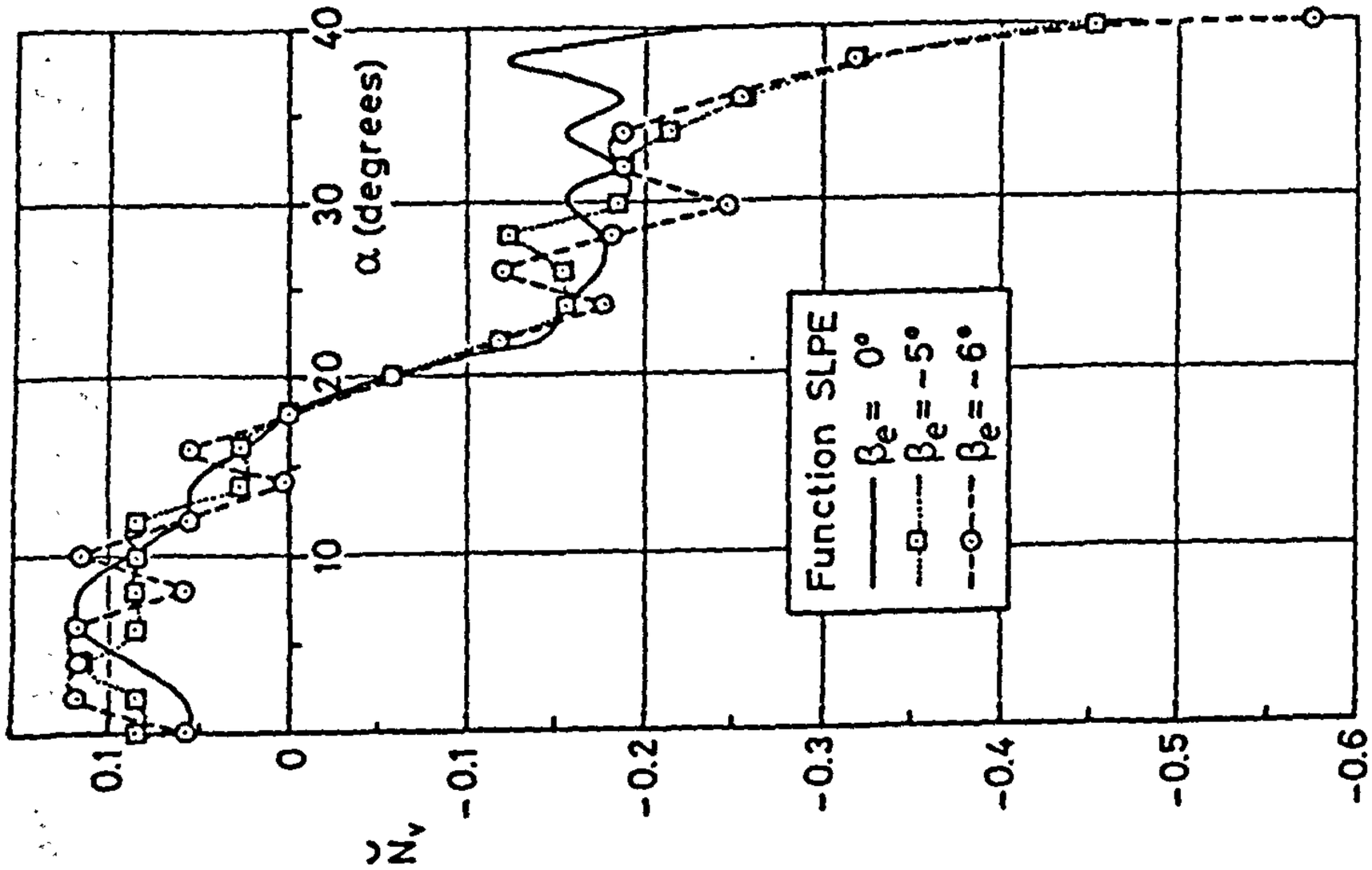

Effect of negative sideslip on N_v

Fig 6.8

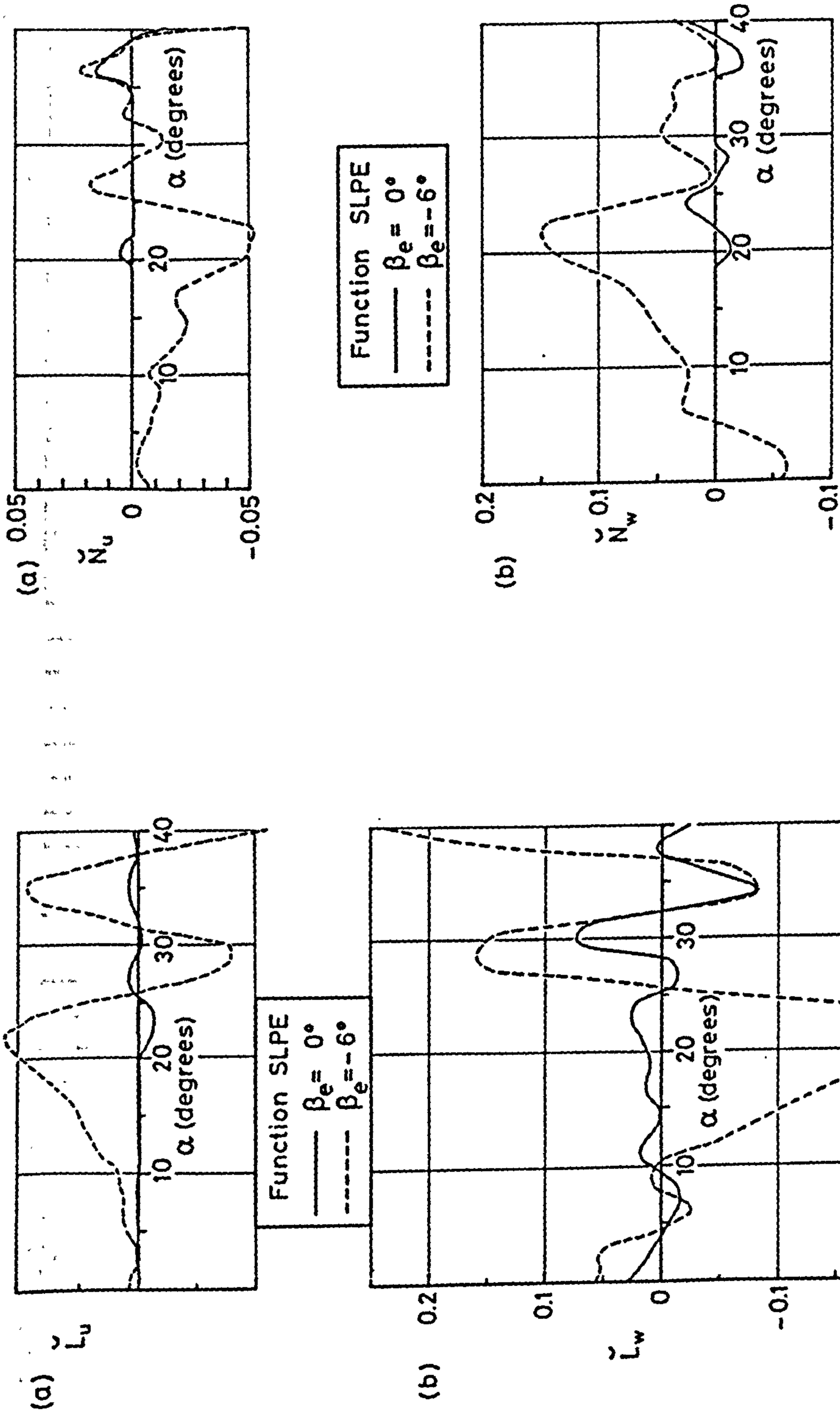

Fig 6.11 Effect of negative sideslip on $\tilde{N}_u$ and $\tilde{N}_w$

Fig 6.10 Effect of negative sideslip on $\tilde{L}_u$ and $\tilde{L}_w$

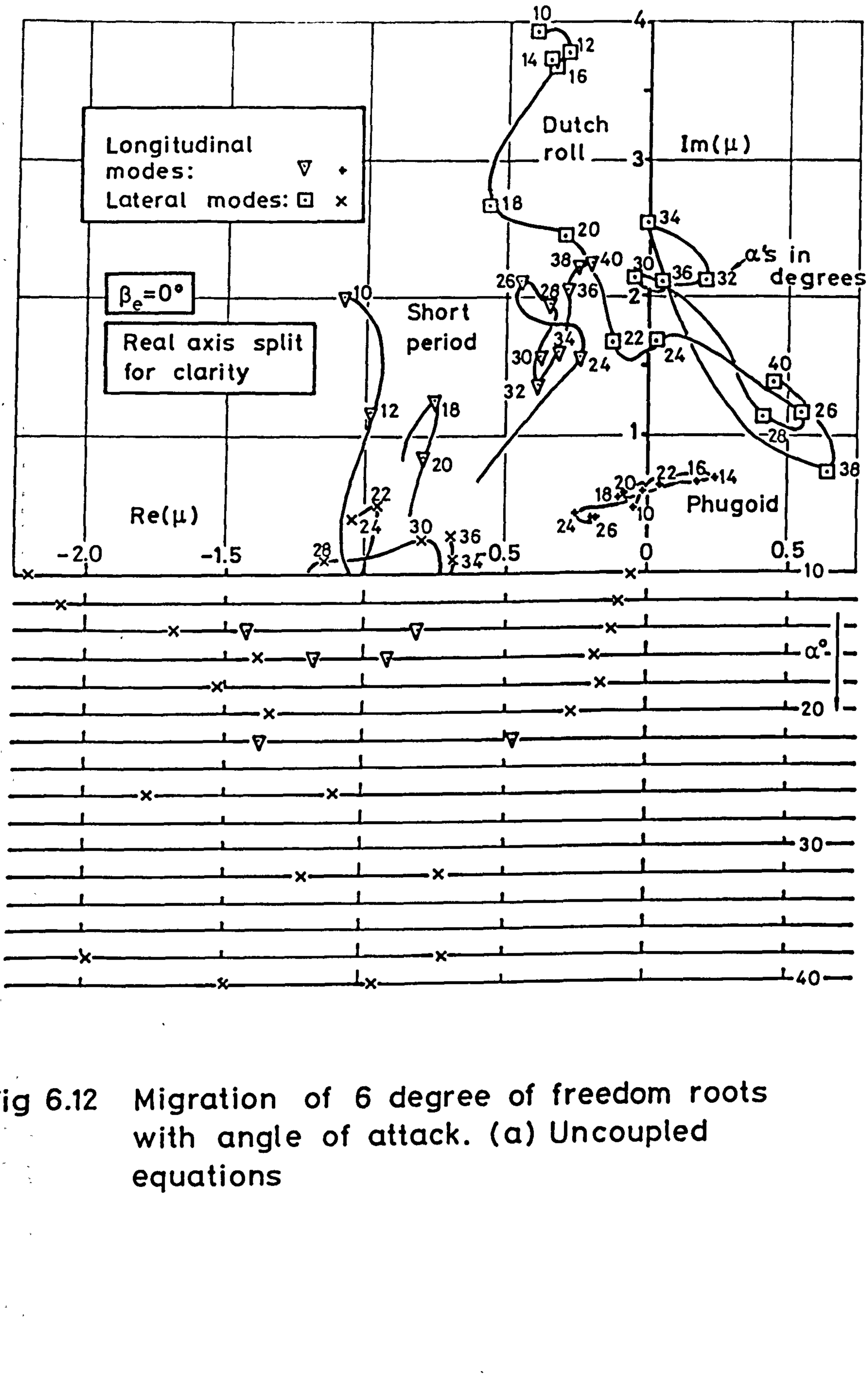

Fig 6.12 Migration of 6 degree of freedom roots with angle of attack. (a) Uncoupled equations

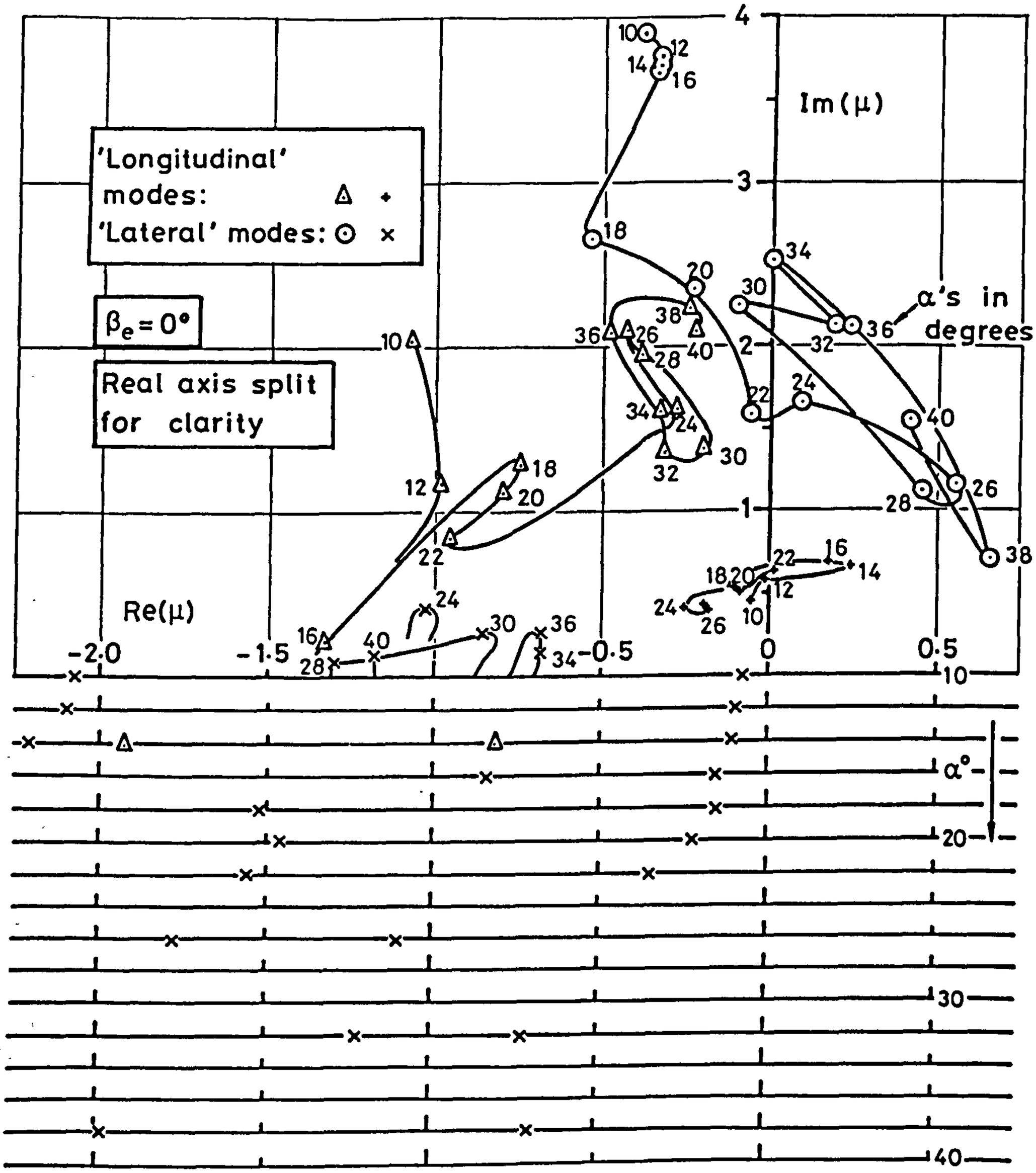

Fig 6.12 (concluded) Migration of 6 degree of freedom roots with angle of attack. (b) Coupled equations

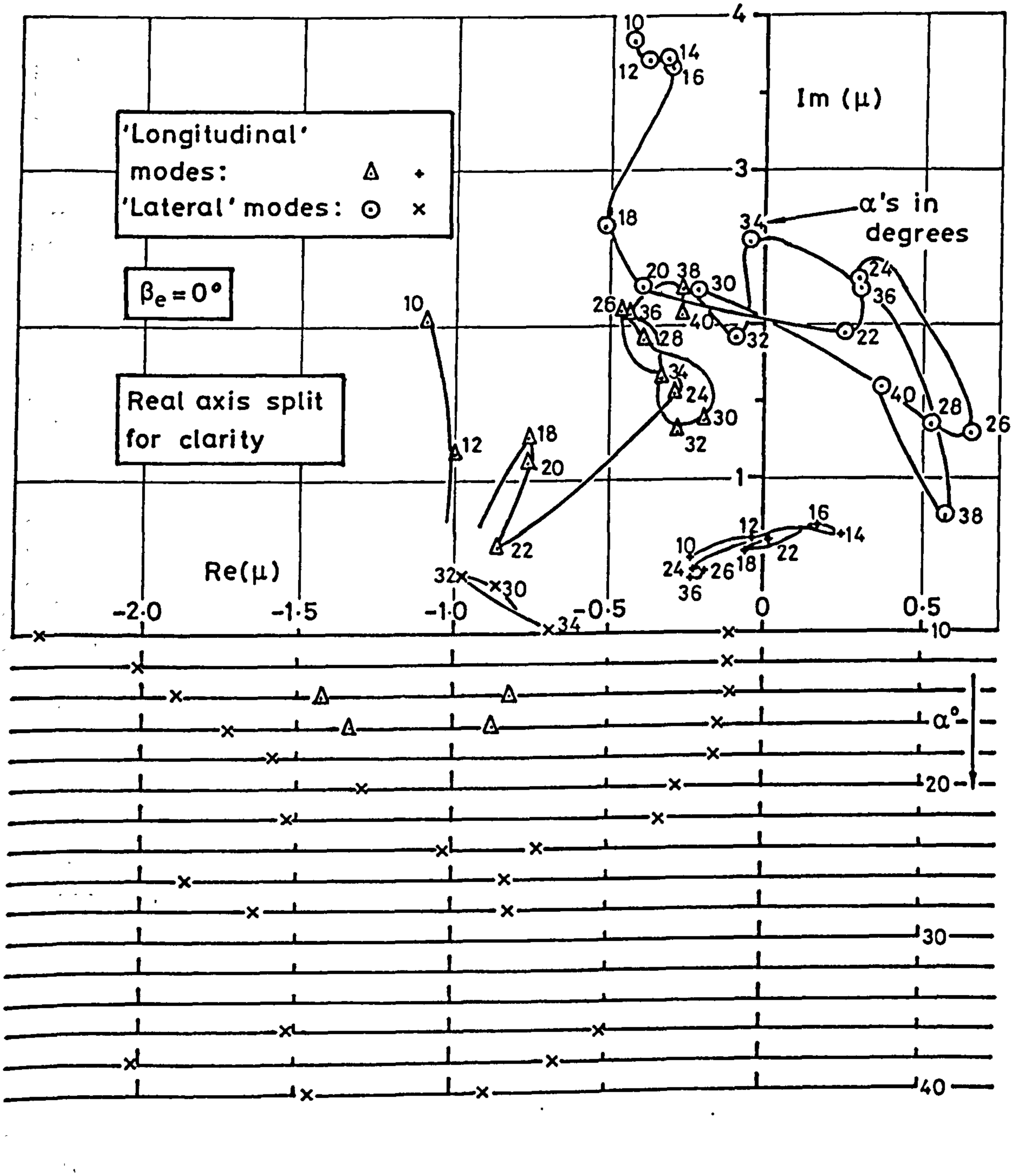

Fig 6.13 Effect of rotary rig data on coupled 6 degree of freedom roots

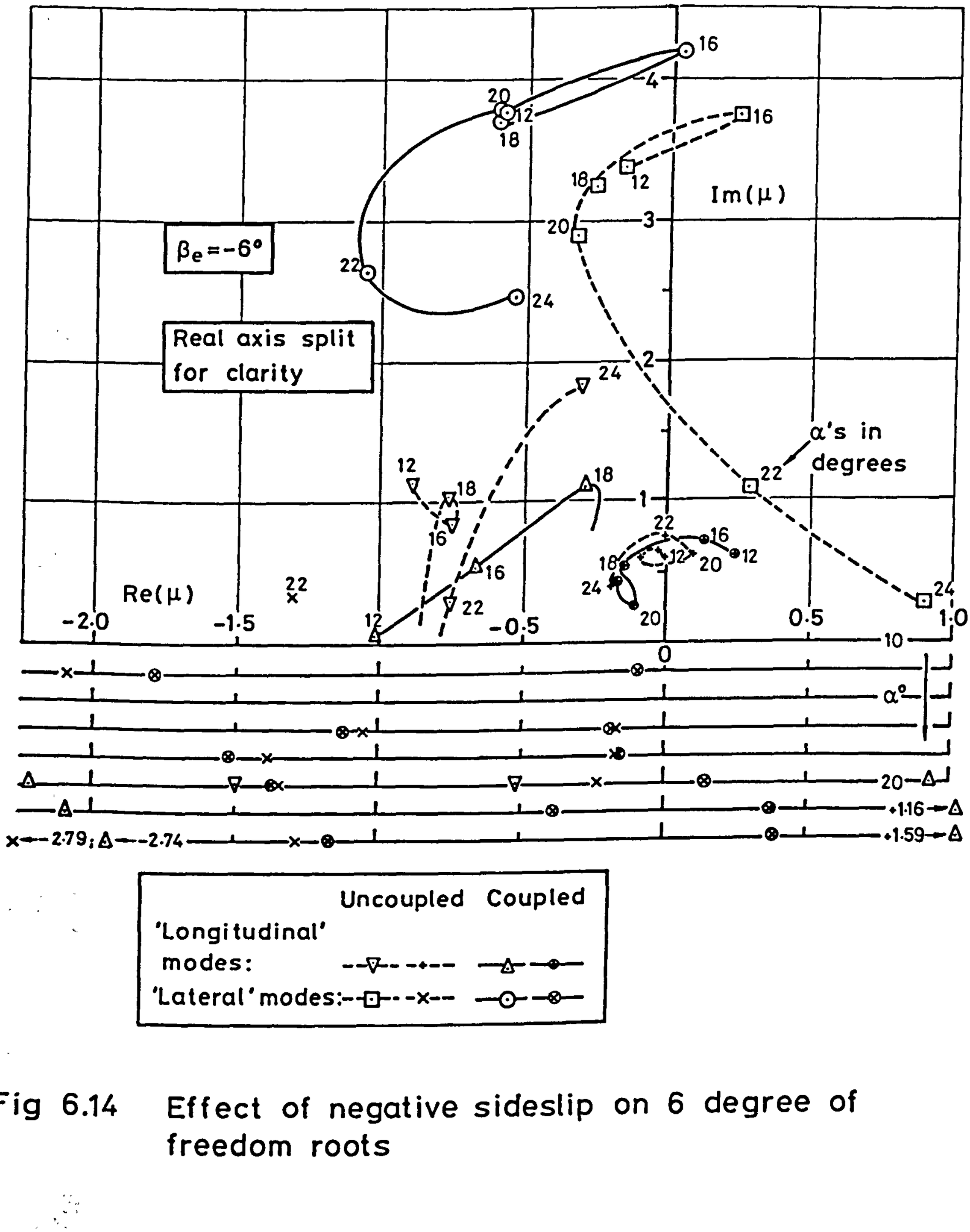

Fig 6.14 Effect of negative sideslip on 6 degree of freedom roots

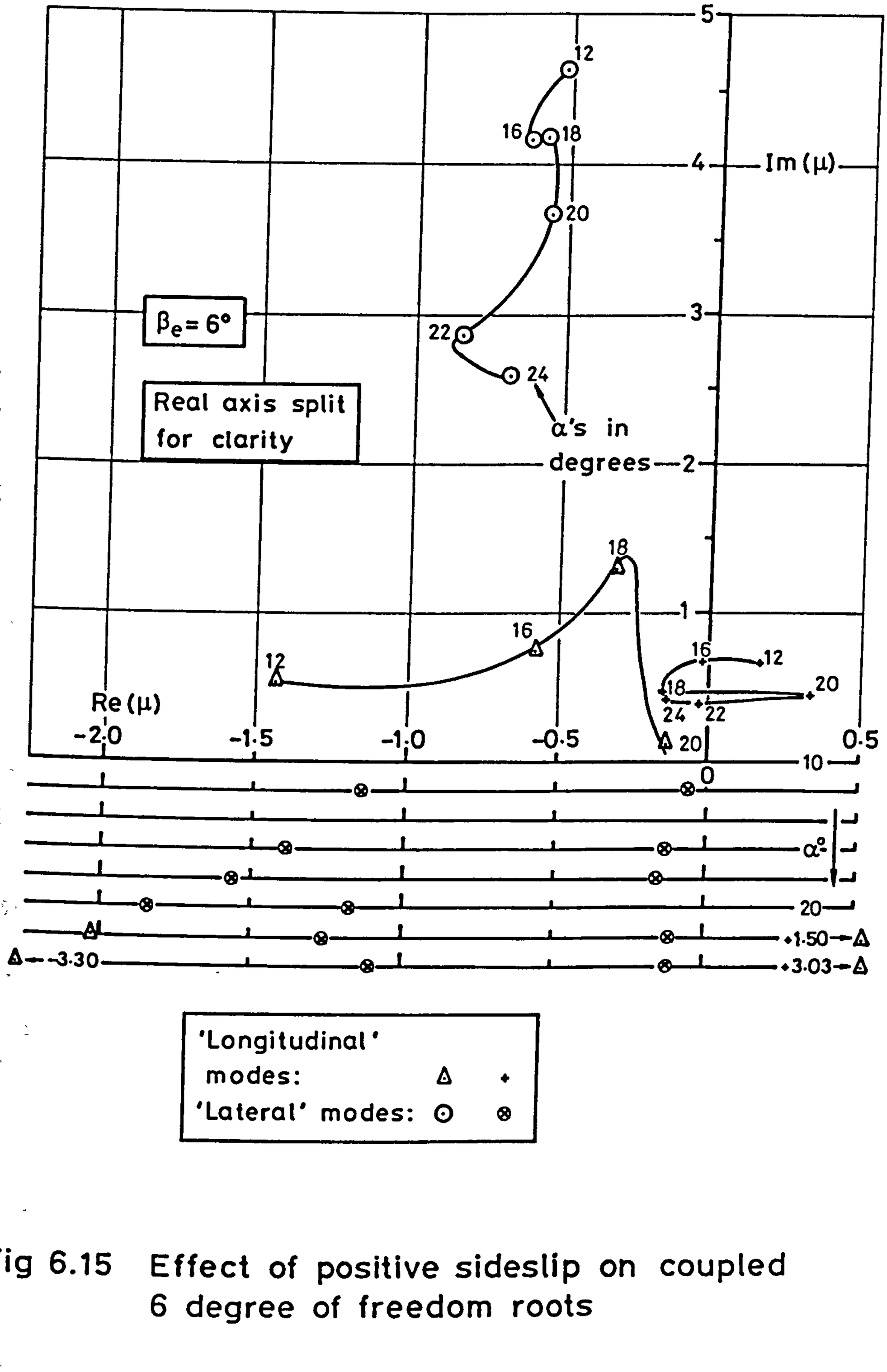

Fig 6.15 Effect of positive sideslip on coupled 6 degree of freedom roots

	Eigenvalues		Eigenvalues
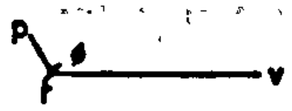	-0.332 ± 3.379i	α = 12°	-0.592 ± 3.781i
	0.244 ± 3.743i	α = 16°	0.030 ± 4.175i
	-0.269 ± 3.266i	α = 18°	-0.613 ± 3.705i
	-0.328 ± 2.893i	α = 20°	0.612 ± 3.795i
	0.295 ± 1.091i	α = 22°	-1.069 ± 2.639i
	0.904 ± 0.280i	α = 24°	-0.505 ± 2.470i

Uncoupled system

Coupled system

$\beta_e = -6°$

Only components greater than 5% magnitude of major component are shown, for each eigenvector

(a) 'Dutch roll'

	Eigenvalues
α = 16° 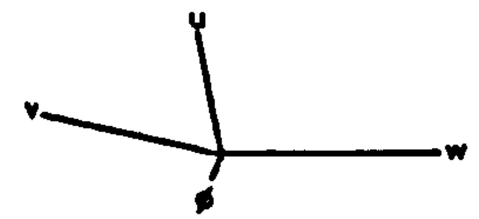	0.140 ± 0.720i
α = 18° 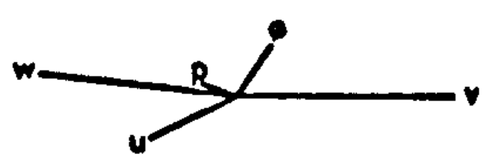	-0.145 ± 0.556i
α = 20° 	-0.106 ± 0.293i
α = 22° 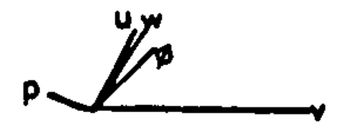	-0.176 ± 0.423i
α = 24° 	-0.178 ± 0.406i

Coupled system

(b) 'Phugoid'

Fig 6.16 Typical eigenvectors at negative equilibrium sideslip

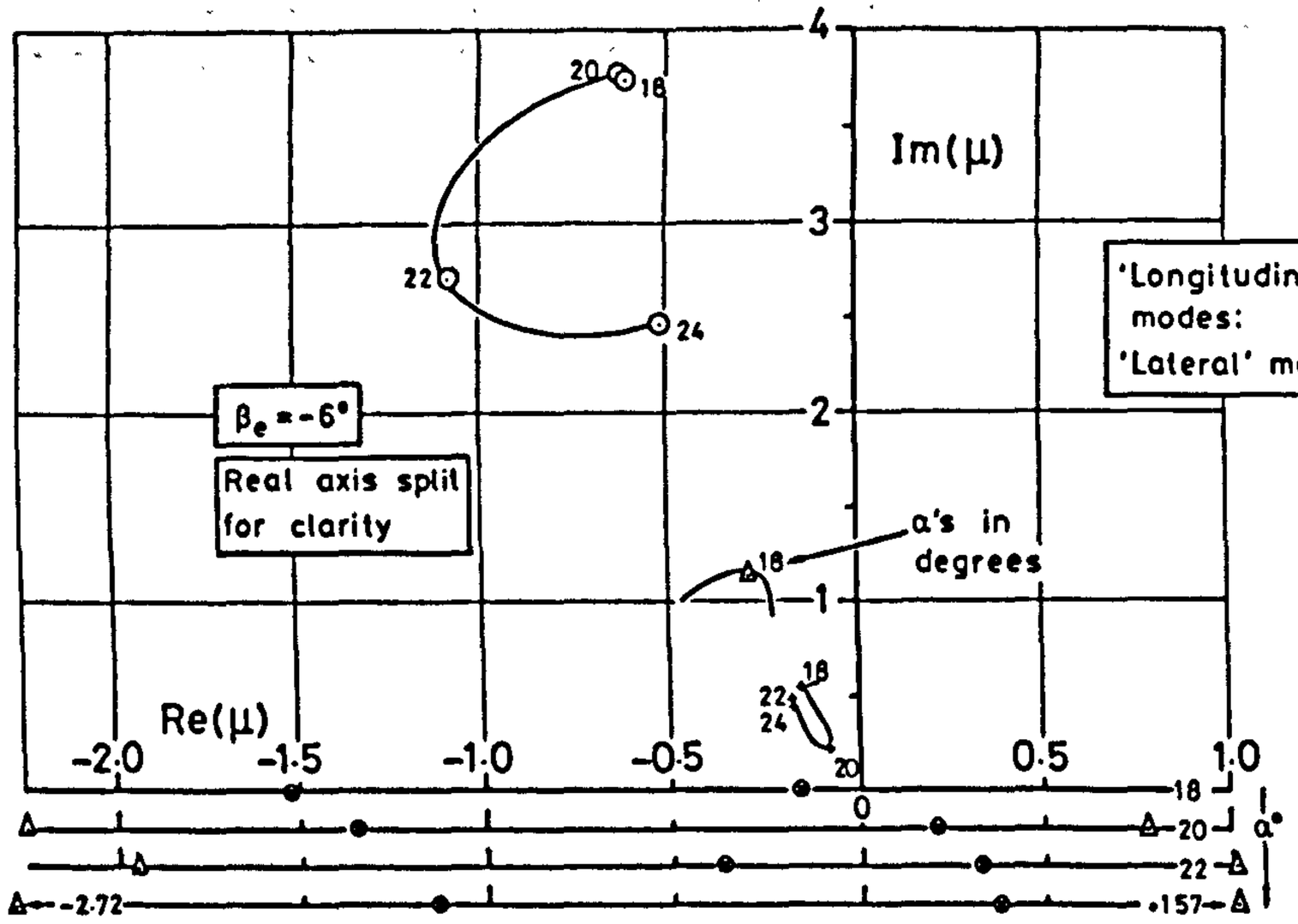

Fig 6.17 Roots at negative equilibrium sideslip with major cross-coupling derivatives present

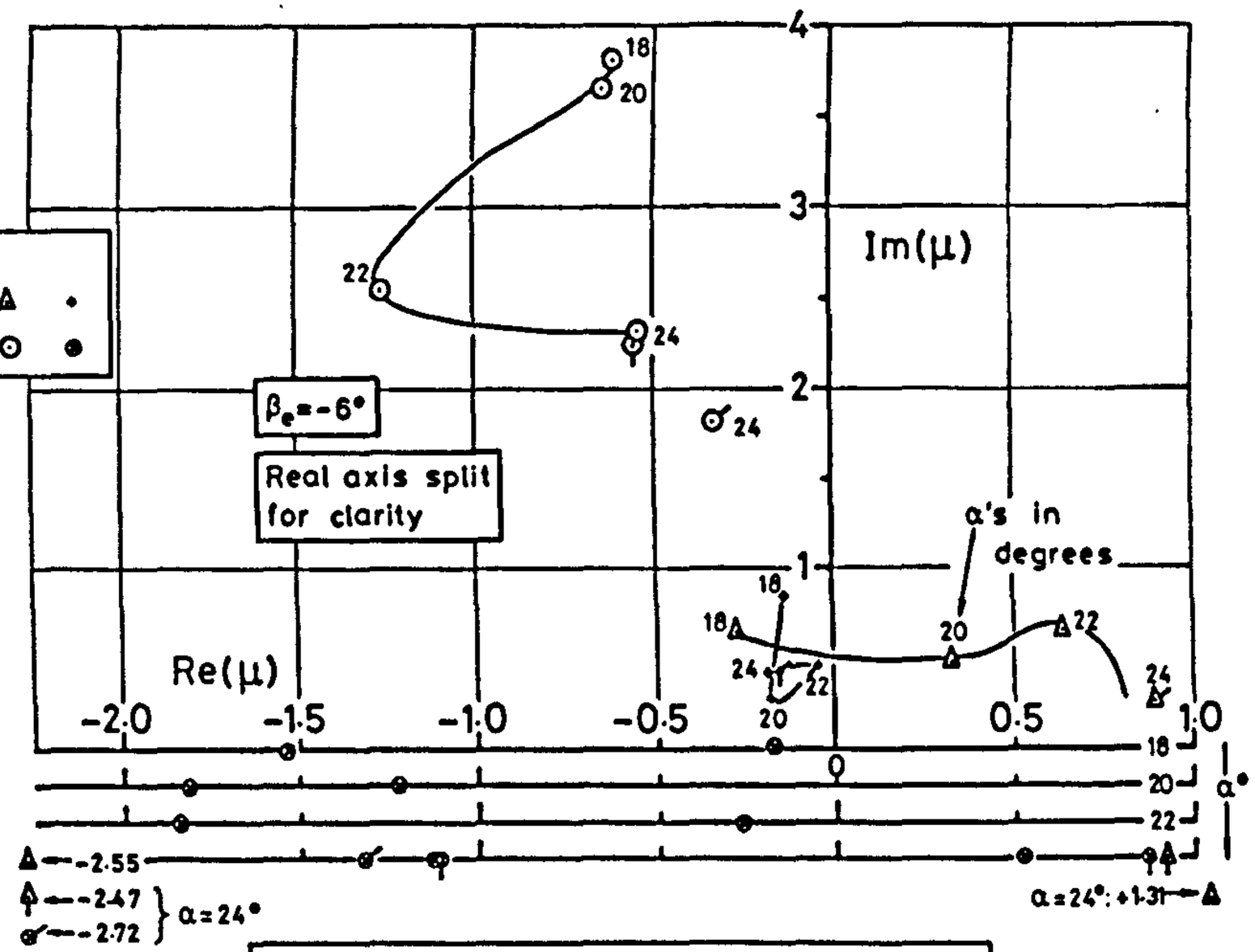

Fig 6.18 Effect, on roots at negative sideslip, of removing $\check{M}_v$

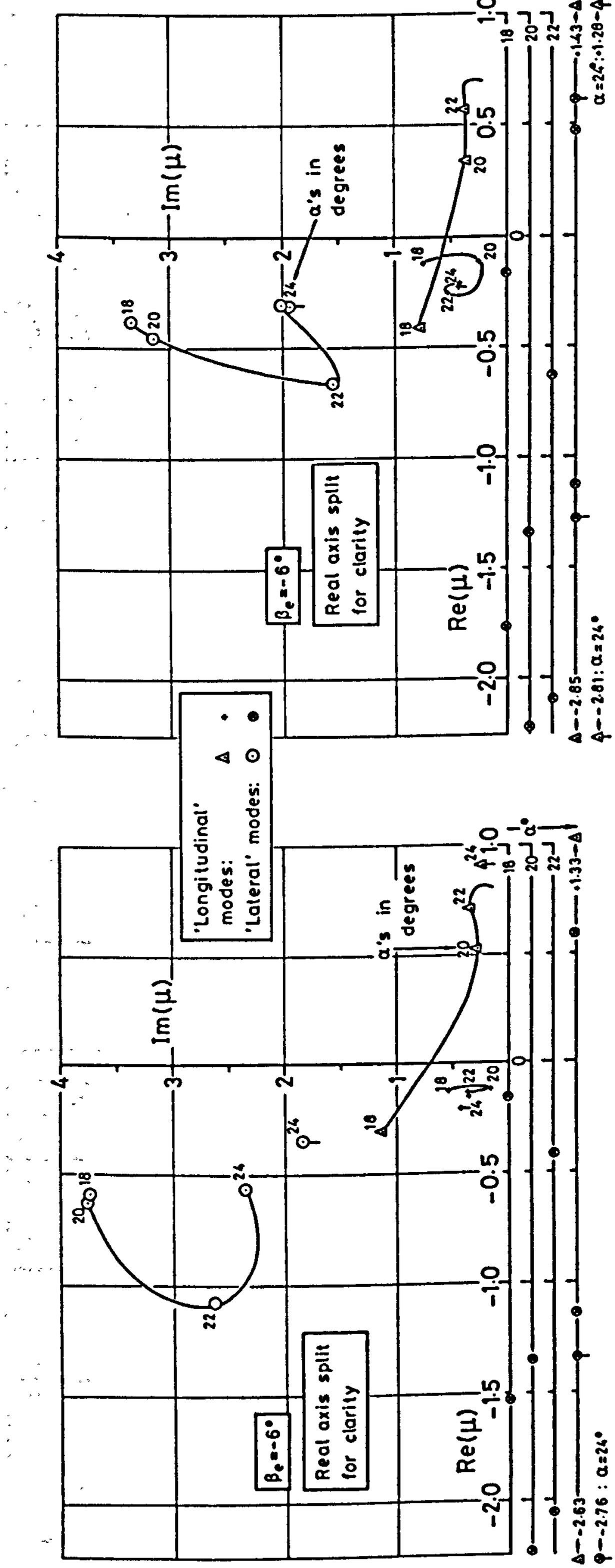

Fig 6.20 Effect, on roots at negative side-slip, of removing $\check{L}_w$

Fig 6.19 Effect, on roots at negative side-slip, of removing $\check{L}_u$

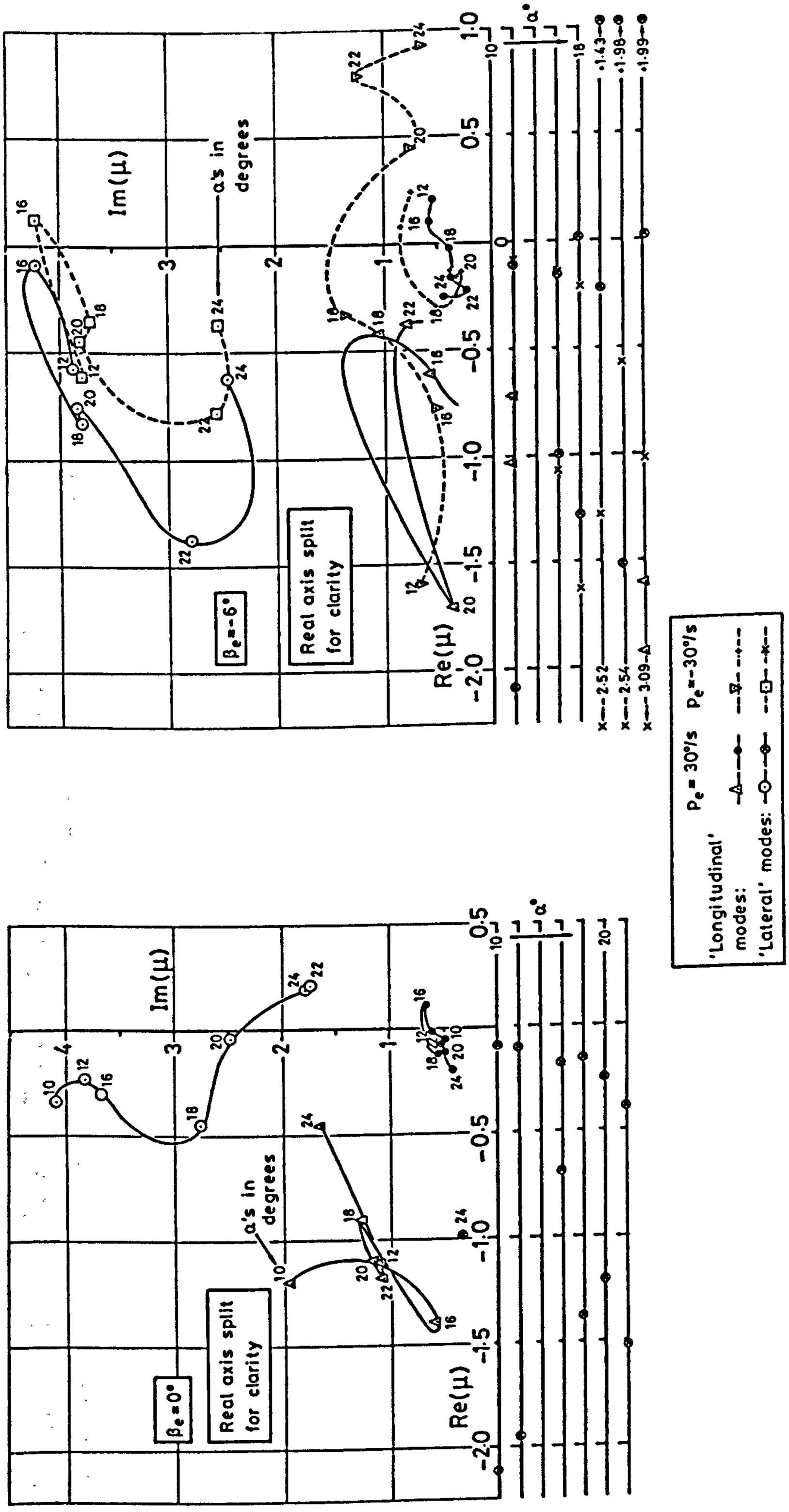

(b) At negative sideslip

(a) At zero sideslip

Fig 6.21 Effect of steady roll rate on coupled 6 degree of freedom roots

Subroutine AERODYN, program SIMUL6

	Static data	Oscillatory data			Rotary data
X^B =	$X(\alpha,\beta)$				
Z^B =	$Z(\alpha,\beta)$	$+\frac{1}{2}\rho V^2 S$ [$\breve{Z}_q(\alpha).q_\gamma$	$+\ \breve{Z}_p(\alpha).p_\gamma$	$+\ \breve{Z}_{\eta_T}(\alpha).\eta_T$	]
M^B =	$M(\alpha,\beta)$	$+\frac{1}{2}\rho V^2 S\bar{c}$ [$\breve{M}_q(\alpha).q_\gamma$	$+\ \breve{M}_p(\alpha).p_\gamma$	$+\ \breve{M}_{\eta_T}(\alpha).\eta_T$	]
Y^B =	$\frac{1}{2}\rho V^2 S$ [$C_Y^B(\alpha,\beta)$	$+$		$+\ \breve{Y}_\zeta(\alpha).\zeta + C_Y^B(\alpha,p^w)$	]
L^B =	$\frac{1}{2}\rho V^2 S\, b$ [$C_l^B(\alpha,\beta)$	$+\ \breve{L}_q(\alpha).q_\gamma + \breve{L}_p(\alpha).p_\gamma + \breve{L}_r(\alpha).r_\gamma + \breve{L}_{\xi_T}(\alpha).\xi_T$		$+\ \breve{L}_\zeta(\alpha).\zeta + C_l^B(\alpha,p^w)$	]
N^B =	$\frac{1}{2}\rho V^2 S\, b$ [$C_n^B(\alpha,\beta)$	$+\ \breve{N}_q.q_\gamma + \breve{N}_p(\alpha).p_\gamma + \breve{N}_r(\alpha).r_\gamma + \breve{N}_{\xi_T}(\alpha).\xi_T$		$+\ \breve{N}_\zeta(\alpha).\zeta + C_n^B(\alpha,p^w)$	]

Fig 6.22 Formulation of 6 degree of freedom, body axis forces and moments

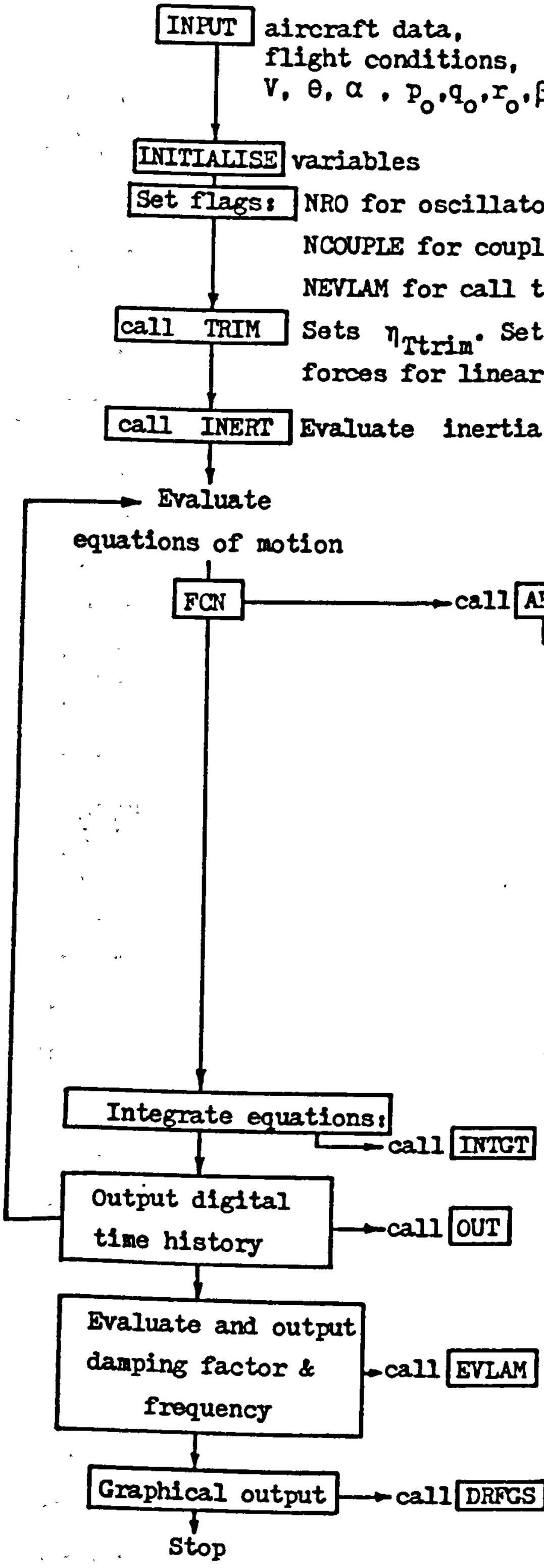

Fig 6.23 Outline flowchart of simulation program SIMUL6

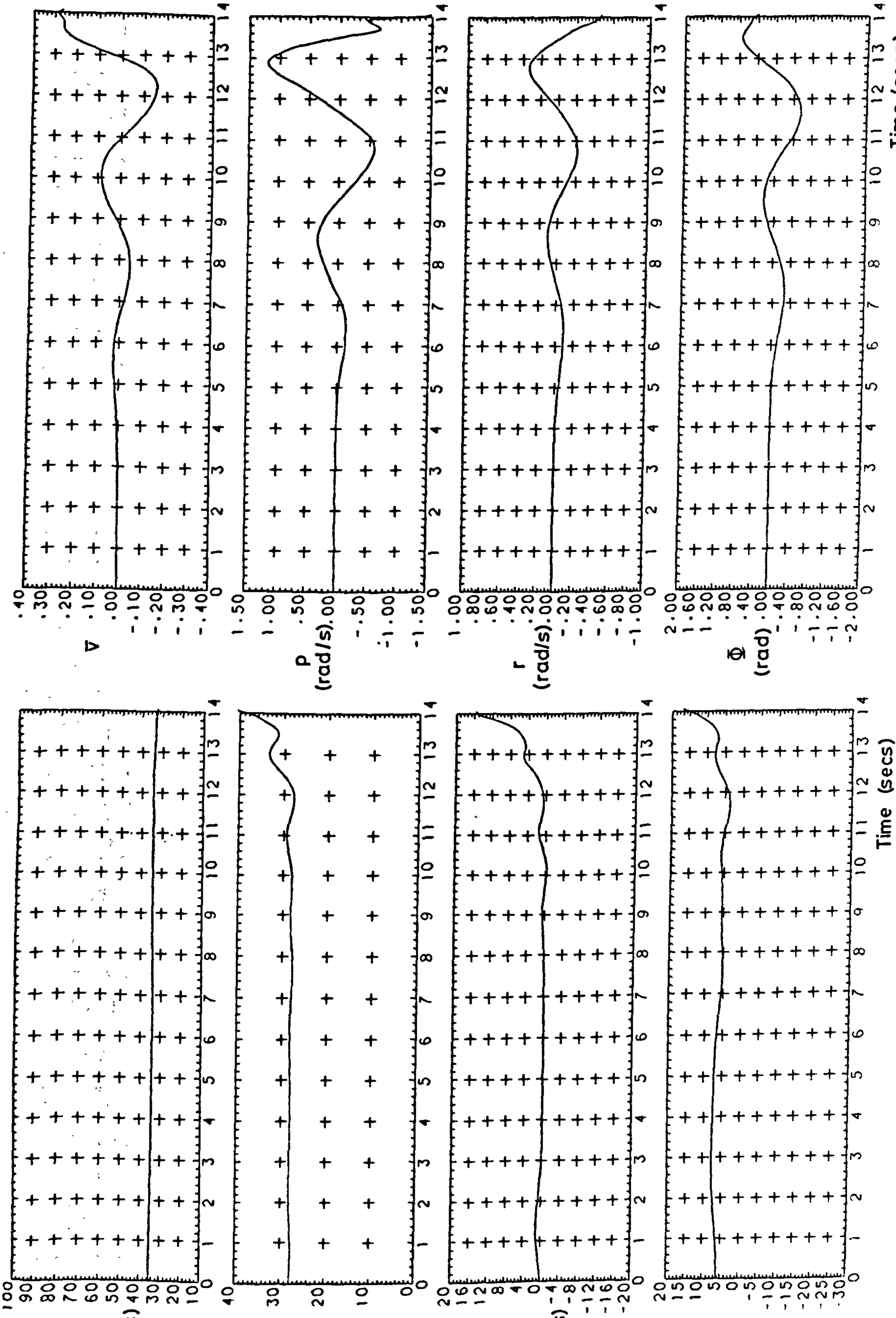

Fig 6.24 Basic HIRM unstable trim at $\alpha = 28°$

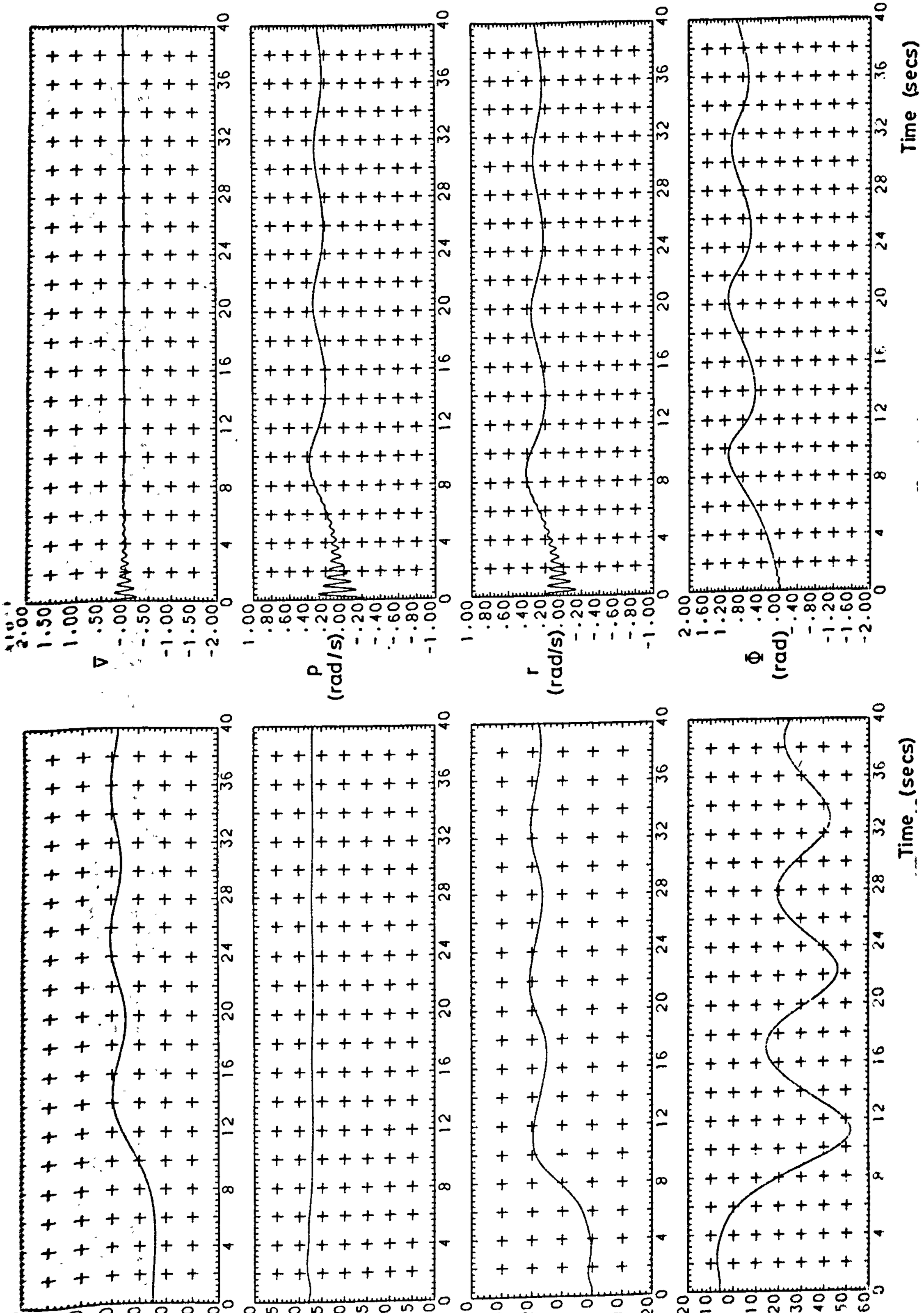

Fig 6.25 HIRM trim at α=28° with $K_{r\beta}$=-0.7

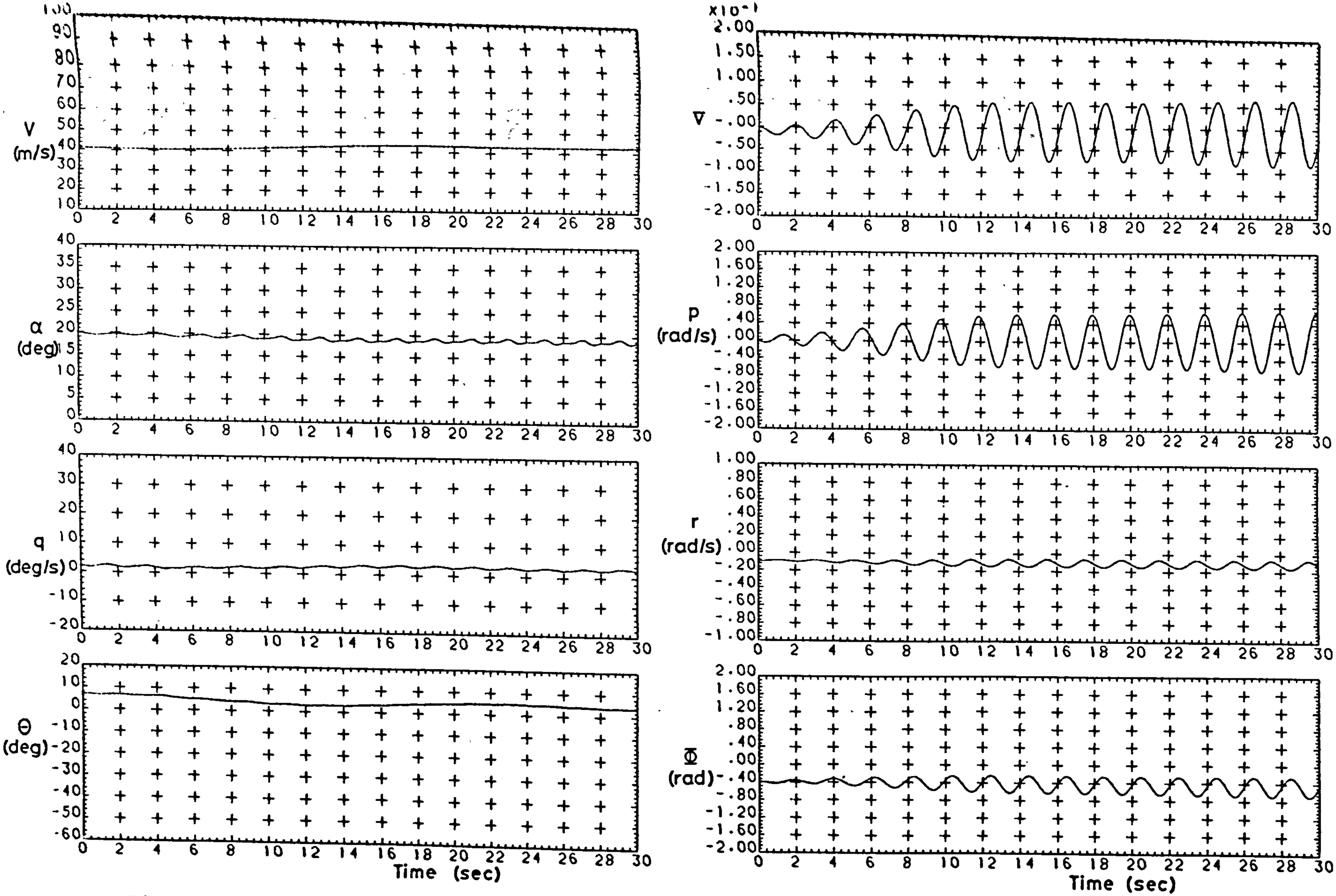

Fig 6.26 Turning flight, case 2 with rotary rig roll damping and cross-coupling derivatives

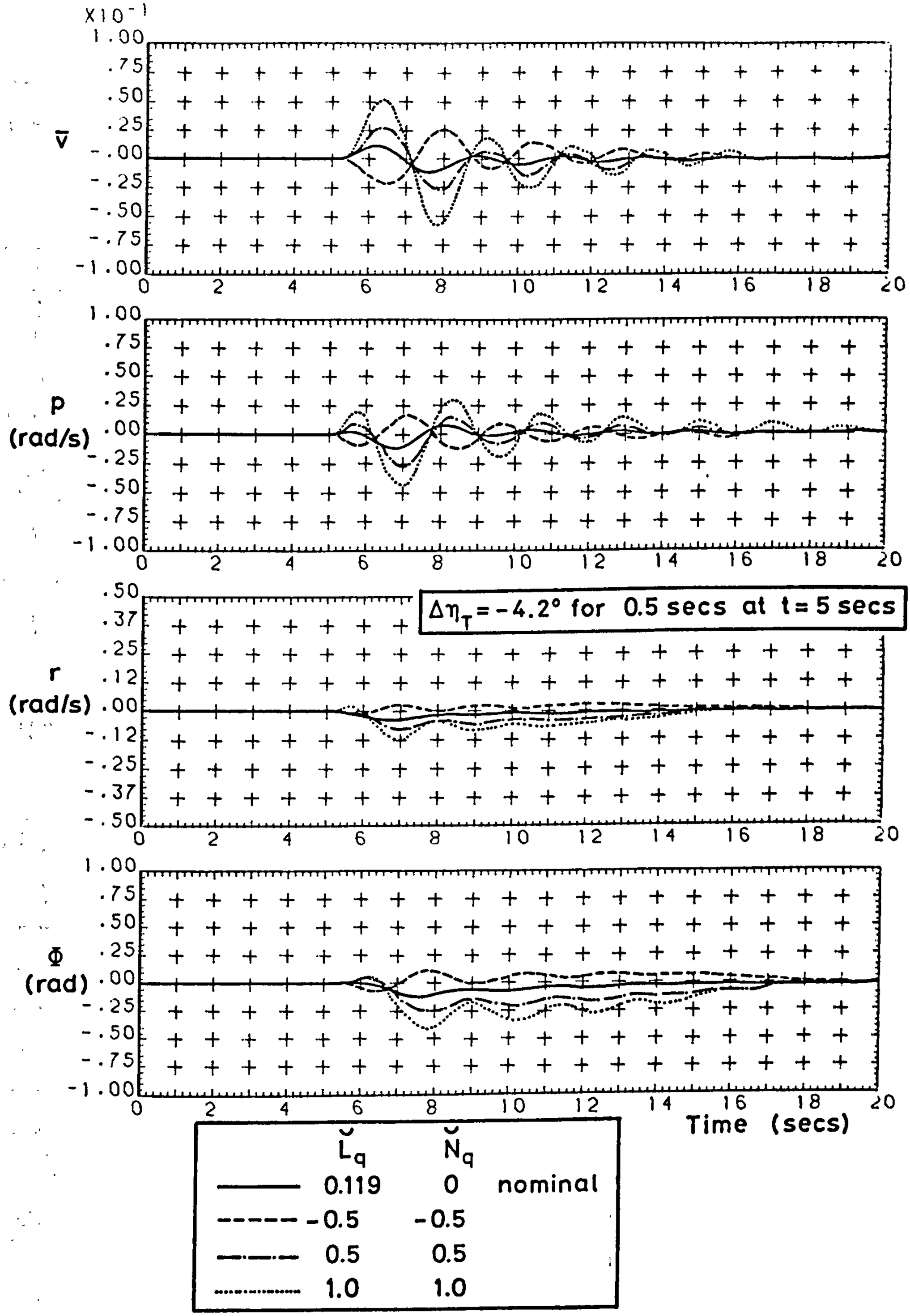

Fig 6.27 Sensitivity of lateral response, at α=18°, to tailplane pulse

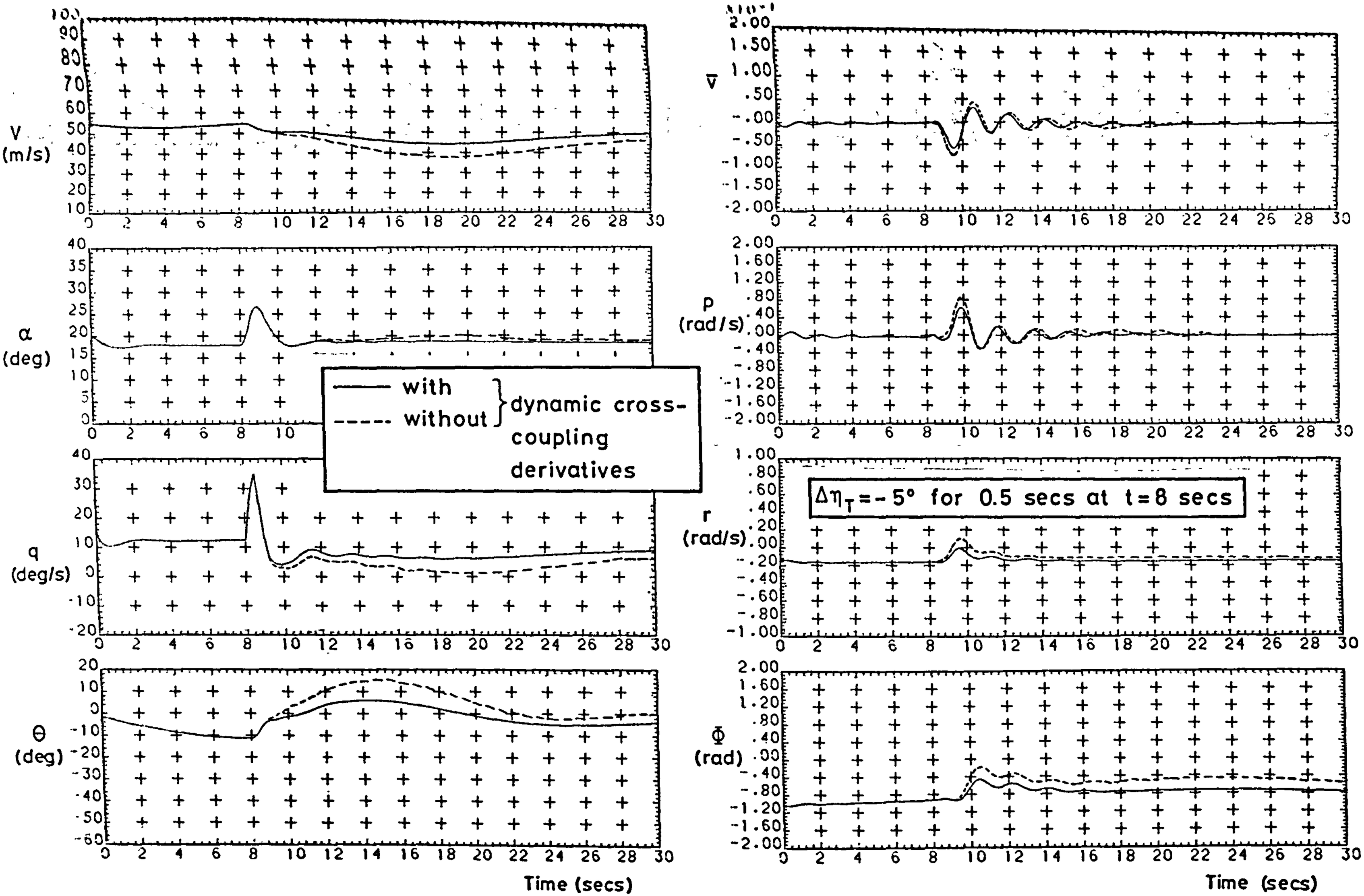

Fig 6.28 Effect of cross-coupling derivatives on stable response in a turn, case 2

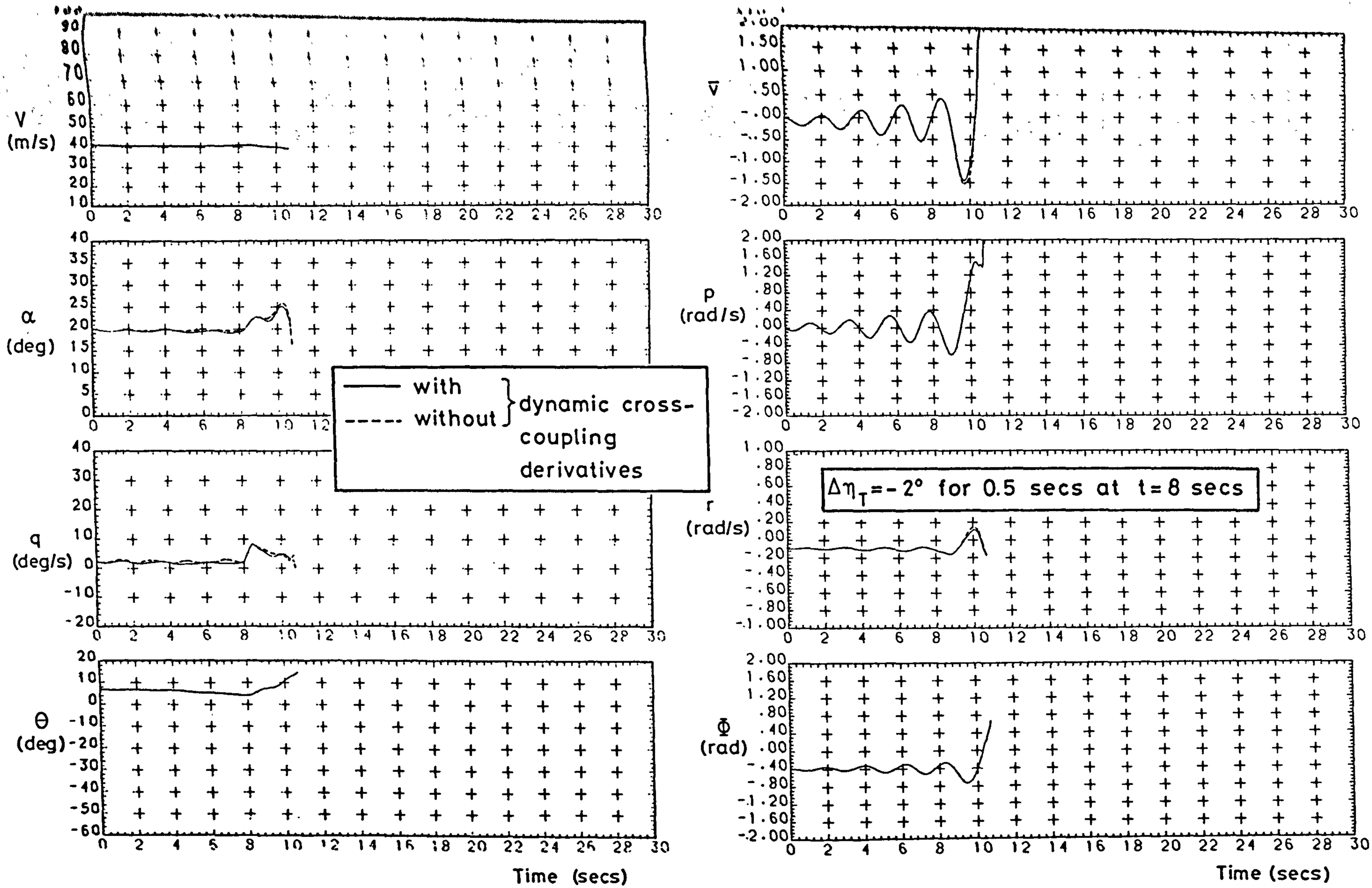

Fig 6.29 Effect of cross-coupling derivatives on response in a turn, case 2, with rotary rig roll damping

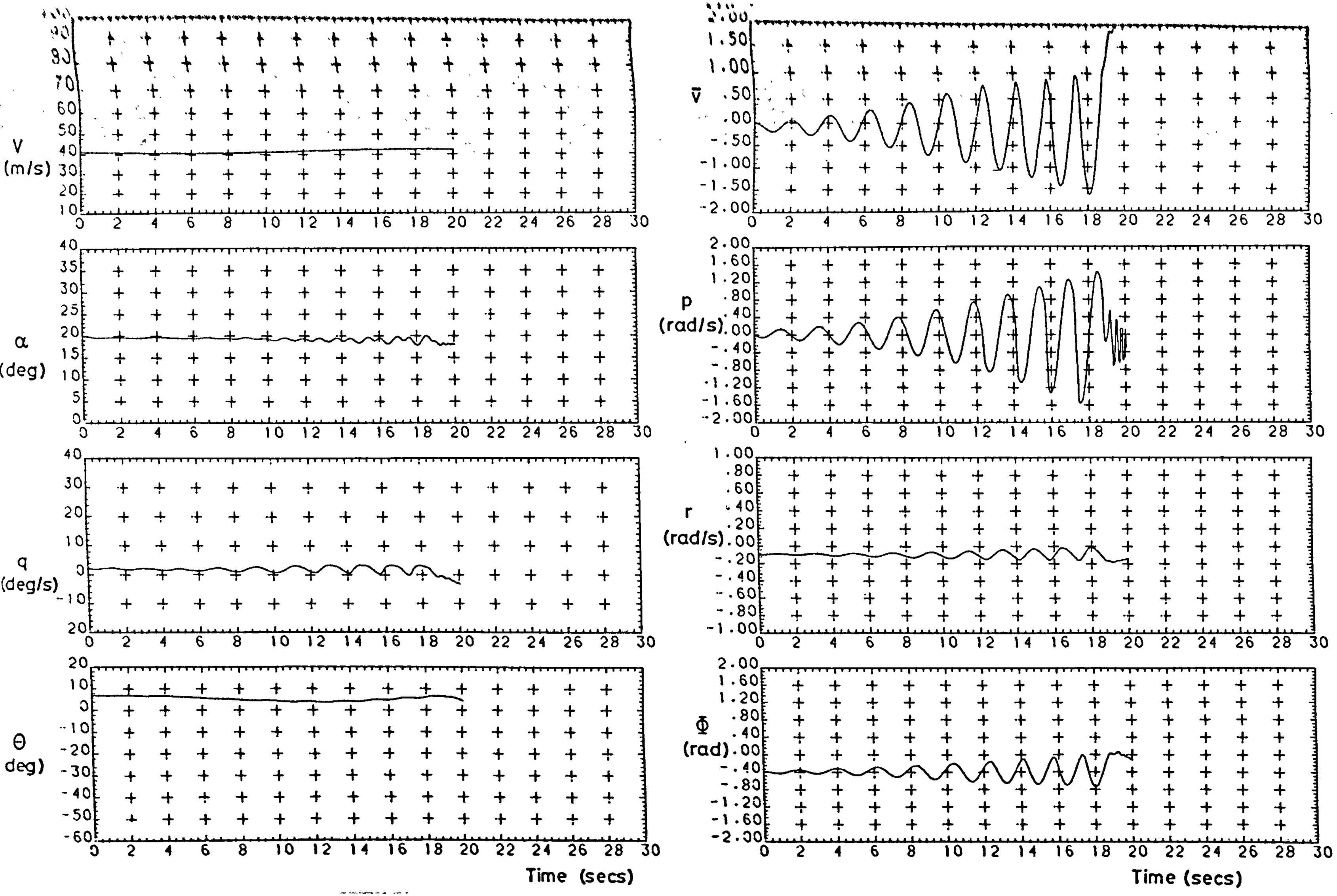

Fig 6.30 Turning flight, case 2 with rotary rig roll damping and no cross-coupling derivatives

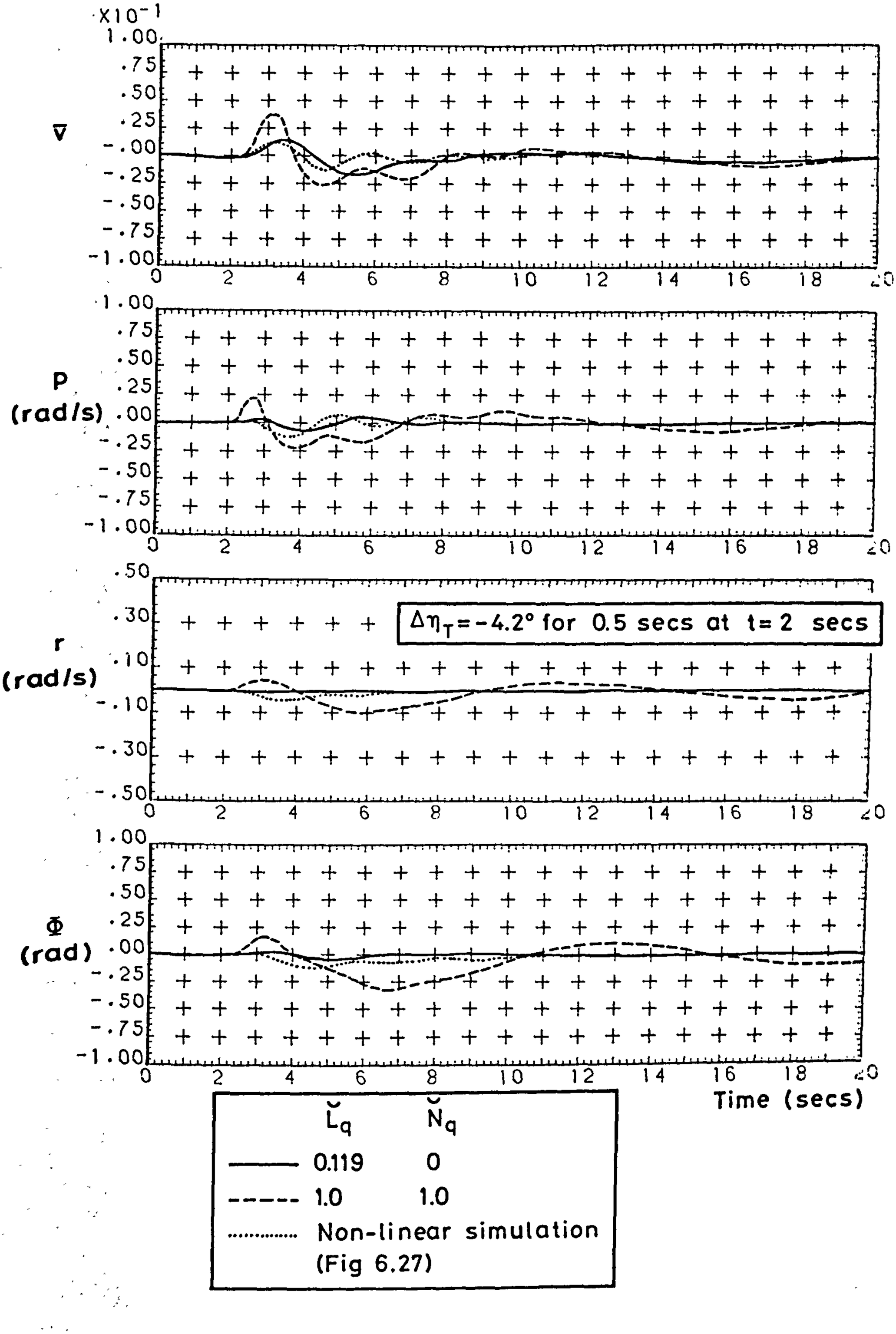

Fig 6.31 Sensitivity of linearised lateral response, at $\alpha = 18°$, to tailplane pulse

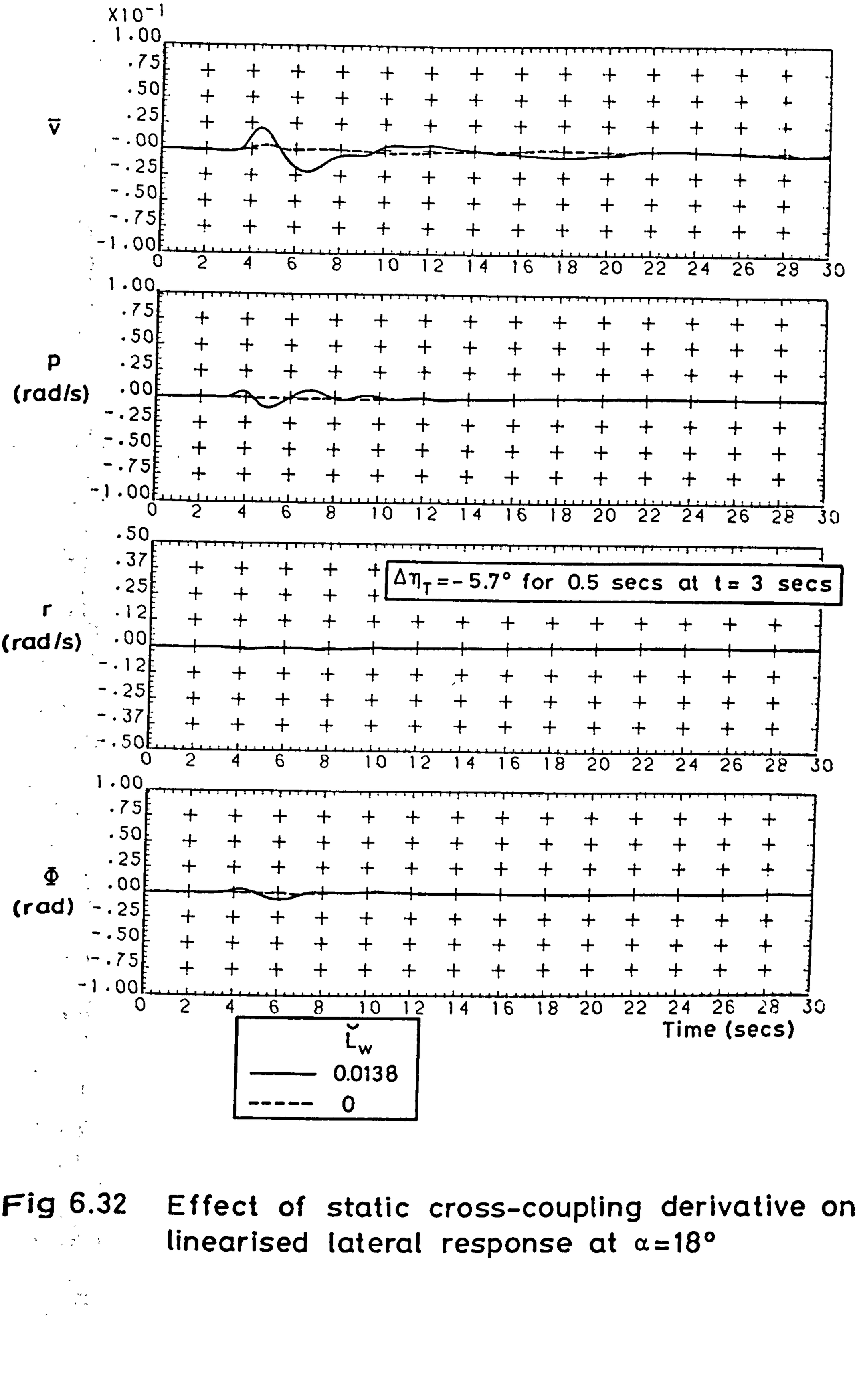

Fig 6.32 Effect of static cross-coupling derivative on linearised lateral response at $\alpha = 18°$

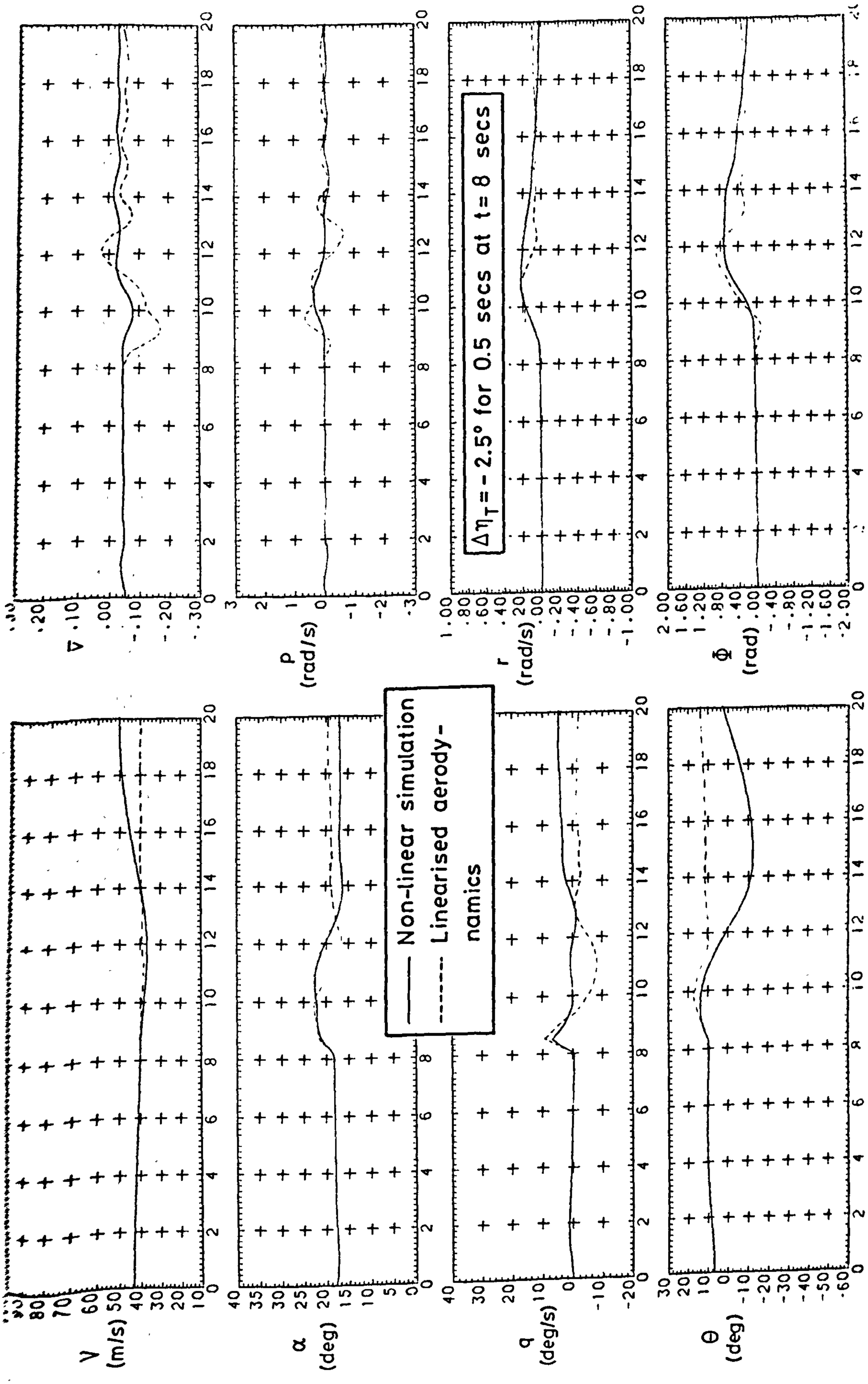

Fig 6.33 Comparison of responses in steady sideslip

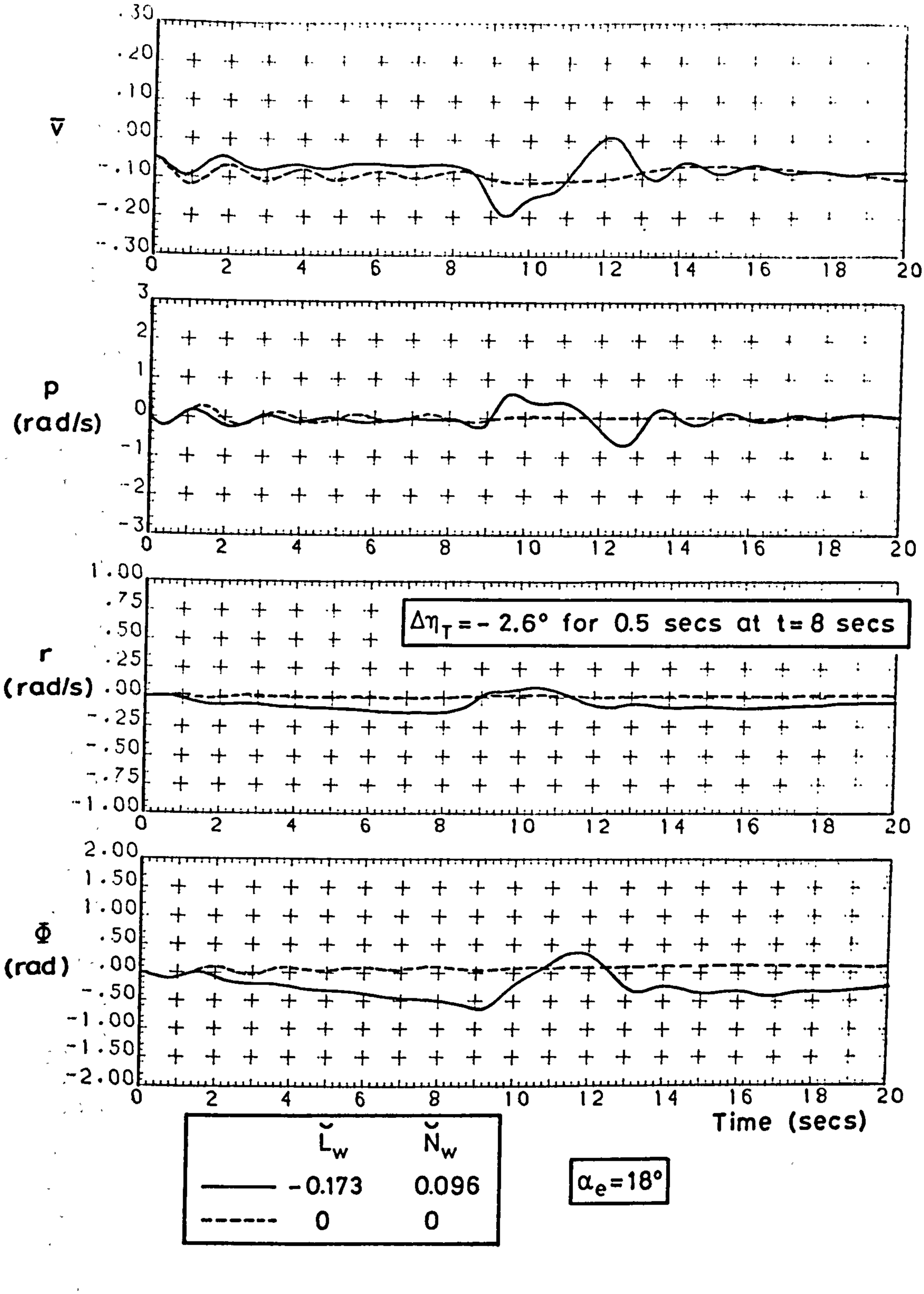

Fig 6.34 Effect of omitting static cross-coupling derivatives, on linearised lateral response in steady sideslip

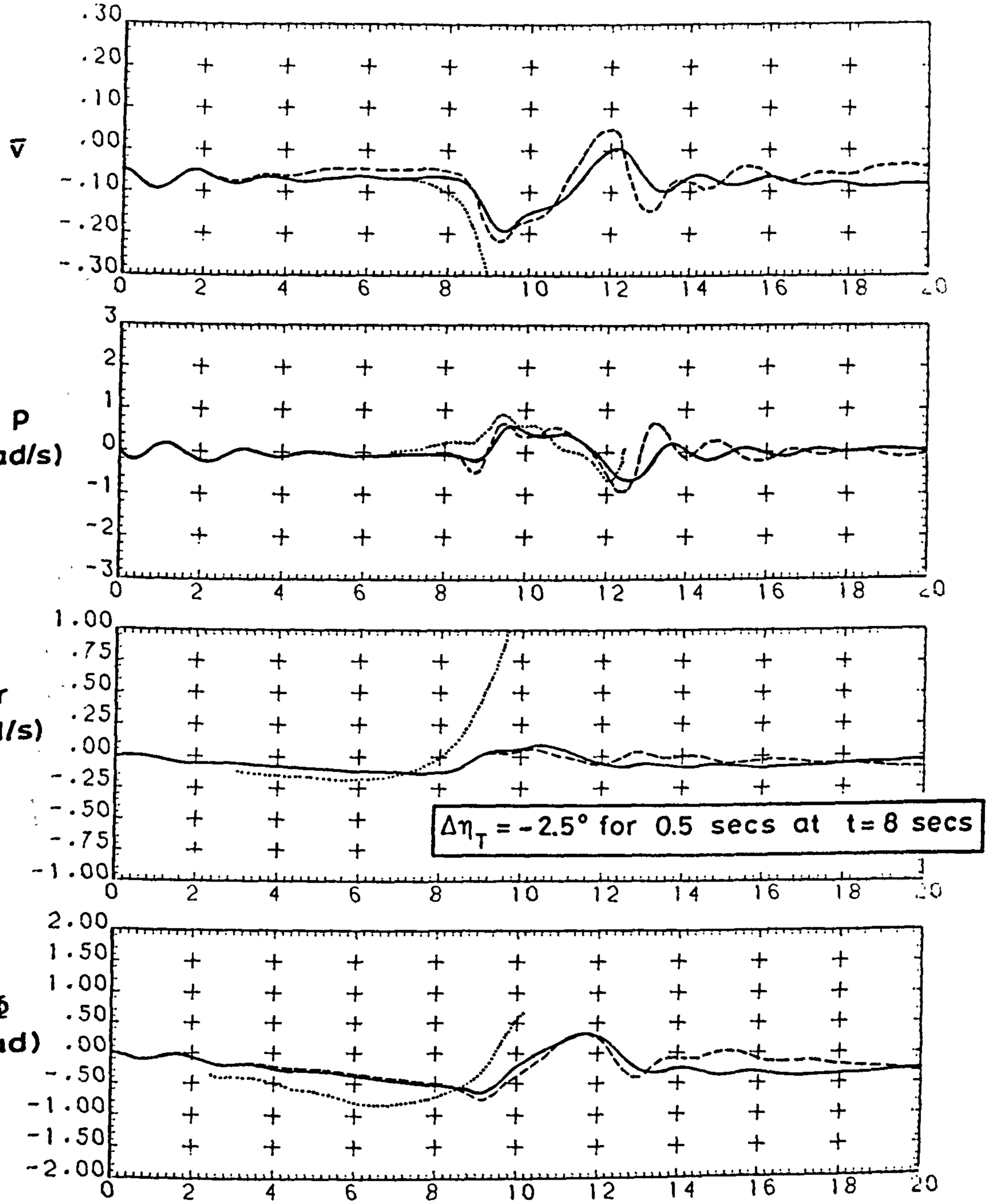

Fig 6.35 Effect of doubling static cross-coupling derivatives, on linearised lateral response in steady sideslip

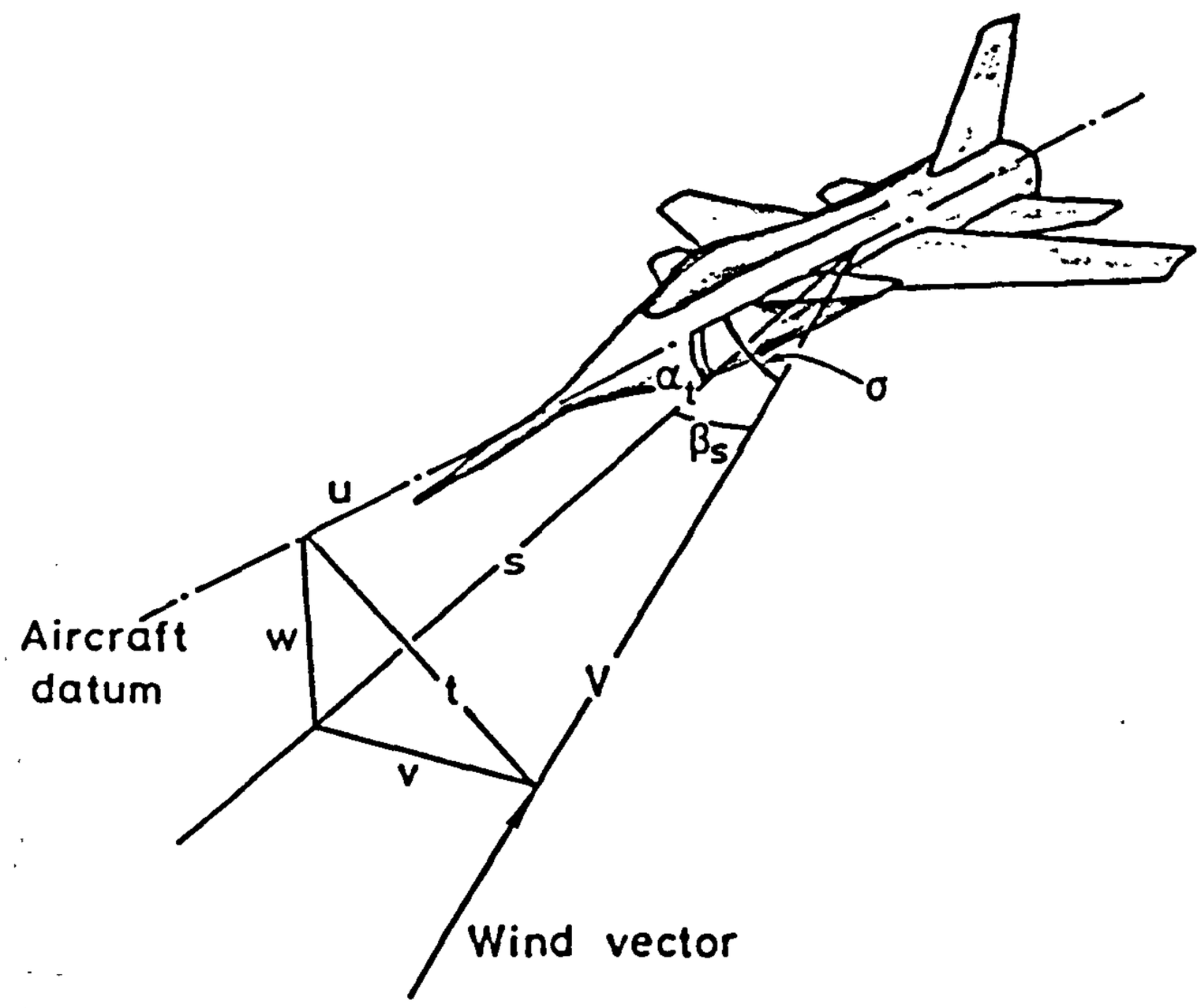

Fig F.1 Relationships between angles